46th Meeting of The Italian Section of The Combustion Institute

Towards Net-Zero Carbon Society

Bari

June 2-5, 2024

Book of Abstract

edited by

Sergio Mario Camporeale, Mario Commodo, Gianluigi De Falco, Christian Hasse, Davide Laera, Giancarlo Sorrentino, Antonio Tregrossi


THE COMBUSTION INSTITUTE
1954

46th Meeting of The Italian Section of The Combustion Institute

Towards Net-Zero Carbon Society

Book of Abstract

Bari
June 2-5, 2024

edited by
Sergio Mario Camporeale, Mario Commodo, Gianluigi De Falco, Christian Hasse, Davide Laera, Giancarlo Sorrentino, Antonio Tregrossi

46th Meeting of The Italian Section of The Combustion Institute
Book of Abstract
ISBN 978-88-88104-29-4
Editors:
Sergio Mario Camporeale, Mario Commodo, Gianluigi De Falco, Christian Hasse,
Davide Laera, Giancarlo Sorrentino, Antonio Tregrossi

ASICI - Associazione Sezione Italiana del Combustion Institute
P. Tecchio, 80, 80125 Napoli
Napoli, June, 2024

The Italian Section of The Combustion Institute
www.combustion-institute.it


THE COMBUSTION INSTITUTE
1954

46th Meeting of the Italian Section of the Combustion Institute
Towards Net-Zero Carbon Society

SUMMARY

PLENARY LECTURES

SESSION I: CARBON-FREE ENERGY CARRIERS: COMBUSTION FUNDAMENTALS

SESSION II: BIOMASS AND WASTE THERMOCHEMICAL PROCESSING, RECYCLING, AND VALORIZATION

SESSION III: CARBON-FREE ENERGY CARRIERS: COMBUSTION APPLICATIONS – PART 1

SESSION IV: LAMINAR AND TURBULENT COMBUSTION, INCLUDING IGNITION, COMBUSTION DYNAMICS AND DETONATION

SESSION V: CARBON-FREE ENERGY CARRIERS: COMBUSTION APPLICATIONS – PART 2

SESSION VI: SOOT, NANOMATERIALS SYNTHESIS, AND LARGE MOLECULES PRODUCTION

SESSION VII: PROPULSION & ENGINES

SESSION VIII: STATIONARY COMBUSTION SYSTEMS AND GAS TURBINES - PART 1

SESSION IX: NOVEL CONCEPTS AND CCUS INCLUDING MULTI-PHYSICS AND MULTI-PHASE PHENOMENA

SESSION X: STATIONARY COMBUSTION SYSTEMS AND GAS TURBINES - PART 2

SESSION XI: REACTION KINETICS

SESSION XII: EMISSION AND CONTAMINANTS MITIGATION, FORMATION AND MONITORING INCLUDING INCINERATION

WORK IN PROGRESS POSTERS


THE COMBUSTION INSTITUTE
1954

PLENARY LECTURES


THE COMBUSTION INSTITUTE
1954

Green metals as recyclable carriers of renewable energy – From global opportunities to combustion physics

Christian Hasse
Institute for the Simulation of Reactive Thermo-Fluid Systems - Darmstadt University of Technology

Abstract
The transformation to a net-zero carbon society is one of the most pressing challenges of our time. Green metal fuels, produced from metal oxides using renewable energy, are emerging as a carbon-free, high energy density replacement for fossil fuels due to their availability and recyclability. Iron in particular is a promising option for a carbon-free cycle since it is non-toxic, safe to transport, easy to store, abundant, and in principle can be recycled an unlimited number of times.

This plenary will deliver two key messages:
1. Metal fuels are a promising carrier of renewable energy for a net-zero carbon society.
2. While previous work on solid carbonaceous fuels provides an excellent starting point for studying metals as energy carriers, the physics of metal fuel combustion is quite different, fascinating, and largely unexplored.

In the first part, iron as a metal fuel is first introduced as a recyclable chemical energy carrier. During the reduction of iron oxides, energy from renewable sources such as wind, hydro, and solar is stored. This energy is released again through combustion and can be used as high-temperature process heat or for the generation of electricity. The product of this zero-CO2 combustion process is solid iron oxide, which can be collected for recycling. One promising application of metals is the retrofit of existing infrastructure. This is demonstrated with a thermodynamic system analysis for a coal-fired power plant to be operated with iron powder in the future. This is followed by a techno-economic analysis, for which different partner countries for reduction and oxidation are considered. Hydrogen and iron are compared as energy carriers on the basis of round-trip efficiency and levelized cost of electricity.
In the second part, selected experimental and numerical results on the combustion physics of iron are presented. First, the oxidation of single iron particles is showcased, and the different phases of ignition and combustion are discussed with a special focus on the coupling of gas phase transport with the condensed phase kinetics. Next, canonical polydisperse iron-air flames, from which typical combustion characteristics such as the reaction front speed can be deduced, are discussed. Going towards multidimensional flames, experimental and numerical results for a laminar self-sustained Bunsen-type jet flames are presented. The

reaction zone structure and the reaction front speed are analyzed. The need for well-controlled and well-characterized experimental conditions to reduce uncertainties is demonstrated by comparison to simulation results. Finally, results for turbulent iron-air flames are presented.

Selected references part 1:

Debiagi, P., Rocha, R.C., Scholtissek, A., Janicka, J., Hasse, C.: Iron as a sustainable chemical carrier of renewable energy: Analysis of opportunities and challenges for retrofitting coal-fired power plants, Renewable and Sustainable Energy Reviews, 165:112579, DOI:10.1016/j.rser.2022.112579, 2022.

Neumann, J., da Rocha, R., Debiagi, P., Scholtissek, A., Dammel, F., Stephan, P., Hasse, C.: Techno-economic assessment of long-distance supply chains of energy carriers: Comparing hydrogen and iron for carbon-free electricity generation, Applications in Energy Combustion Science, 14:100128, DOI:10.1016/j.jaecs.2023.100128, 2023.

Janicka, J., Debiagi, P., Scholtissek, A., Dreizler, A., Epple, B., Pawellek, R., Maltsev, A., Hasse, C.: The potential of retrofitting existing coal power plants: a case study for operation with green iron, Applied Energy, 339:129050, DOI:10.1016/j.apenergy.2023.120950 (preprint 10.48550/arXiv.2303.04000), 2023.

Selected references part 2:

Li, T., Heck, F., Reinuauer, F., Böhm, B., Dreizler, A.: Visualizing particle melting and nanoparticle formation during single iron particle oxidation with multi-parameter optical diagnostics, Combustion and Flame, 245:112357, DOI: 10.1016/j.combustflame.2022.112357, 2022.

Mich, J., Braig, D., Gustmann, D., Hasse, C., Scholtissek, A.: A comparison of mechanistic models for the combustion of iron microparticles and their application to polydisperse iron-air suspensions, Combustion and Flame, 256:112949, DOI: 10.1016/j.combustflame.2023.112949, 2023.

Wen, X., Scholtissek, A., van Oijen, J., Bergthorson, J., Hasse, C.: Numerical modeling of pulverized iron flames in a multidimensional hot counterflow burner, Combustion and Flame, 248:112572, DOI:10.1016/j.combustflame.2022.112572, 2023.

Luu, T. D. Shamooni, A., Kronenburg, A., Braig, D., Mich, J., Nguyen, B.-D., Scholtissek, A., Hasse, C., Thäter, G., Carbone, M., Frohnapfel, B., Stein, O.T.: Carrier-phase DNS of ignition and combustion of iron particles in a turbulent mixing layer, Flow, Turbulence and Combustion, online first, DOI: 10.1007/s10494-023-00526-y, 2024.

Vance, F., Scholtissek, A., Nicolai, H., Hasse, C.: Flame propagation modes for iron particle clusters in air – Part I: transition from continuous to discrete propagation mode under weak convection effects, Combustion and Flame, 260:113265, DOI:10.1016/j.combustflame.2023.113265, 2024.

Vance, F., Scholtissek, A., Nicolai, H., Hasse, C.: Flame propagation modes for iron particle clusters in air -- Part II: transition from continuous to discrete propagation mode under strong convection effects, Combustion and Flame, online first, DOI:10.1016/j.combustflame.2023.113199, 2024.

Ammonia, the 'other' hydrogen for clean ICE

Christine Mounaïm-Rousselle
Laboratoire PRISME - University of Orléans

Abstract

The objective to reach neutral carbon footprint in 2050 accelerates the energy transition. Industries and scientists collaborate for developing zero CO_2 emission solutions for all energy sectors: power, transport and industry. Hydrogen and hydrogen derived fuels, 'e-fuels' will play an important role. Ammonia, one of the simplest electro fuels, is a promising candidate as energy and hydrogen carrier, but it can also be used directly as a zero-carbon fuel, pure or mixed with hydrogen or biofuels. However, the combustion properties of ammonia are far from those of conventional fuels and are still not well known especially for engine relevant conditions. During this talk, the state of art of ammonia combustion in internal combustion engines will be presented with focus on the remaining challenges.

The dual role of Carbon in the energy transition

Matteo Maestri
Department of Energy - Politecnico di Milano

Abstract
The pressing issue of global warming is widely acknowledged to stem from our current energy scenario, which has led to the release of tremendous amounts of CO_2 from the burning of fossil fuels and the extraction of metals for material production, resulting in excessive CO_2 concentrations in the atmosphere. To address this issue and achieve a neutral carbon footprint by 2050, rebalancing CO_2 levels in the atmosphere is crucial. Carbon can play a decisive role in achieving this goal by fulfilling a dual role: (i) developing valorisation routes of CO_2 and biomass to useful molecules and (ii) using carbon as a material rather than a fuel. In this talk, I will showcase two examples of this dual role of Carbon in the energy transition, such as the operando-Raman kinetic analysis of surface carbon formation during methane dry reforming and the multiscale analysis of the synthesis carbon nanotubes from methane at large scale.


THE COMBUSTION INSTITUTE
1954

SESSION I

Carbon-free energy carriers: Combustion fundamentals


THE COMBUSTION INSTITUTE
1954

Hydrogen combustion: mixture rules and rate constants. A case study on the multicomponent pressure dependence of $H+O_2+M=HO_2+M$

M. Primi, T. Dinelli, M. Lea Casagrande, L. Pratali Maffei, A. Cuoci, M. Pelucchi, C. Cavallotti
matteo.primi@polimi.it
*Dept. Chemistry, Materials, and Chemical Engineering, Politecnico di Milano
Piazza Leonardo da Vinci, 32, Milano, Italy

Abstract
Hydrogen combustion has recently been the subject of considerable interest because of its perspective use as energy vector. It has though been shown that the mixture rules used to determine rate constants of termolecular reactions currently implemented in most kinetic simulation software are physically inconsistent when used in the fall-off regime. Also, there is considerable uncertainty in the dependence on the bath gas of the rate constants of some key termolecular reactions. In this context, we developed an approach to study hydrogen reactivity whose final aim is the full a priori revision of the elementary kinetics of hydrogen combustion chemistry. Specifically, we present an efficient and accurate implementation of a method for determining the rate constants of termolecular reactions, we apply it to the study of the $H+O_2+M \rightarrow HO_2+M$ reaction both for single and multiple colliders, and we investigate its impact on kinetic simulations. First, the contribution of intermolecular energy transfer to the reactive process is determined using a 1D master equation model with the collisional kernel described using the single exponential energy transfer model and recombination fluxes computed using Variable Reaction Coordinate Transition State Theory. The energy transfer parameters of the collisional model are then fitted for several colliders (Ar, He, N_2, H_2, CO_2, H_2O) through regression over a large set of experimental rate constants, by interfacing the master equation simulator MESS to a non-linear regression software. Finally, a physically consistent mixture model is implemented for the first time in a kinetic simulator, the OpenSmoke software, and kinetic simulations are performed to study model performances. The simulation results show that the impact of the new sets of rate constants so determined can be significant in some combustion environments.

Introduction
In the last decades, the use of hydrogen has gained significant interest for replacing traditional carbon-based fuels either alone, mixed with CO, CO_2, and H_2O, or as a primary component of synthetic gas. It is particularly suitable for high-temperature, energy-intensive industrial processes [1], as well as for the decarbonization of

heavy/long-distance transport [2]. Furthermore, blending hydrogen with natural gas for household heating and distributing it through existing pipeline systems is already a viable option [3]. However, the utilization of hydrogen blends in commercial applications has been limited due to several technical challenges, which include blowout, flashback, autoignition, combustion dynamics, and environmental impact.
A great accuracy in describing hydrogen reactivity is the first fundamental step in overcoming these challenges. Currently, two main issues limit the accuracy of hydrogen kinetics in systems with a high number of pressure-dependent termolecular reactions, as it happens in atmospheric and combustion chemistry. Firstly, within existing kinetic mechanisms, termolecular reactions are expressed as a function of a reference reaction with a specific collider (usually Argon), and the rates with other colliders are obtained by means of corrective parameters, the third body efficiencies. However, these parameters are often determined through fitting of complex sets of data, with the consequence that they can vary substantially even between similar kinetic mechanisms, leading to non-unambiguous results. Secondly, Burke [4] has demonstrated that the mixture rules used to determine rate constants currently implemented in most kinetic simulation software are physically inconsistent when used in the fall-off regime.
This work aims to develop an efficient and accurate approach to be used to address these methodological shortcomings. Reporting the case study of $H+O_2+M \rightarrow HO_2+M$ reaction, the proposed method has been applied to determine the rate constants of termolecular reactions, both for single and multiple colliders, and its impact has been evaluated through kinetic simulations.

Methods

The proposed approach is implemented in two separate and consecutive steps, as shown in Figure 1. The first has the purpose of determining accurately the energy transfer parameters of different colliders and consequently the rate constant in the presence of a single bath gas. In the second one, the rate constants so determined are used to estimate mixture dependent rate parameters using for this purpose the physically consistent mixture rules proposed by Burke et al. [5] to properly describe multicollider systems.
In the first step of this approach, high pressure rate constants are determined using the ab initio transition state theory based master equation approach (AI-TST-ME) as implemented in EStokTP [6]. In particular, the rate constant for the $H+O_2$ recombination reaction is determined using Variable Reaction Coordinate Transition State Theory (VRC-TST) determining energies as a function of the transitional coordinates at the CASPT2 level using a cc-pVDZ basis set and a full valance active space. The interaction potential was corrected for geometry relaxation and basis set effects.

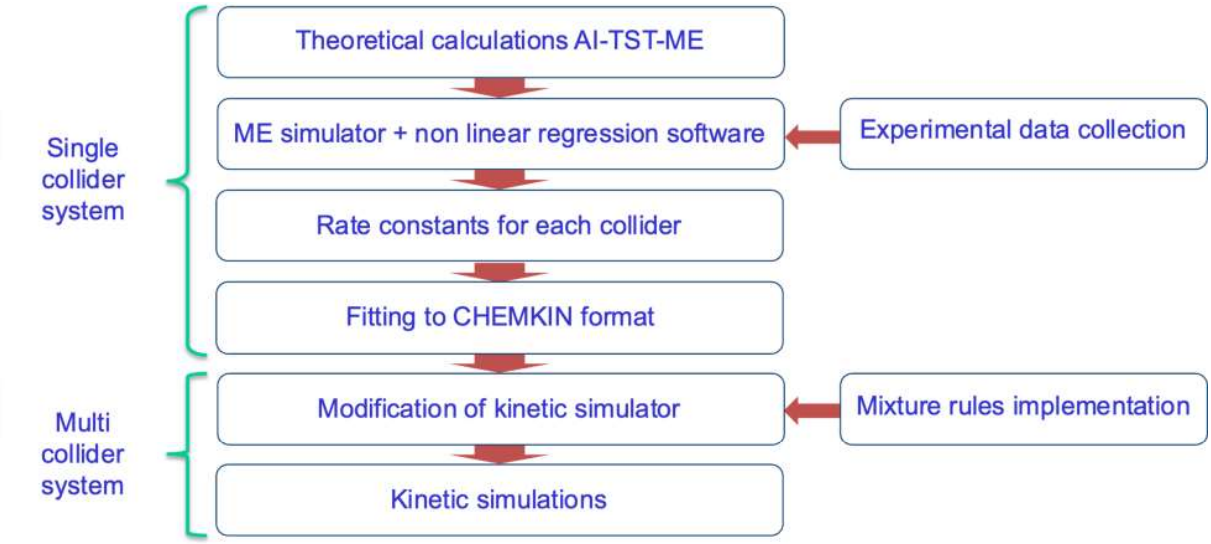

Figure 1. Method conceptual scheme

Afterward, a 1D master equation model was used with the collisional kernel described using the single exponential energy transfer model and recombination fluxes computed using VRC-TST. The master equation used in this work has the following expression:

$$\frac{dn(E)}{dt} = \sum_{i=1}^{M} Z_i[M_i] \sum_{E^I=0}^{\infty} \left(P_i(E,E^I)n(E^I) - P_i(E^I,E)\cdot n(E)\right) - k(E)n(E) \qquad (1)$$

where the subscript i refers to the ith component of the mixture, Z_i is the collision frequency between the reactant and the third body M_i, whose concentration is indicated as $[M_i]$, while *k(E)* is the microcanonical decomposition rate constant of the reactant with energy E. Finally, $P_i(E,E^I)$, also known as collisional kernel, represents the probability that a reactant with energy E^Imoves to energy E due to a collision with an ith mixture component. In this work, the single exponential energy transfer model is exploited and is expressed as:

$$P_i(E,E^I) = \frac{1}{N(E^I)} e^{\left(-\frac{E^I-E}{\alpha_i}\right)} \quad E \le E^I \qquad (2)$$

Where $N(E^I)$ is a normalization constant so that the integral of P_i over all energy states is equal to 1 and α_i is the average energy transferred per down collision. The last one is a semi-empirical parameter that depends on the collider, expressed as:

$$\alpha_i = \alpha_0 \left(\frac{T}{298\,K}\right)^n (E \le E^I)\,, \qquad (3)$$

where α_0 and n are parameters that must be defined for each investigated collider. For this purpose, a regression over more than 500 experimental data has been performed by coupling the master equation solver MESS [7] with a non linear regression software. Eight possible species (Ar, N_2, H_2, CO_2, H_2O, O_2, He, Kr) were investigated as bath gas, representing an exhaustive list of strong and weak colliders.

Once the energy transfer parameters have been determined, rate constants for each individual collider were calculated at pressures up to 100 bar and at temperatures between 300 and 2500 K. Then, the rate constants were fitted and expressed in the modified Arrhenius form that is suitable for implementation in kinetic mechanisms that use the ChemKin format, as is the case for OpenSMOKE++ [8]. For the sake of simplicity, pressure dependence is accounted for using the PLOG ChemKin format, though other methods have been implemented in OpenSMOKE++.
Finally, the linear mixture rule algorithm proposed by Burke et al. [5] was implemented in OpenSMOKE++. This algorithm can briefly be explained as follows: first the reduced pressure, defined as the ratio between the low and high-pressure limit rate constants multiplied by the total concentration is determined and used as a quantitative measure of the width of the falloff regime. Then, the contributions of each collider to the rate constant are estimated at the same reduced pressure rather than absolute pressure as in traditional linear mixture rules. Therefore, rate constants for weak and strong colliders are more similar than values evaluated at the absolute pressure. Finally, the rate constant is determined as a linear sum of the rate constants of each component at the same reduced pressure weighted by their fractional contributions to the reduced pressure [5].
To test the impact of the implemented approach, some kinetic simulations were performed inserting the $H+O_2+M \rightarrow HO_2+M$ rate constant calculated with the systematic approach described above in the CRECK hydrogen mechanism and simulating hydrogen laminar flame speeds.

Results and discussion

The energy transfer parameters obtained from the regressions are reported in Table 1. The total number of rate constants used for the regression is 130 for Ar, taken from six different works, and measured between 298 to 2053 K and at pressures comprised between 0.01 and 950 bar. Differently, 15 works were considered for N_2, collecting 134 experimental rate constants between 298-1908 K and 26 Torr and 950 bar. Regarding H_2O, regression was performed on 84 rate constants from six works, measured between 298 and 1375 K and at pressures from 0.03 and 45 bar. The 39 rate constants used for the regression for O_2 were measured at 0.009-0.04 bar and from 298 to 700 K, whereas 4 experimental data sets were considered for CO_2, consisting of 26 rate constants measured at 1-17 bar from 800 to 1300 K. Concerning H_2, the regression was performed on 23 rate constants measured at 298 K and from 0.09 to 0.8 bar. The data used for Kr are also at room temperature but were measured between 0.09 and 0.16 bar. Lastly, 105 rate constants from 6 works were used for the regression concerning He, with experimental data measured between 298 and 700 K and at pressures from 0.005 to 900 bar. All regressions performed have a correlation index higher than 0.95, which was considered as the minimum acceptable value. Regressions over CO_2 and H_2 have the lowest correlation index, respectively 0.957 and 0.966. It is assumed that this is mainly related to the limited temperature and pressure ranges in which experimental measurements are available. To the best

of our knowledge, we have found in the literature only one other estimate of the collision parameters of these colliders for this reaction [9], which are found to be in reasonable agreement with those determined in this work.

Table 1. Energy transfer parameters calculated for different colliders and correlation index of the regression.

Collider	α_0	n	Correlation index
Ar	33.3	1.048	0.985
He	27.4	1.005	0.990
N_2	49.0	0.927	0.988
O_2	36.6	0.952	0.996
H_2	36.4	0.943	0.966
CO_2	52.5	1.493	0.957
H_2O	158.1	1.394	0.978
Kr	30.9	1.000	0.974

The rate constant in the CRECK Syngas (H_2/CO) mechanism (version 2003, March 2020) [10][11],[12] were updated with new values determined for the $H+O_2+M \rightarrow HO_2+M$ rate constant and used to simulate the laminar flame speeds measured by Sun and Li [13] in hydrogen-air mixtures. It was found that the flame speed is lowered with the updated model, which leads to a better agreement with the experimental data. The main impact of the updated rates is found in the operating conditions where the system is sensitive to the $H+O_2+M \rightarrow HO_2+M$ reaction, thus at pressures of 1-2 bar and temperatures below 1000 K.

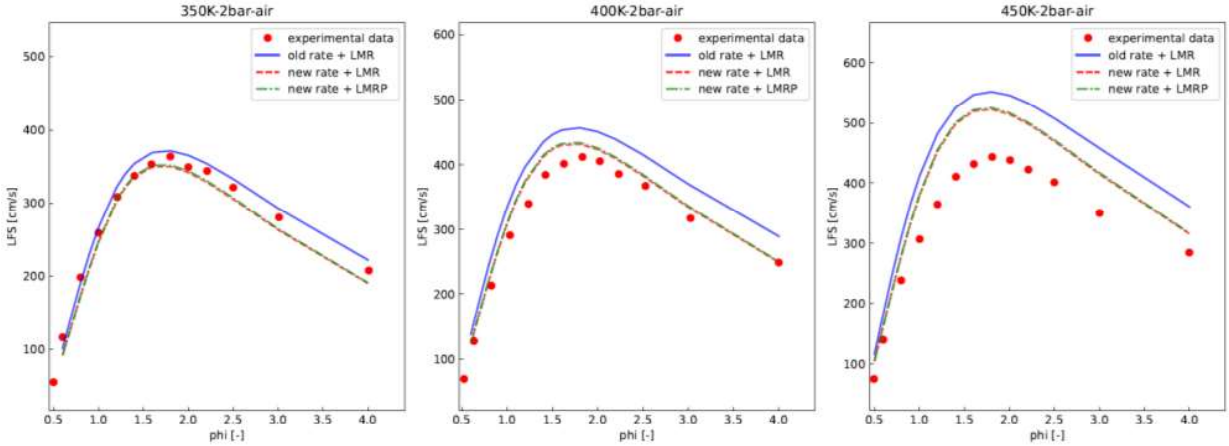

Figure 2. Comparison between LFS predicted using the updated and reference CRECK syngas models with experimental data [13]

Conclusions

Effective collisional parameters and proper dependence of rate constant from mixture composition were determined using a new approach for the $H+O_2$ reaction. Their inclusion in kinetic simulations allowed to improve the agreement with experimental data for what concerns laminar flame speed in some combustion

environments. Future developments include the extension of the new method to other key termolecular reactions in hydrogen combustion and the investigation of mixtures formed by both weak and strong colliders.

References

[1] A. Bhaskar, M. Assadi, H.Nikpey Somehsaraei, "Decarbonization of the Iron and Steel Industry with Direct Reduction of Iron Ore with Green Hydrogen", *Energies.* 13, 758 (2020)

[2] S. Li, N. Djilali, M.A. Rosen, C. Crawford, P. Sui, "Transition of heavy-duty trucks from diesel to hydrogen fuel cells: Opportunities, challenges, and recommendations", *Int. J. Energy Res*. 46, 11718-11729 (2022)

[3] C. Baldino, J. O'Malley, S. Searle, Y. Zhou, A. Christensen, "Hydrogen for heating? Decarbonization options for households in the United Kingdom in 2050", *International Council on Clean Transportation* (2020)

[4] M. P. Burke, R. Song, "Evaluating mixture rules for multi-component pressure dependence: $H+O_2(+M)\rightarrow HO_2(+M)$", *Proc. Combust. Inst.* 36, 245 (2017)

[5] L. Lei, M. P. Burke, "Bath gas mixture effects on multichannel reactions: insights and representations for systems beyond single-channel reactions", *J. Phys. Chem. A* 123, 631-649 (2019)

[6] C. Cavallotti, M. Pelucchi, Y. Georgievskii, S. J. Klippenstein. "EstokTP: electronic structure to temperature- and pressure- dependent rate constants – a code for automatically predicting the thermal kinetics of reactions" *J. Chem. Theory Comput*. 15, 1122-1145 (2019)

[7] Y. Georgievskii, J. A. Miller, M. P. Burke, S. J. Klippenstein, "Reformulation and solution of the master equation for multiple-well chemical reactions" *J. Phys. Chem. A* 117, 12146-12154 (2013)

[8] A. Cuoci, A. Frassoldati, T. Faravelli, E. Ranzi, "OpenSMOKE++: an object-oriented framework for the numerical modeling of reactive systems with detailed kinetic mechanisms" *Comput. Phys. Commun.* 192, 237-264 (2015)

[9] J. V. Michael, M.-C. Su, J. W. Sutherland, J. J. Carroll, A. F. Wagner, "Rate constants for $H+O_2+M\rightarrow HO_2+M$ in seven bath gases" *J. Phys. Chem. A* 106, 5297-5313 (2002)

[10] E. Ranzi, A. Frassoldati, A. Stagni, M. Pelucchi, A. Cuoci, T. Faravelli, "Reduced kinetic schemes of complex reaction systems: Fossil and biomass-derived transportation fuels" *Int. J. Chem. Kinet.* 46 (9), 512-542 (2014)

[11] E. Ranzi, C. Cavallotti, A. Cuoci, A. Frassoldati, M. Pelucchi, T. Faravelli, "New reaction classes in the kinetic modeling of low temperature oxidation of n-alkanes", *Combustion and Flame* 162 (5), 1679-1691 (2015)

[12] E. Ranzi, A. Frassoldati, R. Grana, A. Cuoci, T. Faravelli, A. P. Kelley, C. K. Law, "Hierarchical and comparative kinetic modeling of laminar flame speeds of hydrocarbon and oxygenated fuels", *Progress in Energy and Combustion Science* 38 (4), 468-501 (2012)

[13] Z. Sun, G. Li, "Propagation characteristics of laminar spherical flames within homogeneous hydrogen-air mixtures", *Energy* 116, 116-127 (2016)

A-priori analysis of the flame structure in thermodiffusively unstable NH3/H2/air mixtures

F. D'Alessio *, S. Bottari*, P. E. Lapenna*, F. Creta*
francesco.dalessio@uniroma1.it
*Mechanical and Aerospace Engineering, Sapienza University of Rome, Via Eudossiana 18, Rome, 00186, Italy

Abstract
In this investigation, we adopt a data-driven approach utilizing Direct Numerical Simulation (DNS) data from thermodiffusively unstable NH3/H2-Air mixtures to define progress variables, thereby addressing flame dimensionality concerns. Irreducible error analysis highlights the necessity of incorporating at least three progress variables for a comprehensive depiction of hydrogen-enriched ammonia flames. While two-dimensional models suffice for accurately representing temperature, three-dimensional models are essential for effectively reproducing NO dynamics. Additionally, our investigation of Artificial Neural Network (ANN) models reveals their ability to faithfully replicate DNS data when trained on a subset of that data. However, their performance markedly declines when exclusively trained on a dataset comprising unstretched 1D freely propagating flames. This suggests the critical importance of expanding datasets, particularly by incorporating stretched flames, to bolster the ANN model's capacity.

Introduction
Ammonia (NH3) is a promising energy carrier due to its high volumetric concentration of hydrogen (H2), making it efficient for energy storage and transportation. Its clean-burning nature with zero-carbon emissions has garnered attention as a potential solution to environmental concerns linked with fossil fuels [1]. However, challenges exist for its direct utilization as a fuel, notably its low reactivity and the production of nitrogen oxides (NOx) during combustion, particularly in stationary gas turbines. Strategies like blending with hydrogen or partial cracking aim to enhance reactivity [2], while adopting lean premixed combustion can minimize pollutant emissions.
The efficacy of these strategies depends on factors such as fuel mixture composition and combustion conditions. For instance, the effective Lewis number Le_{eff} of NH3/H2 blends is critical, influencing flame stability and combustion characteristics, particularly in lean mixtures where Le_{eff} falls below a critical threshold Le_0 [3]. Under such conditions, intrinsic flame instabilities (IFI) may occur, affecting various flame features, heat release rates, morphology, propagation, and pollutant formation [4]. These instabilities are governed by two mechanisms: the destabilizing hydrodynamic (Darrieus-Landau, DL) mechanism and the

stabilizing/destabilizing thermal-diffusive (TD) mechanism, driven by local imbalances between thermal conductivity and molecular diffusivity of the controlling reactant [5]. Addressing the flame dimensionality issue is crucial for understanding and modeling these complex combustion processes. One method involves using tabulated chemistry, assuming all relevant chemical properties lie on a low-dimensional manifold (LDM) described by a limited number of transported scalars $\Psi = \psi(C_1, C_2, \ldots, C_n)$. It has been shown that at least two-dimensional LDM is needed to accurately reproduce the non linearities and the fluctuations generated form the IFIs in pure hydrogen premixed flames [6], and many investigations have been carried out that proposed different parametrization. Lapenna et al. [7] proposed a representation in terms of non-dimensional temperature Θ and mass fraction of the deficient reactant Y_{H2} using a simplified irreversible one-step chemistry formulation, while Regele et al. [8] proposed a LDM based on the normalized water vapor mass fraction $Y_{H2O}$and a mixture fraction Z.

In this study, we employ a data-driven methodology using Direct Numerical Simulation (DNS) data from thermodiffusively unstable NH3/H2-Air mixtures. Our goal is to identify relevant "data-driven" Progress Variables by applying Singular Value Decomposition (SVD) to matrices containing chemical species data from DNS or 1D datasets generated using Cantera [9]. Through SVD, we derive Progress Variables that capture correlations within the chemical composition space. These variables are used to reproduce target observables from a DNS dataset, with differences analyzed among various reproduction methodologies. Specifically, Progress Variable definitions extracted via SVD from the training dataset are applied to the testing DNS dataset. Our results show that a model directly trained on DNS data outperforms one trained on a 1D dataset in replicating the DNS dataset. Additionally, through irreducible error analysis, we demonstrate that a minimum of three Progress Variables are needed for a comprehensive description of a hydrogen-enriched ammonia flame and for accurately reconstructing its structural characteristics.

Data and Methods

To evaluate the Low-Dimensional Manifold (LDM) dimension for ammonia/hydrogen mixtures, we utilize two distinct datasets. Firstly, we employ the AH1s DNS developed by D'Alessio et al. [10]. This dataset comprises statistically planar premixed flames consisting of 50% NH3 and 50% H2 by volume in air, operating at an equivalence ratio of $\Phi = 0.5$. These two-dimensional flames are simulated within rectangular computational domains that exhibit periodicity in the transverse direction. A small subset of the DNS is used for training while the whole DNS dataset serves as the final target. Secondly, we utilize a dataset generated via Cantera, comprising 30 unstretched freely propagating one-dimensional flame solutions. These solutions were obtained by spanning the equivalence ratios values in the range $\Phi = [0.45, 0.55]$ in order to capture the local variations of equivalence ratio experienced by an unstable 2D flame due to the presence of the instabilities.

Following the methodology outlined in Najafi et al. (2012) [11], singular value decomposition (SVD) is employed to systematically identify a subset of progress variables that effectively capture the Direct Numerical Simulation (DNS) data while minimizing variance. The DNS data, represented as species mass fractions, is structured into a data matrix denoted as X, upon which SVD is performed, resulting in the decomposition $X = U\Sigma V^T$. Progress variables are subsequently derived from the unitary matrix V^T. Up to four progress variables are denoted as $C_j = \Sigma_i a_{i,j} Y_i$, where $a_{i,j}$ is the weight of species i in progress variable j.

Following the determination of Progress Variables, the concept of the optimal estimator, as elucidated in Trisjono et al. (2015) [12], is applied utilizing the two quantities of interest (QoI) being the temperature T and the NO mass fraction Y_NO. This estimator may adopt diverse forms, such as the conditional average of the QoI concerning the set of progress variables $C_{1,\dots,q}$. For this investigation, aligned with Berger et al. (2018) [6], an artificial neural network (ANN) is trained utilizing 10,000 randomly chosen samples from a DNS field or a 1D flames dataset. The ANN architecture comprises three hidden layers housing 5 neurons each, utilizing sigmoid as activation functions, while the output layer employs a linear activation function. These architectural parameters were judiciously selected to ensure the convergence of results. In particular, the sampling procedure was aided by means of the Kullback-Liebler divergence, employed to evaluate the difference between the dataset and the sample's probability distribution functions. This approach allowed us to select a reasonable sample dimension that was a good compromise between ease of training and retained information. The resultant ANN serves as a surrogate for the optimal estimator of the QoIs, denoted as $\zeta^{ANN,q}$, where q denotes the total count of progress variables employed to represent the QoI.

Subsequently, the irreducible error associated with the optimal estimator is computed by contrasting it with the DNS field, yielding:

$$\epsilon_{irr} = < (\zeta^{TRUE} - \zeta^{ANN,q})^2 | C_{1,\dots,q} > \quad (1)$$

The irreducible error is standardized by the maximum value of the conditionally averaged $\omega_{\dot{N}O}$ with respect to the primary scalar C_1, expressed as:

$$\epsilon_{irr,norm} = \frac{\sqrt{\epsilon_{irr}}}{max(<\omega_{\dot{N}O}|C_1>)} \quad (2)$$

Results and discussion

The analysis of the Irreducible Error for each QoI shows decreasing values as the model dimensionality increases, allowing the assessment of the number of needed Progress Variables to achieve a desired accuracy in the reconstruction. For the QoI Temperature, the Irreducible Error significantly decreases while passing from mono-dimensional models to two-dimensional models, but stops significantly decreasing if models with three or more variables are used. This indicates that two dimensional

models are more than sufficient to achieve an excellent representation of Temperature. For the variable NO the Irreducible Error analysis suggests that at least three variables are required to obtain good reconstruction results as shown in Tab1.

Table 1. Average Irreducible Error normalized by maximum QoI value, according to dimensionality of the model.

	1D	2D	3D	4D
Temperature	0.0526	0.0080	0.0078	0.0042
Y_NO	0.1259	0.0397	0.0149	0.0141

The Artificial Neural Network (ANN) model was initially trained on the DNS dataset to effectively reproduce the specified Quantities of Interest (QoIs). The outcomes, depicted in Fig.1, demonstrate remarkable fidelity, particularly when employing two or more Progress Variables for temperature, and three or more for NO. Subsequently, the same model trained on the 1D dataset was applied to the DNS testing dataset. As illustrated in Fig.2, while the model exhibits comparable results for temperature, it consistently falls short in accurately reproducing NO. Notably, augmenting the dimensionality does not seem to enhance the model's capacity for NO reproduction. This observation prompts the inference that an expanded 1D dataset, incorporating stretched flames, is indispensable for attaining improved results, particularly concerning NO reproduction.

Conclusion

In conclusion, our study utilized a data-driven model combining SVD-derived Progress Variables and ANN interpolation. Trained on both DNS and 1D datasets, the model aimed to replicate NO mass fraction and temperature from a reference DNS dataset. Irreducible Error analysis revealed that at least two Progress Variables were necessary for temperature modeling, and three for NO.

Temperature dynamics were accurately replicated by models trained on both DNS and 1D datasets with at least two Progress Variables. However, superior NO reproduction was achieved only by models directly trained on DNS data, requiring three Progress Variables. Conversely, models trained solely on 1D data showed suboptimal performance in capturing NO behavior.

While the model trained on freely propagating flames proficiently reproduced temperature dynamics, it struggled to accurately characterize NO behavior in unstable flames. Future studies should explore incorporating stretched 1D flames to enhance NO reproduction capability. Overall, our findings contribute to advancing flame modeling understanding, emphasizing the importance of addressing complexities highlighted by Irreducible Error analysis.

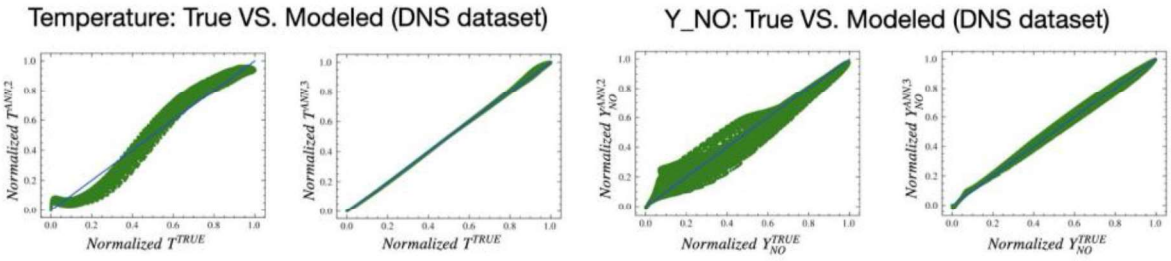

Figure 1. Apriori scatters of presented QoIs. Each plot presents x-axis as the scaled DNS reference dataset values, and the y axis as the values retrieved by the model trained onto the DNS dataset. Above is NO data for 2D and 3D models, while below is Temperature data for 1D and 2D models.

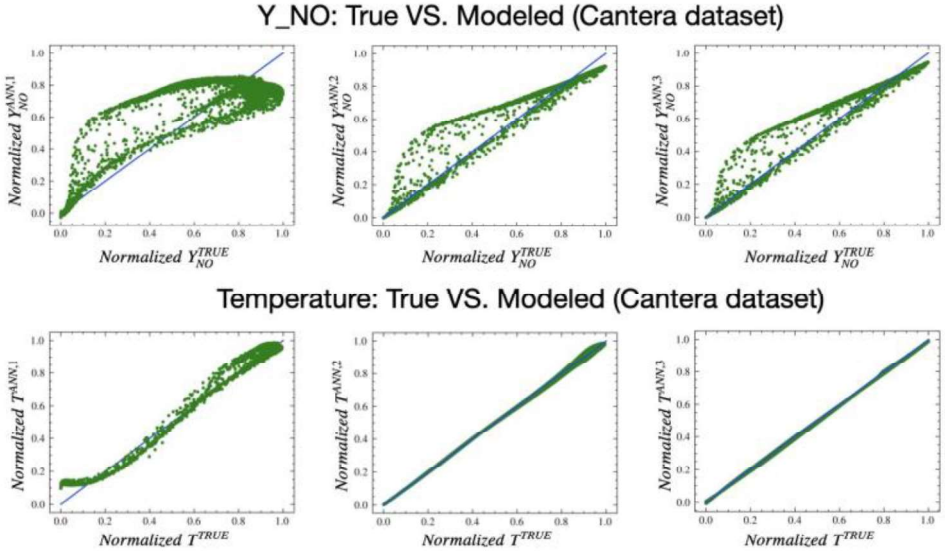

Figure2. Apriori scatters of presented QoIs. Each plot presents x-axis as the scaled DNS reference dataset values, and the y axis as the values retrieved by the model trained onto the 1D dataset. Above is NO data for 1D, 2D and 3D models, while below is Temperature data for 1D and 2D models.

References

[1] A. Yapicioglu, I. Dincer. "A review on clean ammonia as a potential fuel for power generators." Renewable and Sustainable Energy Reviews, 103 (2019), 96–108.

[2] A. M. Elbaz, S. Wang, T. F. Guiberti, W. L. Roberts. "Review on the recent advances on ammonia combustion from the fundamentals to the applications." Fuel Communications, 10 (2022), 100053.

[3] X. Wen, L. Berger, F. vom Lehn, A. Parente, H. Pitsch, M. E. Mueller. "Numerical analysis and flamelet modeling of NOx formation in a thermodiffusively unstable hydrogen flame." Combustion and Flame, 253

(2023), 112817.
[4] M. Matalon. "The Darrieus-Landau instability of premixed flames." Fluid Dynamics Research, 50 (2018).
[5] F. Creta, P. E. Lapenna, R. Lamioni, N. Fogla, M. Matalon. "Propagation of premixed flames in the presence of Darrieus-Landau and thermal diffusive instabilities." Combustion and Flame, 216 (2020), 256–70.
[6] L. Berger, K. Kleinheinz, A. Attili, F. Bisetti, H. Pitsch, M. E. Mueller. "Numerically accurate computational techniques for optimal estimator analyses of multi-parameter models." Combustion Theory and Modelling, 22 (3) (2018), 480–504.
[7] P. E. Lapenna, A. Remiddi, D. Molinaro, G. Indelicato, F. Creta. "A-posteriori analysis of a data-driven filtered wrinkled flamelet model for thermodiffusively unstable premixed flames." Combustion and Flame, 259 (2024), 113126.
[8] J. D. Regele, E. Knudsen, H. Pitsch, G. Blanquart. "A two-equation model for non-unity Lewis number differential diffusion in lean premixed laminar flames." Combustion and Flame, 160 (2) (2013), 240–250.
[9] D. G. Goodwin, H. K. Moffat, I. Schoegl, R. L. Speth, B. W. Weber. "Cantera: An object-oriented software toolkit for chemical kinetics, thermodynamics, and transport processes." Cantera, 2023. Version 3.0.0. doi:10.5281/zenodo.8137090.
[10] F. D'Alessio, C. Matteucci, P. E. Lapenna, F. Creta. "Intrinsic instability of lean hydrogen/ammonia premixed flames: Influence of Soret effect and pressure." Fuel Communications, 19 (2024), 100110.
[11] A. Najafi-Yazdi, B. Cuenot, L. Mongeau. "Systematic definition of progress variables and intrinsically low-dimensional, flamelet generated manifolds for chemistry tabulation." Combustion and Flame, 159 (3) (2012), 1197–1204.
[12] P. Trisjono, H. Pitsch. "Systematic analysis strategies for the development of combustion models from DNS: A review." Flow, Turbulence and Combustion, 95 (2015), 231–259.

EFFECT OF WATER COLLISION EFFICIENCY ON EMISSIONS OF NON-PREMIXED HYDROGEN/AIR FLAMES

R. Concetti*, J. Hasslberger*, M. Klein*
riccardo.concetti@unibw.de
*University of the Bundeswehr Munich, Werner-Heisenberg-Weg 39, 85579, Neubiberg, Germany

Abstract
The present study investigates the role of the high collision efficiency of water on the emissions of nitrogen oxides (NO_x) in the context of non-premixed flames, which have particular relevance in industrial applications. A series of counterflow hydrogen/air flame simulations has been conducted for a range of water loading levels and strain rates. These simulations employ a state-of-the-art chemical mechanism provided by the CRECK group, and a modified version of the mechanism wherein the third-body reaction efficiency of water is inhibited. The outcomes reveal the potential of mitigating emissions due to the properties of water, particularly under circumstances characterized by elevated strain rates.

Introduction
The potential of employing steam injection in combustion systems has been explored as a strategy to mitigate greenhouse gas emissions, notably within methodologies like MILD combustion or Exhaust Gas Recirculation. This approach is considered promising for reducing emissions of NO_x and other deleterious by-products, as documented in the existing literature [1,2]. Nitrogen oxides primarily arise through four pathways:

1. The Zeldovich mechanism or thermal mechanism [3], prevalent under high-temperature conditions.
2. The Prompt or Fenimore mechanism [4], characteristic of rich hydrocarbon combustion.
3. The N_2O mechanism, observed in environments with elevated concentrations of atomic oxygen.
4. The NNH mechanism, prominent under conditions with elevated concentrations of atomic hydrogen.

The importance of the high third-body reaction efficiency of water in affecting the flame structure has been analyzed in previous research by Koroll and Mulpuru [5]. They found that when a hydrogen/oxygen premixed flame is diluted with steam at various concentrations, the reduction in flame speed is less than the value predicted by assuming water to be inert. This effect primarily stems from a specific third-body reaction:

$$H + O_2 + M \leftrightarrow HO_2 + M$$

This particular reaction's relevance has also been recognized in the studies of Lamioni et al. [6] and Attili et al. [7], where it is characterized as a chain-breaking reaction competing with a non-third-body chain-branching reaction. The balance between these reactions depends on the system temperature and can be influenced by the presence of chemical species that affect the strength of third-body reactions, such as water.

The aim of the current study is to investigate the influence of water injection on a canonical counterflow non-premixed flame, with particular attention to the high third-body reaction efficiency of water. The paper presents the theoretical framework in the next section, then proceeds with the presentation and discussion of results, and concludes by outlining the findings.

Theoretical Background

The current investigation explores a counterflow non-premixed flame configuration, wherein fuel and oxidizer are injected from opposite directions with predetermined velocities and separation distance. This configuration inherently exhibits a two-dimensional nature and is characterized by a certain degree of strain. The flame structure of such configurations is notably influenced by the level of strain, rendering it a crucial design parameter also analyzed in this study. To consider different strain rate levels, the relationships delineated by Fiala and Sattelmayer [8] are utilized to specify the boundary conditions for fuel and oxidizer. For each adjustment in strain level, the inlet temperature (T) and inlet flow composition (Y_α) remain constant, while the inlet velocity (u) and distance between the two inlets (d) are varied according to the subsequent scaling rules:

$$u_{new} = u_{old}\left(\frac{a_{new}}{a_{old}}\right)^{\frac{1}{2}};\ d_{new} = d_{old}\left(\frac{a_{new}}{a_{old}}\right)^{-\frac{1}{2}} \quad (1)$$

In this context, a denotes the strain rate, with the subscript indicating the value corresponding to either the preceding (old) or current simulation (new). This method allows for the utilization of prior simulations, adjusted with the updated distance, as initial solutions, thereby facilitating quicker convergence, as explained by Fiala and Sattelmayer [8]. The software utilized for executing the series of batch simulations is Cantera [9], a widely recognized computational platform for modeling chemical kinetics and transport phenomena. In this investigation, a state-of-the-art mechanism proposed by the CRECK group and considering the chemistry relevant to NO_x formation, is adopted [10-12]. The mechanism comprises a total of 159 species and 2459 elementary reactions. Employing this established framework, a sequence of analyses is carried out at various levels of strain rate until extinction is reached, with different levels of water loading in the oxidizer inlet mass (i.e., Y_W between 0% and

10%). Subsequently, the chemical mechanism is adjusted to isolate the impact of the high third-body reaction efficiency of water, with this parameter set to zero for all elementary reactions.

Results and Discussion

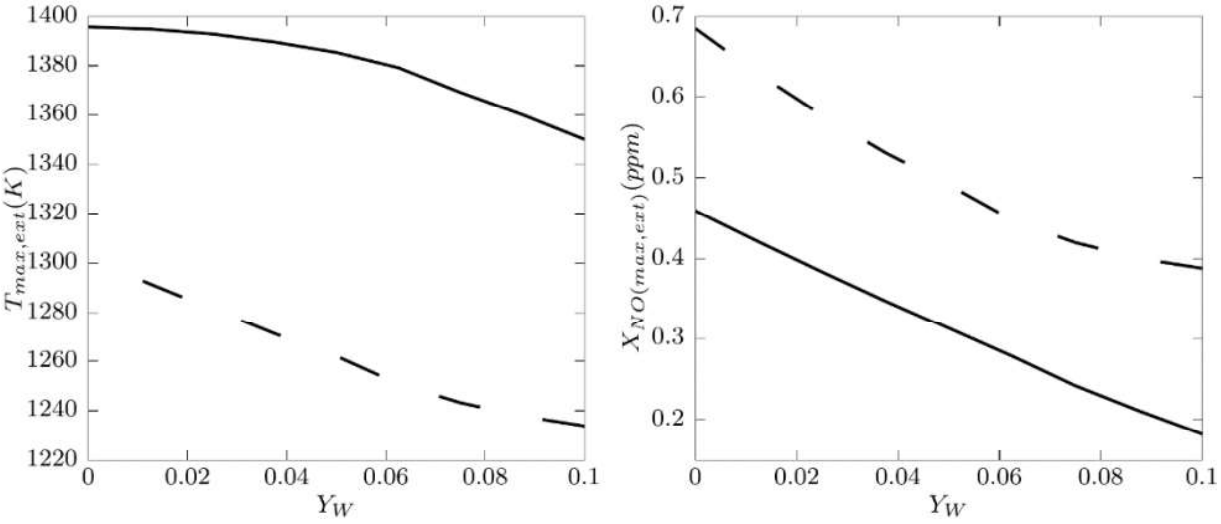

Figure 1. Maximum temperature close to the extinction strain rate ($T_{max,ext}$) and maximum nitrogen monoxide molar fraction close to extinction strain rate ($X_{NO(max,ext)}$) for different levels of water loading by mass (Y_W). The continuous lines refer to the cases with the original chemical mechanism, while the dashed lines refer to the cases with the mechanism without third-body reaction efficiency of water.

The impact of the high third-body reaction efficiency of water at varying degrees of water loading, under strain rate levels close to quenching, is first considered. As depicted in Fig. 1, which illustrates the maximum temperature and the peak NO molar fraction for the considered conditions, it becomes clear that both quantities decrease as the water loading increases. However, upon considering the collision efficiency of water, the maximum temperature under extinction conditions exceeds that observed in cases where the collision efficiency is inactive. This supports observations from literature regarding the higher temperatures achieved with water dilution compared to those predicted when steam is considered inert [5]. Additionally, the sign of curvature of the curves representing the temperature trend changes. If only the Zeldovich mechanism is considered, the outcomes from Fig. 1 might seem counterintuitive, given that elevated temperature conditions typically result in increased NO emissions. However, as written in the introduction, the formation of NO_x proceeds through different pathways. This leads to the inference that the high third-body reaction efficiency of water profoundly affects radicals production (i.e., H and O), thereby exerting a significant influence on nitrogen oxide emissions. The conditions investigated thus far pertain to scenarios approaching flame extinction. In practical scenarios, various levels of strain rate are encountered

depending on the location within the combustion apparatus. Consequently, our attention now turns to examining the evolution of maximum temperature and maximum nitrogen monoxide emissions at different strain rate levels, with water loading levels of 0%, 5%, and 10%.

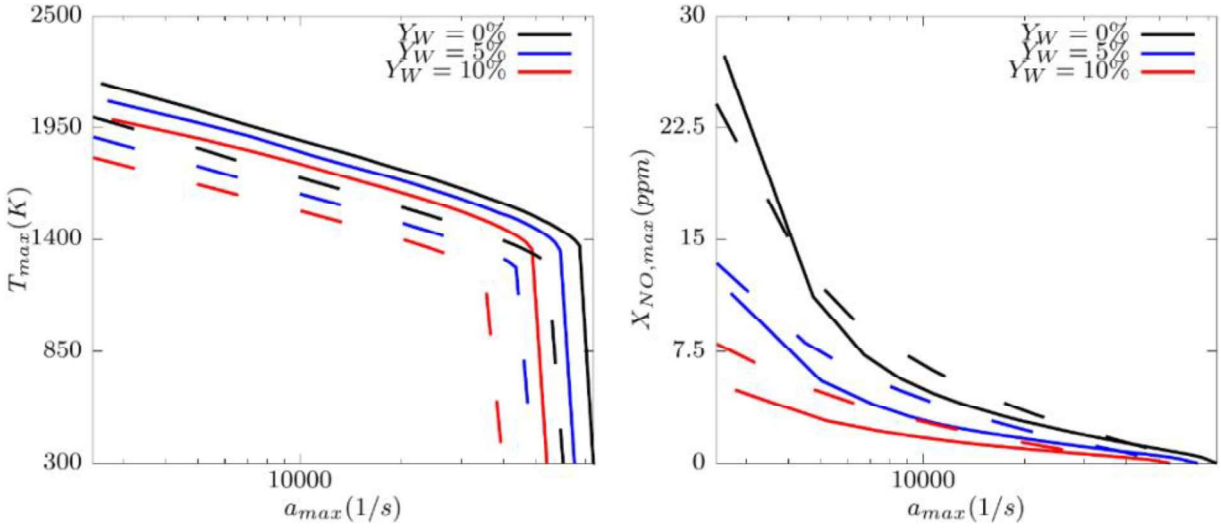

Figure 2. Maximum temperature (T_{max}) and maximum nitrogen monoxide molar fraction ($X_{NO,max}$) as a function of maximum strain rate (a_{max}). The continuous lines refer to the cases with the original chemical mechanism, while the dashed lines refer to the cases with the mechanism without third-body reaction efficiency of water. The different levels of water are indicated in black for 0%, blue for 5% and red for 10%.

Figure 2 illustrates the trends of maximum temperature and nitrogen monoxide molar fraction with strain rate, across the three specified levels of water loading. It becomes evident that the maximum temperature of the systems decreases with increasing strain rate until reaching the quenching level. When the third-body reaction efficiency of water is active, the flame consistently exhibits a higher maximum temperature compared to cases with the modified mechanism. While the temperature demonstrates consistent behavior irrespective of strain rate and water loading, with higher values observed when the collision efficiency is activated, a crossover is observed for the NO emissions: the emissions of NO at 0% water loading are higher with the original mechanism and low strain rate levels, subsequently decreasing as conditions approach quenching. With higher steam concentration, the intersection point shifts toward zero strain rate or disappears entirely. This phenomenon may be explained by the varying significance of the system temperature at different strain rate levels. Near zero strain rate, the elevated maximum temperature is assumed to favor the Zeldovich mechanism [3]. However, as the strain rate grows, the system's maximum temperature decreases, leading to increased prominence of other pathways and their strength is correlated with radical concentrations [2].

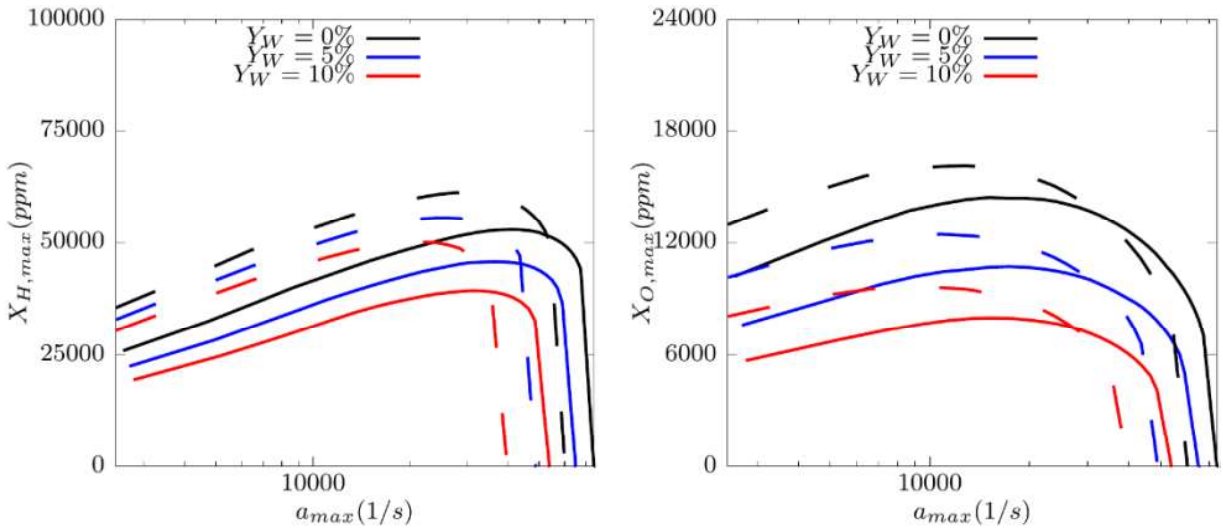

Figure 3. Maximum atomic hydrogen molar fraction ($X_{H,max}$) and maximum atomic oxygen molar fraction ($X_{O,max}$) as function of maximum strain rate (a_{max}). The continuous lines refer to the cases with the original chemical mechanism, while the dashed lines refer to the cases with the mechanism without third-body reaction efficiency of water. The different levels of water are indicated in black for 0%, blue for 5% and red for 10%.

From Fig. 3, it is evident that the concentrations of radicals grow with the strain rate for strain rates being sufficiently smaller than the extinction limit, typically being higher with the modified mechanism. This phenomenon explains the elevated emissions of NO due to the increased importance of the NNH and N_2O mechanisms, despite the lower temperature observed (see Fig. 2), for the modified reaction mechanism with third body efficiency set to zero. Nevertheless, the Zeldovich mechanism remains of paramount importance and Fig. 2 suggests a clear correlation between temperature and NO emissions.

Conclusion

In this study, a series of Cantera simulations were conducted for non-premixed counterflow hydrogen/air flames. The primary objective was to investigate the impact of water injection on NO_x emissions, with specific emphasis on the third-body reaction efficiency of water. It was observed that when the collision efficiency of water is active, the flame exhibits higher temperatures at every strain rate level compared to cases employing a modified chemical mechanism. The production of NO is notably influenced by the collision efficiency; at low strain rates, the original chemical mechanism generates higher pollutant levels when no steam is added, whereas at higher strain rates, the emission of nitrogen monoxide is lower than in cases without collision efficiency. The higher emissions observed with the modified mechanism are attributed to the increased presence of radicals in the flame under moderately high strain rate conditions.

In the next step of this research, we would like to analyze the effect of preheating at conditions typically considered in practical applications.

Acknowledgement
This research, in the frame of project MORE, is funded by dtec.bw – Digitalization and Technology Research Center of the Bundeswehr, which we gratefully acknowledge. dtec.bw is funded by the European Union – Next Generation EU

References

[1] Göke, S., Paschereit, C. O., "Influence of steam dilution on nitrogen oxide formationin premixed methane/hydrogen flames" *J. Propul. Power* 29(1): 249–260, (2013)
[2] Lellek, S., Sattelmayer, T., "NOx-formation and CO-burnout in water-injected, premixed natural gas flames at typical gas turbine combustor residence times", *J. Eng. Gas Turb. Power 140*: 051504, (2018)
[3] Zeldovich, Y. B., "The oxidation of nitrogen in combustion and explosions", *J. Acta. Physicochimica*. 21: 577, (1948)
[4] Fenimore, C., "Studies of fuel-nitrogen species in rich flame gases" *Proc. Comb. Inst.* 17: 661–670, (1979)
[5] Koroll, G., Mulpuru, S. "The effect of dilution with steam on the burning velocity and structure of premixed hydrogen flames", *Proc. Comb. Inst.:* 1811–1819, (1988)
[6] Lamioni, R., Lapenna, P. E., Berger, L., Kleinheinz, K., Attili, A., Pitsch, H., Creta, F., "Pressure-induced hydrodynamic instability in premixed methane-air slot flames" *Combust. Sci. Techno.* 192(11): 1998–2009, (2020)
[7] Attili, A., Lamioni, R., Berger, L., Kleinheinz, K., Lapenna, P.E., Pitsch, H., Creta, F., "The effect of pressure on the hydrodynamic stability limit of premixed flames" *Proc. Comb. Inst.* 38(2): 1973–1981, (2021)
[8] Fiala, T., Sattelmayer, T., "Nonpremixed Counterflow Flames: Scaling Rules for Batch Simulations", *Journal of Combustion* 2014: 484372, (2014)
[9] Goodwin, D. G., Moffat, H. K., Spath, R. L., "Cantera: an object-oriented software toolkit for chemical kinetics, thermodynamics, and transport processes", (2018)
[10] Ranzi, E., Frassoldati, A., Grana, R., Cuoci, A., Faravelli, T., Kelley, A. P., Law, C. K., "Hierarchical and comparative kinetic modeling of laminar flame speeds of hydrocarbon and oxygenated fuels", *Prog. Energ. Combust.* 38: 468-501, (2012)
[11] Ranzi, E., Frassoldati, A., Stagni, A., Pelucchi, M., Cuoci, A., Faravelli, T., "Reduced kinetic schemes of complex reaction systems: fossil and biomass-derived transportation fuels", *Int. J. Chem. Kinet.* 46: 512-542, (2014)
[12] Song, Y., Marrodan, L., Vin, N., Herbinet, O., Assaf, E., Fittschen, C., Stagni, A., Faravelli, T., Alzueta, M. U., Battin-Leclerc, F., "The sensitizing effects of NO2 and NO on methane low temperature oxidation in a jet stirred reactor", *Proc. Comb. Inst.* 37: 667-675, (2019)

ASSESSING THE COMBUSTION BEHAVIOR OF DIMETHYL ETHER AND AMMONIA: A COMPARATIVE STUDY

Francesco Roman Artioli, Luca Granata, Alessandro Stagni*
*alessandro.stagni@polimi.it

Abstract
The mixtures of ammonia/dimethyl ether (DME) are increasing in importance because DME can compensate for the limiting properties of ammonia (like autoignition temperature and flame speed).
This work aims to develop a comprehensive kinetic mechanism describing the pyrolysis and oxidation of the mixtures of the two species. The critical aspects are the binary interactions, which are the focus of this investigation.
Different experimental sets were used to validate the mechanism proposed. The model works reasonably well considering the uncertainty intervals. In addition, different models were used to make a comparison considering the same experimental data.

Introduction
There is a growing interest in utilizing ammonia (NH_3) as an alternative fuel to mitigate greenhouse gas emissions associated with conventional fossil fuels. However, ammonia presents challenges such as a significantly lower burning velocity [1] and higher autoignition temperature [1] compared to traditional fuels.
The aim is to achieve a mixture that performs comparably to existing fuels, thereby enabling the proper utilization of ammonia. It is crucial to select co-fuels that meet specific requirements for burning velocity and ignition behavior.
Oxymethylene ethers (OMEs), as environmentally friendly co-fuels, show great potential in enhancing the oxidation kinetics of NH_3 for various reasons. Firstly, they can be manufactured within a sustainable carbon cycle, thereby facilitating zero-net CO_2 emissions. Additionally, OMEs exhibit desirable characteristics such as high cetane numbers and oxygen content, without containing any carbon-carbon bonds. When blended with conventional fuels, they have been observed to notably decrease soot emissions [2]. Furthermore, OMEs are non-toxic, further highlighting their suitability as sustainable co-fuels. The simplest of the OMEs is DME (or OME_0). In the literature, many mechanisms and experimental studies on the combustion of the mixtures DME/NH_3 are present [3,4]. The objective of this work is to describe the development of a mechanism with predictive features comprehensive of both the pure compounds and mixtures.

Methodology

This work is based on a hierarchical and modular approach. The starting point is to use what has already been developed by Stagni et al for both pure NH_3 and DME [5,6]. The modules have been validated in the respective works. They must be updated with the newest aspects investigated in literature both reactions and reaction paths. Therefore, a new model for the interactions between the two species must be created. Following the hierarchical approach, the first aspect investigated was the C_0-C_1 module starting from the work by Dong et al [7]. The reason was that the combustion of both DME and NH_3 is based on the reactivity of the species included in this module. The effects of this change are very relevant in the case of flame speed because the chemistry of the species up to C_1 is the main in the combustion of dimethyl ether [8]. The single modules about ammonia and DME were slightly changed as mentioned before. The main modifications were made to the module concerning dimethyl ether. The reactions added to the original mechanism are reported in the table below (Table 1). The first two reactions became part of the module due to the sensitivity analysis done for ignition delay times simulations at high temperatures. The mechanism used for this simulation (Dai-Zhang) was proposed by Yin [3]. The sensitivity coefficients of the reactions are not the highest, but these reactions are still present changing the conditions of the system. For this reason, these reactions cannot be ignored (Fig. 1).

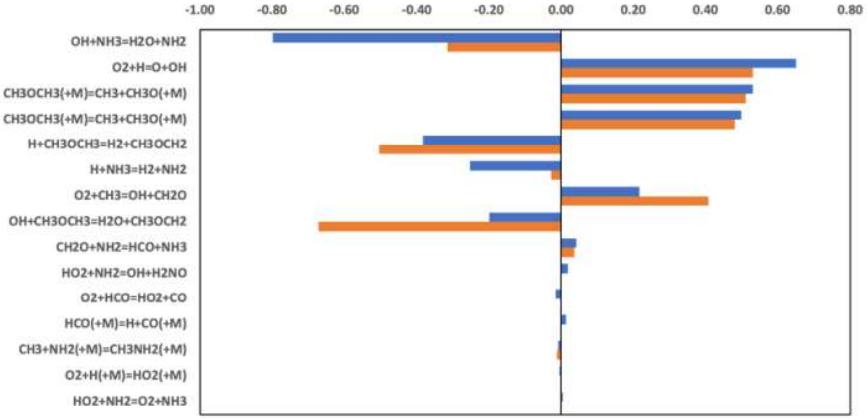

Figure 1. Sensitivity analysis at P=0.14 MPa, ϕ=1 and 5% DME/95% NH_3 (blue bars) and 30% DME/70% NH_3 (orange bars). [9]

The two successive reactions were added by looking at reaction paths not considered, like the ones from Guan et al [10]. After all these modifications, the changed module was used to perform several simulations to prove the validity of the changes. The results of this analysis are not reported here to focus on the results of the mixtures DME-NH_3. The module for the interaction of DME and ammonia is described by two reactions (reported in the last two rows of Table 1). The first reaction has the expression presented in the work of Yin et al [3]. It is shown to be an important reaction through sensitivity analysis. Instead, the second reaction has an expression derived from ab initio calculations. Different studies are available in the literature for this specific reaction. The one chosen is from the work of Cavallotti et al [11]. The reason for this choice is that the rate proposed has been developed considering

a very wide range of temperature conditions (between 300 and 2500 K). The rate was evaluated using an automatic code, for the derivation of kinetics parameters, called EStokTP [11].

Table 1. New interaction reactions were added in the module for DME and DME/NH_3 with references. [9]

Reactions	Reference
$CH_2O + NH_2 \rightarrow HCO + NH_3$	[12]
$CH_3 + NH_2 (+M) \rightarrow CH_3NH_2 (+M)$	[13]
$CH_3OCH_3 + NO_2 \rightarrow CH_3OCH_2 + HONO$	[10]
$CH_3OCH_3 + NO_2 \rightarrow CH_3OCH_2 + HNO_2$	[10]
$CH_3OCH_2 + NH_2 (+M) \rightarrow CH_3OCH_2NH_2 (+M)$	[3]
$CH_3OCH_3 + NH_2 \rightarrow CH_3OCH_2 + NH_3$	[11]

Results

The first result is about a simulation of a Jet Stirred Reactor (JSR). The mixture, at stoichiometric condition, analyzed has the following composition: 50% DME/50% NH_3. In Fig. 2, the plot represents the mole fraction of DME varying the temperature of the reactor (the pressure is constant and atmospheric).

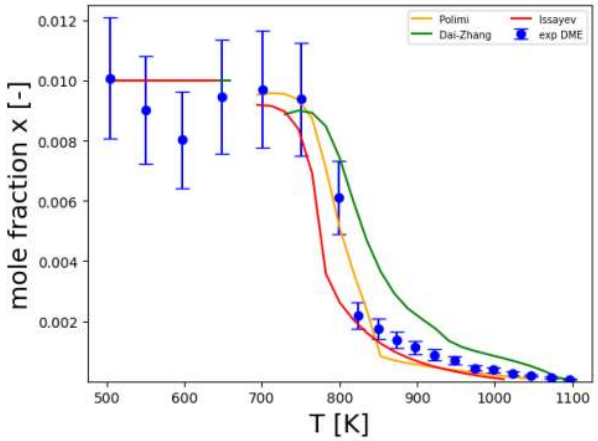

Figure 2. Mole fraction of DME changing the temperature of the JSR. Each color expresses a different mechanism: Polimi (orange), Dai-Zhang (green), and Issayev (red) [4]. The experimental points are from [14].

The curves present some missing points because, as seen in other cases [15], the oscillation issues can affect the low-temperature combustion in a perfectly stirred reactor. This phenomenon does not let the system converge to the steady-state solution, as detailed in the work by Stagni et al [15]. The problem is observed experimentally, and it is reproduced in the numerical simulations.

The laminar flame speed cases are another type of simulation to understand the validity of the mechanism. The first case simulated is about a system with a pressure of 1 bar and an initial temperature of 300 K. Different mole fractions of DME are considered (Fig. 3).

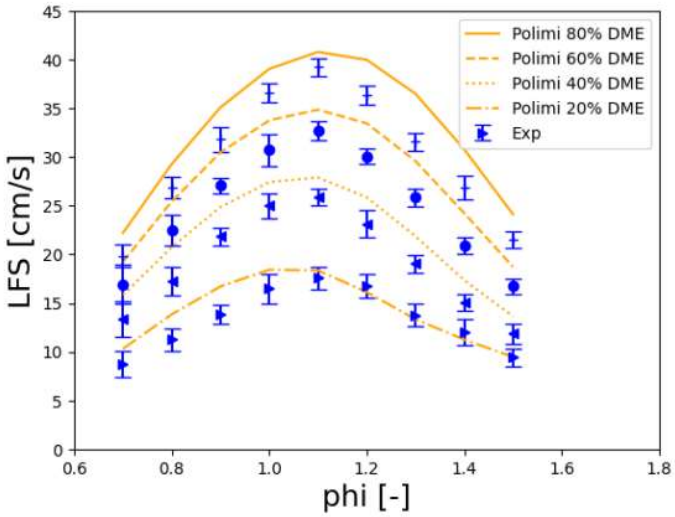

Figure 3. LFS (Laminar Flame Speed) changing the mole fraction of DME. Polimi mechanism (orange). The experimental points are blue [16].

The higher the mole fraction of DME the higher the distance between the model and the experimental data. The results overall have a relative error of around 10%.
The successive case analyzed is about the combustion of pure NH_3 and DME and a mixture of 50% DME/50% NH_3 (Fig. 4). The flames studied are at atmospheric pressure and initially at room temperature (298K).

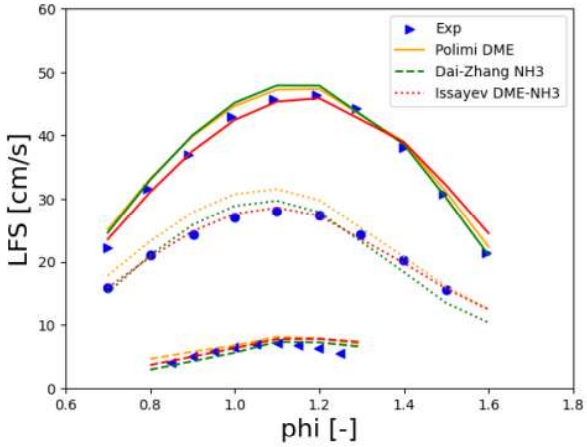

Figure 4. LFS (Laminar Flame Speed) changing the equivalence ratio. Polimi (orange), Dai-Zhang (green), and Issayev (red). The experimental data are from [3].

The curves are different based on the model. The mixtures come from a superposition of the effects related to single components. The important difference in the models is the reactivity of the pure ammonia. This explains the difference also in the mixture of DME-NH_3. Dai-Zhang and Issayev models have a lower speed in the mixtures mainly due to a lower speed of the pure ammonia. A sensitivity analysis was performed for each type of mixture shown (Fig. 5).

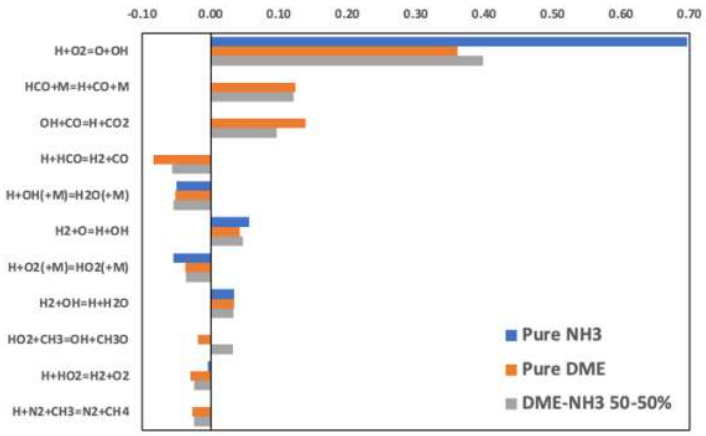

Figure 5. Sensitivity analysis, on the mass-flowrate, of the eleven most important reactions for the mixture 50% DME/50% NH_3.

The sensitivity analysis emphasizes the importance of the reactions in the C_0-C_1 module. The most important reactions, after the main branching reaction, regard the chemistry of carbon. The carbon in the mixture is given by the DME. Therefore, the flame cases are strongly influenced by the DME. This was expected because the addition of DME to ammonia helps in overcoming the lower flame speeds of pure NH_3.

Conclusions

To summarize, this work represents a further stride in advancing the comprehension of combustion of DME/NH_3. The peculiar properties are the base methodology (use of hierarchical and modular approach) and the generality regarding the conditions of development. At the same time, it offers a mechanism applicable with reasonably good results for both the mixtures and the pure components. In fact, new reactions and reactive paths were added based on the sensitivity analysis. In addition, sensitivity analysis was performed on the results that supports the superposition effects mentioned before.

Acknowledgments

This work was founded by the European Union– Next Generation EU. This manuscript reflects only the authors' views and opinions, neither the European Union nor the European Commission can be considered responsible for them.

References

[1] H. Kobayashi, A. Hayakawa, K. D. K. A. Somarathne, and E. C. Okafor, 'Science and technology of ammonia combustion', *Proceedings of the Combustion Institute*, vol. 37, no. 1, pp. 109–133, 2019

[2] R. Zhu, X. Wang, H. Miao, X. Yang, and Z. Huang, 'Effect of dimethoxy-methane and exhaust gas recirculation on combustion and emission characteristics of a direct injection diesel engine', *Fuel*, vol. 90, no. 5, pp. 1731–1737, May 2011

[3] G. Yin *et al.*, 'Experimental and kinetic study on laminar flame speeds of ammonia/dimethyl ether/air under high temperature and elevated pressure', *Combust Flame*, vol. 238, Apr. 2022

[4] G. Issayev *et al.*, 'Ignition delay time and laminar flame speed measurements of ammonia blended with dimethyl ether: A promising low carbon fuel blend', *Renew Energy*, vol. 181, pp. 1353–1370, Jan. 2022

[5] A. Stagni *et al.*, 'An experimental, theoretical and kinetic-modeling study of the gas-phase oxidation of ammonia', *React Chem Eng*, vol. 5, no. 4, pp. 696–711, Apr. 2020

[6] A. Stagni, S. Schmitt, M. Pelucchi, A. Frassoldati, K. Kohse-Höinghaus, and T. Faravelli, 'Dimethyl ether oxidation analyzed in a given flow reactor: Experimental and modeling uncertainties', *Combust Flame*, vol. 240, Jun. 2022

[7] S. Dong *et al.*, 'A new detailed kinetic model for surrogate fuels: C3MechV3.3', *Applications in Energy and Combustion Science*, vol. 9, Mar. 2022

[8] E. Ranzi *et al.*, 'Hierarchical and comparative kinetic modeling of laminar flame speeds of hydrocarbon and oxygenated fuels', *Progress in Energy and Combustion Science*, vol. 38, no. 4. Elsevier Ltd, pp. 468–501, 2012

[9] Granata Luca, 'Kinetic and fluid-dynamic study of ammonia-dimethyl ether mixtures as flexible energy carriers', Politecnico di Milano, 2024.

[10] Y. Guan, R. Liu, J. Lou, H. Ma, and J. Song, 'Computational investigation on the reaction of dimethyl ether with nitric dioxide. II. Detailed chemical kinetic modeling', *Theor Chem Acc*, vol. 139, no. 1, Jan. 2020

[11] C. Cavallotti, M. Pelucchi, Y. Georgievskii, and S. J. Klippenstein, 'EStokTP: Electronic Structure to Temperature- and Pressure-Dependent Rate Constants-A Code for Automatically Predicting the Thermal Kinetics of Reactions', *J Chem Theory Comput*, vol. 15, no. 2, pp. 1122–1145, Feb. 2019

[12] Q. S. Li and R. H. Lü, 'Direction dynamics study of the hydrogen abstraction reaction CH2O + NH2 → CHO + NH3', *Journal of Physical Chemistry A*, vol. 106, no. 41, pp. 9446–9450, Oct. 2002

[13] J. T. Jodkowski *et al.*, ''CHEMICAL PHYSICS LETTERS Kinetics of the cross reaction between amidogen and methyl radicals', 1995.

[14] S. Zhu *et al.*, 'A comparative study of oxidation of pure ammonia and ammonia/dimethyl ether mixtures in a jet-stirred reactor using SVUV-PIMS', *Combust Flame*, vol. 250, Apr. 2023

[15] A. Stagni *et al.*, 'The role of chemistry in the oscillating combustion of hydrocarbons: An experimental and theoretical study', *Chemical Engineering Journal*, vol. 385, Apr. 2020

[16] H. Xiao and H. Li, 'Experimental and kinetic modeling study of the laminar burning velocity of NH3/DME/air premixed flames', *Combust Flame*, vol. 245, Nov. 2022

IMPACT OF THE OPERATING CONDITIONS ON THE CORRELATION BETWEEN OH* AND HEAT RELEASE RATE IN HYDROGEN-AIR FLAMES

F. G. Schiavone*, M. Torresi*, S. M. Camporeale*, D. Laera*
f.schiavone11@phd.poliba.it
*Department of Mechanics, Mathematics and Management, Polytechnic University of Bari, Via Orabona 4, Bari 70125, Italy

Abstract
The correlation between the distributions of OH* concentration and heat release rate (HRR) in laminar hydrogen-air flames is investigated, highlighting the differences observed between premixed and diffusion flames and the impact of the operating conditions. First, one-dimensional premixed hydrogen-air flames are considered, showing a characteristic peak shift between OH* and HRR, which is less pronounced or inexistent when considering diffusion hydrogen-air flames. The impact of unburned gas temperature and pressure is studied, showing that an increase of either of the two quantities corresponds to a reduction in the peak shift. Subsequently, the impact of different flame regime is analyzed by considering high-fidelity numerical simulations of a two-dimensional hydrogen-air triple flame, for which diffusion and premixed branches coexist, confirming the observations made for one-dimensional calculations.

Introduction
The distribution of Heat Release Rate (HRR) is fundamental to analyze and predict the structure and dynamics of flames. Nevertheless, HRR direct measurements are impractical, and chemiluminescence (i.e., the spontaneous light emission from excited chemical species in flames) is used as a tracer [1].
A good correlation between CH*, OH* and CO_2* chemiluminescent emissions and HRR is generally observed for steady hydrocarbon flames [1]. For pure methane (CH_4) flames, the peak-to-peak distance between OH* intensity and HRR distributions is smaller than the spatial resolution of most measurements, making OH* an adequate heat release tracer [2]. A correspondence between OH* emission and HRR distributions has been found also for methane-hydrogen blends [3]. For hydrogen (H_2)-air flames, instead, a rather wide distance between the OH* and HRR peaks has been observed, and the correlation between the two quantities has been shown to fail in lean premixed cellular tubular flames [4]. As observed in [5], the fundamental reason leading to these observed differences lies in the interplay between the H-radical pool, the OH* main formation pathways, which are related to the fuel composition, and the heat release process.
In this work, the impact of operating conditions, in terms of unburned gas

temperature, pressure, flame regime and stretch, on such physical-chemical mechanisms and, consequently, on the HRR-OH* correlation is investigated. To this scope, firstly laminar premixed unstrained one-dimensional (1D) H_2-air flames are computed and compared with strained counterflow premixed and diffusion H_2-air flames under various conditions of unburned gas temperature and pressure. Subsequently, the impact of flame regime is further highlighted by considering a H_2-air two-dimensional (2D) triple flame, for which diffusion and premixed branches coexist, to confirm the observations made for 1D flames.

Methodology

One-dimensional flame calculations are performed with Cantera (www.cantera.org), implementing the multi-component transport model and considering the Soret effect, while 2D numerical simulations are carried out with the compressible solver AVBP (www.cerfacs.fr/avbp7x) developed at CERFACS (Toulouse, France). The San Diego (UCSD) [6] scheme is adopted to describe the combustion process.
The OH* formation and consumption process in hydrogen flames relies on the following three elementary reactions [7]:

$$\mathrm{H + O + M \leftrightarrow OH^* + M}, \quad (1)$$
$$\mathrm{OH^* \rightarrow OH} + h\nu, \quad (2)$$
$$\mathrm{OH^* + M \leftrightarrow OH + M}, \quad (3)$$

with $h\nu$ being the energy of the emitted photon. At temperatures below 2800 K, OH* is mainly formed by the recombination reaction (1), while it transfers its excess energy, returning to the ground state, either by emitting light in the radiative decay reaction (2) or by the non-reactive collisional quenching reaction (3) [7].
The sub-scheme by Kathrotia et al. [7] is here adopted to describe OH* formation and consumption. In all cases, the OH* sub-mechanism is simply added to the main reaction scheme as its impact on the ground species' concentrations is negligible [8].

One-dimensional flames

Firstly, freely-propagating, unstretched 1D premixed H_2-air flames at variable unburned mixture temperature T_u, pressure p and equivalence ratio ϕ are compared. The correlation between OH* and HRR distributions is assessed by considering two parameters: the normalized peak-to-peak distance δ and the error estimator Z_{OH^*}. The first one is computed as the distance between the peaks of OH* and HRR distributions, divided by the laminar flame thickness $\delta_L^0 = (T_b - T_u)/\max(dT/dx)$, where T_b is the burned mixture temperature. The second one, instead, quantifies the global quality of the OH*-HRR correlation and has been defined in [9] as:

$$Z_{\mathrm{OH}^*} = \int_x \left(\frac{|\mathrm{HRR}(x)|}{\max(|\mathrm{HRR}(x)|)} - \frac{|c_{\mathrm{OH}^*}(x)|}{\max(|c_{\mathrm{OH}^*}(x)|)} \right)^2, \quad (4)$$

where c_{OH*} is the OH* molar concentration.
As can be observed in Fig. 1, the worst correlation between the two distributions is obtained for stoichiometric values, for which the value of Z_{OH*} is higher. Moreover, this is positively impacted by an increase of pressure, and negatively impacted by an increase of unburned gas temperature. Still, as indicated by the isolines of δ in Fig. 1a, the largest normalized peak-to-peak distance is obtained for lower temperatures.

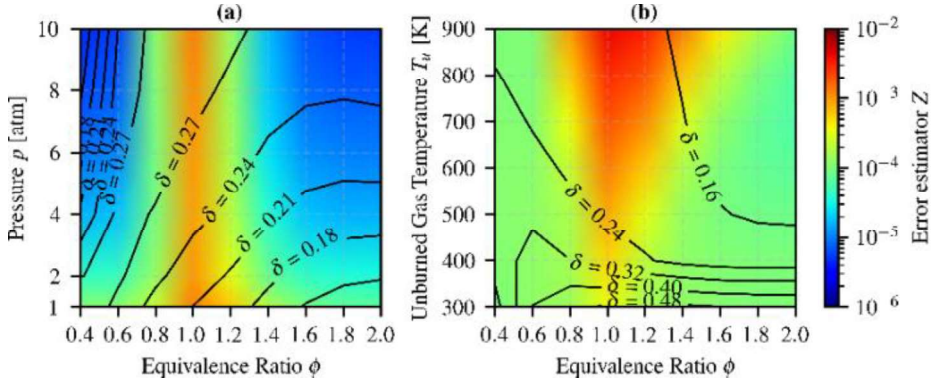

Figure 1. Error estimator Z_{OH*} as a function of ϕ, p and T_u, for T_u = 600 K (a) and p = 1 atm (b). The isolines indicate the corresponding values of δ.

These different trends can be explained by the distributions of OH* concentration and HRR shown in Fig. 2 for stoichiometric flames at three operating points: T_u = 300 K and p = 1 atm (a), T_u = 600 K and p = 1 atm (b), T_u = 600 K and p = 10 atm (c). The computed values of Z are, respectively, 3.53×10^{-4}, 1.26×10^{-3} and 1.25×10^{-3}.

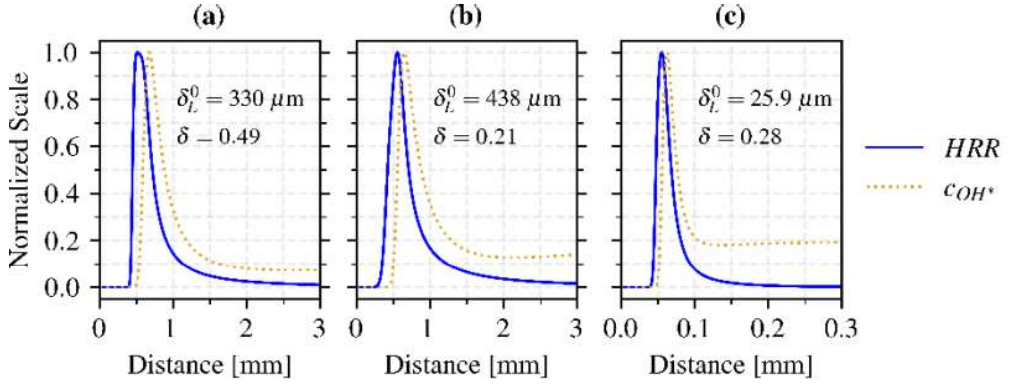

Figure 2. Normalized distributions of HRR and OH* concentration for unstrained premixed flames at ϕ = 1 and T_u = 300 K and p = 1 atm (a), T_u = 600 K and p = 1 atm (b), T_u = 600 K and p = 10 atm (c).

Even though case (a) presents the largest value of δ, the value of Z_{OH*} is the lowest (see Fig. 1a), since the two distributions have the two most similar shapes, mostly due to the reduced equilibrium OH* concentration when compared to the peak one. On the other hand, when increasing T_u and p, the equilibrium OH* concentration increases. Indeed, as the flame temperature increases, OH* production is favored in the post-flame region. The combination of these effects causes a reduction in the

likelihood of the two distributions, with a consequent increase of the value of Z_{OH^*}, even though the value of δ is lower, being the two peaks closer. Consequently, the sole Z_{OH^*} is not sufficient to characterize the correlation between OH* and HRR for H_2-air flames, as it gives a global evaluation of the quality of the correlation, but not an insight into the actual shape and position of the two distributions. As for the impact of operating conditions, it can be observed that, at atmospheric pressure, the peak shift is more accentuated, and is comparable between cases (a) and (b) in terms of physical distance. The different values of δ are in this case due to the increase of flame thickness for higher values of T_u. On the other hand, when pressure increases, the actual physical distance between the peaks is significantly smaller, even though it is more impacting in terms of δ with respect to case (b) due to the reduction of flame thickness given by the pressure increase.

To investigate the impact of flame stretch and regime on the peak shift, 1D stoichiometric twin premixed counterflow flames, for which two jets of premixed fresh gases are opposed to each other, and 1D counterflow diffusion flames, for which a jet of fuel is opposed to a jet of oxidizer, are considered. Flame strain is evaluated as $a = (|u_1| + |u_2|)/d$, where u_1 and u_2 are the inlet velocities of the jets, and d is their distance. The distributions of normalized OH* and HRR are shown, with the corresponding values of δ, in Fig. 3 for $a = 1.0\times10^4$ s^{-1}, a value of strain sufficiently high to highlight stretch effects and, at the same time, not too close to the extinction strain rate, which is approximately 1.8×10^4 s^{-1} for case (a) [5].

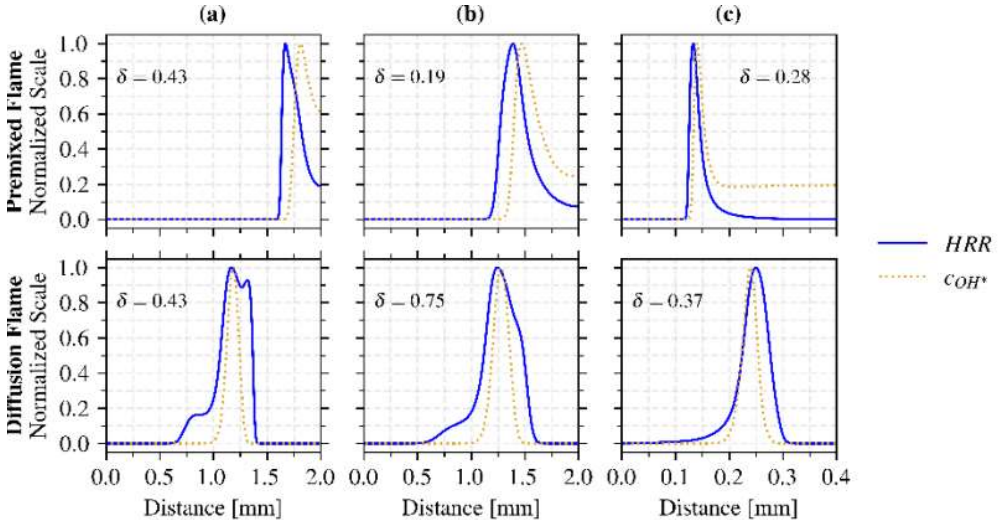

Figure 3. Normalized distributions of HRR and OH* concentration for premixed (top) and diffusion (bottom) counterflow flames at $a = 1.0\times10^4$ s^{-1} and $T_u = 300$ K and $p = 1$ atm (a), $T_u = 600$ K and $p = 1$ atm (b), $T_u = 600$ K and $p = 10$ atm (c).

For the premixed cases, stretch has a limited impact on the peak shift, which remains of the same order of magnitude as in the unstrained case.

On the other hand, the diffusion flames, at least for cases (a) and (b) at atmospheric pressure, show a sensible reduction of the peak shift. Due to the significantly smaller size of the flame front, no appreciable reduction in the peak shift can be found in

case (c). Nevertheless, an agreement in the shape of the distributions, which lacks in the corresponding premixed case, can be observed, sustaining the adequacy of OH* concentration as HRR marker in diffusion H_2-air flames.

Triple flame

The impact of flame regime on the OH*-HRR correlation is further analyzed by considering a 2D triple flame at T_u = 300 K and p = 1 atm, for which three zones can be identified: a lean premixed branch, a rich premixed branch, and a diffusion branch. The HRR fields are shown in Fig. 4 for the premixed (a) and diffusion (b) zones, together with isolines (white) of OH* concentration and the stoichiometric line (black). A sensible axial shift can be observed between the HRR and OH* peaks, with the former being located further down, in the rich premixed zone, while the latter is above, close to the stoichiometric line and in proximity of the triple point. On the other hand, the OH* distribution shows to be better correlated to the HRR one, with the two peaks located in the same region and the OH* field able to capture with sufficient adequacy the HRR variation in the whole zone.

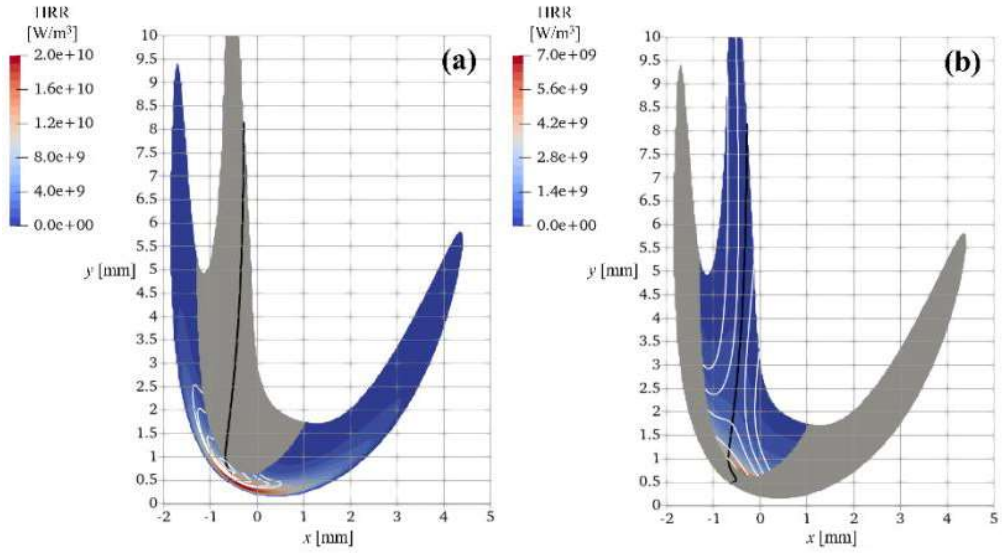

Figure 4. HRR distributions for a triple flame at T_u = 300 K and p = 1 atm in the premixed (a) and diffusion (b) zones, isolines (white) at 90%, 50%, 20%, 10% and 5% of maximum OH* concentration in each zone, and stoichiometric line (black).

Conclusion

In this work, the correlation between heat release rate (HRR) and OH* concentration in hydrogen-air flames has been investigated, focusing on the impact of operating conditions, in terms of unburned gas temperature, pressure, flame regime and stretch. By performing 1D calculations, it has been observed that OH* poorly correlates with HRR for premixed flames, with a sensible shift between the peaks of the two distributions, especially for low pressures, at all equivalence ratios. A similar behavior has been observed also for stretched premixed flames, while a significant improvement in terms of peak shift reduction has been found for diffusion flames.

This behavior has been confirmed also in a 2D triple flame, sustaining the adequacy of OH* as HRR marker for hydrogen-air diffusion flames only, while an error is to be considered for premixed cases. This is especially true for low-pressure cases, which are typical of OH* chemiluminescence experimental measurements.

Acknowledgments
The authors would like to acknowledge CERFACS for the grant to use the AVBP code. High-Performance Computing resources from CINECA (ISCRA-C Project INTONATE), MeluXina/LuxProvide and EuroHPC JU (Project PROMETH2EUS), and CRESCO/ENEAGRID are acknowledged. This work was supported by the Italian Ministry of University and Research under the National Recovery and Resilience Plan funded by the European Union - NextGenerationEU (Project: CNMS named MOST, CUP: D93C22000410001, Spoke 14 "Hydrogen and 11 New Fuels").

References

[1] Lauer, M., Sattelmayer, T., "On the adequacy of chemiluminescence as a measure for heat release in turbulent flames with mixture gradients", *J. Eng. Gas Turbines Power* 132(6): 061502 (2010).

[2] Panoutsos, C. S., Hardalupas, Y., Taylor, A. M. K. P., "Numerical evaluation of equivalence ratio measurement using OH* and CH* chemiluminescence in premixed and non-premixed methane–air flames", *Combust. Flame* 156(2): 273-291 (2009).

[3] Reyes, M., Tinaut, F. V., Giménez, B., Pastor, J. V., "Effect of hydrogen addition on the OH* and CH* chemiluminescence emissions of premixed combustion of methane-air mixtures", *Int. J. Hydrogen Energy* 43(42): 19778-19791 (2018).

[4] Marshall, G. J., Pitz, R. W., "Evaluation of heat release indicators in lean premixed H2/Air cellular tubular flames", *Proc. Combust. Inst.* 37(2): 2029-2036 (2019).

[5] Schiavone, F. G., Aniello, A., Riber, E., Schuller, T., Laera, D., "On the adequacy of OH* as heat release marker for hydrogen-air flames", *Proc. Combust. Inst.*, Manuscript accepted for presentation (2024).

[6] Saxena, P., Williams, F. A., "Testing a small detailed chemical-kinetic mechanism for the combustion of hydrogen and carbon monoxide", *Combust. Flame* 145(1-2): 316-323 (2006).

[7] Kathrotia, T., Fikri, M., Bozkurt, M., Hartmann, M., Riedel, U., Schulz, C., "Study of the H+O+M reaction forming OH*: Kinetics of OH* chemiluminescence in hydrogen combustion systems", *Combust. Flame* 157(7): 1261-1273 (2010).

[8] Graña-Otero, J., Mahmoudi, S. "Excited OH kinetics and distribution in H2 premixed flames", *Fuel* 255: 115750 (2019).

[9] Nikolaou, Z. M., Swaminathan, N., "Heat release rate markers for premixed combustion", *Combust. Flame* 161(12): 3073-3084 (2014).


THE COMBUSTION INSTITUTE
1954

SESSION II

Biomass and waste thermochemical processing, recycling and valorization


THE COMBUSTION INSTITUTE
1954

CHAR:ME: biochar and biomass-derived waste products as sustainable and safe domestic fuel.

Riccardo Caraccio[1], Million M. Afessa[1,2], Andrea Scialabba [3,6], Leonardo Signori [4], Davide Caregnato[5], Daniele Della Toffola[5], Carlo Ferrato[5], Tiziano Faravelli[1], Mauro Bracconi[4], Andrea Turolla[6], Matteo Pelucchi[1]
riccardo.caraccio@polimi.it

[1]Department of Chemistry, Materials and Chemical Engineering, Politecnico di Milano, Italy,
[2]Faculty of Mechanical Engineering, Jimma University, Ethiopia,
[3]Kukula ONLUS, Italy,
[4]Departement of Energy, Politecnico di Milano, Italy,
[5]Blucomb SRL, Italy,
[6]Department of Civil and Environmental Engineering, Politecnico di Milano, Italy

Abstract
Sub-Saharan Africa suffers from extensive forest exploitation, posing large threats to biodiversity and forest cover. The main driving forces are coal production and domestic cooking practices, which have a significant impact on both the environment and human health conditions. To tackle these challenges, the CHAR:ME initiative arises, focusing on repurposing organic wastes into solid fuels (biochar) as alternatives to wood and wood charcoal. Focusing on the Madagascar region of Antsiranana, the project revolves around the development of a new kind of biomass pyrolytic stove to substitute the obsolete technology, currently widely diffuse in these regions. This innovative stove uses biomass briquettes derived from local waste through mechanical compression and bio-drying techniques as feedstock. The gathering of experimental measurements to characterize the available biomass sources was carried out also considering the endangered species involved. Subsequently, the use of advanced scientific methodologies, such as semi-detailed kinetic mechanisms, and 0D and 1D models, were used to determine heating value and yields from the selected feedstock. Then, these models were coupled with full-scale reactor CFD simulation to drive and refine its design. Overall, the project streamlines the entire process from biomass waste generation to reactor operation, advocating for waste recovery and transformation to mitigate adverse environmental and social repercussions. Ultimately, this technology is planned for dissemination on a community scale, addressing the primary challenge of clean cooking in underdeveloped countries as outlined by international sustainability targets.

1. Introduction
The Malagasy Island is considered as a global hotspot of biodiversity, with a varied

and unique composition of flora and fauna. The country is estimated to host over 10'000 different species of plants and 800 species of vertebrates, with rates of endemicity over 80% [1]. In recent years, Madagascar has faced challenges in its development, mainly related to environmental degradation, and biodiversity loss, aggravated by factors like deforestation, population growth, and changing climate patterns. The country's biodiversity has become increasingly threatened, with estimates suggesting that Madagascar has lost at least 44% of its forest cover since the 1950s [2]. Widely diffused among the local population, the exploitation of forests for charcoal and fuelwood, mainly for cooking purposes, poses several concerns on both environmental and social aspects. It is estimated that over 11'000 cases of premature deaths, in Madagascar only, can be associated with pollutants and particulate matter substantially related to these daily activities [3]. The growing charcoal industry, coupled with the extension of agricultural land, is expected to accelerate deforestation, amplifying the impacts of climate change on a continent with a lower level of resources to handle such challenges [4]. The CHAR:ME project aims to propose and implement a sustainable loop to decrease the dependence on fuels from primary forests. This project is aligned with the United Nations's Sustainable Development Goals, encompassing health, clean energy, sustainable cities, responsible consumption, climate action, and life on land.

2. Biomass waste characterization

Focusing on the urban context of Hell-Ville, located on the northern island of Noisy Be, the best sources of available biomass wastes were identified. These mainly included wood shavings and sawdust, but also paper and cardboard, generated by the local carpentry activities. The elemental composition was determined for 5 different samples of local sawdust and for 15 different species of available biomasses. The analyses were performed through a Costech ECS Elemental Analyzer mod. 4010, which allowed for the contemporary measurement of C, H and N content for the samples; O content was determined by difference. Table 1 reports the measured composition of the 5 sawdust samples. Proximate analysis was performed using thermogravimetric analysis (TGA) using a Perkin Elmer SDT Q600. Tests between 30 and 900°C, with a temperature ramp of 10°C/min, both in oxidizing (using air) and inert (using nitrogen) conditions. Through these experiments, it was possible to determine volatile matter, fixed carbon, moisture, and ash contents for all the aforementioned samples. Fig 1. reports the mass loss versus temperature profiles in the presence of nitrogen: all the samples presented similar behavior in these conditions, with an average char yield of 20.71%.

3. Biomass briquetting process

Due to the problems related to the chip-like raw material (e.g., loss of materials during transportation, lower capacity of pyrolysis/gasification processes) and to facilitate processing the feedstock is assembled into briquettes. Through drying and mechanical compression processes, pellets of different dimensions were created

Table 1. Elemental composition of the collected samples (*composition DAF).

Sample	N (wt.%) *	C (wt.%) *	H (wt.%) *	Ash (wt.%)	Moisture (wt.%)
Sawdust_01	0.21 ± 0.02	44.48± 0.2	6.73 ± 0.5	0.00	0.49
Sawdust_02	0.15 ± 0.02	45.60 ± 0.2	7.70 ± 0.5	0.01	0.55
Sawdust_03	0.14 ± 0.02	47.1 ± 0.2	7.18 ± 0.5	0.19	0.60
Sawdust_04	0.37 ± 0.03	45.65 ± 0.2	6.67 ± 0.5	0.69	0.59
Sawdust_05	0.18 ± 0.01	48.81 ± 0.2	7.26 ± 0.5	0.00	0.56

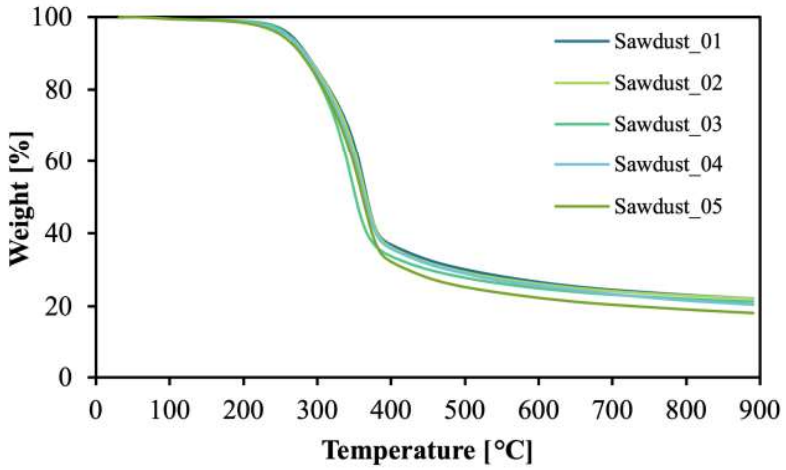

Figure 1. Mass loss profiles of the 5 sawdust samples with nitrogen.

starting from the raw materials previously analyzed. Furthermore, the possibility of mixing other types of available raw materials, such as paper and tapioca starch, was explored in order to increase the mechanical properties of the biomass briquettes. A total of 13 different compositions and compression pressure combinations were tested to find the optimal solution. Considerations about the size of biomass briquettes for improved process efficiency (i.e., for heat and biochar production), while considered as a primary project objective, is outside the scope of this study.

4. Particle Scale Modelling

The elemental analysis of the biomass samples allowed for estimating their chemical compositions, primarily in terms of cellulose, hemicellulose, and lignin, according to the approach by Ranzi et al. [5]. CRECK semi-detailed kinetic mechanism was used to predict the degradation behavior and pyrolysis products distribution. A 0D physical model disregarding heat and mass transfer phenomena was firstly used. Fig 2. reports the predicted curve (line) versus the experimental data (symbols) of the TGA experiments. The model correctly predicts the overall behavior of the samples, properly capturing the initial degradation (mostly due to hemicellulose and cellulose) with some shortcomings in the estimation of the char residue.

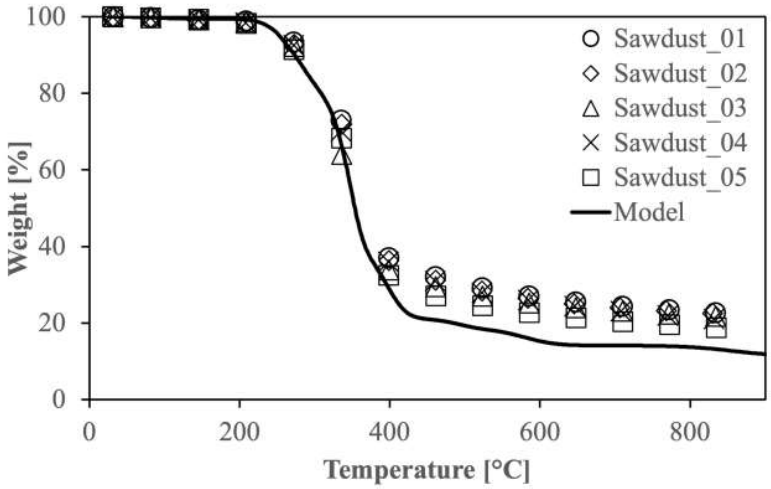

Figure 2. 0D model predictions vs experimental measurements.

The model was then coupled with a 1D isotropic spherical particle model to consider secondary gas-phase reactions and heating behaviors, allowing therefore address more rigorously the biomass briquette behavior. Fig 3a. shows the mass loss curves for a particle of 20 mm diameter considering different temperatures of the environment surrounding the briquette. Fig 3b reports instead the temperature at the core of the particle: the model shows e the expected overshot characteristic of particle-scale biomass degradation, which is due to exothermic charring reactions [6]. Furthermore, both in the 0D and 1D cases, it was possible to evaluate the product distribution and their relative yields, thanks to the detailed chemistry involved within the kinetic scheme.

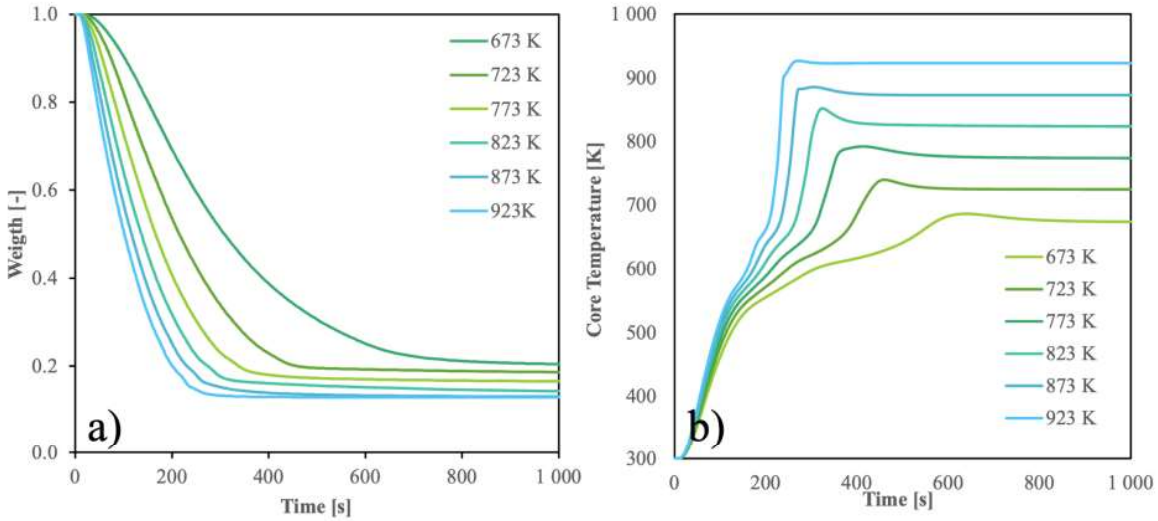

Figure 3. a) mass loss profiles and **b)** Core temperature at different external conditions

5. Pyrolytic hoven

The optimal solution for the design of the pyrolytic hoven is inspired by a "top-lit-up-draft" (TLUD) configuration [7]. A TLUD gasifier stove mainly includes two air

inlets: the first is located near the bottom, while the second is near the top, above the level of the loaded biomass. The fire is started at the topmost part, near the first air inlet; after a short ignition time, the oven moves into pyrolysis conditions, forming char and burning the tar fraction produced. As a result, beside a very stable and clean flame, the oven also produces biochar, which can be further utilized as fuel or stored for other needs. Through efficient air management, the production of pollutants is minimized, making it a far safer alternative than the current uses and currently available technologies (e.g. open fire, clay stoves with poor air and heat management). The technology is easily exploitable locally as the stove can be constructed from simple materials and scraps that are commonly accessible. The oven could easily allow for efficient char gasification by opening the bottom air vent and igniting the residual biochar, producing more clean thermal energy. However, since collecting the biochar is the main goal of this stove, we stop the reactor operations at the end of the pyrolysis step. Preliminary full-scale CFD reactor simulations were carried out. These models allow assessing the effects arising from a variety of fluid flow patterns (e.g. as resulting from shape and characteristic size of briquettes), non-uniform temperature distribution as from heat transfer resistances, and governing chemical reactions in the real device. Experimental measurements at the reactor scale are being performed on a stove prototype to validate the accuracy of the coupled CFD/chemistry models predictions and to further confirm the operational efficiency of the reactor.

6. Biochar Analysis

The previously mentioned (in Section 3.) 13 briquettes were pyrolyzed in the real scale reactor, collecting the residual biochar and analyzing it as in Section 2. obtaining data on TGA degradation profiles and elemental composition for all the samples. Additionally, the same analyses were performed on 3 samples of currently used Malagasy charcoal. From the elemental analysis it was possible to estimate the higher heating value (HHV) of the biochar using the Dulong correlation [8], here reported in Fig. 4. Estimates showed that the biochar produced by the pyrolysis oven has similar performance to the currently used charcoal, making it a suitable substitute for these applications. Furthermore, the use of the proposed oven allows for recovery of the heating energy lost in the charcoal production process, allowing also to further reduce the quantity of biomass used for the cooking activities.

7. Conclusions

The CHAR:ME project targets the design of a new pyrolytic stove for the contextual production of thermal power for cooking purposes and biochar in Sub-Saharan Africa. Moving from the assessment of fundamental physicochemical aspects such as biomass feedstock characterization and chemical kinetics of degradation this work presented preliminary results from the multiscale workflow to design an efficient apparatus, enabling the implementation of new sustainable technologies in underdeveloped countries. During the development of the project, characterization

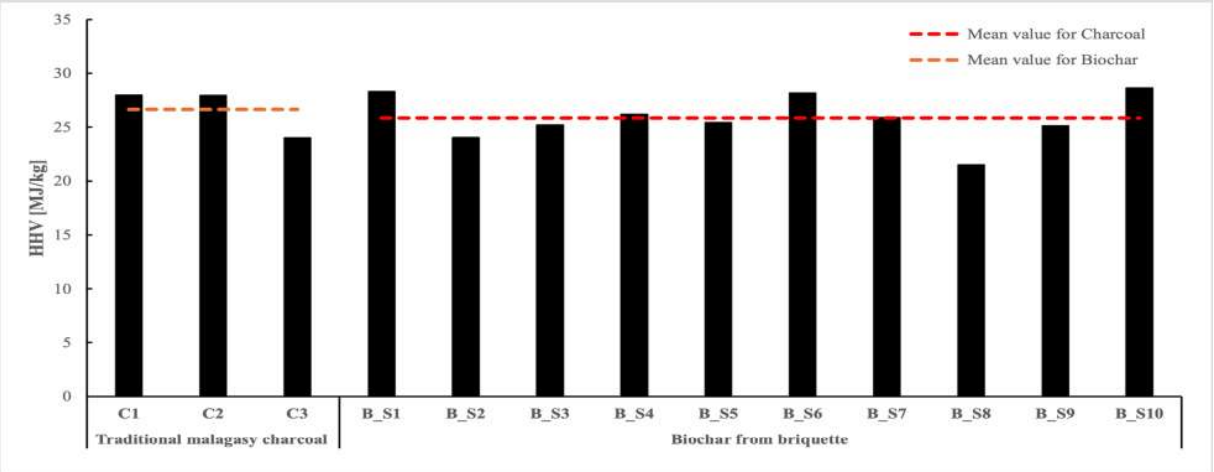

Figure 4. Estimates of the HHV of the analyzed biochar samples

data on many biomasses waste was collected. The use of kinetic models allowed for the prediction of the briquettes' behavior. Full scale reactor CFD simulations and experiments allowed to detect and correct bottle necks on the reactor design. Additional modelling activities (e.g. chemical reactor network) will specifically address flame properties and emissions of NOx and particulate matter to proof the beneficial effects of the proposed technology.

References

[1] S. M. Goodman and J. P. Benstead, "Updated estimates of biotic diversity and endemism for Madagascar," *Oryx*, vol. 39, no. 1, pp. 73–77, Jan. 2005, doi: 10.1017/S0030605305000128.

[2] G. Vieilledent *et al.*, "Combining global tree cover loss data with historical national forest cover maps to look at six decades of deforestation and forest fragmentation in Madagascar," *Biol Conserv*, vol. 222, pp. 189–197, Jun. 2018, doi: 10.1016/j.biocon.2018.04.008.

[3] WHO, "Indoor air pollution: national burden of disease estimates," Jan. 2007.

[4] A. Walsh, "The ordinary ethics of charcoal in northern Madagascar," *Journal of the Royal Anthropological Institute*, vol. 25, no. S1, pp. 108–123, Apr. 2019, doi: 10.1111/1467-9655.13017.

[5] E. Ranzi, P. Eduardo Amaral Debiagi, and A. Frassoldati, "Mathematical Modeling of Fast Biomass Pyrolysis and Bio-Oil Formation. Note I: Kinetic Mechanism of Biomass Pyrolysis," *ACS Sustainable Chemistry & Engineering*, vol. 5, no. 4, pp. 2867–2881, Mar. 2017, doi: 10.1021/acssuschemeng.6b03096.

[6] W. C. Park, A. Atreya, and H. R. Baum, "Experimental and theoretical investigation of heat and mass transfer processes during wood pyrolysis," *Combust Flame*, vol. 157, no. 3, pp. 481–494, Mar. 2010, doi: 10.1016/j.combustflame.2009.10.006.

[7] P. S. Anderson and J. S. Schoner, "Origins, history, and future of TLUD micro-gasification and cookstove advancement," *TLUD Technology*, 2016.

[8] F. Wilfrid and C. P. Martin, *Fuels and Fuel Technology*. Elsevier, 1980. doi: 10.1016/C2013-0-03303-8.

Gasification by O_2-enriched air and steam of two mixed plastic wastes in a large pilot scale fluidized bed gasifier

F. Parrillo*, C. Boccia*, F. Ardolino*, G. Calì, S. Meloni**, A. Pettinau**, U. Arena***

francesco.parrillo@unicampania.it

* Department of Environmental, Biological, Pharmaceutical Sciences and Technologies – University of Campania "Luigi Vanvitelli", Via Vivaldi, 43, 81100 Caserta, Italy

** Sotacarbo S.p.A., Grande Miniera di Serbariu, 09013, Carbonia, CI, Italy

Abstract

Advanced thermochemical technologies for plastic waste valorization represent an interesting alternative to waste-to-energy options. They promote the waste-to-hydrogen and waste-to-chemicals applications, with autothermal steam-oxygen gasification in fluidized bed reactors showing the greatest market potential. The study describes a series of experimental tests carried out at thermal and chemical steady state in a large pilot-scale fluidized bed gasifier, using steam and O_2-enriched air, with increasing fractions of oxygen, for two mixed plastic wastes (MPW). The aim was to investigate the gasification of MPW when the operating conditions gradually change from air-steam gasification to oxygen-steam gasification, with a focus on the effect of the reduced content of nitrogen, the role of steam in the reactor control, and the key process performance parameters. The tests were carried out at various O_2 molar fraction in the enriched-air stream (from 0.21 to 0.49, by keeping fixed the steam-to-carbon ratio at 0.75 mol/mol), and equivalence ratio (from 0.22 to 0.25) for two different mixed plastic waste.

Introduction

Plastic waste is a significant global issue with far-reaching environmental, economic, and social consequences [1]. Developing alternative materials to traditional plastics, improving advancing recycling technologies, and defining waste management schemes are necessary for well addressing the plastic waste problem.

Plastic waste gasification is an advanced thermochemical process that converts plastic waste in a syngas made of CO, H_2, CO_2, CH_4, and other light hydrocarbons, which can be converted into useful products, like transportation fuels and valuable chemicals [2]. One of the advantages of plastic waste gasification is that it can handle a wide variety of plastic types, including mixed or contaminated plastics that may be difficult to recycle through traditional mechanical methods. However, plastic waste gasification still presents several challenges related to the properties of plastic materials; the multi-scale nature of the process; the severe cleaning standards

required for syngas utilization; the scale-up implications [3].
The greatest techno-economic and sustainability potentials of fluidized bed plastic waste gasification [1; 2] are related to waste-to-hydrogen (WtH2) and waste-to-chemicals (WtCh) processes. In both these promising fields, autothermal gasification using steam and oxygen as fluidizing/gasifying media appears the best for a faster and efficient deployment. This is due to the numerous advantages provided by the production of a nitrogen-free syngas, including higher heating values, smaller volumes and unit operations associated, easier gas product separation, and better integration with CCS plants [4]. However, most of the industrial and experimental waste-fueled gasifiers were developed as air-blown rather than oxygen-blown, and only a limited experience exists in autothermal steam-oxygen operations, particularly on large (pilot and demonstrative scale) plants, as confirmed by recent techno-economic analyses [5]. Taking into account these considerations, the study described here reports the experimental results obtained with a large pilot scale, bubbling fluidized bed gasifier (BFBG) [4], operated with mixtures of steam and oxygen-enriched air, at increasing O_2 molar fraction, with two mixed plastic wastes. The aim was investigating the gasification of MPW when the operating conditions gradually change from air-steam gasification to oxygen-steam gasification, with a focus on the effects related to the reduced content of nitrogen, the operating criteria where steam operates as the reactor temperature moderator, and the estimate of reliable values of key process performance parameters.

Materials and methods

The pilot scale gasifier. The pilot scale BFBG employed in this study has a maximum thermal input of 400 kW, with a plastic waste capacity up to 50 kg/h, and a reactor total height (5.73 m) and internal diameter (0.489 m) that are large enough to exclude any scale-related implications [6]. This allows transferring obtained results to larger (even commercial) scale reactors, and it contributes to bridging the gap between research and industrial deployment. More details about the pilot scale gasifier can be found in Parrillo et al. [3].
The experimental procedure. The gasifier requires about 3 hours to be heated up to about 700°C by means of pre-heated blast gases and three electric heaters located along the reactor. At this temperature, the fluidizing gas and the plastic waste flow rates are set to obtain the desired values of the process parameters. Under the selected operating conditions, and without any thermal assistance of external heaters, the reactor gradually reaches thermal and chemical steady states, which are generally maintained for about 2 hours. During this time, gas and solids sampling procedures are activated and measurements of pressure, temperature, blast flow rates, and syngas composition are taken.
The plastic waste and the bed material. The bed material is made of Austrian olivine particles, having a size range of 200-400 μm, with a Sauter mean diameter of 316 μm, a particle density of 2900 kg/m^3 and a bulk density of 1600 kg/m^3. Olivine is a neo-silicate of Mg and Fe, which can be represented by the formula $(Mg,Fe)_2SiO_4$.

The plastic waste are polyolefin blends, named Blu-L and Blu-C, provided by Corepla (Italian Consortium for Plastic Packaging), and prepared by the I.Blu-Company [7] from non-recyclable residues of separated collection of plastics packaging. Table 1 reports its ultimate and proximate analysis (obtained via a LECO Truspec CHN/S), together with low heating value (LHV). Blu-C has a lower carbon content and calorific value than Blu-L and a higher ashes content.

Table 1. Plastic waste characterizations of the plastic waste granules.

	Blu-L	Blu-C
Ultimate analysis, %wt		
C	81.5	76.00
H	12.4	8.2
N	0.29	0.4
S	0	0.30
O	1.56	6.98
Moisture	0.52	0.9
Ashes	3.41	7.6
Proximate analysis, %wt		
Volatile matter	96.0	89.21
Fixed carbon	0.07	2.31
LHV, MJ/kg_{fuel}	38.7	31.1

Results and discussion

The tests with Blu-L and Blu-C were carried out by increasing the oxygen molar fraction (from 21% to 39% for Blu-L and from 21% to 49% for Blu-C) in the enriched-air, by keeping fixed the equivalence ratio value (ER=0.22) and the Steam to Carbon (StC=0.75 mol/mol). The ER value, considered relatively low compared to the typical ranges of autothermal gasification, was established to avoid the risk of overheating the reactor. The fluidization velocity is at constant values (0.5 m/s), able to ensure a good fluidization quality of the bed. A further series of tests was carried out with Blu-C to study the role of the steam in the control of reactor temperature, by increasing ER (in the range 0.21-0.26) and StC (in the range 0.88-1.41 mol/mol). Figure 1 shows the bed temperature obtained by varying the O_2 molar fraction, with Blu-L and Blu-C.

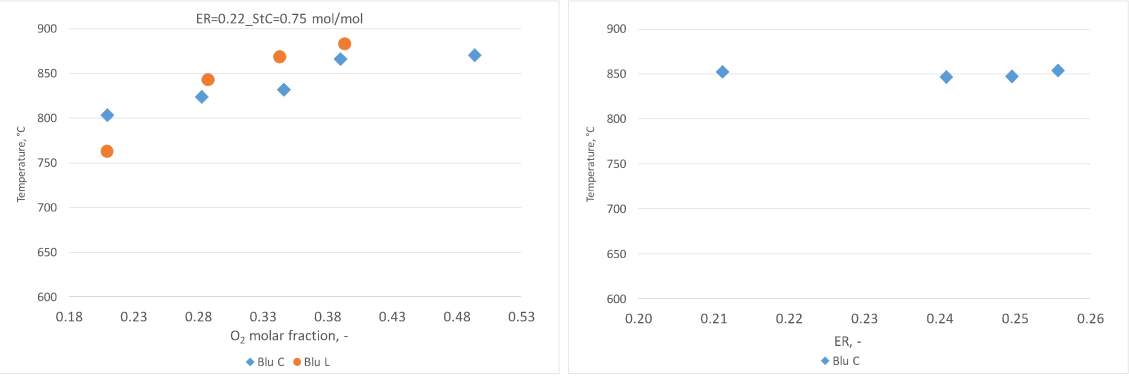

Figure 1. Bed temperature obtained i) by varying the O_2 molar fraction, with Blu-L and Blu-C (left); ii) by varying the ER and the StC to keep the reactor temperature at a constant value (right).

The experimental tests with Blu_L (which has the higher LHV) at increased oxygen content resulted in a progressive increase of bed temperature, since the amount of nitrogen removed was not counterbalanced by a sufficient additional amount of steam. Test with Blu-C (which has the lower LHV) showed a rather similar trend in the bed temperature, but the latter was more easily managed, even with O_2 molar fractions as high as 50%. The role of moderator played by the steam in substitution of the nitrogen appeared crucial: Figure 1 (right) shows that an appropriate increase in the steam flow rate, i.e. an increase of the StO2 ratio, allowed to keep constant the bed temperature, even under higher values of ER.

Figure 2 shows the syngas composition for the comparable tests with Blu-L and Blu-C (top) and for those with Blu-C at a fixed bed temperature (bottom). The reported dry and nitrogen free syngas compositions avoid trends linked to the dilution of the two moderators (nitrogen and steam). For the tested MPWs (Figure 2, top), the higher O_2 percentage in the enriched air indirectly enhances the endothermic reactions involving steam, especially Water Gas and Steam reforming of CnHm, due to the related reactor temperature increase. This explains the increase in terms of CO_2 and H_2, against the reduction of CnHm. Methane and BTX are apparently less influenced by the variations of the involved parameters. The diagram at the bottom of Figure 2, related to test at an almost constant temperature, indicates that ER affects syngas composition mainly in the content of carbon dioxide. The constant temperature along the reactor determines a limited variation of the syngas concentrations of other components.

Figure 3 shows H_2/CO ratio and LHV_{syngas} of the syngas obtained in the comparable tests with Blu-L and Blu-C (top) and by keeping fixed the reactor temperature with Blu-C (bottom). H_2/CO ratio is close to the values of interest for hydrogen and SNG production [2].

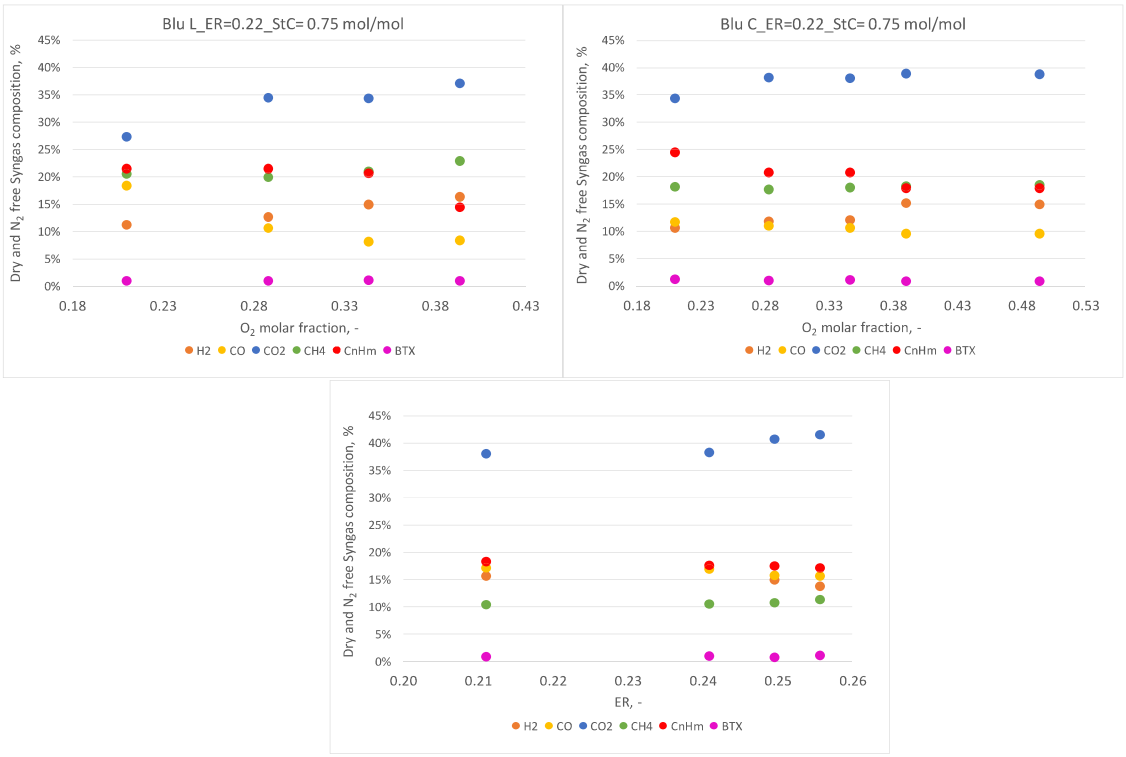

Figure 2. Syngas composition obtained by varying the O_2 molar fraction, with Blu-L (top-left) and Blu-C (top-right), and by keeping bed temperature constant by appropriate variation of ER and StC, with Blu-C (bottom).

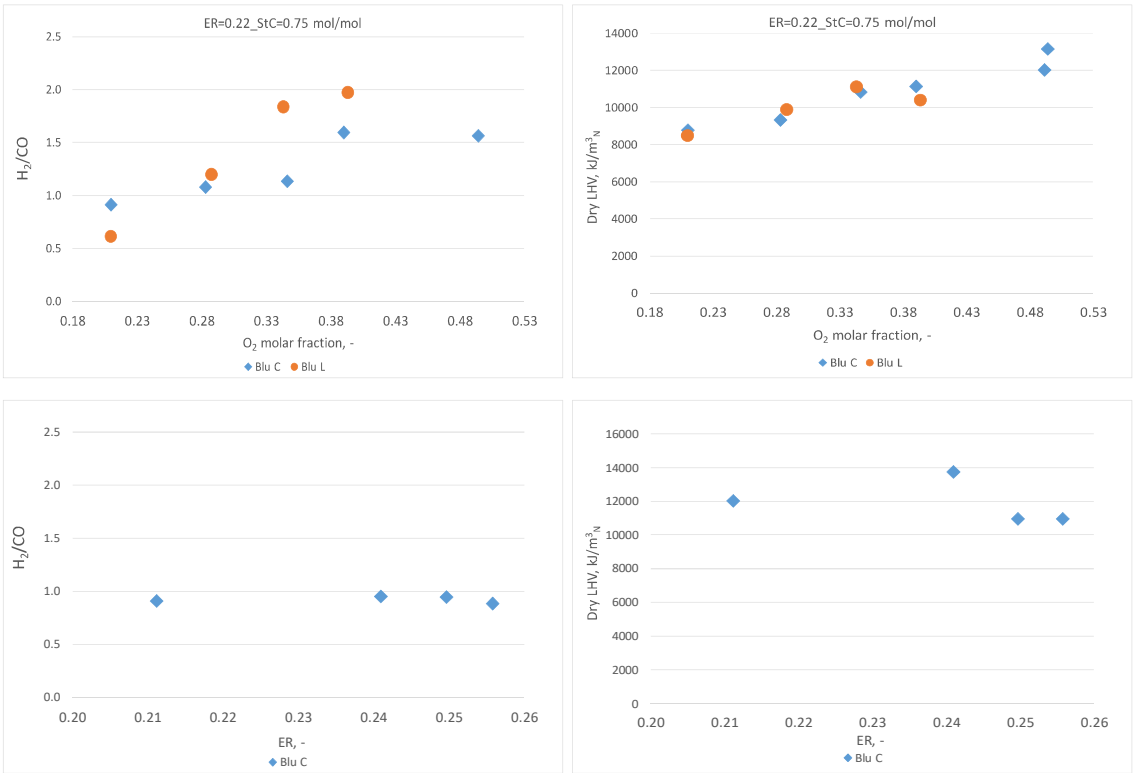

Figure 3. H2/CO ratio and the LHV_{syngas} by varying the O_2 molar fraction, with Blu-L and Blu-C (top), and by varying the ER and the StC with Blu-C (bottom).

Conclusions

The autothermal MPW gasification was investigated by means of pilot-scale experiments in a large bubbling fluidized bed reactor. The gasifier was operated with steam and O2-enriched air, at increasing fractions of oxygen, keeping fixed the equivalence ratio, steam-to-carbon ratio, and steam-to-oxygen ratio. The results indicate that the reactor can be operated as an oxygen-steam gasifier for MPW of moderate-high calorific value, only if an appropriate flow rate of steam can be injected in the reactor. Steam has the key role of moderator of the reactor temperature, whereas it has a limited influence on the syngas composition. The equivalence ratio is an important operating parameter since it largely affects the reactor temperature, which appears the variable that, in turn, more affects the syngas composition.

References

[1] Arena, U., Parrillo, F., Ardolino, F., An LCA answer to the mixed plastics waste dilemma: Energy recovery or chemical recycling? Waste Manage., 171, 662–675 (2023)

[2] Hofbauer, H., and Materazzi, M., "Waste gasification processes for SNG production". In: Materazzi M, Foscolo PU, editors. Substitute natural gas from Waste. Technical assessment and industrial applications of biochemical and thermochemical processes. Elsevier. 105-60 (2019)

[3] Parrillo, F., Ardolino, F., Calì, G., Pettinau, A., Materazzi, M., Sebastiani, A., Arena, U., Plastic waste gasification using oxygen-enriched air and steam: experimental and model results from a large pilot-scale reactor. Waste Manage. 183 pp. 53-62. (2024)

[4] Materazzi, M., Chari, S., Sebastiani, A., Lettieri, P., Paulillo, A., Waste-to-energy and waste-to-hydrogen with CCS: Methodological assessment of pathways to carbon-negative waste treatment from an LCA perspective. Waste Manage. 173, pp. 184-199. (2023)

[5] Afzal, S., Singh, A., Nicholson, S.R., Uekert, T., DesVeaux, J.S., Tan, E.C.D., Dutta, A., Carpenter, A.C., Baldwin, R.M., Beckham, G.T., Techno-economic analysis and life cycle assessment of mixed plastic waste gasification for production of methanol and hydrogen. Green Chem., 25, 5068. (2023)

[6] Cocco, R.A. and Chew, J.W., Fluidized Bed Scale-Up for Sustainability Challenges. 1. Tomorrow's Tools. Ind. Eng. Chem. Res., 63, 2519-2533 (2024)

[7] I.Blu. https://www.iblu.it/en/products.html (2022)

PROCESS MODELING OF THE PRODUCTION OF SYNTHETIC NATURAL GAS FROM BIOMASS-DERIVED SYNGAS

R. Ruggiero*, A. Coppola, M. Urciuolo**, F. Scala*,****
roberto.ruggiero4@unina.it
* DICMaPI, Univeristà di Napoli Federico II, P.le Tecchio 80, 80125, Napoli, Italy
** STEMS, CNR, P.le Tecchio 80, 80125, Napoli, Italy

Abstract
The production of Synthetic Natural Gas (SNG) by syngas obtained from biomass gasification is a challenging process. In particular, since methanation (as Fisher-Tropsh synthesis) is conducted catalytically, strict limits are present in terms of undesired species in the produced gas before the fuel synthesis stage. Moreover, if the syngas is obtained through air-gasification also the hydrogen content should be improved through an appropriate conditioning stage, to obtain a reasonable yield in the desired product. In this work, a brief description of the cleaning and conditioning stages required to improve the quality of the syngas is proposed, and three configurations for the methanation stage of the improved syngas obtained through air gasification of biomass are analyzed and discussed.

Introduction
The synthesis of fuels from renewable sources is considered to be an interesting option for the aim of reducing the carbon footprint of sectors like industries and transport [1]. Numerous approaches can be adopted to reach this objective including biological processes such as the fermentation of sugars, the use of renewable electricity to obtain hydrogen and the so so-called e-fuels, or the use of residual lignocellulosic biomass. The latter is particularly interesting because residual biomass is abundant as a waste stream from other processes, and it is not expensive. In addition, biomass is known to be carbon neutral, since the carbon dioxide emitted by the exploitation of this feedstock is equal to that stored by the biomass during its lifetime. In this work, the focus was put on the synthesis of SNG starting from biomass-derived syngas. In particular, the next section presents the steps required to obtain a valuable product, since the raw syngas obtained through gasification is not suitable for direct synthesis. Cleaning and conditioning stages are required to improve the syngas quality and to make it suitable for methanation. Then three possible configurations for the methanation stage are presented.

Cleaning and conditioning stages
Since biomass has a heterogeneous composition, numerous undesired species can be found in the product syngas, like HCl, H_2S, alkali metals, particulate matter, and tars.

These species and, in particular, tars are related to the operating conditions and the different type of gasification agent (air, oxygen, or steam), and also to the reactor configuration. To obtain a suitable gas for further utilization some requirements have to be satisfied and these limits are related to the use of the gas.

Contaminant	Application			
	IC engine	Gas turbine	Methanol synthesis	FT synthesis
Particulate (soot, dust, char, ash)	<50 mg m^{-3} (PM10)	<30 mg m^{-3} (PM5)	<0.02 mg m^{-3}	n.d.[a]
Tars (condensible)	<100 mg m^{-3}		<0.1 mg m^{-3}	
Inhibitory compounds (class 2-heter atoms, BTX)				<0.01 μL L^{-1} <1 μL L^{-1}
Sulfur (H_2S, COS)		<20 μL L^{-1}	<1 mg m^{-3}	<0.01 μL L^{-1}
Nitrogen (NH3, HCN)		<50 μL L^{-1}	<0.1 mg m^{-3}	<0.02 μL L^{-1}
Alkali		<0.024 μL L^{-1}		<0.01 μL L^{-1}
Halides (primarily HCl)		1 μL L^{-1}	<0.1 mg m^{-3}	<0.01 μL L^{-1}

Figure 1. Typical syngas applications and associated cleaning requirements [2].

In Fig. 1 (taken from [2]), it can be seen that more stringent limits are required when fuel synthesis is considered, in order to avoid catalyst poisoning. In particular, limits related to tar content are quite challenging to be satisfied, since the other contaminants can be more easily removed using sorbents that work at high temperature, such as ZnO [3], Al_2O_3, CaO [4], or by low-temperature operations such as wet scrubbers [2]. In the tar content also molecules like benzene, toluene and xylene are considered, which usually are not removed in other processes such as in CHP applications. To remove heavier tars and part of the BTX contained in the raw gas the approach ideated by ECN named as OLGA process [5] which involves the use of two scrubber columns with liquid rapeseed methyl ester, seems to be the most interesting choice, since it combines good thermal efficiencies and good removal of such undesired species. After this stage, to obtain that specification on the tar levels, a further polishing stage is required like the utilization of an active carbon bed, as done in [6], or a pre-reforming stage where at a temperature of around 500 ºC the gas leaving the process is mixed with steam to obtain the conversion of BTX in syngas. Here also part of the carbon monoxide is converted into carbon dioxide and extra hydrogen trough the water gas shift reaction. In addition, if the syngas has to be used in a fuel synthesis stage like methanation, the ratio between hydrogen and carbon monoxide should be at least equal to three, in order to obtain stoichiometric conditions, otherwise part of the reactants will not react. So to obtain such ratio other stages can be added as the pre-reformer described above or a water gas shift section to improve the hydrogen content, or alternatively hydrogen obtained from the surplus of renewable sources such as wind or solar energy through the electrolysis of water [7] can be added to the syngas to improve the H_2/CO ratio. These are considered as conditioning stages required before the methanation stage.

Fuel synthesis stage

After the correct design of the previous stages, it is possible to convert the upgraded syngas through methanation into SNG. In this work, three schemes have been evaluated based on the syngas obtained through air gasification of wood chips, and improved to reach a ratio between hydrogen and carbon monoxide equal to three using a water gas shift reactor.

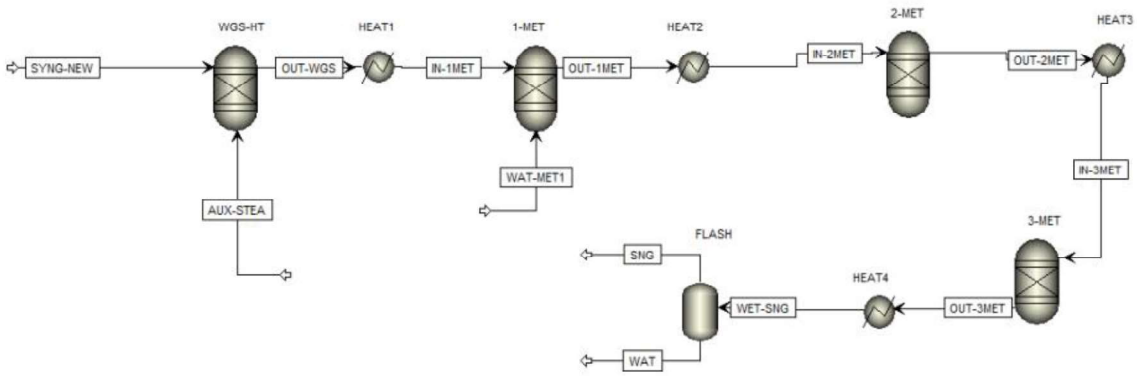

Figure 2. First configuration studied to obtain SNG, named configuration (a)

Figure 2 reports the Aspen flowsheet of the first configuration, which works without the use of external hydrogen. Methanation is carried out in three adiabatic Gibbs reactors, with intermediate cooling, simulating the typical plug flow reactors configuration for this process, as seen in [8]. Temperature and an auxiliary water stream are chosen such to avoid solid carbon formation, to increase the methane yield, and to avoid too high temperature-related issues like sintering of the commonly used Ni catalyst [8]. Then after the last reactor, a flash is used to remove the water obtained from the methanation reactors. In Table 1 the molar composition of the stream that enters the first methanation reactor of the flowsheet, named IN-1METH, and of the stream with the final product named SNG, are reported.

Table 1. Molar composition of "IN-1MET" and "SNG" streams of configuration (a)

Composition (%mol)	**IN-1METH**	**SNG**
CO	5.81	0.02
CO_2	21.11	30.22
H_2	18.37	2.16
CH_4	3.33	12.79
N_2	33.97	48.33
H_2O	17.41	6.48

From this table, it is possible to observe that almost all of the carbon monoxide has reacted and consequently also the hydrogen content has been greatly reduced. However, in configuration (a), which is the easiest configuration studied for the fuel synthesis stage, the final product is rich in CO_2, which has to be removed in a further

stage to improve the SNG characteristics, such as the lower heating value and the Wobbe Index. It must be noted, on the other side, that in this case, as in the Vesta process [8], carbon dioxide acts in preventing high temperatures from being reached. In this way, all the issues related to high-temperature applications are avoided, but of course the methane yield will be reduced.

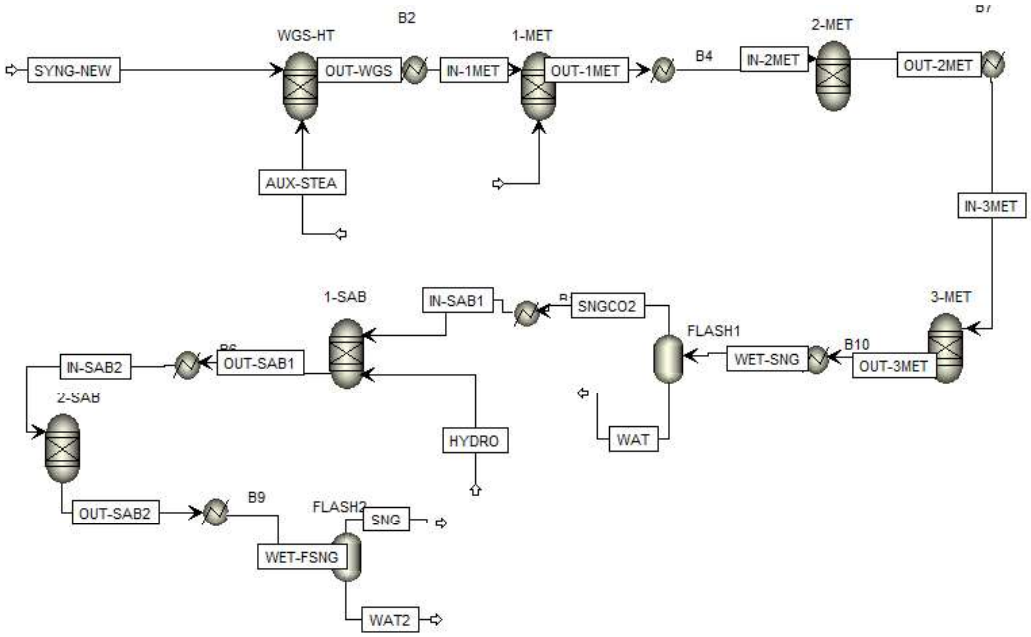

Figure 3. Second configuration studied to obtain SNG, with PtG application, named configuration (b)

Figure 3 reports the second configuration (b), with a power-to-gas application [9], which has been adopted also in [10]. Here hydrogen obtained from renewable sources, like wind or solar energy, can be added to improve the methane yield, converting part of the carbon dioxide that in the first configuration did not react. To reach this goal, two additional Gibbs adiabatic reactors (1-SAB and 2-SAB), working with an initial temperature of 250 °C and with intermediate cooling have been used as suggested in [10]. The quantity of external hydrogen utilized was selected thanks to a sensitivity analysis to balance between the amount of un-reacted hydrogen at the exit and the conversion of carbon dioxide for the scheme described above. In Tab. 2 we can observe that almost half of the carbon dioxide present in the gas that enters the first polishing reactor is converted mainly towards our desired product which is methane. All the simulations were conducted at atmospheric pressure, which is not the best option for a process that involves a decrease of the number of moles, and even if we are considering a favorable working temperature, 250 °C < reactor inlet temperature < 300 °C, the conversion is still far from unity. Working at more elevated pressure or adding additional reactors in series with intermediate cooling would help the system to convert more reactants, in this case mainly hydrogen and carbon dioxide, obtaining a final gas with improved CH_4 content, but at the expenses of a higher plant cost.

Table 2. Molar composition of "IN-SAB1" and "SNG" streams of configuration (b)

Composition (%mol)	IN-SAB1	SNG
CO	0.02	0.34
CO_2	30.22	17.71
H_2	2.16	7.83
CH_4	12.79	22.32
N_2	48.33	45.33
H_2O	6.48	6.47

It was verified then that adding another methanation unit (3-SAB) to configuration (b) working at the same conditions as the other carbon dioxide conversion units, and utilizing the stoichiometric hydrogen required to theoretically completely convert the CO_2 present in the stream IN-SAB1, will lead to a final product in which the main components are: N_2 (41%), CH_4 (31%), CO_2 (4.8%), H_2 (15.5%), H_2O (6,4%), CO (negligible). This limiting case is obtained at p=1 atm and it is shown below in Fig. 4, and named configuration (c).

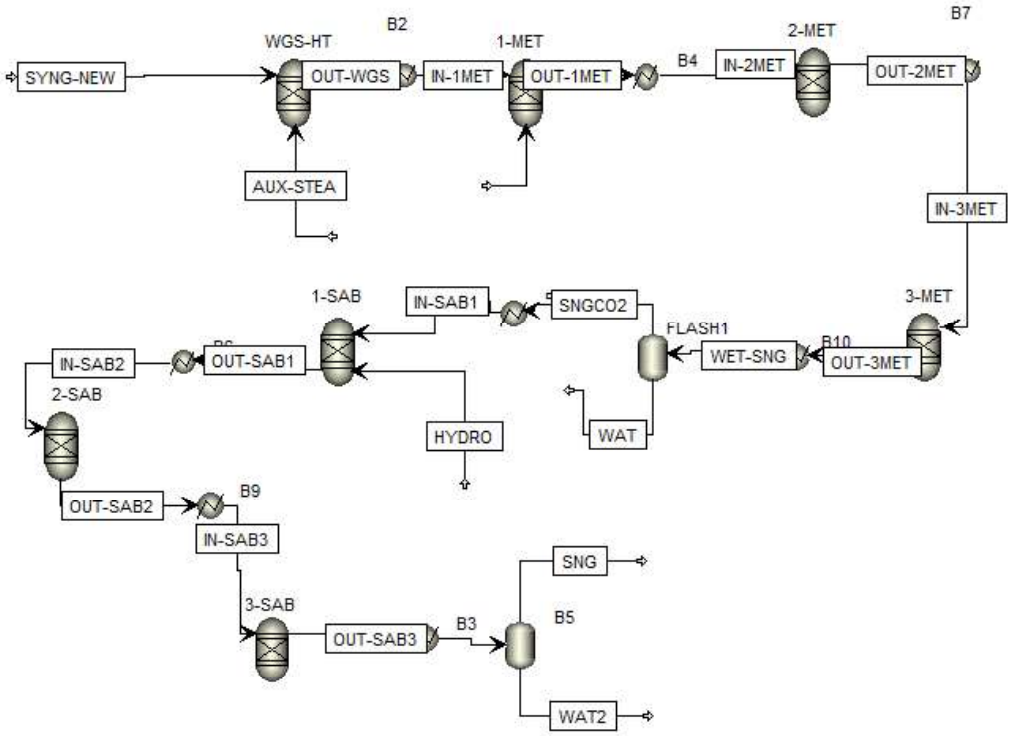

Figure 4. Third configuration studied to obtain SNG, with three additional reactors for CO_2 methanation, named configuration (c).

Next steps

The Olga process and a pre-reforming stage will be integrated into the Aspen model through equilibrium simulations for real syngas with tar-species, to describe this challenging required cleaning stage. Subsequently, a kinetic approach will be

followed to design the units required for the cleaning and the fuel synthesis stages leveraging what was learned from this initial equilibrium approach.

References

[1] Kralova, I., Sjöblom, J., "Biofuels–renewable energy sources: a review." *Journal of Dispersion Science and Technology* 31.3: 409-425 (2010)

[2] Woolcock, P.J., Brown, R.C., "A review of cleaning technologies for biomass-derived syngas." *Biomass and bioenergy* 52: 54-84 (2013)

[3] Tamhankar, S.S., Bagajewicz, M., Gavalas, G. R., Sharma, P. K., & Flytzani-Stephanopoulos, M., " Mixed-oxide sorbents for high-temperature removal of hydrogen sulfide." *Industrial & Engineering Chemistry Process Design and Development*, *25*(2), 429-437 (1986)

[4] Zhao, Y., Liu, G., Huang, J., Veksha, A., Wu, X., Giannis, A., Lim, T.T., Lisak, G.,"Sorbents for high-temperature removal of alkali metals and HCl from municipal solid waste derived syngas." *Fuel*, 321 (2022)

[5] Rabou, L.P., Zwart, R.W., Vreugdenhil, B.J., Bos, L. "Tar in biomass producer gas, the Energy research Centre of the Netherlands (ECN) experience: an enduring challenge." *Energy & Fuels*, *23*(12), 6189-6198 (2009)

[6] Thunman, H., Seemann, M., Berdugo Vilches, T., Maric, J., Pallares, D., Ström, H., Berndes, G., Knutsson, P., Larsson, A., Breitholtz, C., Santos, O., "Advanced biofuel production via gasification–lessons learned from 200 man-years of research activity with Chalmers' research gasifier and the GoBiGas demonstration plant." *Energy Science & Engineering*, *6*(1), 6-34 (2018)

[7] Ozturk, M., Dincer, I. "A comprehensive review on power-to-gas with hydrogen options for cleaner applications.," *International Journal of Hydrogen Energy*, *46*(62), 31511-31522 (2021)

[8] Rönsch, S., Schneider, J., Matthischke, S., Schlüter, M., Götz, M., Lefebvre, J., Prabhakaran, P., Bajohr, S., "Review on methanation - From fundamentals to current projects." *Fuel*, 166: 276–96 (2016)

[9] Thema, M., Bauer, F., Sterner, M., "Power-to-Gas: Electrolysis and methanation status review." *Renewable and Sustainable Energy Reviews*, 112, 775-787 (2019)

[10] Bassano, C., Deiana, P., Vilardi, G., Verdone, N., "Modeling and economic evaluation of carbon capture and storage technologies integrated into synthetic natural gas and power-to-gas plants." *Applied Energy*, *263*, 114590 (2020)

PB FATE DURING PYROLYSIS OF HEAVY METALS CONTAMINATED BIOMASS

Davide Amato*, Paola Giudicianni*, Corinna Maria Grottola*, Fernando Stanzione*, Raffaele Ragucci*
davide.amato@stems.cnr.it
* Institute of Science and Technology for Sustainable Energy and Mobility (STEMS-CNR), V.le Marconi 4, 80125, Naples, Italy

Abstract
In the context of renewable energy and alternative fuels, "unconventional" lignocellulosic biomass is attracting great interest. An example of this biomass is represented by heavy metals contaminated biomass that come from polluted sites (i.e. marginal lands). Pyrolysis is a promising thermochemical valorization treatment for contaminated biomass; however, the presence of heavy metals raises environmental concerns tied both to their release during the process and to the utilization of the contaminated pyrolysis products. Therefore, it is fundamental to consider the heavy metals displacement among pyrolysis products and their chemical speciation when processing heavy metals contaminated biomass.
This work investigates the behavior of lead (Pb) in terms of Pb recovery in the char and its chemical speciation at different pyrolysis temperatures, focusing on the effects of different initial Pb chemical speciation and contamination type (e.g. detrital or authigenic), which correspond to the type of bond between the heavy metal and the biomass tissues.
To this aim, two sets of experiments are conducted. To consider the effect of the initial Pb chemical speciation a chosen biomass, poplar, is doped with two different lead salts, namely lead nitrate ($Pb(NO_3)_2$) and lead acetate ($Pb(CH_3COO)_2$). To simulate different contamination types, the same biomass is demineralized and then doped with lead acetate ($Pb(CH_3COO)_2$) following three different procedures (i.e. dry mixing, wet impregnation and ion exchange). All the doped and the reference feedstocks are then pyrolyzed at three pyrolysis temperatures, 465, 600 and 800 °C, and the produced chars are analyzed to determine Pb content and chemical speciation.
From the obtained results it emerges that while initial Pb speciation has a marginal influence on Pb recovery in char, it clearly affects the chemical form of the retained Pb. On the other hand, different contamination types affect both Pb recovery in char and its chemical speciation, hinting at the relevance of this parameter.

GREEN LITHIUM RECOVERY FROM LFP CATHODES: A STUDY ON AIR-ASSISTED ORGANIC ACID LEACHING

B. Visone*, O. Senneca*, R. Chagtmi*, B. Apicella*
biagio.visone@stems.cnr.it
*Istituto di Scienze e Tecnologie per l'Energia e la Mobilità Sostenibili (STEMS), Naples, Italy

Abstract
Lithium iron phosphate batteries are now getting increasing attention due to their low cost, good cycling stability and high safety characteristics. Enhanced batteries consumption is accompanied by their subsequent discard that, if poorly managed, may cause serious environmental damage as well as severe economic losses.
Since the first adoption of $LiFePO_4$ as a battery component in 1996, numerous cathode recycling methods have been developed, including traditional pyro/hydrometallurgical methods as well as direct regeneration approaches. This paper, after a short review of the most relevant spent cathode treatments, presents preliminary results of a green recovery process, based on the selective extraction of lithium from LFP powders through the combined action of malic acid and oxygen in a semi-batch reactor with continuous air blowing.

Introduction
Driven by the need to cut greenhouse gas emissions and address the depletion of fossil fuels, the adoption of clean technologies has surged at an unprecedented rate in recent years. This trend was accompanied by an increasing need for energy storage devices, which pushed lithium-ion batteries (LIBs) to the forefront.
Currently, the most used LIBs can be classified based on the crystal structure of their cathodes into three types: spinel, layered, and polyanion. Polyanionic compounds, particularly $LiFePO_4$ (LFP) cathodes, have gained increasing success in recent years. This tendency is explained by their low cost and by their long life and high safety due to the strong Fe-O and P-O bonds which make their olivine structure extremely stable [1]. It is natural to assume that such a significant increase in sales of LFP batteries will go hand in hand with an increase in their scrapping and, as their average life is 5-10 years, this will soon become a global issue. Failure to properly dispose of these devices would not only cause serious pollution problems due to the release of toxic compounds into the environment but would also lead to the loss of strategic elements such as lithium and phosphorus, which are considered critical raw materials by the European Union [2]. However, conventional recycling techniques for spent batteries are not as profitable as expected when applied to LFP cathodes due to the lower value of lithium and iron compared to nickel, cobalt and manganese. Researchers are therefore focusing on the development of shorter and less chemical-

intensive processes and the direct regeneration of such materials [3].
This paper presents a short review of the most significant existing literature on the recovery of $LiFePO_4$ cathodes, specifically focused on the most recent and environmentally friendly methods. Moreover, preliminary results obtained performing the selective extraction of lithium from LFP powders through the combined action of malic acid and oxygen in a semi-batch reactor with continuous air blowing was reported.

LiFePO4 cathode recycling

Although not the main culprit in battery degradation, attention is focused on recycling LFP cathodes due to their valuable materials content and production complexity. As shown in Fig. 1a, the initial step to obtain spent cathode powder involves pre-treating retired batteries through discharging, dismantling, and separation. Once the active material is obtained, it is either recovered to restore its electrochemical properties or separated into its components.

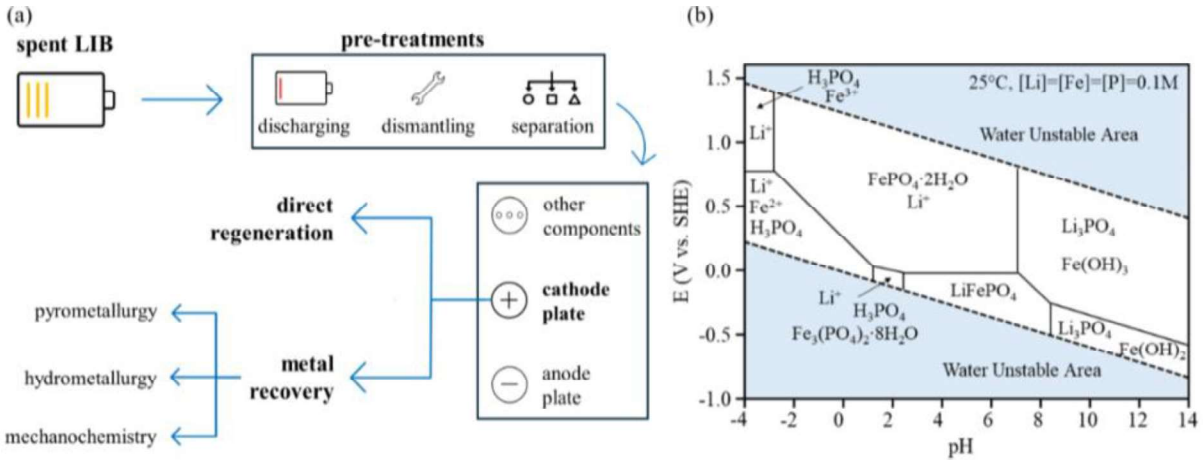

Figure 1. (a) Schematic representation of possible spent LIBs recycling routes. (b) Pourbaix diagram for the Li-Fe-P-H_2O system. Adapted from [4].

Metal Recovery

Following are the main techniques for recovering metals from spent LFP battery cathodes, including pyrometallurgy, hydrometallurgy and mechanochemistry.
Pyrometallurgy is a process that uses high temperatures to cause physical and chemical changes that allow for metal recovery [5]. It was traditionally used to extract valuable metals from ores but has become the go-to technology in the LIBs recycling industry due to its operational simplicity [6]. The extractive pyrometallurgical options used to process spent lithium-ion batteries are roasting/calcination and smelting [7], which differ mainly in operating temperature and atmosphere. Zhang et al. analysed LFP roasting in a sulphatising atmosphere [8]. Results showed that a mild temperature (600°C) reaction with sodium-bisulphate can convert lithium inside the olivine structure of the cathode into water-soluble sulphate, leaving Fe-P-O containing species in the solid state. Carbothermic

reduction (CTR) has also been investigated as a Li recovery procedure [24].
With the advantages of high metal recovery and reduced energy consumption, hydrometallurgical techniques are the preferred ones for spent LFP treatment. The typical hydrometallurgical process consists of a leaching step, aimed at dissolving all or part of the components of the cathode in an aqueous medium, followed by a purification stage. Based on the reagent used to solubilize the cathode, these processes can be categorized into inorganic acid leaching, organic acid leaching and acid-free leaching. An essential element in comprehending the distinctions between these leaching agents is the analysis of Pourbaix diagrams (Fig. 1b). Indeed, wet LFP recovery processes are contingent upon the thermodynamic equilibrium of the Li-Fe-P-H_2O system, which is a function of the pH and redox potential of the solution, as well as the temperature of the system and the liquid phase concentration of the species [4].
Strong inorganic acids can effectively leach Li, Fe and P out of the spent cathode at relatively low temperature as they provide suitable pH conditions for the generation of water-soluble species form the spent cathode powder. Sulphuric acid [9], phosphoric acid [10], pyrophosphoric acid [11] and hydrochloric acid [12] are examples of mineral lixiviants that researchers have investigated. Anyhow, being characterized by large acid consumption and non-selective extraction, these processes require the adoption of complicated metals separation steps and onerous wastewater treatments which limits their economic return. The use of oxidising agents or appropriate pre-treatments can alleviate these problems by enabling selective lithium recovery [4].
In view of the environmental risks associated with the use of mineral lixiviants, organic acids have become a major focus of research in the last few years [13]. This trend can be explained by the fact that, in addition to providing metal leaching efficiencies comparable to those of inorganic acids, these substances offer several advantages such as biocompatibility, mild operating conditions and facile downstream recovery [14]. Zhou et al. [15] proposed a closed-loop process exploiting the synergistic interaction between malic acid and hydrogen peroxide which enabled the occurrence of an in-situ reaction directly converting the olivine structure of $LiFePO_4$ to the olivine structure of $FePO_4$. In the work of Yang et al. [16], relatively cheap acetic acid was used, together with H_2O_2, to achieve Li recovery. By using the cathode plate directly as starting material rather than the previously scratched powder, researchers were able to simplify the recycling process, demonstrating the high selectivity of organic lixiviants towards Al impurities. Leaching with formic acid/H_2O_2 systems was explored by Mahandra and Ghahreman [17]. An oxidant free organic acid treatment was proposed by Chai et al. [18]. Using oxalic acid alone, more than 99% of the lithium present in the spent cathode powder, with only 2.4% Fe moving to the liquid phase, was extracted through a reaction carried out at 90°C for 60 minutes. Attempts to avoid using H_2O_2 are noteworthy because, although it only gives off oxygen and water as decomposition products, it cannot be considered a green reagent due to its energy-

intensive production process [19]. Kumar et al. [20] investigated the possibility of using citrus fruit juices as leaching agents. Lemon juice, paired with hydrogen peroxide, stood out as an excellent reagent owing to its high citric acid content, which provides a suitable pH for selective lithium extraction.

Preliminary results on a green process for lithium recovery from cathodes

In this study, the extraction of lithium from LFP powders was achieved through the combined action of malic acid and oxygen in a semi-batch reactor with continuous air blowing.

Single factor experiments were employed to optimize the leaching parameters.

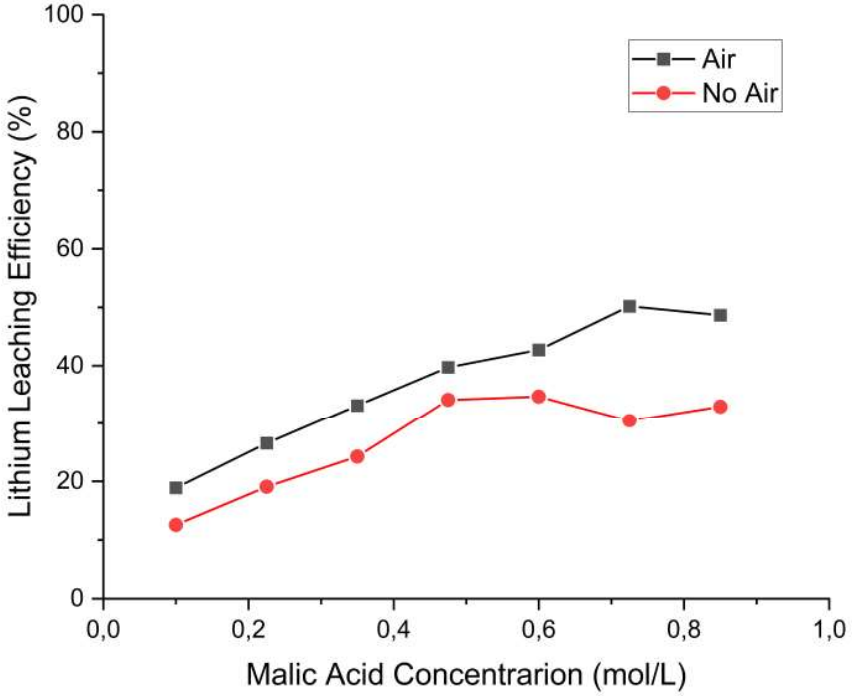

Figure2. Effect of air bubbling on lithium leaching efficiency at T=25°C, S/L=50 g/L, reaction time=3 h, air flowrate= 1 L/min.

The following techniques were used to characterize the raw materials and products of the reaction to evaluate the leaching efficiency and to investigate possible reaction mechanisms: inductively coupled plasma-optical emission spectroscopy (ICP-OES), X-ray diffraction (XRD), X-ray fluorescence spectrometry (XRF), and Fourier transform infrared spectroscopy (FT-IR).

Final remarks

The short review presented in this paper set out to explore the most relevant strategies for spent LFP batteries recycling, highlighting novelty, limitations and possible improvement opportunities. The importance of selective Li extraction together with

the necessity to explore organic acids and inorganic salts as eco-friendly leaching agents has been underlined. This paper also reports preliminary results on air-assisted lithium leaching using malic acid. The obtained results show that continuous air bubbling enhances the ability of malic acid to extract Li from LFP cathodes, suggesting that the proposed process could represent a sustainable route for waste cathodes recovering. Further work is underway to optimise leaching time, temperature and solid-to-liquid ratio, with a view to exploring the deferred addition of acid. This should help to keep the pH constant, thereby improving selectivity for lithium.

References

[1] Y. Xu *et al.*, "Advances and perspectives towards spent LiFePO4 battery recycling," *J Clean Prod*, vol. 434, p. 140077, Jan. 2024, doi: 10.1016/j.jclepro.2023.140077.

[2] European Commission, "Study on the Critical Raw Materials for the EU 2023 – Final Report." doi: 10.2873/725585.

[3] M. Zhang, L. Wang, S. Wang, T. Ma, F. Jia, and C. Zhan, "A Critical Review on the Recycling Strategy of Lithium Iron Phosphate from Electric Vehicles," *Small Methods*, vol. 7, no. 7, Jul. 2023, doi: 10.1002/smtd.202300125.

[4] Q. Jing *et al.*, "E-pH Diagrams for the Li-Fe-P-H2O System from 298 to 473 K: Thermodynamic Analysis and Application to the Wet Chemical Processes of the LiFePO $_4$ Cathode Material," *The Journal of Physical Chemistry C*, vol. 123, no. 23, pp. 14207–14215, Jun. 2019, doi: 10.1021/acs.jpcc.9b02074.

[5] W. Lv, Z. Wang, H. Cao, Y. Sun, Y. Zhang, and Z. Sun, "A Critical Review and Analysis on the Recycling of Spent Lithium-Ion Batteries," *ACS Sustain Chem Eng*, vol. 6, no. 2, pp. 1504–1521, Feb. 2018, doi: 10.1021/acssuschemeng.7b03811.

[6] F. Larouche *et al.*, "Progress and Status of Hydrometallurgical and Direct Recycling of Li-Ion Batteries and Beyond," *Materials*, vol. 13, no. 3, p. 801, Feb. 2020, doi: 10.3390/ma13030801.

[7] B. Makuza, Q. Tian, X. Guo, K. Chattopadhyay, and D. Yu, "Pyrometallurgical options for recycling spent lithium-ion batteries: A comprehensive review," *J Power Sources*, vol. 491, p. 229622, Apr. 2021, doi: 10.1016/j.jpowsour.2021.229622.

[8] L. Zhang *et al.*, "Recovery of LiFePO4 from used lithium-ion batteries by sodium-bisulphate-assisted roasting," *J Clean Prod*, vol. 379, p. 134748, Dec. 2022, doi: 10.1016/j.jclepro.2022.134748.

[9] R. Zheng *et al.*, "Optimized Li and Fe recovery from spent lithium-ion batteries via a solution-precipitation method," *RSC Adv*, vol. 6, no. 49, pp. 43613–43625, 2016, doi: 10.1039/C6RA05477C.

[10] T. Yan *et al.*, "High-efficiency method for recycling lithium from spent LiFePO4 cathode," *Nanotechnol Rev*, vol. 9, no. 1, pp. 1586–1593, Dec. 2020, doi: 10.1515/ntrev-2020-0119.

[11] K. Liu *et al.*, "Application of H4P2O7 as leaching acid in one-step selective recovery for metals from spent LiFePO4 batteries," *Ionics (Kiel)*, vol. 27, no. 12, pp. 5127–5135, Dec. 2021, doi: 10.1007/s11581-021-04273-w.

[12] G. Hu *et al.*, "Direct Recycling Strategy for Spent Lithium Iron Phosphate Powder: an Efficient and Wastewater-Free Process," *ACS Sustain Chem Eng*, vol. 10, no. 35, pp. 11606–11616, Sep. 2022, doi: 10.1021/acssuschemeng.2c03520.

[13] B. Musariri, G. Akdogan, C. Dorfling, and S. Bradshaw, "Evaluating organic acids as alternative leaching reagents for metal recovery from lithium ion batteries," *Miner Eng*, vol. 137, pp. 108–117, Jun. 2019, doi: 10.1016/j.mineng.2019.03.027.

[14] P. Meshram, A. Mishra, Abhilash, and R. Sahu, "Environmental impact of spent lithium ion batteries and green recycling perspectives by organic acids – A review," *Chemosphere*, vol. 242, p. 125291, Mar. 2020, doi: 10.1016/j.chemosphere.2019.125291.

[15] H. Zhou, Y. Zhang, L. Li, and Z. Cao, "Integrated recycling of valuable elements from spent LiFePO4 batteries: a green closed-loop process," *Green Chemistry*, vol. 25, no. 19, pp. 7696–7706, 2023, doi: 10.1039/D3GC02180G.

[16] Y. Yang *et al.*, "Selective recovery of lithium from spent lithium iron phosphate batteries: a sustainable process," *Green Chemistry*, vol. 20, no. 13, pp. 3121–3133, 2018, doi: 10.1039/C7GC03376A.

[17] H. Mahandra and A. Ghahreman, "A sustainable process for selective recovery of lithium as lithium phosphate from spent LiFePO4 batteries," *Resour Conserv Recycl*, vol. 175, p. 105883, Dec. 2021, doi: 10.1016/j.resconrec.2021.105883.

[18] X. Chai *et al.*, "Study on green closed-loop regeneration of waste lithium iron phosphate based on oxalic acid system," *Waste Management*, vol. 181, pp. 168–175, May 2024, doi: 10.1016/j.wasman.2024.03.037.

[19] Y. Tian *et al.*, "Strategies for Sustainable Production of Hydrogen Peroxide via Oxygen Reduction Reaction: From Catalyst Design to Device Setup," *Nanomicro Lett*, vol. 15, no. 1, p. 122, Dec. 2023, doi: 10.1007/s40820-023-01067-9.

[20] J. Kumar, X. Shen, B. Li, H. Liu, and J. Zhao, "Selective recovery of Li and FePO4 from spent LiFePO4 cathode scraps by organic acids and the properties of the regenerated LiFePO4," *Waste Management*, vol. 113, pp. 32–40, Jul. 2020, doi: 10.1016/j.wasman.2020.05.046.


THE COMBUSTION INSTITUTE
1954

SESSION III

Carbon-free energy carriers: combustion applications - Part 1


THE COMBUSTION INSTITUTE
1954

THREE-DIMENSIONAL SIMULATIONS OF FLASHBACK IN PREMIXED HYDROGEN FLAMES WITHIN PERFORATED BURNERS

F. Fruzza*, H. Chu, R. Lamioni*, T. Grenga***,
C. Galletti*, H. Pitsch****

filippo.fruzza@phd.unipi.it

* Department of Civil and Industrial Engineering, University of Pisa, Pisa 56122, Italy
** Institute for Combustion Technology, RWTH Aachen University, Aachen 52056, Germany
*** Faculty of Engineering and Physical Sciences, University of Southampton, Southampton SO17 1BJ, UK

Abstract

Predicting flashback in perforated burners for hydrogen substitution in household appliances is crucial yet challenging. Existing studies predominantly employ two-dimensional (2D) simulations due to lower computational demands, but these may not capture the actual flame dynamics, leading to potentially inaccurate predictions of flashback limits. This study utilizes three-dimensional (3D) simulations to evaluate the effects of the finite length of the slits on the flashback limits of hydrogen-premixed flames. Both steady-state and transient simulations are conducted to estimate flashback velocities and dynamics in realistic slit configurations. Comparisons with 2D results reveal significant underestimations of flashback limits by 2D models, as these models neglect the slit ends where flashback typically initiates.

Introduction

The growing interest in hydrogen as a clean fuel necessitates innovative designs for household and commercial heating devices. These devices, equipped with perforated burners, must be re-engineered for hydrogen to prevent excessive temperatures and flashback phenomena. Significant differences in the physical properties of hydrogen compared to natural gas challenge these adaptations. Recent research has concentrated on understanding the flashback limits for hydrogen and hydrogen-natural gas mixtures, with studies exploring these phenomena both experimentally and numerically [1-5]. However, most numerical studies have utilized two-dimensional (2D) simulations, which are computationally economical but could fail to capture the complete dynamics of flashback, potentially leading to inaccuracies. This research takes a novel approach by employing three-dimensional (3D) simulations to better understand how the finite lengths of slits affect flashback limits in hydrogen-air flames. We aim to determine the accuracy of 2D models in estimating flashback velocities and the impact of slit length on flame behavior and heat transfer mechanisms. Our comprehensive simulations include both steady-state and transient analyses, comparing 2D assumptions against more realistic 3D

configurations to provide a more accurate understanding of flashback dynamics.

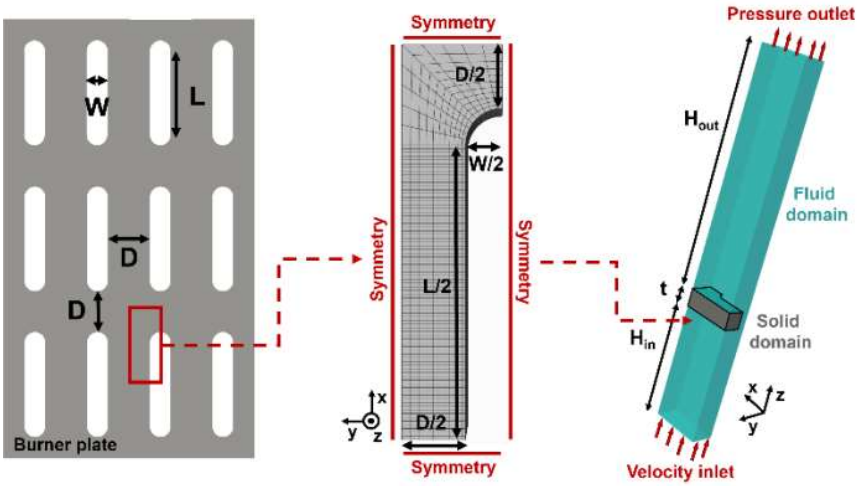

Figure 1. Configuration and computational domain.

Configuration and numerical methods

In this study, we simulate a segment of the perforated plate from a real burner typically used in domestic condensing boilers. We consider 3D configurations representing arrays of holes or slits in various shapes and sizes. The 3D configuration and computational domain are depicted in Figure 1. The computational domain is reduced to a quarter of the entire slit, applying symmetry boundary conditions on the symmetry planes. The numerical fluid domain extends $H_{out} = 4\ mm$ upstream and $H_{out} = 8\ mm$ downstream of the solid plate. The slit width is denoted as W, and the distance between two adjacent slits is D. The length between the centers of the round ends of the slit is denoted as L. With this definition, $L = 0$ corresponds to a circular hole of diameter W. The thickness of the burner plate is $t = 0.6\ mm$, and the slit width is fixed at $W = 0.5\ mm$. The porosity of the burner, $\psi = A_{slit}/A_{tot}$, is adjusted by modifying the distance between slits, D, where A_{slit} and A_{tot} represent the perforated and total plate areas, respectively. We examine H2-air mixtures at various equivalence ratios ϕ. Uniform velocity and temperature $T_u = 300\ K$ are imposed at the inlet, and a pressure of $p = 1\ atm$ is imposed at the outlet. At the fluid-solid interface, a no-slip boundary condition is set for the velocity, and zero-mass flux for the species equations, with the fluid and solid domains thermally coupled through conjugate heat transfer (CHT), which accounts for the interaction between the flame and the burner plate. The governing equations include conservation of mass, momentum, and energy, along with transport and reaction equations for the chemical species, solved on a structured grid with a characteristic cell size of 25 μm in the reaction front region. We employ detailed chemistry using a reduced version of the Kee-58 mechanism, which includes 9 chemical species and 22 reversible reactions. The model incorporates full multicomponent diffusion, Soret diffusion, and radiation. The energy equation is solved within the solid domain, which is modeled using properties of stainless steel used in these burners.

Estimation of flashback velocity

This study employs two different solution approaches to address varied objectives. A steady-state approach is used for parametric variations due to its computational

efficiency, ideal for extensive studies but unsuitable for analyzing flashback dynamics. In contrast, a transient approach, though computationally demanding, enables the study of these dynamics.
In the steady-state method, a stable flame solution is initially obtained with a high inlet velocity using a pressure-based coupled algorithm with second-order spatial discretization. The inlet velocity is then gradually reduced until the solver cannot converge, indicating the critical velocity for flashback. To determine this velocity accurately, the minimum reduction is set to $\Delta V_{in} = 0.01\ m/s$. The flashback velocity is defined as the cold-flow bulk velocity at the slit entry when flashback occurs, calculated as $V_{FB} = 1/\psi\ V_{in}$ at the flashback occurrence.
For the transient approach, simulations cover the entire slit geometry to address potential asymmetries in flashback dynamics, using a second-order scheme for time discretization and a PISO implicit algorithm. The time step within the fluid domain is 1 μs. The solution methodology remains consistent with the earlier description, maintaining a minimum velocity decrement of $\Delta V_{in} = 0.01\ m/s$.

Results and discussion

In a 2D simulation of a slit array, the domain models a cross-section of the slit, assuming it to be infinitely long, which neglects the slit ends. We aim to identify the minimal slit length for which a 3D slit is closely approximated by a 2D model. We conduct steady-state simulations for 3D configurations with slit lengths ranging from 1 mm to 80 mm, comparing these with a consistent 2D model. All 3D geometries share identical cross-sectional profiles to be represented by the same 2D model. The mixture's equivalence ratio is set at 0.6, and the inlet velocity is adjusted to ensure a uniform cold-flow velocity at the slit entry, standardized at 4 m/s. To illustrate how the burner temperature depends on slit length, Figure 2 plots its volume-averaged value in the solid domain as a function of the slit length, including results from the 2D simulation for comparison. This emphasis on burner temperature is crucial, as it significantly influences the flashback velocity [2].

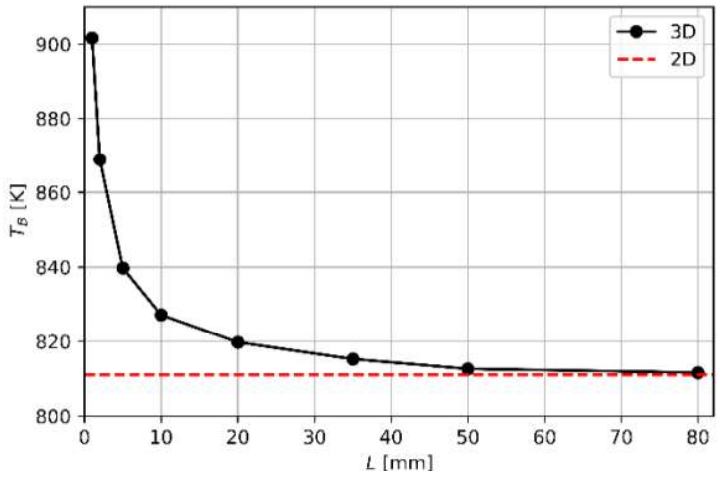

Figure 2. Burner plate temperature as a function of the slit. The dashed line represents the 2D result.

The 2D simulation predicts a burner temperature of 812 K. In contrast, 3D simulations show that at a 1 mm slit length, the burner temperature is 902 K, which decreases to 827 K at 10 mm, eventually aligning with the 2D result around 50 mm. Higher temperatures in shorter slits result from significant heat transfer at the slit ends, where the flame and burnt gases heat

the burner plate. As slit length increases, the influence of the ends diminishes, aligning the 3D results more closely with the 2D conditions. The 2D model effectively represents 3D slit behavior only for lengths exceeding 50 mm. However, slits in practical condensing boiler burners typically range from 0 to 5 mm, indicating that 2D simulations may fail to accurately reproduce the behavior of practical devices.

To explore how the finite length of the slit affects the flashback velocity, and compare 3D and 2D models, we calculate flashback velocities using a steady-state approach for three equivalence ratios, $\phi = 0.6$, 0.8, and 1.0. We examine slits ranging from $L = 0$ to $L = 8\ mm$, with $L = 0$ representing a circular hole. To ensure consistent comparisons, we maintain a fixed porosity of $\psi = 0.2$ by adjusting the spacing between slits. In Figure 3, we present the flashback velocities normalized by the 1D unstretched laminar flame speed as a function of slit length. We also include results for a 2D configuration that simulates an infinite slit, matching the width and porosity of the 3D cases. As expected, for both 2D and 3D simulations, the normalized flashback velocity decreases with increasing equivalence ratio, as the flashback propensity is strongly affected by preferential diffusion effects. We observe a rapid increase in the flashback velocity from $L = 0$ to $L = 1\ mm$. However, for $L > 1\ mm$, the influence of slit length on flashback velocity significantly diminishes, reaching an almost constant value. Notably, unlike the burner plate temperatures shown in Figure 2, where 2D results eventually align with 3D values for larger slit lengths, the flashback velocities in 2D do not converge with those in 3D, being underestimated of approximately 50%.

To explain why the flashback velocity is almost independent of slit length, and why these values do not align with those of the 2D case for larger lengths, a deeper understanding of the flashback is needed. To this end, two transient simulations are conducted: one representing a 2D configuration and another for a 3D slit with a length of $L = 2\ mm$. For both configurations, the slit width is specified as $W = 0.5\ mm$ and the porosity as $\psi = 0.2$. An equivalence ratio of $\phi = 0.6$ is set for the inlet mixture. In Figure 4, we illustrate the flashback event for the 2D configurations. The evolution of the temperature profiles is displayed in four snapshots taken during the occurrence of flashback. As the 2D configuration only considers the transversal section of an actual slit, the flashback dynamics can only be

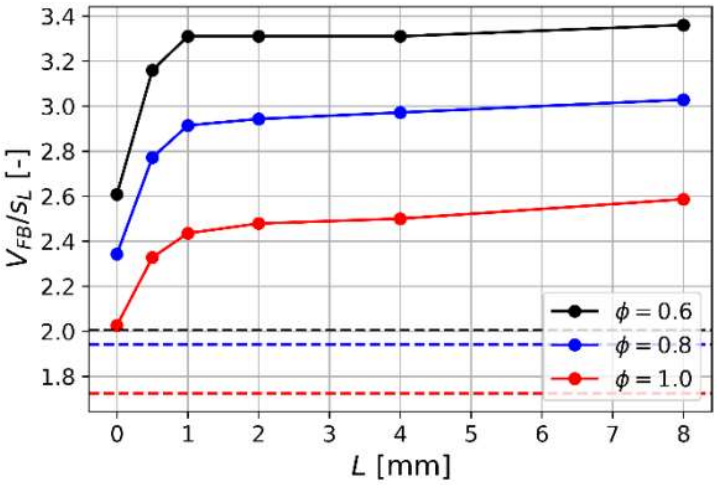

Figure 3. Normalized flashback velocity as a function of the slit length. 2D results are indicated by dashed lines.

represented by the flame crossing the slit starting from the slit side walls. This is imposed by the choice of a 2D domain and could be substantially different from the actual dynamics occurring in a three-dimensional slit.

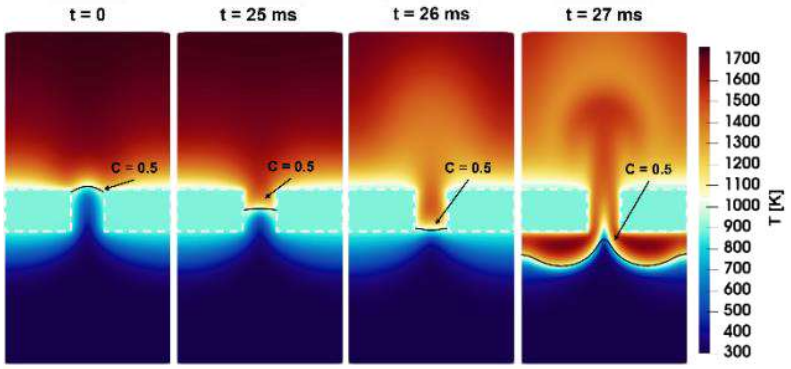

Figure 4. Flashback dynamics in the 2D configuration.

Figure 5 depicts a sequence of four snapshots captured during the flashback occurrence for the 3D configuration. The snapshots illustrate the evolution of the flame front, defined as an iso-surface of progress variable corresponding to $C = 0.5$. The initiation is asymmetric, starting at one end of the slit. From there, the flame front moves backward towards the entrance, traversing the slit entirely on that side, and ultimately driving the entire flashback process. To understand the role of the slit ends and the physical mechanisms involved, a visualization of the last stable flame, is presented in Figure 6. The iso-contour of progress variable at $C = 0.5$ is colored to show temperature (a), local equivalence ratio (b), normalized molecular H_2 consumption rate (c), and displacement speed (d), defined as $S_D = v \cdot n$, where n is the unit vector normal to the iso-surface. A temperature peak is observed at the slit ends where the enclosed geometry enhances heat transfer, resulting in greater pre-heating of the mixture (Figure 6 (a)). In these regions, preferential diffusion effects and Soret diffusion [6] contribute to fuel enrichment of the mixture (Figure 6 (b)). These phenomena lead to an increase in the H_2 consumption rate (Figure 6 (c)), and subsequently, an increase in flame speed, as indicated by the local maxima of displacement speed (Figure 6 (d)). Consequently, this region becomes the initiation zone for flashback, where the local flame speed surpasses the flow velocity, triggering the flashback initiation. The observation of this distinctive dynamics explains why the flashback velocity shows weak dependence on the length of the slit beyond a certain value, as seen in Figure 3. This occurs because the critical region for flashback initiation is consistently located at the slit ends, regardless of the specific value of L. Furthermore, the significant role played by the slit ends underscores that flashback is inherently a three-

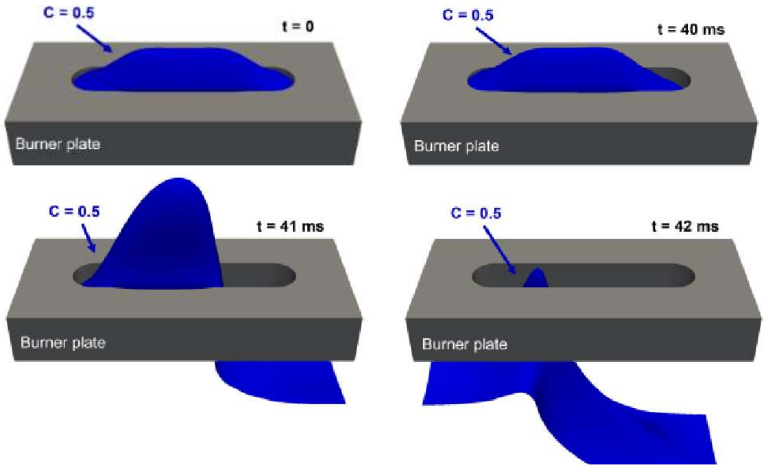

Figure 5. Flashback dynamics in the 3D configuration.

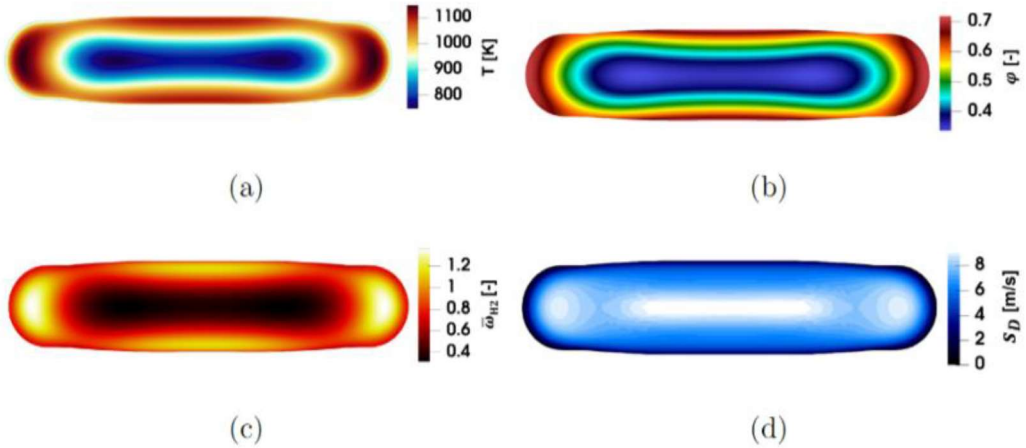

Figure 6. Iso-contour of progress variable (C=0.5) colored by: (a) temperature, (b) equivalence ratio, (C) normalized H_2 consumption rate, and (d) displacement speed.

dimensional phenomenon. Enhanced fuel enrichment and pre-heating at the slit ends cause flashback to initiate at higher inlet velocities compared to 2D configurations. Consequently, the 3D results shown in Figure 3 do not align with those from 2D configurations, where the slit ends are consistently neglected. These results highlight the necessity of using 3D simulations for the accurate estimation of flashback velocities in perforated burners.

References

[1] A. Aniello, T. Poinsot, L. Selle, T. Schuller, Hydrogen substitution of natural gas in premixed burners and implications for blow-off and flashback limits, *Int. J. Hydrog. Energy* 47 (77):33067–33081 (2022).

[2] F. Fruzza, R. Lamioni, L. Tognotti, C. Galletti, Flashback of H2-enriched premixed flames in perforated burners: Numerical prediction of critical velocity, *Int. J. Hydrog. Energy* 48 (81): 31790–31801 (2023)

[3] F. Vance, L. de Goey, J. van Oijen, Development of a flashback correlation for burner-stabilized hydrogen-air premixed flames, *Combust. Flame* 243:112045 (2022)

[4] E. Flores-Montoya, A. Aniello, T. Schuller, L. Selle, Predicting flashback limits in H2 enriched CH4/air and C3H8/air laminar flames, *Combust. Flame* 258:113055 (2023)

[5] F. Fruzza, R. Lamioni, A. Mariotti, M. V. Salvetti, C. Galletti, Flashback propensity due to hydrogen blending in natural gas: Sensitivity to operating and geometrical parameters, *Fuel* 362 (2024) 130838

[6] F. Fruzza, H. Chu, R. Lamioni, T. Grenga, C. Galletti, H. Pitsch, The importance of soret effect, preferential diffusion, and conjugate heat transfer for flashback limits of hydrogen-fueled perforated burners, *submitted to Proc. Combust. Inst.* (2024)

INFLUENCE OF HYDROGEN ADDITION TO METHANE UNDER MILD CONDITIONS

G.B. Ariemma*, G. Sorrentino*, P. Sabia*, M. de Joannon, R. Ragucci*
giovannibattista.ariemma@stems.cnr.it
*Institute of Sciences and Technologies for Sustainable Energy and Mobility (STEMS-CNR), Italy

Abstract
Environmental issues related to CO_2 emissions deriving from power and energy sectors are amongst the most relevant industrial challenges [1]. In particular, an effective approach to address the needed CO_2 emissions reduction is based on the gradual replacement of hydrocarbon-based fuels with hydrogen. However, many techno-economic barriers hinder a straightforward transition to a hydrogen economy [2]. The use of hydrocarbon/hydrogen blends has been proposed as intermediate and bridge solution, thus providing a transition strategy to a carbon-free energy system in the future. In addition, MILD combustion [3] was already proven as suitable and effective technology. However, the step toward the technological readiness of MILD based devices has not yet been completed. In this framework, the present study wants to shed light on the combustion features of methane/hydrogen blends and on the related pollutant emissions in a truly MILD burner. The influence of reactive mixture composition (ϕ) and the hydrogen content in the fuel mixture ($\%H_2$ vol) was highlighted, focusing on oxidation process stability and NO_x emissions. Results confirm the wide fuel flexibility of the MILD combustion process, whose performance is totally released from the fuel mixtures combustion properties. Specifically, results testified the ability of efficiently convert CH_4/H_2 blends by substantially keeping unaffected operating temperatures and NO_x emissions to the levels typically detected for pure methane combustion. In this respect, kinetic analyses highlighted the main reaction involved in NO_x production/consumption for CH_4/H_2 blends and the key role of radical species deriving from both the fuels. In particular, the increased radical pool concentration deriving from the increasing $\%H_2$, along with the resulting decreasing ones from CH_4, balance each other, thus not affecting the NO_x net production.

Acknowledgments
We acknowledge the partial financial support of the European Union NextGeneration EU in the framework of: PE00000021 - NEST - Network 4 Energy Sustainable Transition, Italian Ministry of University and Research Decree n.341 - March 15, 2022 - Spoke 3, CUP B53C22004060006; the National Sustainable Mobility Center - MOST, CN00000023, Italian Ministry of University and Research Decree n. 1033-17/06/2022 - Spoke 12, CUP B43C22000440001; EU initiatives under the National Recovery and Resilience Plan (NRRP-PNRR): “POR H2 AdP MMES/ENEA-CNR”, Mission 2, Component 2, Investment 3.5 "Ricerca e sviluppo sull’idrogeno", CUP: B93C22000630006.

References
[1] IEA, Energy Technology Perspectives 2020. Rep., Int. Energy Agency Paris.
[2] Dincer, I. “Green methods for hydrogen production”, *Int J Hydrogen Energy*, vol. 37, 1954–71 (2012)
[3] Sabia, P., Sorrentino, G., Ariemma, G.B., Manna, M.V., Ragucci, R., de Joannon, M., “MILD Combustion and Biofuels: A Minireview”, *Energy and Fuels* 35:19901–19 (2021)

Thickened Flame model for multi-fuel multi-injection combustion– Pollutant analysis of an ammonia-hydrogen swirled flame

H.J. Vargas Ruiz*,, D. Laera**,***, G. Lartigue***, L. Gicquel****
vargas@cerfacs.fr
*TotalEnergies, Av. Larribau CSTJF, Pau, France
**CERFACS, 42 Av. Gaspard Coriolis Toulouse, France
***Politecnico di Bari, 4 Eduardo Orabona, Bari, Italy

Abstract
An extension of the widely-used Thickened Flame model for Large Eddy Simulations (TFLES) to take into account multi-fuel multi-injection combustion processes is presented. The local variation in fuel composition and equivalence ratio due to differential diffusion and the mixing of differentiated fuel injections is computed from a transported mixture fraction passive scalar tracing the spatial evolution of each fuel stream. This allows to incorporate local fuel composition inhomogeneities into the combustion model and the flame sensor parameters. The proposed modeling is used to predict the ammonia-air swirling flame stabilized by multiple hydrogen injections operated at Cardiff University. To perform such simulations, a novel analytically reduced chemistry scheme for NH_3-H_2-N_2/air combustion is derived and validated at gas turbine operating conditions for multiple ammonia-hydrogen binary fuel blends as well as ternary fuel blends derived from ammonia decomposition. The results of the novel Multi-Fuel TFLES model (MF-TFLES) are compared against the conventional TFLES predictions and assessed via the experimental data at our disposal. The proposed modeling improves the flame shape prediction by assuring the correct application of the artificial flame thickening principles locally and coherently, taking into consideration the multi-fuel complex mixing process. Furthermore, thermal effects on NO_X and flame topology are evaluated by comparing an adiabatic case against one considering wall heat losses.

Introduction
Large Eddy Simulations (LES) have enabled accurate prediction of turbulent reactive flows by limiting the turbulence modeling to the small turbulent scales [1]. This work focuses on the Thickened Flame LES (TFLES) model [2] relying on the premixed flame theory. In this approach, the flame is artificially thickened by a factor $\mathcal{F}$, while conserving the flame speed (S_L^0) and the globally integrated heat release rate [3]. This model is, however, limited to case where (1) perfectly premixed combustion and (2) a mixture uniform unitary Lewis are assumed. The renewed interest in carbon-free fuels such as hydrogen (H_2) and ammonia (NH_3), highlighted limits of the approach previously dismissed, and new combustion modeling

challenges need to be considered for a proper use of the TFLES model in this new framework. Among many for such a vast challenge, two difficulties stand out: first, the correct modeling of unconventional burner technologies with multi-inlet multi-fuel injection systems, and second, the effect of differential diffusion introduced by the presence of H_2 in the fuel blend [4,5]. To the best of the authors' knowledge, none of the previous numerical studies [6,7] have considered the effect of differential diffusion issued by the presence of H_2 in the fuel blend. Furthermore, a configuration with differentiated injection of NH_3 and H_2, such as the one studied by Mashruk et al. [8], inevitably results in a spatially heterogeneous fuel composition in the burner, a feature overlooked by previous studies [6,9]. The present work aims, therefore, at developing a numerical methodology coupling a fuel-agnostic Multi-Fuel TFLES (MF-TFLES) model to a novel NH_3-H_2-N_2 Analytically Reduced Chemistry (ARC) scheme to perform high-fidelity LES of NH_3-H_2 partially-premixed flames with differentiated fuel injection in industrial gas turbine type applications.

Chemical Kinetics Modeling

The Stagni et al. [10] detailed mechanism is selected for reduction. The fully automatic reduction tool ARCANE [11] is used to derive a novel ARC scheme. The initial target fuel is a partially cracked ammonia ternary blend $X_{NH_3} = 0.4285$, $X_{H_2} = 0.4285$, and $X_{N_2} = 0.1430$ in moles. Quantities Of Importance (QOI) are evaluated under a wide range of operating conditions using the premixed freeflame canonical case. That is, 1-20 bar, 300 - 700 K and 0.6-1.6 for pressure, temperature, and equivalence ratio, respectively. The final mechanism, named ARC NH3H2N2_15_211_5_HV for future reference, has 15 species, 211 elementary steps (107 reactions), and 5 QSS species. Both reduced mechanisms showed accurate predictions compared to the basis mechanism and experimental data [12]. *A posteriori* validation of the mechanism is also performed for the whole range of ammonia-hydrogen binary blends ($0 < X_{H_2} < 1$), as well as for all ternary blends derived from ammonia decomposition ($0 < \gamma < 1$). For this exercise, with reported maximum error (e_{rel}^{max}) 10% for S_L^0, 1% for T_{adb}, and 15% for final Y_{NO}.

Turbulent Combustion Modeling

Since the TFLES model is parameterized through 1D reference quantities (δ_{th}^0, S_L^0, etc.), it may be used in partially-premixed configurations provided that the reference fresh state can be locally computed. Usually, the assumption of a mixture constant Lewis number allows TFLES input parameters, namely ϕ, to be computed from the local composition of the reacting mixture using Bilger's mixture fraction definition [13]. While this simplification is generally considered acceptable for heavy carbonated/conventional fuels, it does not hold for lighter fuels with preferential diffusion. Furthermore, the assumption of a uniform fuel composition breaks down in multi-fuel applications with differentiated injection. Given the above limitations, the Multi-Fuel TFLES (MF-TFLES) model is proposed as an extension of the TFLES model for multi-fuel multi-injection partially-premixed combustion. The

objective of these modifications is to cover four scenarios adequately: 1) a homogeneous fuel blend with species having similar diffusion properties; 2) a homogeneous fuel blend with distinct diffusion properties; 3) a differentiated injection of two fuel streams; 4) and the individual injection of each stream (first fuel, second fuel, and oxidizer). To address such scenarios, three reference tanks with assumed constant composition are considered: fuel tank one, fuel tank two, and a single oxidizer tank. A transport equation for a passive scalar per fuel tank is then explicitly resolved by the LES solver in parallel to the transport equations of the chemical scheme species. Each of the two transported passive scalars has, in such a case, the objective to track the evolution of its corresponding fuel mass fraction as if the flow were non-reactive. This work adds the notion of the so-called blend index as the fourth dimension of the reference value look-up table space, allowing for the first time to the best of the authors' knowledge, to correctly parameterize the thickening field in dual-fuel partially-premixed configurations.

Application to a Swirl Burner

The partially-premixed swirled burner experimentally studied by Mashruk et al. [8] is specifically addressed in this work for assessment of the proposed modeling strategy. This burner, displayed in Fig. 1, operates at atmospheric pressure using a fully premixed NH_3-air mixture injected at 288K. Further downstream, a partially-premixed regime is obtained by injecting pure hydrogen, as highlighted in blue in Fig. 1.b. A globally lean equivalence ratio of around 0.65 and a binary NH_3-H_2 fuel blend with $X_{H_2} = 0.3$ are prescribed.

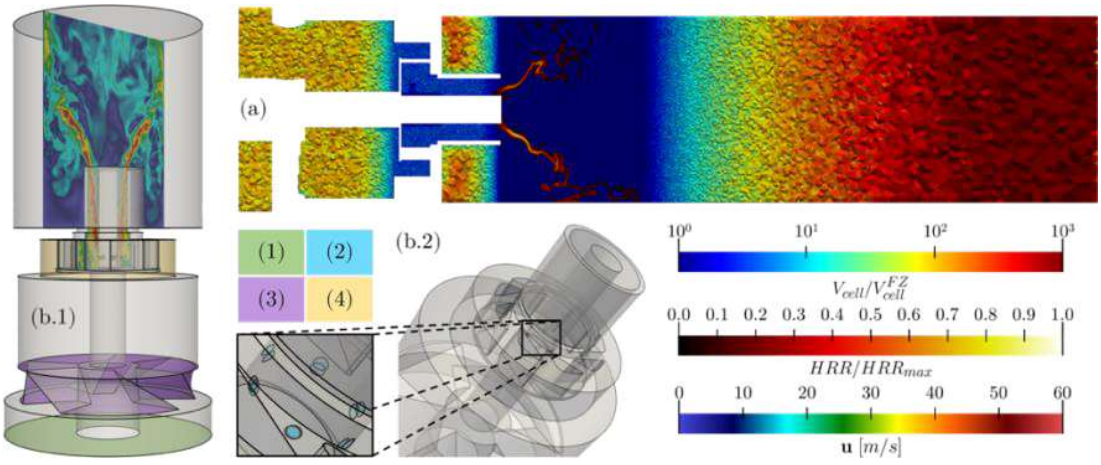

Figure 1. Numerical setup. (a) The cell size distribution normalized by the flame zone target cell volume is displayed. (b.1,b.2) The primary (1) and secondary (2) injection, as well as the axial (3) and the radial (4) swirler are highlighted.

In terms of the computational domain, the burner is described using an 87 million cell unstructured tetrahedral mesh. The primary injection inlet is highlighted in green in Fig. 1.b. The secondary injection system is represented by short-length pipes keeping the injecting tube section untouched. The simulations have been performed

using the parallel explicit cell-vertex code AVBP [14]. The MF-TFLES turbulent combustion model previously detailed is implemented. A 9-point discretization is chosen for a correct flame front resolution. The walls upstream from the burner are no-slip and adiabatic. Heat losses are prescribed for the quartz tube walls.

A reference simulation using the TFLES model (Fig. 2.a) was used to reconstruct the *a priori* effects of the MF-TFLES model (Fig. 2.b). Next, another simulation using the MF-TFLES approach allowed for an *a posteriori* comparison (Fig. 2.c). Misidentification of the of the flame location and misestimation of the required thickening led to the flame being attached to the injector ring.

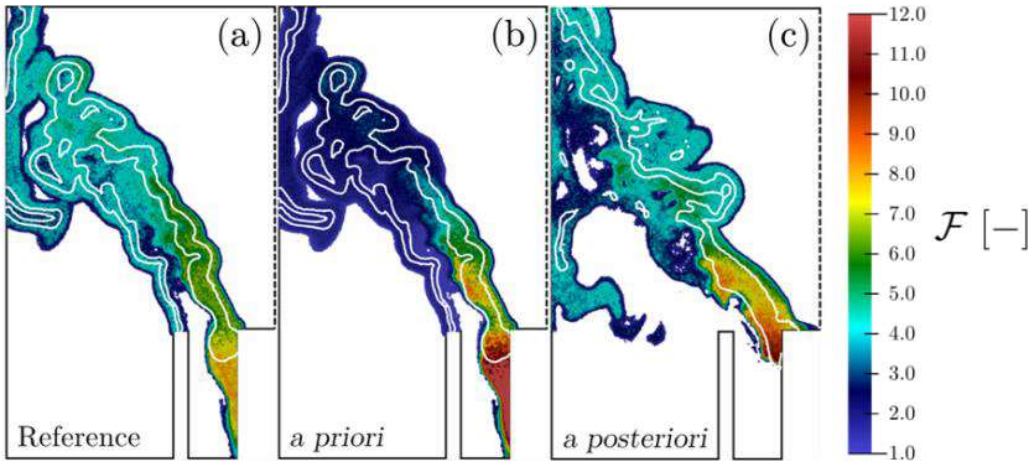

Figure 2. Impact of the MF-TFLES model. TFLES reference appears attached to the injector ring, this branch disappears on the MF-TFLES case (right).

NO_X emissions are highly dependent on the temperature of the burner walls. Therefore, a third simulation considering adiabatic wall for the quartz tube was performed to evaluate heat loss effects on flame topology and NO_X emissions.

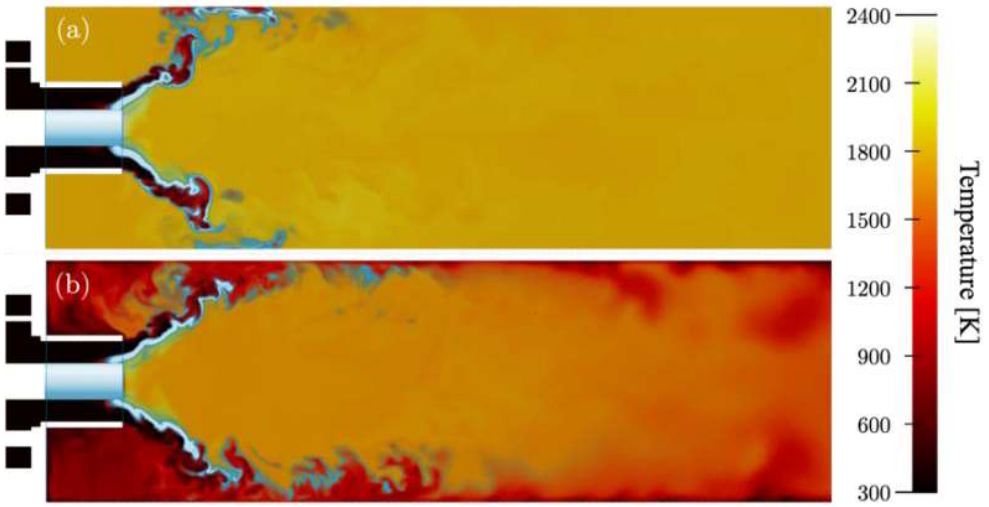

Figure 3. Longitudinal slice of the domain colored by temperature for (a) the adiabatic case and (b) the heat loss case. The flame position is highlighted in blue.

In both simulations, the differentiated injection of hydrogen results in a higher temperature in the central region where the main flame branch attaches to the central rod as illustrated by Fig. 3. This behavior is reinforced by the preferential diffusion of the H_2 molecule. The first observable effect of the heat loss treatment is a temperature reduction near the outer ring of the injector (Fig. 3.b). This ultimately leads to the detachment of the outer branch of the flame which 'unfolds' downstream in the quartz tube. Since the outer branch is detached, unburned fuel leaks downstream through the low temperature zone near the wall.

As expected, NO_X production is also affected by heat losses. Time-averaged solutions considering 20 ms of physical time were used to investigate pollutant concentration. Two sampling methods allowed to evaluate the homogeneity of the pollutant concentration in the radial direction (Fig. 4). In the first approach, pollutant concentrations were sampled using point-probes distributed along the longitudinal axis of the quartz tube. In the second approach, the cross-section integral was computed for 30 planes situated in the same abscissa positions as the point-probes. This analysis revealed strong gas composition heterogeneities in the heat loss case.

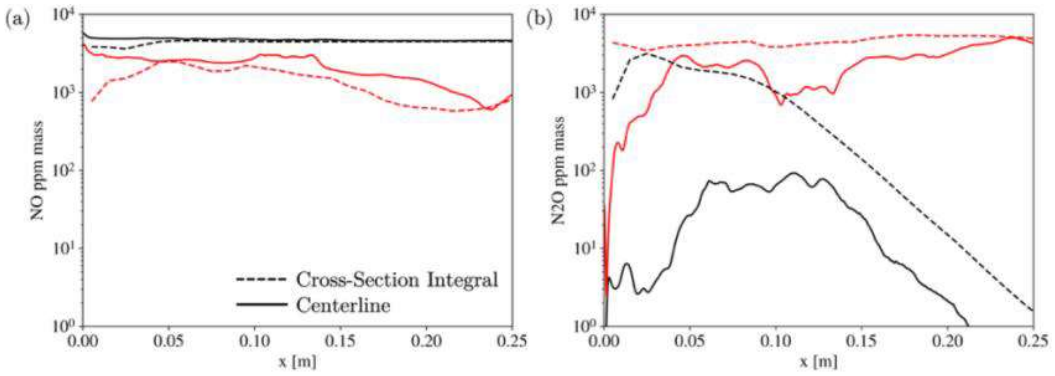

Figure 4. Concentration profiles for (a) NO and (b) N_2O along the quartz tube. Black lines and red lines represent the adiabatic and heat loss case, respectively.

Conclusion

In this work, an ARC for NH_3-H_2-N_2 combustion is coupled to an extension of the TFLES model dealing with differential diffusion and space-inhomogeneous fuel blends in multi-fuel, multi-injection partially-premixed flames. The premixed ammonia-air flame with differentiated hydrogen injection operated at Cardiff University is chosen as a simulation test case. The effect of the MF-TFLES model is evaluated against a reference TFLES model, flame topology effects were observed. Thermal effects are evaluated by comparing an adiabatic case and a heat loss case. Heat losses modify the flame topology resulting in strong exhaust composition heterogeneities and therefore pollutant concentration highlighting the importance of probe placing in experimental configurations. These results may further be used to describe the impact of the flame-turbulence interaction on pollutant formation pathways in decarbonized combustion.

References

[1] Pitsch, H., "Large-Eddy Simulation of Turbulent Combustion," *Annual Review of Fluid Mechanics*, Vol. 38, No. 1, 2006, 453–482.

[2] Colin, O., Ducros, F., Veynante, D., and Poinsot, T., "A Thickened Flame Model for Large Eddy Simulations of Turbulent Premixed Combustion," *Physics of Fluids*, Vol. 12, No. 7, 2000, 1843–1863.

[3] Butler, T. D., and O'Rourke, P. J., "A Numerical Method for Two Dimensional Unsteady Reacting Flows," *Symposium (International) on Combustion*, Vol. 16, No. 1, 1977, 1503–1515.

[4] Nilsen, V., and Kosály, G., "Differential Diffusion in Turbulent Reacting Flows," *Comb. and Flame*, Vol. 117, No. 3, 1999, 493–513.

[5] Im, H. G., and Chen, J. H., "Preferential Diffusion Effects on the Burning Rate of Interacting Turbulent Premixed Hydrogen-Air Flames," *Comb. and Flame*, Vol. 131, No. 3, 2002, 246–258.

[6] Bioche, K., Blondeau, J., and Bricteux, L., "Large Eddy Simulation Investigation of Pressure and Wall Heat Loss Effects on Rich Ammonia-Hydrogen-Air Combustion in a Gas Turbine Burner," Int. J. of Hydrogen Energy, Elsevier Ltd, 47, 85, 2022, 36342–36353.

[7] Zhang, M., Xu, W., Wang, R., Wei, X., Wang, J., Huang, Z., et al., "Wall Heat Loss Effect on the Emission Characteristics of Ammonia Swirling Flames in a Model Gas Turbine Combustor," *Comb. and Flame*, Vol. 256, 2023, p. 112955.

[8] Mashruk, S., Zitouni, S.E, Brequigny, P., et al. , "Combustion Performances of Premixed Ammonia/Hydrogen/Air Laminar and Swirling Flames for a Wide Range of Equivalence Ratios," *Int. J. of Hydrogen Energy*, Vol. 47, No. 97, 2022, 41170--41182.

[9] Agostinelli, P. W., Laera, D., Boxx, I., Gicquel, L., and Poinsot, T., "Impact of Wall Heat Transfer in Large Eddy Simulation of Flame Dynamics in a Swirled Combustion Chamber," *Comb. and Flame*, Vol. 234, 2021, p. 111728.

[10] Stagni, A., Cavallotti, C., Arunthanayothin, S., Song, Y., Herbinet, O., Battin-Leclerc, F., and Faravelli, T., "An Experimental, Theoretical and Kinetic-Modeling Study of the Gas-Phase Oxidation of Ammonia," *Reaction Chemistry & Engineering*, Vol. 5, No. 4, 2020, 696–711.

[11] Cazeres, Q., "Analysis and Reduction of Chemical Kinetics for Combustion Applications," PhD Thesis. Université de Toulouse - Ecole doctorale MEGeP, 2021.

[12] Mei, B., Zhang, J., Shi, X., Xi, Z., and Li, Y., "Enhancement of Ammonia Combustion with Partial Fuel Cracking Strategy: Laminar Flame Propagation and Kinetic Modeling Investigation of NH3/H2/N2/Air Mixtures up to 10 Atm," *Comb. and Flame*, Vol. 231, 2021, p. 111472.

[13] Bilger, R. W. et al., "On Reduced Mechanisms for Methane/Air Combustion in Nonpremixed Flames," *Comb. and Flame*, Vol. 80, No. 2, 1990, 135–149.

[14] Schonfeld, T., and Rudgyard, M., "Steady and Unsteady Flow Simulations Using the Hybrid Flow Solver AVBP," *AIAA Journal*, Vol. 37, No. 11, 1999, 1378–1385.

Numerical Investigation in a Gas Turbine Burner Operating with Hydrogen-Ammonia Blend using Large Eddy Simulation and LES-CRN Methodology

L. Mazzotta*,, R. Meloni*, R. Lamioni***, C. Romano***

luca.mazzotta@bakerhughes.com

*Baker Hughes, Via F. Matteucci 2, 50127, Florence, Italy

**Department of Astronautical, Electric and Energetic Engineering, Sapienza University of Rome, Via Eudossiana 18, Rome, 00184, Italy

***Department of Industrial and Civil Engineering, University of Pisa, L.go L. Lazzarino, Pisa, 56122, Italy

Abstract

A non-premixed burner fed with a blend of ammonia-hydrogen is investigated numerically with the goal to validate the NO_x emission against the corresponding experimental measures, retrieved at atmospheric condition. Although the prediction of the CFD model is satisfactory in line with the experimental data, also a CRN is derived leveraging the time-averaged solution: such model provides a fast and reliable tool to deeply investigate the most significant NO_x formation pathways at the investigated operating conditions.

Introduction

The interest in ammonia as fuel for Gas Turbine (GT) combustors has triggered the development of fundamental research in the last decade [1]. In this context, combustion models embedded into CFD software are yet not fully able to predict several aspects associated with ammonia combustion. NO_x emission quantification is probably the main area where the numerical methodologies need to be improved [2]. It must be also admitted that even the understanding of the most fundamental NO_x formation paths are not always fully clear: the majority of the chemical mechanisms nowadays present in literature struggle on being fully predictive against the corresponding experimental data and very often a good agreement is achieved only on narrow operating windows. Since ammonia is always mixed with other fuels to overcome its chemical drawbacks from a combustion perspective [3] (i.e., natural gas or hydrogen), the challenge is also related to the global proprieties of the blend: depending on the specific operating conditions of the combustor, some NO_x formation paths could be favoured, compromising the generality of a given chemical mechanism. From an industrial perspective, the validation of the numerical approaches is also very often limited to simplified hardware working significantly far from the operating conditions of a modern GT combustor. This is another gap that OEMs should fill in the next future to make ammonia fired GT competitive. In this context, a CFD model as well as a CRN of an industrial burner operated at atmospheric pressure are investigated to develop a procedure able to better

understand the dominant NO_x formation pathways at a specific condition. The details of the test rig and the numerical approaches will be provided in the next sections.

Experimental facility and Campaign

The tests are executed in a single cup BH "*BlueRig*" facility with two independent air lines, one dedicated to the combustion air (Figure 1-a), the second, cooling the flame tube by external convection. The two streams meet at the dilution section placed at the end of the flame tube. Pollutant emissions are sampled downstream the dilution section with the sampled gas sent to a HORIBA PG250 gas analyser.

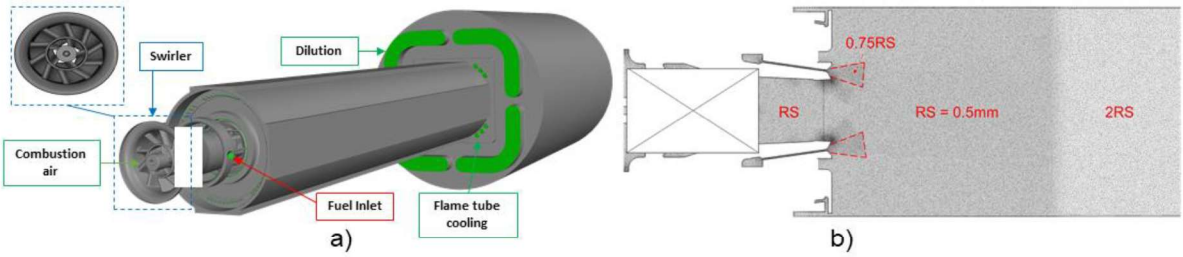

Figure 1: Computational domain (a) and details of the mesh with local refinements in function of the Reference Size (RS) (b).

The burner is a double counter-rotating swirler with two independent fuel lines: a premix and a pilot one [4]. Only the latter is used for the test with ammonia-hydrogen here discussed. Such configuration leads to a non-premixed flame that is dominantly diffusive. The temperature of the air and the global equivalence ratio are set to reach a flame temperature that is fully compatible with the ISO base load of the NOVA^{TM} LT16 engine. A sweep of ammonia content ranging from 0% up to 70% by weight is experimentally investigated [5] and the corresponding NO_x measurements are shown in Figure 2: the latter is selected among all the test points for the numerical investigation.

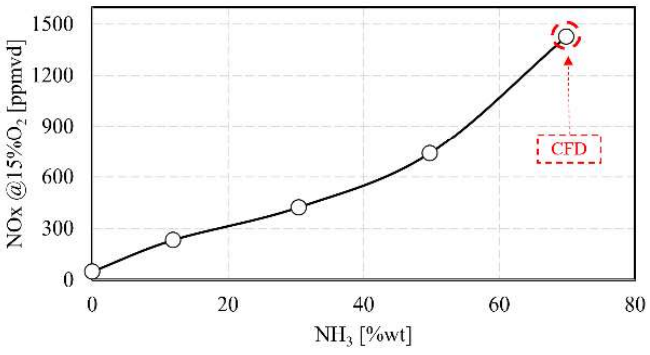

Figure 2: NO_x emissions measurements from the experimental campaign.

Numerical modelling

The commercial code Ansys Fluent is used to obtain the numerical CFD results shown in this work using Large Eddy Simulations (LES). The adopted computational domain is represented in Fig. 1a, while Fig. 1b shows some details of the

computational mesh used for the current investigation, having a total of 27×10^6 polyhedral elements. A Reference Size (RS) equal to 0.5 mm is used as reference to describe the discretization of the domain. The Smagorinsky – Lilly model with dynamic stress closure is employed at the turbulence subgrid scale. The chemistry of the hydrogen/ammonia mixture is modeled using the Flamelet Generated Manifold (FGM) approach [6]. The Stagni et al.'s [7] chemical kinetic scheme, which includes 31 species and 203 reactions, is selected as chemistry set. Additional scalar transport equations for NO and NH_3 are used to better capture nitrogen oxides and unburned ammonia emissions from the LES. Finite Rate closure is used to model the source term for the progress variable. Both spatial and implicit temporal discretization are solved with a second-order upwind scheme along the SIMPLEC scheme for pressure-velocity coupling. The constant time step size is defined in order to maintain the Courant-Friedrichs-Lewy number below unity across the domain, particularly in the flame zone region. After a preliminary wash-out phase, 5 FTT of the burner are simulated to collect statistics. A combined CFD and Chemical Reactor Network (CRN) technique is used to investigate the NO_x formation in the GT system. This approach allows the correct estimation of the number of reactors and their respective volumes, thus obtaining the residence times for each region of the domain. Moreover, the CFD-CRN technique allows to obtain reliable results in terms of NO_x emissions with a relatively low computational cost and, therefore, in a short time, allowing a broad study of the different parameters involved. The CRN to emulate the combustion of NH_3-H_2 mixtures in the complex and dynamic environment of a GT is developed based on the identification of the average zones of the temperature, flow, and radical species, obtained from the LES simulation. The individual reactors with their respective volumes are defined using the open-source software Cantera [8], based on two different types of reactors: the Perfectly Stirred Reactors (PSR), which represent the reactive zone, and the Plug Flow Reactors (PFR), which mimics the unidirectional flow zones of the combustion chamber and the dilution zones due to the injection of cooling air. The CRN is made up of three PSRs, which emulate the Diffusive (DIFF), Flame Zone (FZ) and CORNER regions, and two PFRs, which characterise the post-combustion and cooling zone. This configuration is previously validated in [5] and analysed to establish analytical correlations between the percentage of NH_3 by mass and the network calibration parameter, based on the equivalence ratio of the DIFF reactor. In this work, by exploiting the results obtained from the LES and applying them to the CRN structure, accompanied by the analytical correlations, it is possible to study the evolution of NO_x emissions and compare them with the LES and experimental results.

Results and Discussion

The main instantaneous and time-averaged fields derived from the LES analysis are shown in Figure 3. The axial velocity contour is useful in quantifying the volume associated with the recirculation zones and consequently the regions where fuel is trapped, creating high-temperature zones. As a consequence, the regions with the highest temperature are highlighted in the external recirculation zones where the

temperature is above 1800 K. NO emission is concentrated where the temperature is highest due to the thermal NO_x and fuel-bound mechanisms, the latter due to the significant amount of nitrogen in the fuel mixture. Figure 3 also shows the NO density difference between the flame zone and the post-flame zone where a decrease in temperature leads to a decrease in emissions.

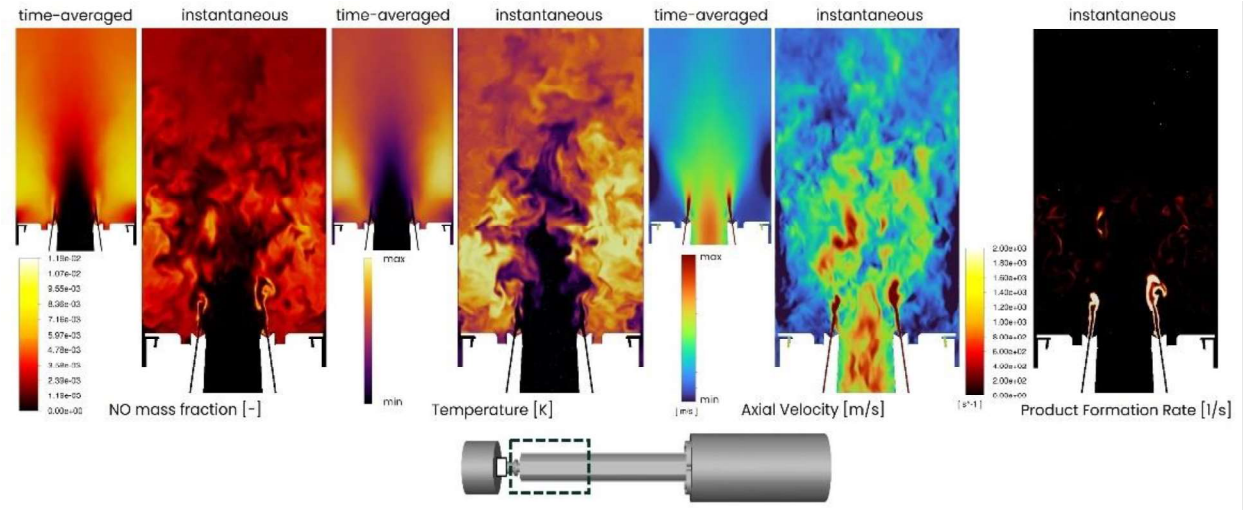

Figure 3: Instantaneous and time-averaged NO mass fraction, temperature, axial velocity and Product Formation Rate fields derived from LES in a longitudinal cross section.

The relationship between the temperature and the NO emissions can be demonstrated looking at the rate of production in the DIFF, in the FZ reactors and the formation pathways shown in Figure 4. In the diffusion zone (see Fig. 4a), the thermal NO_x mechanism derived by Zeldovich's reactions is dominant due to the high temperature present in the flame front. Most of the NO is produced by the reaction $N + OH \leftrightarrow H_2 + NO$.

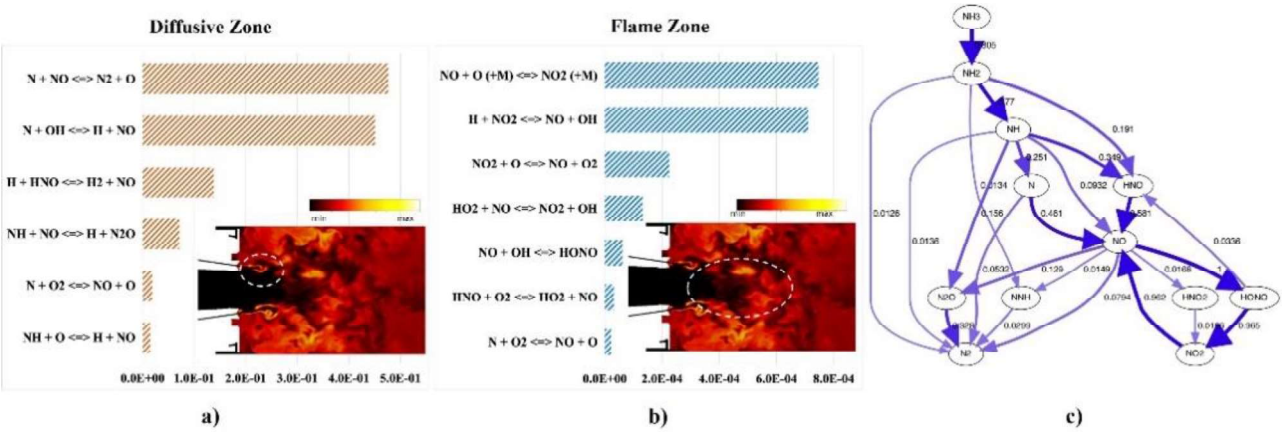

Figure 4: Net Rate of Production (ROP) [Unit: kmol/m^{3}s, Scale: $6x10^{-5}$] of NO in the Diffusive (a) and Flame Zone (b) reactors. Formation pathways following nitrogen species (c). The instantaneous contour plots are retrieved from the LES.

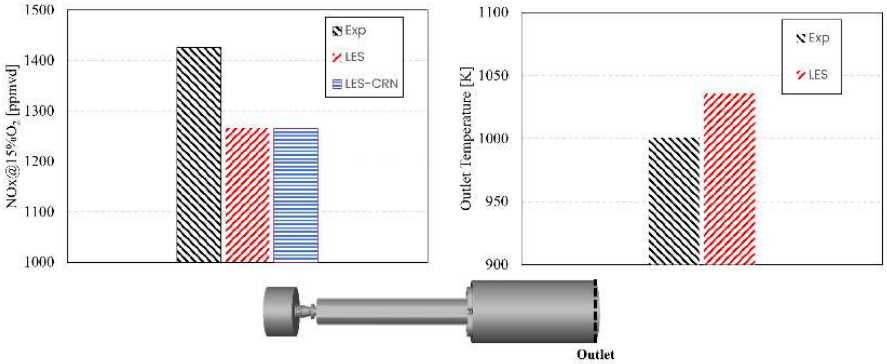

Figure 5: NO_x emission and outlet temperature derived from experimental campaign and numerical simulations.

Regarding the Flame Zone, an increase in the production of NO_2 from the reaction with the third body (NO + O (+M) ⟷ NO_2 (+M)) is observed (see Fig. 4b); with regard to the production of NO, the most important reactions are those linked to the dissociation of NO_2 (H + NO_2 ⟷ NO + OH and NO_2 + O ⟷ NO + O_2). Figure 4c shows a diagram of the most relevant sources of nitrogen oxides in the combustion process due to the dissociation of N-species like NH, NH_2 and HNO. Figure 5 shows the results of the experimental test point and CFD and CFD-CRN simulations in terms of NO_x and exhaust temperature. In terms of emissions, both the LES and CFD-CRN approaches successfully capture NO_x emissions with an error of less than 10% although underestimating it. Opposite to this, there is an overestimation of outlet temperature with an error for LES of less than 3% which corresponds to 30 K.

Conclusion

A LES simulation of a non-premixed burner fed with ammonia-hydrogen mixture under atmospheric conditions is developed and showed good validity compared to experimental data, especially for NO_x emissions. This indicates that the CFD model used is reliable in predicting emissions under specific atmospheric conditions. Furthermore, a CRN based on the time-averaged solution of the LES is implemented. This CRN provides an efficient and reliable approach to analyze in detail the NO_x formation mechanisms under the investigated operating conditions, while allowing a wide sensitivity to the main parameters of interest. The use of this CFD-CRN model can enable a more in-depth investigation of the reaction pathways responsible for NO_x formation, thus providing a better understanding of the chemical processes involved in ammonia-hydrogen combustion. This work focuses on combining advanced numerical modelling approaches with experimental data for a better understanding and prediction of emissions in unconventional combustion systems such as the one studied. The validity of the CFD model and the effectiveness of the proposed CRN provide a solid basis for optimizing the performance of burners fired with ammonia-hydrogen mixtures while reducing NO_x emissions.

Nomenclature

BH	Baker Hughes	*FZ*	Flame Zone
CFD	Computational Fluid Dynamics	*LES*	Large Eddy Simulation
CRN	Chemical Reactor Network	*OEM*	Original Equipment Manufacturing
GT	Gas Turbine	*FGM*	Flamelet Generated Manifold
FTT	Flow Through Time	*PSR*	Perfect Stirred Reactor
PFR	Plug Flow Reactor	*DIFF*	Diffusive Zone

References

[1] A. Valera-Medina, H. Xiao, M. Owen-Jones, W.I.F. David, P.J. Bowen, *"Ammonia for power"*, Progress in Energy and Combustion Science, Vol. 69, 2018.

[2] S. Chaturvedi, R. Santhosh, S. Mashruk, R. Yadav, A. Valera-Medina, *"Prediction of NO_x emissions and pathways in premixed ammonia-hydrogen-air combustion using CFD-CRN methodology"*, Journal of the Energy Institute, Vol. 111, 2023.

[3] J. Li, S. Lai, D. Chen, R. Wu, N. Kobayashi, L. Deng, H. Huang. *"A Review on Combustion Characteristics of Ammonia as a Carbon-Free Fuel"*. *Front. Energy Res* Vol. 9, 2021.

[4] P.C. Nassini, D. Pampaloni, R. Meloni, A. Andreini, *"Lean blow-out prediction in an industrial gas turbine combustor through a LES-based CFD analysis"*. Combustion and Flame, Vol 229, 2021.

[5] C. Romano, M. Cerutti, G. Babazzi, L. Miris, R. Lamioni, C. Galletti, L.Mazzotta, D. Borello, "*Ammonia Blends for Gas Turbine: Preliminary test and CFD-CRN modelling",* Accepted in Proceedings of the Combustion Institute, Milan, 2024.

[6] Oijen, J. A. V., Goey, L. P. H. D., 2000, *"Modelling of Premixed Laminar Flames using Flamelet-Generated Manifolds"*. Combustion Science and Technology,161(1), 113–137.

[7] Stagni A., Cavallotti C., Arunthanayothin S., Song Y., Herbinet O., Battin-Leclerc F., and Faravelli T., 2020, *"An experimental, Theoretical and Kinetic-Modeling Study of the Gas Phase Oxidation of Ammonia"*, React. Chem. Eng., 5(4) pp. 696.711.

[8] D. G. Goodwin et al. "*Cantera: An object-oriented software toolkit for chemical kinetics, thermodynamics, and transport processes"*, https://www.cantera.org 2022.


THE COMBUSTION INSTITUTE
1954

SESSION IV

Laminar and Turbulent Combustion, including ignition, combustion dynamics and detonation


THE COMBUSTION INSTITUTE
1954

INFRARED THERMAL IMAGING AND POLLUTANT EMISSIONS OF ULTRA-LEAN TURBULENT PRODUCER GAS FLAME

M. Z. Qureshi*, C. Caligiuri*, M. Renzi*, V. Benedetti*, F. Patuzzi*, M. Baratieri*
MQureshi@unibz.it
*Faculty of Engineering, Free University of Bolzano, piazza Università 1, 39100, Italy

Abstract
This work aims at supplying some fundamental insights of producer gas combustion and it is developed in the framework of the Green Deal project FRONTSH1P. To this aim, an in-house designed combustion chamber is directly coupled with a fluidized bed gasifier operated with wood packaging waste (e.g., disused pallets). Stable combustion process of producer gas mixtures, also at very-lean equivalence ratio (ER), is achieved and presented as an interesting insight against rising clean energy demand of industrial users with net-zero emissions. Thermal imaging based IR thermography technique is employed and time resolved flame images were viewed for flame temperature field and topology analysis at ER, $\Phi \sim 0.20$ - 0.85. The producer gas flame was quite stable and evenly distributed in the combustion chamber volume at ER = 0.85. Conversely, at lower ER, $\Phi = 0.20, 0.43$, the producer gas flame was strongly unstable due to several competing factors related to fluid dynamics and chemical kinetics. Finally, the re-stabilization opportunity of producer gas flame was revealed with the addition of a small share of methane gas (~ 5% CH_4) at ER, $\Phi \sim 0.20 - 0.25$, which could represent a possible solution to achieve flame stability at ultra-lean combustion. Moreover, CO concentrations of 53 ppm and NO_x emissions of 33 ppm were produced mainly due to fuel-prompt mechanism during ultra-lean combustion of producer gas mixture (G1) 3.70 % CH_4, 18.16 % H_2, 8.69 % CO_2, 21.79 % CO, 7.26 % H_2O, and 40.40 % N_2.

Introduction
The use of clean fuels for thermal energy production still presents several challenges, especially when low Lower Heating Value (LHV) fuels are adopted. Among such fuels, producer gas from biomass and wood wastes gasification represents an interesting low-environmental impact solution to decarbonize high-temperature industrial processes. However, stable and clean combustion of such fuels still need to be investigated in depth. To acquire deep insights into flame instability driving events, the measurement of flame temperature with fast temporal response can be adopted. The use of thermocouples as probing method is a low cost and simple solution, but it does not have a proper response to fast phenomena and could disturb fluid dynamics of the medium. Especially, the thin wire thermocouples are used and

give support to validate kinetic modelling and develop advance non-intrusive techniques for detecting flame temperature. At certain flame temperatures, soot particles and gas molecules emit strong thermal radiations lying in the spectral regions of IR (900 nm – 14000 nm) and VIS range (400 nm – 900 nm), respectively. Magnitude of radiation intensity and underlying spectrum, depending on combustion state, might serve as basis in the development of diagnostic and monitoring tools. For example, detection of black body emissions serves in the development of radiation thermometry and thermography techniques. In recent years, several thermographic studies have been conducted on open pool fires or flames. For example, Sudheer et al. [1] studied open fired gasoline flames; authors inferred flame emissivity mathematically from mass burning rate analysis and compared with experimental emissivity from thermal camera in the spectral range (7.5 – 14 μm). Raj et al. [2] characterized turbulent diffusion flames of gasoline and diesel pool fires of various diameters theoretically and experimentally with IR camera by proposing refine methods. Loboda et al. presented the spectrographic work with reference to black body spectrum and explained the radiation spectra to explore combustion of various vegetation materials, liquid fuels (alcohol, diesel, gasoline), woods and coal. In this work, the optical-based flame imaging technique has been developed for the first time for temperature field and flame topology observations of a confined producer gas flames at lean conditions in a combustion chamber.

Methods

In this work, IR flame imaging technique has been developed for measuring flame temperature field with three biomas-derived green producer gas mixtures G0, G1 and G2 (see **Table 1**). For this purpose, an in-house designed, optically accessible combustion test-rig of upto 30 kW thermal power is operated as shown in Figure 1 (Right). Size of the combustion chamber is 820 mm × 520 mm × 520 mm while burner inernal diameter is 68 mm**.**

Table 1. Producer gas compositions

Gas mixture(s)	Methan flow rate [m^3/h]	CH_4 [% vol.]	H_2 [% vol.]	CO_2 [% vol.]	CO [% vol.]	H_2O [% vol.]	N_2 [% vol.]	LHV [MJ/m^3]
G0	0.00	1.90	18.50	8.85	22.20	7.40	41.15	5.48
G1	0.11	3.70	18.16	8.69	21.79	7.26	40.40	6.04
G2	0.22	4.64	17.98	8.60	21.58	7.19	40.00	6.33

The measurement of producer gas consumption rate is peformed using FCI-ST80 thermal mass flow meter, installed on the spilled outlet pipe of the gasifier and signal is aquired using cDaq NI-9203. Consumption rate of methane flow rate is controlled by Brooks-0254 mass flow controllers. Thermal imaging based IR thermography technique is employed using IR thermal Camera FLIR - A700 of spectral range 7.5 – 14 µm with 30 Hz acquisition frequency. The ZnSe thermal window is located on combustion chamber along the zx-plane and IR camera is placed close to the window facing towards the zx-plane; hence, flame is projected as a 2D image as shown in schematic **Figure 1 (Left)**. Intrusive measurements were also conducted using N type thin wire thermocouples to calibrate emissivity of flame to be utilized in post-processing of flame images. The flue gas emissions were also monitored.

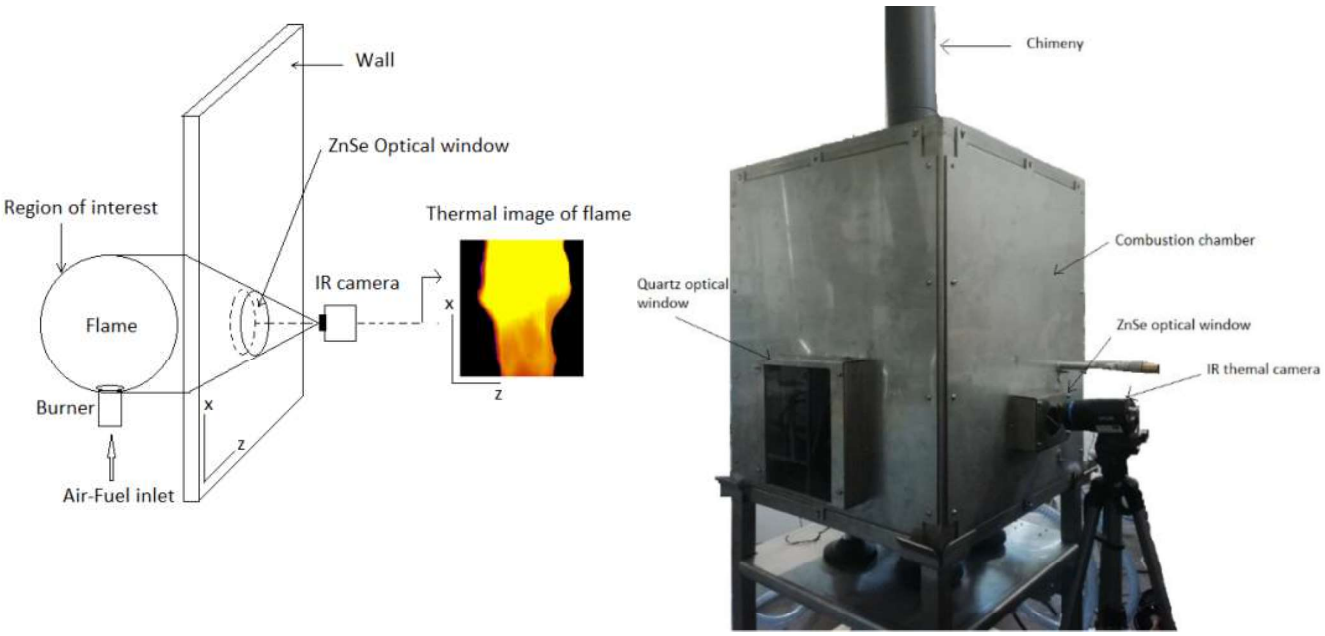

Figure 1. (Left) Schematic diagram of imaging technique. **(Right)** Combustion chamber with optical access

Flame image processing

FLIR thermal camera videos at different thermal loads and equivalece ratio points were recorded and images were processed in three major steps: (1) Emissivity of producer gas flame was corrected with maximum flame temperature measured by thermocouples; to this end, the range of emissivity values of 0.2 to 0.3 was set to match the measured range of temperature values of 900 °C - 1022 °C at lean $\boldsymbol{\Phi}$ ~ 0.65 - 0.85. (2) Pixel size 344 × 357 of flame images was used and pre-processing methods were implemented for identifying the flame zone and its boundaries by applying an edge detection algorithm. To isolate the intense foreground flame from the background, the sobel operation and canny edge detection operation were applied to detect the edges (high gradient intensities in x and z direction) around the flame

boundary, as shown in **Figure 2 (a)**. These images were converted into a binary [0; 1] field in which the area inside the flame boundary represents white region [1], while the remaining (outer) region comprises black [0] region, as shown in **Figure 2 (b)**. In the next step, pixels data of flame region were substituted with color pixels data of FLIR image, as show in **Figure 2 (c)**.

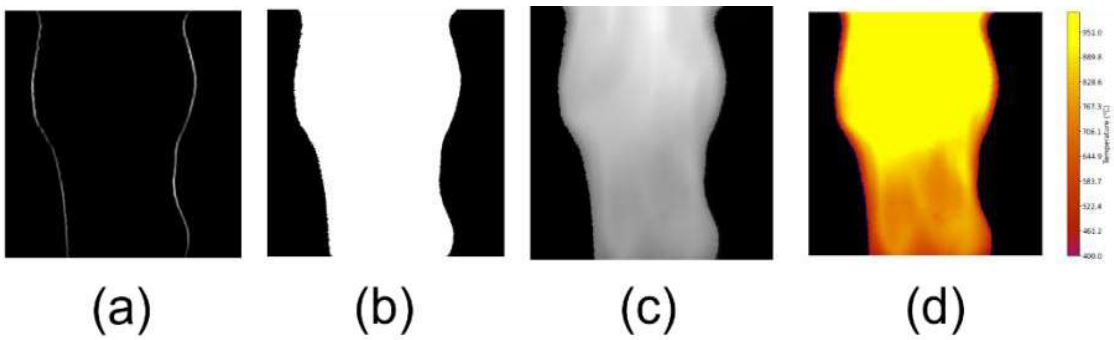

Figure 2. Flame image processing: Edge detection **(a)** Binary field **(b)** Pixel substitution **(c)** Corrected flame image **(d)**.

(3) These pre-processed RGB images were then converted into grey scale images. Using these grey and RGB scale pixel range, a mapping function was built to determine grey scale and thermal data at each pixel of images. A reference location was defined in the zx-plane according to a reference thermocouple coordinate (x, z) in the flame image (including thermocouples). A pixel based correlation factor was defined at that reference location using the grey scale and temperature value, using $Correlation\ factor = Measured\ temperature/Grey\ scale$ was used to rescale and get the corresponding corrected flame temperature, see **Figure 2 (d)**.

Results: Flame visualizations and emissions

The experimental flame data was obtained from the experimental campaign using the described methodology to present flame temperature and flame topologies of G0, G1 and G2 producer gas mixtures**.** Flame images of producer gas compositions, were viewed at 28 kW, 14 kW and 10 kW Thermal Loads (TL) for detecting flame temperature filed and topology analysis at equivalence ratios (ER), $\boldsymbol{\Phi}$ ~ 0.20 - 0.85. It is important to mention that these thermographic images do not depict the exact reaction zone; however, they identify the transition of burned to unburned regions. It appeared that producer gas G0 flame was quite stable and evenly distributed in the combustion chamber volume at ER, $\boldsymbol{\Phi}$ = 0.85. Moreover, the instantaneous flame

images showed analogous flame shapes at consecutives frames, which demonstrated a stable combustion behavior of producer gas G0 as shown in **Figure 3 (Left)**. Conversely, the producer gas flame images that were imaged at lower ER conditions led to the different outcomes. For instance, at ER, $\boldsymbol{\Phi}$ = 0.43, the producer gas G0 flame shapes at consecutive frames were distinct, as shown in **Figure 3 (Center),** due to several competing factors related to fluid dynamics and chemical kinetics. The decrement of flame temperature was noticed at lower ER conditions, which may cause the reactions to be slower and may weaken the role of chemical kinetics associated with producer gas combustion process. In addition, it appears that high flow rates of air, as compared to fuel, contributed to shred the vortical structures that

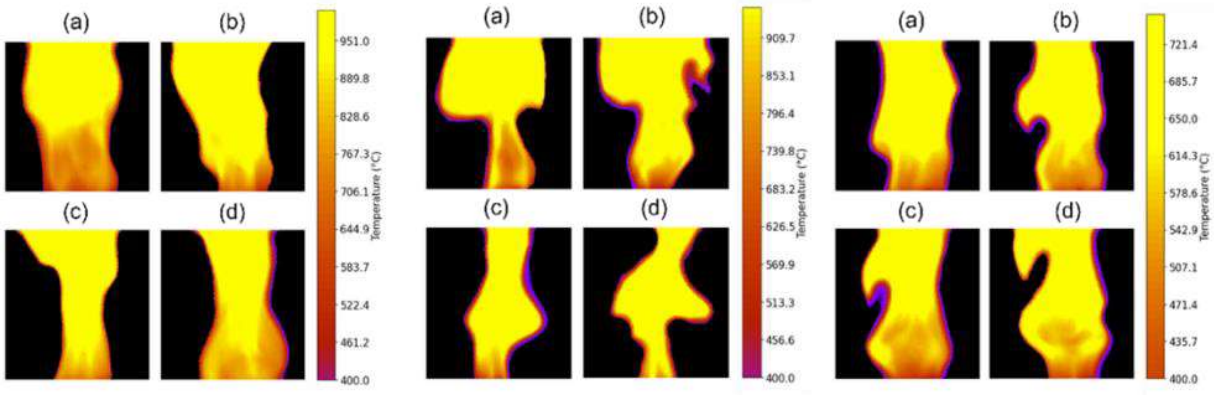

Figure 3. Time resolved flame thermal images of producer gas mixtures: G0, $\boldsymbol{\Phi}$ = 0.85 (Left), G0, $\boldsymbol{\Phi}$ = 0.43 **(Center),** G1, $\boldsymbol{\Phi}$ = 0.25 **(Right)**

perturbed the flame by creating the various branches on flame surfaces. Additionally, the phenomenon of flame neck thinning with uneven distribution was observed, which could be a sign of onset flame instability events. In particular, the flame surface area around flame neck was decreased as compared to flame at downstream location of combustion chamber. Moreover, the phenomenon of flame neck thinning became more evident when flame images were thermographically viewed at a ultra-lean ER, $\boldsymbol{\Phi}$ ~ 0.20 – 0.25. Nevertheless, it was observed that producer gas G0 flame was slightly uplifted due to flame destabilization and moved above the interrogation window. Finally, as shown in **Figure 3 (Right)**, the re-stabilization behavior of producer gas flame in G1 - G2 (only G1 mixture flame image is reported here) was revealed with addition of small share of methane gas (up to 5% CH_4) at ER, $\boldsymbol{\Phi}$ = 0.20, which could be a possible solution of producer gas flame instability at ultra-lean combustion process. This flame topology study has exhibited the flame instability events and occurrence of flame destabilization (close to blow off) events at very lean flame conditions. Morover, the flue gas emissions O_2, CO, CO_2 , and NO_x (NO and NO_2) were monitored at the outlet of combusiton chamber. In particular, CO concentrations of 9020 ppm were found to be at the highest level at ER, $\boldsymbol{\Phi}$ = 0.85, whereas, around 53 ppm were observed at very lean ER, $\boldsymbol{\Phi}$ = 0.20.

Following the same trend, NO_x emissions of 239 ppm concentration were observed at $\boldsymbol{\Phi}$ = 0.85 while the minimum concentration of 33 ppm at ER, $\boldsymbol{\Phi}$ = 0.25. These NO_x and CO pollutants were emitted mainly because of N_2 and CO components present in the fuel mixture.

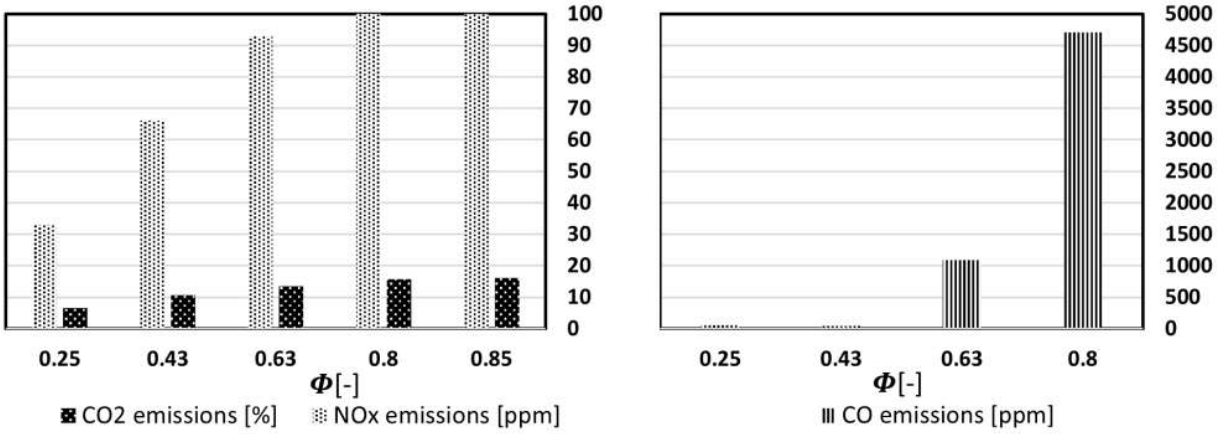

Figure 4. Flue gases: CO_2 and NO_x **(Left)** CO emissions **(Right)**.

Conclusions

In this work, the combined impact of changing TL and lean ER conditions on the producer gas combustion parameters and flame topology are evaluated. Stable combustion operation of producer gas was observed at lean ER = 0.85 conditions; conversely, flame stability concerns at ultra-lean ER, $\boldsymbol{\Phi}$ = 0.2, were encountered. It was revealed that a small share of methane could be a viable solution to overcome producer gas flame instability issues in these conditions. It was concluded that low NOx emissions ~ 35 ppm were produced mainly due to the fuel-prompt NOx mechanism in G1 producer gas flame at ultra-lean combustion.

References

[1] S. Sudheer and S. V. Prabhu, "Measurement of flame emissivity of gasoline pool fires," *Nucl. Eng. Des.*, vol. 240, no. 10, pp. 3474–3480, 2010, doi: 10.1016/j.nucengdes.2010.04.043.

[2] V. C. Raj and S. V. Prabhu, "A refined methodology to determine the spatial and temporal variation in the emissivity of diffusion flames," *Int. J. Therm. Sci.*, vol. 115, pp. 89–103, 2017, doi: 10.1016/j.ijthermalsci.2017.01.016.

A transported thickening factor strategy for multi-regime combustion

Nicola Scopolini*, Simone Castellani*, Antonio Andreini*
nicola.scopolini@unifi.it
* Department of Industrial Engineering, University of Florence, Italy

Abstract
This paper investigates the necessity for a spatial and temporal relaxation of the thickened flame model (TFM) in multi-regime combustion applications. Two definitions of flame index are employed as combustion regime sensor for both the standard model and in a dynamic relaxation strategy. The effectiveness of all modeling approaches is assessed on a Large Eddy Simulation (LES) of a two-dimensional triple flame, which is developed within a shear layer comprising fuel and oxidizer.

Introduction
Numerical modeling of multi-regime flames is inherently complex, as they may simultaneously exhibit different combustion regimes locally. While offering lower relative computational cost, tabulated chemistry approaches are difficult to apply in multi-regime scenarios, due to the complexity of generating a representative tabulation. In contrast, species transport approaches such as the thickened flame model, although computationally expensive, require fewer *a priori* assumptions, and therefore are still one of the main strategies for multi-regime combustion modeling. TFM [1] is based on the artificial thickening of the flame front to enable its resolution on a numerical LES grid, while retaining the original flame speed. This concept is applicable to premixed flames, which exhibit a well-defined flame front and speed. However, this approach cannot be applied to high Damkhöler non-premixed flames [2], as the chemical source term is not the limiting factor for the consumption speed. The current state of the art for multi-regime modeling with TFM involves the application of the dynamically thickened flame model (DTFM) [3] on the premixed zones of the flame, thanks to a regime identifier [4,5]. A subsequent switch to a finite-rate closure no-modelling strategy on the non-premixed areas is then applied. Diffusive flames, in fact, are already thickened on a LES grid, due to the non-resolved stretch. This strategy may result in a spatially discontinuous definition of the thickening factor F when neighbouring cells have different combustion regimes [6]. Furthermore, an abrupt change of the thickening factor between subsequent time steps may lead to localised numerical quenching. The reaction rates are instantaneously divided by F, while time is needed by the flame to recover its thickness. In industrial applications with low-Mach solvers these issues may be significant, as coarser grids and high values of F with larger time step, are often used.

This work aims to study a relaxation in time and space of the thickening strategy via a transport equation of F, coupled with a flame index based on the gradients of mixture fraction and progress variable.

Methodology

Flame index definition

In the standard DTFM the switch between the premixed and non-premixed treatment of the flame is done thanks to a flame regime sensor, usually a scalar. In this paper, two possible definitions of the so-called flame index concept are investigated. The first is the normalized Takeno Flame Index (FI) [7], which is based on the dot product of the fuel and the oxidizer. Since this definition doesn't explicitly account for the mixing process, expressions which include the mixture fraction Z have been introduced in the literature. For this work, the intermediate expression of the Premixedness Index (PMI) proposed by Illana et al. [8] has been used. This flame index is based on the alignment of the direction cosines of the gradients of Z and a reaction progress variable c. If the flame is locally premixed, the gradients will be perpendicular ($PMI = 1$), while in a non-premixed or weakly stratified region, the dot product will be close to 1 ($PMI = 0$).

$$PMI = 1 - \left| \frac{\nabla c}{\|\nabla c\|} \cdot \frac{\nabla Z}{\|\nabla Z\|} \right| \tag{1}$$

Since PMI has a continuous definition, a threshold value is selected to allow a certain degree of mixture stratification.

Thickening relaxation strategy

The relaxation strategy of the TFM takes its cues by the transport equation for the DTFM flame sensor Ω, introduced by Jaravel [9]. The author aim is to regularize and extend the application of F toward the preheat zone of the flame, avoiding numerical issues that arise from the sharp gradients at the flame base. Otherwise, in this work the objective is to smooth the sharp transition between premixed and non-premixed cells, through convective transport of the thickening factor. The application of F in the premixed zones is achieved directly thanks to a source production term, while a sink term is responsible for the gradual switch to the no-model approach, where $F = 1$. Furthermore, since the molecular diffusivity is alone not sufficient to correctly widen the thickened area toward the preheat zone, the actual transported scalar is multiplied by a factor n. Subsequently, the local value obtained is clipped to the minimum between F and F_{max}, given by the desired points needed to resolve the flame front. The following set of equations therefore depicts this dynamic relaxation strategy just outlined.

$$F_{max} = \frac{N}{\delta_T} \Delta x \;\rightarrow\; F_{corr} = n F_{max} \tag{2}$$

$$\frac{\partial F}{\partial t} + \frac{\partial \rho U F}{\partial x_i} = \nabla \cdot (\rho D_F \nabla F) + S_F \tag{3}$$

$$S_F = \begin{cases} \dfrac{F_{corr} - F}{\tau_0} \dot{R}_k + \dfrac{1 - F}{\tau_1} & if\ flame\ index = premixed \\ \dfrac{1 - F}{\tau_1} & if\ flame\ index = non\ premixed \end{cases} \tag{4}$$

Where N is the number of points desired in the flame front, δ_T the flame thermal thickness, Δx a one-dimensional mesh size. S_F is the global source term of the transport equation and $\dot{R}_k$ the kinetic rate of a reaction o k of choice. In addition, τ_0,τ_1 are constants that control the magnitude of the production and destruction of F. Finally, to ensure that the turbulent diffusivity contribution in the flame front is correctly switched off, as in the original DTFM formulation, a hyperbolic tangent sensor Ω is introduced.

$$\Omega = \tanh\left(\frac{F}{F_{trsh}}\right) \tag{5}$$

Where F_{trsh} is a threshold value.

Computational domain and numerical setup

Both the relaxation strategy and the standard DTFM model are investigated with LES of a 2D triple flame, developed in a shear layer of H2 and air at 3 bar. The computational domain is a 100mm x 20mm rectangle with fuel and oxidizer inlets separated by the major axis of symmetry. The boundary conditions for hydrogen and air are 12 m/s at 293 K and 3 m/s at 450 K, respectively. To validate the model, a flame-resolved reference case is discretized on a numerical grid of 40 million uniform quadrilateral elements. The Navier-Stokes equations are solved using the density-based explicit solver AVBP [10] with third-order accurate in time and space schemes. In addition, as the thickened flame model comparisons are performed on the pressure-based implicit solver ANSYS FLUENT 2022R2, a sampling of the inlet velocity profiles of the reference run has been performed, to be used as boundary conditions in the subsequent calculations. A coarser mesh of 3e-4m size is used for all LES simulations of TFM, resulting in a maximum value of $F \approx 22$ in the triple point, for a desired target of 7 points. This high value of the thickening factor is desired to exacerbate the numerical problems arising from an impulsive application of F and to represent coarser grids employed in industrial applications. Nevertheless, a separate run of the DTFM on a finer grid ($F \approx 7$) has been performed, to ensure that results are not overly dependent on the thickening factor value. Table 1 summarizes the numerical grid details.

Table 1. Grid size and relative flame thickness in the triple point.

	Reference	Coarse grid	Fine grid
$\Delta x\ [m]$	$7e-6$	$3e-4$	$1e-4$
$\delta_{T,trp}\ [m]$	$9.4e-5$	$9.4e-5$	$9.4e-5$
N_{trp}	≈ 134	≈ 0.32	≈ 0.96

Second order accurate schemes are chosen for both space and time, with a time step of 5e-6s. Mass diffusivity is accounted for through the mixture average approach, with the inclusion of Soret effects. Due to recent discussions on the direct use of the Bilger mixture fraction to evaluate the local δ_T [11], it has been decided to also investigate the F transport strategy and PMI, with the addition of a passive scalar. Furthermore, all TFM simulations are performed with the efficiency function set to 1. The authors acknowledge that this may not be correct and that it's also necessary to recover the real stretch effects on turbulent flames [12]. Nevertheless, this approach has been chosen to isolate the effects of the discontinuous application of F. The TFM simulations are initially run for 3.6e-2 s, with the source terms deactivated up to a height of 30 mm from the inlet. The aim is first to achieve a stable flame configuration and then subsequently investigate the ability of the flame to propagate upstream. A scheme of the domain and flame shape is depicted in Fig. 1. For the flame chemistry, the reaction scheme of Boivin [13] is chosen, comprising of 9 species and 12 reactions. The third body reaction $H + O_2 + M \rightleftarrows HO_2 + M$ is selected for the source term of equation 4, due to its role on the heat release of the $H2$-air triple flame and its maximum towards the preheat zone [14]. For these same reasons, the definition of the progress variable is $c = Y_{H2O} + Y_{HO2}$.

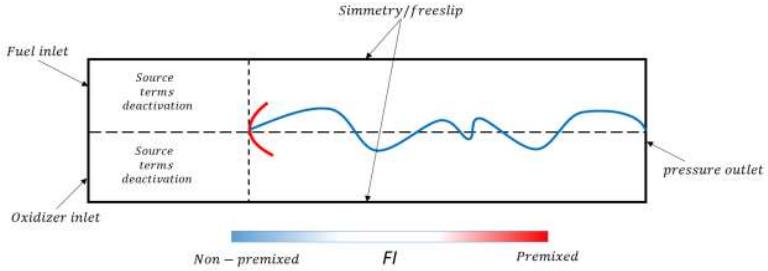

Figure 1. Schematic visualization of the computational domain and boundary conditions, with an added sketch of the expected flame shape.

Results

A 3 mm wide moving window was created based on the stoichiometric mixture fraction and maximum release location, to identify the triple point shift during the simulations. Fig. 2 clearly shows how the standard model experiences detachment for both flame indices, and for the finer grid. The impulsive discontinuous application of F does not allow the flame to anchor at the edge of the zone where the reactions are deactivated, resulting in advection from the domain.

Moving to the F transport simulations, identified as T-TFM, both flame indices capture the ability of the flame to propagate upstream. PMI is helpful in recovering the flame propagation, which is slightly improved using the passive scalar (T-TFM-

PMI-PS). Selecting the right flame index definition is more critical than in the standard DTFM, since the thickening production source is activated whenever the premixed regime is identified. Overestimation of these zones will result in unwanted thickening, as F is advected downstream. On the other hand, underestimation may lead to under-resolution of the flame front, especially in the lean branch of the triple flame.

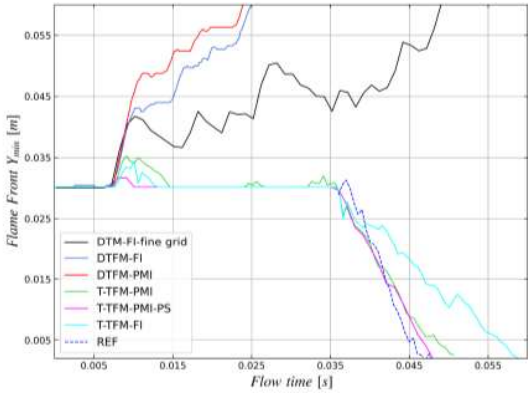

Figure 2. Minimum position of the triple flame front Y_{min} during the flame stabilization and propagation phases.

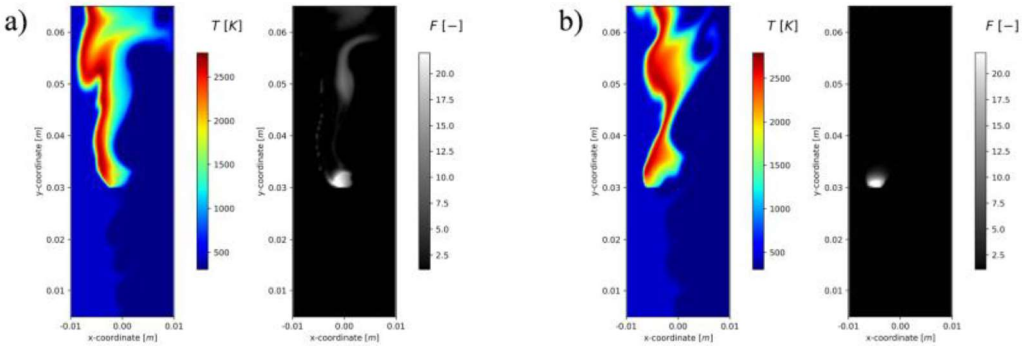

Figure 3. Contours of temperature and thickening factor for the T-TFM during the stabilization phase for FI (a) and PMI (b), respectively.

Figs. 3a and 3b show the effect of the different flame indices on the T-TFM. The PMI (see Fig 3b) results in a much smaller thickened area, localized in the triple flame leading edge. In Fig. 3a FI, on the other hand, produces thickening trails downstream of the front.

Conclusions

The purpose of this study is to demonstrate the need for spatial and temporal relaxation in the application of the thickened flame model in multi-regime flames, and to develop a strategy based on the transport of the thickening factor. In addition, two definitions of the flame index have been studied as a sensor for switching between the thickened model and the no-model approach. The results show that relaxing the thickening factor application helps in recovering the correct behavior of

the reference flame.

References

[1] Colin, O., Ducros, F., Veynante, D., Poinsot, T., "A thickened flame model for large eddy simulations of turbulent premixed combustion", *Physics of Fluids,* 12(7):1843-1863 (2000)

[2] Cuenot, B., Shum-Kivan, F., & Blanchard, S., "The thickened flame approach for non-premixed combustion: Principles and implications for turbulent combustion modeling", *Combustion and Flame,* 239: 111702 (2022)

[3] Legier, J.P., Poinsot, T., Veynante, D., "Dynamically thickened flame LES model for premixed and non-premixed turbulent combustion." *Proceedings of the summer program*. Stanford, CA, (2000)

[4] Aniello, A., Laera, D., Marragou, S., Magnes, H., Selle, L., Schuller, T., Poinsot, T., "Experimental and numerical investigation of two flame stabilization regimes observed in a dual swirl H2-air coaxial injector," *Combustion and Flame*, 249: 112595 (2023)

[5] Castellani, S., Meloni, R., Orsino, S., Ansari, N., Yadav, R., Bessette, D., Boxx, I., Andreini, A. "High-fidelity H2–CH4 jet in crossflow modelling with a flame index-controlled artificially thickened flame model", *International journal of hydrogen energy*, 48(90): 35291-35304 (2023)

[6] Ballotti, A., Castellani, S., Andreini A., "A dynamic thickening strategy for high-fidelity CFD analyses of multiregime combustion", *Proc. ASME Turbo Expo 2024 Turbomach. Tech. Conf. Expo*, London, UK, GT2024-12577 (2024)

[7] Mizobuchi, Y., Tachibana, S., Shinio, J., Ogawa, S., Takeno, T., "A numerical analysis of the structure of a turbulent hydrogen jet lifted flame" *Proc. Comb. Inst.*, 29(2): 2009-2015 (2002)

[8] Illana, E., Mira, D., & Mura, A. (2021) "An extended flame index partitioning for partially premixed combustion" *Combustion Theory and Modelling*, 25(1): 121-157 (2021)

[9] Jaravel T., *Prediction of pollutants in gas turbines using Large Eddy Simulation* (Ph.D. thesis), INP Toulouse (2016)

[10] Schönfeld, T., Rudgyard, M., "Steady and unsteady flow simulations using the hybrid flow solver AVBP", *AIAA J.* 37(11):1378–1385 (1999)

[11] https://cerfacs.fr/hydrogenweek/data/uploads/presentations/tuesday/7-2024_02_27_h2_week_douasbin.pdf

[12] Detomaso, N., Hok, J. J., Dounia, O., Laera, D., Poinsot, T., "A generalization of the Thickened Flame model for stretched flames", *Combustion and Flame*, 258: 113080 (2023)

[13] Boivin, P., Jiménez, C., Sánchez, A. L., Williams, F. A., "An explicit reduced mechanism for H2–air combustion", *Proc. Comb. Inst.*, 33(1): 517-523(2011).

[14] Owston, R., & Abraham, J. "Structure of hydrogen triple flames and premixed flames compared", *Combustion and flame*, 157(8): 1552-1565 (2010)

Laser-induced ignition in a methane/oxygen rocket combustor

D. Passiatore*,, M. Di Renzo*,**, D. Rossinelli**, J. Wang**, G. Iaccarino****
dodipass@stanford.edu
*Department of Engineering for Innovation, University of Salento, Italy
**Center for Turbulence Research, Stanford University, USA

Abstract
This study investigates laser-induced ignition in a model-rocket combustor through computational simulations. The focus is on characterizing successful and unsuccessful ignition scenarios in this extremely stochastic configuration and elucidating the underlying physical mechanisms. Large eddy simulations (LESs) are utilized to explore laser-based forced ignition in a turbulent fresh methane-oxygen mixture, with attention given to the intricate interplay of factors such as initial condition variability and turbulent flow field. Perturbations in laser parameters and initial flow conditions reproduce the stochastic behavior of realistic applications, revealing critical insights into ignition location relative to the fuel-oxidizer mixture. Results will highlight the interplay between hydrodynamic ejections from the laser spark and jet entrainment.

Introduction
In rocket combustors, laser ignition is gaining consideration owing to its mechanical simplicity, controllability, elevated kernel deposition energy, and more efficient lean ignition [1]. Nevertheless, throughout forced ignition, stochasticity arises from the interplay of the ignition kernel with the turbulent fuel-air mixture, along with variations in kernel deposition and location. Characterizing the statistical behavior of stochastic ignition phenomena becomes pivotal for the secure and dependable deployment of these ignition systems. This motivates the investigation of the present work, focusing on laser-forced ignition in a model-rocket combustor [2,3]. The goal of the study is to expose the extreme sensitivity of the process and to use computational tools to gain insights into the physical mechanism at play. To this purpose, large eddy simulations (LESs) are performed to investigate the behavior of laser-based forced ignition in gaseous methane (CH_4)/molecular oxygen (O_2) subscale rocket combustors. Three cases are carried out, one in which the laser is fired in the fuel/oxidizer jet and two in which the laser is fired just outside the fresh reactants; perturbation of some controlling parameters for these last two simulations will lead to different ignition outcomes.

Investigated test case
A sketch of the considered computational geometry is shown in Figure 1. The

combustor is discretized by a curvilinear mesh with a total of 220 million mesh points. Gaseous pure methane (coflow) and oxygen (core center) are injected through the shear coaxial injector and the two streams are separated by an annular wall. The boundary conditions used in the simulations are the Navier-Stokes characteristic boundary conditions (NSCBC), used both at the injector and at the nozzle the inlet velocity profile is set such that the total mass flow rates of oxygen (6.44 g/s) and methane (1.66 g/s) are constant in time. All walls of the combustor are modeled as a no-slip isothermal wall at 300K.

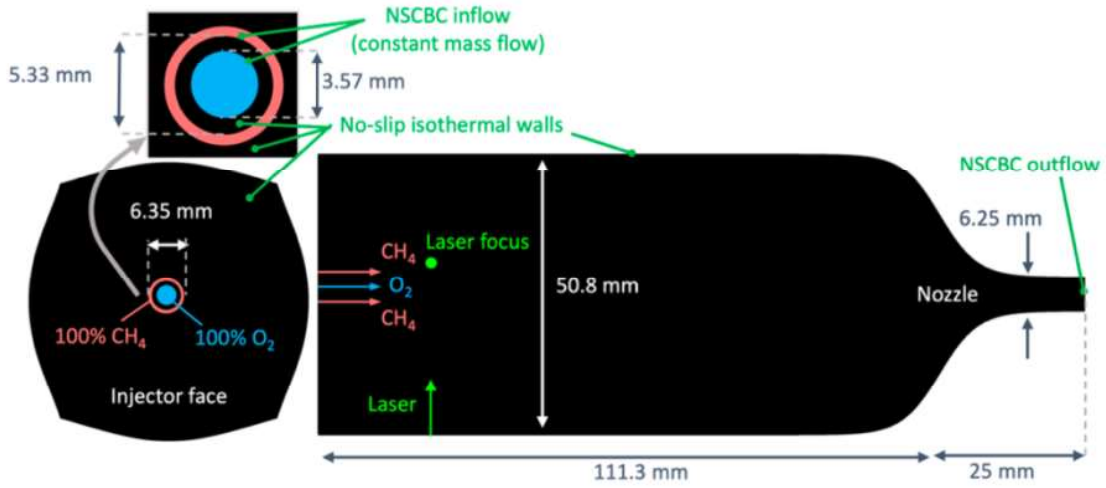

Figure 1. Schematic of the geometry and boundary conditions.

The gas in the chamber is initialized with 100% oxygen at 125 kPa and 300K to approximate the pressure composition after a long priming sequence. To analyze the relatively short dynamics of laser-induced ignition, we target a simulation time window of approximately 11ms, beginning 10ms before laser deployment.
As discussed earlier, the ignition process is stochastic and sensitive to various sources of uncertainty. The inert simulation (i.e., pre-deployment stage) is performed only once, with a two-species inert mixture of methane and oxygen. This stage is necessary to let the turbulent flow field develop and to initiate a good level of premixing of the reactants. Stochasticity of turbulence is reproduced by selecting different laser deposition instants by the end of this pre-ignition phase. The second stage of the simulation is characterized by the deployment phase. The kernel used in [4], and described hereafter, is placed at a specific focal location in the combustor. Different deployment phases (i.e., different simulations) are characterized, not only by the different laser deposition instants but also by perturbations in the deposited energy and geometrical parameters of the kernel (R1 and R2). Reasonable values of both the deposited energy and radii aspect ratio R1/R2 are informed by literature [3,5,6]. A set of these perturbed parameters is selected for each of the following simulations.

Methodology

The LESs described below are conducted using the Hypersonic Task-based Research (HTR) solver described in [7]. Details on the physical models, underlying assumptions, and numerical methods utilized can be found in [2,8,9].
The chemical mechanism considered to compute the reaction rate models combustion of methane, evaluated with a 35-step, 12-species neutral chemical-kinetic reduced mechanism FFCMy-12 extended to near-atmospheric pressures, as previously done in [4]. The laser-induced deposition of thermal energy is modeled through a source term in the total energy conservation, according to [4]. This source term is a function of a target energy value deposited by the laser in the gas, windowed in time by a Gaussian function. An ovoid shape of the kernel is imposed, controlled by the radii of two hemispherical lobes, R1 and R2, connected by a truncated cone. This geometry can faithfully capture laser-induced hydrodynamic effects [5,6].

Results preview

Case 1

For the test case analyzed in this section, the laser is focused inside the jet. This mode of ignition is referred to as direct ignition [3], as the laser deposition occurs in regions where both fuel and oxidizer coexist within the classical flammability limits of the equivalence ratio. If the deposited energy is above the minimum ignition value, sensitivity to the aforementioned parameters is almost negligible, and successful ignition is very likely to occur, as observed in [3]. Therefore, only one case is presented for this ignition mode. Figure 2 shows the flow field of density at different time instants after the laser pulse; an isosurface of temperature is also used to better visualize the flame development. The laser deposition generates a kernel of hot gases that reaches an extremely high temperature by 5μs. At the same time, the laser-generated shock wave can be appreciated. The high temperature generated by the laser, together with the local composition, initiates combustion in the form of a turbulent premixed flame, already at 50μs. The subsequent thermal expansion generates a pressure wave that spans the combustor and is subsequently reflected by the curved walls of the nozzle.

Case 2 and 3

The indirect ignition mode [3], refers to a situation in which the laser is fired outside the propellant jet. This ignition mechanism demonstrates that the interaction between the laser-generated flow and the instantaneous flow field can produce unexpected ignition scenarios. We compare two test cases, nominally identical, with a different combination of the perturbed parameters. Differences between the two sets of control parameters are guided by experimental evidence and will be highlighted in the presentation. Figure 3 shows the kernel evolution for both cases. The shape of the kernel at the first instant is similar, despite the perturbation in the kernel parameters. The origin of the laser-induced ejecta is also visible. By 470μs, the hot gases are

transported close to the region with composition within the flammability limit, initiating combustion.

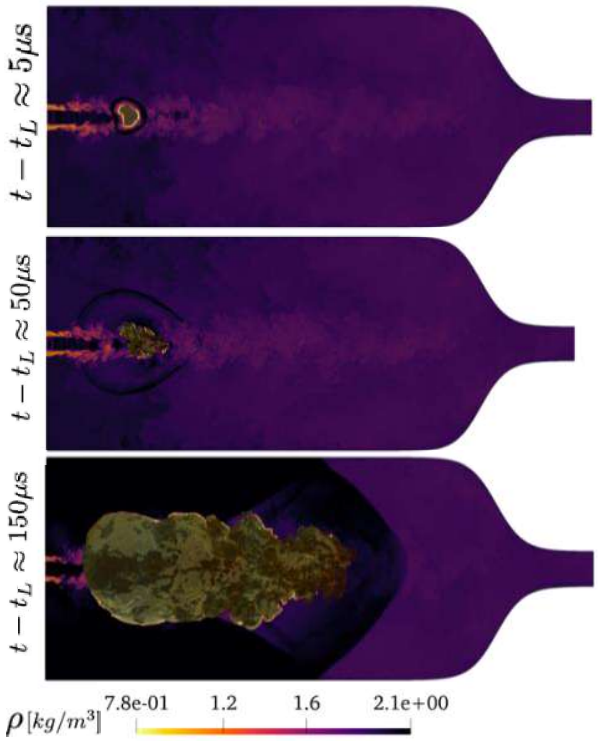

Figure 2. Contour of density field for the direct ignition case. The flame is represented by an isosurface of temperature equal to 1800 K, with arbitrary color scale.

In the other case, the jet oscillations in the downstream section are out of sync with the laser deposition and the hot gases happen to be further away from the flammable region. The last row shows a well-established flame for the igniting case, whereas hot gases in the second one continue to cool down. We use the mixture fraction Z to depict the amount of fuel and oxidizer in a certain region. To achieve ignition, high-temperature gases reaching a well-mixed region of the flow is a necessary (but not sufficient) condition. Tracking the interaction of the stochiometric region and the hot gases provides insights into the early combustion process. In Figure 4, we show a scatter plot of conditioned temperature greater than 1000 K, colored by the heat release rate, as a function of Z; in the same figure, the stochiometric value is marked by a dashed vertical line. This diagram is useful to quantitatively corroborate the two different outcomes of forced ignition, at different time instants.

Conclusive remarks

In the present work, Large Eddy Simulations of laser-induced ignition are performed. The prediction target is a subscale rocket combustor model, composed of partially

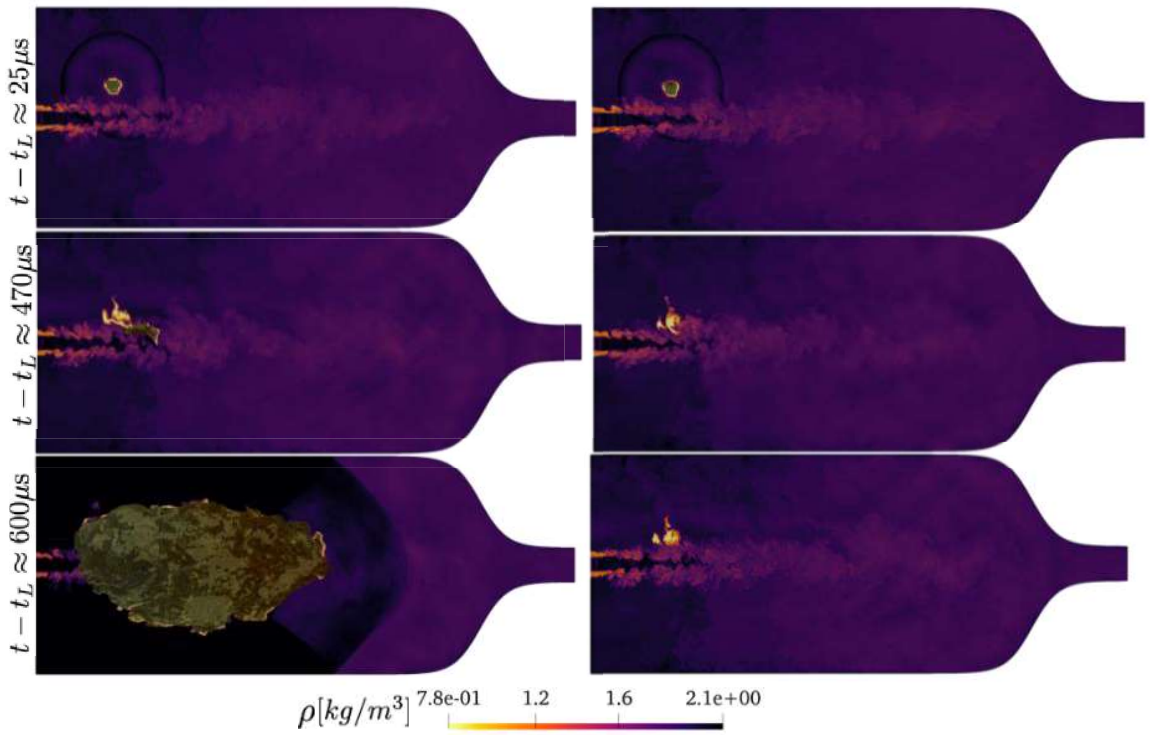

Figure 3. Contour of density field for the indirect ignition case. Igniting case (left column) and not-igniting case (right column).

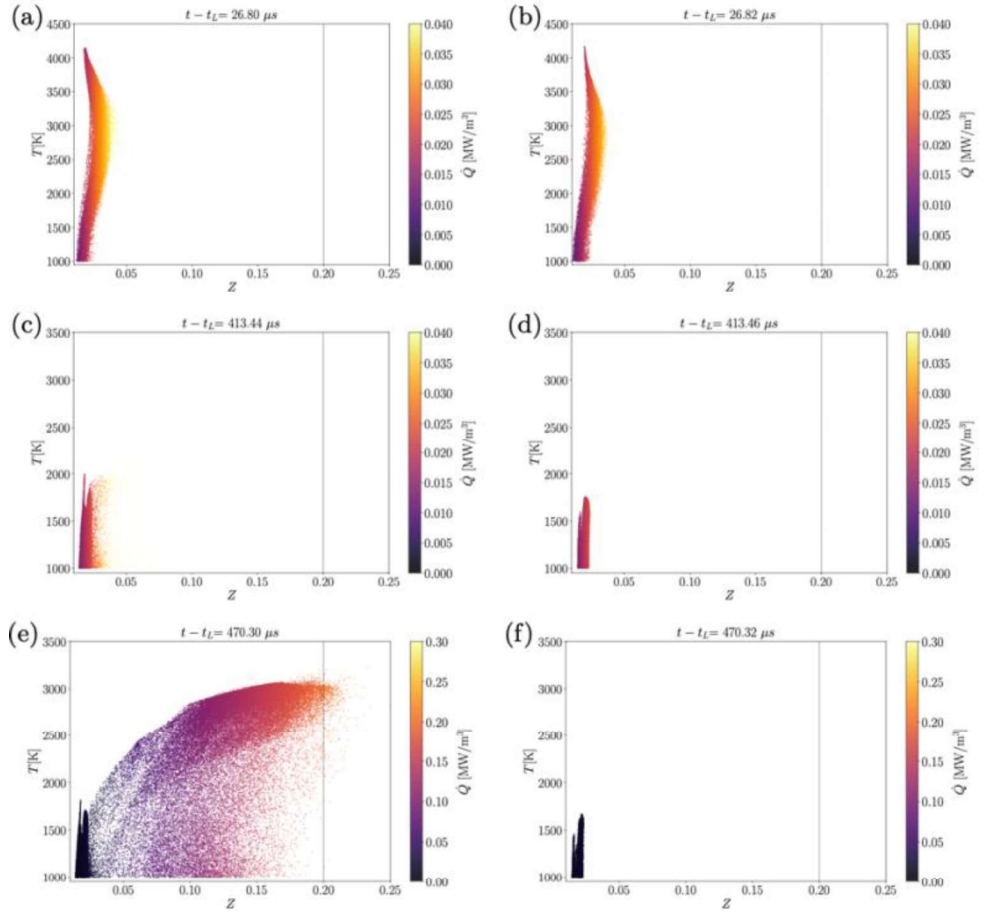

Figure 4. Scatter plot of temperature values greater than 1000 K, plotted against mixture fraction Z for igniting case (left) and not-igniting case (right).

premixed methane and oxygen, locally ignited by a laser-induced spark. It has been shown that, depending on where the energy is focused, the ignition outcome can be particularly sensitive to flow conditions. In realistic configuration, the sources of uncertainties derive mostly from difficulty in controlling the operating conditions, i.e., instantaneous turbulence, focal location, kernel shape. Specific combination of these uncertainties can lead to ignition failure. In this work, we will numerically characterize the sources of uncertainties and prove the coexistence of both ignition and no-ignition for nominally identical conditions.

References

[1] C. Manfletti. Laser ignition of an experimental cryogenic reaction and control thruster: pre-ignition conditions. *Journal of Propulsion and Power*, 30(4):925–933 (2014)

[2] J. Wang, M. Di Renzo, C. Williams, J. Urzay, and G. Iaccarino. Progress on laser ignition simulations of a ch4/o2 subscale rocket combustor using a multi-gpu task-based solver. Center for Turbulence Research Annual Research Briefs, pages 129–142 (2021)

[3] R. Strelau, M. Frederick, W. C Senior, R. Gejji, and C. D Slabaugh. Modes of laser spark ignition of a model rocket combustor. *In AIAA SCITECH 2023 Forum*, page 2377, 2023.

[4] J. M. Wang, M. Di Renzo, G. Iaccarino, H. Wang, and J. Urzay. Laser- induced indirect ignition of non-premixed turbulent shear layers. *Combustion and Flame*, 264:113426 (2024)

[5] J. M. Wang, D. A. Buchta, and J. B. Freund. Hydrodynamic ejection by laser-induced optical breakdown. *Journal of Fluid Mechanics*, 888, 2020.

[6] J. M. Wang, J. F. MacArt, and J. B. Freund. Flow dynamics of laser-induced breakdown at a fuel–oxidizer interface and its effect on ignition. *Combustion and Flame*, 229:111375 (2021)

[7] M. Di Renzo, L. Fu, and J. Urzay. HTR solver: An open-source exascale-oriented task-based multi-GPU high-order code for hypersonic aerothermodynamics. *Computer Physics Communications*, 255:107262 (2020)

[8] T. Zahtila, D. Passiatore, and G. Iaccarino. Progress on multi-fidelity simulations of a laser ignited rocket combustor. *Annual Research Briefs, Center for Turbulence Research*, 2023.

[9] D. Passiatore, J. M. Wang, M. Di Renzo, G. Iaccarino. Computational study of laser-induced modes of ignition in a coflow combustor. *Private communication* (2024)

Bayesian Data Assimilation of Acoustically-Forced Laminar Premixed Conical Flames

Alessandro Giannotta*, Matthew Yoko, Stefania Cherubini, Pietro De Palma, Matthew P. Juniper
*alessandro.giannotta@poliba.it

Abstract
We perform experiments on an acoustically-forced laminar premixed conical flame and assimilate experimental flame position data into a physics-based premixed flame model. The experimental rig is a ducted conical flame supplied by a mixture of methane and ethylene. A high-speed camera captures the dynamics of the perturbed flame, as well as snapshots of the stable flame. We model the flame with a front-tracking solver with an imposed velocity field. We use adjoint-accelerated Bayesian inference to identify the most probable model parameters, given the data. Through this, we create a quantitatively-accurate model with quantified uncertainty bounds. The trained model grants access to unmeasured quantities, such as the fluctuating heat release rate, which cannot be reliably deduced solely from flame emission. This study presents a novel method that combines flame natural emissions with reduced-order models to derive the flame transfer function with uncertainty bounds.

1. Introduction
The efficiency of the mechanism driving thermoacoustic oscillations depends strongly on the phase difference between the heat release rate (h.r.r) and pressure oscillations [1]. Because the phase difference is sensitive to small changes in most parts of a thermoacoustic system, its thermoacoustic behaviour tends to be extremely sensitive to small changes [2]. For the same reason, the outputs of faithful thermoacoustic models are also sensitive to small changes in the model parameters or the models themselves. On the positive side, this means that model parameters tend to be observable from data. In other words, with well chosen experiments, we can (i) tune the parameters of candidate models and (ii) compare candidate models against each other and select the best one [3, 4]. This extreme sensitivity also means that thermoacoustic systems can often be stabilized by making small changes, which is attractive in industrial settings. The h.r.r. rate is difficult to model or simulate a priori [5] so people often turn to experimental measurements. Unfortunately, the fluctuating emission from the flame is not a reliable method for measuring the fluctuating h.r.r. [6]. Alternatives, such as PLIF to identify reaction zones [7] are possibly more accurate but are technically difficult and, in large systems, impractical. The approach in this paper solves this problem by combining experimental measurements with numerical simulations. The natural emission of the flame may not directly give the h.r.r. but it does provide data about the flame position as a function of time. This data can be combined with candidate physics-based

models of the flame. We infer the model parameters and their uncertainties from the data. This model gives, amongst other things, the h.r.r. fluctuations as a function of the velocity fluctuations. This flame model will then be included within a larger model of the thermoacoustic behaviour of the system, whose other parameters are inferred in the same way [8]. The end result will be a quantitatively-accurate physics-based model of the flame and thermoacoustic systems that is interpretable, trustworthy, and extrapolatable.

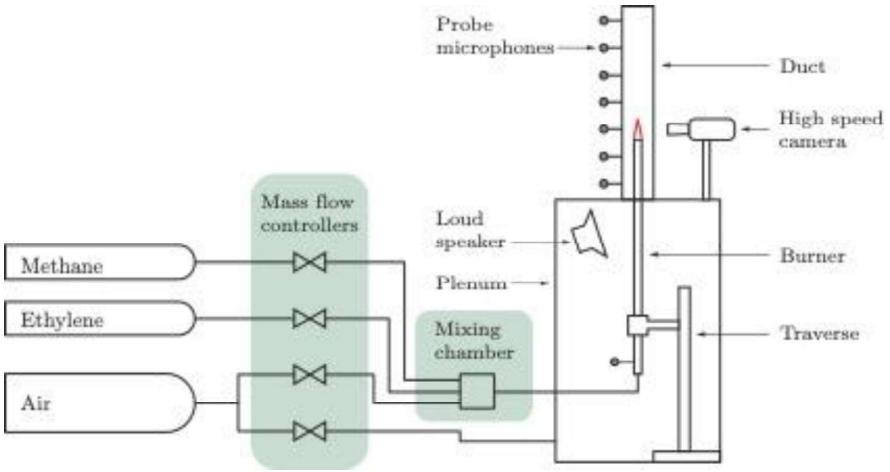

Figure 1. Diagram of the experimental rig.

2. Experiments

The experimental configuration is a laminar premixed conical flame inserted into a vertical duct, as illustrated in Figure 1. The lower end of the duct is fixed to a plenum chamber, through which co-flow air is supplied. The upper end is open to atmosphere. The duct is a 0.8 m long section of quartz tube with an internal diameter of 75 mm. The burner is a 0.85 m long section of brass tubing with an internal diameter of 14 mm. At the injection plane, the nozzle diameter is 9.35 mm. The burner is fuelled by a mixture of methane and ethylene over a wide range of equivalence ratios and fuel mass flow rates. The premixed air and fuel are supplied to the base of the burner via a set of mass flow controllers. A high-speed camera is used to record the flame under both steady and perturbed conditions. The position of the flame-front in the image, is used as the experimental data for data assimilation. The properties of the flame studied in this work are summarised in Table 1. The flame is forced at 230 Hz, which was chosen to be close to the duct's fundamental mode.

Table 1. Summary of the properties of the flame studied in this paper.

Property	Value	Units
Air flow	8.444	[Ln/min]
CH4 flow	0.449	[Ln/min]
C2H4 flow	0.499	[Ln/min]
Equivalence ratio	1.27	[-]

Mean flow velocity	2.45	[m/s]
Mean heat release rate	525	[W]

3. Reduced-Order Model of a laminar premixed Bunsen flame

The flame is approximated by an axisymmetric surface separating the reactants from the products. Each point of the surface is in kinematic equilibrium between the local flame speed and the reactants velocity field. In this study, we adopt a front-tracking method as detailed in Ref [9]. The model can then be expressed compactly through:

$$d\boldsymbol{x}/dt = \boldsymbol{f}(t,\boldsymbol{x};\boldsymbol{p}) \quad (1)$$

where $\boldsymbol{x} = (\boldsymbol{r}, \boldsymbol{z})$ is the state vector defining the flame front position in terms of radial coordinates, $\boldsymbol{r}$, and longitudinal coordinates, $\boldsymbol{z}$. The vector $\boldsymbol{p}$ contains the physics-based parameters, while $\boldsymbol{f}$ is the physics-based nonlinear operator encapsulating the flame-front dynamics. The main feature of the model is that it has been designed to be differentiable with respect to the state and the parameters. The model parameters $\boldsymbol{p}$ are: (i) the flame aspect ratio $\beta = \beta(\bar{u}, S_L)$, which depends on the bulk velocity in the burner tube $\bar{u}$, and the unstretched laminar flame speed S_L; (ii) the nondimensional Markstein length M, which depends on the thermal expansion parameter, the effective Lewis number of the mixture, the Zel'dovich number and the thermal conductivity of the mixture [10]; (iii) the shape parameter μ, which linearly combines a uniform and a parabolic mean velocity profile [11]; (iv) the wavelength of the harmonic perturbation velocity field K; (v) the amplitude of the acoustic forcing ε_V ; (vi) the amplitude of the flame base oscillations λ; (vii) the initial phase of the flame base oscillations φ_0. These seven parameters are sufficient to describe the flame front dynamics qualitatively. All lengths, including the Markstein length, are normalised by the nozzle radius.

4. Bayesian data assimilation

In this section, we introduce the following notation: the data D is the flame position observed in the experiment $\boldsymbol{x_e}$; the model H encodes the reduced-order model described in the previous section such that for a given set of parameters $\boldsymbol{a}$, the model $H(\boldsymbol{a})$ gives a prediction of the flame position $\boldsymbol{x}(\boldsymbol{a})$.

We assume that the model can describe the data and we infer its most probable parameters $\boldsymbol{a_{MP}}$. We propose a prior probability distribution over the parameter values, through which we can encode any prior knowledge. We then use the data, D to perform a Bayesian update on the parameter values:

$$P(\boldsymbol{a}|D,H) = P(D|\boldsymbol{a},H)P(\boldsymbol{a}|H)/P(D|H) \quad (2)$$

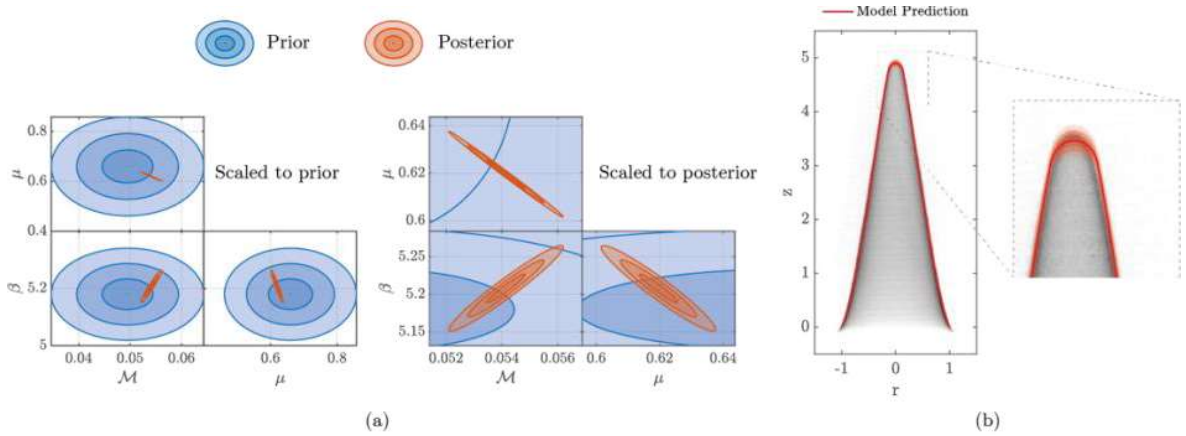

Figure 2. (a) Prior (blue) and posterior (red) probability distributions of the parameters in the steady case. The contours show 1, 2, and 3 standard deviations from the prior and posterior parameter estimations. The parameters are the flame aspect ratio β, the shape parameter for the velocity field μ and the nondimensional Markstein length M. (b) Model prediction (red line) with a confidence interval of 3 standard deviations (red shading) plotted on top of the steady flame image. The panel on the right shows a magnification of the flame tip.

The best estimate of the parameters is that which maximises the left hand side of equation (3). We ignore the denominator because it does not depend on the parameters and we therefore maximise the numerator.
It is convenient to define the cost function, J, as the negative log of the numerator. We then minimise J using a quasi-Newton BFGS method with gradient information provided by adjoint methods. Once we have found the most likely parameters $\boldsymbol{a_{MP}}$, we use Laplace's method [3] to determine their uncertainties. We assume that $P(\boldsymbol{a}|D,H)$ is Gaussian around $\boldsymbol{a_{MP}}$ and approximate the inverse covariance matrix as the Hessian of the cost function.

5. Parameter inference from flame snapshots

The data assimilation process is performed in two steps. From the steady-state flame snapshot we can infer the values of the aspect ratio β, the nondimensional Markstein length M and velocity shape parameter μ. We start by setting a large uncertainty in the prior values of the parameters. Figure 2a shows the prior and posterior probability distribution of the model parameters. The contours show 1, 2 and 3 standard deviations from the prior $\boldsymbol{ap}$ (blue) and posterior $\boldsymbol{a_{MP}}$ (red). In general, the uncertainties in the parameters have been reduced significantly by the data assimilation to quite precise values. Figure 2b shows the model prediction ± 3 standard deviations plotted against the experimental flame-front picture. The largest uncertainties are found at the flame tip, which is the region that is most sensitive to the parameters.
We repeat the process with the images of the acoustically forced flame-front. In this case we use the knowledge gained from the previous step and set large uncertainty in the prior values of K, ε_V, λ and φ_0 . Figure 3 shows the model prediction ± 3

standard deviations, plotted against the experimental flame-fronts, during a limit cycle. As in the steady-state case, the largest uncertainties are found at the flame tip. The discrepancies between the flame-front observations and model predictions are due to model error. This could be reduced by adding more physical phenomena to the model and applying the same data-assimilation process, although this risks creating an elaborate model with too many parameters to be useful. The advantage of the current model is that, even though it contains some model error, it can match the experimental images well at nearly all moments in the cycle. This model, because it contains few parameters, can be trained on a relatively small amount of data.

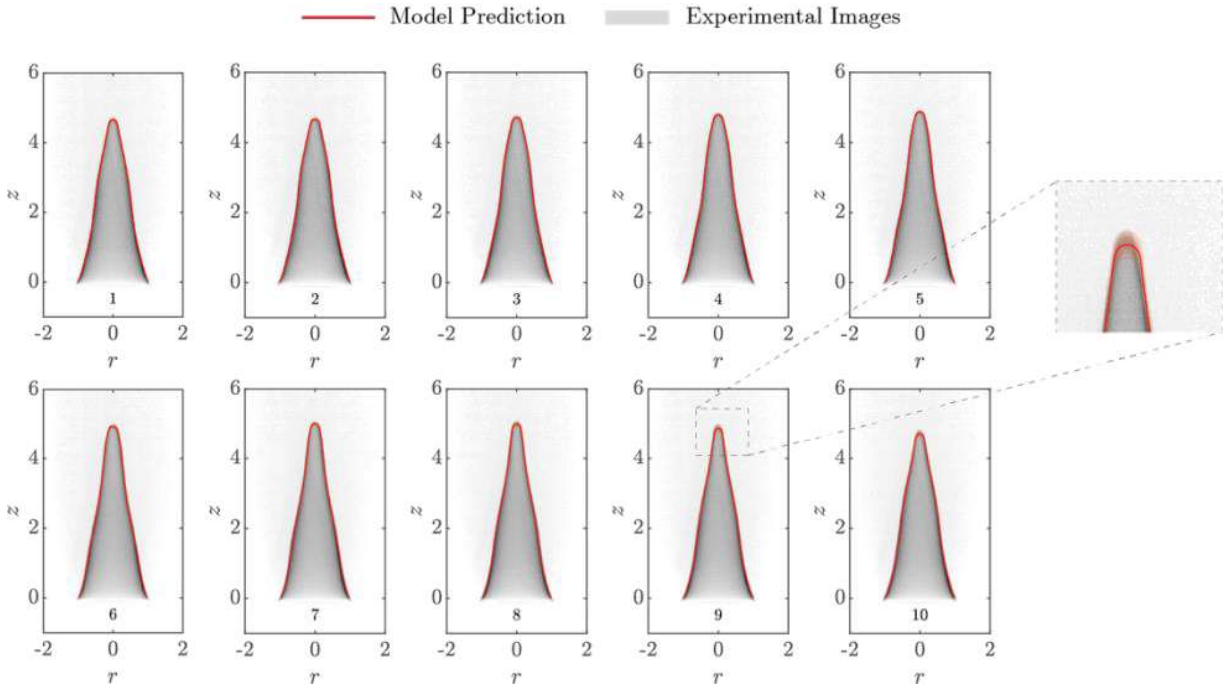

Figure 3. Model prediction (red line) with a confidence interval of 3 standard deviations (red shading) plotted on top of 10 frames of the unsteady flame, captured during a limit cycle.

6. Heat release rate

Once the most probable parameter values are inferred and the flame-front position predictions are obtained, we can estimate the heat release rate. We express the heat release rate, q, as the sum of a steady part, $\bar{q}$, and a perturbation, q'. Figure 4 shows the unsteady heat release rate, q, normalised by the mean heat release rate, $\bar{q}$, plotted over one period. The times at which the snapshots occur are indicated with dots, labelled with the corresponding frame numbers from Figure 3. We see that the trained model allows us to reconstruct a smooth heat release rate signal from sparse observations. We are also able to quantify the uncertainty in the fluctuating heat release rate. Figure 4 also shows the normalised velocity perturbation at the burner rim $u'_Z/\bar{u}$, which gives rise to the heat release rate fluctuations. We are therefore able to use the trained model to quantify the thermoacoustic response of the flame.

For example, by linearising the model around this point, we can calculate the flame transfer function of this flame, with defined uncertainty bounds.

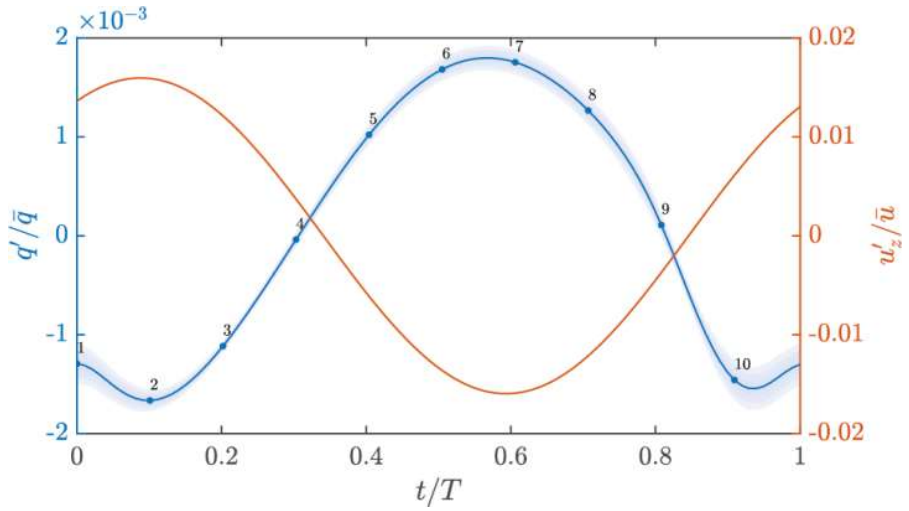

Figure 4. On the left y-axis, we show the normalised heat release rate perturbation, $q'/\bar{q}$, predicted by the model during one period, T, of the limit-cycle (blue line). The numbers on the blue line refer to the frame numbers in Figure 3. The contours show 1, 2, and 3 standard deviations from the maximum a posteriori model prediction. On the right y-axis we show the normalised longitudinal velocity perturbation at the burner rim, $u_z'/\bar{u}$

7. Conclusions

In this study, we perform experiments on an acoustically forced, laminar premixed conical flame in a duct. We use a high-speed camera to record snapshots of the natural emission of the flame while steady and forced. We propose a physics-based reduced-order model of this flame and infer the most probable model parameters from the data. This process (i) turns a qualitatively-accurate model into a quantitatively-accurate model, and (ii) quantifies the uncertainty in the inferred model parameters and the model predictions. The inference process produces a digital-twin of the flame, which provides access to quantities that were not directly measured in the experiments. From observations of the perturbed flame we can infer the fluctuating heat release rate as a response to the velocity perturbation. This is used to calculate the flame's thermoacoustic response through the flame transfer function. We have demonstrated this using snapshots of the natural luminosity of the flame, which can be captured using a basic experimental setup. We can therefore estimate a flame's thermoacoustic response without the need for direct velocity or heat release rate measurements. In future work we will (i) apply this method to a wide range of conical flames, (ii) propose general models for the parameters so that we can predict the behaviour of unseen flames, and (iii) apply the inferred flame transfer functions to a higher level model of the thermoacoustic system.

References

[1] Lieuwen, T. C. and Yang V., "Combustion Instabilities In Gas Turbine Engines: Operational Experience, Fundamental Mechanisms, and Modeling", *volume 210. American Institute of Aeronautics and Astronautics*, 2005.

[2] Mongia H.C., Held T., Hsiao G. and Pandalai R., "Challenges and progress in controlling dynamics in gas turbine combustors". *Journal of Propulsion and Power* 2003; 19(5): 822–829.

[3] Juniper M.P. and Yoko M., "Generating a physics-based quantitatively-accurate model of an electrically-heated Rijke tube with Bayesian inference". *Journal of Sound and Vibration* 2022; 535: 117096.

[4] Yoko M. and Juniper M.P., "Minimizing the data required to train a physics-based thermoacoustic model". In *29th international congress on sound and vibration*, 2023.

[5] Poinsot T., "Prediction and control of combustion instabilities in real engines". *Proceedings of the Combustion Institute* 2017; 36(1): 1–28.

[6] Han Z, Balusamy S and Hochgreb S. "Spatial analysis on forced heat release response of turbulent stratified flames". *Journal of Engineering for Gas Turbines and Power* 2015; 137(6).

[7] Yuan R, Kariuki J, Dowlut A, Balachandran R and Mastorakos E., "Reaction zone visualisation in swirling spray n-heptane flames". *Proceedings of the Combustion Institute* 2015; 35(2): 1649–1656.

[8] Yoko M. and Juniper M.P. "Data-driven modelling of thermoacoustic instability in a ducted conical flame". *In Symposium on Thermoacoustics in Combustion, 11-14 September 2023*, Zurich, Switzerland, pp. 1–12.

[9] Giannotta A., Cherubini S., De Palma P. and Juniper M.P. "The effect of flame curvature and flame base movement on the frequency response of a conical Bunsen flame". *Combustion and Flame*, 2024.

[10] Matalon M. "Intrinsic flame instabilities in premixed and nonpremixed combustion". *Annu Rev Fluid Mech* 2007; 39: 163–191

[11] Yu H, Juniper MP and Magri L. "A data-driven kinematic model of a ducted premixed flame". *Proceedings of the Combustion Institute* 2021; 38(4): 6231–6239.

Analysis of Flame Propagation and Detonation Characteristics in Hydrogen-Oxygen and Ammonia-Oxygen Mixtures

Giacomo Cinieri, Zubair Ali Shah, Maria Grazia De Giorgi*,
mariagrazia.degiorgi@unisalento.it

Abstract
This work investigates detonation in a microdevice for ammonia-hydrogen-oxygen mixtures at 10 bar. The ZND model and the Navier-Stokes equations with skeletal mechanisms are solved. The results are in good agreement with experimental data, where available. Temperature, Chapman-Jouguet parameters, and cellular size are correlated to hydrogen concentration, revealing a clear functional relationship. In flames with low hydrogen composition, the cell size increases and the CJ velocity decreases. In the 2D simulation, starting from a hydrogen/oxygen products hotspot, the time and space to detonation are analyzed, showing good agreement with ZND model. For pure ammonia/oxygen composition, flame does not propagate.Ammonia is a promising compound for the chemical storage of renewable energy produced from non-continuous sources. However, the low reactivity of ammonia necessitates the use of ammonia–hydrogen blends as a fuel for combustion applications.

Introduction
Combustion can manifest in various modes, including laminar flames, deflagrations, and detonations. Deflagrations involve subsonic expansion waves that propagate through the diffusion of heat and mass from the reaction zone to ignite the unburned gases. This burning rate leads to increased turbulence in the unburned gases, establishing a positive feedback loop between turbulence and the reaction zone. Additionally, the flame front interacts with walls and obstacles, further enhancing acceleration. At the same time, the reaction zone is quenched due to flame stretch and mixing of cold reactants with hot products, imposing an upper limit on flame acceleration and finding an equilibrium in deflagration. This is why the interest in Deflagration-to-Detonation Transition (DDT) in micro/meso devices has led to the utilization of hydrogen as an essential fuel component. Without the presence of hydrogen, avoiding flame quenching and the cessation of propagation remain undocumented in the literature. Ignition and flame stabilization processes in supersonic combustion microdevices significantly differ from those observed in the subsonic regime [1]. Flames generate acoustic waves that propagate into the unburned mixture at the local speed of sound. These waves may converge and form precursor shocks, thereby pre-compressing the reactant mixture and elevating its temperature. The fundamental arrangement of a stable detonation wave can be elucidated through the Zeldovich-von Neumann-Döring (ZND) model, comprising

a leading shock and a subsequent reaction zone. Within this framework, the lowest attainable detonation velocity is identified as the Chapman-Jouguet (CJ) speed [2]. Despite the ZND model assumption of a stable detonation wave, empirical and computational investigations have demonstrated that actual detonation waves exhibit instability under flow disturbances. Another issue is the selection of an appropriate kinetic model. On one hand, there's the need to retain information about radicals.On the other hand, a highly detailed mechanism would make simulations computationally heavily demanding. This study aims to shed new light on the detonation of mixtures at high pressure with blends of ammonia and hydrogen, an area where the literature on explosions and detonation is largely unexplored. Flame acceleration and transition to detonation in $NH_3/H_2/O_2$ mixture at atmospheric condition was studied by Zhu et al [3]. This research focuses on investigating detonation within a microdevice containing H_2 / O_2 and NH_3-H_2-O_2 mixtures at 10 bar. The primary objectives include correlating temperature, CJ parameters, and cellular size with hydrogen/ammonia concentration to understand their relationships. Additionally, the research will examine the impact of varying blend compositions on cell size and CJ velocity. Preliminary 2D simulations, starting from a hotspot, will analyze the time and space required for H_2 detonation and its 2D cellular structure.

Methodology

To compute the DDT parameters, we employ a two-pronged approach using both 2D and 1D simulations. For the 2D simulations, we utilize OpenFoam 6 with detonationFoam and Adaptive Mesh Refinement (AMR) technology [4], [5]. For 1D computations, we utilize the Shock and Detonation Toolbox, a collection of MATLAB scripts and functions, fo CJ parameter forecasting and 1D computations. The toolbox is used to calculate CJ velocities, pressure, and temperature for the given fuel mixtures, which are crucial for understanding the theoretical detonation characteristics and serve as a benchmark for 2D simulation results. The 1D computations involve solving the ZND equations to obtain detailed profiles of detonation wave structure, including shock front, reaction zone, and energy release rate. The results from 1D computations provide a foundational understanding of the detonation process, which is compared and validated against the more complex 2D simulations performed with Detonationfoam. An adiabatic duct of 0.9 mm width is the test case, already analyzed by Ramachandran et al. [6] with the PeleC code. A symmetry boundary condition is applied to half the computation cost, knowing the symmetrical flame behavior. Pressure is equal to 10 bar, and the unburned gas is at the temperature of 503 K at stoichiometric conditions. At the beginning of the simulation, the flame front is a y = 1 mm with a temperature of 3075 K for pure hydrogen and 2773 for ammonia blends test cases. 2D simulations with pure ammonia/oxygen test case shows no propagation, proving the importance of hydrogen blending in DDT ammonia mixtures. In Table 1, molar fractions for different mixtures simulated in the paper are provided. The duct is divided into 10^4x16 cells. A Courant number of 0.55 is applied.

Table 1. Molar fractions for different test cases. P = 10 bar, T = 503 K

Test case	*NH_3*	*H_2*	*O_2*	*Test case*	*NH_3*	*H_2*	*O_2*
m1	0.4706	0.1176	0.41	*m5*	0.16	0.48	0.36
m2	0.4	0.2	0.4	*m6*	0.0816	0.5714	0.3469
m3	0.3077	0.3077	0.3846	*m7*	0	0.667	0.333
m4	0.2105	0.4211	0.368				

Bykov et al. mechanism has been used [7]. Ignition delay time and CJ velocity were predicted and compared with experiments respectively in [8] and in [9] in Figure 1.

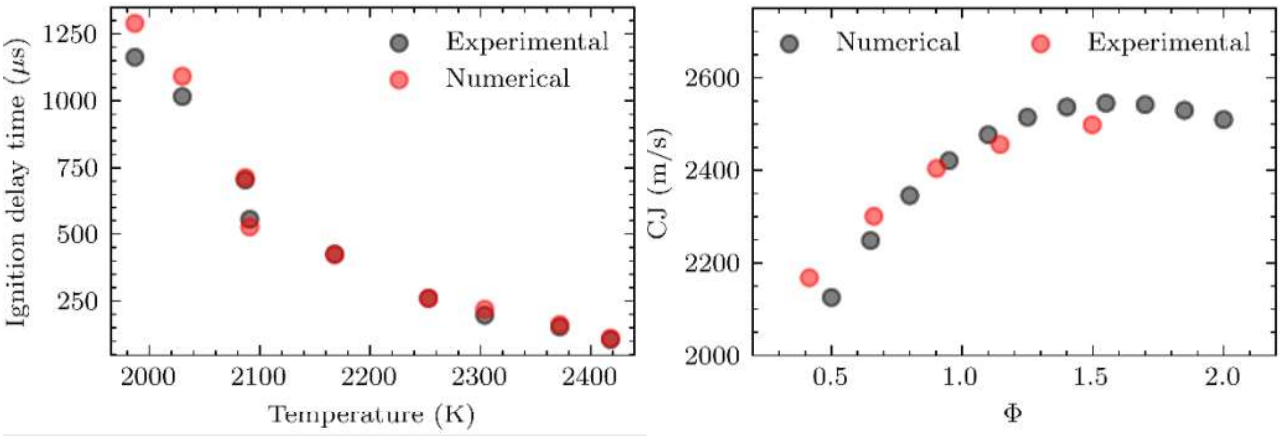

Figure 1. a) IDTs of 0.005715 NH_3/ 0.004285 O_2 / 0.99Ar mixture with p=11 atm [8], b) CJ velocity for NH_3/ O_2, Φ = 1, T=295 K [9].

Results

The Shock & Detonation Toolbox is used to predict the $NH_3/H_2/O_2$ ZND structures at p_0 = 10 atm consistent with the initial condition in Table 1. Figures 2a and 2b illustrate the spatial distribution of temperature and thermicity (heat release beyond the shock) from the ZDN structure (the shock is positioned at x=0 with a velocity corresponding to the CJ value for each mixture). Across the shock wave, the temperature sharply jumps from 2000 K to over 4000 for the pure H_2/O_2 mixture, and to 3700 K for the mixture with the lowest H2 fraction (m1). The heat release is primarily located around 10 μm for most conditions. For NH_3 molar concentrations greater than 0.3077, the peak of thermicity shifts (see Figures 2a-2b. Specifically, for the m1 mixture, this peak occurs at x=28 μm.

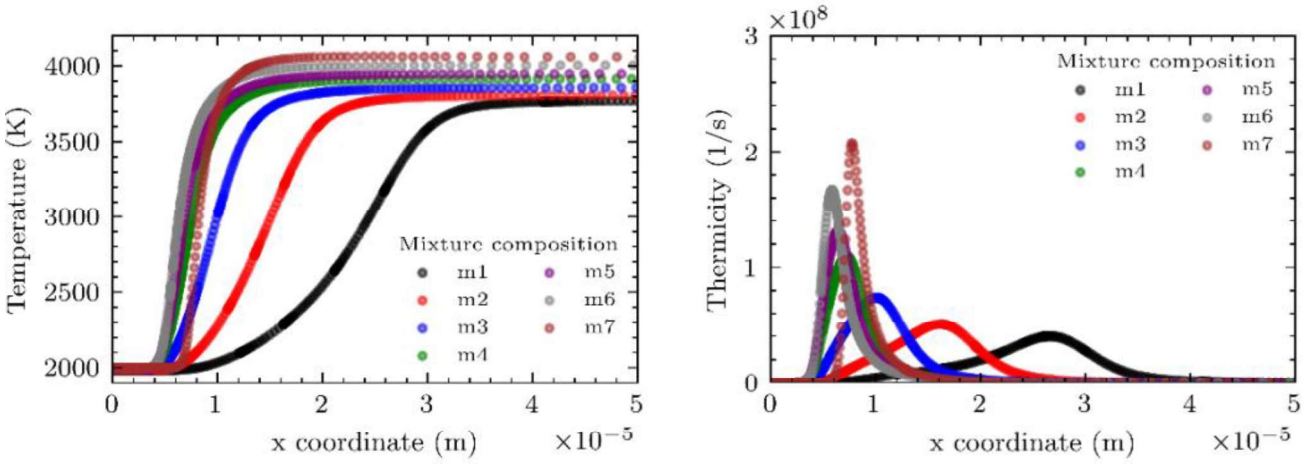

a) b)

Figure 2. Distributions of a) temperature, b) thermicity for different mixture compositions (read Table 1).

In Figure 3, CJ velocity and cellular size (λ) with Ng et al. model correlation [10] are computed. CJ increases from 2495 m/s to 2835 m/s. The λ value decreases from 1 cm to 2.4 mm for m6 to the final value of 3.2 mm for pure H_2 case.

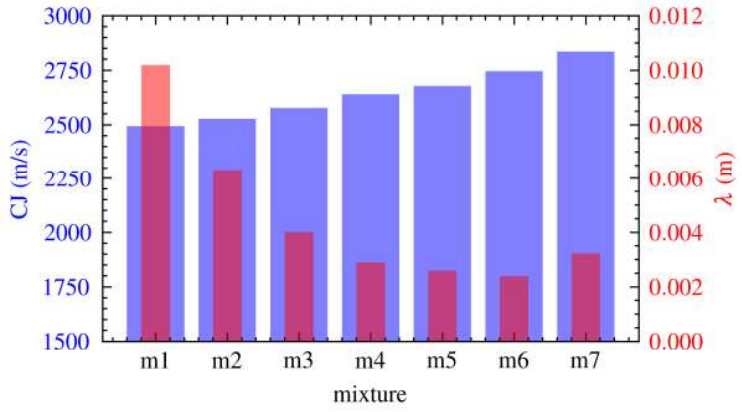

Figure 3. Computed CJ velocity and cell size as functions of NH_3/H_2 molar ratio a in stoichiometric NH3/H2/ O2 mixtures.

DDT 2-D results for m7 mixture are presented compared with PeleC solver simulation results performed in [6]. For hydrogen-oxygen DNS, Li et al. mechanism is used, already widely validated in literature for different pressure conditions [8]. The flame propagates at a velocity of 550 m/s, and the DDT initiates around 155 μs.Figure 4a illustrates the flame front propagation, which aligns well with previously reported results. Figure 4b depicts the axial pressure time sequence, showing the distribution and evolution of shock waves. The pressure in the detonation increases from 10 to 14 bar within $1.6e^{-4}$ s. The temperature increases from 3700 K to over 4000 K during detonation.

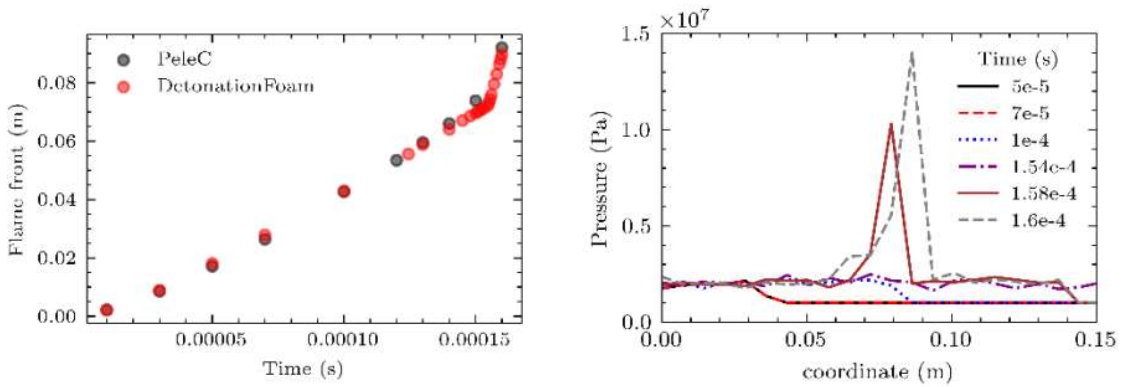

a) b)

Figure 4. 2D-time sequence of a) flame front position, b) pressure in the midline for m7 mixture.

Figure 5 depicts the shape evolution of the flame front from ignition to DDT.

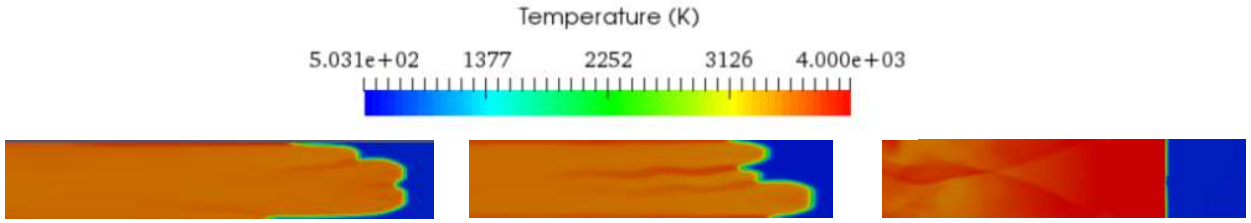

t = 1.4e-4 s t = 1.5 e-4 s t = 1.555 e-4 s

Figure 5. DDT time sequence of temperature distributions at flame front for m7 mixture.

Figure 6 illustrates the detonation and the cellular structure of the phenomenon at t=1.555e^{-4} s. The cell size λ at the completed transition (t = 1.57e-4 s) measures 3.05 mm, which is in good agreement with the results shown in Figure 3.

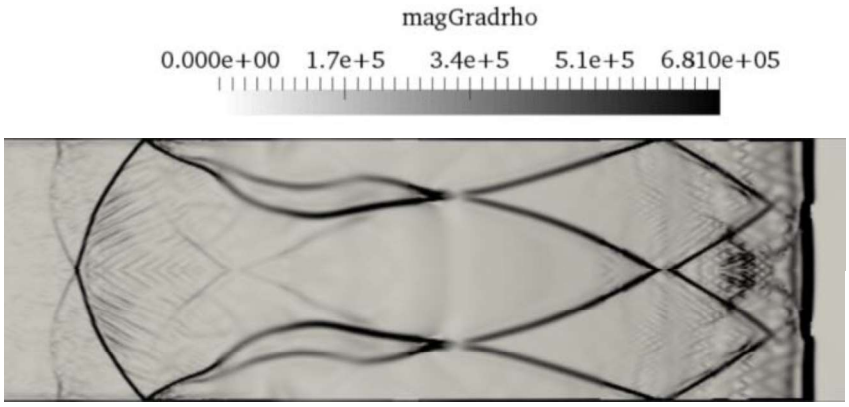

Figure 6. Numerical Schlieren visualization for m7 mixture at t = 1.555 e-4 s.

Conclusions

In this work, the characteristics of flame deflagration and detonation in a channel

filled with pure H_2/O_2 and $NH_3/H_2/O_2$ at 10 bar have been investigated. The fully compressible Navier-Stokes equations, coupled with the perfect gas equation of state, are solved using detonationFoam. The ZND model is analyzed using the Shock & Detonation Toolbox for seven different mixture compositions, providing Chapman-Jouguet (CJ) parameters, cellular sizes, and shock thermal characteristics. As H_2 concentration increases, the temperature and thermicity rise, and the shock width shifts to the left, shortening to a few micrometers. For the H_2/O_2 condition, a 2D DDT analysis reveals a detonation initiation time of 1.6e-4 seconds and a detonation distance of 0.089 meters. The cellular structure is confirmed with a size of 3 mm, which is in good agreement with ZND model predictions.

Funding

The present project has been funded by PRIN 2022 ROADMAP (202225ZCSE) - CUP F53D23001510006.
Giacomo Cinieri has been funded by Apulia Region, POC PUGLIA. FESRTFSE 014/2020 RIPARTI project.

References

[1] F. S. Billig, 'Research on supersonic combustion', *Journal of Propulsion and Power*, vol. 9, no. 4, pp. 499–514, Jul. 1993, doi: 10.2514/3.23652.
[2] F. A. Williams, *Combustion Theory*. CRC Press, 2018.
[3] R. Zhu, X. Fang, C. Xu, M. Zhao, H. Zhang, and M. Davy, 'Pulsating one-dimensional detonation in ammonia-hydrogen–air mixtures', *International Journal of Hydrogen Energy*, vol. 47, no. 50, pp. 21517–21536, Jun. 2022, doi: 10.1016/j.ijhydene.2022.04.265.
[4] J. Sun, Y. Wang, B. Tian, and Z. Chen, 'detonationFoam: An open-source solver for simulation of gaseous detonation based on OpenFOAM', *Computer Physics Communications*, vol. 292, p. 108859, Nov. 2023, doi: 10.1016/j.cpc.2023.108859.
[5] 'Explosion Dynamics Laboratory'. Accessed: May 05, 2024. [Online]. Available: https://shepherd.caltech.edu/EDL/PublicResources/sdt/
[6] S. Ramachandran, N. Srinivasan, Z. Wang, A. Behkish, and S. Yang, 'A numerical investigation of deflagration propagation and transition to detonation in a microchannel with detailed chemistry: Effects of thermal boundary conditions and vitiation', *Physics of Fluids*, vol. 35, no. 7, p. 076104, Jul. 2023 .
[7] V. Bykov, M. Stein, and U. Maas, 'Study of mechanism of ammonia decomposition and oxidation: From NOx reduction to ammonia auto-ignition problem', *Proceedings of the Combustion Institute*, vol. 39, no. 4, pp. 4267–4275, Jan. 2023, doi: 10.1016/j.proci.2022.07.048.
[8] J. Li, Z. Zhao, A. Kazakov, and F. L. Dryer, 'An updated comprehensive kinetic model of hydrogen combustion', *Int J of Chemical Kinetics*, vol. 36, no. 10, pp. 566–575, Oct. 2004, doi: 10.1002/kin.20026.
[9] R. Zhu, M. Zhao, and H. Zhang, 'Numerical simulation of flame acceleration and deflagration-to-detonation transition in ammonia-hydrogen–oxygen mixtures', *International Journal of Hydrogen Energy*, vol. 46, no. 1, pp. 1273–1287, Jan. 2021, doi: 10.1016/j.ijhydene.2020.09.227.
[10] Ng, Hoi Dick, Yiguang Ju, and John H. S. Lee. 2007. Assessment of Detonation Hazards in High-PressureHydrogen Storage from Chemical Sensitivity Analysis. International Journal Of Hydrogen Energy 32 (1): pp. 93-99.


THE COMBUSTION INSTITUTE
1954

SESSION V

Carbon-free energy carriers: combustion applications - Part 2


THE COMBUSTION INSTITUTE
1954

Analysis of the NO_x formation pathways in a partially premixed burner operated with pure hydrogen

R. Meloni*, G. Babazzi*, L. Mazzotta*,, D. Borello*****
roberto.meloni@bakerhughes.com
*Baker Hughes, Via F. Matteucci 2, 50127, Florence, Italy
**Department of Astronautical, Electric and Energetic Engineering, Sapienza University of Rome, Via Eudossiana 18, Rome, 00184, Italy
***Department of Mechanical and Aerospace Engineering, Sapienza University of Rome, Via Eudossiana 18, Rome, 00184, Italy

Abstract
The need of reliable CFD models able to predict the performance of pure hydrogen combustion is becoming strategic for the development of new burner designs for GT. So, in this research paper, the results of a species-transport based model applied to the HYLON burner will be presented. Both the attached and the lifted flame configuration are investigated and discussed showing an excellent agreement with the experimental measurements. Furthermore, the CFD solutions are coupled with a CRN to estimate the NO_x emission, considering all the possible formation pathways.

Introduction
Hydrogen combustion represents one of the biggest challenge gas turbine manufacturers have to deal with, especially in the context of low NO_x emissions. The hitch consists in finding a design able to guarantee low emissions avoiding thermo-acoustic instabilities as well as flashback/flame holding [1]. An additional roadblock in the design space is represented by the lack of reliability of the CFD models for hydrogen combustion. Computationally cheap models based on pre-tabulated chemistry are totally unreliable since they are not able to capture some fundamental hydrogen properties (i.e., response to the strain rate, preferential diffusion). On the other side, models relying on the species transport, despite their high computational costs, are not free of uncertainties when applied to high-pressure and high-temperature conditions. It must be also considered that detailed measures able to characterize a pure hydrogen flame at these conditions are totally missing in literature. This deficiency is limiting the assessment of the actual prediction capabilities of the numerical models for industrial applications. More often instead, their validation must leverage single-swirler tests at low pressure where the optical access allows the execution of quantitative measures. Radical chemiluminescence and PIV can be performed to fully characterize the flame length and its morphology providing crucial information for the optimization of the numerical models. The same kind of approach is presented in this work for the HYLON burner [2]. The prediction capabilities of a species transport-based model will be evaluated comparing the numerical results against detailed measures. An insight on the NO_x

emission for the two investigated operating conditions will be discussed as well.

Test Rig and Computational Mesh Resolution

The computational domain is prepared referring to the material reported in [2] where also the operating conditions characterizing the burner in the *Attached* (*A*) and *Lifted* (*L*) configuration are detailed. Figure 1-a shows the employed geometry with a close up of the HYLON burner, unveiling the details of both the radial passages of the air and the fuel line. The latter is characterized by a swirler mounted close to the burner exit providing an additional swirler that enhances the flame stabilization in the primary zone. Instead, Figure 1-b reports the size of the computational mesh in the most important regions of the model. The finest mesh resolution, equal to about 50 µm, is applied in the final part of the burner and where the flame gets stabilized in the primary zone as demonstrated by the contour plot of the normalized HRR for the flame *A*. The mesh remains extremely fine (~300 µm) right outside these regions and progressively coarser elsewhere, reaching a maximum of 600 µm. The total mesh count is of approximately 25 million polyhedral elements.

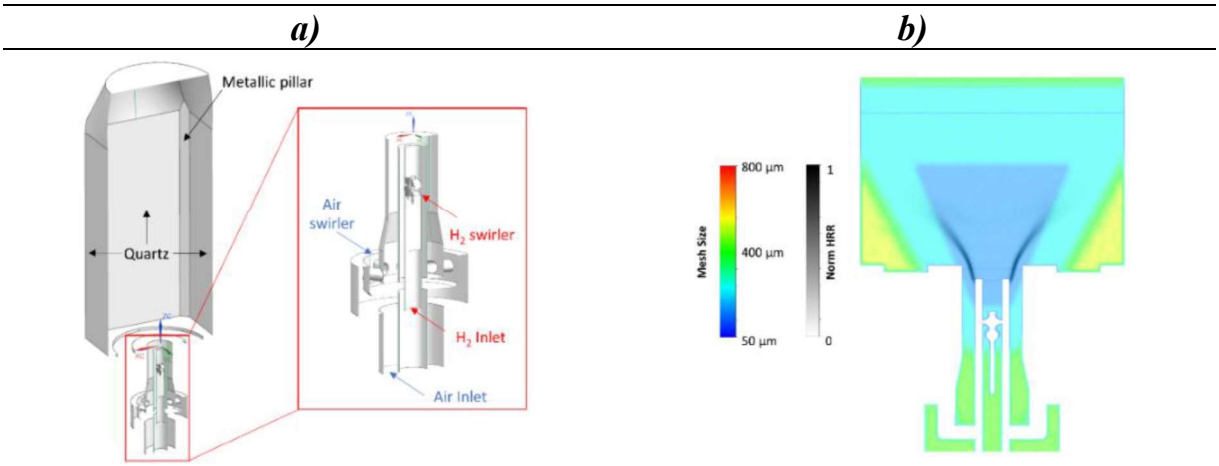

Figure 1. *Combustion test rig with detailed view of the HYLON burner (a) and mesh inside the swirler and the primary zone (b).*

As it will be discussed in the next paragraph, the grid plays a crucial role in the performance of the combustion model in the large-eddy simulation context. This mesh is able not only to resolve most of the turbulent length scales, as demonstrated by Aniello et al. [3] where a similar discretization strategy is adopted, but it can also accurately model the diffusive and the premixed regime both present in a stratified flame. While the former requires a high resolution to properly capture the mixing among species, the premixed regime needs a fine mesh to accurately reconstruct the species profiles in the flame front thickness, according to the TFM [4].

Enhanced-Thickened Flame Model and Numerical Settings

The closure of the chemical source term of each species transport equation depends on the local value of the flame index, calculated according to Eq. 1:

$$FI = \frac{\nabla Y_{H2} \cdot \nabla Y_{O2}}{|\nabla Y_{H2} \cdot \nabla Y_{O2}|} \quad (1)$$

If the FI is negative (diffusive regime), the finite rate closure is adopted, while the TFM formulation is applied for positive values (premixed flame), characterized by a fixed flame propagation speed and a chemically controlled fuel consumption. So, the formulation of the transport equation of each species $\tilde{\varphi}$ can be written as:

$$\frac{\partial \bar{\rho}\,\tilde{\varphi}}{\partial t}+\frac{\partial \bar{\rho}\,\widetilde{u_j}\,\tilde{\varphi}}{\partial x_j} = \frac{\partial}{\partial x_j}\left(\bar{\rho}(EFD + (1-\Omega)D_t)\frac{\partial \tilde{\varphi}}{\partial x_j}\right)+\frac{E}{F}\dot{\omega}(\tilde{\varphi}) \quad (2)$$

with E and F the efficiency function and the thickening factor, respectively. These two parameters are simply set to unity for $FI < 0$ or calculated by a user-defined function according to the Colin's formulation for E [4] and Eq. 3 for F:

$$F = \Omega(F_{max} - 1) + 1 \quad (3)$$

The maximum thickening factor is calculated as $F_{max} = \Delta x\, N/LFT(\Phi)$. The actual mesh resolution (Fig. 1-b), Δx, can limit F_{max} to values close to 5 having chosen a number of points $N = 10$ inside the flame front thickness ($LFT(\Phi)$). The flame front is identified through the sensor Ω, calculated considering $H_2 + OH \rightarrow H_2O + H$ as reference reaction. The reduced mechanism by Boivin et al. [5] made of 9 species and 12 reactions is used. Mass flow rates are imposed at air and H_2 inlets while a pressure outlet is placed at the end of the quartz. The temperature at the metallic pillars and at quartz liner are adopted according to the measured data.

Results and Discussion

Flame morphology

The comparison between the experiments and numerical model in terms of flame shape and position is reported in Figure 2, showing the HRR for the former and the OH* for the latter. The CFD is able to predict both the flame configurations varying the overall air mass flow rate. Flame A is characterized by the anchoring of the flame root at the lip of the hydrogen injector where, as demonstrated by Aniello et al. [4], the fuel is trapped by a local recirculation eventually leading the heat release region to be confined between the shear layer and the external recirculation zone. The combustion model can also correctly predict the weak HRR in the core of the swirler flow, downstream the H_2 injector, barely visible in Figure 2-a. Conversely, the higher air bulk velocity in Flame L overcomes the local laminar flame speed at the H_2 lip preventing the flame stabilization and promoting a lift-off. Also, the location of the OH* peak is well captured.

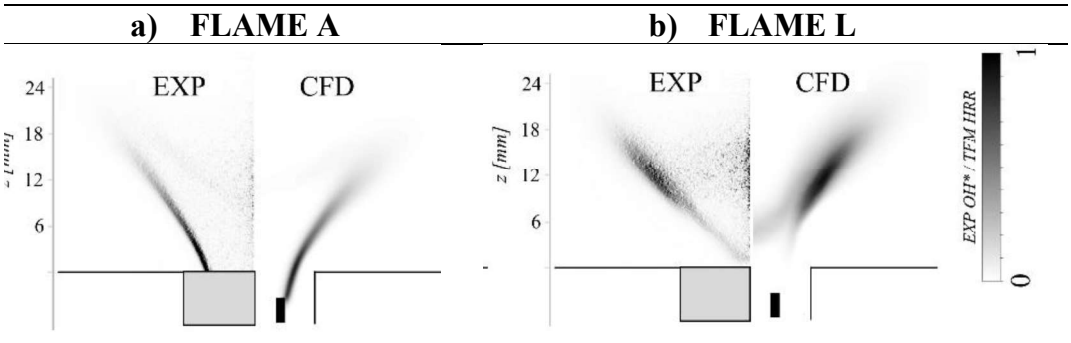

Figure 2. *Experimental Abel-deconvoluted OH* vs CFD HRR for flame A (a) and L (b).*

Figure 3 shows the HRR conditioned with the flame index at the stoichiometric iso-surface: while Flame A burns totally in diffusive mode anchored to the H_2 injector, Flame L has a mixed combustion regime: the flame lift-off gives H_2 sufficient time to mix with a benefit in terms of NO_x reduction [3].

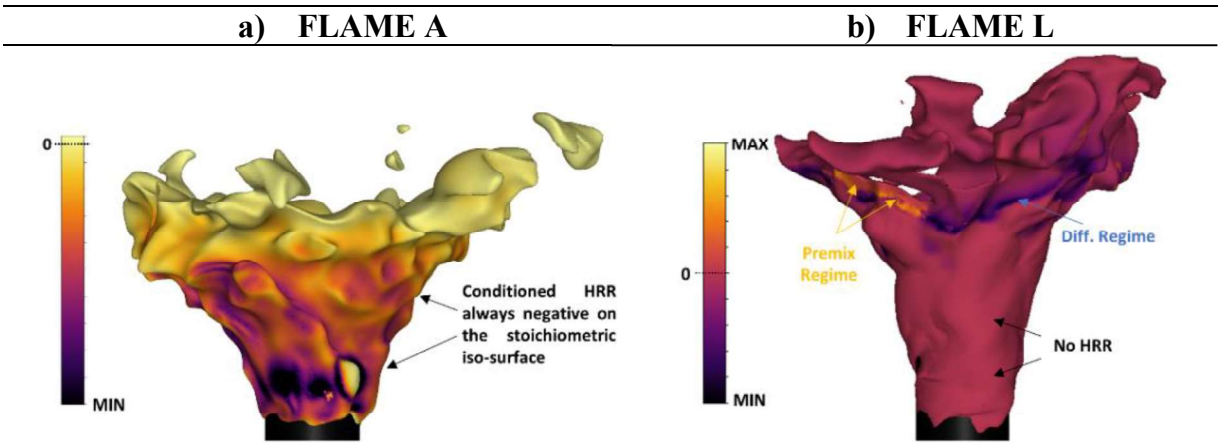

Figure 3. *Instantaneous normalized FI- conditioned HRR for Flame A (a) and L (b).*

Reactive velocity profiles

For sake of brevity, only the contour plots of velocity magnitude and axial velocity profiles at $z = 5$ and $z = 15\,mm$, reported in Figure 4, are here discussed. Regarding the velocity magnitude fields, the opening angle of the swirled air as well as the interaction of the jets with the walls are quite well predicted in both conditions. Some minor differences are present for Flame L. First of all, a more intense central recirculation zones is obtained: this can be observed also from the radial velocity profiles at low x-coordinate values. Additionally, the numerical results show also a more axially extended high velocity field closer to the walls. These small differences for the lifted flame could be related to the outlet boundary placed at the end of the quartz without considering any interaction with the atmosphere outside the flame tube that can play a role when the mass flow rate is increased. On the other side, the radial profiles for Flame A seems not have relevant discrepancies against the PIV. While there is an overlapping of the numerical with the experimental results at $z = 5$ mm, a small underprediction of the peak velocity is found at $z = 15$ mm.

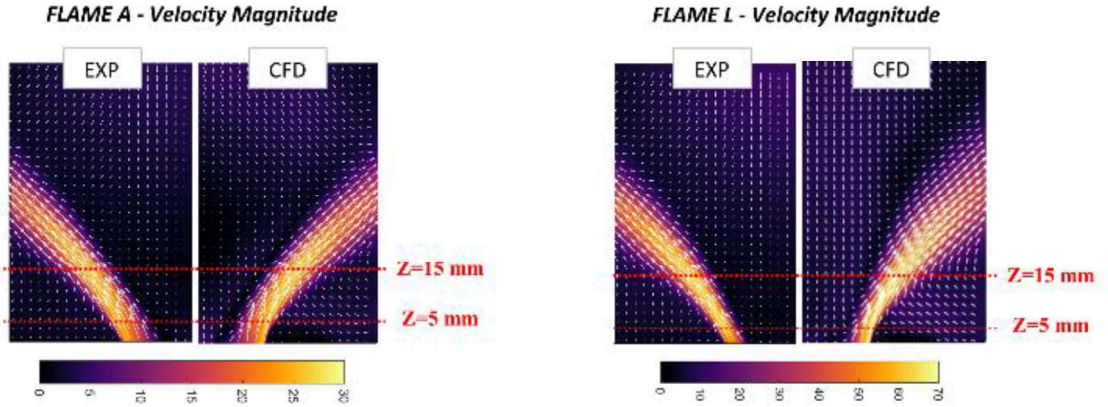

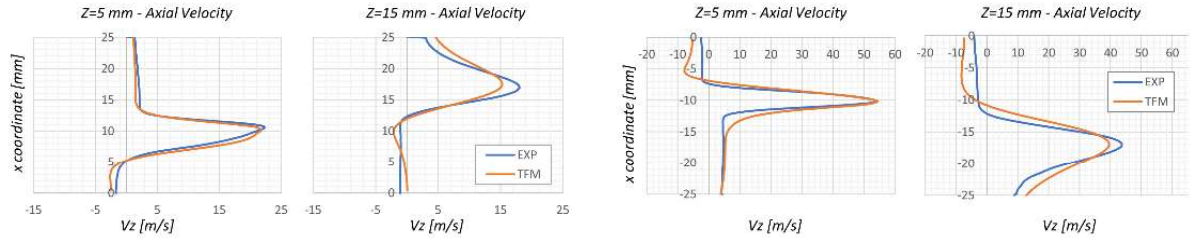

Figure 4. *Velocity profiles comparison in reactive conditions.*

CFD-CRN methodology and results

The CFD-CRN methodology is used to quantify NO_x emissions in the exhaust section. It is a simplified approach for analysing complex systems, such as those typical of gas turbines and perform a wide range of sensitivity to several parameters. Figure 5 shows the different reactors through which both flames are schematized.

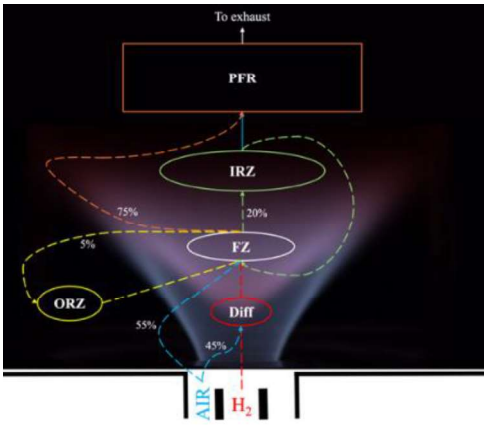

Figure 5. *CRN scheme adopted to quantify NO_x for both flames.*

Three PSRs representing the FZ and the two recirculation zones (IRZ and ORZ) are employed. A diffusion zone is used to consider the formation of the high temperature in the flame front. This zone is obtained by splitting the air to obtain the stoichiometric equivalence ratio. Additionally, a PFR denotes the inclusion of a unidirectional flow zone. By analysing the axial velocity field and HRR from the LES, it is possible to obtain the volumes to be associated to the FZ and I/ORZs, respectively and obtain the residence times of each zone. The split percentages between the different volumes are obtained by CFD. The kinetic scheme of Stagni et al. [6] was used, with all the main reactions characterizing NO_x formation within it. Figure 6b demonstrates that the NO emission derived from the LES-CRN analysis are predicted with an error of less than 4%. To assess the consumption and production contributions of the main reactions derived from the NO_x formation mechanisms (thermal and NNH) of both flames (A and L), the ROP values were compared within the flame zone, as shown in Figures 6a,c. High flame temperature (greater than 1850 K) promotes the NO formation in the burnt gases through the Zeldovich route and the residence time will determine the NO concentrations. In fact, $N+NO <=> O+N_2$ results the main reaction responsible for the NO reduction, as shown in Fig. 6c, while consumption of NNH prevails for the lifted flame.

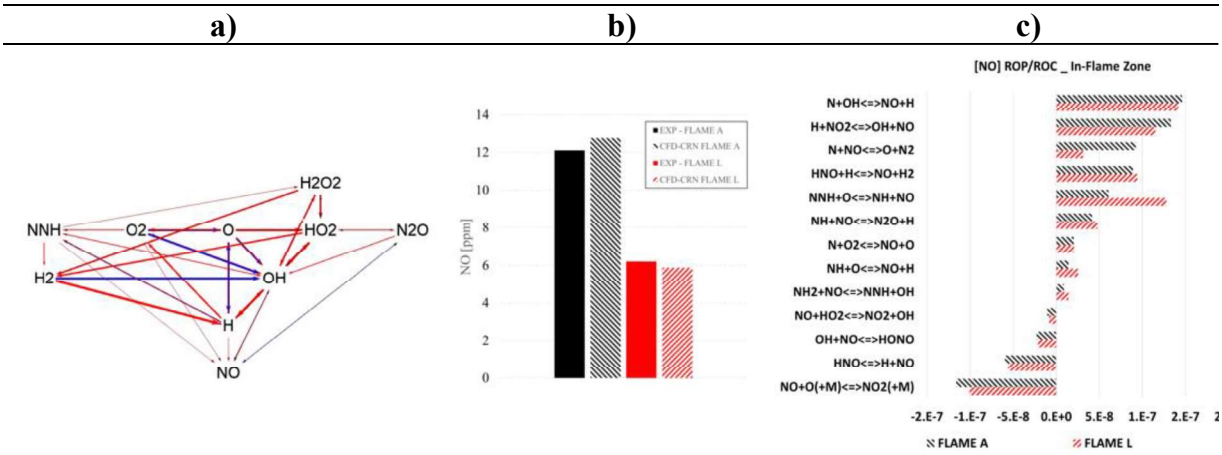

Figure 6. *(a) NO formation pathway in the FZ; (b) NO emissions results: LES-CRN vs data; (c) absolute ROP [mole/cm^3-sec] for the main NO reactions inside the FZ.*

Conclusion

In the present work, the results of a customized TFM are compared with detailed measures of the HYLON burner. The findings characterizing the flame front are in line with the experimental OH* maps for both the attached and lifted flame configuration. Also the reactive flow fields are in good agreement with the PIV data. A CRN for the assessment of the NO emission is built on top of the CFD solution, providing a good agreement with the experimental measures for both flames.

Nomenclature

CFD	*Computational Fluid Dynamics*	*HRR*	*Heat Release Rate*
CRN	*Chemical Reactor Network*	*PIV*	*Particle Image Velocimetry*
FI	*Flame Index*	*TFM*	*Thickened Flame Model*
PFR	*Plug Flow Reactor*	*PSR*	*Perfectly Stirred Reactor*
ORZ	*Outer Recirculation Zone*	*IRZ*	*Inner Recirculation Zone*
ROP	*Rate Of Production*	*FZ*	*Flame Zone*

References

[1] T. Lieuwen, Y. Neumeier, B. T. Zinn (1998). *"The Role of Unmixedness and Chemical Kinetics in Driving Combustion Instabilities in Lean Premixed Combustors"*, Comb. Science and Technology, 135:1-6, 193-211

[2] https://tnfworkshop.org/hydrogen-flames/

[3] A. Aniello, D. Laera, S. Marragou, H. Magnes, L. Selle, T. Schuller, T. Poinsot, *"Experimental and numerical investigation of two flame stabilization regimes observed in a dual swirl H2-air coaxial injector"*, Comb. Flame, Vol. 249, 2023

[4] O. Colin, F. Ducros, D. Veynante, T. Poinsot, *"A thickened flame model for large eddy simulations of turbulent premixed combustion"*, *Phys. Fluids 12* (2000) 1843-63

[5] P. Boivin, C. Jiménez, A.L. Sánchez, F.A. Williams, "An explicit reduced mechanism for H_2–air combustion", Proceedings of the Combustion Institute, Vol 33, 2011.

[6] Stagni, A., Cavallotti, C., Arunthanayothin, S., Song, Y., Herbinet, O., Battin-Leclerc, F., and Faravelli, T., 2020. "*An experimental, theoretical and kinetic-modelling study of the gas-phase oxidation of ammonia*". React. Chem. Eng., 5, pp. 696–711

Flashback limits of H_2 premixed laminar flames: impact of Soret and multicomponent diffusion

A. Cuoci*, B. Naud, M. Arias-Zugasti***, A. Frassoldati***

alberto.cuoci@polimi.it

* CRECK Modeling Lab, Department of Chemistry, Materials, and Chemical Engineering, Politecnico di Milano, Milano (Italy)

** Modelling and Numerical Simulation Group, CIEMAT, Madrid (Spain)

*** Departamento de Física Matemática y de Fluidos, Universidad Nacional de Educación a Distancia (UNED), Madrid (Spain)

Abstract

This paper presents a detailed numerical investigation of the flashback limits of hydrogen premixed laminar flames, with a focus on the impact of the Soret effect and multicomponent diffusion. Employing the advanced "1+M" diffusion model, we compare its performance against the traditional mixture-averaged (MA) approach to explore the implications on safety and efficiency of combustion devices, particularly in micro-perforated burners.

Our study highlights the critical role of the Soret effect, which is shown to significantly influence flashback limits, especially under lean conditions. Without accounting for the Soret effect, both MA and "1+M" models underestimate the propensity to flashback, potentially compromising safety. The results demonstrate that, even if the "1+M" model provides more accurate predictions, the MA model's conservative estimates offer a less computationally demanding alternative that still ensures safety against flashback.

The findings emphasize the importance of incorporating accurate diffusion modeling in the design of hydrogen-fueled systems, as it is essential for predicting and mitigating flashback risks.

Introduction

Fossil fuels have been a primary energy source since the industrial revolution, significantly contributing to global greenhouse gas emissions and accelerating climate change. In sectors like residential heating, which heavily relies on natural gas (NG), there is a pressing need for sustainable alternatives. As of 2022, approximately 49% of U.S. households and a similar proportion in Europe use NG for heating, generating considerable CO_2 emissions annually [1]. Transitioning to zero carbon-ready boilers that use green hydrogen (H_2), produced from renewable sources, is seen as a promising solution to harmonize with the variability of renewable energy while mitigating environmental impacts.

However, hydrogen's unique properties, such as high reactivity, flammability limits, and flame speed (about six times that of NG) introduce new challenges in

combustion technology. These properties affect flame propagation and stability, particularly in premixed burner configurations designed for compact combustion chambers. The risk of flashback, where the flame moves upstream into the burner, poses significant safety concerns, and leads to reduced flexibility of practical combustion devices [2].
While traditional theories on flame stabilization provide some insights, they do not fully address the complexities of real-world applications where factors like flame-wall interactions and preferential diffusion play crucial roles. Recent studies [3-6] have emphasized that hydrogen's increased flame speed is not the only factor contributing to flashback. Instead, the interaction between the flame and the burner walls, facilitated by preferential diffusion, is also critical.
In this paper we numerically investigated the enhanced flashback propensity of hydrogen in simplified burner configurations. More specifically, the objective was to better characterize the impact of Soret effect and advanced multicomponent diffusion models (with emphasis on the "1+M" model [7]) on the flashback limits of H_2/air mixtures.

Numerical Methodology

In this study, we investigated the flashback limits in a multi-slit burner configuration, commonly used in domestic boilers. For simplicity, a planar geometry was adopted, in line with the one proposed by Vance et al. [4].
The slit width is W=1 mm, the distance between the slits is D=1 mm, and the plate thickness is t=0.6 mm. The computational domain extends 10 mm downstream and 3 mm upstream from the burner plate. The burner plate is modeled with properties typical of stainless steel used in domestic boilers. Premixed gases are introduced at a uniform velocity with a temperature of 300 K. The mesh comprises rectangular cells, refined near the burner plate and flame front to capture thermal gradients effectively, with ~40,000 cells in the largest configuration.
The flow within the burner is laminar, with Reynolds' numbers ranging from 100 to 1000 under various operating conditions. We employed the laminarSMOKE++ code, which solves conventional transport equations for momentum, species, and energy in laminar flows [8, 9]. The diffusion fluxes are modeled using the conventional mixture-average (MA) formulation or the more accurate "1+M" multicomponent diffusion model, recently proposed in [7]. Boundary conditions include a fixed pressure at the outlet (1 atm) and no-slip conditions on the burner surface. Symmetry conditions to mimic the entire burner setup are adopted along the sides. Radiative heat transfer and gravitational effects are neglected.
The solid region's energy equation is solved in steady-state conditions to decouple it from the gaseous phase dynamics, a method proven effective in similar studies [3-6]. Each simulation begins with a high inlet velocity for stability, then systematically lowers the velocity to determine the minimal specific power that sustains a steady flame without flashback.

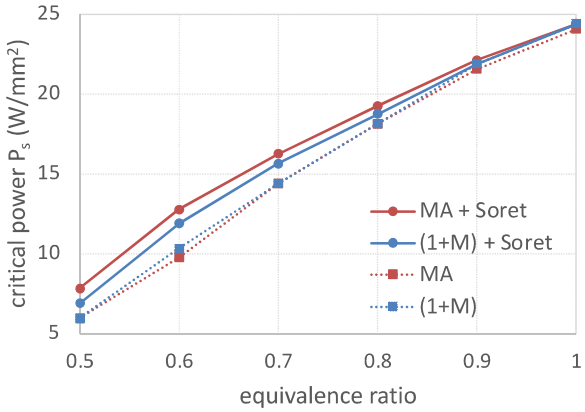

Figure 1. Critical specific power (P_s) at flashback conditions as a function of the equivalence ratio $\boldsymbol{\phi}$.

Results and Discussion

Figure 1 shows the flashback curves, i.e. the critical specific powers (P_S) at critical conditions as a function of the equivalence ratio ϕ, for different diffusion models. As expected, the critical power increases with the equivalence ratio, because of the increased reactivity of the mixture, which enhances the propensity to flashback. If the Soret effect is not included in the calculations, the mixture-averaged (MA) and the 1+M formulations do not show any significant differences. The inclusion of Soret effect increases the critical power, especially at lower equivalence ratios (i.e. lean conditions). Thus, not including the Soret effect in the numerical simulations leads to an underestimation of the flashback propensity and this could be potentially dangerous in applications. No significant differences can be observed between the MA and 1+M formulations at large equivalence ratios. At lean conditions, the two formulations show some deviations: more specifically, the MA formulation tends to slightly overestimate the flashback propensity. In general, the results show that the MA formulation can reproduce quite well the results of the more accurate (but also more expensive) 1+M formulation. Since the MA formulation tends to slightly overestimate the critical power, its adoption for quantifying the flashback propensity can be considered a good alternative to more complex and expensive multicomponent diffusion models (such as 1+M).

The different enhanced flashback propensity due to the Soret effect can be explained and discussed by looking at some specific fields (see Figure 2): temperature, scaled H_2 consumption rate $\hat{\Omega}_{H_2} = \frac{\Omega_{H_2}}{\Omega_{H_2,1D}^{max}}$, scaled H elemental mass fraction $\hat{Z}_H = \frac{Z_H - Z_{H,in}}{Z_{H,in}}$, and scaled enthalpy $\hat{h} = \frac{h - h_{in}}{C_{P,u}(T_b^0 - T_u)}$. In the definitions above, the H_2 consumption rate is scaled with the maximum consumption rate of a 1D adiabatic, flat premixed flame $\Omega_{H_2,1D}^{max}$. The H elemental mass fraction is scaled with the corresponding inlet value $Z_{H,in}$. h_{in} is the inlet specific enthalpy, $C_{P,u}$ and T_u are the specific heat coefficient and temperature at inlet conditions, and T_b^0 the adiabatic flame temperature. $\hat{Z}_H$ can be used to quantify local stratification in composition due to

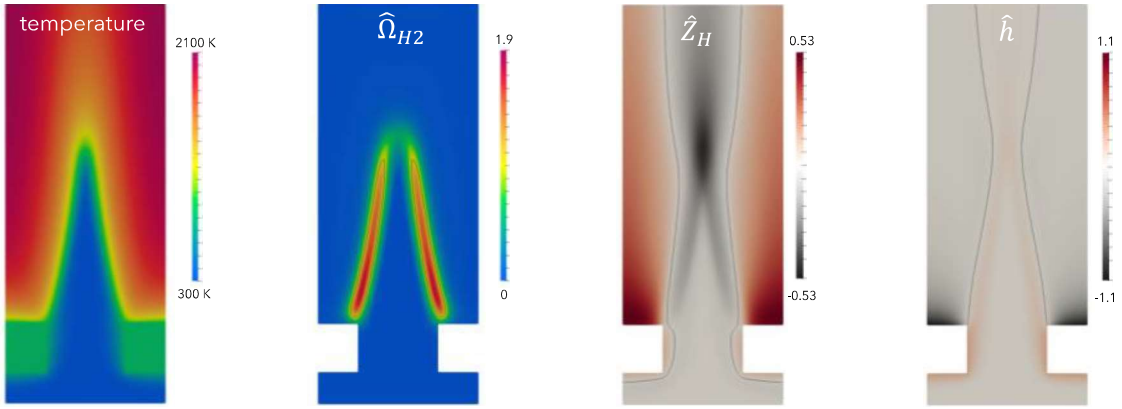

Figure 2. Temperature, scaled H_2 consumption rate $\widehat{\boldsymbol{\Omega}}_{\boldsymbol{H_2}}$, scaled H elemental mass fraction $\widehat{\boldsymbol{Z}}_{\boldsymbol{H}}$, and scaled enthalpy $\widehat{\boldsymbol{h}}$ for $\boldsymbol{\phi = 0.70}$ and P=21 W/mm^2.

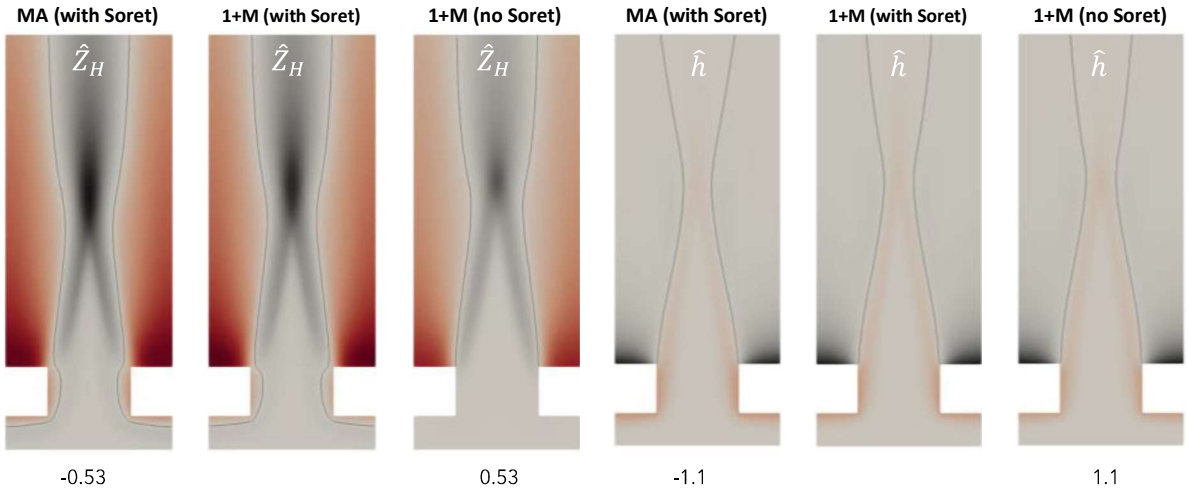

Figure 3. Scaled H elemental mass fraction $\widehat{\boldsymbol{Z}}_{\boldsymbol{H}}$ and scaled enthalpy $\widehat{\boldsymbol{h}}$ for $\boldsymbol{\phi = 0.70}$ and P=21 W/mm^2 when different diffusion models are adopted.

preferential diffusion effects. $\hat{h}$ allows to identify the effects of heat exchange with the burner plate: positive values mean local preheating, while negative values heat loss. From Figure 2, it is clear that the flame burns stronger close to the base and weaker at the tip. This is strictly related to preferential diffusion and stratification of the mixture, which becomes richer close to the burner walls and leaner at the tip. Moreover, there is a significant heat loss along the top wall of the burner. Since the overall system is adiabatic, the heat loss is returned to the gas phase along the lateral and bottom walls, where the inlet mixture is preheated.

Figure 3 shows a comparison between the simulations carried out with the MA and 1+M models (including the Soret effect) and the simulation carried out with the 1+M model without the Soret effect. No significant differences can be observed in terms of scaled enthalpy $\hat{h}$. However, without the Soret effect, no stratification of the inlet mixture can be observed along the bottom and the side walls of the burner, which is on the contrary clearly apparent in MA and 1+M formulations. Indeed, thanks to preheating, Soret diffusion pushes light species (mainly H_2 and H) close to the burner

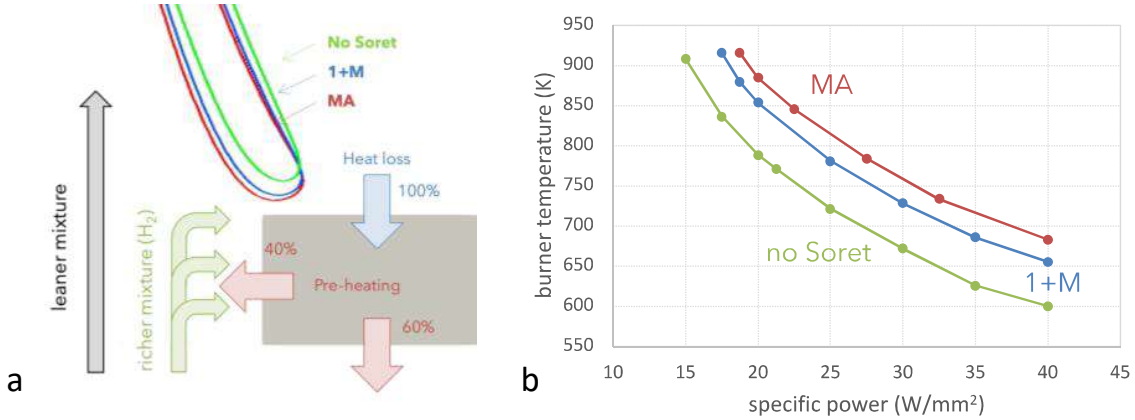

Figure 4. a) Impact of Soret effect and heat loss on flame stabilization ($\boldsymbol{\phi = 0.70}$ and P=21 W/mm^2). The colored curves are the iso-contours of scaled H_2 consumption rate at $\boldsymbol{\widehat{\Omega}_{H_2} = 1}$ (adapted from Vance et al. [3]). b) Average burner temperature for $\boldsymbol{\phi = 0.70}$ with different diffusion models.

walls, so the mixture approaching the flame base becomes locally richer. Since the MA and 1+M models including the Soret effect result in richer mixtures, this explains their higher reactivity and thus their higher propensity to flashback.

Figure 4a reports the iso-contours of $\hat{\Omega}_{H_2}$, considered as a measure of the reactivity of the flame. As expected, without Soret effect, the flame burns weaker (being leaner) and the distance between the reactive region and the top wall is larger. When we include the Soret effect (both MA and 1+M formulations), we have the opposite: the flame burns closer to the top wall. The heat loss through the top wall (not here reported) is now larger, thus producing a larger preheating along the side and bottom walls. Higher preheating means stronger Soret diffusion and therefore higher local enrichment of the flame, which then makes the flame stronger. Thus, this is a self-sustained mechanism [3], which is also confirmed by the larger average temperatures reached by the burner, reported in Figure 4b.

Conclusions

This study provides a numerical investigation of flashback propensity of hydrogen premixed laminar flames, elucidating the influence of the Soret effect and advanced multicomponent diffusion models. By comparing the 1+M diffusion model with the conventional mixture-averaged (MA) model, our analysis reveals that neglecting the Soret effect leads to an underestimation of flashback propensity, particularly under lean conditions, which could pose significant risks in real-world applications. The simulations show that while the MA and 1+M models perform similarly under rich conditions, discrepancies emerge at leaner mixtures. The 1+M model provides a more accurate prediction of flashback limits, but the MA model's tendency to slightly overestimate the critical power offers a conservative and less computationally expensive alternative for assessing flashback risks.

The simulations also highlight the importance of considering local composition stratifications and heat transfer effects in predicting flashback behavior. The

inclusion of the Soret effect enriches the hydrogen content near burner walls, increasing local reactivity and thus the propensity for flashback. This indicates a critical feedback mechanism where heat loss at burner walls enhances local preheating and, subsequently, the strength of the flame due to stronger Soret diffusion.

In practical terms, these findings stress the need for incorporating advanced diffusion models and the Soret effect into the design criteria of hydrogen combustion systems to enhance safety and efficiency. For future research, expanding the scope to include varied burner geometries and operating conditions would further refine our understanding of hydrogen's behavior in combustion settings.

References

[1] Energy Information Administration, Annual Energy Outlook 2023 (2023)

[2] Lamioni, R., Bronzoni, C., Folli, M., Tognotti, L., Galletti, C., "Feeding H_2-admixtures to domestic condensing boilers: Numerical simulations of combustion and pollutant formation in multi-hole burners", *Applied Energy* 309: 118379 (2022)

[3] Vance, F.H., De Goey, P., van Oijen, J.A., "The effect of thermal diffusion on stabilization of premixed flames", *Comb. Flame* 216: 45-57 (2020)

[4] Vance, F.H., De Goey, P., van Oijen, J.A., "Development of a flashback correlation for burner-stabilized hydrogen-air premixed flames", *Comb. Flame* 243: 112045 (2022)

[5] Flores-Montoya, E., Aniello, A., Schuller, T., Selle, L., "Predicting flashback limits in H_2 enriched CH_4/air and C_3H_8/air laminar flames", *Comb. Flame* 258: 113055 (2023)

[6] Fruzza, F., Lamioni, R., Tognotti, L., Galletti, C., "Flashback of H_2-enriched premixed flames in perforated burners: Numerical prediction of critical velocity", *Int. J. Hydrogen Energy* 48(81): 31790–31801 (2023)

[7] Naud, B., Cordoba, O., Arias-Zugasti, M., "Accurate heat (Fourier) and mass (Fick and thermodiffusion) multicomponent transport at similar cost as mixture-averaged approximation", *Comb. Flame* 249: 112599 (2023)

[8] Cuoci, A., Frassoldati, A., Faravelli, T., Ranzi, E., "Numerical modeling of laminar flames with detailed kinetics based on the operator-splitting method", *Energy Fuels* 27(12): 7730–7753 (2013)

[9] Cuoci, A., Frassoldati, A., Faravelli, T., Ranzi, E., "OpenSMOKE++: An object-oriented framework for the numerical modeling of reactive systems with detailed kinetic mechanisms", *Comput. Phys. Commun.* 192: 237–264 (2015)

PREDICTIVE SURROGATE MODEL FOR NOx EMISSIONS IN GAS TURBINE SYSTEMS FED WITH AMMONIA/HYDROGEN BLENDS

R. Lamioni*, A. Mariotti*, M.V. Salvetti*, C. Galletti*
rachele.lamioni@unipi.it
* Dipartimento di Ingegneria Civile e Industriale, University of Pisa, Pisa 56126, Italy

Abstract
Renewable energy sources must be widely integrated to face climate change. One important option that can be produced from surplus solar and wind energy is hydrogen, which may be used as an alternative fuel for technologies that are already in use. On the other hand, ammonia, that it is easily liquefied and distributed through the existing infrastructure, can act as an excellent hydrogen carrier.
This study aims to investigate the feasibility of using ammonia/hydrogen mixtures in gas turbines by applying numerical techniques with low computational cost. A chemical reactor network (CRN) based surrogate model is developed to estimate the effect of operational and model parameters on NOx emissions in a gas turbine fed with ammonia/hydrogen mixtures. To this purpose, we use Uncertainty Quantification (UQ) to calibrate the network and identify which operational and model qualities have the greatest impact on the estimation of NOx emissions.

Introduction
Gas turbines are an integral part of the global energy scenario, requiring initiatives to reduce carbon emissions and improve environmental sustainability. Hydrogen (H_2), derived from renewable energy sources, and ammonia (NH_3), used as its stable carrier, are among the leading alternative fuels under consideration due to their favorable storage characteristics. However, the different thermo-chemical properties of H_2 and NH_3 present unique challenges. Hydrogen is highly reactive compared to conventional fuels and has a high adiabatic flame temperature, which can result in increased thermal NOx emissions and flame instability (flashback). Conversely, ammonia is less reactive, characterized by low flame speeds that can lead to flame extinction (blow-off) and it can contribute to higher NOx production due to its fuel-bound nitrogen.
Considering these challenges, it is imperative to conduct comprehensive research on these fuels to assess their viability as substitutes for fossil fuels. Effective strategies like staged combustion and the blending of fuels, particularly blending ammonia with more reactive fuels such as methane or hydrogen, the latter obtained from ammonia cracking, have shown promise in improving the combustion characteristics of ammonia [1].
The investigation of new fuel mixtures through experimental setups or detailed numerical simulations using Computational Fluid Dynamics (CFD) can be

prohibitively expensive and time-consuming, given the need to investigate a wide range of conditions such as mixture composition, equivalence ratio, injection pressure, and temperature.
In this context, the Chemical Reactor Network (CRN) approach, first introduced by Bragg [2], emerges as a cost-effective and computationally efficient alternative. This methodology simplifies the representation of complex thermochemical and flow fields by dividing them into a network of discrete volumes modeled as canonical chemical reactors - typically Perfectly Stirred Reactors (PSRs) and/or Plug Flow Reactors (PFRs). These interconnected reactors exchange mass and heat and are designed to encapsulate the essential characteristics of the overall flow and thermos-chemical field.
However, the application of CRN to gas turbines is challenging, as it should replicate faithfully the intricate dynamics which is characterized by zones of varying temperature, flow, and chemical species concentration. Accurately modeling these complexities using zero-dimensional reactors that build the CRN is crucial.
Indeed, the effectiveness of the CRN model is highly dependent on the network configuration which should be devised by considering the flow features [3-4] as well as on model parameters as the chemical schemes. The latter may pose significant issues in case of novel fuels, because of the limited validation in literature.
The reliability of the approach is constrained by potential errors arising from network modeling and the calibration of model parameters. To address these limitations, Uncertainty Quantification (UQ) techniques are applied to quantify the propagation of uncertainties related to both operational and modeling parameters, and to assess the confidence level of the model. This type of analysis can be used to develop high fidelity and resolution models (surrogate models) based on the original CRN model, providing a useful tool for identifying the parameters that have a greater weight on the estimates of the quantities of interest analyzed and the relative range of interest (i.e., NOx and unburned NH_3).

Case study

The case study is the high-pressure generic swirl burner (HPGSB), housed within the high-pressure optical chamber (HPOC) [5]. The HPGSB uses quartz windows and a cylindrical quartz burner confinement to provide optical access to the flame. The HPGSB is modular and can be operated with a wide range of swirl numbers. Previous works [5-6] include further information on the design and operation of this high-pressure combustion rig test facility.

Numerical approach

The CRN code is written in Python using Cantera [7], an open-source software for thermodynamics and reaction kinetics. To investigate a fully CRN method without the use of CFD or other information, the CRN is developed using a simple one-stage configuration, with the flame zone as a PSR reactor and the post-combustion zone, characterized by unidirectional flow using a PFR reactor as shown in Figure 1.

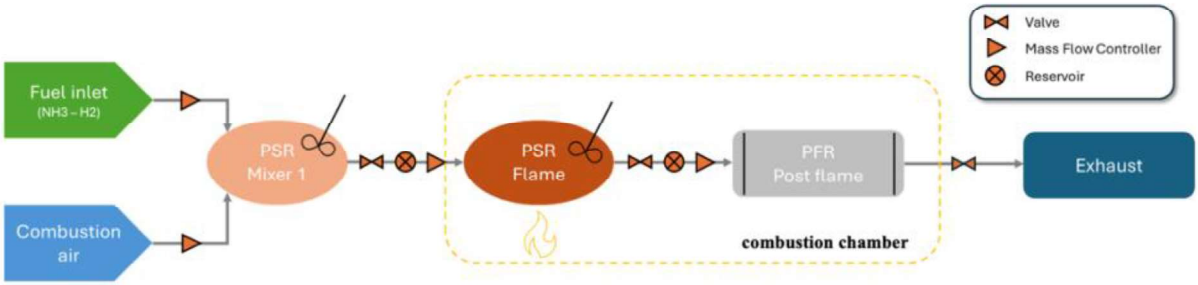

Figure 1. One stage Chemical Reactor Network structure.

Figure 1 exhibits an additional non-reactive PSR reactor (Mixer 1) that has the purpose of mimicking the mixing zone outside the combustion chamber for the characterization of premixed processes such as those being investigated on the HPGSB setup [4]. In this simple one-stage CRN, the model parameters are reduced to the kinetic mechanism used and the fraction of the flame volume V_F/V_T, which is the portion of the chamber occupied by the flame compared to the total of the chamber, with the mixer being an external and analytically defined element. In this scenario, we are investigated and quantified the uncertainty of operating and modeling parameters by assessing their impact on the selected quantities of interest, such as NOx and unburned NH_3.

The idea is to consider operating or modeling parameters not as deterministic variables, but rather through analytical sampling with an appropriate Probability Density Function (PDF), and to assess how uncertainty propagates at a computational level on the quantification of the desired outputs. This methodology can lead to direct calibration through comparison with experimental data or to a retro-calibration and CRN optimization phase, eliminating the parameters that do not influence the estimate of NOx emissions or unburned NH_3, optimizing the performance of the system and improving the confidence and robustness of the model. The propagation of uncertainty of the paraments is evaluated by developing a low-cost surrogate model that is trained on the outcomes of CRN simulations at specific points on a grid of size N, where N is the number of input parameters studied (N = 4).

Table 1: Operating and model parameters with their range.

Operating parameters	**Range**
Ammonia content NH_3 [%vol]	20 - 90
Equivalence ratio ϕ [-]	0.35 - 1.40
Inlet temperature T_{in} [K]	430 - 700
Model parameter	
Flame PSR volume fraction [$\%V_F/V_T$]	10 - 80

Table 1 presents the parameters and the respective distribution range. The surrogate model is developed through the advanced Monte Carlo approach [8], using a polynomial best-fit method, beginning from simulations of the original CRN at known quadrature points. These grid points are calculated using Newton Cotes quadrature formulas [8]. The surrogate model is a polynomial correlation with multiple variables (our operational and model parameters) that calculates our variable of interest, which in this case is NOx emissions in the parameter space, $NOx = f(\%NH3,\ \phi,\ T_{in}, \%V_F/V_T)$.
This model is used to conduct a global sensitivity analysis, determine the parameters that have the least influence on the CRN analysis, and generate response surfaces for NOx emissions.

Results: global sensitivity analysis
The global sensitivity analysis is conducted through the results obtained from our surrogate model in terms of PDFs and Sobol' indices of the quantity of interest, such as NOx emissions.

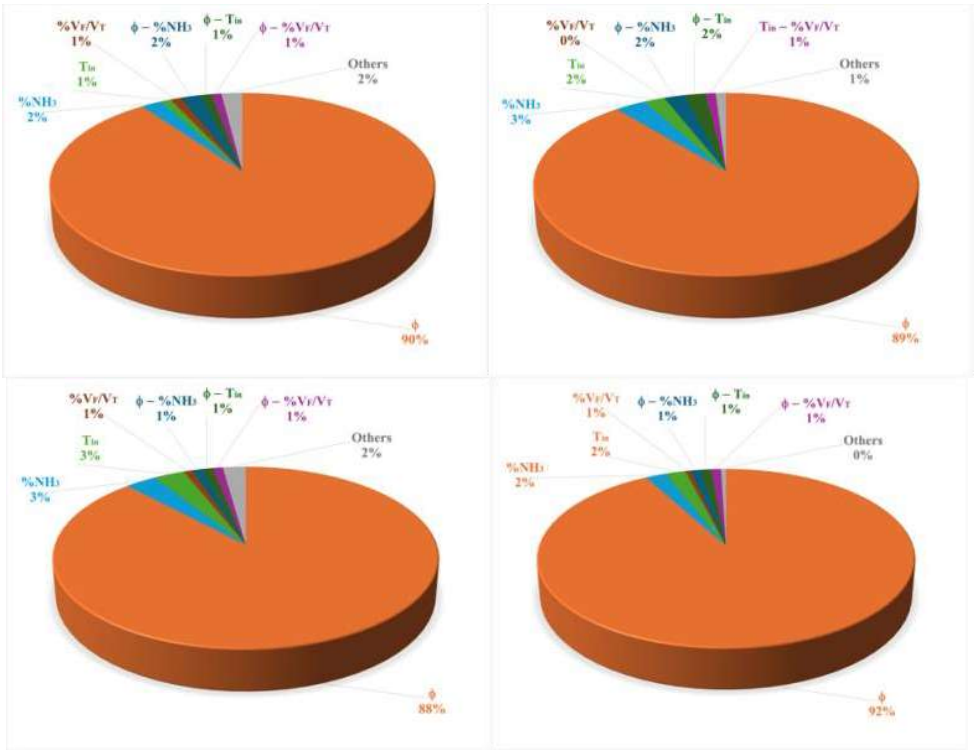

Figure 2. Sobol' indices for NOx emissions at different kinetic mechanism (a) Gotama et al. (b) Stagni et al. (c) Okafor et al. (d) Kaust et al.

These indices describe a variance-based statistical technique for global sensitivity analysis, which measures the individual importance of each parameter, as well as their joint effect on the quantity of interest, i.e., NOx emissions. In the first step, the impact of the kinetic mechanisms on the prediction of NOx emissions is evaluated

by analyzing four chemical schemes: Stagni et al [9] with 31 species and 203 reactions, Gotama et al [10] with 32 species and 165 reactions, Okafor et al. [11] with 59 species and 256 reactions and Kaust et al. [12] with 38 species and 263 reactions.

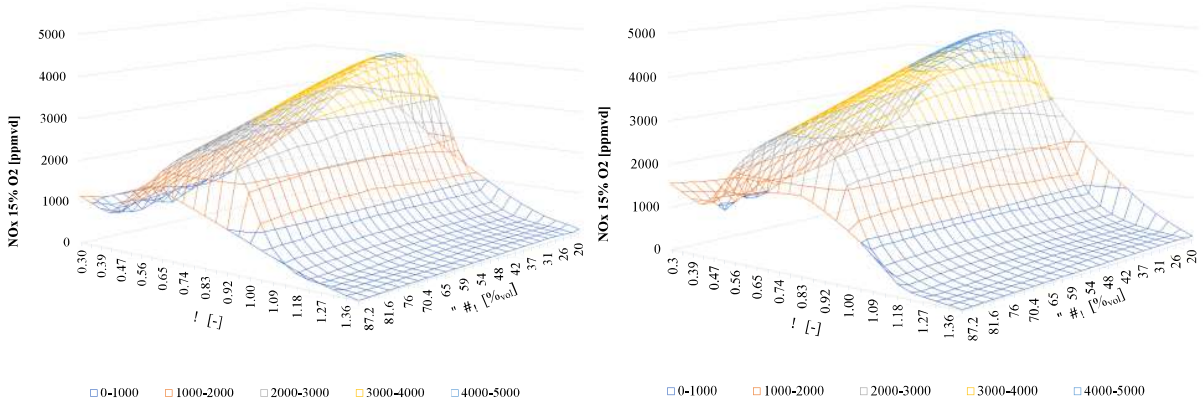

Figure 3. Maps (slice at T_{in} and $\%V_F/V_T$ constant) for NOx emissions at different kinetic mechanism (a) Gotama et al. [10] (b) Stagni et al. [9].

Figure 2 shows the Sobol' indices for NOx emissions by varying the kinetic schemes in the surrogate model. We can note that the equivalence ratio (ϕ) has the greatest influence on the estimation of NOx, with an index value equal to Iϕ = 90% -89%-88%-92% for the Gotama et al. [10], Stagni et al. [9], Okafor et al [11], and Kaust et al. [12] mechanisms respectively. The influence of the other parameters and their coupling is almost negligible. It should also be noted that the parameter related to the model (volume fraction of the flame reactor compared to the total volume of the combustion chamber) is 0%-1%, regardless of the kinetic mechanism analysed. This indicates that the influence of this parameter does not affect the estimation of NOx emissions compared to the other operating parameters. This does not mean that the estimation of the emissions is not quantitatively influenced by this parameter, but that by trying to characterize a wide range of configurations at the same time, the overall effect on the trend obtained is irrelevant. To visualize the trend of NOx emissions in a map, we consider a slice within the four-dimensional parameter space, fixing two parameters at a time, such as T_{in} and $\%V_F/V_T$, as shown in Figure 3, where only two kinetic mechanisms are considered (Stagni et al. [9] and Gotama et al. [10]). We can note that varying the kinetic schemes, the NOx emissions behavior agrees with each other, with a strong dependence on the equivalence ratio.

Conclusion

A surrogate model based on the single-stage CRN is developed to emulate the gas turbine system fed with ammonia/hydrogen mixtures. The surrogate model is used to perform a global sensitivity analysis of NOx emissions to operating and modelling parameters. The model allows the construction of operational maps of NOx emissions in parameter space. It also allows estimation of the effect of individual parameters and their coupling on the prediction of NOx emissions.

The surrogate model offers the possibility of providing concrete support for the definition of experimental setups, while highlighting the confidence level of the estimates and the robustness of such models.

References

[1] Singh A. S., et al. Experimental and computational (chemical kinetic+ CFD) analyses of self-recuperative annular tubular porous burner for NH_3/CH_4-air non-premixed combustion, *Chemical Engineering Journal* 2023.

[2] Bragg S., Application of reaction rate theory to combustion chamber analysis, *Aeronautical Research Council London*, 1953.

[3] Andreini A., Facchini B., Gas Turbines Design and Off-Design Performance Analysis with Emissions Evaluation, *Journal of Engineering for Gas Turbines and Power* 126 2004.

[4] Falcitelli, M., et al. Modelling practical combustion systems and predicting NOx emissions with an integrated CFD based approach. *Computers & chemical engineering*, 26 2002.

[5] Pugh D., et al. Influence of steam addition and elevated ambient conditions on NOx reduction in a staged premixed swirling NH_3/H_2 flame, *Proceedings of the Combustion Institute* 37 2019.

[6] Valera-Medina A., et al. Premixed ammonia/hydrogen swirl combustion under rich fuel conditions for gas turbines operation, *International Journal of Hydrogen Energy* 44 2019.

[7] Goodwin D. G. et al. Cantera: An object-oriented software toolkit for chemical kinetics, thermodynamics, and transport processes*, https://www.cantera.org 2022*.

[8] Virtanen P., and SciPy Contributors. Fundamental Algorithms for Scientific Computing in Python. *Nature Methods*, 17 2020.

[9] Stagni A. et al. An experimental, theoretical, and kinetic-modeling study of the gas-phase oxidation of ammonia. *Reaction Chemistry & Engineering* 5 2020.

[10] Gotama G. J. et al. Measurement of the laminar burning velocity and kinetics study of the importance of the hydrogen recovery mechanism of ammonia/hydrogen/air premixed flames. *Combustion and Flame* 236, 2022.

[11] Okafor E. C. et al. Experimental and numerical study of the laminar burning velocity of CH_4–NH_3–air premixed flames. *Combustion and Flame*, 187, 2018.

[12] Szanthoffer A. G. et al. Testing of NH_3/H_2 and NH_3/syngas combustion mechanisms using a large amount of experimental data. *Applications in Energy and Combustion Science*, 14 2023.

EXPLORING HYDROGEN LOW NOX (HYLON) BURNER WITH LARGE EDDY SIMULATIONS

M. Fiaschi*, S. Nambully*, S. Liu*, E. Pomraning*,
D. Lee*, M. D'Elia*
matteo.fiaschi@convergecfd.com
* Convergent Science GmbH. Hauptstrasse 10, 4040, Linz. Austria.

Experimental Investigation of Hydrogen Jet for Direct Injection in ICE

A Montanaro*, G. Meccariello, L. Allocca
alessandro.montanaro@stems.cnr.it
STEMS – CNR, Naples, Italy

Abstract
Hydrogen is considered as one of the potential clean fuels because of its zero-carbon nature and it has attracted considerable attention in the automotive industry for transition toward zero-emission. Since the H_2 jet dynamics play a significant role in the fuel/air mixing process of direct injection spark ignition (DISI) engines, the current study focuses on experimental hydrogen jet characterization in terms of mass flow rate measurements and morphology investigation under a wide range of engine-like conditions by a Compressed Hydrogen Gas (CHG) injector used for typical direct injection applications. A measuring system, suitable for the gaseous fuels, was used for measuring the instantaneous flow rate as well the dynamic behavior of the injection system. High-speed z-type schlieren imaging was applied in a constant volume chamber to investigate the evolution and shockwave structures of highly under-expanded H_2 jets.

Introduction
Combustion supplies more than 80% of the global energy used in transportation, power generation, as well as industrial, commercial, and residential heat. As combustion continues to be a significant part of the world energy mix, it must be made sustainable with continued developments of technology and fuels. Advanced combustion technologies offer pathways for greatly reducing carbon emissions in all the major energy sectors. In this contest, the hydrogen (H_2) represents an attractive energy carrier for decarbonizing the transport sector, since it has the potential to address both Greenhouse gas emissions (GHG) and pollutant emission problems [1-6]. Despite the above advantages, the development of H_2-ICEs is still in the conceptual and prototype stage, due to several drawbacks mainly related to the very low density of hydrogen. More, fuel injection equipment, including injectors, high-pressure on-board pumps, cryogenic pumps, and tender couplings are key technology gaps impeding faster penetration of H_2 combustion technologies. The decrease in volumetric efficiency and the onset of abnormal combustion phenomena can be potentially solved by directly injecting H_2 into the cylinder during the compression (at high pressure) or intake (at low-medium pressure) strokes, in the so-called direct injection (DI) engines [7-9]. Due to the possibility of different injection strategies and the variation of in-cylinder back-pressure, the comprehensive knowledge of hydrogen injection spray behavior and characteristics is fundamental

for improving the combustion process in DI H_2-ICE. In this contest, the present work aims to deal the hydrogen jet behavior in terms of mass flow rate measurements and morphology investigation under a wide range of engine-like conditions. The spatial and temporal evolution of the H_2 jet was studied by a z-type schlieren optical setup by injecting through a H_2 injector into a constant volume combustion vessel for a wide range of operative conditions.

Experimental Background and Method

The gas was delivered through a hydrogen pintle "outwardly opening" injector equipped with a cap on the nozzle tip. The gas supply system consists of a pressurized tank containing hydrogen connected to the injector via a line which includes the presence of a pressure regulator, a storage tank to reduce the gas pressure oscillations during the injection events, and a pressure sensor to collect the injection pressure just upstream the injector entrance. The injection rate measurements were realized through the Mexus AIR 2.0 device. This shot-to-shot device applies a variant of Zeuch's method to calculate the injection rate of a gas injector. The used device is equipped with two pressure sensors and a thermocouple to measure the pressure and the temperature inside the injection chamber. The two pressure sensors are used to get an accurate and highly resolved absolute pressure inside the chamber: a piezoresistive sensor gives the absolute pressure and the piezoelectric one gives a pressure signal with a high resolution needed for the injection rate calculation. The spatial and temporal H_2 jet characterization was studied injecting hydrogen at room temperature into an optically accessible constant volume combustion vessel (CVCV) controlled in temperature and pressure to replicate the typical thermodynamic engine conditions. Schlieren optical technique, in the classic Z-type configuration, was used to acquire the H_2 jet images for a wide range of engine-like conditions by a high-speed CMOS camera. The desired ambient pressures were realizing by delivering nitrogen inside the vessel. More details of the experimental apparatus can be found in [10]. A customized procedure developed in C# environment with the help of some image-processing libraries was implemented to process the images and ensure adequate enhancement to allow the measurement of the jet macroscopic characteristics. Further details on the adopted image processing procedure were reported in [11, 12].

Results and Discussions

The mass flow rate measurements were carried out for single injection strategies for three different injection pressures (20, 30, and 40 bar) and energizing time (1.25, 2.25, and 3.0 ms) by keeping constant ambient pressure at 3.0 bar.

In Figure 1, the mass flow rate profiles vs time are reported for three investigated injection pressures. For confidentiality reasons agreed with the industrial partner, the trends relating to the mass flow rate measurements are shown in a dimensionless way, not affecting this the complete understanding of the phenomenon with respect to the injection conditions. The area under each profile corresponds to the amount of

the hydrogen injected per stroke. The profiles clearly show the injection pressure effect on the total amount of injected fuel, grater is the injection pressure more fuel flows through the nozzle exit. The rise time is function of the injection pressure indicating a prompter answer of the injecting system at highest pressures. More, the injection pressure affects the total duration of the process in the sense that higher pressures result in slightly longer durations.

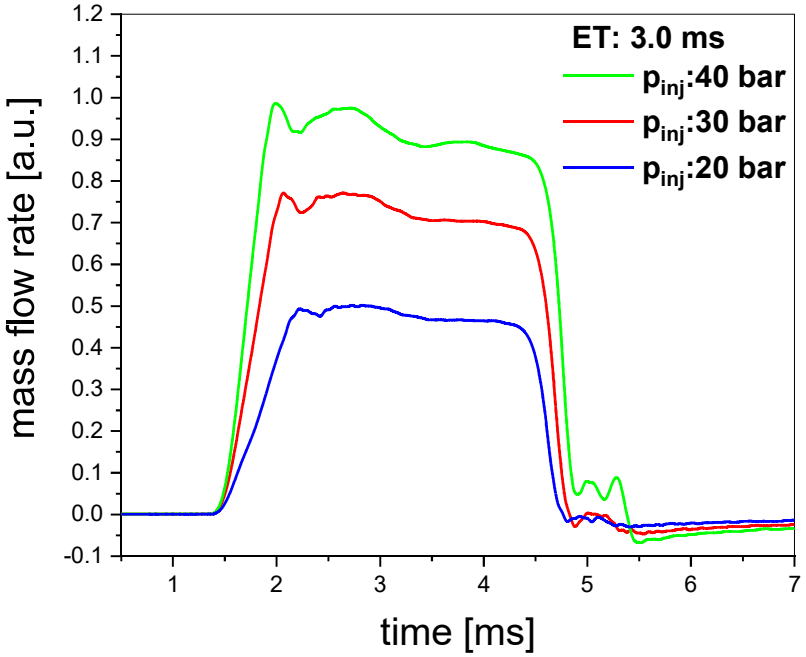

Figure 1 Effect of the injection pressure on mass flow rate profiles

Schlieren visualizations were used to determine the macroscopic jet characteristics of H_2 and its inner structure mainly in terms of gas spread, tip penetrations, and the shockwave formation inside a pressurized vessel. Left side of figure 2 depicts the volume occupied from the injected H_2 in the vessel at the explored ambient pressures of 1.5, 3.0, and 4.5 bar and injection pressures of 20, 30, and 40 bar, at 0.56 ms from the start of injections. N_2 gas was used to realize the desired ambient pressure at ambient temperature of 276 K. Schlieren characterization of hydrogen mixing revealed sensitivity to small flow change. The breaking effect of the gas density is instantly evident on jet morphology resulting in a shorter, larger, and denser jet with increasing of the N_2 pressure, at equal injection pressure. The increase of the injection pressure translates in greater quantities of delivered fuel at higher momentum. More, H_2 jet tends to disperse toward radial direction when p_{inj} is decreased. Jet penetration (right side of figure 2) was measured as the maximum distance in the axial direction between the injector nozzle and the jet tip; the limit of penetration measurements was given by the quartz windows clearance equal to 66 mm. The window optical limit was quickly reached at the lowest backpressure due to the lowest effect of the filling brake in the combustion vessel. All the curves start with a slight concavity upwards, more accentuated at low backpressures, propagating

then almost linearly up to the saturation phase. It is interesting to note the drastic change of the jet tip speed by increasing the injection pressure up to 40 bar, with a quasi-linear behavior of the curves up to reaching the window limit.
When a compressible fluid is injected at high pressure into the combustion chamber, choked flow conditions can occur in the exit section of the nozzle (as well inside it), resulting in the formation of shock waves and discontinuities that influence the process mixing in the downstream area. The formation of these under-expanded structures, recognizable by the presence of "barrel shock" in the structure of the jet, depends mainly on the ratio between the pressure upstream of the injector nozzle (p_{inj}) and the pressure inside the cylinder (p_{amb}), defined "net pressure ratio" (NPR) [12, 13]. The jet undergoes an evolution of its structure passing from subsonic to moderately under-expanded up to strongly under-expanded with appearance of Mach disk. In figure 2, the Mach disks at the exit of the nozzle are well evident at the highest NPR meaning a combination of low p_{amb} and high p_{inj}. The height of the Mach disks increased during the initial phases, after that it reached a quasi-stable value with a pronounced and growing trend as the NPR ratio increases.

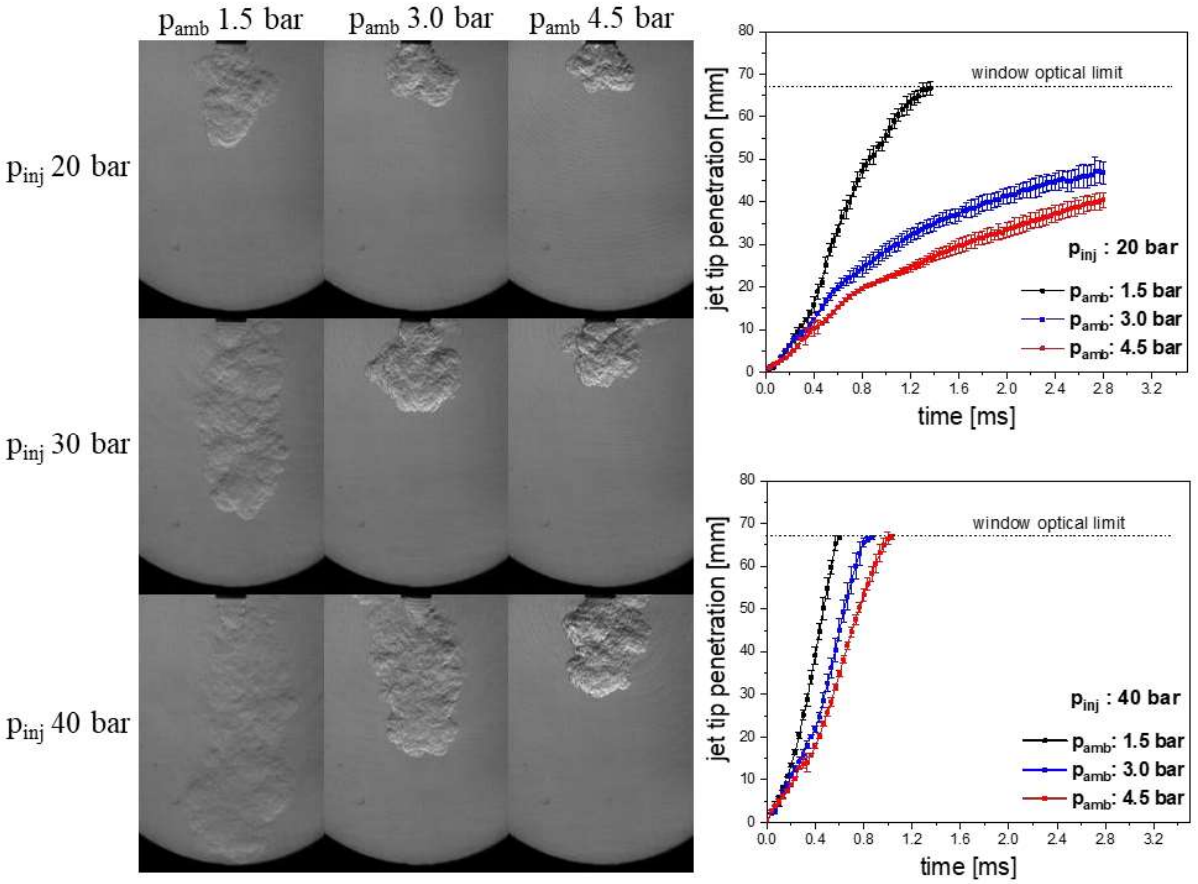

Figure 2 Effects of injection and ambient pressure on H_2 jet morphology and tip penetrations.

Conclusions

In the present study, comprehensive investigations on the hydrogen jet behavior, generated by a Compressed Hydrogen Gas (CHG) injector under different operative conditions, were performed in terms of mass flow rate measurements and morphology investigation. A measuring system, suitable for the gaseous fuels, was used for measuring the instantaneous flow rate while the jet morphology was studied in a constant volume vessel at different back pressures by the cycle-resolved schlieren imaging technique. Mass flow rate measurements showed a high repeatability with a very low RMS of the collected results for all the injection strategies demonstrating a strong stability of the entire injection system as well as accuracy of measurements obtained through the used device. Strong effects of the ambient pressure were carried out on jet evolution resulting in decreasing of both tip penetration and jet area with increasing of the ambient pressure. More, due to the compressibility of the gas, the local density inside the jet increased with increasing of ambient pressure. In conclusion, the illustrated results aim to improve the knowledge of under-expanded jets evolution under a wide range of operative conditions and could be useful to provide a robust data set to develop advanced CFD numerical models.

References

[1] Dilara P., “The future of clean cars in Europe: EU Green Deal and EURO 7”, 4th Sino-EU workshop on New Emissions Standards and Regulations for Motor Vehicles March 3-5, 2021.

[2] Stępień, Z. A Comprehensive Overview of Hydrogen-Fueled Internal Combustion Engines: Achievements and Future Challenges. Energies 2021, 14, 6504, https://doi.org/10.3390/en14206504

[3] Hosseini, S.E.; Butler, B. An overview of development and challenges in hydrogen-powered vehicles. Int. J. Green Energy 2020, 17, 13–37.

[4] Dougherty, W.; Kartha, S.; Rajan, C.; Lazarus, M.; Bailie, A.; Runkle, B.; Fencl, A. Greenhouse gas reduction benefits and costs of a large-scale transition to hydrogen in the USA. Energy Policy 2008, 37, 56–67.

[5] Yip, H.L.; Srna, A.; Chun Yin Yuen, A.; Kook, S.; Taylor, R.A.; Heng Yeoh, G.; Medwell, P.R.; Chan, Q.N. A review of hydrogen direct injection for internal combustion engines: Towards carbon-free combustion. Appl. Sci. 2019, 9, 4842.

[6] Y.H. Teoh, H.G. How, T.D. Le, H.T. Nguyen, D.L. Loo, T. Rashid, et al., “A review on production and implementation of hydrogen as a green fuel in internal combustion engines”, Fuel, 333 (2023), Article 126525.

[7] Mohammadi, A.; Shioji, M.; Nakai, Y.; Ishikura, W.; Tabo, E. Performance and combustion characteristics of a direct injection SI hydrogen engine. Int. J. Hydrogen Energy 2007, 32, 296–304.

[8] Oikawa, M.; Ogasawara, Y.; Kondo, Y.; Sekine, K.; Takagi, Y.; Sato, Y. Optimization of hydrogen jet configuration by single hole nozzle and high

speed laser shadowgraphy in high pressure direct injection hydrogen engines. Int. J. Automot. Eng. 2012, 3, 1–8.

[9] Yip, H.L.; Srna, A.; Yuen, A.C.Y.; Kook, S.; Taylor, R.A.; Yeoh, G.H.; Medwell, P.R.; Chan, Q.N. A Review of Hydrogen Direct Injection for Internal Combustion Engines: Towards Carbon-Free Combustion. Appl. Sci. 2019, 9, 4842. https://doi.org/10.3390/app9224842.

[10] Duronio, F., De Vita, A., Allocca, L., Montanaro, A., Ranieri, S., and Villante, C., "CFD Numerical Reconstruction of the Flash Boiling Gasoline Spray Morphology," in Conference on Sustainable Mobility, SAE International, sep 2020, https://doi.org/10.4271/2020-24-0010.

[11] Montanaro, A., Allocca, L., De Vita, A., Ranieri, S. et al., "Experimental and Numerical Characterization of High-Pressure Methane Jets for Direct Injection in Internal Combustion Engines," SAE Technical Paper 2020-01-2124, 2020, https://doi.org/10.4271/2020-01-2124.

[12] Allocca, L., Montanaro, A., Meccariello, G., Duronio, F. et al., "Under-Expanded Gaseous Jets Characterization for Application in Direct Injection Engines: Experimental and Numerical Approach," SAE Technical Paper 2020-01-0325, 2020, doi:10.4271/2020-01-0325.

[13] Pham Q., Chang M., Kalwar A., Avinash Kumar Agarwal, Park S., Choi B., Park S., Macroscopic spray characteristics and internal structure studies of natural gas injection, Energy, 263 (2023), 126055, https://doi.org/10.1016/j.energy.2022.126055.

HIGH PRESSURE DIRECT NUMERICAL SIMULATION OF TURBULENT PREMIXED $NH_3/H_2/N_2$ – AIR SLOT FLAME AT φ=1.5

D. Cecere, M. Cimini, S. Carpenella, E. Giacomazzi
donato.cecere@enea.it
TERIN-DEC-CCT Laboratory, ENEA, C.R. Casaccia, S.M. di Galeria (Rome), Italy

Abstract
This study explores the flame dynamics of a premixed $NH_3/H_2/N_2$-air slot flame at high equivalence ratio and pressure, relevant for clean combustion technologies. The main goal is to shed some light on the interaction between chemical kinetics and turbulent flow structures, providing insights into NO_x emissions and combustion efficiency. Key findings highlight the effect of the H_2 preferential diffusion on the flame local equivalence ratio, which decreases for negative curvatures, resulting in a NO peak that exceeds the corresponding value in laminar flames. In the post flame zone, the NO concentration is lower than 150 dry-ppm. The results offer critical data for optimizing fuel mixtures and operating conditions in industrial applications to achieve lower emissions and improved performance.

Introduction
The International Energy Agency (IEA) identifies hydrogen and its derivatives, like ammonia, as carbon-free energy carriers, pivotal in global efforts to decarbonize energy systems [1], and for balancing renewable energy intermittency. To ensure power supply security, gas turbines, known for their electrical efficiency and power density, require fuel-flexible combustion systems to reliably operate with various compositions, including H_2 blends and NH_3. Despite challenges like low flame speed, NO_x production [2], stability and reactivity, NH_3 presents advantages over H_2 due to higher density, simpler production, and lower cost-effective energy storage [3]. Due to the convenience of NH_3, it is often feasible to locally generate the needed H_2 by partially thermally and/or catalytically cracking ammonia, obtaining a $NH_3/H_2/N_2$ blended mixture to be used in combustion systems. In this context, recent findings suggest that adopting a two-stage Rich-Quench-Lean (RQL) strategy enhances flame stability and lowers emissions in ammonia-fired combustors [4]. In fact, in rich-fuel operation, NO_x emissions are minimized, and excess NH_3 is converted into H_2 via pyrolysis. Then, introducing secondary dilution air downstream allows the remaining H_2 to react under fuel-lean conditions, ensuring low emissions and high efficiency. Moreover, staged combustion under high pressure (> 20 bar) can achieve NO_x emissions comparable to natural gas turbines [5]. The available literature highlights the role of NH_3 as a potential alternative to replace conventional hydrocarbons in combustion processes. Nevertheless, few

studies have been performed to understand the synergistic interaction between the turbulent flame dynamics and the NH_3 combustion phenomenon. For this reason, this study aims to investigate a rich premixed slot jet flame of $NH_3/H_2/N_2$ at high pressure, by means of Direct Numerical Simulations (DNS), providing a clear understanding of the flame structure, stabilization, and NO_x formation.

Case Description and Numerical Setup

This study addresses the resolution of the three-dimensional, reactive, and unsteady compressible Navier-Stokes equations to explore the combustion characteristics of a slot premixed jet flame fueled by an $NH_3/H_2/N_2$ mixture with an equivalence ratio of φ=1.5. The fuel mixture is injected through a slot into a co-flow of equilibrium burnt flue gases under a pressure of 25 bar. The mixture composition for the case under investigation consists of 5% NH_3, 15% H_2, and 80% N_2 by volume. The co-flow gases have an adiabatic temperature set to 2133 K, while the fuel stream temperature is 750 K, a typical value consistent with the thermal decomposition of ammonia. The co-flow speed is 7 m/s, and the fuel speed is 35 m/s. The Reynolds number of the unburned stream is approximately 41505, resulting in a Kolmogorov scale η around 10 μm. The nominal Karlovitz number (Ka) is 38.92, while the nominal Damköhler number (Da) is 1.43.

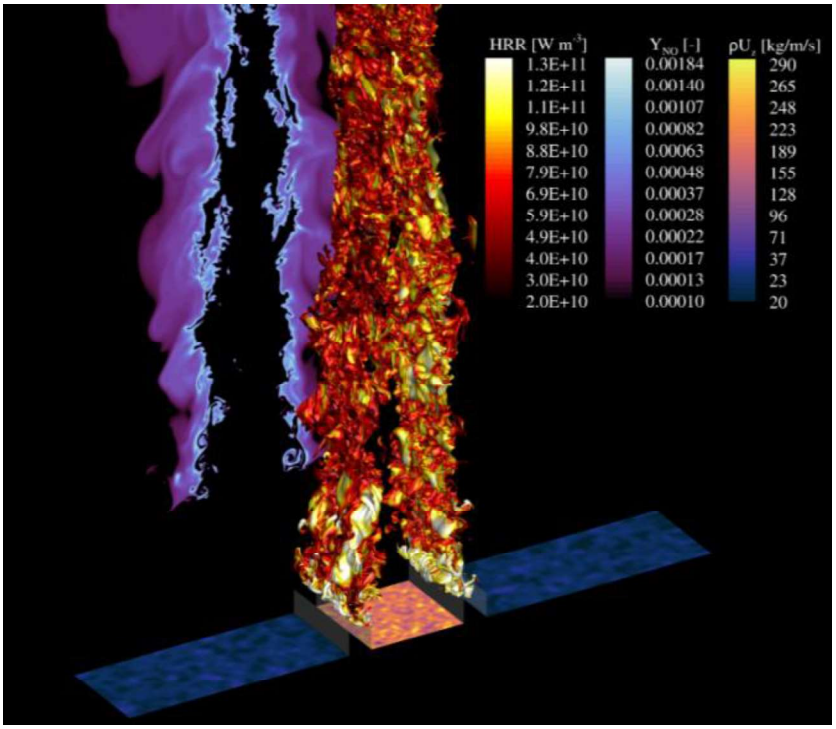

Figure 1. Volume rendering of an isosurface of T=1500 K colored with the Heat Release Rate (HRR, black body colormap), NO slice at z=0 (oceanography dense colormap), and momentum fluctuations slices at the slot inlet. Instantaneous taken at t=0.0052 s from the start of the simulation.

The dimensions of the computational domain are $L_x \times L_y \times L_z = 8.75H \times 6.25H \times H$ in the streamwise (x), crosswise (y), and spanwise (z) directions, respectively. The jet and the coflow are separated by walls of thickness $H/4$, similar to the setup used by Luca et al. [6] and Berger et al. [7] in their studies. The final DNS grid consists of $N_x \times N_y \times N_z = 3000 \times 864 \times 600$ grid points, resulting in approximately 1.55 billion cells.

Jiang's enhanced $H_2/O_2/N_2$ mechanism, tailored for NOx formation in high-pressure NH_3 combustion. Molecular transport in the mixture is modeled using the Hirschfelder and Curtiss expression, considering the Soret thermo-diffusive effect and pressure gradient diffusion. The Wilke's formula for viscosity and the Mathur's expression for the thermal conductivity are used to evaluate mixture-average properties. Preferential diffusion is modelled based on the Hirschfelder and Curtiss law.

The DNS simulation is performed using the ENEA in-house HeaRT code [8], which exploits a staggered finite-difference scheme to solve compressible, reactive Navier-Stokes equations, with second-order accurate centered diffusive flux calculations and AUSM$^+$-up method for convective terms. Extended non-reflecting boundary conditions account for variable transport properties and local heat release. Homogeneous and isotropic turbulence is prescribed in the central premixed jet mixture and coflow burned gases using synthetic generation methods. The flame regime, based on the inlet parameters, falls within the thin reaction zones (TRZ) according to the Borghi-Peters diagram.

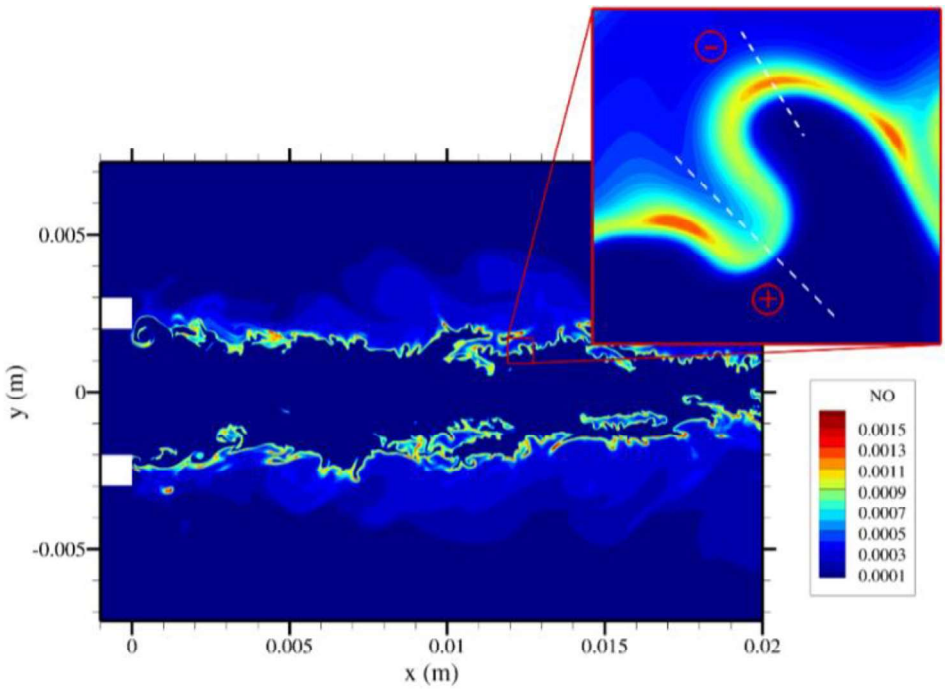

Figure 2. Slice at z=0 m and zoomed-in view of NO mass fraction profile.

Results

Figure 1 depicts the configuration of the slot turbulent flame and includes an isosurface based on the temperature field, which is color-coded by the HRR. Additionally, it shows a slice at $z = 0$ illustrating the NO mass fraction and a slice of the momentum x-component at the inlet. Above the duct exit, the flame becomes quickly wrinkled by turbulent vortices, resulting in a prompt increase in fuel consumption due to the enhancement of the flame surface. In this simulation, turbulence plays a key role in the synergistic interaction with the combustion process. When the flame front becomes turbulent it tends to corrugate considerably, generating a chaotic path of alternating positive and negative curvatures. The effect of curvature on combustion plays a crucial role in the NO formation, due to the local enrichment of the mixture that can lead to a decrease in NO and vice versa (the equivalence ratio varies in the range 1.36-1.85 increasing for positive curvatures).

Reaction paths analysis reveals that NO production peaks are located at strong negative curvatures, for values of the local equivalence ratio around 1.4 smaller the nominal one. In these region (for $c = 0.8$, $c = Y_{H_2O}/Y_{H_2O,Max\ Lam}$) being the progress variable defined with H_2O mass fraction) the most relevant production rate path is the HNO path. The relevant concentration of OH, O at negative curvature regions promotes their reaction with the high concentration of N radicals (more than 150% greater than positive curvature) to form NO and HNO radicals. The most important path in the NO consumption is the N_2O and N_2 paths [9].
Inside the flame a continuous region of alternating positive and negative curvatures was chosen for the purpose of analyzing the NO formation behavior (see Fig. 2). A rake line was used to sample the flow field and extract all the major features needed for this analysis from the zones of maximum and minimum curvature.

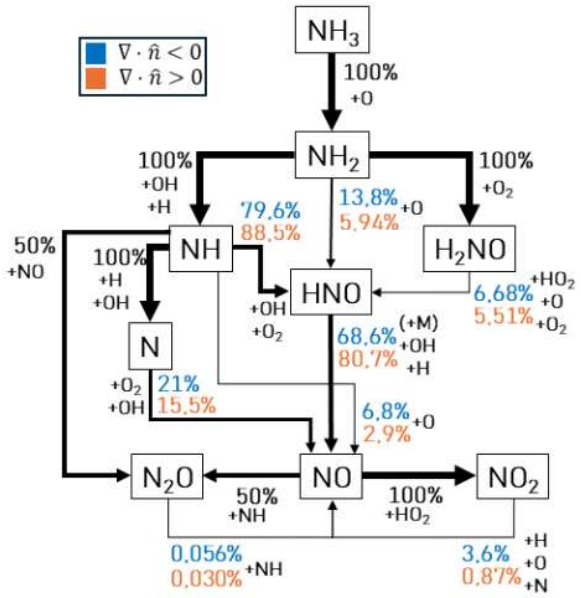

Figure 3. Local reaction path diagram of NO formation via N in the flame zone of negative (blue font color) and positive (orange font color) curvature.

The flux diagram in Fig. 3 is evaluated in the local point of maximum curvature (positive and negative) to better describe the NO formation reaction path via N. The diagram also embeds the species involved in every reaction of the pathway, emphasizing the role of the reactions that occur in the process. The results show that, when the curvature is negative, the local production of NO is driven by the HNO decomposition with a third body. This is in agreement with the study of [9], which performed a study of the curvature effects on the NO formation in turbulent $NH_3/H_2/N_2$-air premixed flames at 1 atm. The second and third leading mechanism in the formation of NO are due to the reaction of O_2 with N, and the reaction of H with HNO. Other four reactions that are visible in Fig. 3 contribute in a minor way to the NO production. These are: i) the reaction of OH with HNO; ii) the reaction of H with NO_2; iii) the reaction of O with NH and iv) the reaction of OH with N. When the curvature becomes positive, the major production mechanisms remain unaltered. Nevertheless, the conversion of HNO in the NO production process gains weight, while the conversion of N and NH loses relevance. This behavior can be explained by the fact that zones with positive curvature are affected by a greater H_2 concentration that reacts, producing H_2O with O and OH favoring their depletion.

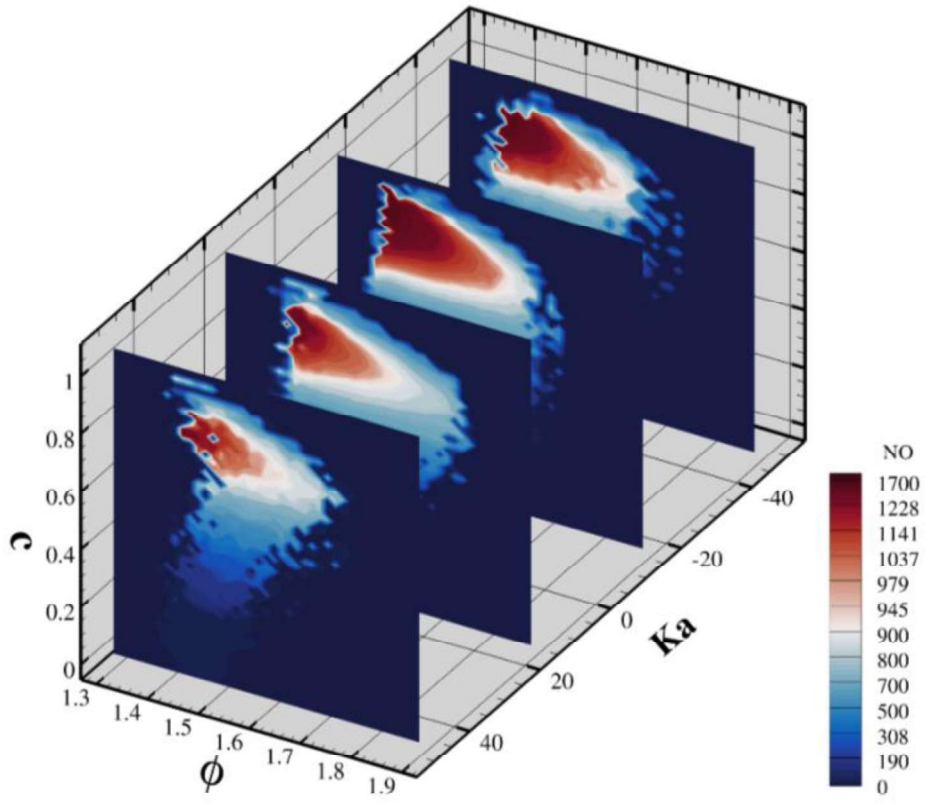

Figure 4. Mean NO value (dry-ppm) as a function of ϕ, c and the local Ka.

Figure 4 presents a three-dimensional visualization of the mean NO (dry-ppm) pollutant as a function of φ, c, and the local $Ka = (S + S_d \nabla \cdot \hat{n})\tau_F$, where S is the strain, S_d is the displacement speed, $\nabla \cdot \hat{n}$ is the curvature, and $\tau_F = \delta_F / S_L$ the characteristic laminar flame time. The NO maximum values are located for negative

Ka and equivalence ratios less than the nominal one, while on the contrary minimum values are attained for positive Ka and $\phi > 1.7$. The NO peaks have been identified, as for the laminar flame, for $c \approx 0.86$, a c value greater than that of the maximum HRR.

In the post flame zone ($c > 0.9$) the NO concentration has a peak around 150 dry-ppm, greater than that of the laminar flame post flame zone (< 10 ppm) since in the latter NO. This is explained by the fact that the laminar flame equilibrium NO values are taken at residence times substantially higher than those in modern gas turbine combustors (where typical values are in the 5-20 ms range).

References

[1] International Energy Agency. Global Hydrogen Review. Technical report, IEA, Paris, 2021.
[2] U.J. Pfahl et al. Combust. Flame, 123:140–158, 2000.
[3] C. Zamfirescu and I. Dincer. Fuel Process. Technol., 90:729–737, 2009.
[4] E.C. Okafor et al. Proc. Combust. Inst., 37:4597–4606, 2019.
[5] S. Gubbi et al. ACS Energy Letters, 8:4421–4426, 2023
[6] S. Luca et al. J. Prop. Power, 341(1):153 – 160, 2018.
[7] L. Berger et al. Combustion and Flame, 244:112254, 2022.
[8] E. Giacomazzi, D. Cecere, M. Cimini, S. Carpenella, Energies, 16, 2023.
[9] S. Karimkashi et al. Combustion Science and Technology, 1-30, 2023.


THE COMBUSTION INSTITUTE
1954

SESSION VI

Soot, Nanomaterials synthesis, and Large Molecules production


THE COMBUSTION INSTITUTE
1954

Towards an improved description of carbonaceous particle morphology

A. Nobili*, M. Pelucchi*, A. Frassoldati*, T. Faravelli*
tiziano.faravelli@polimi.it
**CRECK Modeling Lab, Department of Chemistry, Materials and Chemical Engineering "G. Natta", Politecnico di Milano, P.zza Leonardo da Vinci 32, 20133 Milano, Italy.*

Abstract
Carbon nanoparticle (CNP) formation from hydrocarbon combustion is of high interest not only for the study of pollutant (soot) emissions, but also in the area of advanced materials. CNP optical and electronical properties, relevant for practical applications, significantly change with their morphology and nanostructure. This work extends a detailed soot kinetic model, based on the discrete sectional approach, to explicitly incorporate the description of CNP polydispersity, maintaining the CHEMKIN-like format. The model considers various nanosized primary particles, generated from liquid-like counterparts through the carbonization process. The model is validated against literature experiments from 11 laminar flames, in both premixed and counterflow configuration, over a wide range of operating conditions (P=1–5 atm, T_{max}=1556-2052 K). The model captures the measured trends of the analyzed CNP properties. Model deviations from the experiments are also discussed.

Introduction
Recent scientific research is driving a paradigm shift on carbonaceous nanoparticles (CNPs) produced from hydrocarbon combustion, looking more and more often at them as attractive materials for new practical applications rather than as harmful pollutants [1].
The strong variation of CNP physical and chemical characteristics as their size and nanostructure evolve in flames was highlighted in several studies. Their size-specific electronic and optical properties were measured and modeled [2], demonstrating the variation of ionization energies and optical band gaps with particle diameter. Regarding CNP morphology, it is known that polydisperse aggregates are formed by primary particles of different sizes [3]. Great efforts have been made to develop kinetic models that can describe this polydispersity in flames. For example, Thomson and coworkers [4] developed an advanced sectional model, based on the solution of transport equations for the number density of aggregates and primary particles. Kraft and coworkers [3] proposed a detailed population balance model (PBM), which describes the evolution of carbonaceous particles by solving the Smoluchowski equation [5]. These models were successfully applied in both one and two-dimensional flame simulations to predict several soot measurements.
This work presents the first discrete sectional model fully written in CHEMKIN format able to predict CNP morphology in terms of primary particle diameter (D_{pp})

profiles, particle size distribution (PSD) and H/C ratio along 1D laminar flames. One of the main advantages of the proposed model is that neither the solution of many additional equations other than those for mass, energy, momentum, and species, nor post-processing steps of numerical results obtained through simplified methods are required. Moreover, the proposed model allows to account for the different reactivity of aggregates that share equivalent mass but possess different surface areas due to the presence of primary particles of different sizes.

Kinetic model

The main features of the discrete sectional model developed by the CRECK modeling group were described in previous works [4]. Large PAHs and CNPs are discretized into 25 sections of lumped pseudo species, called BINs, from 20 to over 10^8 C-atoms. Based on a recent theoretical study on large PAHs [5], aromatic species with >100 C-atoms are modeled as persistent radicals.

In this work, the assumption of primary particles (BIN12, D_p=10 nm) with a single fixed size, adopted in previous versions of the model [4,6], is removed to account for polydispersity. This enables an improved description of the morphology and in turn of the surface reactivity of carbonaceous particles. Carbonaceous particles are distinguished between liquid-like particles (BIN-L) and solid primary particles with an onion like nanostructure (BIN-PP), as shown in Fig. 1. Once the first liquid-like particles (BIN5, D_p=2 nm) form through inception of gas-phase large PAHs, they can Coalesce or Grow ("C&G") towards larger BIN-L (vertical arrows in Fig. 1) or undergo carbonization from Liquid to Solid ("LtoS") primary particles BIN-PP (horizontal arrows in Fig. 1). Indeed, it was experimentally observed that incipient particles are liquid-like amorphous carbonaceous materials [7]. Then, an interplay of physicochemical phenomena governs the transition from liquid-like to solid particles. This transition is driven by the carbonization process. Dobbins [7] proposed a first-order Arrhenius rate constant for the conversion of CNP precursors to carbonaceous species in diffusion flames of eight different hydrocarbon fuels. This rate is here used as reference to model particle carbonization.

Primary particles can then form larger BIN-PP through coagulation and growth (vertical arrows in Fig. 1) or Aggregate ("A") into fractals (diagonal arrows in Fig. 1). The combination of primary particles of different size within the same aggregate would result in an enormous number of BINs. To limit the total number of species in the proposed model, each primary particle is assumed to aggregate forming monodisperse entities, with a fractal dimension D_f = 1.8 [8]. Different monodisperse aggregates (e.g., BIN-AG-I, BIN-AG-II) with equal mass are considered in the model (Fig. 1).

The reference rate parameters for aggregation of solid particles and aggregates are adapted from previous versions of the model [4,6]. The collision efficiency (γ) proposed in [6] is considered to account for the temperature, particle H/C ratio and size dependency of aggregation reactions. For coalescence, which involves at least one liquid-like particle (BIN-L), different rates are considered. In particular, a

unitary collision efficiency ($\gamma = 1$) is assumed. Moreover, based on the molecular dynamic (MD) simulations performed in [9], coalescence rates are scaled with respect to the volume ratio of the colliding entities.

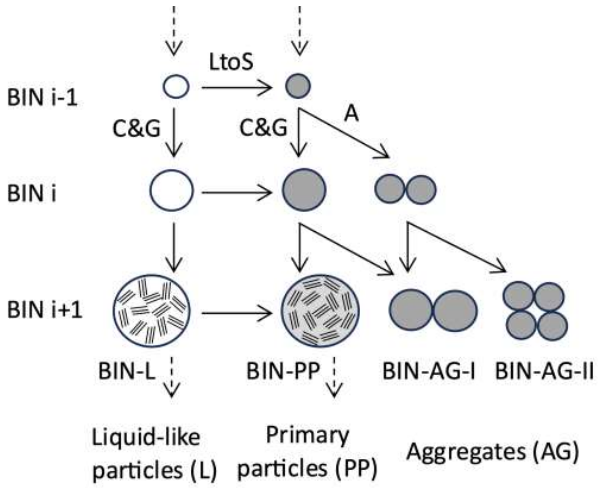

Figure 1. Schematic representation of the polydisperse CRECK model. The arrows represent different reaction classes: carbonization, i.e., the transition from liquid to solid particles ("LtoS"), coalescence and surface growth ("C&G"), and aggregation ("A").

Reaction classes for inception, surface growth, dehydrogenation and oxidation with their reference rate parameters are taken from previous versions of the CRECK model [4,6]. The overall model, coupled with detailed gas-phase chemistry up to 5-ring aromatics [6] and it is fully written in CHEMKIN format. Numerical simulations are carried out with the OpenSMOKE++ framework [10].

Results and discussion

Model validation is performed by comparison with data from 11 laminar flames, whose operating conditions are summarized in Table 1. The selected flames include three different configurations: premixed flat flames established on the McKenna-type burner (LPF), premixed burner-stabilized stagnation flames (BSSF) and counterflow diffusion flames (CFDF).

The series of premixed ethylene flames experimentally studied by Xu and Faeth [11] and the series of counterflow diffusion ethylene flames by Amin et al. [12] are selected to assess the model performances against literature data of average primary particle diameter (D_{pp}), at different equivalence ratios (ϕ = 2.34-2.94) and pressures (P = 2-5 atm) in the premixed and in the counterflow configuration, respectively.

In the series of premixed flames, the model captures the increase of average primary particle diameter (Fig. 2a) as the equivalence ratio increases. A good quantitative agreement between measurements and simulations is obtained for both carbonaceous particle properties at ϕ = 2.34 and 2.64, while larger deviations occur at ϕ = 2.94.

Table 1. Laminar flames investigated.

#Flame	Type	T_{max}, K	P, atm	$^{*}\phi/^{**}Z_{st}$	$^{*}v_0$, cm $s^{-1}/^{**}K_G$, s^{-1}	L, mm	Ref.
F1	LPF	1644	1	2.34	6.8	30	[11]
F2	LPF	1600	1	2.34	6.8	30	[11]
F3	LPF	1556	1	2.34	6.8	30	[11]
F4	CFDF	1983	2	0.17	30	8.2	[12]
F5	CFDF	2016	3	0.17	30	8.2	[12]
F6	CFDF	2037	4	0.17	30	8.2	[12]
F7	CFDF	2052	5	0.17	30	8.2	[12]
F8	BSSF	1783	1	2.06	8	5	[13]
F9	BSSF	1832	1	2.06	8	10	[13]
F10	LPF	1700	1	2.40	4	14	[14]
F11	LPF	1770	1	2.40	5	16	[14]

*Equivalence ratio (ϕ) and cold gas velocity (v_0) for premixed flames. **Stoichiometric mixture fraction (Z_{st}) and global strain rate (K_G) for counterflow flames.

The evolution of D_{pp} profiles along the axial coordinate of the flame at different equivalence ratios is well reproduced, with maximum deviations by a factor of ~1.2 at ϕ = 2.94. Importantly, Fig. 2a shows the improved predictive capability of the proposed model, which accounts for CNP polydispersity, with respect to its previous version [4], which instead assumes monodisperse aggregates constituted by fixed size primary particles (D_{pp}=10 nm, red dashed line in Fig. 2a).
In the series of counterflow flames F4-F7, the polydisperse model also captures the increase of D_{pp} (Fig. 2b). However, the measured peak D_{pp} is characterized by a more pronounced increase from 2 to 5 atm, i.e., from 13 to 52 nm, respectively, compared to the model predictions, i.e., from 28 to 40 nm. Moreover, the model predicts a steeper increase of the D_{pp} profiles from ~0.45 cm from the fuel nozzle toward the particle stagnation plane, where the larger primary particle diameters are reached. On the other hand, the model captures the increasing slope of the D_{pp} profiles from 2 to 5 atm as well as the shift of the peak D_{pp} location towards larger distances from the fuel nozzle as pressure increases (Fig. 2b).
Another key morphological property of CNPs is the particle size distribution (PSD). The PSD measurements of Shao et al. [13], performed in a series of BSS ethylene flames (F8-F9 in Table 2) at different height above the burner (H_p) are selected to analyze the related model predictions (Fig. 2c). The proposed model satisfactorily describes the transition from the unimodal to the bimodal distribution with the increase of particle residence time from H_p = 5 mm to 10 mm. The clear development of the throat at H_p = 10 mm obtained with the proposed model represents another relevant improvement in the description of the PSD evolution with respect to its previous version [6], which considers neither CNP polydispersity nor the scaling of coalescence rates with the volume ratio of the colliding entities described above.

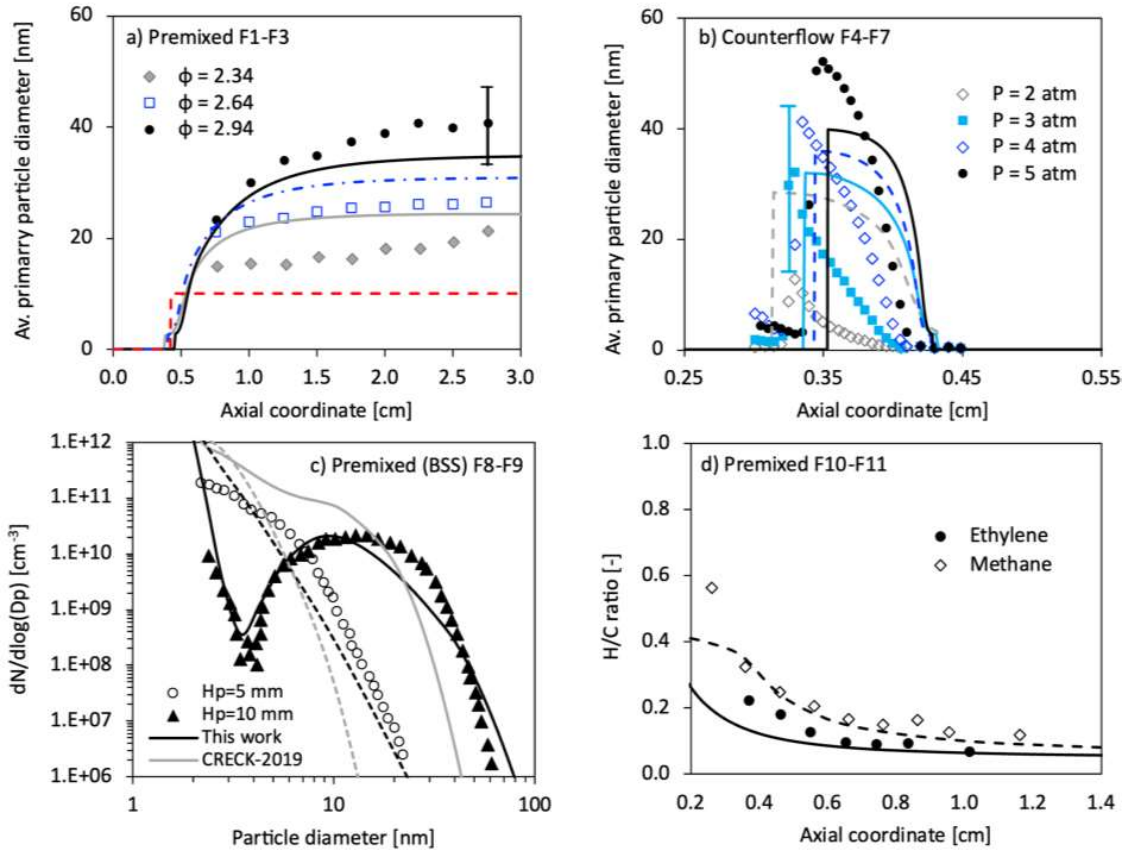

Figure 2. Average primary particle diameter profiles in a) laminar ethylene premixed (F1-F3) [11] and b) counterflow flames (F4-F7) [12]. Particle size distribution at H_p=5 and 10 mm in BSS ethylene flames (F8-9) [13]. H/C ratio profiles in ethylene (F10) and methane (F11) premixed flames [14]. Symbols: experiments; lines: model simulations.

Finally, the model is validated against experimental data of particle H/C ratio in two laminar premixed flames fueled by ethylene and methane by Russo et al. [14]. Model simulations well capture the formation of more dehydrogenated carbonaceous particles in the ethylene flame (F10) with respect to those produced in the methane flame (F11), due to the related lower fuel H/C ratio (2 for C_2H_4 and 4 for CH_4). These results highlight the good model description of carbonaceous nanostructure, which significantly determines not only the reactivity [2] but also the optical and electronic properties of CNPs, as discussed in the introduction of this work.

Conclusions

A novel detailed discrete sectional model for CNP formation has been presented in this work. The main novelty introduced is the description of CNP polydispersity achieved by considering the formation of primary particles with different sizes from liquid-like counterparts through the carbonization process. Compared to previous versions of the model, this allows to predict the evolution of average primary particle diameters (D_{pp}) measured in both premixed and counterflow diffusion ethylene flames. The model also captures the measured trends of particle size distribution

(PSD) and particle H/C ratio. Future studies are necessary to perform more accurate rate estimation of key processes like carbonization, coalescence and aggregation, characterized by the largest uncertainties, but significantly affecting model predictions of CNP morphology.

References

[1] Lindstedt R.P., Michelsen H.A., Mueller M.E., "Special issue and perspective on the chemistry and physics of carbonaceous particle formation", *Combust Flame* 113042 (2023).
[2] Liu C., Singh A. V., Saggese C., Tang Q., Chen D., Wan K., Vinciguerra M., Commodo M., De Falco G., Minutolo P., D'Anna A., Wang H., "Flame-formed carbon nanoparticles exhibit quantum dot behaviors", *Proceedings of the National Academy of Sciences* 116: 12692–7 (2019).
[3] Botero M.L., Eaves N., Dreyer J.A.H., Sheng Y., Akroyd J., Yang W., Kraft M., "Experimental and numerical study of the evolution of soot primary particles in a diffusion flame", *Proceedings of the Combustion Institute* 37: 2047–55 (2019).
[4] Nobili A., Cuoci A., Pejpichestakul W., Pelucchi M., Cavallotti C., Faravelli T., "Modeling soot particles as stable radicals: a chemical kinetic study on formation and oxidation. Part I. Soot formation in ethylene laminar premixed and counterflow diffusion flames", *Combust Flame* 243: 112073 (2022).
[5] Nobili A., Pratali Maffei L., Baggioli A., Pelucchi M., Cuoci A., Cavallotti C., Faravelli T., "On the radical behavior of large polycyclic aromatic hydrocarbons in soot formation and oxidation", *Combust Flame* 111692 (2021).
[6] Pejpichestakul W., Frassoldati A., Parente A., Faravelli T., "Kinetic modeling of soot formation in premixed burner-stabilized stagnation ethylene flames at heavily sooting condition", *Fuel* 234: 199–206 (2018).
[7] Dobbins R.A., "Soot inception temperature and the carbonization rate of precursor particles", *Combust Flame* 130: 204–14 (2002).
[8] Schenk M., Lieb S., Vieker H., Beyer A., Gölzhäuser A., Wang H., Kohse-Höinghaus K., "Morphology of nascent soot in ethylene flames", *Proceedings of the Combustion Institute* 35: 1879–86 (2015).
[9] Hawa T., Zachariah M.R., "Coalescence kinetics of unequal sized nanoparticles", *J Aerosol Sci* 37: 1–15 (2006).
[10] Cuoci A., Frassoldati A., Faravelli T., Ranzi E., "OpenSMOKE++: An object-oriented framework for the numerical modeling of reactive systems with detailed kinetic mechanisms", *Comput Phys Commun* 192: 237–64 (2015).
[11] Xu F., Sunderland P.B., Faeth G.M., "Soot formation in laminar premixed ethylene/air flames at atmospheric pressure", *Combust Flame* 108: 471–93 (1997).
[12] Amin H.M.F., Roberts W.L., "Soot measurements by two angle scattering and extinction in an N2-diluted ethylene/air counterflow diffusion flame from 2 to 5 atm", *Proceedings of the Combustion Institute* 36: 861–9 (2017).
[13] Shao C., Campuzano F., Zhai Y., Wang H., Zhang W., Mani Sarathy S., "Effects of ammonia addition on soot formation in ethylene laminar premixed flames", *Combust Flame* 235: 111698 (2022).
[14] Russo C., Tregrossi A., Ciajolo A., "Dehydrogenation and growth of soot in premixed flames", *Proceedings of the Combustion Institute* 35: 1803–9 (2015).

THE EFFECT OF OZONE ON SOOT FORMATION IN PARTIALLY PREMIXED LAMINAR METHANE/AIR FLAMES

A. Pignatelli, L. Basta*, F. Sasso*, F. Picca*, M. Commodo***, P. Minutolo***, A. D'Anna***

alessia.pignatelli@unina.it

* Dipartimento di Ingegneria Chimica, dei Materiali e della Produzione Industriale, Università degli Studi di Napoli Federico II, P.le Tecchio 80, 80125 - Napoli (Italy)

** Dipartimento di Fisica, Università degli Studi di Napoli Federico II, Via Cinthia 21, Napoli, 80126, Italy

*** Istituto di Scienze e Tecnologie per l'Energia e la Mobilità Sostenibili, Consiglio Nazionale delle 14 Ricerche, P.le Tecchio 80, 80125 - Napoli (Italy)

Abstract

Soot is globally considered as a strongly harmful compound to people's health as to the environment [1]. For this reason, the identification of technologies and methods able to reduce the release of soot particles is a hot topic in the research field. The introduction of active molecules in the burners seems to have a strong potential and among them, ozone represents a good candidate. In this study, the effect of ozone addition on soot formation in partially premixed laminar methane flame has been investigated. Two equivalence ratios (Φ) were analyzed, equal to 15 and 25, respectively. Soot particles collected in the centerline of the flames at several heights above the burner have been examined in terms of size, morphology, and chemical/structural characteristics, by differential mobility analysis, atomic force microscopy, and Raman spectroscopy respectively. The Raman spectroscopy analysis indicates that ozone addition promotes the formation of slightly larger aromatic soot constituents. Moreover, within the selected experimental conditions and ozone concentration of several hundred parts per million, the flame temperature is unaffected regardless of the presence or absence of ozone. Consequently, it can be inferred that the observed modifications in soot characteristics are predominantly attributed to chemical factors. The observed effects are all consistent with a possible chemical interaction of atomic oxygen, resulting from the decomposition of ozone in the post-flame zone, with aromatic π-radicals, precursors of the soot particles.

Introduction

Combustion of hydrocarbon fuels plays a central role in our everyday life, but the understanding of the mechanisms involved in this process is an active and ongoing research field. In the last decades, great attention has been given to the investigation of the byproducts of incomplete combustion, especially soot. Soot particles can strongly differ in terms of size, nanostructure, and chemical composition according

to the combustion conditions. Factors influencing this variability include flame temperature, fuel composition, pressure, residence time, and premixing level. Innovative experimental [2-4] and theoretical methods [5,6] have recently contributed to enrich our comprehension of soot formation and evolution in flame. A significant breakthrough stands in the identification of π-radicals as critical intermediates in the inception and growth of soot particles. Recent investigations supported the existence of molecular clustering reaction pathways driven by radical-chain reactions of π-radicals whose understanding could strongly contribute to the clarification of the main mechanisms involving soot formation [2,5].
Several studies investigated the soot formation in purely diffusive flames [7-10], but the analysis of partially premixed flames can be extremely useful due to the use of this type of flame in a large class of practical devices.

Experimental Setup

A partially premixed flame arises when the fuel is mixed with a sub-stoichiometric amount of air - to generate a local fuel-rich mixture - before reaching the reaction zone, where additional air becomes available. The effects of partial premixing on soot formation have been explored using diverse techniques [11-14]. In this work, the effect of ozone on particle nucleation and soot formation is analyzed by investigating a partially premixed laminar flame of methane and air, operated at two different equivalence ratios, i.e. different amounts of the primary air added to the fuel stream, equal to 15 and 25, respectively. The experimental conditions are reported in Table 1.

Table 1. Experimental Conditions.

Flame	Φ	O_3 [ppm]	Q_{CH4} [l/min]	Q_{PA} [l/min]	Q_{SA} [Nl/nh]
Φ15	15	-	0.4	0.50	4000
$Φ15_{O3}$	15	570	0.4	0.50	4000
Φ25	25	-	0.4	0.32	4000
$Φ25_{O3}$	25	500	0.4	0.32	4000

The fuel flow rate (Q_{CH4}) remains constant for both flames, as does the secondary air flow rate (Q_{SA}), which is provided to stabilize the flame. The variable factor is the primary air flow (Q_{PA}), responsible for generating the two Φ values. The burner was the same as in previous studies [14]; a schematic representation is reported in Figure 1. The ozone was produced by an ozone generator Model 1001 Jelight Company Inc. For both flames, the ozone concentrations were dictated by the limitations of the ozone generator, which grantees a maximum conversion of oxygen into ozone equal to 0.25% c.a. The resulting concentrations were measured via a Model 205 Dual Beam Ozone Monitor (2B Technologies).

The exhausts of the flames were collected using a horizontal stainless steel tubular probe with a 1 cm outer diameter and an orifice of 0.2 mm. A turbulent N_2 diluent flow was provided so to avoid particle aggregation and quench chemical reactions of the flame exhausts. The flame products were collected at different heights above the burner (Z), so to have a clear picture of the evolution of the particles in the flame.

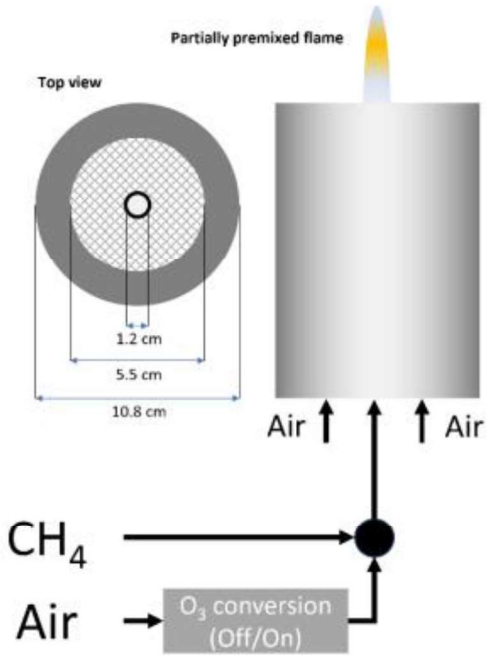

Figure 1. Schematic of the co-flow partially premixed burner setup.

Results

For each flame, the analysis of the effects of ozone on the produced soot was performed by using RTD signal analysis, particle size distribution function investigations, temperature measurements, semi-contact AFM, and Raman Spectroscopy.

Temperature does not significantly change after the introduction of ozone, probably due to the low concentrations involved in this study.

As reported in Figure 2, for both equivalence ratios, PSDs register a decrease in particle number in the upper part of the flame. This can be due either to a higher oxidation reactivity of the soot from ozone addition compared to the normal one, or a lower concentration and nucleation of soot because of the ozone injection into the flames.

Semi-contact AFM allows to investigate the morphology of the soot particles, highlighting a larger number of collected particles, surface coverage, and collected volume of the particles for higher equivalence ratios. 3-dimensional visualization of the AFM images shows a lower height of the collected particles in the ozone-doped flame. It is notable that the heights of the particles collected in the flames after ozone addition correspond to that of PAHs of only a few layers (bin spacing approximately

corresponding to the PAHs interlayer distance). Moreover, the base radius follows the same trend, decreasing with reducing Φ and with ozone.

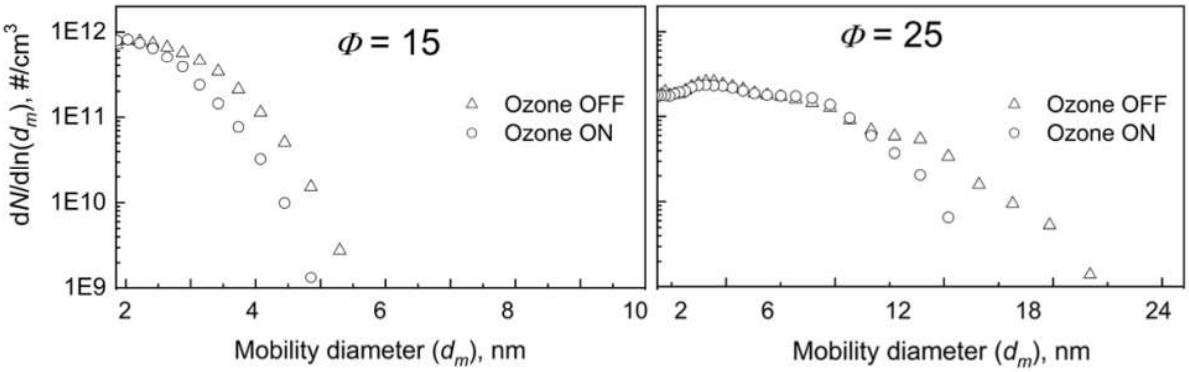

Figure 2. Particle size distributions (PSDs) along the flame centerline with and without ozone injection collected at Z= 49 mm. Φ equal to 15 and 25 are reported on the left and right side, respectively.

Raman spectroscopy has been used to assess the effect of ozone addition on soot chemical/structural characteristics. O_3 promotes the growth of the aromatic size, evidenced by the larger D/G ratio and a better graphitic structure shown by the deeper valley between D and G peaks. This effect can be tentatively assigned to the removal of resonantly stabilized radicals. In fact, in the flame without O_3, a higher amount of such radicals, which arise from non-hexagonal defects, would favour crosslinks between aromatics and, thereby, reduce HACA growth producing smaller aromatic structures. The observed effect when introducing ozone is consistent with a chemical interaction of atomic oxygen with aromatic π-radicals, precursors of the soot particles, resulting in a reduced clusterization of soot molecular constituents. Furthermore, the interaction of the atomic oxygen with the aromatic π-radicals in incipient particles can also alter their growth through coagulation.

Conclusions

This study aims to investigate the effects of ozone in flame. From these results, the introduction of O_3 in flame and the consequent presence of atomic oxygen seems to affect the soot formation mechanisms. For each flame condition, soot particles show an altered number and dimension after the introduction of the active molecule, as well as different morphology and chemical structure. Further analysis is currently investigation so to highlight the main variables affecting the production of soot and to univocally individuate an innovative combustion methodology able to reduce pollutant emissions [15,16].

References

[1] Xi, J., Yang, G., Cai, J., Gu Z., "A Review of Recent Research Results on Soot: The Formation of a Kind of Carbon-Based Material in Flames", *Front. Mater*., Vol 8, (2021)

[2] Lieske, L-A, Commodo, M., Martin, J.W., Kaiser, K., Benekou, V., Minutolo, P., et al. "Portraits of Soot Molecules Reveal Pathways to Large Aromatics, Five-/Seven-Membered Rings, and Inception through π-Radical Localization", *ACS Nano* 17:13563–74 (2023).

[3] Faccinetto, A., Irimiea, C., Minutolo, P., Commodo, M., D'Anna, A., Nuns, N., et al. "Evidence on the formation of dimers of polycyclic aromatic hydrocarbons in a laminar diffusion flame. *Commun Chem* 3:112, (2020).

[4] Johansson, K.O., Head-Gordon, M.P., Schrader, P.E., Wilson, K.R., Michelsen, H.A. "Resonance-stabilized hydrocarbon-radical chain reactions may explain soot inception and growth", *Science* 361:997–1000 (2018).

[5] Frenklach, M., Mebel, A.M. "On the mechanism of soot nucleation". Physical Chemistry Chemical Physics 22:5314–31 (2020).

[6] Martin, J.W., Pascazio, L., Menon, A., Akroyd, J., Kaiser, K., Schulz, F., et al. "π-Diradical Aromatic Soot Precursors in Flames". *J Am Chem Soc* 143:12212–9 (2021).

[7] Karataş, A.E., Gülder, Ö.L. "Soot formation in high pressure laminar diffusion flames". *Prog Energy Combust Sci* 38:818–45(2012).

[8] Vander Wal, R.L. "Soot precursor carbonization: Visualization using LIF and LII and comparison using bright and dark field TEM". *Combust Flame* 112:607–16, (1998).

[9] D'Anna, A., Rolando, A., Allouis, C., Minutolo, P., D'Alessio, A. "Nano-organic carbon and soot particle measurements in a laminar ethylene diffusion flame". *Proc. Comb. Inst,* 30:1449-56, (2005).

[10] Kholghy, M.R., Afarin, Y., Sediako, A.D., Barba, J., Lapuerta, M., Chu, C., et al. "Comparison of multiple diagnostic techniques to study soot formation and morphology in a diffusion flame". *Combust Flame* 176:567–83(2017).

[11] McEnally, C.S., Pfefferle, L.D. "Experimental study of nonfuel hydrocarbons and soot in coflowing partially premixed ethylene/air flames". *Combust Flame* 121:575–92, (2000).

[12] Arana, C.P., Pontoni, M., Sen, S., Puri, I.K. "Field measurements of soot volume fractions in laminar partially premixed coflow ethylene/air flames". *Combust Flame* 138:362–72, (2004).

[13] Huang, C-H., Vander Wal, R.L. "Partial premixing effects upon soot nanostructure". *Combust Flame* 168:403–8, (2016).

[14] De Falco, G., Sirignano, M., Commodo, M., Merotto, L., Migliorini, F., Dondè, R., et al. "Experimental and numerical study of soot formation and evolution in co-flow laminar partially premixed flames". *Fuel* 220:396–402, (2018).

[15] Stankovich, S., Dikin, D.A., Dommett, G.H.B., Kohlhaas, K.M., Zimney, E.J.,

Stach, E.A., et al. "Graphene based composite materials". *Nature* 442:282–6 (2006) 220:396–402.

[16] D'Alessio, A., D'Anna, A., Minutolo, P., Sgro, L.A., "Nanoparticles of Organic Carbon (NOC) formed in flames and their effects in urban atmosphere" in Bockhorn, H., D'Anna, A., Sarofim, A.F., Wang, A. (Eds) Combustion Generated Fine Carbonaceous Particles. KIT Scientific Publishing, Karlsruhe 205-230, (2009)

FLAME-SYNTHESIZED TiO_2-C NANOCOMPOSITE FILMS: UNVEILING RESISTIVE SWITCHING PHENOMENON FOR MEMORY STORAGE APPLICATIONS

Abdul Khalique*, Mario Commodo, Patrizia Minutolo**, Gianluigi De Falco**, Andrea D'Anna***
abdul.khalique@unina.it
* Dipartimento di Ingegneria Chimica, dei Materiali e della Produzione Industriale, Università degli Studi di Napoli Federico II, P.le Tecchio 80, 80125 - Napoli (Italy)
** Istituto di Scienze e Tecnologie per l'Energia e la Mobilità Sostenibili, Consiglio Nazionale delle Ricerche, P.le Tecchio 80, 80125 - Napoli (Italy)

Abstract
A composite nanostructured thin film of TiO_2-C has been fabricated through a facile one-step flame-based synthesis using a customized honeycomb burner and then collected via thermophoretic deposition. Titanium (IV) isopropoxide (TTIP) solution was used as a precursor for TiO_2 nanoparticles and ethylene/air premixed gas was the fuel source of carbon compounds. The produced nanocomposite film is analyzed with Raman spectroscopy to examine the presence of both TiO_2 and carbon peaks. The produced nanocomposite film was further investigated for optical bandgap determination through UV-Vis spectroscopy and its electrical characteristics through current-voltage (I-V) measurements. The TiO_2-C nanocomposite film exhibited capacitive coupled resistive switching behavior, unveiling great potential for non-volatile memory storage applications.

Introduction
Titanium dioxide (TiO_2) nanoparticles produced through several methods have been extensively studied for their physiochemical characteristics for the last two decades for their wide applications including biosensors, gas sensors, pigments, photocatalysts, etc [1]. Additionally, its high chemical activity under UV irradiation makes it a primary choice to be used as an active component of solar cells as well as a reaction catalyst. It is well known that TiO_2 nanoparticles exhibit significantly higher activity than the bulk material, and this is correlated with a greater active surface area. UV irradiation of TiO_2 nanoparticles produces electron-hole pairs that participate in catalytic activities on the particle surface because of photon energy absorption[2]. An inverse process is followed up with it called charge recombination. Reports suggested that such recombination of the electron-hole pairs is probably due to the energy band gap[3]. The transition of the electron from the conduction band to the valence band is directly related to the band gap, so the higher the band gap, the lesser the chance of electron transition. As a result, when TiO_2 is exposed to sunlight, the lower the band gap, the higher the proportion of usable energy because

lower energy photons are needed to excite the electrons that are present in the valence band. As of today, several techniques are being utilized for the band gap reduction of the TiO_2 including structural modification with the incorporation of carbon. The carbon doping provides enhanced absorption capacity to the crystalline TiO_2 making it a porous structure by introducing additional defects and vacancies into the TiO_2 lattice. Different methods are adopted to produce TiO_2-C nanocomposites including sol-gel method, hydrothermal method, flame aerosol synthesis, thermal decomposition and reduction method in order to obtain particles with different sizes, shapes, and crystal structures[4]. Recently, the flame-based synthesis method has been increasingly adopted for producing a variety of organic and inorganic nanoparticles thin films, and powders with different properties due to its compliant approach and industrial-level scalability.

Recently, flame-formed TiO_2-C have been reported to exhibit significant improvement in their photocatalytic performances. Besides the photocatalytic characteristics, the two-step flame-synthesized TiO_2-C thin films have revealed an interesting resistive switching effect [5]. This discovery paves the way for an interesting application of TiO_2-C nanocomposite films for non-volatile memory storage devices. The resistive switching phenomenon is attributed to the memristor, the fourth component of the circuit that was discovered in 1971 by Leon Chua[6]. This phenomenon attracted the substantial attention of the scientific community towards investigation of this symmetric fourth component of the circuit. That discovery opened the door for designing more complex integrated circuits with enhanced technical capabilities. Since then, several organic and inorganic composite materials have been produced with resistive switching behaviour along with an interesting capacitive coupled switching phenomenon.

Experimental

The experimental setup for the facile one-step flame synthesis of TiO_2-C nanocomposite thin films consists of a customized vertical honeycomb burner. Using pre-heated air as the carrier gas, a high-pressure syringe pump (Model 410 from KD Scientific, Holliston, MA, USA) was utilized to supply the atomized 0.5 Molar precursor solution of TTIP in ethanol to the reactor at a flow rate of 900 µL/min along with the spray air (60 Nl/h). The spray solution was carried to the burner with the help of secondary air through the line (60 Nl/h). The burner and its connected supply lines were heated up to 450K with the help of heating tapes to avoid the condensation of the syringe-fed TTIP solution. Furthermore, the premixed ethylene (45 Nl/h) and air (200 Nl/h) were supplied through the bottom of the honeycomb burner as the source of carbon nanoparticles. The system is capable of any variation in the concentration or the flow rate of the precursor solution or the carbon source to obtain different sizes and morphology of the produced nanocomposite films. TiO_2-C nanocomposite films are produced in this flame condition of vapor-fed 0.5M TTIP precursor solution and the premixed ethylene/air and thermophoretically collected on different substrates mounted on a rotating disk

15 cm above the burner surface rotating at a speed of 460 rpm set through a voltage regulator. Additionally, the CNP thin films have been produced with the same setup under similar conditions in the absence of TTIP precursor sending only ethanol through the syringe pump for the comparative study of the CNP film and TiO_2-C nanocomposite film.

Surface polished aluminum substrate was used for the Raman analysis of the produced nanocomposite film through a Raman microscope (model Xplora, from Horiba, Kyoto, Japan) equipped with a 100 × 0.9 NA objective and laser beam with an excitation wavelength of 532nm. For absorption analysis, UV-vis spectrophotometer (model 8453 from Agilent, Santa Clara, CA, USA) was used to obtain the spectra of produced film on quartz slides. To investigate the electrical behavior of the film the OSSILA x200 source measuring unit coupled with Linkam HFS600E-PB4 with T95 system controller was utilized. The nanocomposite films were deposited on 'Micrux ED-IDE1-Au' gold-coated electrodes.

Results and Discussions

Raman Analysis

The Raman Spectra of the CNPs thin film and TiO_2-C Nanocomposite film are shown in Fig. 1.

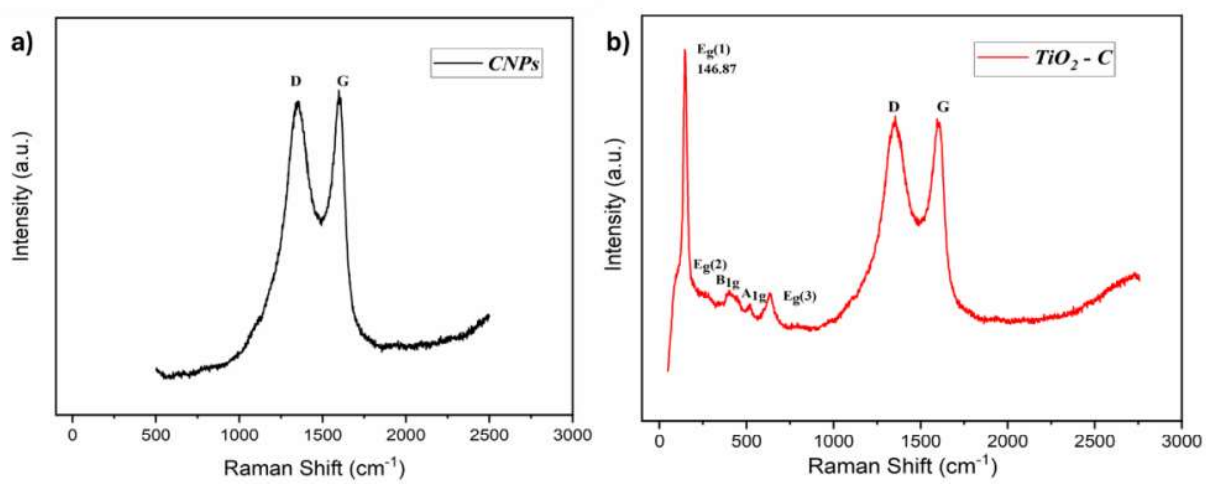

Figure 1. Raman spectrum of **(a)** CNPs thin film, and **(b)** TiO_2-C nanocomposite thin film.

The normalized Raman spectrum in Fig 1 (a) exhibits the characteristics of a standard carbon compound with D band and G band at 1350 cm^{-1} and 1600 cm^{-1} respectively with no further peak signals indicating the successful deposition of pure CNPs thin film. Fig 1 (b) shows the peaks at 146.87 cm^{-1}, 200 cm^{-1}, 402 cm^{-1}, 517 cm^{-1}, and 640 cm^{-1} attributed to the E_g, E_g, B_1g, (B_1g/A_{1g}), and E_g active anatase modes of TiO_2. There is a little positive shift of 2.87 cm^{-1} in the primary peak of TiO_2 with respect to its standard 144 cm^{-1} which suggests the blue shift due to incorporation of low band gap compound i.e., carbon. With that, the D band and G band in the spectrum

corresponds to the most likely interconnection of CNPs and TiO_2 NPs, hence forming a nanostructured TiO_2-C composite thin film.

Absorption

Absorption of the TiO_2-C nanocomposite thin film is studied to investigate the energy band gap variation with respect to the pure TiO_2. Titania has remained a primary choice among semiconductor metal-oxides for various application due to its stable energy bandgap of 3.2 eV that is often engineered through incorporation of different organic and inorganic compounds to get desired behavior and performance for different applications. Employing the Tauc model, the optical band gap is experimentally determined from the UV-visible absorption spectrum:

$$\sqrt{\alpha h\upsilon} = B\left(h\upsilon - E_g^{opt}\right) \quad (1)$$

Here in Fig. 2, TiO_2-C nanocomposite thin film is reported with a reduced energy bandgap with respect to the pure TiO_2.

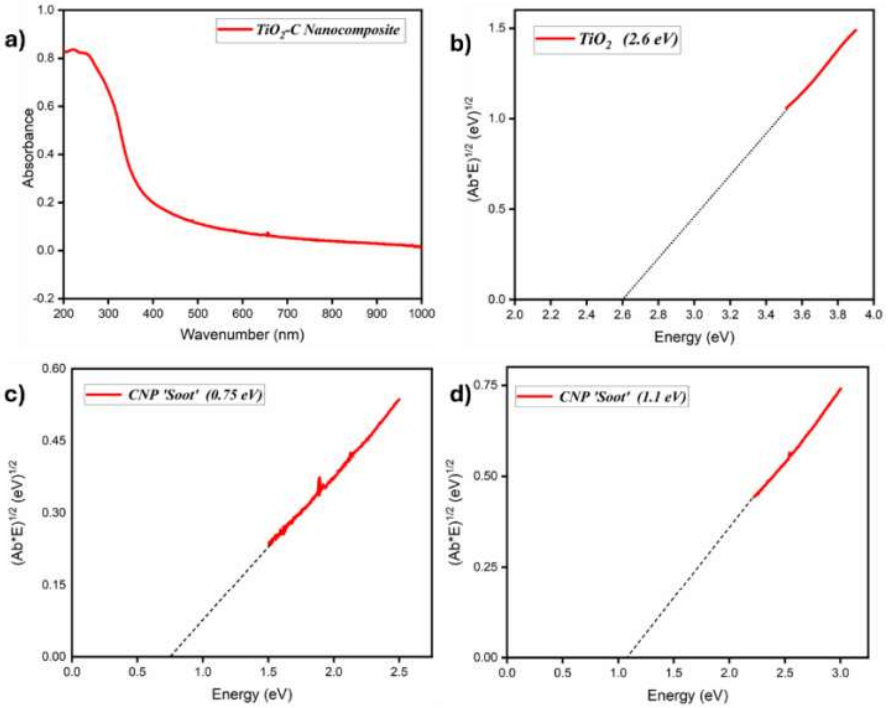

Figure 2. (a) UV-Vis absorption spectrum of the TiO_2-C nanocomposite thin film,**(b-d)** Tauc plot of the produced film to determine bad gape.

Fig. 2 (a) shows the complete absorption spectrum of the TiO_2-C nanocomposite film measured on the quartz. Employing the Tauc model, Fig. 2 (b-d) shows the Tauc plot visualized in different ranges of the spectrum for determining the optical bandgap. It is evident from the Fig. 2(b) that there is a significant reduction in the bandgap of TiO_2 from standard 3.2 eV to 2.6 eV apparently due to the CNPs incorporation. Whereas, in Fig. 2 (c-d) the Tauc plot corresponds to the bandgap of 0.75 eV and 1.1 eV attributed to the presence of CNPs.

Electrical 'Current-Voltage' Measurement (I-V)

As the memristor was introduced, the idea of a fourth circuit element has garnered a lot of interest as it allows for the creation of increasingly intricate integrated circuits using memristors to meet increasingly demanding technical specifications. Herein, an interesting resistive switching phenomena is observed in the produced TiO_2-C nanocomposite thin film. In Fig. 3 the curves measured at a voltage scan rate VSR of 0.2 v/s are shown.

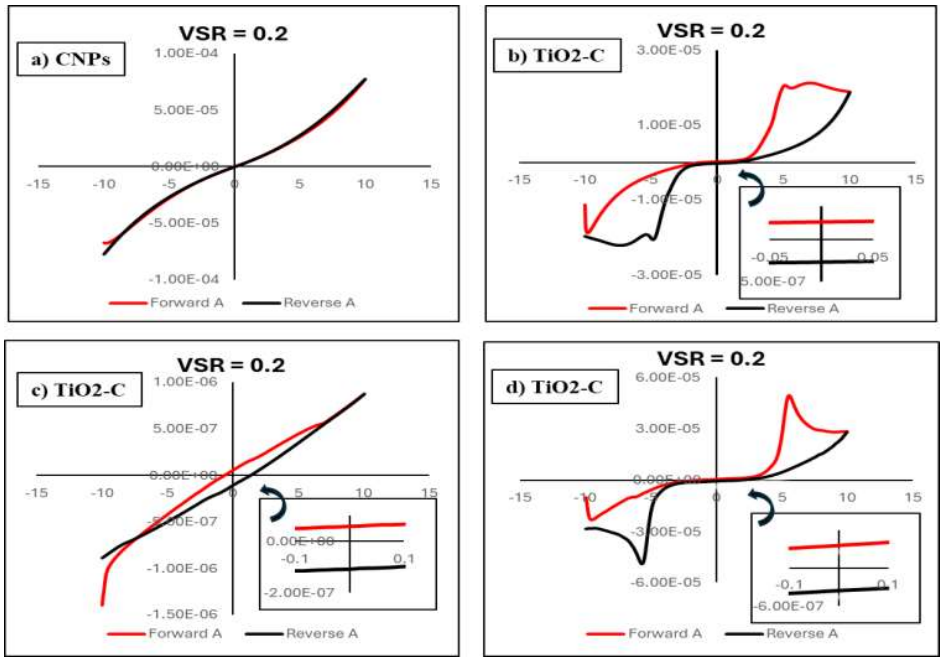

Figure 3. Current-Voltage ***(I-V)*** curves of the **(a)** CNPs thin film, **(b)** TiO_2-C nanocomposite on the synthesis day, **(c)** TiO_2-C nanocomposite after putting them in dark 'deactivation', **(d)** TiO_2-C nanocomposite after exposure to the solar light irradiation 'reactivation'.

The I-V measurements of TiO_2-C nanocomposite film unveiled the capacitive coupled resistive switching phenomenon that is observed in the non-zero crossing I-V curves, generally termed as non-pinched I-V hysteresis. Fig. 3 (a) shows a typical non-ohmic I-V curve attributed to the carbon compound of the 0M flame that produced pure CNPs film. Whereas the I-V curves of the TiO_2-C nanocomposite films in fig. 3 (b-d) exhibit an interesting activation and deactivation phenomenon of the switching behavior under exposure to the solar light irradiation and dark condition respectively. Fig. 3 (b) represents the I-V measurement taken on the synthesis day showing substantial bipolar switching. Fig.3 (c) shows the I-V measurements taken after a span of 05 days under dark. The switching phenomenon completely disappeared with a significant reduction of the current by up to 02 order of magnitude as illustrated in the Fig.3 (c) suggesting deactivation of the nanocomposite film due to the presence of TiO_2. Furthermore, upon exposure to the

solar light irradiation for 05 days the switching behavior re-appeared again with an increase in the current value equivalent to the initial measurement of the nanocomposite film as shown in Fig. 3 (d). Such activation/deactivation behavior in the produced film hints toward its great potential to be utilized for sensors and non-volatile memory storage devices.

Conclusion

The TiO_2-C nanocomposite films were successfully produced through a facile one-step flame synthesis technique. Raman analysis revealed its composite formation and a noticeable blue shift in the primary peak of anatase attributed to the incorporation of low bandgap carbon compound. Substantial reduction in the optical band gap was observed due to the presence of CNPs. The extensive investigation of the I-V revealed the capacitive-coupled memristive effect along with an interesting activation/deactivation phenomenon of the switching mechanism under solar light irradiation/darkness. Such fascinating electrical properties of the produced nanocomposite film pave the way for deep insights into exploring its advance applications.

Acknowledgement

The authors thank the PRIN 2022 PNRR project P2022HKE88: "FLAMENCO" for financial support.

References

[1] P. Rajaram, A. R. Jeice, and K. Jayakumar, “Review of green synthesized TiO2 nanoparticles for diverse applications,” *Surfaces and Interfaces*, vol. 39, p. 102912, Jul. 2023, doi: 10.1016/J.SURFIN.2023.102912.

[2] T. Chen, J. Xie, and P. Gao, “Ultraviolet Photocatalytic Degradation of Perovskite Solar Cells: Progress, Challenges, and Strategies,” *Advanced Energy and Sustainability Research*, vol. 3, no. 6, p. 2100218, Jun. 2022, doi: 10.1002/AESR.202100218.

[3] H. Li, D. Wang, H. Fan, P. Wang, T. Jiang, and T. Xie, “Synthesis of highly efficient C-doped TiO2 photocatalyst and its photo-generated charge-transfer properties,” *J Colloid Interface Sci*, vol. 354, no. 1, pp. 175–180, Feb. 2011, doi: 10.1016/J.JCIS.2010.10.048.

[4] G. Kholodnaya, R. Sazonov, and D. Ponomarev, “TiO2@C nanocomposites – from synthesis to application: A review,” *Fullerenes, Nanotubes and Carbon Nanostructures*, vol. 29, no. 7, pp. 487–526, 2021, doi: 10.1080/1536383X.2020.1820994.

[5] M. Commodo *et al.*, “Resistive Switching Phenomenon Observed in Self-Assembled Films of Flame-Formed Carbon-TiO2 Nanoparticles,” *Materials 2021, Vol. 14, Page 4672*, vol. 14, no. 16, p. 4672, Aug. 2021, doi: 10.3390/MA14164672.

[6] L. O. Chua, “Memristor—The Missing Circuit Element,” *IEEE Transactions on Circuit Theory*, vol. 18, no. 5, pp. 507–519, 1971, doi: 10.1109/TCT.1971.1083337.

Carbon production by thermal methane cracking in tubular quartz reactor

E. Busillo*, A. Nobili, F. Serse**, M.P. Bracciale*, P. De Filippis*, M. Pelucchi**, B. de Caprariis***
emmanuel.busillo@uniroma1.it
* Department of Chemical Engineering, Materials and Environment, Sapienza University of Rome, Via Eudossiana 18, 00184, Roma, Italy
** CRECK Modeling Lab, Department of Chemistry, Materials and Chemical Engineering "Giulio Natta", Politecnico di Milano, Piazza Leonardo da Vinci 32, 20133, Milano, Italy

Abstract

Methane cracking is explored as a bridge technology that enables the production of hydrogen while capturing carbon in the form of valuable materials, which could potentially lower hydrogen production costs and reduce carbon emissions. The process of methane (CH_4) cracking consists in the conversion CO_2-free of methane molecules into carbon and hydrogen

$$CH_{4(g)} = C_{(s)} + 2H_{2(g)} \quad (1)$$

The valorization of the carbon product plays a crucial role in reducing H_2 prices and improving overall process economics. To achieve this, a comprehensive understanding of the complex network of reactions involved in methane thermal cracking is essential, particularly in relation to the formation of valuable carbon and unwanted byproducts such as carbon nanoparticles. The study focuses on the experimental analysis and kinetic modelling of methane cracking in a tubular quartz reactor, exploring the morphology of the carbon products. The experimental investigation of pure methane cracking in a tubular quartz reactor, was conducted operating within a temperature range of 875–975 °C and varying initial flow rates of CH_4 (30, 45, and 60 ml/min). The data obtained from experiments were compared to the outcomes of kinetic simulations conducted on a heterogeneous plug flow reactor with specific dimensions (length = 20 cm, diameter = 1.5 cm) using the OpenSMOKE++ framework [1]. The reactor model, which includes details of the sectional area, total inlet and outlet flow, and stream composition in mass fractions, has been previously explained in [2]. Surface deposition properties are defined by the superficial site fraction density ($\Gamma = 8 \times 1014$ #/cm^2) and surface composition expressed as surface fraction adopting a 50/50 ratio of armchair to zigzag edges, which is based on estimates from prior research studies [3,4]. The detailed chemical kinetic mechanism utilized in this study comprises three main components:

1) gas-phase mechanism incorporating detailed high-temperature kinetics from

hydrogen and methane to polycyclic aromatic hydrocarbons (PAHs) formation;

2) carbon nanoparticle formation mechanism, validated against soot measurements in flames and flow reactors, utilizing a discrete sectional approach to describe large gas-phase aromatic species, soot particles, and aggregates;
3) solid carbon deposition mechanism based on previous research [2], involving a variety of surface species and reactions to describe the reactivity of armchair and zigzag sites on a graphite substrate;

These mechanisms collectively comprise a total of 244 species and 9493 reactions, encompassing various physical and chemical processes such as inception, growth, dehydrogenation, particle coalescence, and aggregation to model the evolution of soot. Results of quantitative measurements of CH_4 conversion obtained from mass spectrometry data and the identification of key aromatic precursors acquired by GC/MS are depicted in the figures (Fig. 1, 2). The empirical findings and simulated outcomes align closely within the margins of experimental uncertainties. Methane conversion diminishes under two conditions: firstly, as the initial flow rate rises while temperature remains constant, due to a reduction in the mean residence time; and secondly, as temperature decreases while the initial flow rate remains fixed. When the flow rate is constant, a temperature shift from 875 to 975 ◦C corresponds to a methane conversion increase of approximately 28–30%. The maximum conversion rate is achieved at the highest temperature and residence time, with methane conversion reaching around 35% at T = 975 ◦C.

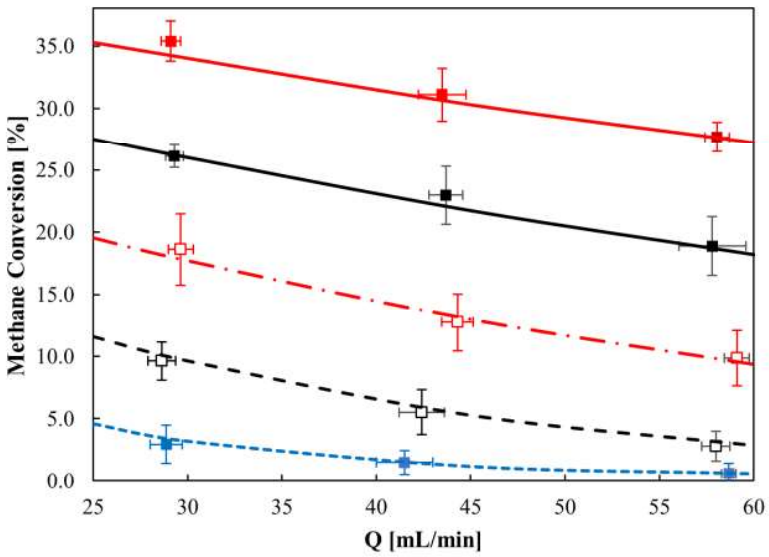

Figure 1. Methane conversion as a function of initial flow rates (25 – 60 ml/min) at different temperatures: 875 (blue), 900 (dashed black), 925 (dash-dotted red), 950 (black) and 975 °C (red). Symbols – experimental data; lines – model results.

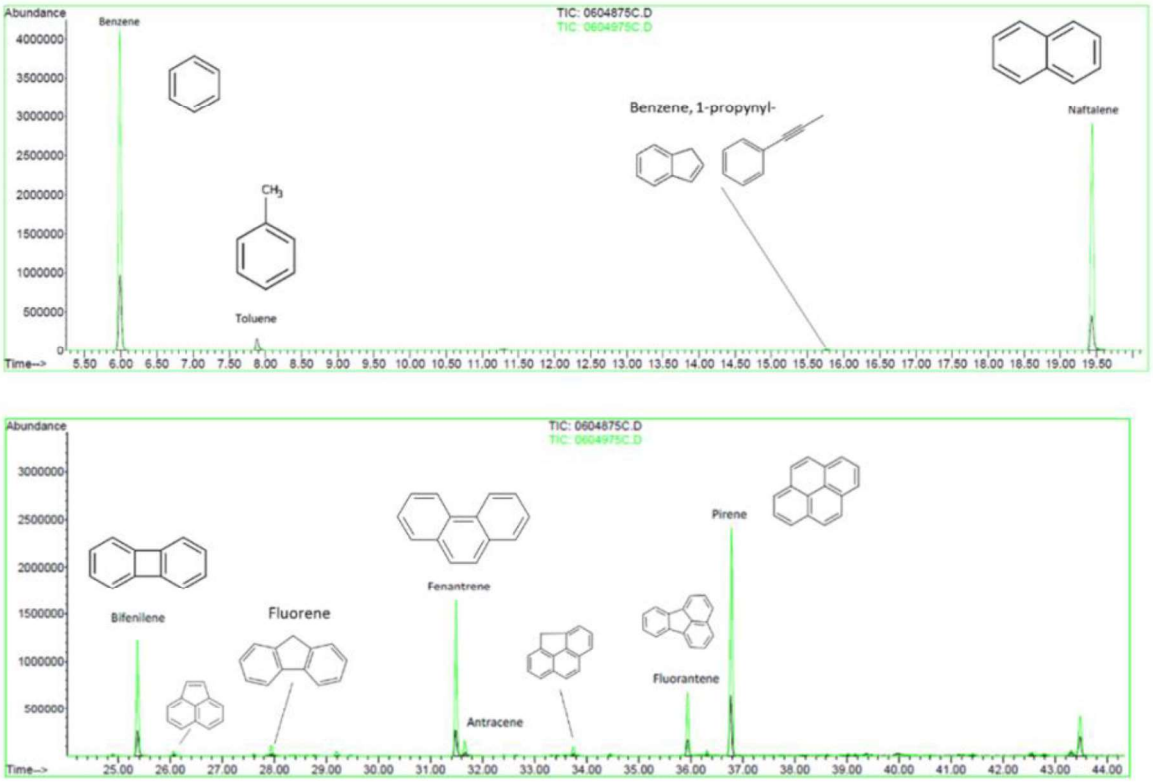

Figure 2. Chromatograms obtained from the injection into the GC/MS of gas samples taken from the top of the reactor.

The analysis of reaction intermediates revealed benzene, toluene, and PAHs such as naphthalene, phenanthrene/anthracene and pyrene. Benzene derivatives, biphenylene and fluoranthene have also been detected. Detailed analysis and characterization of the carbon products allowed for the exploration of the different morphologies for deposited carbon at reactor walls (Fig. 3 a, c) and carbon nanoparticles found in the gas phase (Fig. 3 b, d). The latter consist in fractal-like particles with dimensions of approximately 200–300 nm. On the other hand, deposited carbon is characterized by a carbonaceous matrix with interconnected hemispheres reaching sizes of up to 10 μm. Stacked dense carbon layers contribute to a thickness of 9–10 μm. The observed microstructures could be influenced by the chemical species deposited and their sticking characteristics. The mode of deposition (autocatalytic sticking mode of C_2 versus random deposition mode of C_6) affects the growth dimensionality. The transition between different microtextured pyrocarbons is expected to be linked to a threshold concentration of heavy polyaromatic molecules, which influence surface coverage and growth orientation. Vertical expansion of islands is attributed to lower adhesion energy on the substrate compared to cohesive energy within the pyrocarbon. As a result, proper control of gas-phase reactions is essential for regulating island growth and achieving the desired form of carbon.

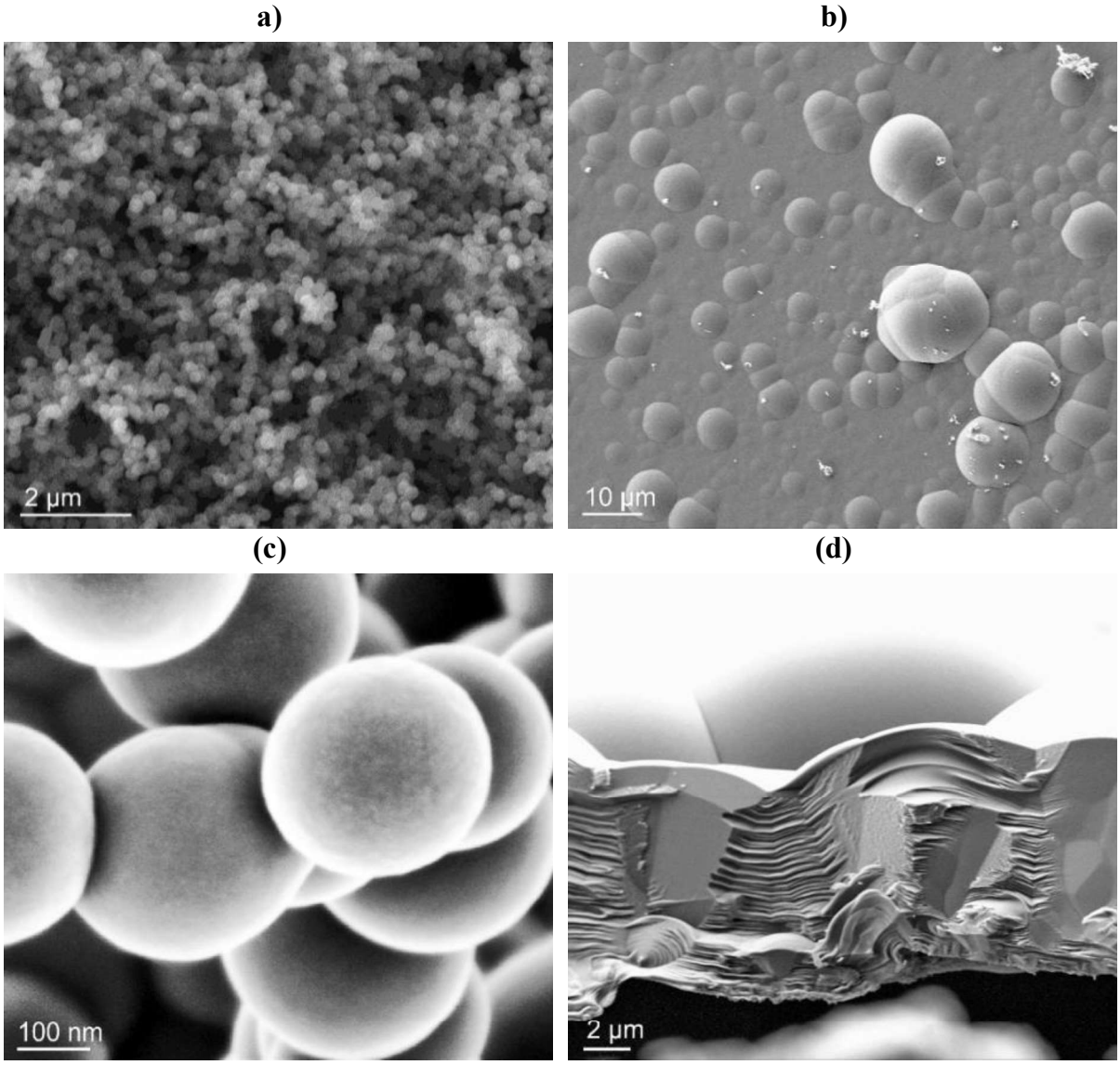

Figure 3. SEM images of the carbons collected: **a)** from the gas phase; **b)** from the reactor wall at T = 925 °C, Q_0 = 30 mL/min and t = 1.5h. **c)** and **d)** micrographs represent the magnification of particles collected from the gas flow and the cross section of the flake collected from the reactor wall, respectively.

At the experimental condition of this work micro filamentous carbon structures with semispherical tip and homogeneous diameter resembling catalyst-free vapor grown carbon fibers [5] and carbon micro-trees already reported in catalyst-free propylene [6] and in methane deposition [7] have been observed. An example for such structures is represented in Fig. 4, a. The scheme of the proposed mechanism for the formation of these peculiar carbon arrangements is depicted in Fig. 4, b. Filaments could have been formed from early carbon structures grown in the gas-phase owed to high residence time of the gas inside the heated zone and to the low S/V ratio of the experimental reactor, thus suggesting a complex interaction between

homogeneous processes and deposited carbon morphology.

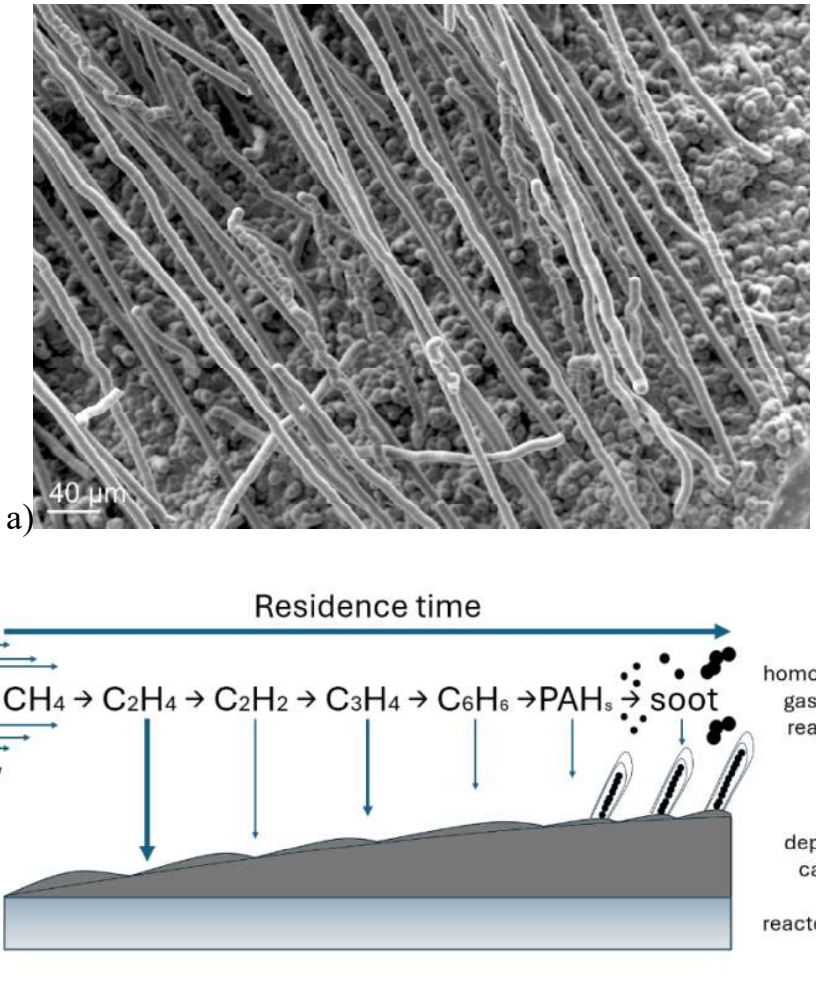

Figure 4. SEM Image of carbonaceous filaments produced at 925 °C after 3 h of reactor operation (a) and a scheme of the proposed mechanism for such filament formation (b)

In conclusion, this study delves into the experimental investigation of methane pyrolysis for carbon and hydrogen production, conducted within a tubular quartz flow reactor. By varying temperature and flow rates, the research elucidates the significant impact of these parameters on methane conversion rates. Through quantitative measurements and identification of key intermediates, such as aromatic and polyaromatic species, the study leveraged an existing kinetic model to interpret the observed results effectively. Moreover, the analysis of collected carbonaceous materials revealed distinct morphologies indicative of different formation mechanisms, heavily influenced by operating conditions and gas-phase composition. This nuanced understanding suggests a complex interplay between homogeneous and heterogeneous processes, further emphasized by the presence of carbon filaments with varying characteristics. Looking ahead, the study advocates for the extension of the kinetic model to encompass detailed pathways of aromatic species, polyaromatic hydrocarbons, carbon nanoparticles and surface deposition. Such

enhancements, coupled with systematic experimental characterization, hold the promise of providing stakeholders with advanced chemical kinetics and reactor modeling tools. These tools, in turn, are vital for driving the design of innovative technologies geared towards efficient hydrogen and valuable carbon materials production via hydrocarbon pyrolysis. Thus, this research paves the way for future advancements in the field, bridging the gap between fundamental understanding and practical applications.

References

[1] Cuoci, A., Frassoldati, A., Faravelli, T., Ranzi, E., "OpenSMOKE++: an object-oriented framework for the numerical modeling of reactive systems with detailed kinetic mechanisms", *Comput. Phys. Commun*. 192: 237–264 (2015)

[2] Serse, F., Ding, Z., M. Bracconi, M., Maestri, M., Nobili, A., Giudici, C., Frassoldati, A., Faravelli, T., Cuoci, A., Pelucchi, M., "A comprehensive kinetic framework for solid carbon deposition and hydrogen production from the pyrolysis of light hydrocarbons streams", *Carbon Trends*. 11: 100263 (2023)

[3] Frenklach, M., Wang, h., "Detailed surface and gas-phase chemical kinetics of diamond deposition", *Phys. Rev. B*. 43: 1520–1545 (1991)

[4] Lacroix, R., Fournet, R., Ziegler-Devin, I.P., Marquaire, P.M., "Kinetic modeling of surface reactions involved in CVI of pyrocarbon obtained by propane pyrolysis", *Carbon*. 48:132–144 (2010)

[5] Zou, J.Z., Zeng, X.R., Xiong, X.B., Tang, H.L., Li, L., Liu, Q., Li, Z.Q., "Preparation of vapor grown carbon fibers by microwave pyrolysis chemical vapor deposition", *Carbon*. 45: 828–832 (2007)

[6] Fan, Z., Tan R., He, K., Zhang, M., Peng, W., Huang, Q., "Low temperature growth of catalyst-free carbon micro-trees", *J. Mater. Sci*. 50:13–20 (2015)

[7] Ajayan, P.M., Nugent, J.M., Siegel, R.W., Wei, B., Kohler-Redlich, P., "Growth of carbon micro-trees", *Nature*. 404:243–243 (2000)

MONITORING CARBON CONTENT COMPOSITION OF NANOPARTICLES GENERATED IN A PREMIXED ETHYLENE AIR FLAME

F. Picca*, M. Commodo, P. Minutolo**, A. D'Anna***
francesca.picca@unina.it
* Dipartimento di Ingegneria Chimica, dei Materiali e della Produzione Industriale - Università degli Studi di Napoli Federico II, P.le Tecchio 80, 80125, Napoli, Italy
**Istituto di Scienze e Tecnologie per L'Energia e La Mobilità Sostenibili (STEMS)-CNR, 80125, Napoli, Italy

Abstract
The study investigates the composition and properties of carbonaceous nanoparticles formed in a premixed laminar ethylene-air flame. The work aims to understand the evolution of these particles within the flame, from nucleation to growth, regarding their structural composition particularly focusing on the fractions of organic carbon (OC) and elemental carbon (EC). Experimental analysis involves thermo-optical-transmission (TOT) measurements and Raman spectroscopy of particles collected at different residence times. Results reveal a prevalence of organic carbon at lower residence times, transitioning to elemental carbon at longer residence times. Raman spectroscopy confirms the presence of characteristic carbon bands and highlights variations in the fluorescence background, correlating with the dominance of organic carbon during nucleation and early particle growth. The study contributes to a deeper understanding of carbonaceous nanoparticle formation in flames and provides valuable insights into their composition and properties.

Introduction
The investigation into the formation of soot particles, categorized as carbonaceous nanoparticles, during high-temperature incomplete combustion of hydrocarbon fuels remains a central focus within the combustion research community. Studies on the properties of soot particles underscore their sensitivity to various combustion parameters [1–4]. Indeed, the flame conditions significantly influence the size and composition of the particles, which undergo complex chemical and physical transformations during fuel-rich combustion. The evolution of soot particles within flames starts from nucleation to growth and maturation, resulting in a diverse array of structural and optical characteristics. Understanding the underlying chemistry and physics of this process is paramount for mitigating carbon particle emissions from combustion systems, given the significant concerns regarding their impact on human health, environmental quality, and climate change [5]. Concurrently, the production of carbonaceous particles has spurred interest in flame synthesis, an innovative

approach for generating nanomaterials, particularly of the carbon variety [6–8]. The diverse array of generated combustion materials holds immense potential for promising advancements that can improve our quality of life. To utilize this potential there is a pressing need for a deeper understanding of the mechanisms underlying their formation. Combustion processes yield a diverse array of carbonaceous compounds starting from gas-phase polycyclic aromatic hydrocarbons (PAHs), often serving as precursors to soot particles. These PAHs, once nucleated, undergo processes of coagulation, coalescence, and mass growth through heterogeneous solid-gas phase reactions. A formation of larger particles, whose size typically increases with residence time [2], happens. The composition and properties of these particles produced at different residence times may vary, particularly in terms of organic carbon (OC) and elemental carbon (EC) fractions [9–10]. These variations in composition give rise to a range of properties that are significant for diagnostic purposes. To address these challenges, evaluating the composition of soot particles in terms of EC and OC fractions is essential. Thermo-optical-transmission (TOT) analysis serves as a standard method for quantifying carbon concentration and distinguishing between OC and EC components. Additionally, there is a need for chemical characterization of the materials under study. Raman spectroscopy offers valuable insights into the chemical structural evolution of various nanoparticles in terms of their molecular composition and arrangement.
In this work, we have investigated carbon aerosols produced in various residence times in the flame by TOT measurements and Raman spectroscopy to characterize their structural composition and optical properties in correlation with their OC and EC content.

Experimental

In this study, an analysis of carbonaceous nanoparticles produced in a premixed laminar ethylene-air flame was conducted. The flame was stabilized on a water-cooled sintered steel McKenna burner with a diameter of 6 cm, where the cold gases reached the burner at a velocity of 9.8 cm/s. The chosen fluxes led to a flame characterized by a (C/O) atomic ratio of 0.67, ϕ=2.01. To collect the particles, a tubular dilution stainless-steel probe constituted by an orifice with diameter of 0.6 mm was employed, allowing for the extraction of carbonaceous particles from the flame centerline. The sampled flow was mixed immediately with a turbulent N_2 diluent flow, achieving a dilution ratio on the order of 1:350, and then directed to a filter holder containing a 47 mm pre-fired quartz filter. A representation of the experimental setup is depicted in Fig. 1a.
The premixed flame enabled the collection of combustion products at various distances from the burner surface, *Z*, corresponding to different residence times. Nanoparticles were collected from *Z*=6mm to *Z*=10 mm, with each filter undergoing a total sampling duration of 5 hours. Subsequently, the particles collected on the quartz filter underwent offline characterization through TOT and Raman measurements.

For TOT analysis, a rectangular filter piece (1.5 × 1 cm) from the central portion of the filter was utilized with a Lab OC-EC Aerosol Analyzer from Sunset Laboratory Inc., following the NIOSH870 method. During the analysis, the sample undergoes two phases: first, the sample is exposed to He gas while the temperature is ramped up, causing OC to evolve from the filter and then, in an oxidized environment, to CO_2 a flame ionization detector (FID). After the first cooling phase, a mixture of helium and oxygen is introduced, and the temperature is ramped up in steps again. Some fraction of OC pyrolyzes rather than evaporate generating a pyrolytic carbon (PC). The PC is supposed to have similar optical proprieties of EC, so it has to be considered to avoid overestimating EC. The carbon generated during this oxidizing phase is converted to CH_4 for quantification and is defined as EC. After a second cooling phase, CH_4 is injected for FID signal calibration. Since OC and EC show different behavior in the visible region of light, a laser (λ=670 nm) monitors filter transmittance through the filter to separate PC from EC by defining a "split point". Before the split point the measured signal is attributed to OC, after the split point is attributed to EC. The split point is numerically defined when laser transmittance equals the mean of the first 10 seconds of ambient temperature analysis.
Raman spectroscopy analysis was conducted using a Horiba XploRA Raman microscope system equipped with a 100× objective (NA 0.9, Olympus) and a frequency-doubled Nd: YAG laser (λ = 532 nm) as the laser source. To prevent structural changes in the sample due to thermal decomposition and ensure optimal resolution, laser beam power, exposure time, and other instrumental parameters were meticulously selected. Spectra were acquired with a laser beam power set at 10% of attenuation and an accumulation (exposure) time of five cycles, each lasting 30 seconds. Five randomly selected spots per sample were averaged to enhance statistical relevance, and all spectra were subsequently baseline-corrected and normalized to the maximum of the G peak at approximately 1600 cm^{-1}.

Results

Fig. 1a shows the outcomes of the filter sampling procedure. Next to the representation of the experimental setup, the images of five filters, coated with carbonaceous material, are presented. These filters are displayed sequentially, with increasing residence times, from bottom to top. A preliminary qualitative assessment reveals a progression in coloration from light brownish to darker brown, except for the visibly darker sample at *Z*=9 mm, which appears to diverge from this pattern.
In Fig. 1b the thermogram of the filter acquired at *Z*=7 mm is reported. In the first He phase the OC is determined. When the temperature increases again and with the oxidized ambient the PC is generated until the split point. After that, the carbon is defined as EC. The EC/TC and OC/TC ratio values gained from TOT analysis are reported in Table 1. The OC reported in table 1 has to be considered as OC_{TOT} =OC+PC. The data indicate a prevalence of organic carbon at lower residence times, particularly at Z=6 mm, where gas-phase molecular compounds dominate, and initial nucleation of molecules commences. With longer residence times, the organic

carbon content diminishes in favor of elemental carbon.

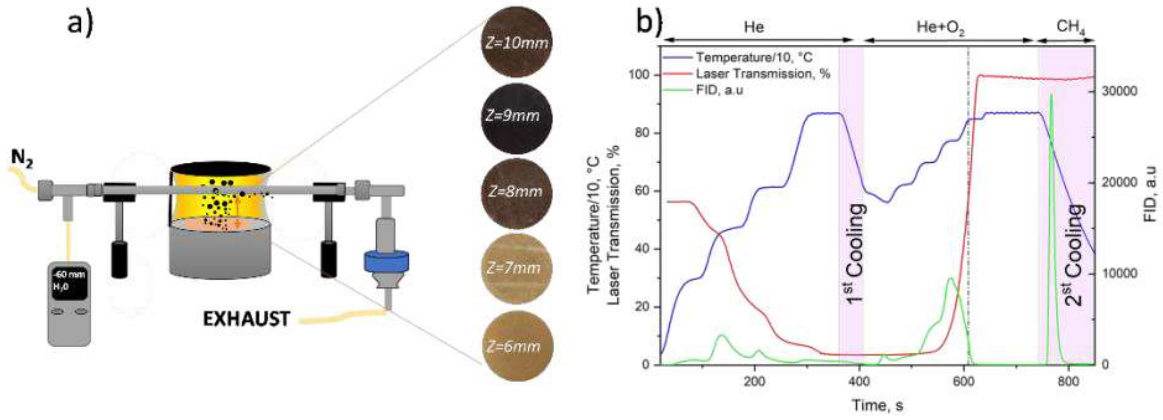

Figure 1 a)Experimental set-up on the left; filters acquired at different times on the right; b) Thermogram showing the ramp temperature program, blue line; measured laser transmission in red line; FID signal in green line. The vertical dashed line shows the split point which divides the EC from OC.

Table 1

Z, mm	EC/TC	OC/TC	m/I(G)	H/C
6	0.05±0.01	0.95±0.10	23.23 ±9.26	0.78±0.11
7	0.19±0.02	0.81±0.09	10.56±2.67	0.63±0.05
8	0.35±0.04	0.65±0.07	6.18±1.68	0.53±0.05
9	0.38±0.04	0.62±0.06	3.63±0.44	0.45±0.02
10	0.38±0.04	0.62±0.07	2.22±0.17	0.38±0.01

Fig. 2a displays the results of Raman spectroscopy. Each Raman spectrum exhibits the characteristic D and G bands typical of carbon compounds. It is noteworthy that the Raman spectra at lower residence times exhibit a split at the G-band, warranting further investigation. The fluorescence background contribution, reported in Table 1, is calculated from the Raman spectra and, consistent with the TOT findings, demonstrates a significant contribution at lower residence times, coinciding with the onset of nucleation, where organic carbon predominates. Indeed, as shown in Fig. 2b, an increasing trend in OC/TC as a function of photoluminescence is observed with a considerable difference between lower and higher residence time. In Table 1 also the Hydrogen to Carbon (H/C) ratio is reported. The H/C ratio, calculated from the m/I(G) and using Equation 1 [11], correlates with this trend, Fig. 2c. At lower residence time where is predominant the organic carbon fraction also the H furnishes its major contribution.

$$H[at.\%] = 21.7 + 16.6 * \log\left(\frac{m}{I(G)}\right) \quad (1)$$

As residence time increases, the particles approach a predominantly carbonaceous composition, with a gradual decrease in hydrogen and organic carbon contribution. The values derived from this investigation are in close agreement with the existing literature [12, 13].

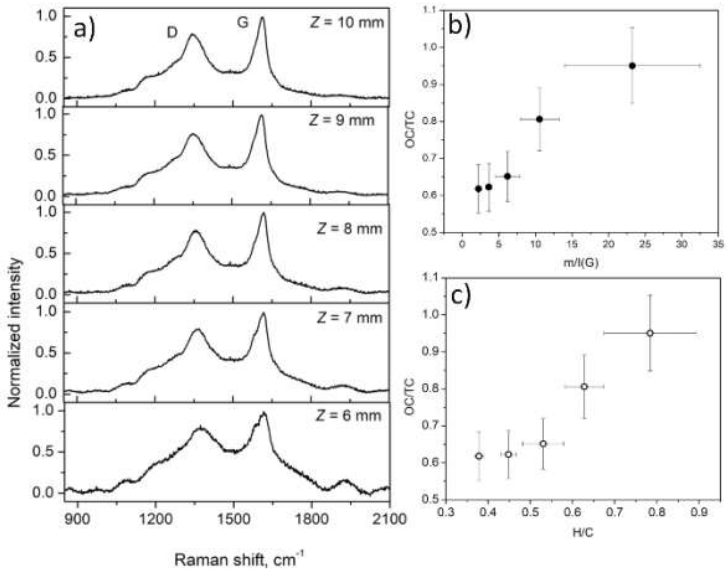

Figure 2 a) Raman spectra of all the 5 acquired filters; b) representation of OC/TC ratio as a function of m/I(G); c) representation of OC/TC ratio as a function of H/C.

Conclusions

The combined use of TOT analysis and Raman spectroscopy allows for describing the evolution of OC and EC fractions as a function of residence time within a lightly sooting laminar premixed ethylene/air flame. The results underscore the prevalence of organic carbon at the early stages of particle formation, transitioning to elemental carbon increasing at higher residence time. The joint of these two techniques reveals quite marked differences in chemical composition among the generated particles. Where the photoluminescence is higher, there is a great H contribution derived from mainly organic carbon. These conditions, rich in H, could be the ideal set in the nucleation step, through polymerization reaction by aromatic radical involvement. Conversely, at higher residence times, aligning with the formation of more coagulated, aggregated nanoparticles, the variation in organic carbon content, H percentage, and photoluminescence signals appear well correlated to each other. Nevertheless, the relative intensity of the two main Raman signals, the D and the G bands typically used to follow graphitization and/or the amorphization of carbonaceous materials, remains mostly unchanged in the examined conditions. The process of carbonization and dehydrogenation occurring during the early evolution of the nascent soot does not involve the planar growth of the aromatic constituents but probably mainly the formation of cross-links through the aromatic domains composing the particles. This, in turn, may be responsible for the change of optical, electronic, and other physical properties of the particles during their evolution in

flame often observed in the literature.

Acknowledgment This work was supported by PRIN – "Investigating atmospheric fate and Toxicological properties of Biofuels Emitted ultrafine particles with a SimulaTion chamber (IT-BEST)"

References

[1] Abid, A.D., Heinz, N., Tolmachoff, E.D., Phares, D.J., Campbell, C.S., Wang, H.: "On evolution of particle size distribution functions of incipient soot in premixed ethylene-oxygen-argon flames", *Combust Flame*. 154: 775-788 (2008).

[2] Commodo, M., De Falco, G., Bruno, A., Borriello, C., Minutolo, P., D'Anna, A.: "Physicochemical evolution of nascent soot particles in a laminar premixed flame: From nucleation to early growth", *Combust Flame.* 162: 3854–3863 (2015).

[3] Gu, C., Lin, H., Camacho, J., Lin, B., Shao, C., Li, R. et. al. "Particle size distribution of nascent soot in lightly and heavily sooting premixed ethylene flames", *Combust Flame.* 165: 177–187 (2016).

[4] Commodo, M., De Falco, G., Minutolo, P., D'Anna, A., "Structure and size of soot nanoparticles in laminar premixed flames at different equivalence ratios", *Fuel*. 216: 456–462 (2018).

[5] Bond, T.C., Doherty, S.J., Fahey, D.W., Forster, P.M., Berntsen, T., Deangelo, B.J., et al., "Bounding the role of black carbon in the climate system: A scientific assessment". *J. Geophys. Res.* 118: 5380–5552 (2013).

[6] Murayama, H., Tomonoh, S., Alford, J.M., Karpuk, M.E., "Fullerene production in tons and more: From science to industry" *Fuller.Nanotub. Carbon Nanostructures* 12:1-9 (2004).

[7] Memon, N.K., Tse, S.D., Al-Sharab, J.F., Yamaguchi, H., Goncalves, A.M.B., Kear, et al. "Flame synthesis of graphene films in open environments". *Carbon*. 49: 5064-5070 (2011).

[8] Liu, H., Ye, T., Mao, C., "Fluorescent carbon nanoparticles derived from candle soot" *Angew.Chem.Int.Ed.*.46:6473-6475 (2007).

[9] Minutolo, P., Gambi, G., D'Alessio, A., "The optical band gap model in the interpretation of the UV-visible absorption spectra of rich premixed flames". *Symposium (International) on Combustion*. 26: 951–957 (1996).

[10] Bocchicchio, S., Commodo, M., Sgro, L.A., Chiari, M., D'Anna, A., Minutolo, P., "Thermo-optical-transmission OC/EC and Raman spectroscopy analyses of flame-generated carbonaceous nanoparticles" *Fuel*. 310: 122308 (2022).

[11] Casiraghi, C., Piazza, F., Ferrari, A.C., Grambole, D., Robertson, J., "Bonding in hydrogenated diamond-like carbon by Raman spectroscopy", *Diam Relat Mater*. 14:1098-1102 (2005).

[12] Faccinetto, A., Irimiea, C., Minutolo, P., Commodo, M., D'Anna, A., Nuns, N., et al. "Evidence on the formation of dimers of polycyclic aromatic hydrocarbons in a laminar diffusion flame" *Commun Chem*. 3, (2020).

[13] Buijnsters, J.G., Gago, R., Jimńez, I., Camero, M., Agulló-Rueda, F., Gómez-Aleixandre, C, "Hydrogen quantification in hydrogenated amorphous carbon films by infrared, Raman, and x-ray absorption near edge spectroscopies" *J Appl Phys*. 105, 093510 (2009).

Exploring Flame-Formed Carbon Nanoparticle Thin Films for Sensing Applications

L. Basta*, P. Darvehi, G. De Falco**, M. Commodo**, A. Aloisio*, P. Minutolo**, and A. D'Anna*****

luca.basta@unina.it

* Dipartimento di Fisica Ettore Pancini, Università degli Studi di Napoli Federico II, Complesso Universitario di Monte S. Angelo, Edificio 6, Via Cinthia, 21, 80126, Napoli, Italy (L. Basta, A. Aloisio)

** Istituto di Scienze e Tecnologie per l'Energia e la Mobilità Sostenibili, Consiglio Nazionale delle Ricerche, P. le Tecchio 80, 80125, Napoli, Italy (P. Darvehi, G. De Falco, M. Commodo, P. Minutolo)

*** Dipartimento di Ingegneria Chimica, dei Materiali e della Produzione Industriale, Università degli Studi di Napoli Federico II, P.le Tecchio 80, 80125, Napoli, Italy (A. D'Anna)

Abstract

Carbon-based nanostructured materials offer exciting potential due to their unique properties. This research explores using flame synthesis as a simple and cost-effective method, to create carbon nanoparticles (CNPs) for sensor applications. Thermophoretic sampling then deposits CNPs as thin films, ideal for miniaturized sensors. By controlling flame and sampling conditions, CNP properties like size, structure, and composition can be tuned. These CNP films exhibit good electrical conductivity, biocompatibility, and sensitivity, making them promising candidates for gas and temperature sensors. The resulting films are conductive, lightweight, and biocompatible, making them ideal for sensor applications. This study demonstrates a one-step process for creating active components for rapid and sensitive temperature and gas sensors using flame-synthesized CNPs without further treatment, highlighting the potential of this approach for rapid and cost-effective sensor development.

Introduction

Carbon-based advanced materials exhibit remarkable versatility and have been revealed to hold great potential for functional applications due to their exceptional combination of good electrical conductivity, high chemical and thermal stability, ideal optical properties, and low toxicity. Indeed, their use in energy harvesting media, optoelectronic and sensing devices, and flexible active materials, among numerous other potential applications, have been recently gathering more and more interest [1]. This has fueled significant advances in the development of novel carbon-based nanomaterial synthesis routes.

In particular, thanks to the spontaneous formation of carbon nanoparticles (CNPs) in fuel-rich flames, these highly reactive environments have been exploited as a starting

point for production techniques of several carbon materials, such as fullerenes, carbon nanotubes, carbon black, graphene, and soot [2]. Among them, CNPs which are formed at the early growth stages (starting from the inception point) exhibit particularly interesting properties, even without pre- or post-deposition treatments, such as chemical surface functionalization or temperature treatment. In fact, at the beginning of the formation process CNPs are constituted of large polyaromatic molecules (PAHs) that can aggregate via physical van der Waal forces and chemical cross-linking [3,4]. Moreover, at higher flame residence time, through coagulation and surface reactions, particles can grow, and larger primary particles can be formed [5]. Hence, a fine tailoring of both the flame reactor and the flame synthesis parameters allows for the tunable production of CNPs that possess engineered properties, such as size, amorphous versus graphitic-like composition ratio, and electrical and optical characteristics [6,7].

Furthermore, in those practical applications that require thin film production, like the miniaturization of electronic devices or the development of battery electrodes, flame synthesis offers an effective bottom-up assembly method [8,9]. Indeed, nanostructured, self-assembled uniform thin films can be produced via thermophoretic sampling, which relies on the thermophoretic force that pushes flame-generated particles from the hot flame toward a cold substrate rapidly inserted into the flame [10]. The resulting deposition mechanism has been shown to present a ballistic-like nature and to produce a self-affine, fractal, and porous structure, made of voids and grains [6]. Notably, the properties of the generated film depend on the properties of the original precursor particles, together with the total deposition time [11]. Hence, there has been a lot of interest in using CNP thin films in sensing applications due to their capacity to conduct electricity, their biocompatible, very sensitive, flexible, and lightweight nature, as well as the ease of their production.

Here we report on the development of cost-effective temperature and gas sensors via a straightforward one-step process based on the synthesis of CNPs in flames and subsequent particle thermophoretic sampling, without the need for any further physico-chemical treatment. The response of the resulting sensing devices toward ambient temperature or ethanol vapor exposure is investigated, confirming the potential of the flame-synthesis procedure to produce effective active layers for rapid and sensitive sensors.

Experiment

A laminar premixed ethylene/air flame at atmospheric pressure stabilized on a water-cooled sintered bronze McKenna burner with a diameter of 6 cm is used for the production of the carbon nanomaterial in fuel-rich, sooting conditions. The flame equivalent ratio is $\phi = 2.32$ (carbon to oxygen atomic ratio of 0.77) and the cold gas velocity is $v = 9.8$ cm/s. The height above the burner (HAB), which in this system directly corresponds to the flame residence time, is set to 10 and 14 mm, in order to collect CNPs up to 25 nm of average diameter [12]. Thin-film Inter Digitated gold electrodes (from Micrux, ED_IDE1-Au) are utilized as substrates, with a channel

width-to-length ratio of W/L = 49000. The self-assembly of the CNP thin films is obtained by exploiting thermophoretic deposition via multiple quick insertions of 100 ms each (see Fig. 1a), for a total deposition time in the range of 1 to 5 s, depending on the number of insertions (from 10 to 50). A rapid insertion time is set in order to prevent excessive heating of the substrate which would cause a decrease in the thermophoretic force and, therefore, negatively affect the sampling efficiency. Atomic Force Microscopy (AFM) is performed to obtain the morphological characterization of the samples, using a Scanning Probe Microscope NTEGRA Prima (from NT-MDT), operating in a semi-contact mode with supersharp silicon probes (from NANOSENSORS, SSS-NCHR) with a tip radius of 2 nm (nominal). Structural properties are extracted with Raman spectroscopy measurements, performed with an Xplora Raman microscope (from Horiba), using a 532 nm laser beam of less than 1 mW optical power and a 100x objective lens with numerical aperture NA = 0.9. To obtain the electrical characterization the samples are put on a variable-temperature probe stage (from Linkam, HFS600E-PB4) with tungsten probes and electrical connectors mounted in a gas-tight chamber (see Fig. 1b). Current-voltage (*I-V*) curves are run using a Source Measuring Unit (from Ossila, SMU x200). A controlled atmosphere of variable ethanol concentrations is obtained with a controlled evaporator mixer (from Bronkhorst, CEM).

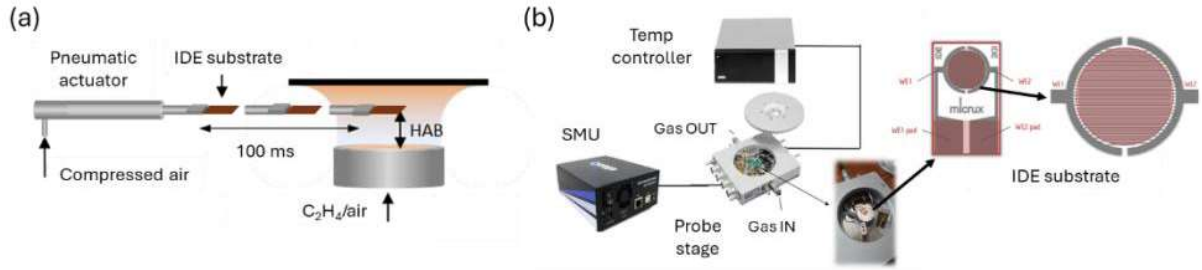

Figure 1. Scheme of the (a) thermophoretic sampling process and of the (b) electrical measuring and sensing setup (with a detailed zoom of the IDE substrate).

Results and Discussion

The surface morphology was visualized with semi-contact AFM (as shown in Fig. 2a). The collected CNP thin film exhibits a granular structure with higher and lower concentrations of grains, typical of thermophoresis-based and other ballistic-like deposition procedures. Underneath the CNP film, the electrode pattern is still recognizable, both in the AFM image and in the height profile taken across the electrodes (as shown in Fig. 2b). With different numbers of insertions and, therefore, different total insertion times, the amount of collected carbon material can be varied. Moreover, by collecting at different HAB values, particles of diverse sizes and varying electrical characteristics can be selected. Indeed, by changing the flame residence time, different regimes of the soot formation process can be explored, and particles from either the nucleation (at lower HAB) or the coagulation (at higher HAB) zones can be gathered. It has already been reported that CNPs of different sizes and levels of growth present different electronic bandgap values. The latter

decreases with the increasing of the particle size, coherently with both a quantum confinement size-dependent effect and a variation in the chemical composition [7,13]. This parameter tuning allows CNP films of variable thickness and electrical properties, and an optimal value can be reached. For thin-film-based electrical measuring techniques, for instance, it is usually advantageous to obtain active films possessing a high resistance. High resistivity films, in fact, allow a low current flow and, therefore, both a negligible self-heating effect and a lower electrical power consumption. This would be obtained with a low amount of material that still is enough for the creation of a continuous percolative network of semiconductive CNPs. On the other hand, when the collected carbon material increases, the complexity of the film surface increases as well, as can be derived from higher surface roughness and developed interfacial area ratio values measured with AFM in case of a higher quantity of collected CNPs. As a result, the active surface exposed to the ambient temperature or atmosphere composition increases as well, allowing for an improved sensitivity. Therefore, here, we collected CNPs at different HABs (with a similar number of insertions), opting for a lower HAB = 10 mm when avoiding self-heating was crucial and a higher HAB = 14 nm otherwise.

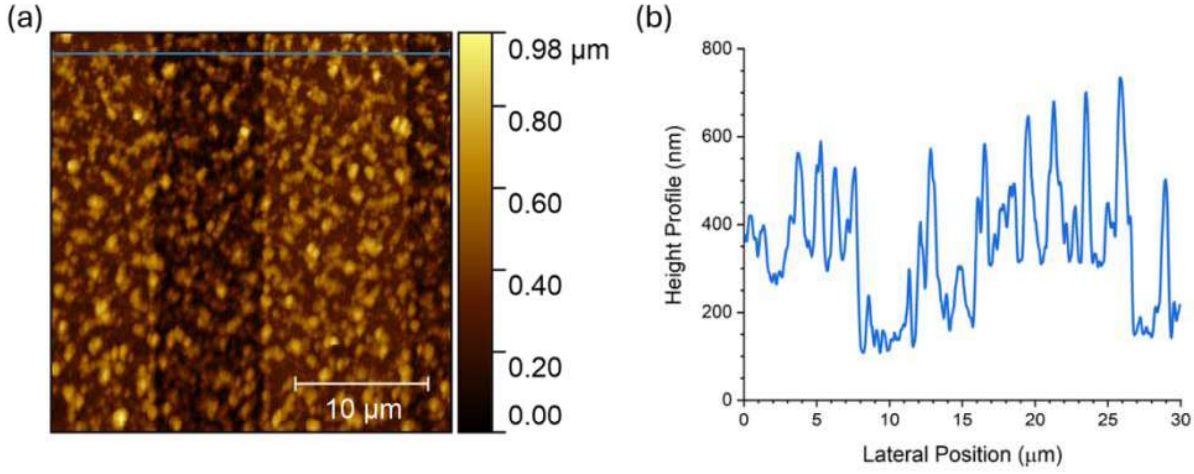

Figure 2. (a) AFM height image of an exemplary 30 × 30 µm^2 area on the sample with 20 insertions at HAB = 14 mm. The CNP self-assembled thin film covers the whole surface of the sample (both the higher gold contact areas and the lower glass gap regions). (b) Height profile collected along the blue line in panel (a), showing the height jump between the covered gold contacts and the covered glass gaps.

In our granular CNP thin films, the current flow is allowed via the tunneling of electrons between neighboring particles which form a continuous percolative network between the electrodes. This phenomenon can be enhanced by the thermal excitation of the electrical carriers. Indeed, increasing the temperature, the number of excited carriers increases, and, therefore, the current rises (as shown in Fig. 3a). This temperature-dependent current response can be exploited to develop a temperature sensor that possesses a high absolute temperature coefficient of resistance ($TCR \sim -100 \times 10^{-4}\ K^{-1}$, denoting a good sensitivity toward

temperature changes) and a reliable response calibration from room temperature (RT) up to 85 °C (with a calibration fit residual lower than 0.1 K) [14]. In contrast, if exposed to gas molecules with a polar nature, such as ethanol, their physical adsorption on CNPs can induce charge transfer and the freezing of electrical carriers. This results in an increase of the film resistance with the increase of the ethanol concentration in the atmosphere (as shown in Fig. 3b). Hence, a sensor for ethanol gas has been designed and tested for a gas concentration between 0 and 2.9%, obtaining fast response and recovery times (both shorter than 20 s) and great sensitivity (up to $0.22\ 1/(ethanol\ concentration\%)$) [15].

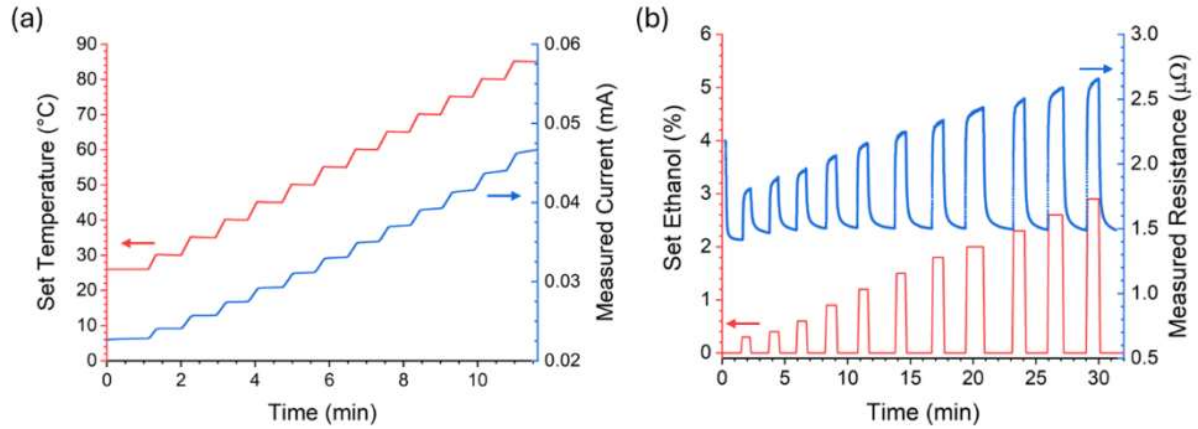

Figure 3. (a) Current response (shown as the blue curve) measured at 10 V on the sample with 40 insertions at HAB = 10 mm during a stepwise temperature increase from RT up to 85 °C (red curve). (b) Resistance response (shown as the blue curve) measured at 2 V on the sample with 50 insertions at HAB = 14 mm during the variation of ethanol concentration (red curve).

Conclusions

In this work, flame-based synthesis of carbon nanoparticles was demonstrated to be a feasible technique for the production of nanostructured thin films to be used as active layers in sensing electronic devices. The electrical response of the CNP thin-films to temperature and atmosphere gas composition was studied revealing good sensitivity and reliability. This, together with the ease and low cost of the material microfabrication process, and the non-toxicity and biocompatibility of carbon-based materials, makes these films ideal for sensing devices in several conditions. Moreover, the synthesis technique illustrated here allows the depositing of the film on a variety of substrates and with arbitrary design. That paves the way to embed temperature and gas sensors in a variety of commercial products where temperature analysis and ethanol gas detection are required.

References

[1] Li, Z., Wang, L., Li, Y., Feng, Y., Feng, W., "Carbon-based functional nanomaterials: Preparation, properties and applications", *Compos Sci Technol* 179:10–40 (2019).

[2] Camenzind, A., Caseri, W. R., Pratsinis, S. E., "Flame-made nanoparticles for nanocomposites", *Nano Today* 5:48–65 (2010).
[3] D'Anna, A., "Combustion-formed nanoparticles", *Proceedings of the Combustion Institute* 32 I:593–613 (2009).
[4] Schulz, F., Commodo, M., Kaiser, K., De Falco, G., Minutolo, P., Meyer, G., D'Anna, A., Gross, L., "Insights into incipient soot formation by atomic force microscopy", *Proceedings of the Combustion Institute* 37:885–892 (2019).
[5] Baldelli, A., Trivanovic, U., Sipkens, T. A., Rogak, S. N., "On determining soot maturity: A review of the role of microscopy- and spectroscopy-based techniques", *Chemosphere* 252:126532 (2020).
[6] De Falco, G., Commodo, M., Bonavolontà, C., Pepe, G. P., Minutolo, P., D'Anna, A., "Optical and electrical characterization of carbon nanoparticles produced in laminar premixed flames", *Combust Flame* 161:3201–3210 (2014).
[7] Veronesi, S., Commodo, M., Basta, L., De Falco, G., Minutolo, P., Kateris, N., Wang, H., D'Anna, A., Heun, S., "Morphology and electronic properties of incipient soot by scanning tunneling microscopy and spectroscopy", *Combust Flame* 243:111980 (2022).
[8] Kanakaraj, R., Sudakar, C., "Candle soot carbon nanoparticles as high-performance universal anode for M-ion (M = Li+, Na+ and K+) batteries", *J Power Sources* 458: 228064 (2020).
[9] Benelmekki, M., Erbe, A., *Frontiers of Nanoscience*. Elsevier Ltd, 2019, pp. 1–34.
[10] Dobbins, R. A., Megaridis, C. M., "Morphology of Flame-Generated Soot As Determined by Thermophoretic Sampling", *Langmuir* 3:254–259 (1987).
[11] De Falco, G., Commodo, M., Barra, M., Chiarella, F., D'Anna, A., Aloisio, A., Cassinese, A., Minutolo, P., "Electrical characterization of flame-soot nanoparticle thin films", *Synth Met* 229:89–99 (2017).
[12] Sgro, L. A., Basile, G., Barone, A. C., D'Anna, A., Minutolo, P., Borghese, A., D'Alessio, A., "Detection of combustion formed nanoparticles", *Chemosphere* 51:1079–1090 (2003).
[13] Liu, C., Singh, A. V., Saggese, C., Tang, Q., Chen, D., Wan, K., Vinciguerra, M., Commodo, M., De Falco, G., Minutolo, P., D'Anna, A., Wang, H., "Flame-formed carbon nanoparticles exhibit quantum dot behaviors", *Proc Natl Acad Sci U S A* 116:12692–12697 (2019).
[14] Minutolo, P., De Falco, G., Commodo, M., Aloisio, A., D'Anna, A., "Temperature Sensing with Thin Films of Flame-Formed Carbon Nanoparticles", *Applied Sciences (Switzerland)* 12:7714 (2022).
[15] Darvehi, P., Basta, L., Commodo, M., Minutolo, P., D'Anna, A., "Application of flame-formed carbon nanoparticle films for ethanol sensing", *Particuology* 91:202–210 (2024).


THE COMBUSTION INSTITUTE
1954

SESSION VII

Propulsion & Engines


THE COMBUSTION INSTITUTE
1954


THE COMBUSTION INSTITUTE
1954

SESSION VIII

Stationary Combustion Systems and Gas Turbines - Part 1


THE COMBUSTION INSTITUTE
1954

LES evaluation of PaSR and Extended FGM model on the DLR F400S.3 mGT burner

G. Generini*, A. Andreini*, T. Lingstädt, P. Kutne****
giulio.generini@unifi.it

*Heat Transfer and Combustion group - University of Florence
50139, Via S. Marta 3, Florence, Italy
**German Aerospace Center (DLR)
70569, Pfaffenwaldring 38-40, Stuttgart, Germany

Abstract
The paper approaches a computational evaluation of the DLR micro-Gas Turbine (mGT) burner F400S.3 describing the turbulent combustion through the partially stirred reactor (PaSR) and the Extended Flamelet Generated Manifold (FGM) combustion models. High-fidelity Large Eddy Simulations (LES) were conducted performing a sensitivity analysis on the burner walls' thermal boundary conditions and the combustion model used, comparing the numerical results with the experimental OH*-chemiluminescence distribution. The results showed good agreement regarding the flame shape and reactivity prediction when non-adiabatic thermal boundary conditions were applied at the burner walls and the PaSR model was implemented. On the contrary, the FGM model exhibited underprediction in flame length and reactivity.

Introduction
The utilization of energy carriers, such as hydrogen (H_2), has become increasingly significant in facilitating reliable and demand-centered power and heat supply despite the lack of large-scale infrastructure for hydrogen transport. In this regard, Decentralized Combined Heat and Power (CHP) systems became relevant as they provide high overall efficiency and require only a limited amount of H_2, which can be produced locally [1]. micro-Gas Turbines (mGT) have become the preferred choice for these systems: their low maintenance, high load capability and fuel flexibility have made them an interesting option for CHP generation [2]. However, while the properties of mGTs are well-suited for traditional fuels like natural gas and synthesis gases, the H_2 combustion characteristics present unique challenges that must be carefully evaluated. Therefore, technical challenges need to be addressed to ensure safe and reliable operation. Many studies regarding hydrogen fuelling in mGTs are available in the literature. Calabria et al. [3] were able to experimentally reach 15% H_2 on the AE-T100 Ansaldo Green Tech mGT, underlining the necessity for a burner geometrical redesign to reduce the risk of combustion anomalies onset for higher %H_2. Cappelletti et al. [4] proceeded with a numerical re-design of the burner reaching 100% H_2 computationally while avoiding flashback and self-

ignition. Devriese et al. [5] evaluated, on a different burner, how the fuel nozzle geometry and flame stabilization method influences NO_x emissions. Similarly, Hohloch et al. [6] emphasized how flame stabilization influences the risk of self-ignition and flashback in the mixing zone and how, for H2 fuelled mGT burners, jet-stabilized combustion systems should be preferred over swirl-stabilized ones.
This work aims to investigate the German Aerospace Center (DLR) mGT burner F400S.3 numerically, focusing on a sensibility analysis on the burner walls thermal boundary conditions and combustion model. Initially, a Reynolds-Averaged Navier Stokes Conjugate Heat Transfer (RANS CHT) analysis of the burner was conducted to compute the combustor wall temperature distributions, which were then used as boundary conditions for Large Eddy Simulations (LES). Then, the PaSR and Extended FGM (introducing Stretch and Heat Loss and Gain effects on the flame) combustion models were evaluated on the burner by comparing the CFD results with the experimental OH*-Chemiluminescence data. The PaSR model shows good agreement with the experimental results when non-adiabatic thermal boundary conditions were set at the burner walls. On the contrary, the Extended FGM model underestimates the flame length and lift-off.

Combustion Modelling

Two different turbulent combustion models were implemented within the domain of interest: the Extended Flamelet Generated Manifolds (FGM) and the Partially Stirred Reactor (PaSR) models.
The Extended FGM model [7] is an enhanced version of the traditional FGM approach, including the stretch and heat loss and gain effects on the flame. To achieve this, a correction to the progress variable source term $\dot{\omega}_c$ is performed by multiplying the standard Finite Rate (FR) turbulent source term by a correction factor $\Gamma(\kappa, \psi, Z)$. Γ is tabulated, in a pre-processing step, as a function of the flame stretch κ, the heat loss and gain parameter ψ and the mixture fraction Z. For the sake of brevity, further information regarding the formulation of the Extended FGM model, is provided in [8] for the RANS framework and in [7] for LES. In this regard, additional details concerning κ and ψ formulations can be found in [9].
The Partially Stirred Reactor (PaSR) model [10] is a finite rate chemistry model based on the assumption that the combustion takes place in reactive structures, referred to as "fine scales", which occupy part of the computational cell volume. The PaSR model is generally used for cases where the high dilution levels and the intense mixing between reactants and combustion products lead to a distributed reaction mechanism, resulting in high Reynolds and moderate Damköhler numbers. Additional information regarding the model could be found in [11] and [12], respectively for the RANS and LES frameworks.

Geometry and Numerical Set-up

The DLR F400S.3 burner, shown in Fig. 1, is a reverse-flow jet-stabilized hydrogen-fuelled atmospheric combustor [6]. Air enters the combustor in counter-current with

respect to the flue gases flowing between the inner and outer flame tubes. The fuel is divided between two different lines: the pilot line, characterized by a diffusive flame, is used for ignition and a further stabilization of the main line partially premixed flame, properly a jet-stabilized flame. The jet-stabilized combustion system creates a high turbulence level recirculation region, promoting the mixing between the fresh fuel-air mixture and the flue gases before combustion while stabilizing the flame. This is beneficial for hydrogen combustion as it reduces the extension of low-velocity regions and avoid combustion instabilities typical for this fuel.

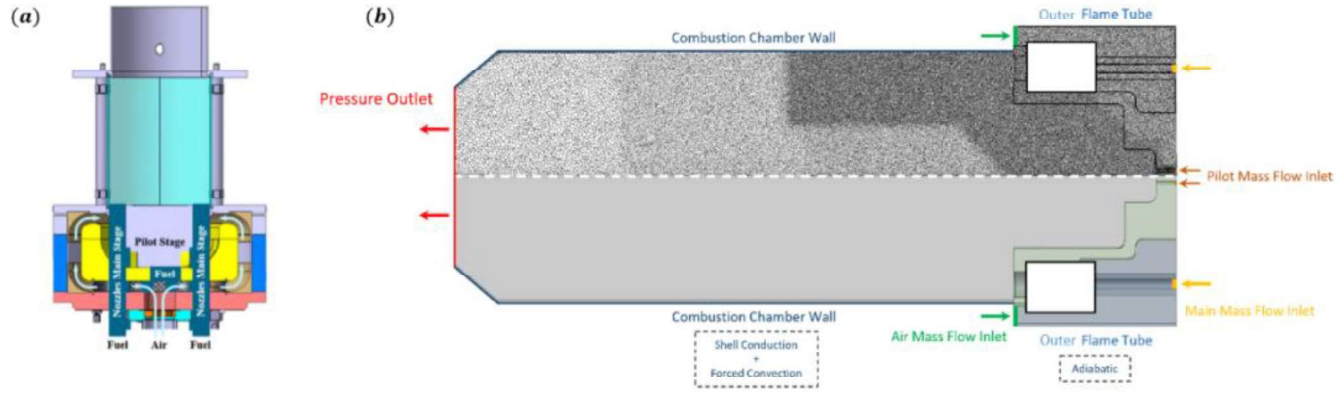

Figure. 1 (a) Experimental Test Case [9]; (b) Computational domain and spatial grid

The Navier-Stokes equations were solved with the pressure-based code ANSYS Fluent 2023 R2, on a 72° sector of the complete burner domain, taking into account the burner periodicity. Initially, to obtain the walls temperature distributions to set as boundary conditions for the LES, a RANS CHT analysis was run on the burner. Here, the combustion chamber wall was simulated as a shell conduction wall, applying the quartz material properties implemented as temperature-dependent polynomials. To take into account the external air flow field cooling effect on the quartz wall, determined by an outlet fan used to promote the flue gas suction, forced convection was modelled. The CHT computational grid, shown in Fig. 1, is composed of approximately 1.4e7 polyhedral cells, obtained by processing an initial hybrid mesh of 24e6 tetrahedral cells with 5 layers of prism adjacent to solid walls. The mesh for the LES CFD analyses was obtained through a similar procedure, neglecting the solid domain in its creation: a polyhedral mesh of about 1.1e7 cells was computed. The chemical reaction mechanism DC1S09, comprising 9 species and 23 reactions, developed by DLR, was used in both the Extended FGM model, for solving of mono-dimensional laminar premixed flamelets and the PaSR model for species transport. For the RANS CHT analysis, the k-ε Realizable with Enhanced Wall Treatment and the COUPLED pressure-velocity coupling scheme were employed, concurrently solving the turbulent combustion using the PaSR combustion model. In the LES context, the effect of unresolved eddies is modelled using the Dynamic Smagorinsky-Lilly formulation which dynamically evaluates the Smagorinsky constant. Turbulent

combustion was analysed with both the Extended FGM and PaSR combustion models. Additionally, the SIMPLEC algorithm was adopted for the pressure-velocity coupling with a constant time step of 1e-6 s to ensure a convective Courant number below 5 in the zones of interest. Second-order schemes are used in both space and time using an implicit formulation for this last one. Finally, identical boundary conditions, as shown in Fig. 1, were set for all cases.

Results and Discussion

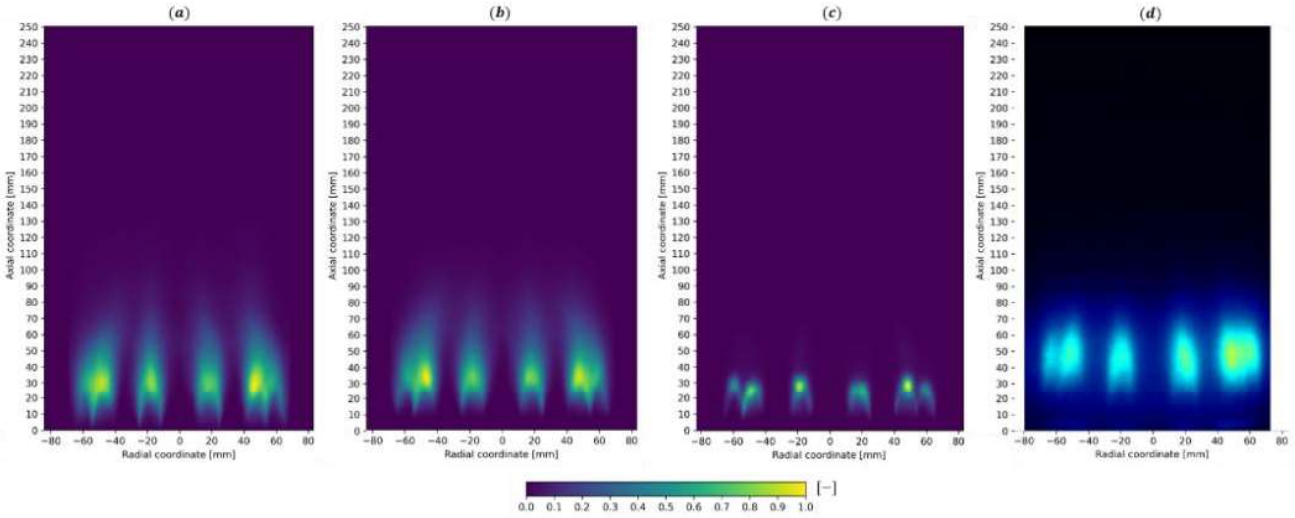

Figure 2 CFD calculated LOS integrated equivalent with (a) PaSR Model with adiabatic walls, (b) PaSR Model with RANS CHT wall temperature distributions, (c) Extended FGM with RANS CHT wall temperature distributions and Experimental OH*-Chemiluminescence (d)

OH*-Chemiluminescence data from experiments (see [6] for further information) were compared with the numerical results by integrating the mean normalized Heat Release Rate (HRR) along the line of sight (LOS) axis to generate the equivalents for comparison with the measured data (Fig. 2). Due to the experimental set-up, the comparison of results is performed only evaluating the partially-premixed main flame.

As mentioned earlier, a RANS CHT analysis was first performed to compute the wall temperature distributions to set as boundary conditions for the LES calculations. Keeping the turbulent combustion model constant (PaSR model) (Fig. 2a and 2b), the thermal boundary conditions introduce flame heat loss, which increases flame lift-off while keeping the flame topology nearly unchanged (Fig. 2b). Despite the improved results obtained by setting non-adiabatic thermal wall boundary conditions, a similar computational setting in the Extended FGM model does not yield comparable results (Fig. 2c). This is mainly due to the fact that the model underestimates the effect of products recirculation on the premixed flame. The model's chemistry tabulation is performed without taking into account the effect of a different oxidant composition determined by the turbulent flow field, which

directly brings the pilot and the main flame products onto the premixed flame itself. This is confirmed in Fig. 3a, which provides the laminar flame speed as a function of the mixture fraction for both H2-Air and H2-vitiated-air mixtures at the domain temperature and pressure boundary conditions, computed through the Unity-Lewis and Multicomponent (non-Unity Lewis) transport model. The vitiated-air composition was obtained by computing the species mass fraction on a constant radius surface (shown in Fig. 3b) vertically slicing the combustion chamber, wisely close to where the premixed flame stabilizes, to take into account the influence of both the pilot and main flame products recirculation on the same premixed flame. The normalized mean Heat Release Rate (HRR) distribution on a plane slicing the domain where the premixed flame stabilizes is also shown in Fig. 3b, overlapped with normalized mean radial velocity vectors to better visualize the extension of the recirculation region and thus the path followed by the combustion products.

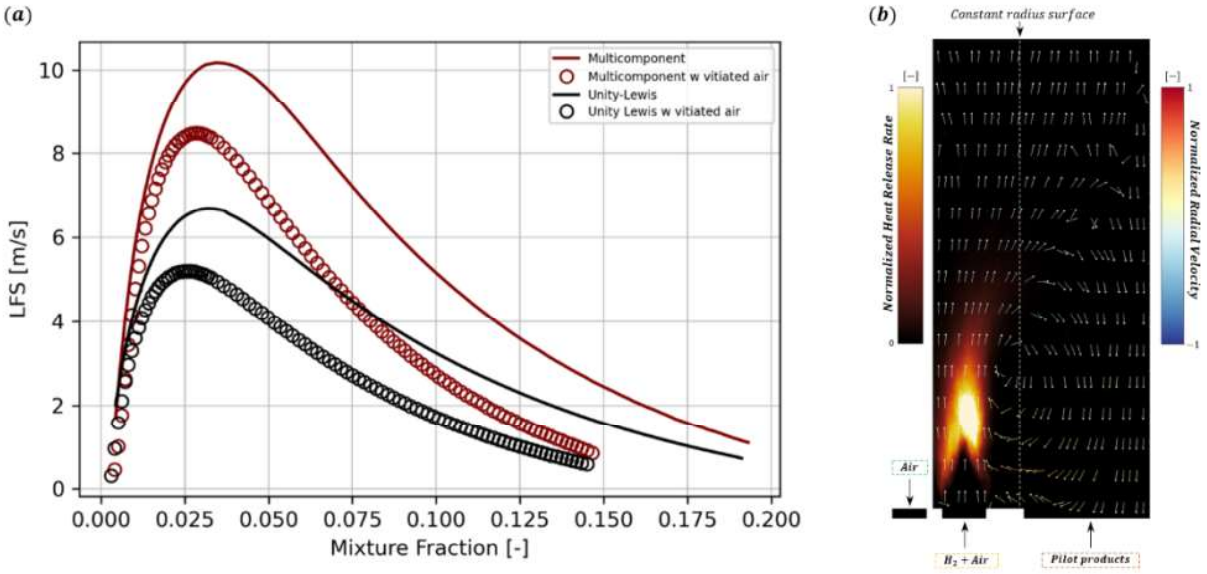

Figure 3 (a) Laminar flame speed as a function of mixture fraction; (b) Normalized mean Heat Release Rate (HRR) distribution overlapped with mean radial velocity vectors.

Conclusions

In this study, the F400S.3 DLR mGT burner was numerically described using Large Eddy Simulations (LES). A sensitivity analysis was performed on the wall thermal boundary conditions and the turbulent combustion model by comparing the Computational Fluid Dynamics (CFD) results with experimental OH*-Chemiluminescence data. Introducing wall temperature distributions obtained from a RANS CHT analysis as thermal boundary conditions for the combustion walls and evaluating turbulent combustion using the PaSR model, the flame characteristics and topology were well captured. The PaSR model is not affected by the limitations of the Extended FGM model, such as its neglect of the recirculation effect of the combustion products on the chemistry tabulation. In this regards, the PaSR model appears to be able to describe adequately the flame

characteristics.

References

[1] Maghanki, M. M., Ghobadian, B., Najafi, G., Galogah, R. J., "Micro combined heat and power (MCHP) technologies and applications", *Renewable and Sustainable Energy Reviews*. 28:510-524 (2013)

[2] Banihabib, R., Assadi, M. A., "Hydrogen-Fueled Micro Gas Turbine Unit for Carbon-Free Heat and Power Generation", *Sustainability*.

[3] Calabria, R., Chiariello, F., Massoli, P., Reale, F., "CFD Analysis of Turbec T100 Combustor at Part Load by Varying Fuels", *Proceedings of the ASME Turbo Expo 2015*, Montreal, Quebec, Canada.

[4] Cappelletti, A., Martelli, F., Bianchi, E., Trifoni, E., "Numerical Redesign of 100kw MGT Combustor for 100% H2 fueling", *Energy Procedia*. 45:1412-1421 (2014)

[5] Devriese, C., Penninx, G., de Ruiter, G., Bastiaans, R., De Paepe, W., "The CFD Design and Optimisation of a 100 kW Hydrogen Fuelled mGT", *Proceedings of the ASME Turbo Expo 2020*, Virtual, Online.

[6] Hohloch, M., Lingstädt, T., Kutne, P., "Experimental Analysis of the Hydrogen Capability of a Fuel Flexible Jet Stabilized Syngas Micro Gas Turbine Combustor Under Atmospheric Conditions". *Proceedings of the ASME Turbo Expo* 2023, Boston, USA.

[7] Langone, L., Sedlmaier, J., Nassini, P.C., Mazzei, L., Harth, S., Andreini, A., "Numerical Modeling of Gaseous Partially Premixed Low-Swirl Lifted Flame at Elevated Pressure", *Proceedings of the ASME Turbo Expo* 2020, Virtual, Online.

[8] Klarmann, N., Sattelmayer, T., Geng, W., and Magni, F., "Flamelet Generated Manifolds for Partially Premixed, Highly Stretched and Non-Adiabatic Combustion in Gas Turbines", *54th AIAA Aerospace Sciences Meeting*, San Diego, California, USA.

[9] Generini, G., Andreini, A., Bianchi, E., "Combustion Modelling of the T100 Micro-Gas Turbine burner including the influence of the stretch and heat loss/gain effects on the flame", *Proceeding of the ASME Turbo Expo 2024*, London, England.

[10] Chomiak, J., *Combustion: A Study in Theory, Fact and Application,* Abacus Press/Gorden and Breach Science Publisher, New York, 1990.

[11] Ferrarotti, M., Li, Z., Parente, A., "On the role of mixing models in the simulation of MILD combustion using finite-rate chemistry combustion models", *Proceedings of the Combustion Institute*, 37(4):4531-4538 (2019).

[12] Li, Z., Cuoci, A., Parente, A., "Large Eddy Simulation of MILD combustion using finite rate chemistry: Effect of combustion sub-grid closure", *Proceedings of the Combustion Institute*, 37(4): 4519-4529 (2019).

The impact of HEFA on Emissions and Performances of a Micro Gas Turbine Using Combustion Vibrations Detection

C. Allouis, A. Amoresano*, G. Langella*, G. Quaremba***
Corresponding author: G. Langella - giuseppe.langella@unina.it
* Dipartimento di Ingegneria Industriale – Università degli Studi di Napoli Federico II, via Claudio 21, 80125, Naples, Italy.
** Istituto di Scienze e Tecnologie per l'Energia e la Mobilità Sostenibile - CNR, via G. Marconi 7, 81025, Naples, Italy.

Abstract
The paper reports a quantitative comparative assessment of particulate matter emissions from a Micro Gas Turbine (MGT) for power generation, providing electrical power up to 30kWe powered by conventional aviation kerosene and its blend with Sustainable Aviation Fuel (SAF). The analysis was based on emission concentrations and particle size distributions. Different liquid fuels, including commercial JP8, blends of JP8 with HEFA, were tested under fixed load. Primarily attention has been focused on the measures of the micro vibrational distributions and their correlation with gas turbine emission and performances, by a chaos theory approach.

Introduction
The field of researching and testing new Sustainable Aviation Fuels (SAF) for air transport is becoming a rising challenge. This is confirmed by the recently European Parliament in 2023 [1], where The *RefuelEU* aviation rules are part of the "Fit for 55 package", the EU's plan to reduce greenhouse gas emissions by at least 55% by 2030 compared to 1990 levels and to ensure the EU becomes climate neutral by 2050. They seek to encourage the aviation sector to use sustainable aviation fuels in order to cut emissions. Previous research program were undergone using HEFA ("Hydrotreated Esters and Fatty Acids"), e.g. ITAKA—Initiative Towards Sustainable Kerosene for Aviation [2], BFSJ—Production of a fully synthetic jet fuel from timber and other biomass, BIOREFLY—Industrial scale demonstration biorefinery on lignin-based aviation fuel [3]. The aim of these projects was to promote the use of alternative jet fuels derived from non-conventional sources. Environmental and Health effects of emissions from aircraft engine reviews present a negative effect on climate change and air pollution [4-6]. In the literature, the positive impact of Sustainable Air Fuels on the carbon footprint has been confirmed. The positive impact of SAF on air quality, particularly in airport areas and their vicinity, should be considered separately [7-9]. Currently, one of the major issues of air pollution is particulate matter. Scientific studies indicate that airport areas are contaminated with nanoparticles [10]. In the context of aviation, these particles can result from the combustion of jet fuels and are associated with adverse respiratory

effects and environmental damage. SAF's cleaner combustion profile, attributed to its renewable feedstocks and advanced production processes, leads to a notable reduction in particulate matter emissions compared to conventional aviation fuels. This positive environmental impact aligns with global efforts to enhance air quality and mitigate the adverse health effects associated with particulate matter exposure [11]. The objective of the research presented in this article was to conduct a quantitative comparative assessment of particulate matter emissions from a MGT for power generation, providing electrical power up to 30kWe powered by conventional aviation kerosene and its blend with SAF. The analysis was based on emission concentrations and particle size distributions. Different liquid fuels, including commercial JP8, blends of JP8 with HEFA, were tested under fixed load. Primarily attention has been focused on the measures of the micro vibrational distributions and their correlation with gas turbine fueling.

Experimental set-up

The Micro Turbine Capstone C30 is a turbine of last generation system with a maximum power output of 30kWe with 26% electrical efficiency and up to 90% combined heat power efficiency. It is widely used in the aeronautical field; in particular, as energy provider for the aircrafts on parking. It can be also operated with different liquid fuels. The fuel supply system is composed of three nozzles (one main and two auxiliaries). In this paper, JP8 as fuel and its blend with HEFA at 20%v/v, at 40%v/v, at 60%v/v, 80%v/v and 100%v/v were used. The choice of HEFA is to verify an eventual difference between fuels in terms of machine performance. The Micro Gat Turbine (MGT) rotation was set at 85000rpm close to its maximum speed (i.e., 90000rpm) for all the fuels. All parameters of the turbine (i.e., rotational speed of the turbine, power output, exhaust gas temperature, etc.) were continuously acquired every two seconds by means of a PC and analyzed at the end of test. The vibrational signals were acquired by means of two unidirectional micro accelerometers, model PCB 352 C22. The acquired data through the accelerometers have been synchronized with each other and were stored in the computer. Synchronization here means that the accelerometer signals were acquired in parallel and aligned on a time basis through a LMS SCADAS data acquisition system. Hence, no electromechanical synchronization system was used for each accelerometer signal (e.g., tachometer signal). Front and side views of the turbine and the location of the accelerometers are shown in fig.1 (left and right respectively). Exhaust gas emissions (O2, CO, CO2) were recorded with continuous gas analyzer Hartmann&Braun, while the real-time particulate distribution functions in the range 7 nm-10 μm) were acquired using an electro-impactor ELPI™.

Methods

The proposed method for distinguishing regular from chaotic dynamics is successful if the noise-level is sufficiently small but also because the balanced dynamics of turbine are essentially stationary and deterministic. Many methods desensitize the

test performed on noisy signals but damps the ability to detect slow growth of the features as well as the signature for time series data of moderate length. For such a reason each accelerometric signal was sampled at 102 400 Hz for 10s, for a total of 1 025 024 sampled points. The calculations were performed by using the MATLAB® software. The nonlinear method introduced in this work consists primarily in the decomposition of the accelerometric signal into two mutually orthogonal components [12] for projecting them on a plane other than phase space. More detailed about the method are given in ref [13].

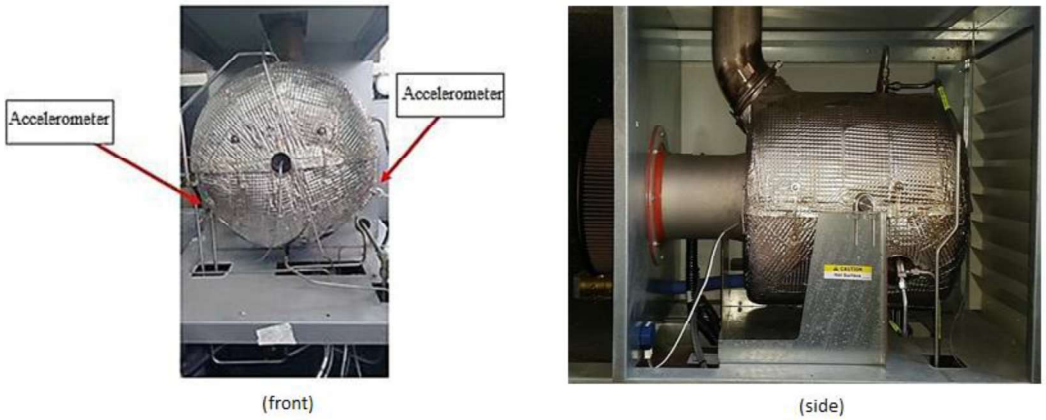

Figure 1 - Turbine with location of accelerometers: front and side view

Results and Discussions

The addition of the biokerosene HEFA in the JP8 did not present any macro-mechanical problem concerning the normal MGT working conditions. For each blend change, we waited for the MGT to thermally and electrically (load) stabilize. The data were acquired after ~30 minutes after the change. Each blend was repeated three times. The presented data represent the average of the measurements. For room reason, not all the results will be presented. From the stable gases emission values presented in Table 1 for the main fuels, we can observe than the addition of HEFA enhances a light decrease of the carbon monoxide and particulate matter, while the nitrogen oxides are stables. This tendency has also been found by Gawron and Bialecki [7] using different turbine rpm modes.

Table 1: Emission values@26kWe

	O_2	**NO_X**	**CO**	**Particulate**
	%	ppm (mg/Nm^3)@15%O_2	ppm (mg/Nm^3)@15%O_2	mg/Nm^3
JP8	18,3	11 (23)	10 (12)	0,23
JP8 – 20%vol. HEFA	18,3	10 (22)	9 (11)	0,22
100%vol. HEFA	18,4	10 (22)	8 (10)	0,20

The time-averaged particle distribution functions are presented in Figure 2 for the different fuels. Dimensions higher than 10 microns were blocked though a cyclone filter in order to focus on small particles. Once again, it is worth to note the positive effect on HEFA addition in JP8. The particle concentration decreased by two orders of magnitude while passing from JP8 to HEFA. The reduction is more evident for particle with diameter higher than 200 nm. Moreover, the bimodal tendency of the JP8 plot tends to disappear while increasing the HEFA concentration in the fuel blend. The positive tendency from HEFA addition has also been found by Jasinski and Przysowa for particle dimension lower than 200 nm [14]. The absence of aromatic compounds could be the main reason of this phenomenon and further kinetics analysis will be performed to assess this assumption.

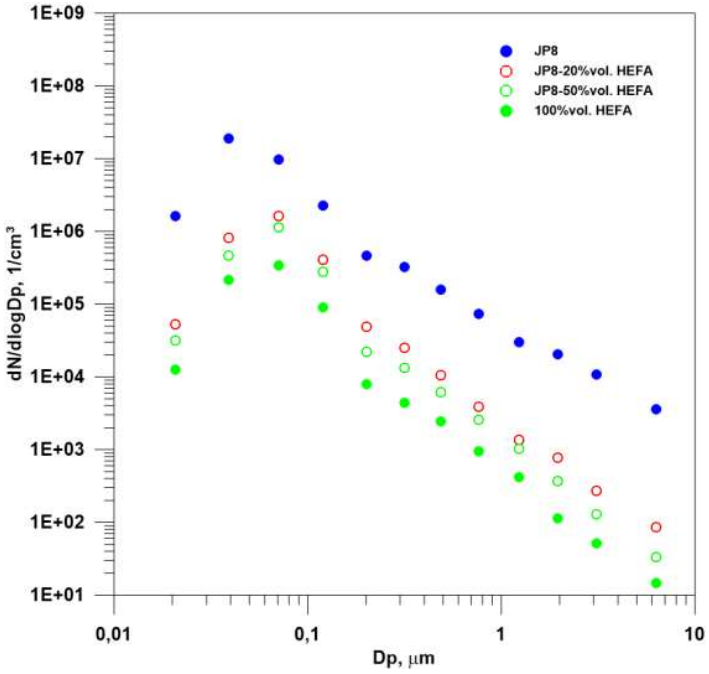

Figure 2 – Averaged particle size distribution functions.

A further mathematical method based on non-linear analysis was performed on data acquired by the accelerometers and processing results are plotted in Figure 3 that represents the instability map for each blend. The mapping of c versus z well illustrates the chaos state of the different blends. It shows that the JP8 looks much more stable compared to its blends with HEFA. The full use of HEFA creates a bigger chaos state compared to JP8. Once again, this tendency could be explained by a "quasi homogeneous" combustion with a lack of intermediate components, e.g. aromatic compounds that kinetically stabilize the combustion. Further investigations need to be performed in that sense. This stability occurs around the high frequency (~2.4 kHz) found by the mathematical analysis. To better understand the role of HEFA in the vibrational aspect of the MGT, the instability was plotted versus the

HEFA concentration in the blends using the MGT rpm variation.

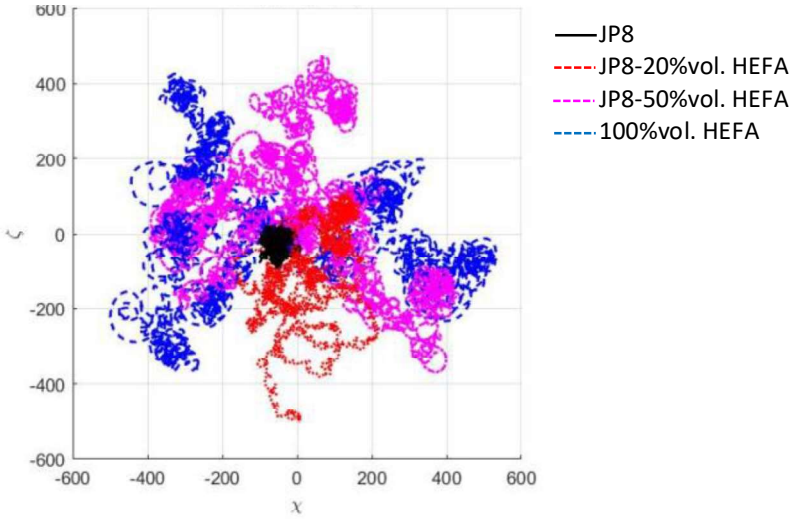

Figure 3 – mapping of c versus z of the different blends.

Figure 4 represents the rpm variation of the MGT for the three sets of measurements performed for each blend. This figure clearly shows that something happens for blends containing 20%vol. and 40%vol. of HEFA. The instability observed for this blends could be due to the competition of the different kinetics of biokerosene and kerosene during their combustion.

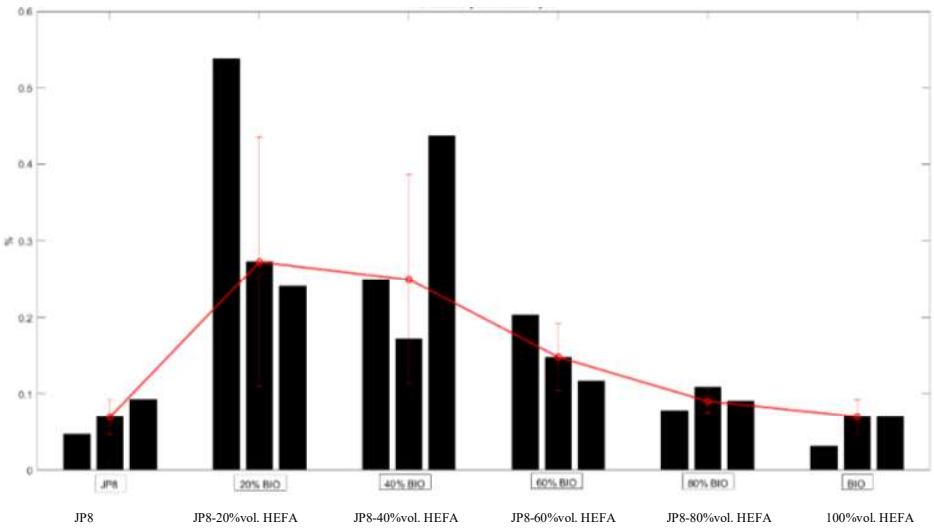

Figure 4 – rpm variation of the MGT vs. blends

Conclusions

A Chaos theory approach based on statistic and non linear mathematical models has been applied for the interpretation of vibration signal acquired on a micro gas turbine for power generation. The technique has shown interesting potential for detecting the correlation between emissions and performances and the use of some Sustainable Aviation Fuels, in particular for HEFA, in different blending conditions.

References

[1] European Parliament website concerning European airports target : https://www.europarl.europa.eu/news/en/press-room/20230911IPR04913/70-of-jet-fuels-at-eu-airports-will-have-to-be-green-by-2050, 13-09-2023.

[2] Velarde C., "Initiative towards sustainable kerosene for aviation—ITAKA project". In: IATA 2015 report, p 25–27. https://www.iata.org/publications/Documents/2015-report-alternative-fuels.pdf, (2015)

[3] Buffi M., Chiaramonti D., "Medina AV Strategies toward experimental assessments of new aviation renewable fuels and blends: the BIOREFLY project". Energy Procedia 105:433–438, (2017).

[4] Braun-Unkhoff M., Riedel U., Wahl C., "About the emissions of alternative jet fuels". CEAS Aeronaut J 8:167–180. C (2017).

[5] Chishty W., Davison C., Bird J., Chan T., Cuddihy K., McCurdy M., Barton P., Krasteva A., Poitras P. "Emissions assessment of alternative aviation fuel at simulated altitudes", ASME Turbo Expo. Vancouver, USA, 6–10 June (2011)

[6] Şöhret Y., Kaya N., Özerdem MB., Karakoc TH., "Contribution of alternative fuels to aircraft exhaust gas emission reduction", 7th international exergy, energy and environment symposium IEEES'7. Valenciennes, France 27–30 April (2015).

[7] Gawron B.; Białecki T., "Impact of a Jet A-1/HEFA blend on the performance and emission characteristics of a miniature turbojet engine", Int. J. Environ. Sci. Technol. 15, 1501–1508, (2018).

[8] Gawron B.; Białecki T., Janicka A.; Suchocki T. "Combustion and Emissions Characteristics of the Turbine Engine Fueled with HEFA Blends from Different Feedstocks", Energies, 13, 1277 (2020).

[9] Przysowa R.; Gawron B.; Białecki T.; Łęgowik A.; Merkisz J.; Jasiński R., "Performance and Emissions of a Microturbine and Turbofan Powered by Alternative Fuels", Aerospace, 8, 25, (2021).

[10] Moore R.H.; Shook M.A.; Ziemba L.D.; DiGangi J.P.; Winstead E.L.; Rauch, B.; Jurkat, T.; Thornhill, K.L.; Crosbie, E.C.; Robinson, C.; et al. "Take-off engine particle emission indices for in-service aircraft at Los Angeles International Airport", Sci. Data, 4, 170198 (2017).

[11] Kurzawska P.; Jasiński R., "Overview of Sustainable Aviation Fuels with Emission Characteristic and Particles Emission of the Turbine Engine Fueled ATJ Blends with Different Percentages of ATJ Fuel", Energies, 14, 1858 (2021).

[12] Kantz H. and Schreiber T., "Nonlinear Time Series Analysis, Cambridge University" Press, Cambridge, (1997).

[13] Allouis C., Amoresano A., Capasso R., Langella G., Niola V., Quaremba G., "The impact of biofuel properties on emissions and performances of a micro gas turbine using combustion vibrations detection", Fuel Processing Technology 179, 10-16, (2018).

[14] Jasinski R., Przysowa R., "Evaluating the Impact of Using HEFA Fuel on the Particulate Matter Emissions from a Turbine Engine", Energies, 17, 177 (2024).

Validation of a virtual chemistry combustion model in a fully technically premixed burner

R. Meloni*, G. Babazzi*, C. Romano*, S. Castellani, A. Andreini****
roberto.meloni@bakerhughes.com
*Baker Hughes, Via F. Matteucci 2, 50127, Florence, Italy
**Department of Industrial Engineering, University of Florence, Italy

Abstract
In this paper a technically fully premixed burner fed with pure hydrogen is investigated through two different versions of the Thickened Flame Model. The main difference lies in the chemistry treatment: while the first is based on a detailed chemistry, the second embeds an in-house developed virtual chemistry mechanism. The models are validated against detailed flame imaging using the OH* radical to detect the flame front morphology and position. The results got through the virtual chemistry are in excellent agreement with the detailed mechanism allowing a strong reduction of the computational effort.

Introduction
Reactive CFD simulations represent nowadays a pillar in the design of modern GT combustors. Moreover, the most accurate combustion models like the Thickened Flame Model (TFM), based on the resolution of primitive variables (so-called species transport), have proven their reliability in capturing the most relevant aspects characterizing the performance of a combustion system, such as flame morphology, emissions and thermo-acoustic instabilities [1-2]. The main drawback of this approach is represented by the high computational cost driven by the need to properly discretize the flame front through extremely fine grids. This requirement is particularly severe when the system is operated at elevated pressure and aggressive fuels like hydrogen are burnt since the flame front can reach a thermal thickness of few micron. A significant computational time reduction can be reached adopting skeletal mechanisms avoiding the transport of those species that are not essential even if this doesn't fully resolve the issue when industrial geometries are simulated. Another option is the employment of global chemical schemes with a single or two steps, as per the original TFM formulation. Unfortunately, such approach lacks generality and even the use of optimized chemical mechanisms must be accurately verified. The virtual chemistry methodology [3] can combine the accuracy provided by a detailed/skeletal chemistry set with the extremely low wall-clock time of a global mechanism. This result can be achieved through customized algorithms able to extend their applicability to a wide range of operating conditions without compromising the accuracy of those parameters that are essential to make the TFM predictive. In this work, a virtual chemistry for pure hydrogen combustion is derived

and embedded within the TFM model. Its performance are measured against a skeletal mechanism and, more importantly, against the experimental measurements characterizing a technically fully premixed industrial burner.

Test Rig Description

The experiments are executed along an atmospheric rig with optical access for detailed imaging (Figure 1). The optical access is ensured by windows on the external casing and quartz windows on the flame tube allowing the visualisation of the primary zone. A Phantom VEO-640L camera is coupled with an IRO-x intensifier. A Nikon UV 85 m lens with a bandpass filter set at 310 +/- 2 nm is employed for the measure of OH* used as heat release rate marker. The sampling frequency is 400 Hz while the gate is equal to 0.4 ms. The time-averaged flame position is retrieved through 1000 samplings. Two independent air lines are installed: the first providing the combustion air and the cooling of the metallics pillars sustaining the quartz through internal passages, the second cooling the quartz and the metallic pillars by external convection.

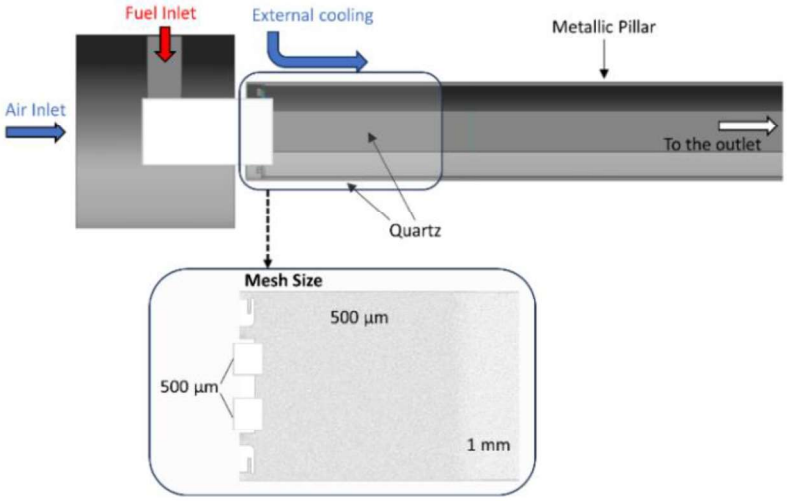

Figure 1. *Combustion test rig (top) and computational mesh in the primary zone (bottom). Design details of the premixer are omitted as well as the external casing.*

The investigated burner is technically fully premixed: the fuel is injected through several jets in cross flow inside the premixing channels ensuring an enhanced mixing with air. In the investigated test condition, pure hydrogen is used. Since the mass flow rates are controlled during the test, the corresponding values are used in the CFD model as boundary conditions. The flame temperature and the pressure drop at which the rig is operated correspond to the values of the NOVA LT16® at ISO base load conditions [4]. Regarding the thermal boundary condition at the combustor walls, an external heat transfer coefficient is coupled with the measured temperature.

TFM: Reference vs Virtual Chemistry Formulation

The two combustion models are indeed different in their mathematical formulation, even if both are based on the TFM. The reference model employs a Flame Index (*FI*,

Eq. 1), to switch from the TFM for the premixed regime to a finite-rate closure for the diffusive one, as explain in [1].

$$FI = \frac{\nabla Y_{H2} \cdot \nabla Y_{O2}}{|\nabla Y_{H2} \cdot \nabla Y_{O2}|} \quad (1)$$

Eq. 2, representing the transport equation of the generic scalar φ, is modified as follows: when the FI is negative, the efficiency function E and the thickening factor F are imposed equal to 1, leading to the finite-rate closure. Conversely, for positive FI, they are calculated according to the original TFM formulation [5].

$$\frac{\partial \bar{\rho}\,\tilde{\varphi}}{\partial t} + \frac{\partial \bar{\rho}\,\tilde{u}_j\,\tilde{\varphi}}{\partial x_j} = \frac{\partial}{\partial x_j}\left(\bar{\rho}(EFD + (1-\Omega)D_t)\frac{\partial \tilde{\varphi}}{\partial x_j}\right) + \frac{E}{F}\dot{\omega}(\tilde{\varphi}) \quad (2)$$

The thickening factor F leverages the flame sensor Ω to apply the artificial thickening only inside the flame front:

$$F = \Omega(F_{max} - 1) + 1 \quad (3)$$

with $F_{max} = \Delta x\, N/LFT(\Phi)$. The adopted mesh resolution inside the primary zone, Δx, (Figure 1) can limit F_{max} to values close to around 6, having chosen a number of points $N = 8$ inside the flame front thickness ($LFT(\Phi)$). The reference reaction for the calculation of the flame sensor Ω selected within the skeletal mechanism of Boivin et al. [6] is $H_2 + OH \rightarrow H_2O + H$. Despite the differentiation between the premixed and the diffusive regime proposed by the reference combustion model, the low fuel unmixedness at the flame front makes the latter practically negligible: Figure 2, shows that the FI is always positive inside the flame front location identified by the contour plot of Ω. Basing on this finding, the VC model is developed without any combustion regime differentiation.

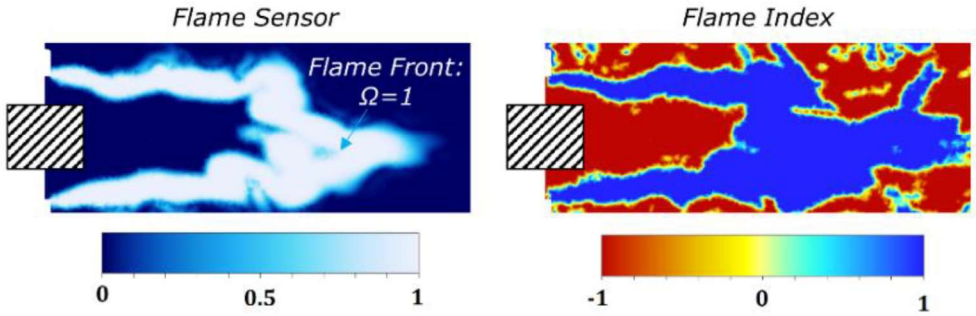

Figure 2. *Flame Sensor (left) and Flame Index (right) proving that the combustion regime is dominantly premixed.*

The virtual chemistry, originally introduced by Callier et al. [3], is based in this study on a single-step irreversible reaction:

$$(a_F F + a_O O)(1 - a_k) + a_k(a_P P) \rightarrow a_P P \quad (4)$$

where O is the oxidiser, F the fuel, P the generic product and a is the stochiometric mass coefficient. a_k controls the amount of products included in the reactants. The introduction of the products into the reactants prevents the autoignition enabling the correct laminar flame thickness prediction. Every species in the reaction is a virtual

entity and must be based according to the specific conditions that the mechanism aims to reproduce. The information needed for the virtual species definition are the Schmidt number, the $NASA7$ polynomial coefficients, and the molecular weight W. Finally, the Prandtl number and the laminar viscosity μ have to be determined as overall mixture properties, not depending on the mixture composition. Indeed, the Pr is constant, while the laminar viscosity is defined as a polynomial function of the temperature. The forward reaction rate is subjected to optimisation: all the parameters that define the Arrhenius expression as well as all the other mentioned quantities are subjected to an optimization process. These control variables are the parameters calibrated to reproduce the performance of a detailed reaction mechanism in the specific thermodynamic conditions of interest. The algorithm maximises a fitness function that is evaluated by means of Cantera as difference between a reference solution based on the detailed mechanism and the virtual mechanism prediction. This calibration is achieved through a genetic algorithm that is schematically reported in Figure 3.

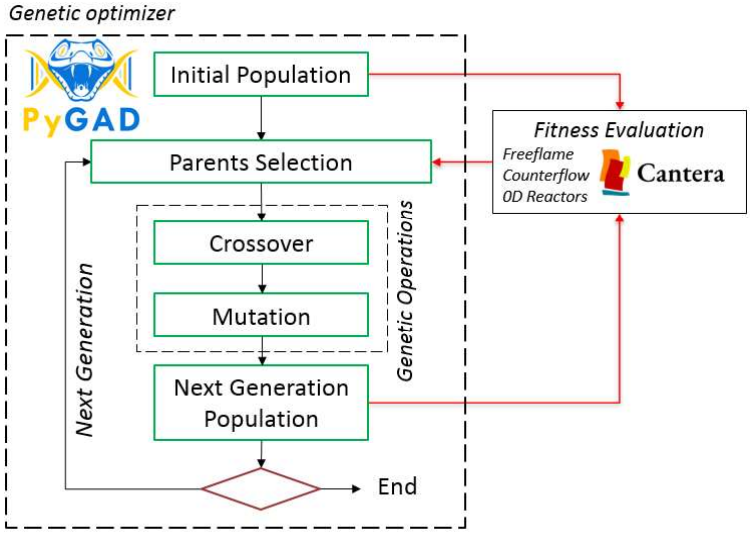

Figure 3. *Genetic optimizer workflow for the calculation of the virtual chemistry.*

Results and Discussion

Flame morphology

The numerical HRR is used to retrieve the predicted flame shape and position and Figure 4 reports the comparison with the experimental OH^* map: the numerical fields are integrated in orthogonal direction to calculate the Line of Sight (LoS) and make them comparable with the chemiluminescence. The dashed horizontal line helps to identify the experimental flame length and highlight the differences with the numerical results. It can be seen that the reference TFM, based on the skeletal mechanism, is affected by a limited difference in terms of flame length. The small difference that can be detected is the rate of decay between the OH^* and the HRR intensity: moving from the flame front, the intensity of OH^* drops in few millimetres while a smoother decay is present for the HRR in the reference numerical case. The same drawback is present in an even more significant way for the VC simulation:

here a more intense signal is present downstream the main heat release region. Such defect is due to a small overprediction of the heat release on the product side using the virtual single step mechanism. Despite that, the flame morphology seems to be reproduced quite accurately also with this approach.

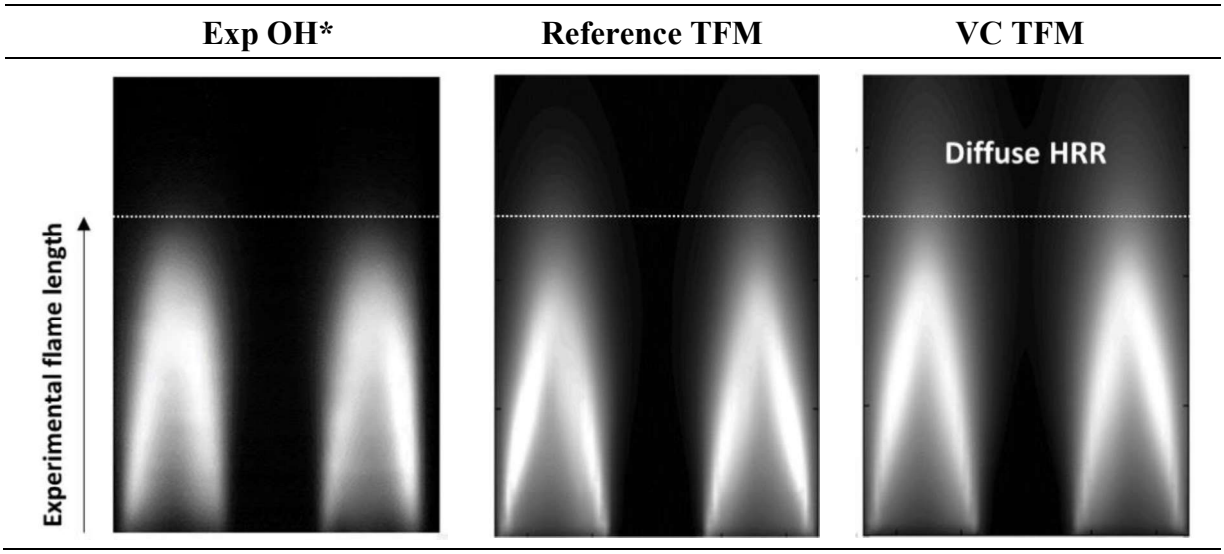

Figure 4. *Experimental time-averaged OH* LoS (left), time-averaged HRR LoS for reference TFM (centre) and the VC model (right). Colorbar: 0-black, maximum-white.*

Another interesting comparison between the reference TFM and the VC approach can be done in terms of fuel mixing: the mixture fraction is calculated according to Bilger's formulation in the former while it is transported through a user defined scalar in the latter. In the reference case, the laminar flame properties, tabulated as a function of the mixture fraction, are influenced by H_2 preferential diffusion. This is not totally correct since the tabulated laminar properties shouldn't be influenced by the strain rate. Conversely, when the mixture fraction is transported, the influence of the H_2 preferential diffusion on the laminar properties is neglected making the approach more consistent. The corresponding differences can be observed in Figure 5 reporting the mixture fraction fields on a longitudinal plane for one of the several burner-tubers with overlapped the iso-line of the HRR at 90%. It can be seen that the reference TFM is characterized by a slightly lower mixture fraction within the flame front while minor differences are observed elsewhere. This is demonstrated also by the contour plots of the mixture fraction at the tuber exit and by the corresponding mixture fraction radial profiles: the maximum difference among them falls at about 70% of the radial span and is less than 0.5%.

Regarding the computational cost, the VC allows a drastic reduction of the delivery time that can be quantified in about -63% compared to the reference TFM. This saving can be significantly higher when such approach is applied to even more complicated chemistry sets, like for example natural gas or blends between different fuels.

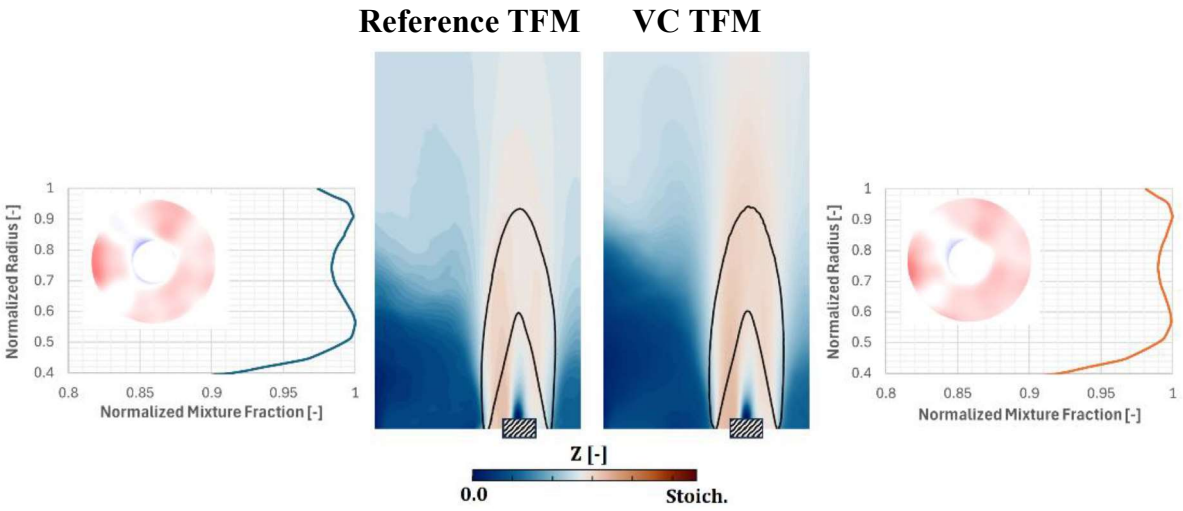

Figure 5. *Mean mixture fraction from the Reference TFM (left) and the VC case (right). The graphs report the profile at the burner exit.*

Conclusion

In this paper, a virtual mechanism for pure hydrogen combustion has been derived and validated against detailed experimental flame imaging and a skeletal mechanism. The comparison with the test data shows a good prediction of the flame morphology while a not relevant difference can be appreciated against the results obtained with the skeletal mechanism. The discrepancy in terms of fuel mixing between the two models can be related only to different numerical strategies. As next step, the virtual chemistry approach will be validated against data for hydrogen-natural gas blends.

Nomenclature

CFD	*Computational Fluid Dynamics*	*HRR*	*Heat Release Rate*
CPU	*Central Processing Unit*	*LoS*	*Line if Sight*
FI	*Flame Index*	*TFM*	*Thickened Flame Model*
GT	*Gas Turbine*	*VC*	*Virtual Chemistry*

References

[1] S. Castellani, R. Meloni, S. Orsino, N. Ansari, R. Yadav, D. Bessette, I. Boxx, A. Andreini, *"High-fidelity H_2–CH_4 jet in crossflow modelling with a flame index-controlled artificially thickened flame model"*, Int J Hydrogen Energy, Vol 48, 2023

[2] P. W. Agostinelli, D. Laera, I. Chterev, I. Boxx, L. Gicquel, T. Poinsot, *"Large eddy simulations of mean pressure and H_2 addition effects on the stabilization and dynamics of a partially-premixed swirled-stabilized methane flame"*, Comb. Flame. Vol 249, 2023.

[3] M. Cailler, N. Darabiha, D. Veynante, B. Fiorina, *"Building-up virtual optimized mechanism for flame modelling"*. Proc. Combust. Inst. 36 (2017) 1251–1258.

[4] https://www.bakerhughes.com/gas-turbines/novalt-technology/novalt16

[5] O. Colin, F. Ducros, D. Veynante, T. Poinsot, "*A thickened flame model for large eddy simulations of turbulent premixed combustion"*, Phys. Fluids 12 (2000).

[6] P. Boivin, C. Jiménez, A.L. Sánchez, F.A. Williams, *"An explicit reduced mechanism for H_2–air combustion"*, Proceedings of the Combustion Institute, Vol 33, 2011.

LEAN BLOW-OUT ANALYSIS FOR THE PERFORMANCE ASSESSMENT OF DIFFERENT BURNER DESIGNS THROUGH A HIGH-FIDELITY CFD APPROACH

G. Lemmi*, S. Castellani*, S. Galeotti*, A. Picchi*, R. Becchi*, A. Andreini*, G. Babazzi, R. Meloni****

gianmarco.lemmi@unifi.it

*Department of Industrial Engineering, University of Florence, Italy

**Baker Hughes, Via F. Matteucci 2, 50127, Florence, Italy

Abstract

Carbon Capture and Storage (CCS) systems play an increasingly essential role in reducing carbon footprint in Gas Turbine (GT) power generation. However, efficient GT-CCS integration requires high Exhaust Gas Recirculation (EGR) rates to boost CO_2 content at the CCS inlet, posing challenges to conventional combustion systems by reducing oxygen levels. Developing innovative technical solutions is critical to extending combustor operability under high EGR rates. This study employs a high-fidelity Computational Fluid Dynamics (CFD) approach to conduct a comprehensive Lean Blow-Out (LBO) analysis, identifying burner designs with broader operability limits at high EGR levels. Due to the computational intensity, cost-effective accuracy is crucial. Hence, all simulations use a validated extended FGM turbulent combustion model.

Introduction

In the ongoing global energy transition towards carbon-neutral alternatives, the urgency to curb emissions from existing power plants is paramount [1]. Within the realm of GT power generation, CCS systems may serve as a viable temporary solution for reducing CO_2 emissions [2]. However, their integration with GT systems requires high EGR rates to maximise CO_2 concentration at the CCS inlet, thus lowering oxygen levels and potentially limiting combustion system operability [3]. Overcoming flame instability under high EGR conditions requires innovative technical solutions to broaden operability limits. In this context, CFD has the potential to play a pivotal role in identifying flame stability limits across various EGR levels and burner configurations. However, industry demands pose a dual challenge: the need for a robust turbulent combustion model capable of accurately addressing near-blow-out phenomena, and the requirement for extensive CFD simulations during the design phase to evaluate technical solutions' impact on flame stability under varying EGR levels, emphasising the imperative to manage computational costs.

In this study, an enhanced version of the FGM model, previously validated by the

authors, is employed to address both objectives. The primary objective of this work is to conduct a comprehensive LBO analysis through a Large Eddy Simulation (LES) approach, assessing flame stability between different burner design solutions under heavy CO_2-diluted air conditions. The computational setup will be outlined in the subsequent section, followed by a description of the numerical LBO procedure. The Results and Discussion will offer a direct comparison of volume-averaged chamber temperature and flame topology among the different design burners investigated.

Experimental Rig and Numerical Setup

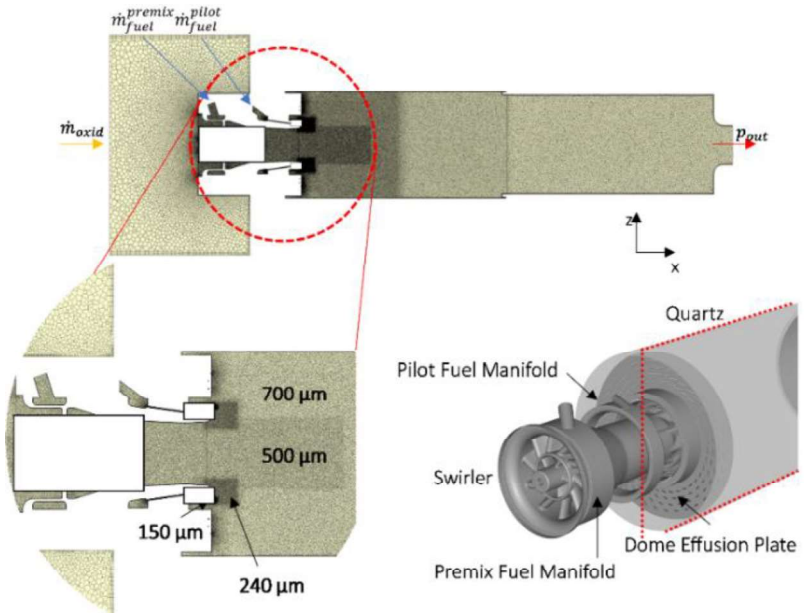

Figure 1. Detailed view of the burner-dome assembly and view of the grid in a longitudinal plane. The employed local sizings are also reported.

Tests are conducted in an optically accessible rig housing an industrial burner supplied by two fuel lines [4]. Fuel is injected by the main premixer through a counter-rotating swirler to ensure uniform mixture delivery into the combustor. In contrast, the pilot line facilitates flame stabilisation by directly delivering gas into the primary zone. The rig operates at atmospheric pressure, with heavily CO_2-diluted air to simulate a real EGR system set to 573 K and Natural Gas with high C2+ content as fuel, featuring an inlet temperature of 291 K, defining test point 95 (TP95) for lean blow-out analysis.

The computational domain encompasses the entire burner geometry (Figure 1), employing a fully unstructured mesh comprising 22 polyhedral cells. Local refinements are applied within the chamber to accurately capture local mixing and flow dynamics. Simulations utilise the commercial pressure-based code ANSYS Fluent® 2022 R1, employing an unsteady high-fidelity LES approach. The WALE subgrid-scale model addresses unresolved turbulence effects [5], while the PISO algorithm governs pressure-velocity coupling with a constant time-step of 1e−5s [6].

Second-order schemes are utilized for both space and time discretization. The outlet maintains constant atmospheric pressure, with wall temperatures prescribed based on thermocouple data. For turbulent combustion modelling, this study utilizes an enhanced version of the FGM approach, incorporating flame stretch and heat loss effects in a pre-calculated table (Γ-table), influencing combustion reactivity directly. For detailed model description and validation, readers are referred to [7].

Numerical Lean-Blow-Out Procedure

The primary aim of this analysis is to determine the burner geometry with the widest flame operability under high CO2 dilution levels in the air. The analysis workflow involves systematically reducing the mass flow rate until encountering lean blow-out [8]. The first step of the analysis consists of an LES of the given geometry under the TP95 operating conditions, here identified as S0. Following stabilization, a 10% reduction in fuel mass flow rate is applied, maintaining the pilot split constant at 30%. Subsequent reductions of 5% in fuel mass flow rate are iteratively implemented until flame extinction occurs. Volume-averaged temperature and volume integral of heat release monitors are employed to identify the onset of LBO conditions. This procedure is repeated for four different burner geometries, denoted as G0, G1, G2, and G3, with specific design characteristics as follows:

- G0: N holes of equal diameter D, with a non-axisymmetric distribution.
- G1: N holes of equal diameter D, with an axisymmetric distribution.
- G2: 2N holes of equal diameter (0.7 D), with an axisymmetric distribution.
- G3: Similar to G1 but with holes tilted in the direction of the swirled flow.

Results and Discussion

Figure 2a displays the area-weighted averaged mixture fraction plots computed on a cross-sectional plane of the flame tube, illustrating the fuel drop steps applied to each geometry. Similar flow times were employed for each geometry during corresponding steps to facilitate visual comparison, as shown in Figure 2a. Small differences arise based on the timing of flame stabilisation occurrence. Each LBO simulation required a total flow time of approximately 0.55s. Considering an estimated flow-through-time (FTT) of about 0.014s, this corresponds to approximately 40 FTTs. The dashed line represents the applied boundary conditions' steps. When reducing the fuel mass flow rate, it takes approximately 2.5 FTTs to uniformly fill the chamber with the new mixture.

Figure 2b illustrates the volume-averaged normalised temperature plots as a function of flow time for each simulated geometry. Trends indicate higher temperatures for G1-G2-G3 configurations compared to G0 under operating conditions with a 15% reduction in fuel mass flow rate (S2). During this phase, G1, G2, and G3 geometries exhibit stable pilot-anchored flames, whereas G0 displays a heavily lifted and elongated flame, as depicted in Figure 3. Conversely, a trend reversal is observed with a 20% reduction in fuel mass flow rate (S3), with the G0 configuration maintaining higher temperatures inside the flame tube compared to other geometries.

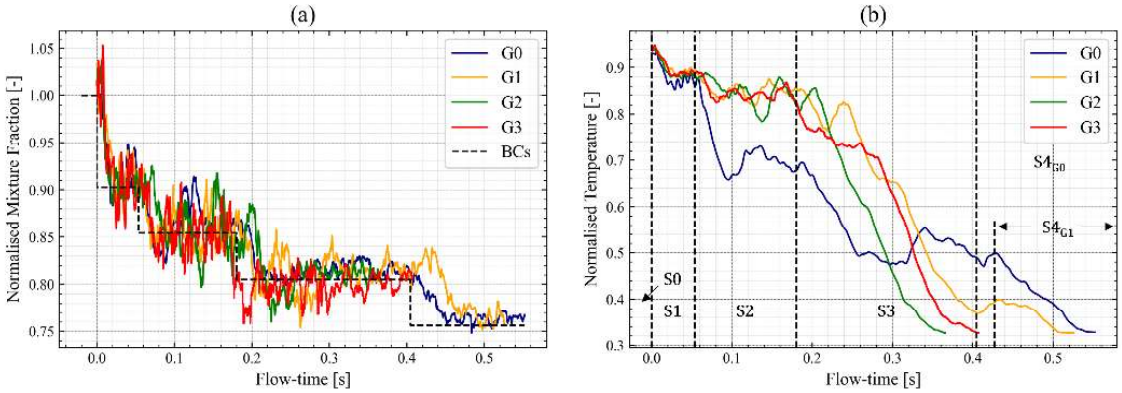

Figure 2. Area-weighted and volume-averaged normalised mixture fraction (a) and temperature (b) plots as a function of the flow time for each simulated geometry.

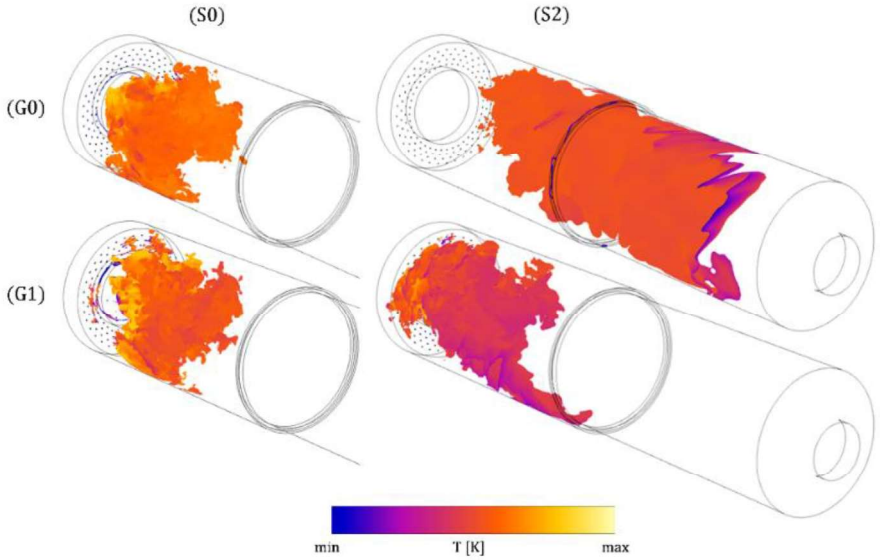

Figure 3. Iso-surface of Progress Variable = 0.5 coloured by temperature for G0 and G1 geometries under 0% (S0) and 15% (S2) fuel mass flow rate reduction.

Under these conditions, the G0 solution sustains stable near-blow-out (BO) conditions, while both G2 and G3 encounter lean blow-out (LBO), with G1 approaching it but not completely experiencing it.

Figure 4 illustrates instantaneous temperature fields on the midplane of the burner for the G0 and G1 design solutions at each fuel reduction step. Both geometries exhibit clear flame length elongation as the fuel mass flow rate decreases. Notably, the G1 geometry demonstrates less susceptibility to this behaviour during the initial two fuel drops (S1-S2), with the flame remaining anchored to the pilots and a high-temperature field observed immediately after the dome. However, a significant decrease in flame stability is observed thereafter, with the flame localised exclusively in the latter portion of the flame tube. In contrast, the G0 geometry displays a more linear trend with the reduction in fuel mass flow rate, with a higher average temperature during the S3 operating condition.

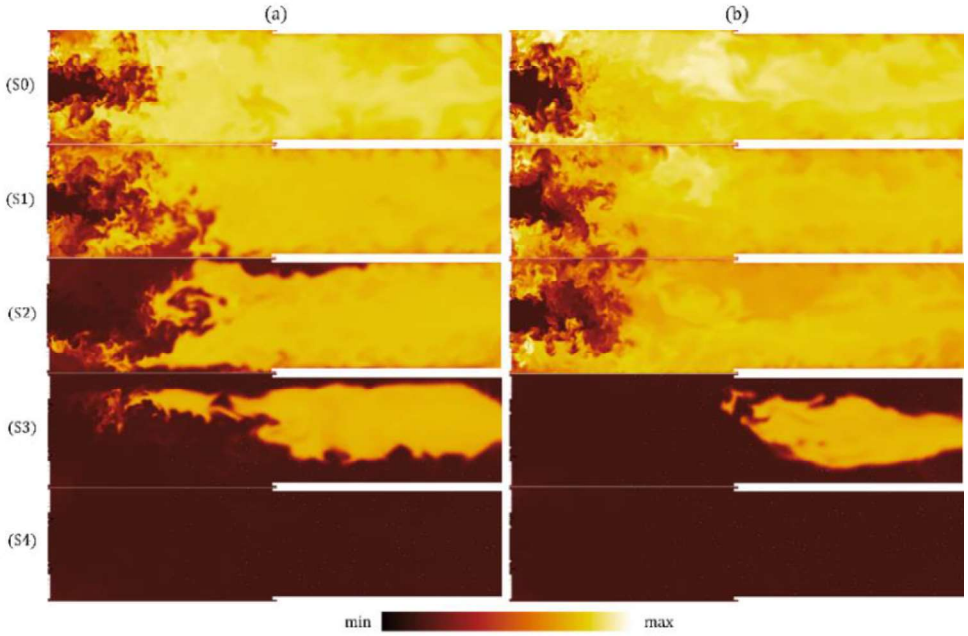

Figure 4: Instantaneous temperature contours on the midplane of the burner for the G0 (a) and G1 (b) design solutions at each fuel reduction step.

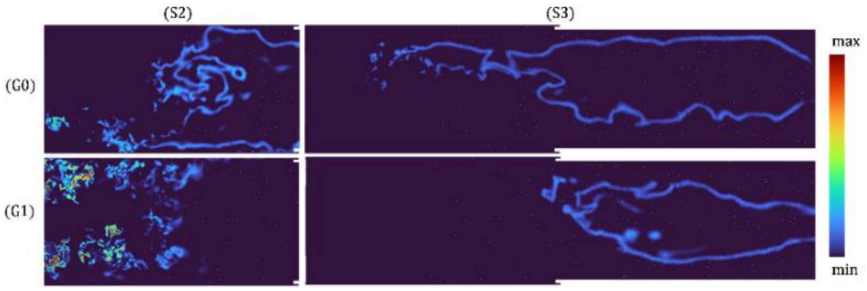

Figure 5: Instantaneous heat-release contours on the midplane of the burner for the G0 and G1 design solutions at steps 2 and 3.

This is further supported by the heat-release contours (Figure 5), indicating that the G0 still maintains a peak of heat release immediately after the pilot jets' region, while the G1 confines it at the end of the flame tube, suggesting an approaching lean blowout (LBO) condition. All solutions ultimately experience lean blowout after a 25% fuel drop. These results closely align with experimental data, with differences ranging from approximately 0.5% to 3% depending on the definition of LBO.

Conclusion

The study delved into the influence of burner geometry on flame stability under highly CO_2-diluted air conditions using LES-based LBO numerical analysis. Through systematic fuel mass flow rate reductions, flame behaviour was analyzed across various burner configurations. Results highlight certain geometries' superior flame stability, showing reduced susceptibility to elongation and LBO. These findings emphasise the pivotal role of burner design in addressing combustion

challenges linked to high EGR rates. Further validation against experimental data underscores the effectiveness of the approach, with the enhanced FGM model maintaining consistency while managing computational costs.

Acknowledgement
The present research activity was carried out in the framework of TRANSITION (fuTure hydRogen Assisted gas turbiNeS for effective carbon capTure IntegratiON). This project has received funding from the Europen Union's Horizon Europe research and Innovation programme under Grant Agreement No 101069665. The Authors gratefully acknowledge this financial support.

Funded by
the European Union

References

[1] A. Pape-Salmon et al., "Low-Impact Renewable Energy Policy in Canada: Strengths, Gaps and a Path Forward", Pembina Institute, 2003 [Online], Available: https://www.jstor.org/stable/resrep00232.5. [Accessed 08 12 2023].

[2] M. Boot-Handford et al., "Carbon capture and storage update", *Energy & Environmental Science,* vol. 7, 2014, https://doi.org/10.1039/C3EE42350F.

[3] A. M. ElKady et al., "Exhaust Gas Recirculation in DLN F-Class Gas Turbines for Post-Combustion CO2 Capture", *ASME Turbo Expo 2008,* vol. 3, pp. 847-854, 9-13 June 2008, https://doi.org/10.1115/GT2008-51152

[4] S. Romano et al., "Modeling of Natural Gas Composition Effect on Low NOx Burners Operation in Heavy Duty Gas Turbine", *Journal of Engineering for Gas Turbines and Power,* vol. 143, 2021, https://doi.org/10.1115/1.4049819

[5] F. Ducros et al., "Wall-Adapting Local Eddy-Viscosity Models for Simulations in Complex Geometries", *Numerical Methods for Fluid Dynamics VI,* 1998.

[6] R. Issa et al., "The computation of compressible and incompressible recirculating flows by a non-iterative implicit scheme", *Journal of Computational Physics,* vol. 62, pp. 66-82, 1986, https://doi.org/10.1016/0021-9991(86)90100-2

[7] G. Lemmi et al., "FGM vs ATF: a comparative LES analysis in predicting the flame characteristics of an industrial lean premixed burner for gas turbine applications", JFUECO, 2024, https://doi.org/10.1016/j.jfueco.2024.100117

[8] P. C. Nassini et al., "Lean blow-out prediction in an industrial gas turbine combustor through a LES-based CFD analysis", *Combustion and Flame,* 2021, https://doi.org/10.1016/j.combustflame.2021.02.037

Experimental and numerical study of the effect of CO_2/N_2 dilution to simulate EGR in GT combustor

S. Galeotti*, A. Picchi*, R. Becchi*, G. Lemmi*, R. Meloni, G. Babazzi**, A. Andreini***

sofia.galeotti@unifi.it

*Department of Industrial Engineering, University of Florence, Italy

**Baker Hughes, Via F. Matteucci 2, 50127, Florence, Italy

Abstract

This work presents the experimental comparison between the use of CO_2 or N_2 to dilute combustion air, in order to simulate Exhaust Gas Recirculation in a gas turbine combustor. Tests have been performed on an industrial burner operated in a tubular single sector test rig at ambient pressure with natural gas as fuel. Comparison is made in terms of flame shape with OH* chemiluminescence imaging, pollutant emissions and dynamic behavior. Significant differences have been observed in terms of CO emissions, and data have been used to validate a reactor network with Cantera, in order to study what happens with intermediate compositions of the oxidant, targeting real EGR conditions.

Introduction

While the employment of Exhaust Gas Recirculation (EGR) is a well-established technique in Internal Combustion Engines to limit NO_x emissions, its adoption in Gas Turbine engines hasn't yet found a practical application due to its expensive and complex installation that doesn't justify the emissions reduction when compared to already established DLN combustion technologies. EGR becomes an interesting option in GT engines considering the possibility of increasing the CO_2 content of the exhaust gases to improve the efficiency of Carbon Capture and Storage (CCS) units. However, the decrease in oxygen content of the combustion air is extremely challenging in terms of combustion stability. CO and UHC emission increase therefore limits the achievable EGR level [1].

European project TRANSITION (fuTure hydRogen Assisted gas turbiNeS for effective carbon capTure IntegratiON) fits in this context with the purpose of developing advanced combustion technologies for natural gas fired Gas Turbines to permit engine operations with high EGR rates, eventually leading to an increase of the CO_2 content in the exhaust gases. Achieving this goal would allow a drastic reduction of the CCS costs and units' size [2].

Recreating real EGR composition in lab scale is quite challenging because of the associated costs and plant complications. During the experimental campaign CO_2 addition in the airflow feeding the burner has been chosen to reproduce EGR, because it offers the opportunity to manage storage better than mixtures with nitrogen. In the present work the effect of such choice is evaluated, comparing the behavior of an industrial burner fueled with natural gas when combustion air is

diluted with CO_2 or N_2 in order to match the same inlet oxygen level, which is a key similarity parameter between real and simulated EGR.

Test rig and burner

The burner was investigated in the reactive test cell of the THT Lab of the University of Florence, with the single sector tubular test rig, reported in Figure 1a. The external vessel is equipped with two perpendicular optical windows for the flame visualization. The combustion chamber is made of a 2.5 mm thick cylindrical quartz liner, cooled by forced convection with a fraction of the incoming air that flows in the annulus between the liner and the confining vessel, not used in the combustion process. The dome plate is cooled through a series of inclined effusion holes.
Combustion air is diluted with CO_2 or N_2 to reach a certain inlet oxygen content. Inert gases are injected in the main air flow line upstream of the electric heater used to increase the flow inlet temperature, in order to deliver to the test section a homogeneous mixture, both in terms of temperature and composition. Natural gas is taken from the domestic line, and fuel composition is analyzed after each test.

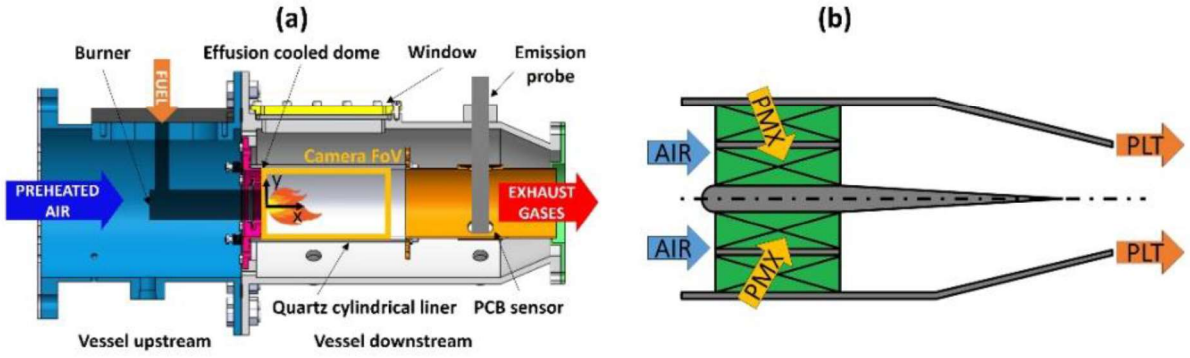

Figure 1. Cross section of the reactive test rig (a) and burner schematic (b)

The investigated burner is a lean premixed burner developed by Baker Hughes for industrial gas turbine applications. A thorough description of the burner geometry and its design can be found in [3], and a sketch is reported in Figure 1b. It is composed by two counter-rotating swirlers and a center body with an air purge. Two independent fuel lines are present: the pilot line (PLT) injects the fuel directly in the combustor chamber through circumferentially equally spaced holes, helping the flame stabilization. The premix line (PMX) delivers the fuel at the tip of the inner swirler, so that it mixes with the airflow thanks to the strong turbulence created by the shear layer generated between the two swirlers.

Operating conditions and measurement techniques

The experimental campaign has been performed at ambient pressure with natural gas as fuel. The purpose of the investigation is to evaluate the effect of the oxidizer composition in reproducing the lack of oxygen due to EGR, diluting the airflow entering the test rig with CO_2 or N_2. Comparison between the two conditions is made by targeting the same inlet oxygen mass fraction Y_{O2}, which has been varied to

simulate different EGR levels. Test are performed with constant thermal power, leading to decreasing adiabatic flame temperature with lower Y_{O2}, especially for the CO_2 case, while differences are lower for the N_2 dilution (see Fig. 3c). The ratio of the fuel flow injected with the premix line and the total fuel flow rate is denoted as PMX%, and has been kept constant at 40%, as well as the inlet temperature of the oxidizer at 300°C and the burner pressure drop at 4.2%.
An emission probe is employed to analyze the exhaust composition through a HORIBA PG350. The probe is made of several radially spaced holes and it is plunged into the flame tube to extract the exhaust gases. After being extracted, the gases flow through a thermally insulated pipeline kept at 150 °C, are dried by a HORIBA PSS-5H refrigerator and finally reach the gas analyzer. The gas analyzer is properly calibrated before each test with a rack of calibrated gas mixture tanks.
Chemiluminescence of the OH* radical was employed to detect the reaction zone and its position in various operating conditions. For OH* chemiluminescence measurements a high-speed camera (Phantom M340) was coupled with the Hamamatsu image intensifier through a relay lens. In addition, a UV lens and bandpass filter (CWL=310 +/- 5nm) were mounted on the image intensifier to be able to capture the OH* transition, which has its peak emission intensity in the UV spectrum at around 310 nm. Images were acquired at 1000 Hz with a 0.5 ms intensifier gate.
A dynamic pressure sensor (PCB) is also installed on the test rig to monitor pressure oscillations, with an acquisition frequency of 12.8 kHz.

Cantera reactor network and thermo-kinetic study

In order to gain a comprehensive understanding of how the oxidizer composition affects the thermo-kinetics of the combustion process, Laminar Flame Speed (Sd), and Extinction Strain Resistance (ESR) were evaluated with Cantera. The first was done with FreeFlame class, while the CounterflowDiffusionFlame function was employed to model the counterflow diffusion flame and determine the maximum extinction strain rate. The evaluation of S_d and ESR was done targeting a constant adiabatic flame temperature.
Additionally, experimental data in terms of pollutant emissions have been used to tune and validate a reactor network representing the combustor with CO_2 or N_2 dilution, in order to be able to study intermediate oxidizer composition, and therefore the real EGR case. Three distinct Perfectly Stirred Reactors (PSRs) were implemented to represent the main flame, pilot flames, and corner regions of the combustor, while two Plug Flow Reactors (PFRs) were utilized to model the dilution zone. Experimental conditions were targeted for the CO_2 and N_2 dilutions cases, while an in-house algorithm was utilized to estimate the mixture composition for the real EGR case (dry), matching the inlet oxygen mass fraction and thermal power. Furthermore, the CO_2 dilution case was run also considering the CO_2 at the inlet as inert.

Results and discussion

Figure 2 presents the laminar flame speed and extinction strain rate, estimated with Cantera. With CO_2 dilution laminar flame speed is lower, with increasing difference with respect to real EGR as the inlet oxygen content decreases. Considering as first approximation that turbulence remains unaltered, the lower laminar flame velocity of CO_2 dilution case leads lower Damkohler numbers, thus moving toward diffuse combustion regimes, with a thickening of the flame front.

Regarding the extinction strain rate, as expected it decreases with lower inlet oxygen fraction, and with CO_2 dilution flame extinction is reached for lower values of the strain rate, thus indicating a reduced combustion stability. Therefore, CO_2 dilution creates more challenging conditions for flame stability compared to N_2 dilution or real EGR, which results in an intermediate condition.

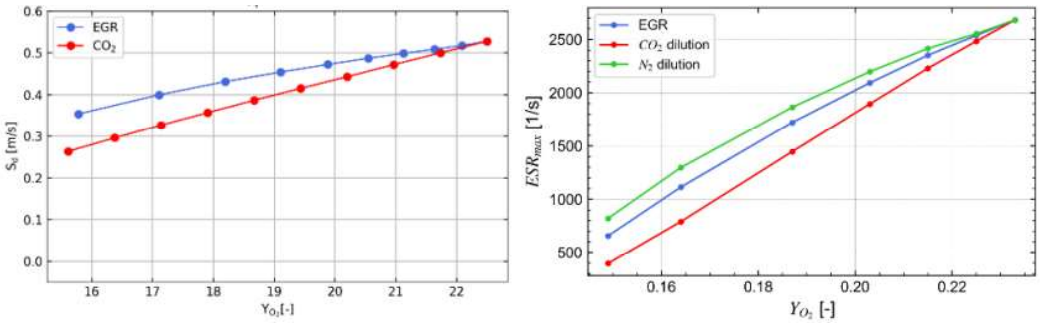

Figure 2. Comparison of Laminar Flame Speed (S_d) and Extinction Residence Time (ESR)

Figure 3 shows the results of CO and NO_x emission measurements (EXP profiles), together with the results of the reactor network (RN profiles). Experimental data highlight significant differences in CO levels between N_2 and CO_2 dilution, especially at low Y_{O2}. The reactor network is able to capture the two different exponential trends, with values close to the measured ones. If the CO_2 at the inlet is considered as inert, CO values are much smaller and comparable to the ones of N_2 dilution case. Therefore, the thermal effect has very little impact, and very high CO levels for the CO_2 dilution case are due to equilibrium effects for high CO_2 concentration. Real EGR case turns out to be much closer to the N_2 dilution curve, indicating that testing with CO_2 is a very conservative condition in terms of CO emissions.

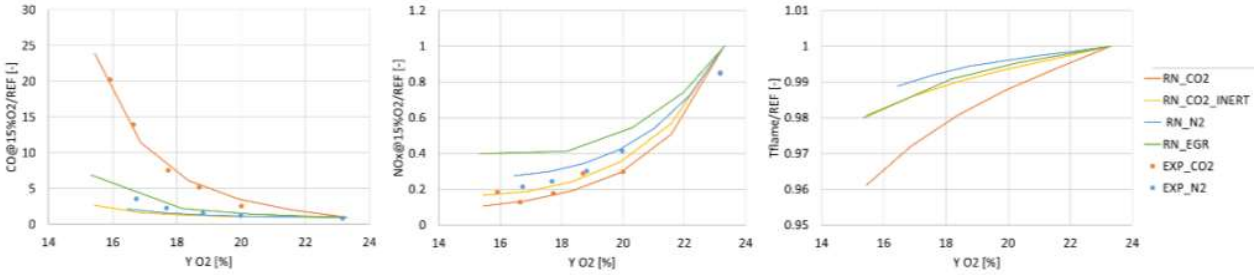

Figure 3. CO and NOx emission measurements (EXP) compared with the results of the reactor network (RN), and adiabatic flame temperature

Regarding NO_x emissions experimental values are slightly higher in the case of N_2 dilution, because of the higher adiabatic flame temperature. The reactor network confirms this trend and shows even higher values in the case of real EGR, since NO_x are also recirculated.

The time averaged OH* chemiluminescence maps identifying the burner flame structure and position are reported in Figure 4. As observed in previous works [4] the flame lifts off from the burner exit and shifts downstream with CO_2 dilution. The oxygen content depletion leads to a slowdown of the reaction process, as showed by the decrease in laminar flame speed. Indeed, the reaction zone becomes more widespread, reaching an extension that almost covers the whole combustion chamber.

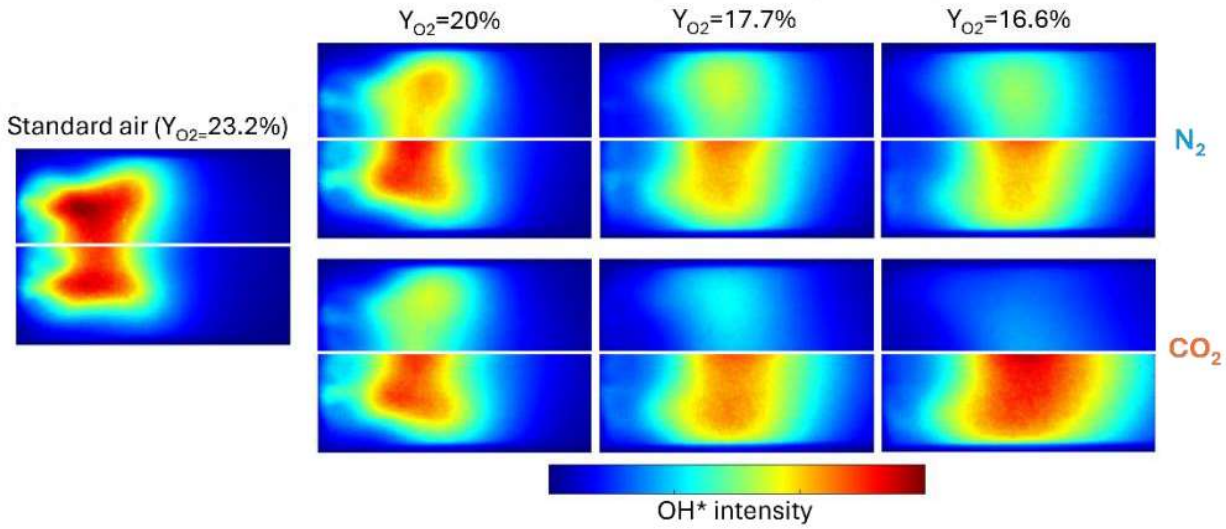

Figure 4. Time-averaged OH* chemiluminescence images (Upper halves: absolute OH* intensity, lower halves: normalized with each maximum)

Comparing the upper halves of the images, the reduction of OH* intensity with lower inlet oxygen content is much more evident with CO_2 dilution, but considering normalized images the differences become negligible, and the shape and position of the reaction zone is approximately the same. Only at very low inlet oxygen content length of the reaction zone increases with CO_2 dilution, but this is an effect related to the lower values with which the images are normalized.

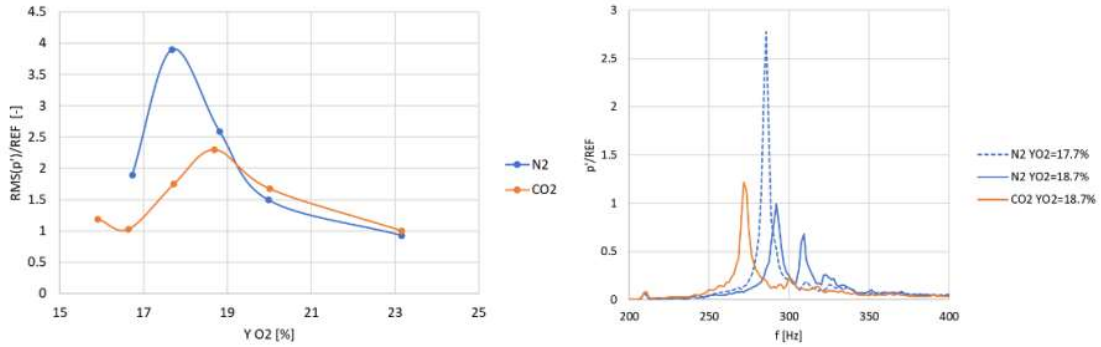

Figure 5. Measured RMS of pressure oscillation amplitude as a function of inlet oxygen level (a) and frequency spectrum (b)

The dynamic behavior is also affected by the oxidizer composition, as shown by Figure 5. A non-monotonic trend of the amplitude of pressure oscillations with inlet oxygen level has been observed with CO_2 dilution. A maximum is still present also with N_2 dilution, with higher peak and shifted to lower values of O_2 mass fraction. This effect is still related to the lower laminar flame speed in the case of CO_2 dilution, which gives rise to a more distributed flame, which partially dampens the oscillations and slightly reduces their peak frequency.

Conclusion

In the present work differences in terms of pollutant emissions, flame structure, and dynamic behavior due to oxidant composition were investigated, in order to evaluate the effect of the experimental strategy of reproducing the absence of oxygen due to EGR by diluting the combustion air with CO_2 or N_2.
Emission measurements revealed very high CO levels with CO_2 dilution, and the Cantera reactor network is able to reproduce the trend of the experimental data, showing that with real EGR CO values would be closer to the one's measured with N_2 dilution. OH* chemiluminescence intensity reduction is more pronounced with CO_2 dilution, but normalized images show that the shape and position of the reaction zone is very similar. The dynamic behavior is also affected by the oxidizer composition, with higher pressure fluctuations with N_2 dilution for the investigated conditions.
These results support the validity of the experimental strategy to use CO_2 dilution to reproduce EGR, in the perspective of a general preliminary screening, considering different burners and various solutions to improve flame stability. In fact the choice turns out to be very precautionary in terms of CO emissions, while in terms of thermoacoustic instabilities N_2 dilution with nitrogen is more critical.

Acknowledgement

Funded by the European Union

This project has received funding from the European Union's Horizon Europe research and Innovation program under Grant Agreement No 101069665

References

[1] ElKady, A. M., Evulet, A., Brand, A., Ursin, T. P., Lynghjem, A. "Exhaust Gas Recirculation in DLN F-Class Gas Turbines for Post-Combustion CO2 Capture". *Proc ASME Turbo Expo*, pp. 847–854 (2008)

[2] Tabbi Wilberforce, A.G. Olabi, Enas Taha Sayed, Khaled Elsaid, Mohammad Ali Abdelkareem, "Progress in carbon capture technologies", Science of The Total Environment, Vol 761, 2021

[3] M. Cerutti, N. Giannini, G. Ceccherini, R. Meloni, E. Matoni, C. Romano, G. Riccio, "Dry low NOx emissions operability enhancement of a heavy-duty gas turbine by means of fuel burner design development and testing", Proc of ASME Turbo Expo, GT2018-76587, Oslo, Norway, 2018

[4] Galeotti, S., Picchi, A., Becchi, R., Meloni, R., Babazzi, G., Romano, C., and Andreini, A. "Experimental characterization of an industrial burner operated with simulated EGR", Applied Thermal Engineering, 2024


THE COMBUSTION INSTITUTE
1954

SESSION IX

Novel concepts and CCUS including multi-physics and multi-phase phenomena


THE COMBUSTION INSTITUTE
1954

Integrated CO_2 Capture and Methanation from a SO_2-bearing flue gas: S-tolerance and regeneration of the dual function material

S. Cimino, E.M. Cepollaro, L.Lisi
stefano.cimino@cnr.it
* STEMS- CNR, Napoli, Italy

Abstract
The combined CO_2 capture and methanation with Dual Function Materials (DFM) is emerging as a vibrant field of research for its potential to increase the efficiency and reduce the cost of current multistage CCU processes.
In this work, a DFM containing Ru (1% wt) and Li (3% wt.) dispersed onto γ-Al_2O_3 was extensively tested in the integrated CO_2 capture and methanation process to assess the effects of the main species (O_2 and H_2O) as well as of poisonous impurities (SO_2) in realistic flue gases. The ageing study with up to 100ppmv SO_2 demonstrated a remarkable tolerance to sulfur poisoning coupled with a slow loss of CO_2 capacity due to long-term S-accumulation.

Introduction
Reversing global temperature rise requires mitigating greenhouse gas emissions from the industry and energy sectors. As the world will still rely on fossil fuels in the mid-term, and there are sectors which cannot be easily decarbonised or only partially so, carbon capture and utilization (CCU) technologies are required for the ambitious net zero carbon emission target to be met [1-2]. Recently, the integration of CO_2 capture and its direct conversion into valuable fuels or intermediates such as methane, CO or syn-gas is emerging as a vibrant field of research due to the potential to achieve a circular carbon economy while cutting the costs and increasing the efficiency of the energy-intensive multistep CCU technologies that are currently available [1-2]. In particular, many authors have recently demonstrated that the integrated CO_2 capture and in-situ methanation (ICCM) can be performed over Dual Function Materials (DFMs) [1-4], which combine at the nanoscale a CO_2 sorbent phase (e.g. alkali (hydro)oxides/carbonates) with a methanation catalytic active phase (e.g. Ni or Ru). The process is then operated in a chemical looping mode mediated by the DFM which is alternatively exposed to a CO_2-rich atmosphere (capture stage), and an H_2 stream (methanation stage) (Figure 1). Since both CO_2 adsorption and methanation are exothermic the ICCM process can be run isothermally in the 250-350 °C range by harvesting the sensible heat of typical flue gases and without any further energy input, utilizing either fixed bed reactors with alternate feeds or interconnected fluidized bed reactors with circulating DFM [2].

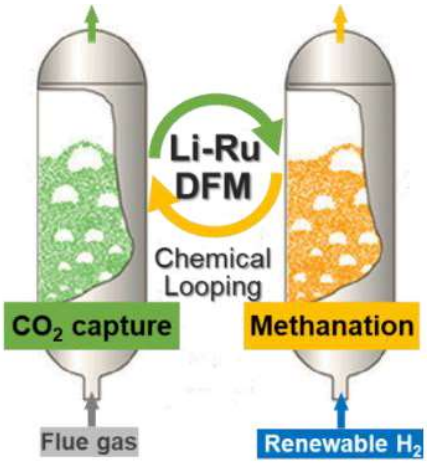

Figure 1. Schematic representation of the Integrated CO_2 Capture and Methanation process with a Li-Ru DFM circulating within interconnected fluidized bed reactors.

In this work we set out to investigate the performance of a DFM containing Li and Ru dispersed on γ-alumina during the ICCM with a more realistic flue gas including O_2, H_2O and SO_2 impurities (up to 100ppm), which can severely poison catalytic metal sites for hydrogenation. The ageing study involved more than 100 capture and methanation cycles in a fixed bed reactor operated in the temperature range 260 – 320 °C with alternate feed conditions.

Experimental

Ru and Li were dispersed sequentially within 1mm Al_2O_3 spheres by impregnation with water solutions of nitrate precursors. Their loadings in the final DFM were deliberately kept low (ca. 1 % and 3 % wt., respectively) to better highlight the possible sulfur-poisoning effects on both the sorption and catalytic functionalities.
Combined CO_2 capture and methanation tests were performed in a fixed bed quartz reactor with an annular section (d_{in}=4mm, d_{out} =10 mm) that was loaded with ca 2.3 cm^3 (packed-volume) of Li-RuA DFM. The reactor was operated at atmospheric pressure and at fixed temperature (260-320 °C) and total inlet flowrate (20 Sl/h) by switching alternatively the feed between the CO_2 capture and methanation phases. During the first step a feed gas stream containing 5% vol. CO_2 in N_2 with the possible additional presence of 0.25% O_2 and/or 1.5% H_2O as well as 10-100 ppmv SO_2 was stepwise admitted to the reactor and flowed over the DFM. After an intermediate purge (2 min, pure N_2), the methanation phase was started by switching the feed to 15% vol. H_2 in N_2. Continuous gas analyzers (ABB Optima Advance) were used to measure the molar fractions of CO_2, CH_4, CO, and SO_2, H_2S.

Results and Discussion

Textural and morphological properties of the fresh Li-RuA material as well as its parent RuA catalyst are presented in Table 1. The dispersion of Li on RuA induced a 9.2% increase in the density of the resulting DFM spheres (stabilized in air after reduction). However, the specific surface area of Li-RuA was lowered from 180

down to 145 m^2 g^{-1}, suggesting a deeper modification of the original textural properties. In particular, the Pore Size Distribution analysis indicates Li-addition caused an evident enlargement of the mesopores (Table 1) whose median size passed from 9.4 nm for RuA up to 10.9 nm for Li-RuA. XRD patterns indicate Li addition induced the formation of the mixed $LiAl_5O_8$ crystalline phase which shares the same spinel structure of γ-alumina. The characteristic dimensions of the Ru crystallites in RuA and Li-RuA, estimated by Scherrer's equation, were equal to 10.3 and 10.6, respectively (Table 1): therefore, Li addition and the subsequent reduction of the DFM at 450 °C did not alter the initial metal dispersion.
Temperature-programmed methanation tests performed by co-feeding CO_2 and H_2 over the DFM bed (not-shown) indicated that Li-addition significantly boosted the catalytic activity of Ru/A in the whole temperature range so that the temperature for 10% conversion decreased from 293 °C down to 265 °C while the activation energy was poorly unaffected (T_{10}, E_a in Table 1).

Table 1. Summary of the characterization results for (reduced) DFMs: Density of the spheres, Specific surface area (S_{BET}), pore size by N_2 physisorption; size of Ru (d_{Ru}) crystallites from XRD data; apparent activation energy (E_a) and temperatures for 10% conversion (T_{10}) for the catalytic hydrogenation of gaseous CO_2.

	Density	S_{BET}	Pore size	d_{Ru}	S	E_a	T_{10}
	g cm^{-3}	m^2 g^{-1}	nm	nm	% wt.	kJ/mol	°C
RuA	1.40	180	9.4	10.3	-	71	293
Li-Ru/A	1.53	145	10.9	10.6	-	81	265
S-Li-Ru/A	1.59	133	11.3	16.5	2.1[a]	71	303[b]

[a] estimated from TG analysis supposing the decomposition of Li_2SO_4 into Li_2O
[b] S-aged DFM sample recovered to air and tested without any further pretreatment

Figure 2 presents the typical transient CO_2, CH_4, and CO concentration traces as well as the temperature profiles recorded at the exit of the DFM bed during standard cycles run at a fixed preheating (280 °C). As soon as admitted to the reactor, CO_2 was quickly captured by the DFM so that its concentration dropped to zero after ca. 25 seconds independently from the presence of O_2 or H_2O in the feed stream; thereafter, it started to raise progressively until the overall capacity was mostly saturated (within 4 min). The contribution from the reactor hold-up can be visualized by the dashed line in Fig. 2a. Some weakly bonded CO_2 was spontaneously desorbed from the DFM during the intermediate purge phase under N_2 flow (required to avoid gas mixing) before H_2 was admitted to the reactor. At that point, CH_4 formation occurred with an apparent initial rate that was not affected by the eventual presence of O_2 or H_2O during the previous stage. The peak production of CH_4 (up to 3.5% by volume) was achieved within 25s, being slightly lower when the simulated feed gas contained some H_2O, due to the lower amount of CO_2 stored on the DFM. Simultaneously, a very low amount of CO was formed (≤40ppm, Fig. 2c), and it

became almost undetectable for the humid flue gas case. Limited thermal desorption of CO_2 was observed at the beginning of the hydrogenation phase (Fig. 2a), driven by the heat released by the exotherm of the catalytic reaction, which indeed caused a temperature increase recorded at the exit of the DFM bed (Fig. 2d). The maximum and minimum values of ΔT_{exit} were measured when the flue gas contained O_2 or H_2O, respectively.

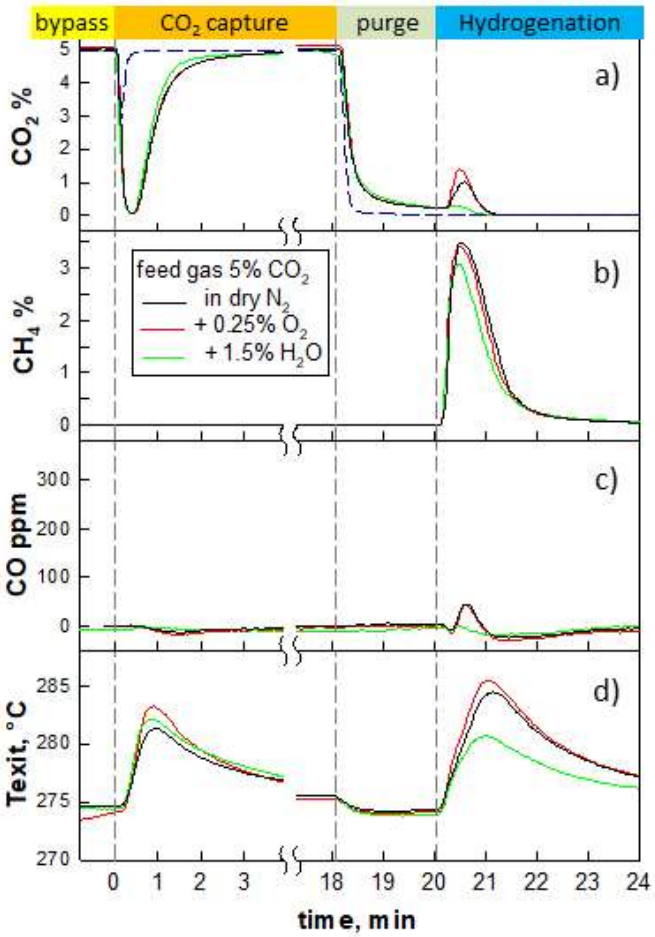

Figure 2. Integrated CO_2 capture and methanation cycles on Li-Ru/A DFM at 280 °C with 3 different feed gas compositions: 5% CO_2 in N_2, with the addition of +0.25% O_2 or +1.5% H_2O. Temporal profiles of CO_2 (a) CH_4 (b) and CO (c), and corresponding temperature at the exit of the catalytic bed (d).

Interestingly, also the CO_2 capture process caused similar temperature increases due to the exothermic nature of the surface reactions involved, which increased in the presence of O_2 in the flue gas (Fig. 2d). In particular, at temperatures exceeding 200 °C Ru can be easily oxidized during adsorption and then reduced back to its metal form during the methanation step: both the oxidation of Ru by O_2 and the reduction of RuO_x by H_2 are exothermic reactions which therefore contribute to enhancing the heat release during both half cycle (Fig. 2d).

Eventually, we set out to investigate the performance and stability of the Li-RuA DFM over time when SO_2 (10 or 100 ppm) was co-fed with CO_2 in the simulated flue gas also containing H_2O and O_2. During the capture step, the exit gas

concentration of SO_2 quickly dropped to zero while, during methanation, the Li-RuA DFM did not emit any measurable H_2S (nor SO_2) but retained all of the sulfur fed to the reactor. This is not surprising given the strong affinity of alkali-based sorbents for SO_2 leading to the formation of stable sulfite/sulfates [3]. Therefore, the general performances measured during the ageing study at 280 °C are presented in Figure 3 in terms of the CO_2 uptake, CH_4 production, CO_2 conversion, and CH_4 selectivity, as a function of the total amount of sulfur stored on the DFM. In particular, empty and close symbols refer to tests performed with either 10 or 100 ppm of SO_2, respectively. For comparison purposes, the black dash-dotted lines report data relevant to our previous results obtained with a Na-RuA DFM [3].

Initially, the Li-RuA DFM showed remarkable tolerance to the presence of SO_2 in the flue gas so that all process outcomes were almost unaltered up to ca 70 $\mu mol/g_{DFM}$ of stored S. Thereafter, the CO_2 capture capacity and the corresponding CH_4 production started to decrease progressively following almost parallel trends, while the CO_2 conversion and CH_4 selectivity remained close to their original values or even increased slightly. This is a clear indication that SO_2 competed with CO_2 for the same basic adsorption sites of the DFM, which, once saturated with S-species, were not restored during the hydrogenation phase. Notably, the intrinsic catalytic methanation activity of Ru sites was substantially preserved even at high S-loadings. Furthermore, the performance enhancement measured over the Li-based DFM as compared to its Na-based counterpart (ca 35-40% larger capture capacity and methane production, Fig. 3 b,c) was steadily preserved along with the growing S-load over time on stream.

The removal efficiency for SO_2 approached a breakthrough condition (90%) at ca 800 $\mu mol_{SO2}/g_{DFM}$: at that point, the residual CO_2 uptake and CH_4 production were reduced to ca 25% of their original values. Some H_2S started to be detected during the hydrogenation phase once the S-loading on the DFM approached the saturation level and the feed SO_2 concentration was raised to 100 ppm.

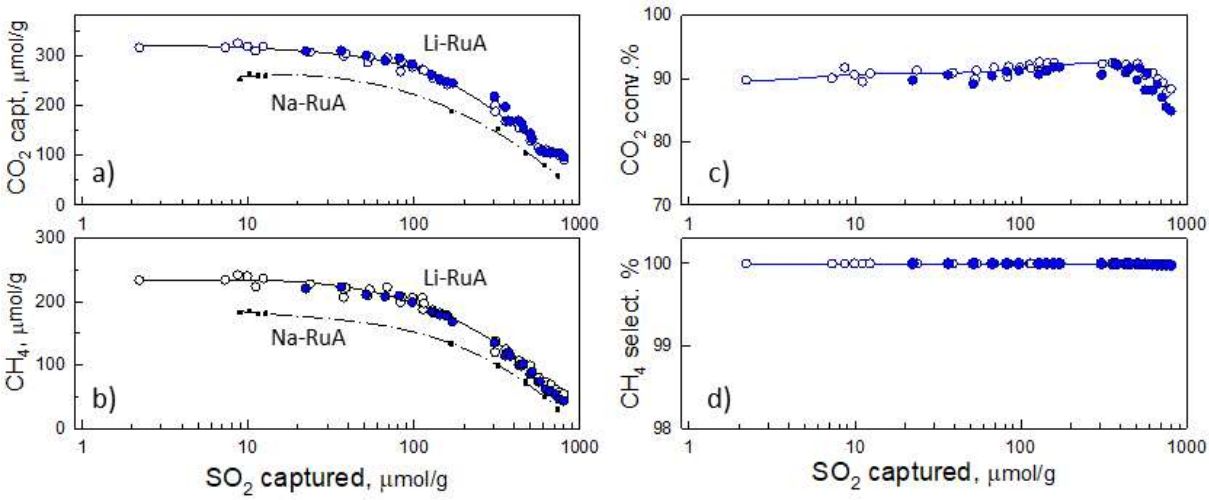

Figure 3. ICCM performance data with Li-RuA DFM operating at 280 °C with a simulated flue gas containing 5% CO_2, 1.5% H_2O, 0.25% O_2, and 10 or 100 ppmv SO_2 (open or closed symbols, respectively).

While S-species captured on the strong basic sites of the Li-RuA DFM appear too stable to be hydrogenated at 280 °C, it is suggested that more weakly bonded SO_x ad-species on a mostly saturated DFM surface can spill-over onto adjacent catalytic sites to form H_2S, provided that Ru sites are not covered by CO_x species involved in the formation of methane [3].
It should be mentioned that Ru-based catalysts are generally prone to severe poisoning effects by sulfur-bearing compounds under reducing atmospheres due to the easy formation of inactive metal sulfide species [5]: at variance, we only observed a marginal loss of activity (as measured by the CO_2 conversion and CH_4 selectivity), even in those last experiments run with a highly sulfated DFM when H_2S was detected in the product stream (Figure 3 c,d) and RuS_x species were likely formed during the methanation phase.
Post-ageing characterization of the sulfurized DFM, after more than 100 cycles during 50 days at reaction temperatures, indicated a high stability of its textural properties and a relatively limited increase of the average size of Ru nanoparticles due sintering (Table 1). Accordingly, the residual intrinsic methanation activity of the S-aged Li-Ru/A was comparable to the reference RuA catalyst, suggesting it only lost the initial promoting effect of Lithium due to the extensive formation of the corresponding sulfates (Tab. 1). A clear self-poisoning effect was observed during gas phase methanation tests for temperatures above 290 °C (not shown): this is attributed to the formation of RuS_x species by reaction (temperature activated) of Li-sulfates with nearby Ru nanoparticles [5]. Notably, exposure of the sulfurized (poisoned) DFM to oxidizing conditions such as those encountered during the CO_2 capture stage can easily decompose inactive RuS_x species, by this way self-regenerating the original catalytic activity for the following methanation stage.

References

[1] Merkouri, L.-P., Reina, T.R., Duyar, M.S. “Closing the Carbon Cycle with Dual Function Materials”, *Energy & Fuels* (2021).
[2] S. Sun, H. Sun, P.T. Williams, C. Wu, “Recent advances in integrated CO_2 capture and utilization: a review”, *Sustain. Energy Fuels* 5: 4546–4559 (2021)
[3] Cimino, S., Cepollaro, E.M., Lisi, L., “Sulfur tolerance and self-regeneration mechanism of Na-Ru/Al2O3 dual function material during the cyclic CO2 capture and catalytic methanation”, *Appl. Catal. B.317*: 121705 (2022).
[4] Porta, A., Matarrese, R., Visconti, C.G., Castoldi, L., Lietti, L., “Storage Material Effects on the Performance of Ru-Based CO_2 Capture and Methanation Dual Functioning Materials”, *Ind. Eng. Chem. Res.* 60: 6706–6718 (2021)
[5] Kuzmenko, D., Nachtegaal, M., Copéret, C., Schildhauer, T.J., “Molecular-level understanding of support effects on the regenerability of Ru-based catalysts in the sulfur-poisoned methanation reaction”, *J. Catal.* 375: 74–80 (2019)

A FLUIDIZED BED AUTOTHERMAL REACTOR FOR SOLAR-POWERED SUSTAINABLE PROCESSES

S. Padula*, M. Troiano*,, C. Tregambi*,***, R. Solimene* and P. Salatino****

stefano.padula@stems.cnr.it

*Istituto di Scienze e Tecnologie per l'Energia e la Mobilità Sostenibili (STEMS), Consiglio Nazionale delle Ricerche, Italy

**Dipartimento di Ingegneria Chimica dei Materiali e della Produzione Industriale (DICMaPI), Università degli Studi di Napoli Federico II, Italy

***Dipartimento di Ingegneria, Università degli Studi del Sannio, Italy

Abstract

In the last decades Concentrating Solar Thermal (CST) technologies have been successfully employed in the power sector and might prove a viable solution to decarbonize heavy industry and transportation in future years. Solar-driven chemical processes can be targeted to produce sustainable fuels and commodities, but this advancement will require the development of innovative chemical reactors. The present study advances the concept of a Directly Irradiated Fluidized Bed Autothermal Reactor (DIFBAR). This novel reactor incorporates an internal solid-solid heat exchanger that allows to preheat the reactants, by recovering the sensible energy of the products. This paper presents new experimental results, considering the Calcium Looping (CaL) process as a reference case-study. Cold flow and high temperature experiments are carried out, testing a natural calcarenite (a $CaCO_3$-based sand) as reactant, mixed with black proppants particles to enhance the absorption of solar radiation.

Introduction

Concentrated solar thermal (CST) technologies are based on a set of sun-tracking mirrors (heliostats), that focus solar rays on a receiver. In the last twenty years the production of electricity by CST-powered plants has reached commercial maturity [1]. The development of large scale CST plants has catalyzed the interest toward the application to the chemical and fuel industry, that is today a wide and diverse field of research. Many applications involve gas-solid processes, that can be carried out at temperatures compatible with the most advanced solar receivers [2]. These processes can produce solar fuels and chemicals by the thermochemical conversion of biomasses or the chemical looping of metal oxides [3]. Another field of interest is the thermochemical energy storage (TCES): solar energy drives an endothermic reaction, whose products are stored and employed to release heat through the reverse exothermic reaction [4]. Calcium looping (CaL) is one of the most promising

processes because of the combination of high operating temperatures, energy density and low cost. It based on the reversible reaction:

$$CaCO_3 \rightleftharpoons CaO + CO_2 \quad (1)$$

Solar energy is used to drive the endothermic decomposition (calcination) of calcium carbonate ($CaCO_3$), that produces calcium oxide (CaO) and carbon dioxide (CO_2). Then, the reverse reaction (carbonation) is conducted to release energy.
As no limitations occur on the side of heliostat engineering, major efforts must be directed to the development of reactor technologies [5]. Fluidized bed reactors have been widely recognized as an adequate solution for the deployment of CST-driven thermochemical processes [6], thanks to their excellent heat transfer properties and flexibility. This paper is dedicated to the study of a Directly Irradiated Fluidized Bed Autothermal Reactor (DIFBAR) [7]. This innovative reactor type recovers the sensible energy of reaction products to preheat the reactants in an internal solid-solid heat exchanger, following the principle of autothermal reactors. In this way the conversion of solar to chemical energy is maximized. Recently a lab-scale prototype has been set up for the proof of concept [8]: the study characterized the experimental apparatus with inert sand as bed inventory and went on to demonstrate the operation as chemical reactor by performing the calcination of magnesium carbonate particles at 600-750°C.
On the other hand, the selection of suitable materials is crucial for the success of any solar-driven process. This study studies the application of the DIFBAR to the CaL processes, testing a natural calcarenite (a $CaCO_3$-based sand) as reactant. In order to compensate their poor absorptivity of solar radiation, reactant particles are mixed with black proppants with a 1:3 mass ratio. A calcination test at temperatures between 700-800°C was performed by irradiating the lab-scale prototype with a 10 kW_e solar simulator, followed by a carbonation test with a CO_2-rich stream at 550-600°C under non-irradiated conditions.

Experimental set up

Figure 1 pictures the DIFBAR prototype. The prototype is made of stainless steel and insulated with rock wool blankets and ceramic shells. It is equipped with four mass flow controllers, eight pressure transducers and sixteen K-type thermocouples at various heights. Setpoints and measuring signals are handled by a LabView application.
During calcination experiments, a fluidizing air stream (Q_1) entrains the solids through the riser (a) to the solar receiver (b). There, the particles are exposed to a concentrated solar radiation passing through a circular aperture of 100mm and sealed by a quartz window. Then the solids flow through the annulus tube (c) and are returned to the storage reservoir (d). The particles in the annulus and in the riser exchange heat counter-currently. The reservoir can be fluidized by a secondary air stream (Q_{res}) fed through a sparger. Two additional air streams can be fed (Q_3 and

Q_4), to provide a gas-sealing for the reservoir and the receiver. The Q_3 stream also regulates the solid discharge rate from the annulus into the reservoir and is set so as to keep constant the bed level inside the annulus for any circulation rate. During carbonation experiments, the solar receiver is not operated, whereas the reservoir is operated as a FB reactor with a 15% CO_2–air mixture stream. Concentrated solar radiation is simulated with a 10kW$_e$ Xenon arc lamp and an elliptical reflector (high-flux solar simulator). Electric heaters are used to heat up the reservoir during start-up phase (max. power 1.5kW) and to keep its temperature during the carbonation test.

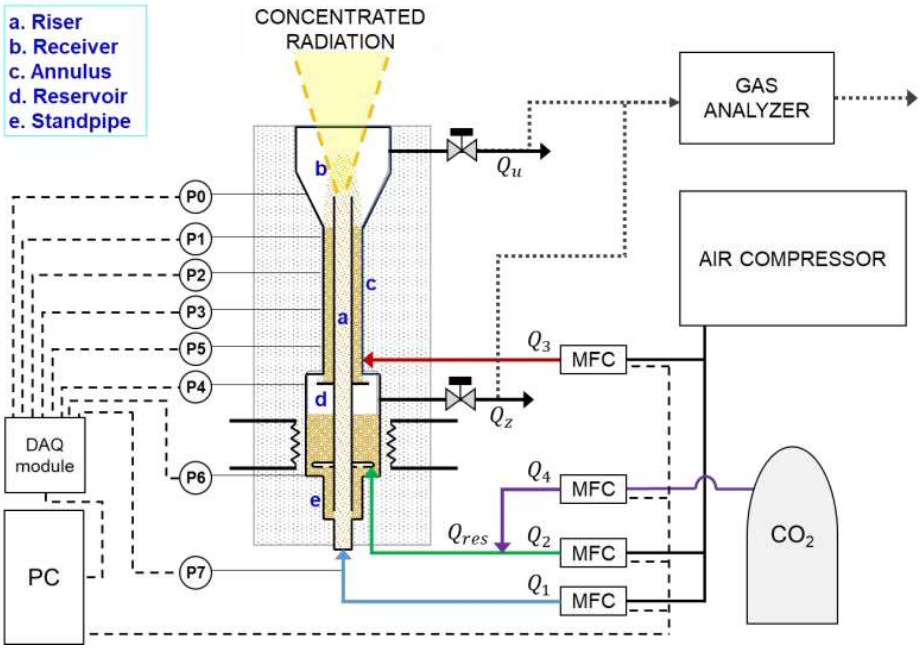

Figure 1. Experimental set-up: (a) prototype scheme and (b) photograph**.**

A mixture of calcarenite sand and black proppants with 1:3 mass ratio and a total mass of 1.4 kg was used as bed inventory. The calcarenite is a natural rock from Apulia (Italy), composed by 91%$_w$ of $CaCO_3$, as estimated from thermogravimetric experiments. The two solids were sieved in different size ranges in order to separate the reactant after the experiments for subsequent analysis. Size ranges were selected to ensure desired fluidization conditions in the reactor.

Table 1. Materials properties

Material	**Size range [μm]**	**Bed density [kg/m^3]**	**Minimum fluidization velocity [cm/s]**
Black proppants	90-300	1830	3.5
Calcarenite	300-420	1175	11.8
Mixture	-	1664	4.8

The steady temperature profile proves the efficiency of the heat exchanger during calcination. Outlet CO_2 concentration were measured with an online gas analyzer to monitor the course of the reactions. After the carbonation experiment the reactant was sampled and analyzed to assess the final conversion.

Results

Figure 2 shows the mass flux of the calcarenite-black proppant mixture through the riser (G_r) obtained by cold flow experiments. The solids mass flux linearly increases from 0 to 40 kg/(m^2s) for gas velocities between 1.8 and 2.0 m/s. The figure also reports the fraction of calcarenite particles fed to the receiver (α). This measure shows a slight increase with the fluidizing velocity, but is in general quite close to the value 25%. This demonstrates that the particles are well-mixed inside the riser and no segregation occurs inside the reservoir.

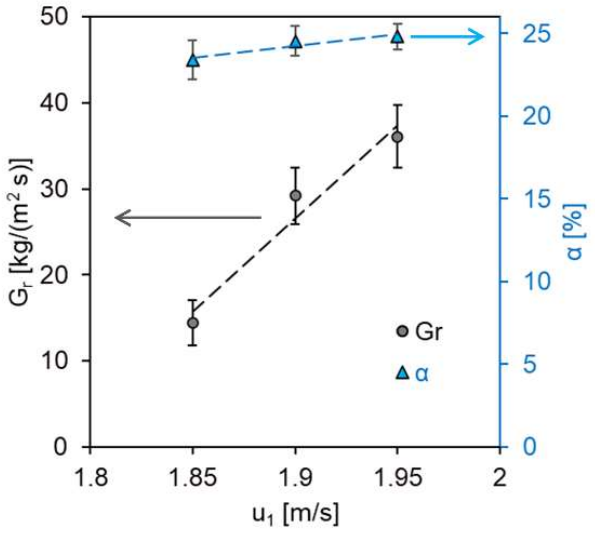

Figure 2. Solids mass flux (G_r) and calcarenite fraction (α) in the riser.

Figure 3 shows the results of a calcination experiment. The internal heat exchanger allows to preheat the reactants from 550°C to 750°C (Fig. 1a).
To increase the residence time of the reactants in the receiver and allow calcination, a fill-and-empty strategy was adopted, resulting in oscillating receiver temperature (T11) and CO_2 concentration (Fig. 1b). The outlet CO_2 concentration is close to reaction equilibrium conditions (9% CO_2 at 750°C).

Figure 4 reports the reservoir temperature and CO_2 concentration during the carbonation test, carried out right after the end of calcination. The final carbonation degree was 55% after a total reaction time of 1.5h at 550-600°C. This results are in line with similar experiments carried out with Sardinian limestone [9].

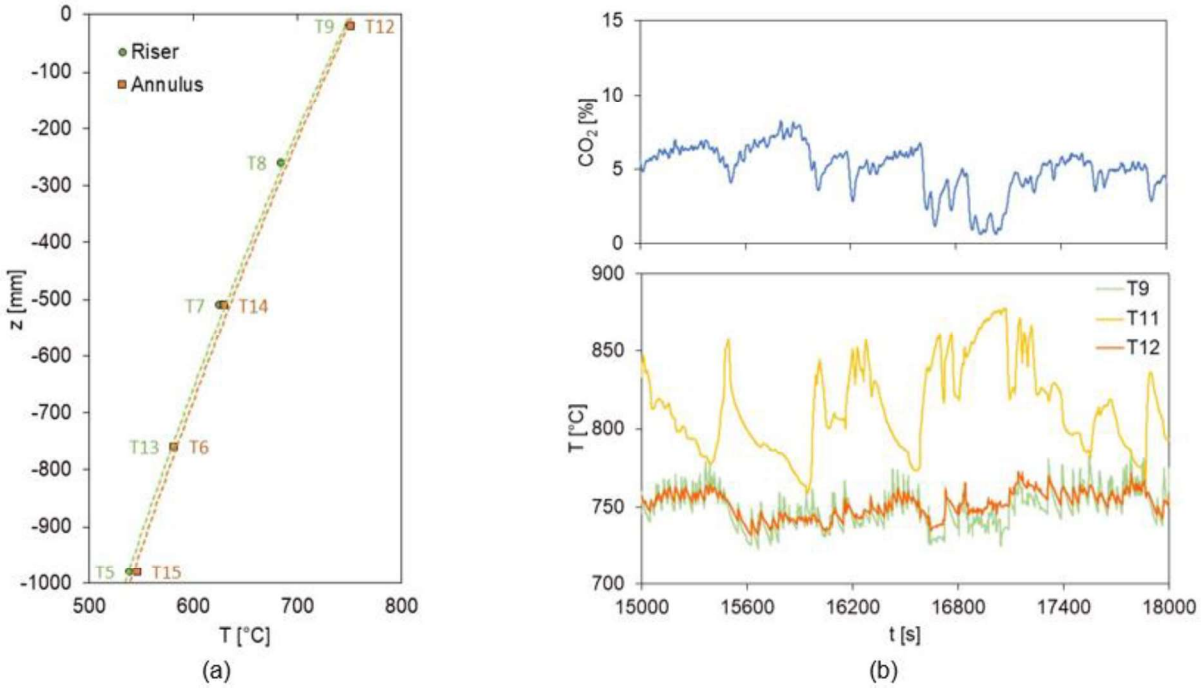

Figure 3. Calcination results: (a) temperature profile of the internal heat exchanger, (b) CO_2 outlet concentration and receiver temperatures.

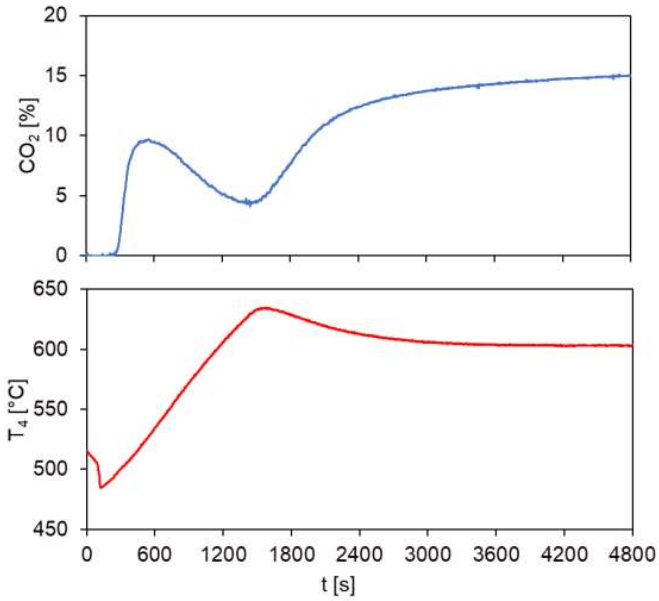

Figure 4. Carbonation results: CO_2 outlet concentration and reservoir temperature.

Conclusions

Altogether these experiments show the potentiality of the DIFBAR as a solar reactor and its key operating variables. In particular the results highlighted that the calcarenite is a valid material for TCES with results comparable to limestone and that mixing it with black proppants is a viable strategy to compensate its poor absorptivity in a directly irradiated reactor. Next experiments will scrutinize the effect of the mass ratio of the solids mixture.

Acknowledgements
The study has been supported by the Ministry of University and Research (MUR) - Italy, in the frame of the project PRIN 2022 PNRR – P202224CPL - REchargeable THErmochemical Energy Battery for Energy Storage from renewable sources (reThebes).

References

[1] Merchán, R.P., Santos, M.J., Medina, A., Calvo Hernández, A., "High temperature central tower plants for concentrated solar power: 2021 overview", *Renewable and Sustainable Energy Reviews* 155: 111828 (2022).
[2] Nathan, G.J., Lee, L., Ingenhoven, P., Tian, Z., Sun, Z., Chinnici, A., Jafarian, M., Ashman, P., Potter, D., Saw, W. "Pathways to the use of concentrated solar heat for high temperature industrial processes", *Solar Compass* 5: 100036 (2023).
[3] Yadav, D., Banerjee, R., "A review of solar thermochemical processes", *Renewable and Sustainable Energy Reviews*, 54: 497-532, (2016).
[4] Prieto, C., Cooper, P., Inés Fernández, A., Cabeza, L.F., "Review of technology: Thermochemical energy storage for concentrated solar power plants", *Renewable and Sustainable Energy Reviews*, 60: 909-929, (2016).
[5] Alvarez Rivero, M., Rodrigues, D., Pinheiro, C.I.C., Cardoso, J.P., Mendes, L.F., "Solid–gas reactors driven by concentrated solar energy with potential application to calcium looping: A comparative review", *Renewable and Sustainable Energy Reviews*, 158: 112048, (2022).
[6] Tregambi, C., Troiano, M., Montagnaro, F., Solimene, R., Salatino, P., "Fluidized Beds for Concentrated Solar Thermal Technologies—A Review", *Front Energy Res*, 9: 618421, (2021).
[7] Tregambi, C., Padula, S., Galbusieri, M., Coppola, G., Montagnaro, F., Salatino, P., Troiano, M., Solimene, R., "Directly irradiated fluidized bed reactor for thermochemical energy storage and solar fuels production", *Powder Technol*, 366: 460–469, (2020).
[8] Padula, S., Troiano, M., Tregambi, C., Solimene, R., Salatino, P., "Directly irradiated fluidized bed autothermal reactor (DIFBAR): Hydrodynamics, thermal behaviour and preliminary reactive tests", *Fuel*, 346: 128222, (2023).
[9] Padula, S., Troiano, M., Tregambi, C., Solimene, R., Salatino, P., "Experimental investigation of Directly Irradiated Fluidized Bed Autothermal Reactor (DIFBAR) for thermochemical processes", *Powder Technology*, under review.

Evaporation and Combustion of Suspended Droplets with Buoyancy-Driven Flows

E. Cipriano*, A. Frassoldati*, T. Faravelli, A. Cuoci
edoardo.cipriano@polimi.it
*CRECK Modeling Lab, Department of Chemistry, Materials, and Chemical Engineering "G. Natta", Politecnico di Milano, Piazza Leonardo da Vinci, 32, Milano, 20133, Italy

Abstract
Numerical models for droplet combustion typically assume spherical symmetry, simplifying the fluid dynamics in favor of a detailed description of the combustion chemistry. This study relaxes that hypothesis by presenting a comprehensive numerical framework that includes: i) interface-resolved evaporation; ii) surface tension effects; iii) complex gas-phase kinetics; iv) radiation. This model employs the volume-of-fluid approach for the description of the two-phase system, and it enables the description of deformable droplets, in motion or suspended on a solid fiber. Despite the increased computational time, this model can directly resolve multidimensional phenomena, such as buoyancy-driven flows, droplet deformation, liquid internal recirculation, and non-spherical flames. This research helps to improve our understanding of droplet combustion dynamics, and it can be used to correct predictions from simplified models, accounting for multidimensional fluid dynamics phenomena.

Introduction
Alternative liquid fuels are recently studied as possible alternatives to fossil fuels. To deepen our understanding of the combustion of alternative liquid fuels we must combine the experimental investigation with mathematical models able to predict the correct consumption dynamics of fuel droplets. This work proposes a comprehensive numerical model that can simulate phase change in a gas-liquid system, assuming low Mach number, constant ambient pressure, subcritical conditions, and variable thermodynamic and transport properties. The resulting model is used to simulate isolated droplets suspended on a solid fiber at different gravity conditions. This configuration, widely used in experimental works, helps to simplify the spray combustion problem by neglecting the interactions between different droplets, and by focusing on the evaporation and combustion characteristics of a single droplet. The big novelty with respect to the previous literature works is that, in this study, we pursue the direct solution of the multidimensional system without relying on sub-grid-scale correlations.

Governing Equations
The control volume over which the system of equations is solved comprises two immiscible phases separated by a zero-thickness interface. The characteristic

function H is used to distinguish between the two phases:

$$H(\boldsymbol{x},t)=\begin{cases}1 & \text{if liquid phase}\\ 0 & \text{if gas phase}\end{cases} \tag{1}$$

where $\boldsymbol{x}$ is the space coordinate, while t is the generic simulation time.
The transport of the gas-liquid interface obeys the equation [1]:

$$\frac{DH}{Dt}=\frac{\partial H}{\partial t}+\boldsymbol{u}_{\boldsymbol{\Gamma}}\cdot\nabla H=0 \tag{2}$$

where $\boldsymbol{u}_{\boldsymbol{\Gamma}}$ is the interfacial velocity. The governing equations for each phase derive from a set of conservation laws on mass, momentum, chemical species, and mass fractions [2]:

$$\nabla\cdot\boldsymbol{u}=\beta\frac{DT}{Dt}+M\sum_{i=1}^{NS}\frac{1}{M_i}\frac{D\omega_i}{Dt} \tag{3}$$

$$\rho\frac{D\boldsymbol{u}}{Dt}=-\nabla\cdot\boldsymbol{\tau}-\nabla p_d-\boldsymbol{g}\cdot\boldsymbol{x}\nabla\rho \tag{4}$$

$$\rho\frac{D\omega}{Dt}=-\nabla\cdot\boldsymbol{j_i}+r_iM_i \tag{5}$$

$$\rho Cp\frac{DT}{Dt}=-\nabla\cdot\boldsymbol{q}-\left(\sum_{i=1}^{NS}Cp_i\boldsymbol{j_i}\right)\cdot\nabla T+\dot{Q}_r+\nabla\cdot\dot{\boldsymbol{q}}_{rad} \tag{6}$$

which are solved for the velocity $\boldsymbol{u}$, pressure p, temperature T, and chemical species mass fractions ω_i, while the density ρ is updated using an Equation of State. According to the low-Mach formulation, the pressure gradients in the continuity equation are neglected with respect to the expansion due to temperature and composition changes. The term β is the thermal expansion coefficient, while M and M_i are the molecular weight of the mixture and of the chemical species i, respectively. The viscous stress tensor in the momentum equation is computed by neglecting the compressible part: $\boldsymbol{\tau}=-\mu(\nabla u+(\nabla u)^T)$ where μ is the dynamic viscosity. The pressure is linked to the dynamic pressure p_d by the hydrostatic contribution: $p_d=p-\rho\boldsymbol{g}\cdot\boldsymbol{x}$, with $\boldsymbol{g}$ the gravitational acceleration. Eq. (5) comprises the diffusive fluxes, computed using Fick's law, and the reaction rate r_i. The temperature equation (6) includes the heat conduction term $\boldsymbol{q}$, calculated using Fourier's law, the enthalpy changes due to the chemical species diffusion, where Cp is the heat capacity, the heat of reaction $\dot{Q}_r$ and the radiation heat fluxes $\dot{q}_{rad}$. In this work we neglect the heat transfer between the solid suspender and the gas-liquid system. Therefore, the only effect of the solid fiber that we consider is the droplet suspension by the action of the surface tension force.

Equations (3-6) are valid in the gas and in the liquid phase separately, but they must

be coupled with appropriate gas-liquid interface boundary conditions, obtained by integrating Eq. (3-6) across a portion of the interface. Introducing the jump notation for a generic variable: $[\phi] = \phi_l - \phi_g$ the following set of jump conditions is obtained [3]:

$$[\boldsymbol{u}]_\Gamma \cdot \boldsymbol{n}_\Gamma = \dot{m}[1/\rho]_\Gamma \tag{7}$$

$$[p]_\Gamma = \sigma\kappa - \dot{m}[\boldsymbol{u}]_\Gamma \cdot \boldsymbol{n}_\Gamma + [\boldsymbol{\tau} \cdot \boldsymbol{n}_\Gamma]_\Gamma \cdot \boldsymbol{n}_\Gamma \tag{8}$$

$$[\rho(\boldsymbol{u} - \boldsymbol{u}_\Gamma) \cdot \boldsymbol{n}_\Gamma]_\Gamma = 0 \tag{9}$$

$$[\rho\omega_i(\boldsymbol{u} - \boldsymbol{u}_\Gamma) \cdot \boldsymbol{n}_\Gamma + \boldsymbol{j}_i \cdot \boldsymbol{n}_\Gamma]_\Gamma = 0 \tag{10}$$

$$[\lambda\nabla T \cdot \boldsymbol{n}_\Gamma]_\Gamma = \sum_{i=1}^{NS} \dot{m}\Delta h_{ev,i} + \epsilon\sigma_{SB}(T_\infty^4 - T_\Gamma^4) \tag{11}$$

which is solved to obtain every information about the interface: vaporization rate $\dot{m}$ for each chemical species, interface temperature, mass fractions, and mole fractions. The velocity jump is due to the Stefan flow contribution, the pressure jump includes the surface tension force, where σ is the surface tension coefficient, while κ is the interface curvature. The terms n_Γ and t_Γ indicate the interface normal and tangential vectors, respectively. The interface enthalpy balance (Equation 11) includes the interface radiation term, where ϵ is the emissivity, σ_{SB} is the Stefan-Boltzmann constant, while T_∞ is the gas phase bulk temperature.
The interface is assumed to be at thermodynamic equilibrium conditions, and therefore, the system of jump conditions is closed by including the vapor-liquid equilibrium relationships, which expresses the continuity of the chemical species fugacity f_i and of the temperature across the interface.

$$[f_i]_\Gamma = 0 \tag{13}$$

$$[T]_\Gamma = 0 \tag{14}$$

In this work, Raoult's law is used for the VLE, assuming an ideal liquid mixture, an ideal gas mixture, and negligible Poynting correction.

Numerical Discretization

The set of equations described in the previous section is integrated using the Finite Volume Method on adaptive Cartesian grids, using quad/octree discretization [4]. The transport of the interface is performed using the geometric Volume-of-Fluid approach [3], which discretizes Eq. (2) by keeping the sharp nature of the characteristic function taking advantage of the planar interface reconstruction. The jump conditions (7-11) are introduced into the governing equations (3-6) using the Whole Domain Formulation [3], by expressing them as source terms localized at the gas-liquid interface. Details about the numerical methods for solving the

incompressible multicomponent phase change equations are reported in Cipriano et al. [5], whose model is extended in this work by including variable thermodynamic and transport properties, low-Mach compressibility effects, and chemical reactions.

Results: Droplet Evaporation

The model presented in this work was validated with pure evaporation cases by comparing our simulation results with experimental data and with a well-validated 1D model that assumes spherical symmetry [6].

The first test case is the evaporation of a n-heptane droplet in microgravity at different pressure (1, 5, 10, 20 atm) and temperature (~450, 550, 650, 750 K) conditions. The initial droplet diameter is 0.7 mm, and the simulation is performed by exploiting the axial symmetry. Fig. 1 shows the trend of the square droplet diameter in time. We notice that our model and the 1D model are in excellent agreement at every operative condition. However, there is a delay between the numerical results and the experimental data which increases with pressure, and which is more evident for lower temperature conditions.

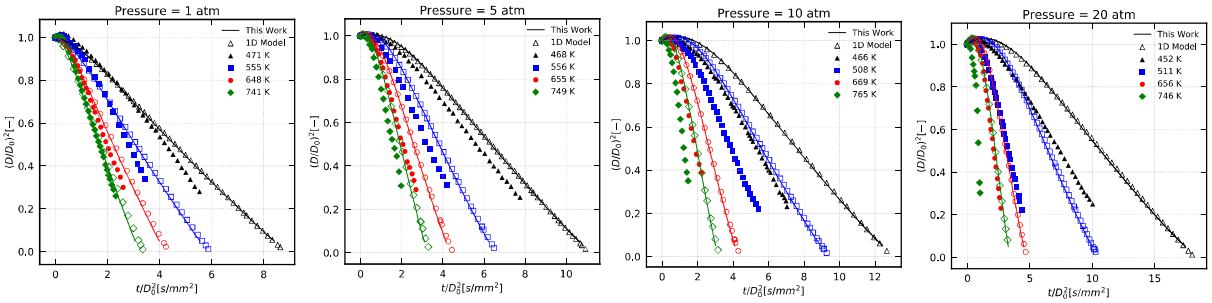

Figure 1: Square diameter decay in time for n-heptane droplet evaporation in microgravity.

The ability of our model to resolve droplets at different gravity conditions is exploited to explain the discrepancies between the numerical models and the experiments. To this purpose, we re-simulate the Nomura et. al [7] droplets at different gravity values: $1/100\boldsymbol{g}$, $1/10\boldsymbol{g}$, $1\boldsymbol{g}$, where $\boldsymbol{g}$ is the Earth's normal gravity value, where the value of $1/100\boldsymbol{g}$ is the residual gravity measured by [7] for the parabolic flight experiments. Fig. 2 shows that the introduction of gravity shifts the numerical results toward the experimental data, with more intensity at high pressure and low temperature, in agreement with the functional dependency of the Grashof number, which measures the importance of the natural convective fluxes.

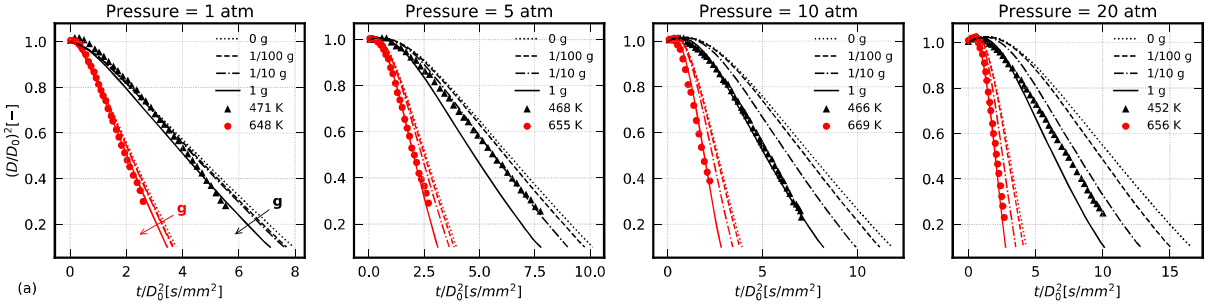

Figure 2: Effect of the residual gravity on the evaporation of n-heptane droplets.

The effects of the interface radiation and of the heat conduction from the solid fiber on Nomura et al. [7] droplets have already been studied by other authors. However, those studies cannot explain the pressure dependency of the gap between the experimental data and the numerical results, which was highlighted for the first time in this work using direct numerical simulations.
The evaporation of droplets in normal gravity conditions was validated by comparing our model with experimental data [8]. This test case considers n-decane droplets with different initial diameters (0.4, 0.52, 0.6, 0.7 mm), at ambient temperature 773 K, droplet initial temperature 328 K, at pressures 1 and 5 atm. Fig. 3 shows that our model captures the same trends of the experimental data for the droplet consumption rate at different initial diameters.

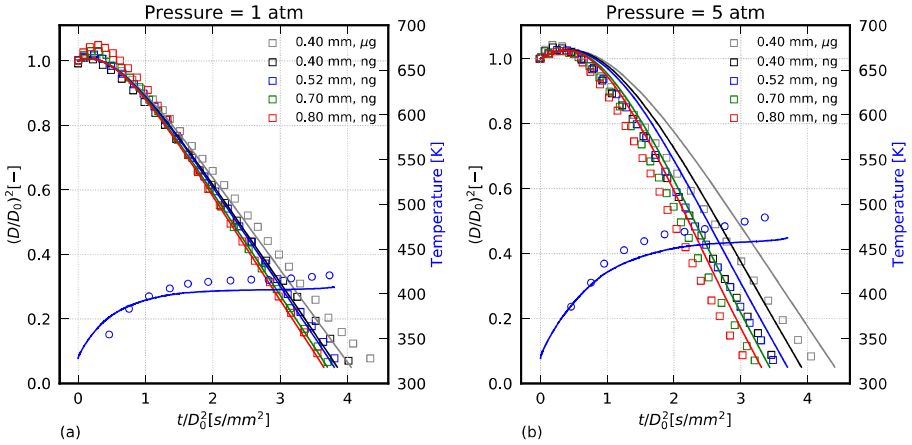

Figure 3: Square diameter decay in time for n-decane droplet evaporation in normal gravity.

Results: Droplet Combustion

The same study on the influence of pressure and buoyancy on the droplet consumption rate should be performed with combustion cases. Such study can highlight the different burning rates of droplets in microgravity and in normal gravity conditions, at different ambient temperatures and pressures. The results from this study are useful to obtain expressions and correlations that correct 0D and 1D models that cannot directly solve multidimensional phenomena. In this test case, we considered the combustion of methanol droplets at different pressures (5, 10, 15 atm), with an initial diameter of 0.5 mm. Fig. 4 reports the square droplet diameter in time from our model, both in microgravity and in normal gravity conditions. The comparison with OpenSMOKE++ shows a displacement that require further investigation, but both models show the same physical trend: in microgravity the burning rates of the droplets increases with increasing ambient pressure. In normal gravity conditions this effect is magnified, and the consumption of the droplets is strongly increased because of natural convective fluxes and because of the different flame position and geometry.

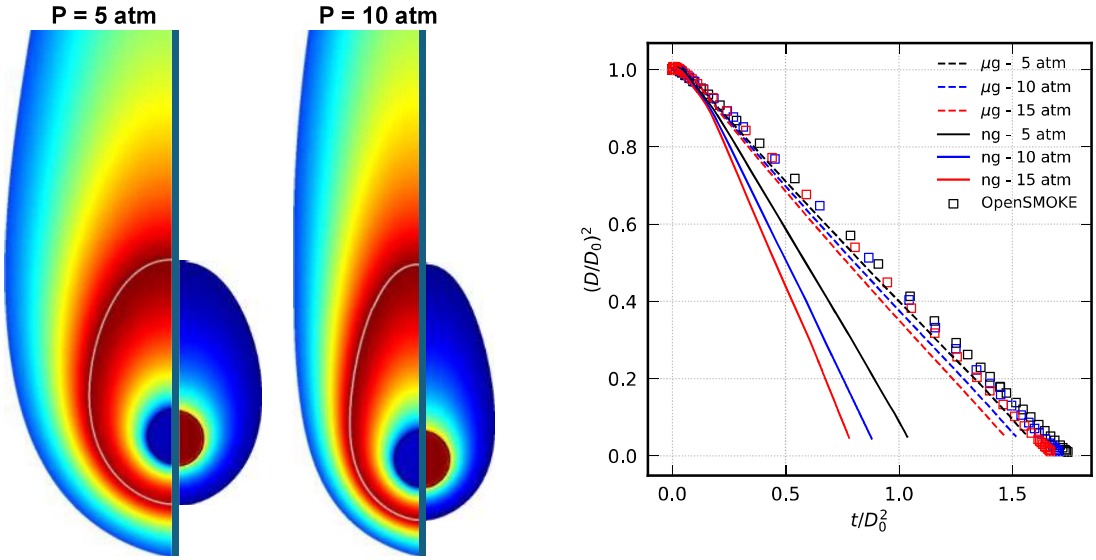

Figure 4: Maps of the temperature and fuel mass fraction (left); square diameter decay for the methanol combustion in microgravity and in normal gravity conditions (right).

References

[1] Drew, D.A., "Mathematical modeling of two-phase flow", *Annual review of fluid mechanics* 15: 261-291 (1983)

[2] Pember, R. B., Howell, L. H., Bell, J. B., Colella, P., Crutchfield, W. Y., Fiveland, W. A., & Jessee, J. P., "An adaptive projection method for unsteady, low-Mach number combustion", *Combustion Science and Technology* 140: 123-168 (1998)

[3] Scardovelli, R., & Zaleski, S., "Direct numerical simulation of free-surface and interfacial flow", *Annual review of fluid mechanics* 31: 567-603 (1999)

[4] Popinet, S., "Gerris: a tree-based adaptive solver for the incompressible Euler equations in complex geometries", *Journal of computational physics* 190: 572-600 (2003)

[5] Cipriano, E., Frassoldati, A., Faravelli, T., Popinet, S., & Cuoci, A., "Multicomponent droplet evaporation in a geometric volume-of-fluid framework", *Journal of computational physics* 507 (2024)

[6] Cuoci, A., Mehl, M., Buzzi-Ferraris, G., Faravelli, T., Manca, D., & Ranzi, E., "Autoignition and burning rates of fuel droplets under microgravity", *Combustion and Flame* 143:211-226 (2005)

[7] Nomura, H., Ujiie, Y., Rath, H. J., Sato, J. I., & Kono, M., "Experimental study on high-pressure droplet evaporation using microgravity conditions", *Proc. Comb. Inst.* 26:1267-1273 (1996).

[8] Murakami, Y., Nomura, H., & Suganuma, Y., "Experimental study on unsteadiness of n-decane single droplet evaporation and effect of natural convection on droplet evaporation at high pressures and temperatures", *Transactions of the japan society for aeronautical and space sciences, aerospace technology japan,* 19:647-653 (1996).

Bio-crude production and inorganics elements distribution during the hydrothermal liquefaction of tannery sludge

F. Di Lauro*, G. Marotta, M. Balsamo**, F. Montagnaro**, P. Salatino*, R. Solimene*****

* Dipartimento di Ingegneria Chimica, dei Materiali e della Produzione Industriale, Università degli Studi di Napoli Federico II, Piazzale Vincenzo Tecchio 80, 80125, Napoli, Italy.
** Dipartimento di Scienze Chimiche, Università degli Studi di Napoli Federico II, Complesso Universitario di Monte Sant'Angelo, 80126, Napoli, Italy.
***Istituto di Scienze e Tecnologie per l'Energia e la Mobilità Sostenibili, Consiglio Nazionale delle Ricerche, Sede Secondaria, Piazzale V. Tecchio 80, 80125, Napoli, Italy.

e-mail of the corresponding author: giusy.marotta@unina.it

Abstract
Tannery sludge (TS) is the major waste in leather industry. The wastewater treatment of tanning plants produces large amounts of sludge contaminated with chromium, which disposal is a hard issue to deal. In this context, hydrothermal liquefaction (HTL) is an innovative thermochemical process to convert contaminated biomasses into bio-fuels. In this study, a tannery sludge was chosen as substrate to perform the HTL process. The HTL tests were carried out in a 500 mL batch reactor for different reaction times (0–10 min) and temperatures (250°C, 275°C, 300°C and 350°C). Results proved that under the best operating conditions (350ºC and 10 min) it is possible to obtain a bio-crude yield (on dry and ash-free basis) of 29.5% with an associated energy recovery of 44.1% (higher heating value of 36.1 MJ/kg). ICP-MS analysis of the three HTL products (bio-crude, aqueous phase and solid residue), showed that the inorganic elements are mainly concentrated in the solid residue. Finally, UV-vis analysis of Cr showed that it is present in reaction products in its trivalent form, thus demonstrated that HTL, in this study at least, avoids the undesired oxidation of Cr(III) to Cr(VI).

Introduction
About 6.9 Gt/year of raw leathers are produced worldwide [1], with a considerable release into the environment of hazardous sewage sludge, contaminated by heavy metals. In particular, basic chromium (III) sulphate salt is used as a tanning agent. However, only 60% of the total amount of chromium is effectively used during the tanning process, binding with animal skin collagen. The rest of chromium remains in the tanning bath and is subsequently discharged into the wastewater, whose treatment produces the tannery sludge [2]. Therefore, new routes for the valorization

of these contaminated waste must be identified to achieve a more sustainable production of leathers. In this context, hydrothermal liquefaction (HTL) represents an emerging process for the energy valorization of tannery sludge, by converting it into liquid bio-fuels and avoiding the high-energy demanding dehydration step commonly associated with conventional thermochemical processes [3]. Indeed, HTL is generally carried out in a hot, pressurised water environment (200–375°C and 40–200 bar) for sufficient time to convert the organic matter of the tannery sludge (TS) into bio-crude as target product, together with gas and aqueous phases, and a solid residue as co-products [4]. Moreover, not aiming at the complete oxidation of the organic component, HTL process potentially limits the oxidation of Cr in its more harmful hexavalent form. In this study, a tannery sludge was adopted as substrate for the HTL process to produce bio-crude. HTL tests were carried out in a 500 mL batch apparatus for reaction times ranging from 0 to 60 min and temperatures of 250, 275, 300°C and 350°C, also to assess the possible formation of bio-crude during the thermal transients. Bio-crude samples obtained under the best operating conditions, were also chemically and energetically characterized by proximate and ultimate analysis and Mahler bomb calorimeter. Moreover, the distribution of inorganic elements (with particular reference to heavy metals) in the different HTL products was assessed by ICP-MS analysis. Lastly, the distribution and speciation of chromium in the HTL products was studied by UV-vis analysis.

Tannery sludge

Chromium-rich industrial sludge from a tanning wastewater treatment plant was used as a substrate to perform HTL tests. By proximate analysis, TS consists of 18.46% moisture, 50.13% volatile material and 31.41% ash, while no fixed carbon was detected. Moreover, a total C content of 33.61% was detected by ultimate analysis, along with 5.10% H, 2.44% N and 4.07% S, and a Cl content equal to 0.35% on dry basis. The high percentage of S is due to high amount of sulfates used in the tanning process (about five times higher on dry basis than S content of a municipal sludge, as reported in [5]). Regarding the energy properties of TS, on a dry basis, the average value of higher heating value HHV is 14.90 MJ/ kg. Lastly, the metal content of TS, on dry basis, was obtained by inductively coupled plasma-mass spectrometry (ICP-MS), according to which Ca is the most abundant metal, with a concentration of 49.64 g/kg, followed by Fe (24.77 g/kg), Cr (22.52 g/kg), Si (8.74 g/kg), Al (4.77 g/kg), Na (4.32 g/kg), Zn (1.16 g/kg) and Mg (1.01 g/kg). The Cr(total) content obtained by atomic absorption spectroscopy is about 25.38 g/kg on dry basis, while no Cr(VI) was detected in the sludge by UV-vis analysis.

Experimental apparatus for HTL and products separation procedure

The HTL tests were performed in a 500 mL batch autoclave reactor [6] equipped with a pressure measurement and control system, an internal loop coil to ensure the fast cooling of the system, a magnetic stirrer, a tubular electric heater surrounding the reactor coupled with a thermocouple and PID systems for the temperature setting

and measurement. A layer of rock wool and a band heater, respectively on the top and the bottom of the reactor, were used to optimize the thermal transient. More details on reactor configuration are reported in our previous work [7]. Briefly, the reactor was loaded with a slurry of 10%$_{wt}$ biomass content, consisting of 30 g (on dry basis) of parent sludge, together with distillated water, after which the head space of reactor was purged with N_2. Then, the system is pressurized to obtain a pressure of about 200 bar at the temperature selected for the reaction. HTL tests were conducted at temperatures (T) of 300 °C and 350 °C, and for isothermal residence times (t) ranging from 10 to 60 min. Moreover, the possible formation of bio-crude during the thermal transients was assessed by stopping heating as soon as the reactor reached a temperature of 250°C, 275°C, 300°C and 350°C. After the HTL test, the solid-liquid mixture recovered from the reactor was filtered on a Büchner under vacuum. The solid phase was subjected to a Soxhlet extraction with dichloromethane (DCM) to recover the bio-crude from the pores of solid, and then oven-dried at 105°C for 24 h. The bio-crude fraction extracted from DCM was recovered for subsequent distillation. The liquid fraction was separated into bio-crude and aqueous phase by centrifugation for 10 min at 4000 rpm using a NEYA BASIC ventilated apparatus. The bio-oil was recovered using 20 g of DCM and mixed with the bio-crude fraction extracted from DCM by Soxhlet procedure. Finally, the bio-crude was distilled under vacuum distillation at 0.4 bar to get the evaporation of the solvent. Finally, the yield of the products was calculated as the mass of product obtained compared to that of sludge loaded (on a dry basis). Moreover, after the separation protocol, the bio-crude samples were subjected to a Mahler bomb calorimeter for the HHV determination, and the energy recovery (ER) was estimated according to the following equation:

$$ER = \frac{\mathrm{HHV}_{bio-crude}}{\mathrm{HHV}_{biomass}} Y^{db}_{bio-crude}$$

Results and discussion

Figure 1 shows the yields on dry basis of bio-crude (a), water-soluble compounds (b), solid residue (c) and gas phase (d) at different reaction times as a function of the operating temperature. For both the temperatures investigated of 300°C and 350°C, the yield of HTL products remains almost constant, showing that the effect of the isothermal reaction time is negligible. In detail, for the test carried out at 350ºC, the bio-crude yield slightly increases from 0 to 10 min (18.2%), remains about constant until 40 min and then decreases to 60 min (15.8%), probably due to the reactions of polymerization/cracking of the bio-crude for long reaction times with the consequent increase in the yields of the solid residue and gas phase from 40 to 60 min. A similar trend, shifted to longer times, was obtained for tests carried out at 300°C. The yield of bio-crude slightly increases from 0 to 30 min (17.1%), remains constant up to 50 min and then decreases to 60 min (15.4%). In addition, the yield of the solid residue between 0 and 60 min decreases slightly from 61.18% to 56.77% and from 54.70% to 52.91%, respectively at 300 and 350°C. Lastly, the yield of the gas phase does not follow a clear, with a slight increasing trend from 1.6% to 6.5% at 300°C and from

3.9% to 8.1% at 350°C. The bio-crude samples with the maximum yield, (29.5% at 350°C–10min and 27.8% at 300°C–30min on dry and ash-free basis), were chemically and energetically characterized. Similar HHV values were obtained for both samples (36.1 MJ/kg at 350°C and 35.5 MJ/kg at 300°C); while the slight difference in *ER* (44.1% at 350°C and 41% at 300°C) is determined by the slightly higher yield of the bio-crude obtained at 350°C. About the chemical composition, Cl content of samples is one order of magnitude lower than its concentration in the starting biomass (0.001% at 350°C and 0.028% at 300°C, on dry basis). The S content in the bio-crude is similar to the one detected in the parent sludge (3.32% at 350°C and 3.34% at 300°C, on dry basis). The high S content in the bio-crude can be ascribed to the presence of basic chromium sulphates which are used in tanning process.

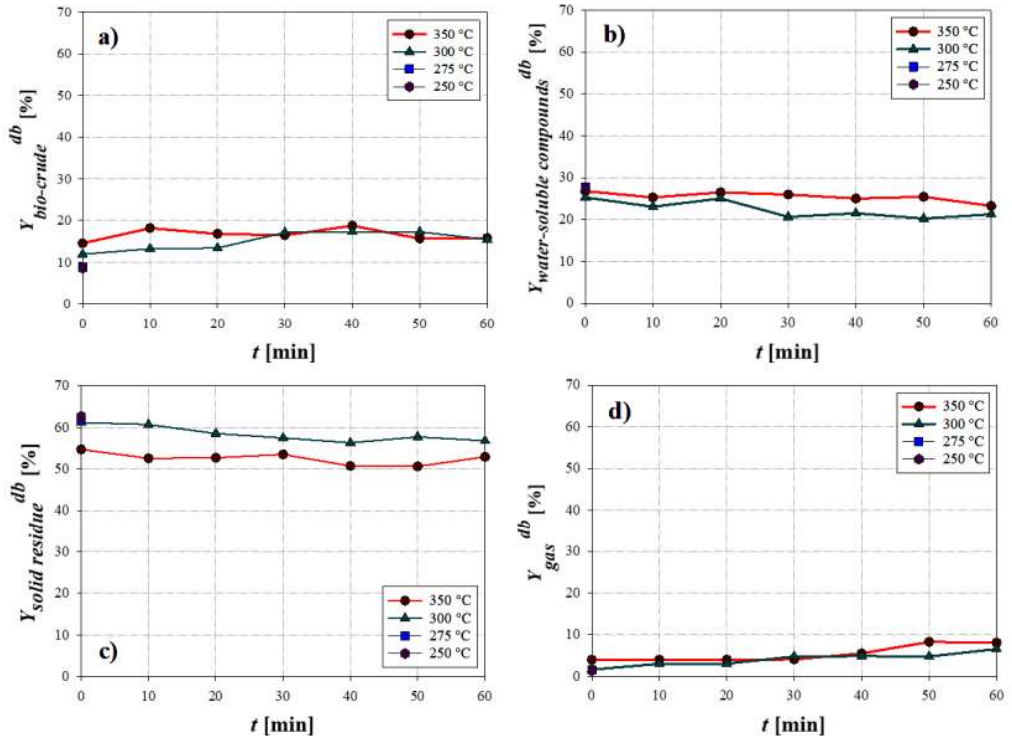

Fig. 1. Yield of a) bio-crude b) water-soluble compounds c) solid residue and d) gas yields as a function of time and for different temperature.

Table 1 shows the distribution of inorganic elements in the three HTL products. The investigated elements are mainly concentrated in the solid residue, while some of them are found in traces in the bio-crude and in the aqueous phase. In detail, Ca is the most abundant in the solid residue, followed by Fe and Cr. About the Cr distribution in the HTL products, solid residue has a Cr content of 29.0 g/kg at 300°C and 45.87 g/kg at 350°C, and it is almost all the Cr of the parent sludge. Cr in the solid residue is two orders of magnitude higher than that of the bio-crude (0.15 g/kg at 300°C and 0.14 g/kg at 350°C) and four orders of magnitude higher than that of the aqueous phase (0.004 g/kg at 300°C and 0.00044 g/kg at 350°C). However, even if at very low concentration, the presence of Cr, as well as of Fe, found in both bio-crude samples could require additional metals removal techniques. The speciation of

Cr during the HTL process was assessed by UV-vis analysis of the HTL products for the best operating condition in terms of bio-crude yield (350°C–10min). Results show that, the Cr(VI) content was not detected by UV-vis analysis in all HTL products. This result confirms the potential use of TS in the HTL process, avoiding the problem of Cr oxidation found in other thermochemical processes (i.e. combustion, gasification).

Table 1. ICP-MS analysis for solid residue (SR), bio-crude (BC) and aqueous phase (AP) obtained in TS hydrothermal liquefaction tests, (not detection, n.d.).

Element	SR-300-30 [g/kg]	SR-350-10 [g/kg]	BC-300-30 [g/kg]	BC-350-10 [g/kg]	AP-300-30 [g/kg]	AP-350-10 [g/kg]
B	0.012	n.d.	n.d.	n.d.	n.d.	n.d.
Na	1.50	1.61	n.d.	0.041	0.84	1.06
Mg	3.71	2.70	n.d.	n.d.	n.d.	0.0058
Al	13.53	24.29	0.027	0.48	0.0017	0.00051
P	17.23	7.96	0.0027	0.012	0.021	0.0014
K	0.68	0.23	n.d.	n.d.	0.14	0.050
Ca	92.86	78.49	0.050	0.049	0.25	0.032
Ti	0.003	0.004	n.d.	n.d.	n.d.	n.d.
V	0.030	0.037	0.0062	0.0067	0.00054	0.00054
Cr	29.00	45.87	0.15	0.14	0.0040	0.00044
Mn	0.28	0.015	n.d.	n.d.	n.d.	n.d.
Fe	40.92	54.15	1.12	1.18	0.00049	n.d.
Co	0.010	0.012	0.00002	n.d.	n.d.	n.d.
Ni	0.099	0.051	0.0064	n.d.	n.d.	n.d.
Cu	0.20	0.13	n.d.	n.d.	n.d.	n.d.
Zn	1.18	3.58	n.d.	n.d.	n.d.	n.d.
As	0.054	0.012	0.0022	n.d.	0.00040	0.00012
Zr	0.0001	0.0021	n.d.	n.d.	n.d.	n.d.
Mo	0.0004	0.0032	n.d.	n.d.	n.d.	n.d.
Ba	0.57	0.067	0.00023	0.0012	0.00055	0.00032
Pb	0.043	0.045	n.d.	n.d.	n.d.	n.d.

Conclusion

Tanning industry annually produces a large amount of sludge, contaminated mainly with chromium compounds. The disposal of this hazardous waste in landfill leads to high management costs and secondary pollution issues. A sustainable development means the identification of new technologies for the valorization of the heavy metals contaminated biomasses, as tannery sludge. To this end, the hydrothermal liquefaction process was applied to a tannery sludge to produce an energy vector. The HTL tests were carried out in a 500 mL batch reactor for different reaction times and temperatures, proving that in the best operating conditions (350ºC and 10 min) it is possible to obtain a bio-crude yield (on a dry and ash-free basis) of 29.5% with an associated energy recovery of 44.1% (HHV of 36.1 MJ/kg). The distribution of inorganic elements in the three HTL products, obtained through ICP-MS analysis, showed that the elements are mainly concentrated in the solid residue, with values

up to 4 orders of magnitude higher than those shown in the bio-crude and aqueous phase. Finally, UV-vis analysis of Cr showed that it is present in reaction products in its trivalent form, demonstrating that HTL under the adopted conditions did not oxidize Cr(III) in its more harmful hexavalent state.

Acknowledgments

The authors acknowledge funding from the project funded under the National Recovery and Resilience Plan (NRRP), Mission 4 Component 2 Investment 1.3 - Call for tender No. 1561 of 11.10.2022 of Ministero dell'Università e della Ricerca (MUR); funded by the European Union – NextGenerationEU. Project code PE0000021, Concession Decree No. 1561 of 11.10.2022 adopted by Ministero dell'Università e della Ricerca (MUR), CUP – E63C22002160007, Project title "Network 4 Energy Sustainable Transition – NEST". Part of the research activities carried out in the framework of the Programma per il Finanziamento della Ricerca di Ateneo (FRA) 2022 of the University of Naples Federico II (Project "Eco-sustainable Production of bIofuels from the Conversion of sludges through hydrothermal liquefaction" (EPIC)).

References

[1] Zhuo Y., Chen Z., Gong H., and Yang Z., “Chromium speciation in tannery sludge residues after different thermal decomposition processes”. J. Clean. Prod. 314 (2021) 128071.

[2] Kavourasa P., Pantazopoulou E., Varitis S., Chrissafis K., Dimitrakopulos G.P., Mitrakas M., Zouboulis A.I. Karakostas Th., and Xenidis A., “Incineration of tannery sludge under oxic and anoxic conditions: Study of chromium speciation”. J. Hazard. Mater. 283 (2015) 672–679.

[3] Wang K., and Tester J.W., “Sustainable management of unavoidable biomass wastes”. Green Energy and Resources. 1 (2023) 100005.

[4] Basar I.A., Liu H., Carrere H., Trablyb E., and Eskicioglu C., “A review on key design and operational parameters to optimize and develop hydrothermal liquefaction of biomass for biorefinery applications”. Green Chem. 23 (2021) 1404–1446.

[5] Di Lauro F., Balsamo M., Solimene R., Alfieri M.L., Manini P., Migliaccio R., Salatino P., and Montagnaro F., “Characterization of Biocrude Produced by Hydrothermal Liquefaction of Municipal Sewage Sludge in a 500 mL Batch Reactor”. Ind. Eng. Chem. 63 (2024) 995–967.

[6] Di Lauro F., Balsamo M., Solimene R., Salatino P., and Montagnaro F., “Hydrothermal Liquefaction Process to Obtain Sludge-Derived Bio-Fuels: Setup of the Experimental Apparatus and Preliminary Tests”. Chem. Eng. Trans. 92 (2022) 475–480.

[7] Balsamo M., Montagnaro F., Di Lauro F., Salatino P., Solimene R., “Effect of Heating Rate on the Performances of HTL Applied to a Sewage Sludge”. Chem. Eng. Trans. 105 (2023) 313–318.

EFFECT OF NANOSECOND PLASMA DISCHARGE ON IGNITION DELAY TIME OF AMMONIA/AIR MIXTURE

Zubair Ali Shah*, Mingming Zhu, De Giorgi Maria Grazia***
mariagrazia.degiorgi@unisalento.it
*Department of Engineering for Innovation, University of Salento, Via per Monteroni, 73100 Lecce, Italy
**School of Water, Energy and Environment, Cranfield University, College Rd, Wharley End, Bedford MK43 0AL, UK

Abstract
Plasma-assisted ignition and combustion is now a very attractive subject due to its numerous applications in the fields of transportation and power generation using zero-carbon fuels. Plasma discharge can improve combustion by producing a high number of chemically active particles that influence the chemical process. This numerical study investigated the effect of nanosecond plasma discharge on ignition delay time (IDT) of ammonia/air mixture at low and intermediate temperatures (850 - 1100 K) under atmospheric pressure. Employing ZDPlasKin and CHEMKIN codes, coupled with a validated kinetic mechanism, the study aims to assess the combustion enhancement of ammonia by plasma. The results showed that using the 20 pulses plasma discharge, the IDT was reduced from 210.55 s to 3.01 s and the flame temperature increased from 2388.5 K to 2433.1 K at an initial temperature of 850 K and pressure of 1 atm.

Introduction
Among the various greenhouse gases, carbon dioxide (CO_2) emitted from the combustion of fossil fuels is identified as the primary contributor to this global warming trend [1]. Recognizing the urgency of addressing climate change, many countries globally are adopting substantial measures to transit towards cleaner and more sustainable energy sources [2, 3]. Ammonia (NH_3) emerges as a promising solution to address aspects of the impending energy crisis. It has gained considerable attention as a carbon-free fuel and hydrogen carrier. In addition, ammonia enjoys well-established storage and transportation infrastructures, rendering the long-term storage and transport of ammonia a cost-effective solution [4]. While ammonia offers numerous advantages, there are several challenges that must be addressed before its direct utilization in combustion devices like compression ignition (CI) and spark ignition (SI) engines. These challenges include high resistance to autoignition (with an octane number around 130) [5], a narrow flammability range, slow flame speed, NOx emission, and a high latent heat of vaporization. Recent review articles [6,7], contemplate ammonia as a prospective future fuel, acknowledging the need to

navigate and resolve these challenges for its effective integration. Identifying ammonia as a potential future fuel necessitates a comprehensive understanding of its oxidation processes.

The ignition delay time (IDT) stands out as a crucial characteristic in the combustion of fuels within practical energy devices. In the context of NH_3 combustion, it's noteworthy that the high ignition temperature and ignition energy of NH_3 pose limitations on its practical application as a fuel. Therefore, investigating the ignition characteristics of NH_3 and exploring methods to enhance NH_3 ignition is necessary. The present study specifically addresses this challenge by utilizing non-equilibrium plasma. Because plasma discharge has the potential to enhance ignition by generating chemically active particles that influence chemical reaction mechanisms that dominate the ignition process. This numerical investigation focuses on the impact of nanosecond plasma discharge on the IDT of ammonia/air mixtures at low and intermediate temperatures (850-1100 K) under atmospheric pressure.

Numerical Methodology

Numerical modeling has been performed by coupling a zero-dimensional plasma kinetic model (ZDPlasKin) [8] and the chemical kinetic model (CHEMKIN) [9]. ZDPlasKin was used to analyze the nanosecond repetitive pulse discharge and CHEMKIN was used to predict the IDT. The plasma enhancement ignition process is divided into discharge and ignition phases due to the significant difference in the time scales of the two phases. The discharge phase is characterized by the transfer of energy and the activation of neutral particles. A significant number of active particles are created during the plasma discharge phase such as NH_2, NH, H, O, O_3, and OH which are delivered as the active species into the ignition process of the NH_3/air mixture in the ignition stage, simulating the whole process of plasma-enhanced ammonia ignition. Simulations of plasma discharges are performed using the validated Plasma Kinetic Mechanism [11] and modified Mei's ammonia combustion mechanism [12]. Mei's ammonia combustion mechanism is selected because it can accurately capture the laminar flame speeds (S_L) and IDT [12,13] within the experimental uncertainties. Furthermore, the Mei mechanism was discovered to better predict NO than other mechanisms [14]. The rate constants of significant reactions are modified from recent experimental, numerical, and review studies for better performance at low and intermediate temperatures, and O_3 sub-mechanism reactions from ZH Wang et al. [15] are added to the base mechanism. The general methodology can be summarized in Figure 1 using the numerical procedure flowchart.

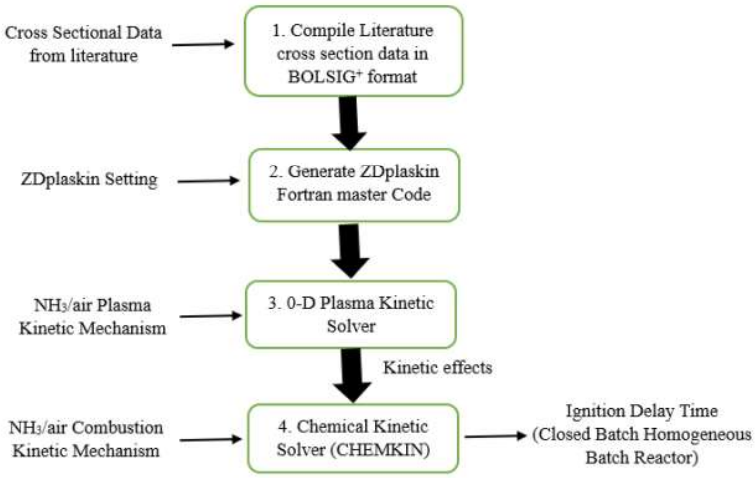

Figure 1. A detailed diagram of the numerical modeling approach with integration of ZDPlasKin and CHEMKIN

Validation

To assess the validity of the updated reaction mechanism used in this investigation, a validation analysis was performed by comparing experimental [16] and numerical data [17-19]. To investigate the IDT of the NH_3/air mixture, different mechanisms were employed in numerical simulations using CHEMKIN [9]. In this study, IDT is defined as the time when the temperature gradient reaches its maximum and the Closed Homogeneous Batch Reactor module was employed to calculate the IDT. Figure 2 highlights that present, Stagni et al. [17] and Han et al. [18] mechanisms have good agreement with the IDT experimental values. However, the mechanisms proposed by Okafor et al. [19] tend to slightly overestimate the experimental values under current conditions.

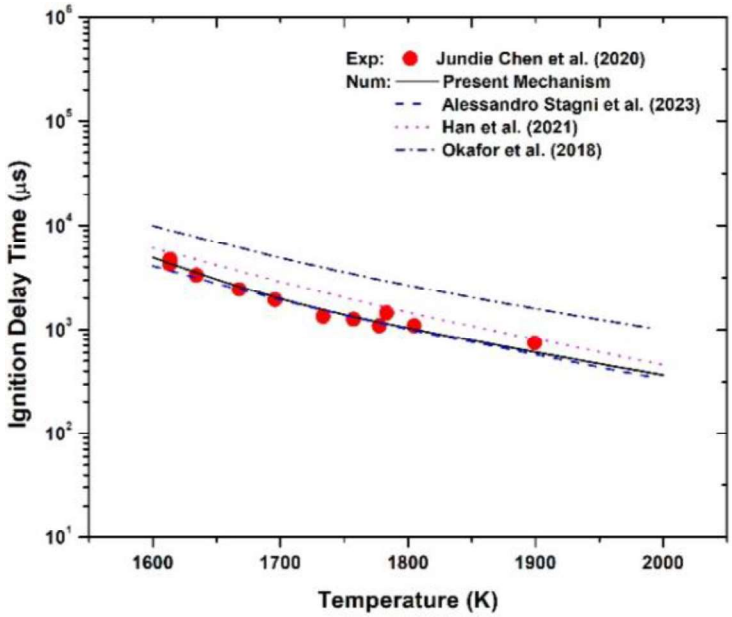

Figure 2. IDTs of $0.04375NH_3/0.03281O_2/0.92344Ar$ mixture as a function of temperature at a pressure of 1.2 atm and $\phi = 1.0$. Symbols represent the experiment data, and lines depict the simulated results of the current and prior models.

Results

The current analysis was conducted to investigate the effect of initial temperature and plasma discharge with 20 sequential pulses by keeping the E/N 180Td constant on IDT and flame temperature of NH_3/air mixture in the range of low and intermediate temperature (850 - 1100 K) under atmospheric pressure. During the plasma discharge active particles (O, H, OH, NH, NH_2, and O_3) presented in Table 1 are generated due to ionization, excitation, dissociation reactions, and recombination of electron-ion reactions.

Table 1. Production of species with 20 sequential pulses of plasma discharge in NH_3/air mixture at, E/N = 180Td, P = 1 atm, ϕ = 1.0 with PRF = 50 kHz used in the CHEMKIN.

Temperature K	Maximum mole fraction of species					
	O	H	OH	NH	NH_2	O_3
850	0.00306	0.00331	0.00127	0.000383	0.00392	2.07513E-5
900	0.00267	0.00283	0.00109	0.000328	0.00336	1.45403E-5
950	0.00230	0.00239	0.000934	0.000278	0.00285	1.01764E-5
1000	0.00198	0.00204	0.000803	0.000237	0.00243	7.09373E-6
1050	0.00170	0.00173	0.000685	0.000201	0.00207	4.87725E-6
1100	0.00145	0.00146	0.000581	0.000170	0.00175	3.25817E-6

The results showed that using the 20 pulses plasma discharge, the IDT was reduced from 210.55 s to 3.01 s and the flame temperature increased from 2388.5 K to 2433.1 K at an initial temperature of 850 K as shown in Figure 2. The ignition delay time of the combustion under the plasma case is significantly shorter and the flame temperature higher than that of the case without plasma, indicating that the excitation of the plasma promotes the reaction and provides new reaction pathways in boosting low-temperature NH_3 ignition.

It can be seen in the NH_3/air mixture, that the initial temperature has a significant influence on the IDT without a plasma case. As the initial temperature increases, the IDT decreases significantly. When the initial temperature increases from 850 K to 1100 K, the ignition delay time is reduced from 210.55 s to 0.36 s and the flame temperature gradually increases from 2388.5 K to 2514.1 K. In the case of plasma, the initial temperature has an insignificant impact on the NH_3/air mixture. The IDT decreases gradually as the initial temperature increases, but the difference is not as significant as that for the case without plasma. As the initial temperature increases from 850 K to 1100 K, the IDT decreases from 3.01 s to 0.038 s and flame temperature increases from 2433.1 K to 2531.5 K.

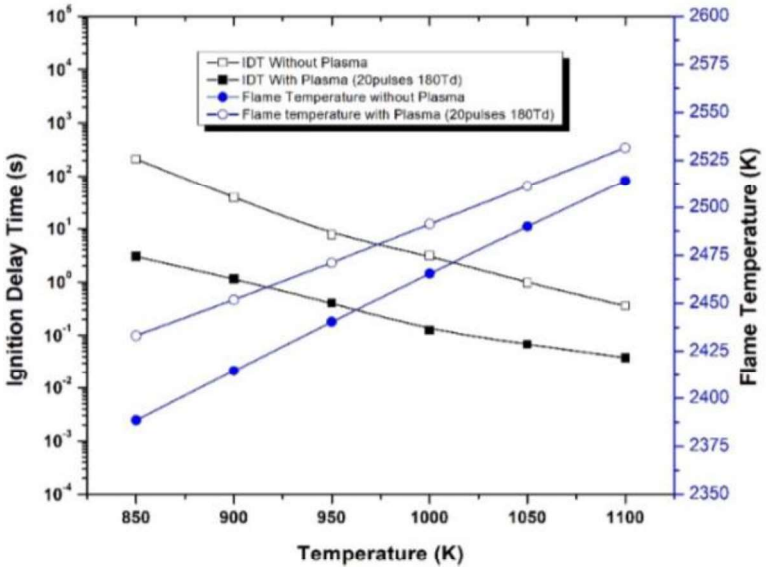

Figure 2. IDT and flame temperature without and with 20 sequential pulses of plasma discharge in NH_3/air mixture at, E/N = 180Td, P = 1 atm, ϕ = 1.0 with PRF = 50 kHz.

Conclusion

This numerical investigation focuses on the impact of nanosecond plasma discharge on the IDT of an ammonia/air mixture for low and intermediate temperatures (850 - 1100 K) under atmospheric pressure. The results revealed the IDT of the ammonia combustion under the plasma case is significantly shorter and the flame temperature higher than that of the case without plasma. Employing a 20 pulses plasma discharge, the IDT was reduced from 210.55 s to 3.01 s and the flame temperature increased from 2388.4 K to 2433.1 K at an initial temperature of 850 K.

Funding

The work was supported in part by Project MOST Research Project: Sustainable Mobility Center (Centro Nazionale per la Mobilità Sostenibile – CNMS) CUP Progetto: F83C22000720001; Codice del Progetto: CN00000023.
The work was funded also by the PRIN - “Intermingle Mild-oxidation and Plasma Roadmaps for hydrOgen/ammOnia energy-Vectors” - IMPROOVE- CUP: F53D23009670001

References

[1] L. Al-Ghussain, “Global warming: review on driving forces and mitigation”, *Environ. Prog. Sustain Energy* 38: 13-21 (2019).
[2] T. Haasz, J.J. Gomez Vilchez, R. Kunze, P. Deane, D. Fraboulet, U. Fahl, E. Mulholland, “Perspectives on decarbonizing the transport sector in the EU28”, *Energy Strategy Rev* 20: 124-132 (2018).
[3] X. Pan, H. Wang, L. Wang, W. Chen, “Decarbonization of China's transportation sector: in light of national mitigation toward the Paris Agreement goals”, *Energy* 155: 853-864 (2018).
[4] A. Valera-Medina, H. Xiao, M. Owen-Jones, W.I.F. David, P.J. Bowen, “Ammonia for power”, *Prog. Energy Combust. Sci.* 69: 63-102 (2018).

[5] P.J. Feibelman, R. Stumpf, “Comments on potential roles of ammonia in a hydrogen economyda study of issues related to the use of ammonia for onboard vehicular hydrogen storage”, *Sandia Natl. Lab* (2006).

[6] A. Valera-Medina, F. Amer-Hatem, A. Azad, I. Dedoussi, M. de Joannon, R. Fernandes, P. Glarborg, H. Hashemi, X. He, S. Mashruk, “Review on ammonia as a potential Fuel: from synthesis to economics”, *Energy Fuels* 35: 6964–7029 (2021).

[7] Zubair Ali Shah, Ghazanfar Mehdi, Paolo Maria Congedo, Domenico Mazzeo, Maria Grazia De Giorgi, “A review of recent studies and emerging trends in plasma-assisted combustion of ammonia as an effective hydrogen carrier” *International Journal of Hydrogen Energy* 51: 354-374 (2024).

[8] Pancheshnyi S, Eismann B, Hagelaar G J M and Pitchford L C 2008 Computer code ZDPlasKin (available at: www.zdplaskin.laplace.univ-tlse.fr)

[9] Lutz A E, Kee R J and Miller J A 1988 SENKIN: a FOR-TRAN program for predicting homogeneous gas phase chemical kinetics with sensitivity analysis Report No. SAND87-8248 (Sandia National Laboratories)

[10] L.G. Piper, “Energy transfer studies on N2(X 1Σ+g, v) and N2(B 3Πg)”, *J. Chem. Phys.* 97: 270–275 (1998).

[11] Mohammad Shahsavari, Alexander A. Konnov, Agustin Valera-Medina, Mehdi Jangi, “On nanosecond plasma-assisted ammonia combustion: Effects of pulse and mixture properties”, *Combustion and Flame* 245: 112368 (2022).

[12] B. Mei, X. Zhang, S. Ma, M. Cui, H. Guo, Z. Cao, Y. Li, “Experimental and kinetic modeling investigation on the laminar flame propagation of ammonia under oxygen enrichment and elevated pressure conditions”, *Combust. Flame* 210: 236–246 (2019).

[13] Taaresh Sanjeev Taneja, PraiseNoah Johnson, Suo Yang, “Nanosecond pulsed plasma assisted combustion of ammonia-air mixtures: Effects on ignition delays and NO x emission”, *Combustion and Flame* 245: 112327 (2022).

[14] P. Sabia, M.V. Manna, A. Cavaliere, R. Ragucci, M. de Joannon, “Ammonia oxidation features in a jet stirred flow reactor. The role of NH2 chemistry”, *Fuel* 276: 118054 (2020).

[15] Wang ZH, Yang L, Li B, Li ZS, Sun ZW, Aldén M, Cen KF, Konnov AA, “Investigation of combustion enhancement by ozone additive in CH4/air flames using direct laminar burning velocity measurements and kinetic simulations”, *Combustion and Flame* 159: 120–129 (2012).

[16] Jundie Chen, Xue Jiang, Xiaokang Qin, Zuohua Huang, “Effect of hydrogen blending on the high temperature auto-ignition of ammonia at elevated pressure”, *Fuel* 287: 119563 (2021).

[17] Alessandro Stagni, Carlo Cavallotti, “H-abstractions by O2, NO2, NH2, and HO2 from H2 NO: Theoretical study and implications for ammonia low-temperature kinetics”, *Proceedings of the Combustion Institute* 39: 633–64 (2023).

[18] Han X, Lubrano Lavadera M, Konnov AA, “An experimental and kinetic

modeling study on the laminar burning velocity of NH3+N2O+air flames", *Combust Flame* 228: 13–28 (2021).

[19] E.C. Okafor, Y. Naito, S. Colson, A. Ichikawa, T. Kudo, A. Hayakawa, H. Kobayashi, "Experimental and numerical study of the laminar burning velocity of CH4 −NH3−air premixed flames", *Combust. Flame* 187: 185–198 (2018).


THE COMBUSTION INSTITUTE
1954

SESSION X

Stationary Combustion Systems and Gas Turbines - Part 2


THE COMBUSTION INSTITUTE
1954

Comparison of Different Instability Criteria for the Characterization of the Dynamical State of Combustion Systems

E. Giulietti*, E. Giacomazzi*, C. Stringola*, C. Romano**
eugenio.giacomazzi@enea.it
*TERIN-DEC-CCT Laboratory, ENEA, C.R. Casaccia, S.M. di Galeria (Rome), Italy
**Baker Hughes, Florence, Italy

Abstract
Although investigated for many years, real-time monitoring of combustion dynamics is still an important issue in modern gas turbine operation. In this article, attention is focused on two quantities, radiant energy, and pressure, that can be sampled in combustion systems. Based on such quantities, and with the aim of selecting the best operational index to detect instability precursors, different strategies are here defined and compared.

Introduction
Great effort is currently dedicated to the development of fuel-flexible lean-premixed gas turbines able to burn fuel mixtures with variable hydrogen content. Lean premixed combustion offers the advantage of low NO_x emission, but it is highly sensitive to external perturbations, especially to variations in the equivalence ratio of the mixture; this issue tends to promote the onset of self-sustained large amplitude pressure oscillations called thermoacoustic instabilities, due to the resonant coupling between unsteady combustion processes and pressure waves in the combustion chamber [1,2]. Such instabilities enhance heat transfer to combustor walls, deteriorate combustion efficiency, increase pollutant emission, and, in extreme cases, can produce structural damages leading to the loss of control of the power plant or propulsion system. While the global mechanism of thermoacoustic instabilities is known, identifying in real-time the responsible initial mechanism and its precursors remains a difficult task.
This article describes the results of real-time monitoring of a turbulent lean-premixed flame by means of an optical system called Optical Diagnostics of Combustion (ODC), developed, validated, and patented in ENEA [3-6], and a pressure transducer. With the aim of looking for the best index for real-time identification of instability precursors, different indexes are suggested and compared.

Monitoring quantities and sensors
Turbulence-chemistry interaction results in an unsteady variation of the flame shape and the local reaction rates, thus, causing a broadband noise level, commonly referred to as combustion noise. During combustion instabilities three physical mechanisms interact in a highly nonlinear and unsteady manner, i.e., vortex motion

(vorticity), heat release (entropy waves) and acoustic fluctuations, and the flame itself can be influenced by noise and acoustic waves up to a resonant interaction.
The main and direct outputs that an observer in front of a combustion process can capture are radiant energy (light emission), thermal energy (light emission in the NIR or IR range) and noise (pressure waves).
The most basic measurable quantity to monitor and characterize unstable combustion is dynamic pressure [1], by means of microphones and pressure transducers. Since acoustic waves propagate throughout the entire combustion system, they can be placed far from high temperature regions. In enclosed systems, flames can be strongly influenced by the acoustic characteristics of the combustion chamber; therefore, the acoustic signature of a burner may change when it is installed in different combustion chambers (including the effects of dampers and cooling systems).
Many features make radiant energy sensors appealing. Such devices are optical; hence, they are not intrusive. Exhibiting large bandwidth up to several kHz or even tens MHz, they are suitable for the study of flame dynamics and combustion instabilities or unsteady pulsed combustors as well as for the development of fast-response controllers.
The naturally occurring flame chemiluminescence in UV-VIS range is related to heat release and has proven to be extremely useful in characterizing unstable combustion in lean premixed combustion. Chemiluminescence is the radiative emission from electronically excited species. Its intensity is determined by the competition between the chemical reactions that produce such excited species and the collisional quenching reactions. In particular, emission from OH (282.9 nm; 307-309 nm) and CH (387 nm; 431.5 nm) radicals, occurring at distinctly different and relatively narrow-wavelength intervals, are good indicators of heat release rate [7] and flame front location. Single detectors, such as photomultipliers (PM), photodiodes (PD) or avalanche photodiodes (APD), coupled with bandpass filters at selected central wavelengths, are the most common option to detect radiant energy [4].

Classical criteria for thermo-acoustic instabilities

The classical *Rayleigh's criterion* [8] states that when the pressure and heat-release fluctuations, p' and H_R', are in phase, a system becomes unstable:

$$\int_V \int_0^\tau p' H_R' dt dV > 0 \quad (1)$$

When the magnitude of the phase between p' and H_R' is less than 90° they are in phase, and the instability is locally amplified. Conversely, when these fluctuations are out of phase (i.e., in the range 90°-180°), the instability is damped.
Rayleigh's criterion is a necessary but not sufficient condition for instability to occur (loss mechanisms are neglected). *Chu's criterion* [8] is more accurate:

$$\int_V \int_0^\tau T' H_R' dt dV > 0 \quad (2)$$

It requires temperature and heat release fluctuations, T' and H_R', to be in phase for the instability to grow. An extended version of the above criteria also exists [8].

The suggested experimental instability criteria

Once introduced classical instability criteria, it is worth looking for some measurable integral (in space) quantities linked to T' and H'_R, that can be correlated to pressure fluctuations p'. It is observed that total radiation emitted by flames consists of two types of sources: the first one is chemiluminescence, while the second one is thermal emission associated to the Planck function [4,9,10]:

1. since the intensity of light emission (radiant energy) in the UV-VIS range (chemiluminescence) is proportional to the production rate of some molecules (e.g., CH, OH, C2 radicals), chemiluminescence can be used as an indicator of reaction rates and heat release rate fluctuations, i.e., H'_R [7];
2. since the intensity of light emission in the IR range (thermal energy) is proportional to the temperature of the field according to the Planck function, it can be used as an indicator of temperature fluctuations, i.e., T' [9,10].

With these statements, it is possible to evaluate instantaneously and in real-time three instability criteria, T'-H'_R (mimicking the Chu's criterion), p'-H'_R (mimicking the Rayleigh's criterion), and p'-T', by cross-correlating the three quantities, H'_R and T' being measured via radiant energy sensors, and p' via acoustic sensors.

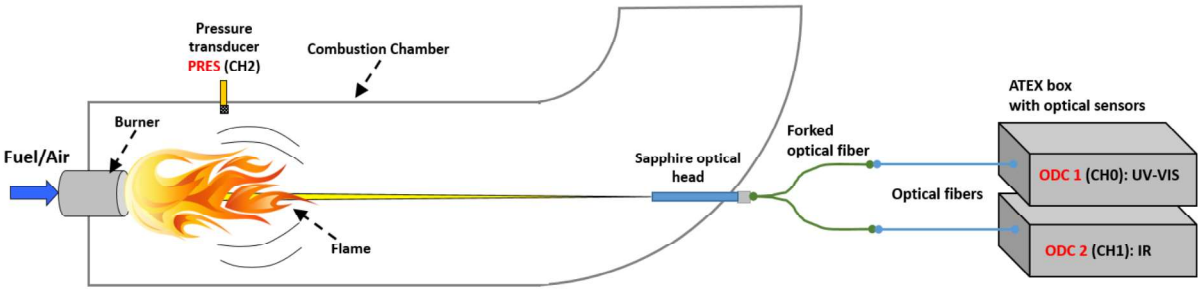

Figure 1. Sketch of the experimental set-up.

Experimental set-up

The two integral radiant energy signals related to the UV-VIS and NIR ranges are sampled by means of the ODC system developed and patented at ENEA [3-6]. ODC methodology lets to characterize in real time the dynamics of unstable conditions, chemical species, and temperature, and estimate the average flow speed.

The ODC system has an optical sapphire head with an angle of view of nearly 20 degrees, that samples radiant energy from a wide reacting region to capture eventual growing of instability precursors in different parts of the flame. The optical head is connected to two avalanche-photodiodes (APD) by means of a bifurcated optical fiber bundle (Fig. 1). The first APD works in the UV-VIS range (300-550 nm, coupled to a pass-band optical filter limiting the actual range to 320-550 nm) linked to the heat release fluctuations, H'_R, and the second one in the NIR range (900-2600 nm, coupled to a high-pass optical filter) linked to the temperature fluctuations, T'.

The industrial burner investigated in this work has a central swirled premixed burner and a pilot coaxial burner, operated at 60 kW_t, ambient pressure, and fed with a mixture of natural gas (94.6/0.5/4.2/0.6 %vol. of $CH_4/C_3H_8/C_2H_6/N_2$) and air.

Combustion dynamics characterization

The burner consists of a pilot and a premixed module; the combustion and cooling air mass flow rates are constant during operation; the total fuel mass flow rate is also constant (nominal equivalence ratio ~0.56), split between the two modules (see black curve in Fig. 2). The flame switches from stable to unstable mode by increasing the premixed contribution. Figure 2 shows the time evolution of radiant energy and pressure raw signals (the ODC almost always identifies the same frequency peaks detected by the pressure transducer). Five time-windows (from A to E), each of 1 s, were examined as representative of different operating conditions (thermoacoustic instability conditions are reached in B and E). Figure 3 shows the history of the pressure peak amplitude in two frequency ranges, [0-320] Hz and (320-4.000] Hz, evidencing two unstable conditions exhibiting the greatest acoustic emission.

Three ramping up/down cycles are operated in ~8000 s: the energy provided to the system is constant (fuel flow rate). The first has a slow 40-100% premix split ramp in ~2000 s, visible in the ODC UV-VIS signal all over the time, but only at the peak unstable condition (100% split) in the NIR (likely due to the inertia of the combustor walls); the fast ramping down in ~500 s is visible in both signals. The second cycle has a ramp 0-80% premix split in ~700 s, turns quickly to 60% for ~1250 s, then to 0% very quickly; no instabilities are exhibited due to the system thermal inertia, i.e., they are prevented by the hotter condition: the energy provided through the fuel is constant but much lower than that stored by the combustor walls during the previous unstable condition and slowly released, as evidenced by both monotonically decreasing ODC radiant energy signals. The third cycle has a ramp 0-100% premix split in ~1500 s (faster than in the first cycle), then turns back to 0% very quickly; after the second cycle the temperature of the combustor walls lowered although it is likely higher than at the start of the first cycle: hence, the system exhibits an unstable condition seen by both ODC radiant energy signals, especially by NIR.

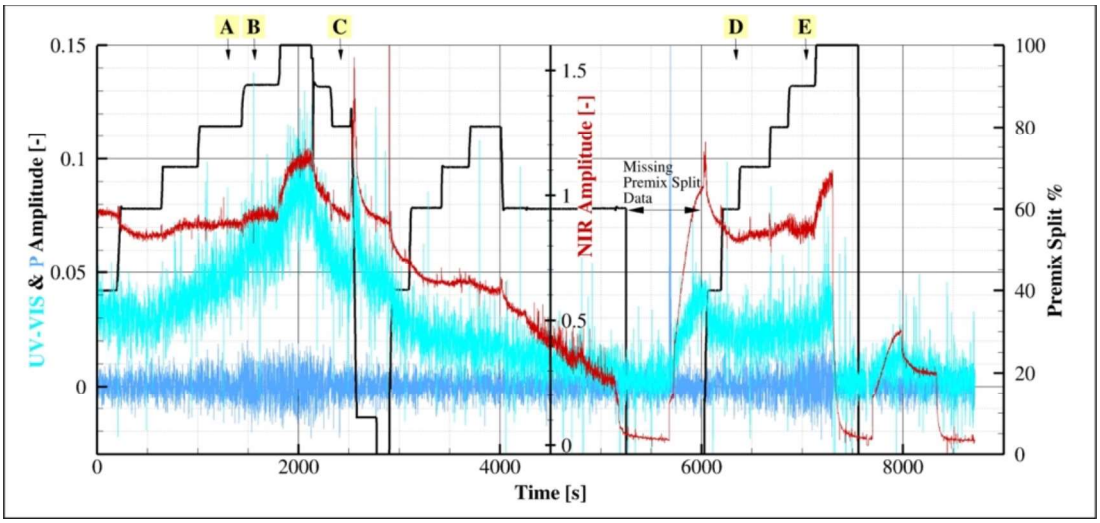

Figure 2. Time-history of the ODC optical signals in the UV-VIS (heaven, left axis) and NIR (red, central axis) ranges, and of the pressure signal (blue, left axis).

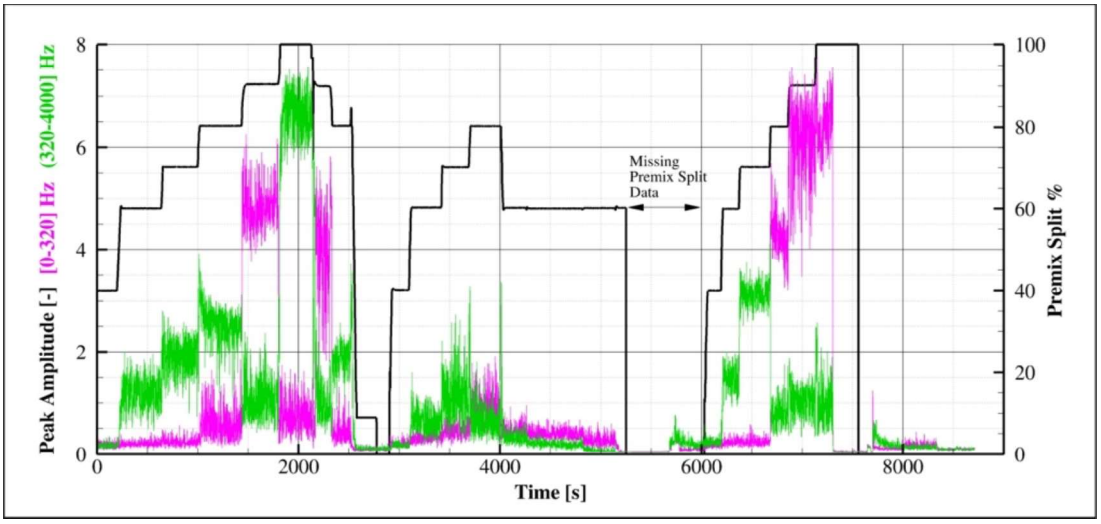

Figure 3. Time-history of the amplitude of the pressure peak in the frequency ranges 0-320 Hz (fuchsia) and 320-4000 Hz (green).

The *cross-correlation indexes* T'-H_R', p'-H_R' and p'-T', shown in in Fig. 4, are remarkably sensitive in all cases; the cross-correlation index between the ODC NIR optical signal and the pressure signal, i.e., p'-T', performs better than the others, reaching values between 0.5 and 0.65. The indexes T'-H_R' and p'-H_R' look very similar: this could imply that T' and p' are interchangeable; besides, the lower performance could be justified by the low signal to noise ratio observed for the UV-VIS contribution, H_R'.

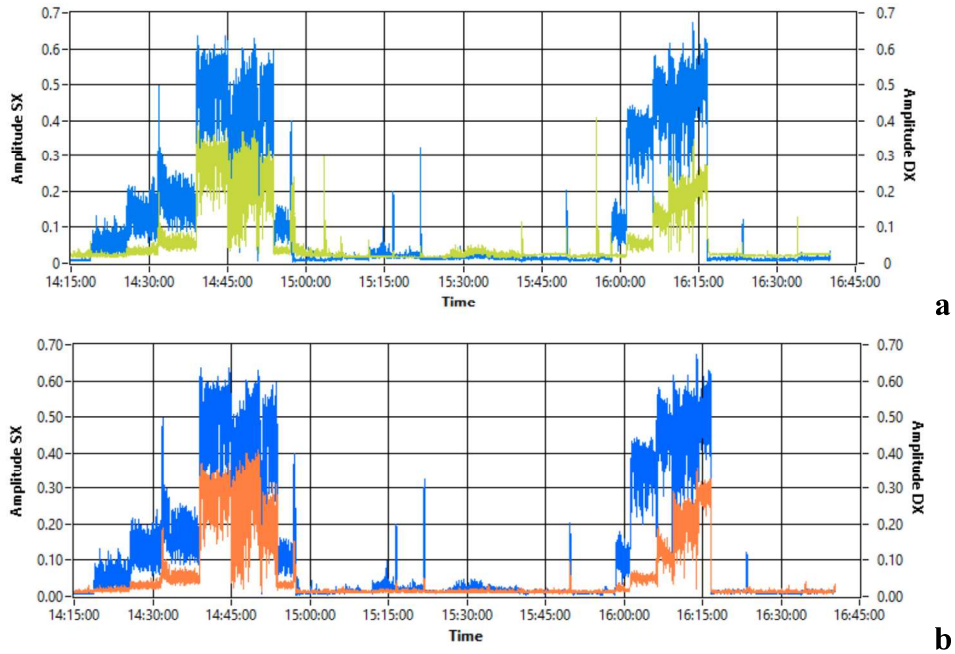

Figure 4. Time-history of the cross-correlation indexes between the ODC signals in the UV-VIS and NIR ranges (light green), the ODC NIR and pressure signals (blue), and the ODC UV-VIS and the pressure signals (orange).

Conclusions and future work

Sampling flame radiant energy using a photodiode and employing cross-correlation indices has shown promise as a practical method for monitoring the dynamic state of combustion systems and identifying thermoacoustic instability conditions in real-time. This strategy also has the potential to reduce monitoring hardware by substituting the flame detector with a robust optical sapphire head.
Future work will aim to enhance the optical signal sampled in the UV-VIS range by reducing the number of junctions between optical fibers and utilizing a more sensitive GaP (Gallium Phosphide) optical sensor operating in the 150-550 nm range. With these new features, the performance of the cross-correlation indices will be reassessed to determine whether combustion instabilities can be detected solely using the ODC system, focusing on monitoring the T'-H'_R index.

Acknowledgments

Special thanks to Nuovo Pignone Tecnologie Srl, a part of the Baker Hughes group, for generously granting access to their facility and providing the experimental data.

References

[1] Lieuwen T., Yang V., "Combustion instabilities in gas turbine engines: operational experience, fundamental mechanisms, and modelling", Progress in Astronautics and Aeronautics, 210:611–34, 2005.
[2] Giulietti E., "Combustion instabilities in Gas Turbine - A new methodology for combustion monitoring", LAP LAMBERT Academic Publishing, 2015.
[3] Bruschi R., Giacomazzi E., Stringola C., CasasantaV., Manfredi F., Caruggi M., "Diagnostics of Flow Dynamics Bringing to the Onset of Thermo-Acoustic Instabilities in Gas-Turbine Combustors", 14th IFRF Members' Conference, Noordwijkerhout, The Netherlands, 11-14 May 2004.
[4] Giacomazzi E., Troiani G., Giulietti E., Bruschi R., "Effect of Turbulence on Flame Radiative Emission", *Experiments in Fluids*, 44-4:557-564, 2008.
[5] Giacomazzi E., Giulietti E., Stringola C., Cassani S., Pagliari L., Chiocchini S., "Combustion Monitoring in Gas Turbines and enhanced stability at very lean conditions", Proc. ASME Int. Gas Turbine Inst., ASME TURBO Expo: Power for Land, Sea, and Air, GT2014-25506, Dusseldorf, Germany, 2014.
[6] Chiocchini S., Pagliaroli T., Camussi R., Giacomazzi E., "A Mutual Nearest Neighbours Based Chaotic Synchronization Index to Detect Thermo-Acoustic Coupling in Gas Turbine Combustion Instabilities'", Proc. ASME Turbo Expo 2016: Turbine Technical Conference and Exposition, GT2016, Seoul, South Korea, June 13-16, 2016.
[7] Hardalupas Y. and Orain M., "Local measurements of the time-dependent heat release rate and equivalence ratio using chemiluminescent emission from a flame", Combustion and Flame, 139-3:188-207, 2004.
[8] Nicoud F., Poinsot T., "Thermoacoustic instabilities: Should the Rayleigh criterion be extended to include entropy changes?", Combustion and Flames, 142:153-159, 2005.
[9] Planck M., "The Theory of Heat Radiation", New York, 2nd edition, 1959.
[10] Gaydon A.G. and Wolfhard H.G., "Flames: Their Structure, Radiation, and Temperature", Chapman and Hall, London, 4th edition, 1978.

CHALLENGES IN MODELLING INDUSTRIAL BURNERS FOR DESIGN PURPOSE: A CASE STUDY FOR GASEOUS AND LIQUID FUELS

G. Rossiello*, L. Morandi, D. Carucci**, D. Ettorre***, T. Vela*, S.B. Ahmadpanah*, and M. Torresi*****

Corresponding author: gianluca.rossiello@seamthesis.com (Gianluca Rossiello)
* SEAMTHESIS Srl, Via IV Novembre, 156 – 29122 Piacenza, ITALY
** Termotecnica Industriale Srl, via Dante, 16 – 20121 Milano, ITALY,
*** DMMM, Department of Mechanics, Mathematics and Management, Polytechnic University of Bari, Via Re David, 200 – 70125 Bari, ITALY

Abstract

This article deals with the use of CFD simulations as design tool for the development of heavy-duty burners. The newly designed 50 MW burner operates, singularly in a combustion chamber, with both gaseous and liquid fuel. The focus is on two aspects of modelling: one related to gaseous fuel, and the other to low boiling point liquid.
First, for refinery gas feeding, attention is drawn on the geometry and boundary conditions suitable for the injection nozzles of external spuds, considering either the injection directly on exit surfaces of nozzles on spud tip, or the internal volume of the spuds and each hole geometrically included in the computational domain. The two simulations show no relevant difference for the given ratio between hole diameter and depth.
As a second example, the liquid fuel feeding is considered for the same burner: in this case the challenges come from light naphtha feeding, due to low boiling point. Indeed, it is shown how, employing a standard atomizer designed for light oil, the functioning of the burner inside the combustion chamber is totally unsatisfactory, with delayed combustion and carbon monoxide at furnace exit. For modelling validation purpose, the same numerical test is run with a gasoil, obtaining a suitable solution, well known for the coupling of this kind of air/steam assisted atomizer with gasoil. This second test proves the suitability of such numerical modelling: indeed, in the end it is shown a third result obtained by completely redesigning the atomizer to operate with low boiling point fuel, showing a completely satisfactory behavior.
Finally, this study underlines how CFD simulations give quantitative and affordable support to designers for such complex and challenging problems, anticipating and replacing, to a certain extent, experimental testing, in the early stages of design and when testing is not viable for some reason.

Context and motivation

The ongoing energy transition from fossil to renewable sources is a real challenge for industry and for the energy market, requiring a combination of fuel flexibility,

thermal efficiency, and low emissions to properly manage fossil fuels, waste, and new and renewable energy carriers, both gaseous and liquid, reducing fuel consumption and expensive after-treatment of flues [1].
In this context, advanced design tools are needed to meet market needs: in particular, for steam boiler design, it is essential to improve and refine simulation capabilities to properly handle a wide range of liquid and gaseous fuels with performance even exceeding that of standard fuels [2-4]. Experimental campaigns are extremely expensive, with few plants available for full scale testing, and require careful commissioning and management to give accurate measurements. Moreover, the testing give back, as best option, affordable performance parameters, but nothing regarding the interpretation of such results, neither in depth understanding of flame behavior or physical phenomena taking place in general. In this context, CFD analysis can be an extremely useful and strategic tool both for the analysis and development of individual equipment – for example burners, air intake openings, etc. – both for the optimization of the whole system.

Problem description

The object of the present study is the modelling of a single heavy-duty industrial burner of a boiler furnace fed with both gas and liquid fuel. The burner has a total of 9 gas lances with three nozzles each, and a Y-jet air/steam assisted spray atomizer. In the case of liquid fuel supply, a standard atomizer is first studied, comparing the performance obtained with light naphtha supply with that resulting using the physical properties of standard diesel fuel. The operating conditions considered are 100% load corresponding to 48.71 MW of thermal input for refinery gas, and 48.35 MW thermal input for liquid fuel. The compositions and main physical properties of gaseous and liquid fuels are summarized in Table 1 and Table 2, respectively.

Table 1. Refinery gas composition [% Volume] and physical properties.

	CH4	H2	C2H6	C3H8	N2	MW	LHV
Units	%	%	%	%	%	kg/kmole	MJ/kg
	51	25.5	4	16.2	3.3	17.967	47.818

Table 2. Liquid fuel composition [% Volume] and physical properties.

	C6H6	C5H12	C6H14	MW	LHV
Units	%	%	%	kg/kmole	MJ/kg
	54	23	23	78.312	42.717

Numerical modelling and boundary conditions.

CFD analyses are conducted with the Ansys Fluent-v17.2 [5]. The computational domain is discretized with a polyhedral mesh of about 7.5 million elements with orthogonal prismatic cells next to the walls. For each configuration, a steady state computation is performed with turbulence modeled by a RANS approach and

standard 2 equations closure. The non-premixed model is used to account for gas phase reaction, with tabulated chemistry by a probability-density-function approach based on the hypothesis of chemical equilibrium, with tabulated data (PDF-Table) computed in pre-processing. Compressible ideal gas approach is employed for the equation of state and in addition, the domain-based weighted sum of grey gases model is used to calculate the gas radiative properties and the radiant heat transfer is calculated by the Discrete Ordinates method (DO). The Discrete Phase Model available in Ansys Fluent is employed for description of liquid droplets, with constant velocity of 70 m/s and direction perpendicular to the nozzle exit surface and with a Rosin-Rammler distribution for the diameter of particles, with 70 μm for mean value, 21 μm as minimum one, and 140 μm for the maximum.
The vaporization temperature and boiling temperature used in the simulations are respectively 262 K and 353 K for the light naphtha, and 400 K and 589 K for the fuel-oil. The flow rate of combustion air input is calculated by the design value of the excess air, which is 12.5% for both gaseous and liquid fuel full load operation. For the furnace walls, a convective heat transfer coefficient of 2800 W/m^2-K is considered, which also accounts for the phenomenon of fouling, with water-cooling temperature of 255 C. For radiation, internal emissivity coefficient is set to 0.6.

Directionality testing with gaseous fuel

The first case study shown in this work concerns the gaseous fuel modelling and operation of the burner in the combustion chamber of the steam generator. The correct representation of boundary condition is at least as essential as the proper and modelling in order to obtain accurate results, with reliable assessment of flame behavior affordable estimation of relevant performance parameters. Hence, the focus here is on the injection of fuel jets into the furnace from external gas spuds nozzles. The physical phenomenon under investigation is the supercritical discharge of a high-pressure gas flow from convergent nozzles into the low-pressure volume of the combustion chamber. The well-known flow is characterized by conical oblique shocks, high Mach number internal jets, and successive normal shocks alternated with expansion fans. Through this complex flow structure, the adaptation of fuel streams to the downstream low-pressure field occurs. The direction and momentum of such fuel jets is affected by the modelling of flow and the representation of boundary conditions: while the former aspect is described in the previous section, the latter is discussed here. In particular, two alternatives are considered. In a first simulation, the internal volume of gas spuds is included in the domain, and the nozzles are modelled as passage ducts, discharging into the furnace. In a second simulation just the outlet section of the nozzle on the tip of each spud are considered as inlet surfaces. So, in the first case an overall mass flow rate is imposed for each of eh 9 spuds, while in the second it is imposed on each of the 27 nozzles (3 nozzles on each spud). The two simulations show similar results, almost overlapping, both for the streamlines of jests (see Figure 2) and for the flame behavior. This proves that the ratio of nozzle diameter to the length of the hole (12 mm and 15 mm,

respectively) is sufficiently high to make upstream inertial effect and 3D flow behavior through the drilled volumes almost negligible. Finally, to illustrate the flame shape and the burner-furnace behavior, we show in Figure 3 the contour plot of temperature and carbon monoxide fields.

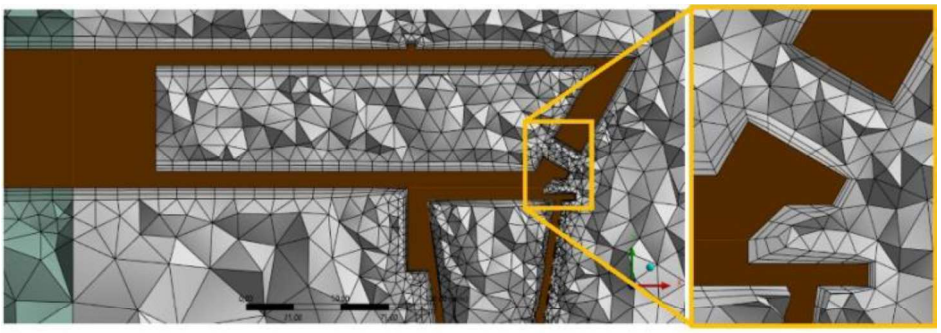

Figure 1:Geometry used for case 1, with nozzle volume modelled.

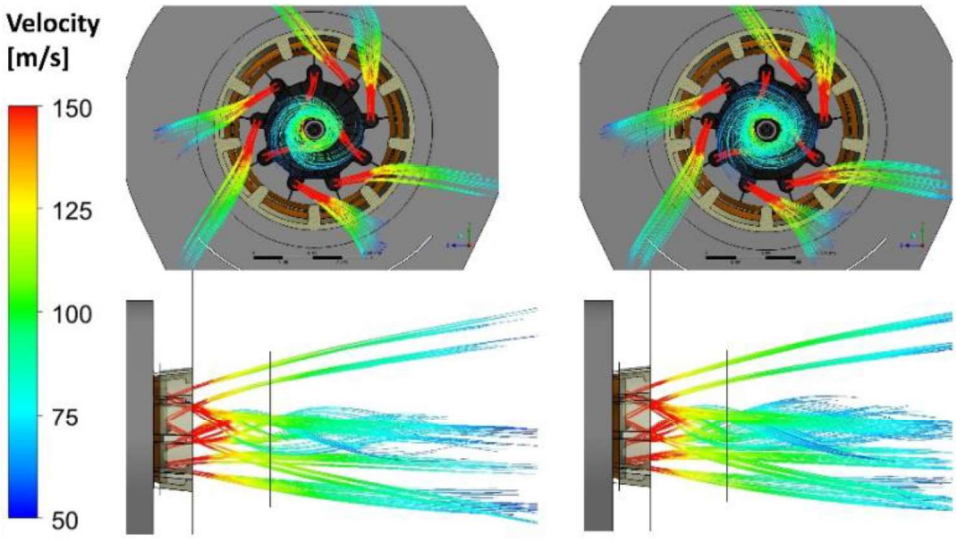

Figure 2 Streamline of fuel (refinery gas) coming out from nozzles, coloured by velocity magnitude: model with holes included (left) vs model with exit surfaces.

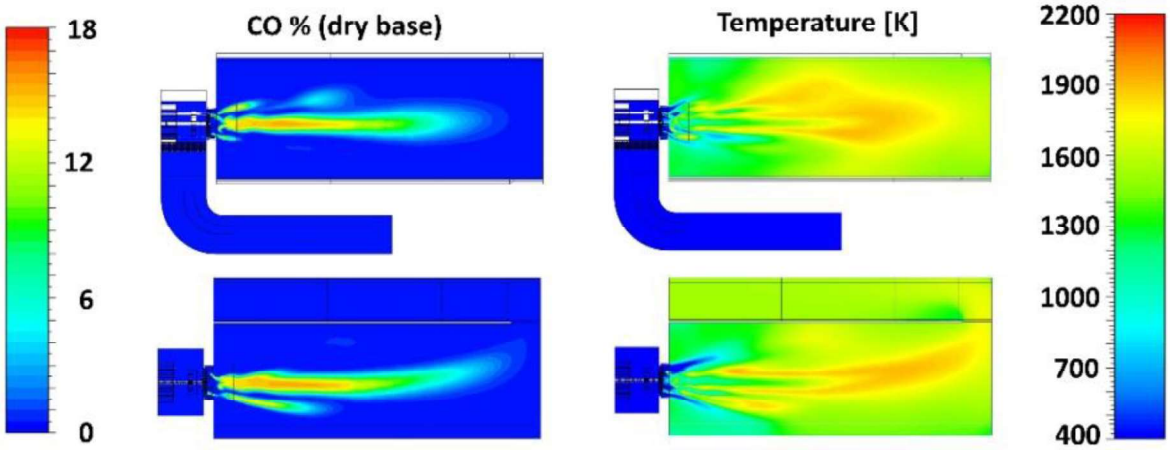

Figure 3:Refinery gas CFD solution: temperature (right) and CO (left) fields.

Analyses of spray combustion for liquid fuel feeding

The second part of this study is focused on liquid fuel combustion modelling of the burner inside the combustion chamber. In particular, three results are shown. The first one refers the simulation with light naphtha feeding, a low boiling point liquid fuel, using a "standard" Y-jet air-assisted atomizer. The solution obtained for the flame shape is completely unsatisfactory, as shown in the first column of Figure 4, since the combustion is delayed, and CO oxidation is not complete at combustion chamber exit. This behaviour is due to extremely fast evaporation of liquid fuel at nozzle atomizer exit, as is clearly visible in the picture in the third (last) row: this issue can be imputed either to modelling inaccuracy, or to bad atomizer operation.

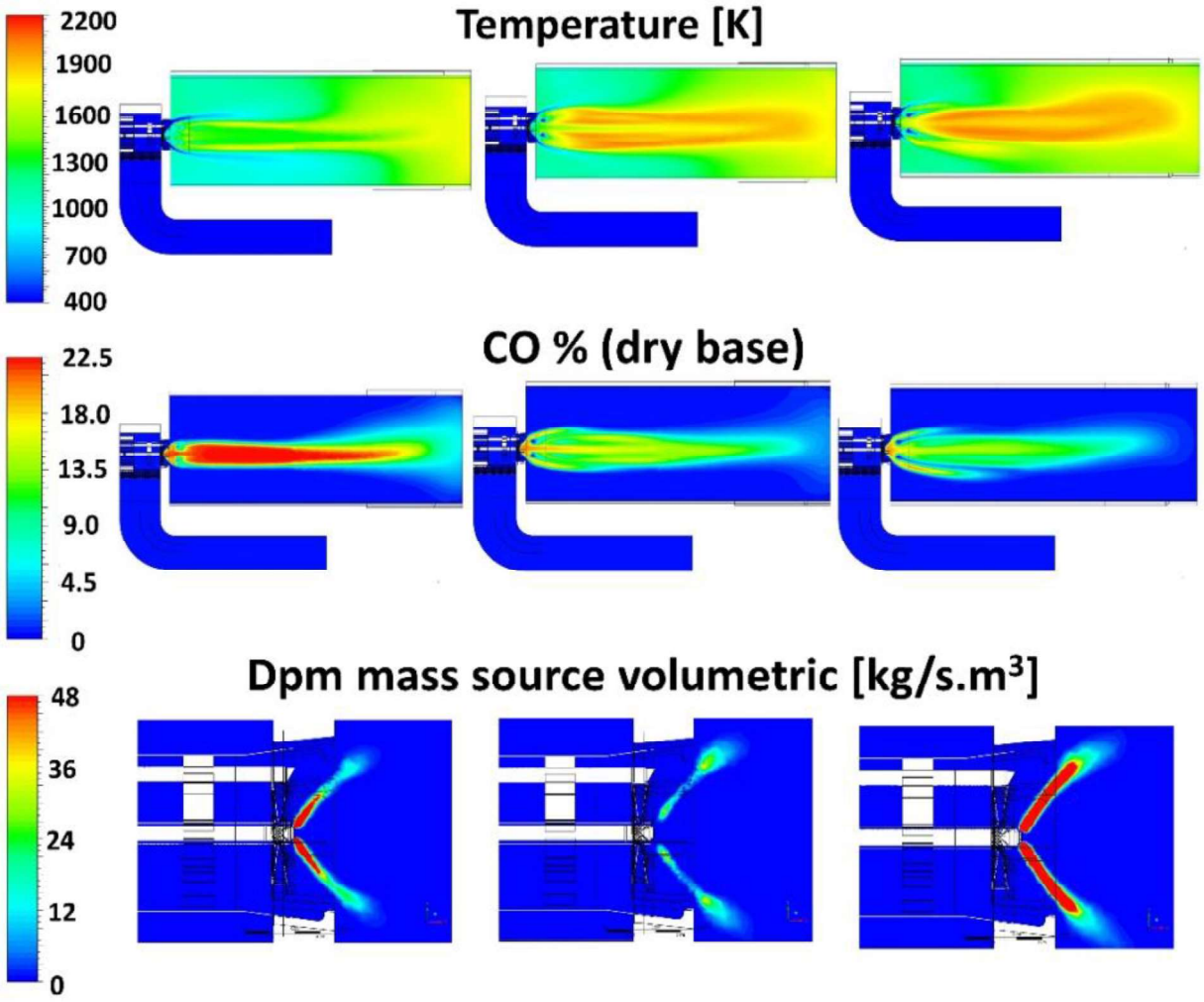

Figure 4:Liquid fuels CFD solutions: temperature (first row), CO (second row) and vapor mass source (third row) fields; the first column refers to Case-1 (light naphtha and initial atomizer), the second column refers to Case-2 (fuel-oil and initial atomizer) third column refers to Case-3 (light naphtha, redesigned atomizer).

To address this point, a second simulation is taken into consideration, which is identical to the first one except for the liquid droplets, for which fuel-oil physical properties replace those of light naphtha. The idea is to replace a low-boiling point

liquid fuel, with a diesel oil for which this kind of atomizers has been developed, giving a well-known and satisfactory flame behaviour. Indeed, in the second column of Figure 4 the numerical solution of this second case is shown, proving that the overall model captures the expected flame characteristics. This step is used as a validation of the modelling approach, and allows then a proper redesign of the atomizer, finally giving with light naphtha a completely satisfactory combustion behaviour, as illustrated in the last column of Figure 4. The final flame behaviour is similar to that of the fuel oil case, even if the light naphtha is a low boiling point fuel, and even if the evaporation pattern of the newly designed atomizer is completely different from the initial Y-jet atomizer used in the case-1 and case.2 simulations.

Conclusion

In this work an example is given of how CFD modelling and simulation can be exploited for the design and optimization of a heavy-duty burner. In particular, gaseous and liquid fuel operation are simulated, focusing on modelling and functioning aspects.

For the refinery gas feeding it is proven that the modelling of internal spud volumes and nozzle holes in not required for the considered geometry, and that the burner design is completely satisfactory as for its flame shape and coupling with the combustion chamber.

Concerning liquid fuel, the CFD simulations proves the inadequacy of a standard Y-jet air assisted atomizer to operate with low boiling point fuel like light naphtha. A second simulation with the same atomizer and fuel-oil is used to verify the modelling of liquid droplets and spray combustion. Finally, the numerical simulation are exploited to redesign the atomizer for low boiling point liquid fuel, obtaining a completely satisfactory behavior of flame and complete combustion at furnace exit.

References

[1] WEO-2021 World Energy Outlook, International Energy Agency, Paris, France, 2021.

[2] Park, J. K., Park, S., Kim, M., Ryu, C., Baek, S. H., Kim, Y. J., Kim, H. H., Park, H. Y., “CFD analysis of combustion characteristics for fuel switching to bioliquid in oil-fired power plant,” Fuel, 159, 2015, 324-333.

[3] Liu, H., Zhang, L., Li ,Q., Zhua, H., Deng, L., Liu, Y., Che, D., “Effect of FGR position on the characteristics of combustion, emission and flue gas temperature deviation in a 1000 MW tower-type double-reheat boiler with deep-air-staging”, Fuel, 246, 2019, 285-294.

[4] Laubscher, R., van der Merwe, S., “Heat transfer modelling of semi-suspension biomass fired industrial water tube boiler at full- and part-load using CFD”, Thermal Science and Engineering Progress, 25, 2021, 100969.

[5] ANSYS Fluent, Users and Theory Guide, ANSYS, Inc., v.17.2, 2017.

ANALYSIS OF THERMOACOUSTIC INSTABILITES IN A MICRO GAS TURBINE

C. Vankelekom*, F.G. Schiavone **, W. De Paepe*, D. Laera **
christophe.vankelekom@student.umons.ac.be
*University of Mons (UMONS), Thermal Engineering and Combustion Research Unit, Mons, Belgium
**Department of Mechanics, Mathematics and Management, Polytechnic University of Bari, Bari, Italy

Abstract
Global warming, environmental impact, pollution and air quality are the main concerns of this century. One way to limit the impact is to reduce our fossil fuel consumption for electricity production using renewable energy sources. This solution, however, is intermittent and non-dispatchable. To help the energy transition, thermal-based power generation as micro gas turbines (mGTs) offer many prospects, thanks to their flexible operation, such as short start-up times. Nevertheless, thermoacoustic instabilities can occur, and a way to identify, quantify and even prevent them is of fundamental importance. With this work, we aim to numerically characterize the onset of these instabilities in the MTT EnerTwin mGT fuelled with natural gas, to gain a better understanding of the mechanisms leading to flame-acoustic coupling in these devices.

Introduction
The thermoacoustic combustion instabilities is an unsteady non-linear phenomenon generated by the coupling between heat release rate fluctuations and acoustic waves. This kind of instability is dangerous because pressure fluctuations may produce vibrations inside the system that could further damage the components. Fully compressible Large Eddy Simulations (LES) have been proved to be a powerful tool to investigate this phenomenon in either laboratory scales [1] or industrial gas turbines [2]. Nevertheless, such methodology has never been applied in micro gas turbines (mGTs) with very small-scale combustor. The present work aims at filling this gap by proposing a LES study on thermoacoustic instabilities in a mGT. At first, stable flame is characterized. LES predict a fully premixed V-shape flame burning in very lean conditions. Acoustic properties of inlet and outlet boundary conditions are then varied to trigger the thermoacoustic modes. Differently from standard gas turbines, unstable modes at very high frequencies, i.e., 920 and 2260 Hz, are predicted and are in line with experimental recordings performed in the TRMI laboratory at UMONS (Belgium). The applied procedure has been proved to be relevant to analyse thermoacoustic instabilities via numerical LES simulations.

Experimental set-up

The considered burner is integrated in the MTT EnerTwin micro gas turbine, exploiting the typical recuperator Brayton cycle layout. It combines heat and power generation and produces up to 3 kWe and up to 21.5 kWth. A simplified scheme of the experimental set-up of this mGT, available in the laboratories of UMONS, with the different sensor locations where P, T and $\dot{V}$ (pressure, temperature, and volumetric flow rate, respectively) are measured, is presented in Fig. 1a. The mGT is equipped with a concentric co-flow cylindrical partially pre-mixed combustor, a scheme of which is provided in Fig. 1b. The air (blue arrows) is distributed over the primary zone, bypassing through the swirler and the secondary and tertiary zones thanks to dilution holes (denoted with the letter A). This swirler is composed of 7 blades, inducing the swirling motion of the air, and has 14 fuel injectors, placed upstream of the blades where fuel (in this study, methane) is injected (red arrows). Finally, in nominal operation, the combustor operates at a pressure of 2.8 bar with an air mass flow rate of 45 g/s at 975 K and a methane mass flow rate of 0.43 g/s at 380 K. As a result, the global equivalence ratio is equal to 0.165. These operating conditions are used for the numerical simulation of the combustor.

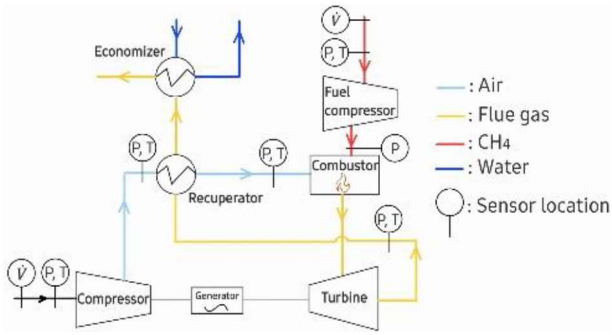

(a)

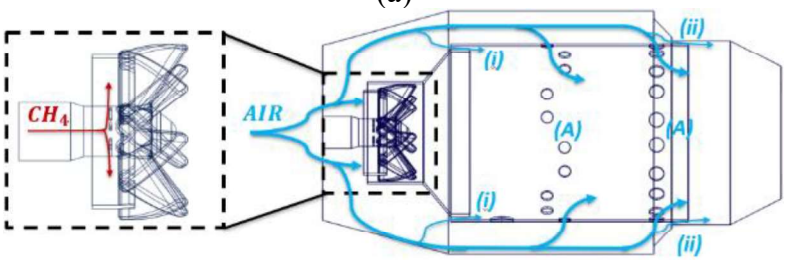

(b)

Figure 1. (a) Simplified scheme of the mGT set-up with the component links and sensor locations. (b) Combustor geometry with a local view on the swirler region where methane is injected upstream of the swirler and air is divided through several passages: swirler, dilution holes (A), inlet gap (*i*) and outlet gap (*ii*).

Numerical set-up and methodology

To investigate thermoacoustic instabilities, fully compressible Large Eddy Simulations are used to solve the reacting multi-species Navier-Stokes equation. The mesh used has 25 million tetrahedral elements and is refined in the flame region with a cell size of 0.35 mm. A smooth transition towards the outlet is achieved to reach a

maximum size of 3 mm. These simulations are performed with the AVBP code developed at CERFACS (https://www.cerfacs.fr/avbp7x/). Firstly, to characterize the stable flame, thermoacoustic coupling is prevented imposing a non-reflective outlet via Navier-Stokes Characteristic Boundary Conditions (NSCBC) [3]. Walls are considered as no-slip and with heat losses for the ones closer to the flame region. The flux through the wall is evaluated by giving the thermal resistance, equal to $2.5 \cdot 10^{-5}$ m²K/W, computed as the ratio of the wall thickness and the heat conductivity. For the combustion model, a dynamic version of the thickened flame model (DTFLES) is applied [4] coupled with the Charlette efficiency function [5, 6] with $\beta = 0.5$. To model the small turbulence scales, the SIGMA model is used as subgrid stress tensor [7]. Pure methane is considered as fuel and its oxidation is described with a modified version of the two-step BFER mechanism [9] (more details are reported in the next section). Once the reactive flow is converged, the results are used to compute the acoustic modes with FEniCS (https://fenicsproject.org/), a code solving the Helmholtz equation with a Finite Element Method. Finally, the thermoacoustic analysis is carried out by varying the relaxation factor at the inlet and outlet (NSCBC) to trigger thermo-acoustic instability [9].

Chemical mechanism for partially pre-mixed flame

The used chemical mechanism consists of two chemical reactions (1) and (2). To correctly predict the velocity and thickness of the flame for the operating condition in this work, an optimization is performed by changing the coefficients of the Arrhenius reaction rate constant equations (Eqs. (1) and (2)) and the Pre-Exponential Adjustment (PEA) functions (Eqs. (3) and (4)):

$$CH_4 + 1.5\,O_2 \Rightarrow CO + 2\,H_2O \qquad k_1 = A_1\, f_1(\phi)\, T^{\beta_1}\, e^{\left(\frac{-E_{a1}}{RT}\right)} [CH_4]^{n_{CH_4}}\, [O_2]^{n_{O_{2,1}}} \quad (1)$$

$$CO + 0.5\,O_2 \Leftrightarrow CO_2 \qquad k_2 = A_2\, f_2(\phi)\, T^{\beta_2}\, e^{\left(\frac{-E_{a2}}{RT}\right)} [CO]^{n_{CO}}\, [O_2]^{n_{O_{2,2}}} \quad (2)$$

$$f_1(\phi) = \frac{2}{1+\tanh\left(\frac{\phi_{0,1}-\phi}{\sigma_{0,1}}\right) + B_1\left[1+\tanh\left(\frac{\phi-\phi_{1,1}}{\sigma_{1,1}}\right)\right] + C_1\left[1+\tanh\left(\frac{\phi-\phi_{2,1}}{\sigma_{2,1}}\right)\right]} \quad (3)$$

$$f_2(\phi) = \frac{1}{2}\left[1+\tanh\left(\frac{\phi_{0,2}-\phi}{\sigma_{0,2}}\right)\right] + \frac{B_2}{2}\left[1+\tanh\left(\frac{\phi-\phi_{1,2}}{\sigma_{1,2}}\right)\right] + \frac{C_2}{2}\left[1+\tanh\left(\frac{\phi-\phi_{2,2}}{\sigma_{2,2}}\right)\right]\left[1+\tanh\left(\frac{\phi_{3,2}-\phi}{\sigma_{3,2}}\right)\right] \quad (4)$$

The optimization was performed to minimize the root mean square of the velocity difference predicted by the BFER and GRI 3.0 detailed mechanisms computed by using Cantera (https://cantera.org/). The optimized values (reported in red) of the novel *"CH4_6_2_CV"* mechanism are summarized in Table 1 where standard BFER parameters are also reported (in black). For the PEA functions, only the parameters $\phi_{2,1}$ has been modified from a value of 1.6 to 1.68. The Prandtl and the Schmidt

numbers for each species are imposed as equal to 0.5, keeping a constant Lewis number equal to 1. Figure 2 shows the improvement with the new mechanism (blue curve), with respect to the classic BFER (black curve) especially for lean mixtures.

Table 1. Parameters of the Arrhenius reactions rate constant equations for the CH4_6_2_CV (red) and standard BFER (black) schemes.

j	A_j	β_j	$E_{a,j}$	$n_{O_{2,j}}$	n_{CH_4}	n_{CO}
1	4.9×10^9 8.21×10^7	0	3.55×10^4 4.41×10^4	0.65 0.542	0.5 0.2	/
2	2×10^8 1×10^8	0.7	1.2×10^4	0.5	/	1

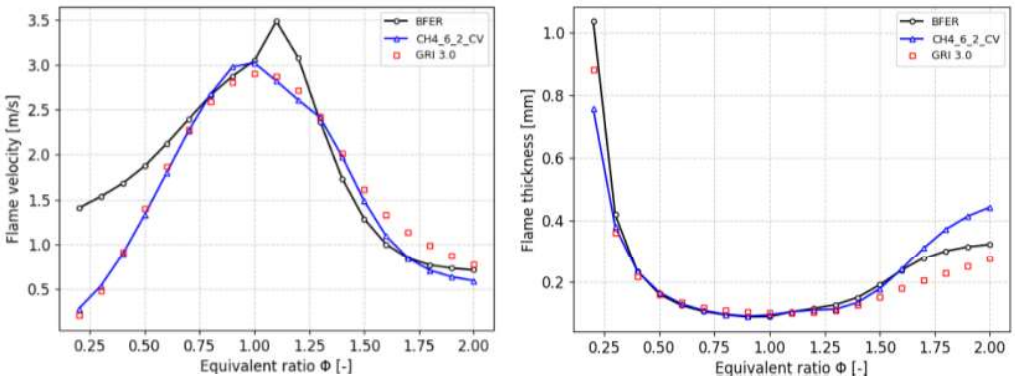

(a) (b)

Figure 2. Comparison of the 1D flame velocity (a) and thickness (b) between the GRI 3.0, BFER and the new CH4_6_2_CV mechanisms.

Reactive flow results: stable flame

Figure 3a depicts an instantaneous 3D contour of the heat release rate coloured by the DTFLES thickening factor and local equivalence ratio: LES predicts a classical V-shape flame stabilized over the swirler nose. Figure 3b reports a scatter plot of temperature over local equivalence ratio. The flame mainly burns in lean regime with the most probable value around ϕ=0.55, confirming the need of using the improved CH4_6_2_CV mechanism.

Then, the time averaged of the temperature field over 5 flow-through times is reported in Fig. 4. It provides a better visualization of the flame detachment from injector walls, shown by the white iso-contour of heat release rate at 10% of the maximum value, as a consequence of heat losses.

Thermoacoustic studies

By analysing the spectrum of pressure probes located at the inlet of the combustor (Fig. 5a-left), differently from the stable flame (black curve), no clear resonant peaks are observed.

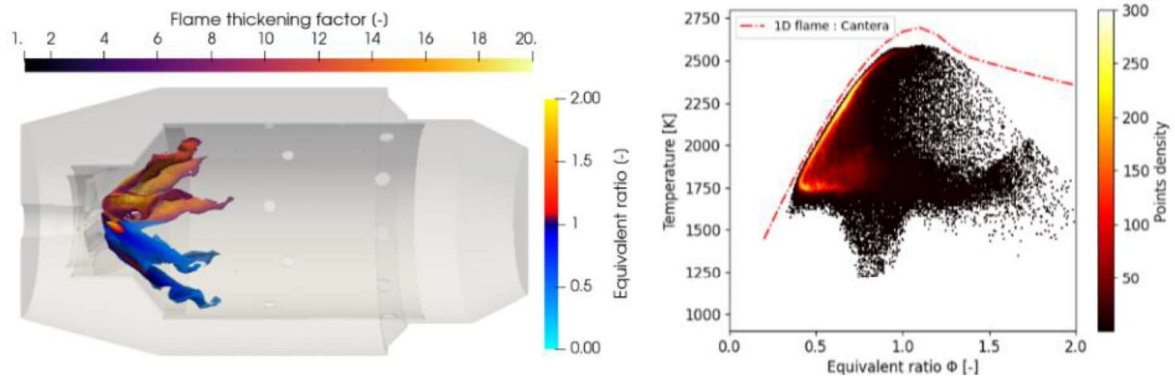

(a) (b)

Figure 3. (a) Heat release rate region coloured by the flame temperature and equivalence ratio (b) scatter plot of temperature over local equivalence ratio.

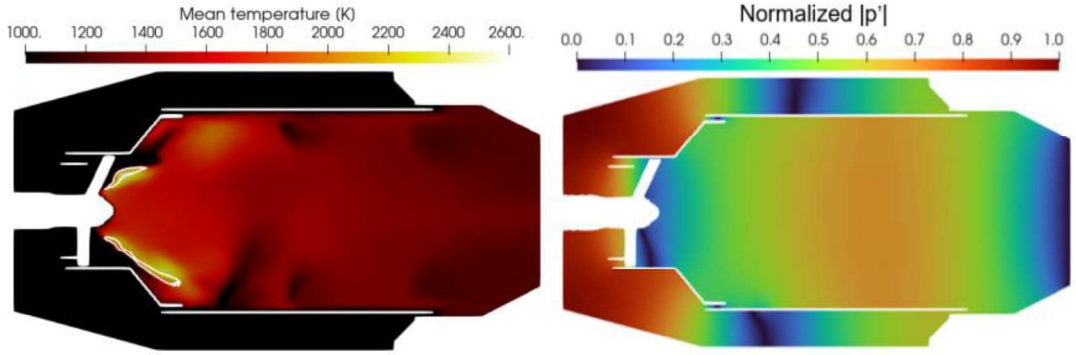

(a) (b)

Figure 4. (a) Time averaged of the temperature field over five flow-through times and the iso-contour of heat release rate (white lines) at 10 % of the highest value. (b) Second acoustic mode evaluated by FEniCS.

On the contrary, some unstable modes are triggered (red curve) at a frequency of ~ 900 Hz and 2200 Hz when a relaxation factor of $60 \cdot 10^3\ s^{-1}$ is applied at both inlet and outlet. These correspond to the first and second acoustic modes, respectively, evaluated by FEniCS (Fig. 4b). The peaks are recorded also in the heat release rate spectrum confirming the thermoacoustic coupling (Fig. 5a-right). A trace of the two modes can be also found in the pressure spectrum of sound recorded during the mGT tests with an external microphone (Fig. 5b), indicated with blue and red line, which validates the LES predictions.

Conclusions

Reactive fully compressible LES simulations have been performed on the MTT Enertwin mGT combustor. The results showed a stable V-shape flame without any acoustic mode except when the relaxation factor at inlet and outlet are changed. Frequency peaks are excited at approx. 900 and 2200 Hz which are close to those coming from the experimental data, proving the reliability of the applied procedure.

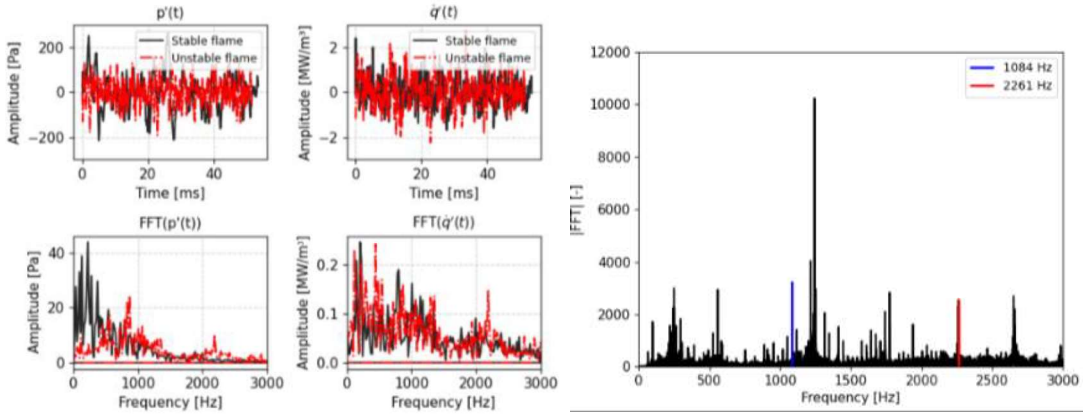

(a) (b)

Figure 5. (a) FFT analysis of the pressure and heat release rate signals where black and red are the stable and unstable flame respectively. (b) FFT analysis of the sound emitted by the mGT while operating at nominal condition.

Acknowledgments

HPC resources from EuroHPC JU (Project PROMETH2EUS) on MeluXina/LuxProvide and from CRESCO/ENEAGRID are acknowledged.

References

[1] Agostinelli, P. W., Laera, D., Boxx, I., Gicquel, L., & Poinsot, T. (2021). Impact of wall heat transfer in Large Eddy Simulation of flame dynamics in a swirled combustion chamber. *Combustion and Flame* 234, 111728.

[2] Gicquel, L. Y., Staffelbach, G., & Poinsot, T. (2012). Large eddy simulations of gaseous flames in gas turbine combustion chambers. *Progress in energy and combustion science* 38(6), 782-817.

[3] Poinsot, T.J., Lelef, S.K., Boundary conditions for direct simulations of compressible viscous flows, *Computational Physics* 101(1):104-129 (1992)

[4] Legier, J.P., Poinsot, T., Veynante, D., *Dynamically thickened flame LES model for premixed and non-premixed turbulent combustion*, Proceedings of the summer program, 2000, p. 157-168.

[5] Charlette, F., Meneveau, C., Veynante, D., "A power-law flame wrinkling model for LES of premixed turbulent combustion Part I: non-dynamic formulation and initial tests", *Combustion and Flame* 131:159-180 (2002)

[6] Charlette, F., Meneveau, C., Veynante, D., "A power-law flame wrinkling model for LES of premixed turbulent combustion Part II: dynamic formulation", *Combustion and Flame* 131:181-197 (2002)

[7] De Santis, A., Clements, A.G., Pranzitelli, A., Ingham, D.B., Pourkashanian, M., "Assessment of the impact of subgrid-scale stress models and mesh resolution on the LES of a partially-premixed swirling flame", *Fuel* 281: 118620 (2020)

[8] Franzelli, B., Riber, E., Gicquel, L., Poinsot, T., "Large eddy simulation of combustion instabilities in a lean partially premixed swirled flame", *Combustion and Flame* 159:621-637 (2012)

[9] Selle, L., Nicoud, F., Poinsot, T., "Actual impedance of nonreflecting boundary conditions: Implications for computation of resonators", *AIAA* 42: 958-964 (2004)

MODELLING AND FULL-SCALE TESTING OF A 35 MW HEAVY-DUTY MILD BURNER

D. Ettorre*, A. Puzo*, T. Vela, S.B. Ahmadpanah**, A. Saponaro***, M. Torresi*, and G. Rossiello****
corresponding author gianluca.rossiello@seamthesis.com
* DMMM, Department of Mechanics, Mathematics and Management, Polytechnic University of Bari, Via Re David, 200 – 70125 Bari, ITALY
** SEAMTHESIS Srl, Via IV Novembre, 156 – 29122 Piacenza, ITALY
*** Centro Combustione Ambiente SpA (CCA, Sofinter group), via Milano km 1,600, 70023 Gioia del Colle (BA), ITALY

Abstract
This research is focused on the experimental testing of a Ultra Low-NOx burner for steam generators, at its full capacity of 35 MW of fuel thermal input, and on the CFD modeling and simulation in three operating conditions, with comparison of NOx emissions coming from numerical results against experimental data.
First, the burner and the experimental test-rig, represented by a 48 MW boiler by the CCA facilities in Italy, are shown and illustrated, along with the testing conditions and the results obtained in terms of performance and emissions, in three different operating conditions. In all three cases the burner is fed with natural gas, the first being the baseline. In the second test condition steam is injected to reduce the NOx production, while in the third one EFGR (External Flue Gas Recirculation) is employed, keeping constant the steam mass flow rate, thus accomplishing the 1-digit target on the nitrogen oxides emissions.
In the second part CFD simulations are shown to give much insight in the burner operation and flame behavior inside the furnace, and to compare the overall results obtained in terms of performance, *i.e.*, NOx emissions predicted. The NOx modeling is carried out on the computed combustion temperature and species fields, and the outlet levels compared to the experiments. The results obtained prove that the chosen modeling is enough accurate to represent properly the main features of the complex physical phenomena involved, and the NOx estimation is found to be quite accurate to employ extensively the CFD tools for a detailed design process.

Context and motivation
Energy production and process industries account for more than one-third of global primary energy demand. The main source of this energy is still fossil fuel combustion. Since NOx is one of the most harmful emissions from combustion, the development of technologies that reduce its emission is of primary importance for industrial combustion applications. Combustion technology greatly influences NOx formation, and its development is the first essential step in limiting emission levels.

To strongly decrease the NOx emissions, new generation of Low-NOx burners (LNBs) is being developed [1]. The LNBs technology includes strategies such as air/fuel staging and flue gas recirculation, not necessarily as an alternative but often in synergy [2]. A particular mention deserves the MILD (Moderate or Intense Low Oxygen Dilution) combustion technology [3-5] where a dilution of the comburent air together with an increase of its temperature above the fuel self-ignition temperatures allows the delocalization of the oxidation reaction avoiding temperature peaks and NOx formation.
The key themes of this work are the analysis of the results of full-scale experimental tests on an industrial burner conducted on a dedicated test rig, and a comparison with CFD (Computational Fluid Dynamics) fluid dynamic simulations performed on the burner and combustion chamber assembly. Moreover, the research aims at identifying the potential of the MILD combustion applied to large scale industrial burners and to assess the effectiveness of specific techniques such as EFGR and steam injection for NOx emission reduction, also showing how NOx emission evaluation by CFD is suitable for very large-scale test equipment and compares well even with low NOx levels under extreme MILD combustion conditions.

Problem description and experimental results
CCA has developed a new Ultra-low NOx burner, in the 35 and 45 MW scale, which have been studied and optimized by means of CFD analysis and tested in full scale at the CCA facility in Gioia del Colle (Italy).
The test rig, in which the experimental tests performed on the burner are carried out, of the Center for Combustion Environment (CCA) (Figure 1), is equipped with a test combustion chamber for burners up to 48 MW thermal size, including feeding systems (gas, liquid and solid pulverulent), flue gas cooling (water-steam circuit, with evaporator tubes, superheater banks and condenser), flue gas treatment system with bag filters, and flue gas expulsion.

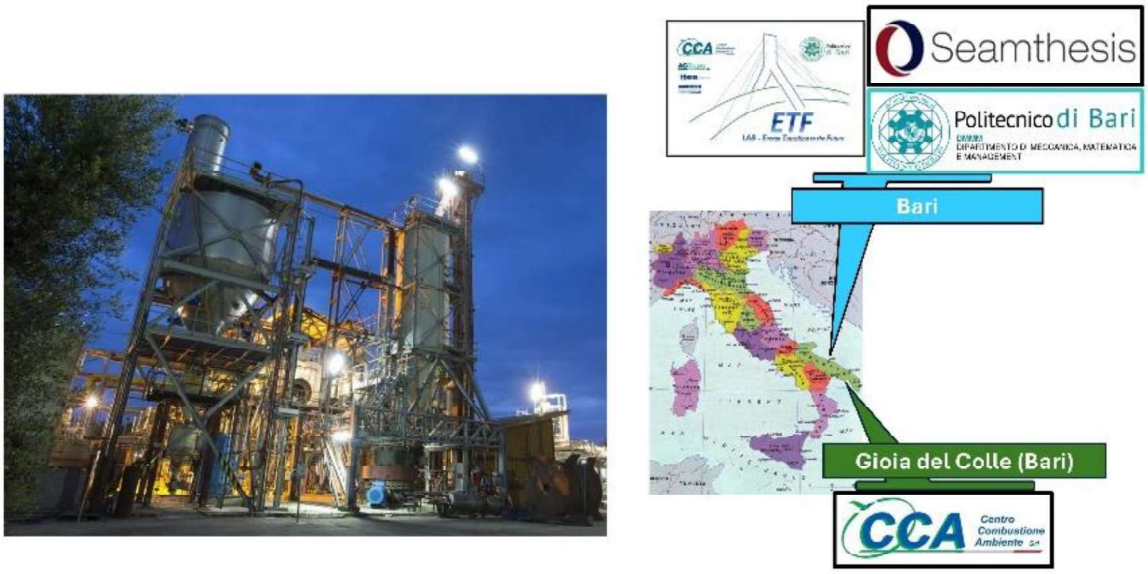

Figure 1. CCA 48 MW test-rig in Gioia del Colle (right) and 35 MW burner (left).

These tests are conducted by keeping constant the thermal input of 35 MW thermal referred to the lower heating value of the fuel, i.e., natural gas. This corresponds to 100% of the nominal load and the air flow rate is made to vary to test different excess air values, as well as the steam flow rate and the recirculation rate of external flue gas to evaluate its effect on NOx reduction.
During the tests, the quantities of interest are measured and recorded, Figure 2 shows the history of a test day, where NOx and CO are shown in ppm on a dry basis and normalized to a flue gas oxygen content of 3 percent on a dry basis. Also shown in Figure 2 is the dry oxygen content in flue gas (in percent) and the EFGR flow rate (in t/h). Six subdivisions are visible in the graph, representing the time intervals over which the results are averaged to identify significant operating points. Once the experimental testing has taken place, three main operating conditions of interest are identified: the baseline in period A (neither combustion gas recirculation nor steam injection is present), a second with steam injection in interval B, and a third with combined steam and combustion gas recirculation action in interval E.

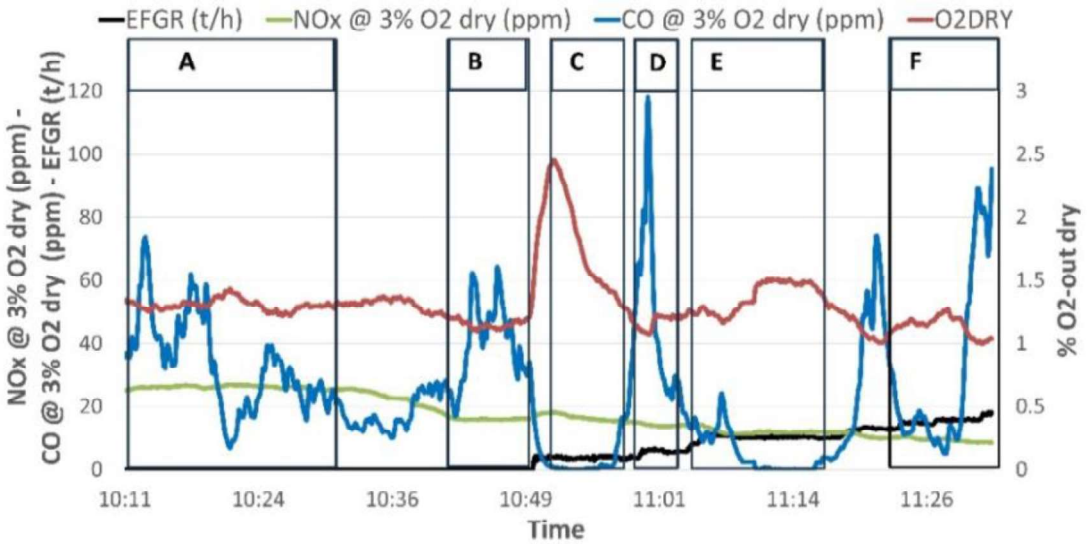

Figure 2. Test history chart (EFGR, O_2, NOx, CO) and operating points identified.

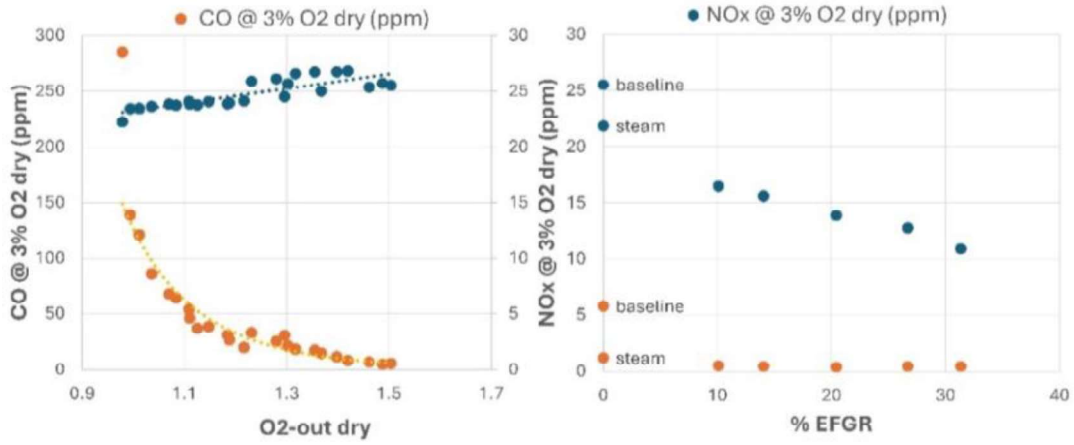

Figure 3. NOx and CO emissions depending on: (right) O_2 content in flue gases (*i.e.*, air excess**)**, and (left) External Flue Gas Recirculation rate (%).

Figure 3 shows on the left the trend of CO and NOx production as a function of oxygen content obtained as a result of the analysis performed on the flue gases.
On the right are shown the trends of reaction products (CO and NOx) as a function of the percentage of recirculation of the flue gases obtained during the test. It is clear from those trends that the presence of EFGR, with low residual oxygen contents in the flue gas, generates a reduction in emissions in terms of NOx and CO production.

Numerical modeling and results

The quantities of interest associated with each case considered are shown in Table 1 and used to define the inputs for CFD setup and to perform the comparison of numerical simulation results against experimental testing. The fuel flow rate, the flow rate of combustion air input, are exploited. Emission values, in particular, are used to verify and validate the results of the experimental analyses.

Table 1. Magnitudes of interest for the cases considered.

Grandezza	**Units**	**Case 1: BASELINE**	**Case 2: STEAM**	**Case 3: STEAM + EFGR**
MFR air	*Kg/s*	*13.345*	*13.246*	*13.449*
MFR fuel	*Kg/s*	*0.79*	*0.79*	*0.79*
MFR H2O vapour	*Kg/s*	*0*	*0.239*	*0.239*
MFR EFGR	*Kg/s*	*0*	*0*	*2.869*
O_2 dry	*%*	*1.3*	*1.14*	*1.48*
NOx dry, 3@O_2	*ppm*	*26*	*16*	*12*
CO dry, 3@O_2	*ppm*	*50*	*50*	*0*

CFD analyses are conducted with the Star-CCM+ simulation suite [6]. The computational domain, depicted in Figure 4 on the left, is discretized with a polyhedral mesh of about 5 million elements with orthogonal prismatic cells next to the walls and generating smaller cells close to complex geometries (Figure 4 on the right), like the swirler and the gas spud, to correctly capture flows and combustion details.

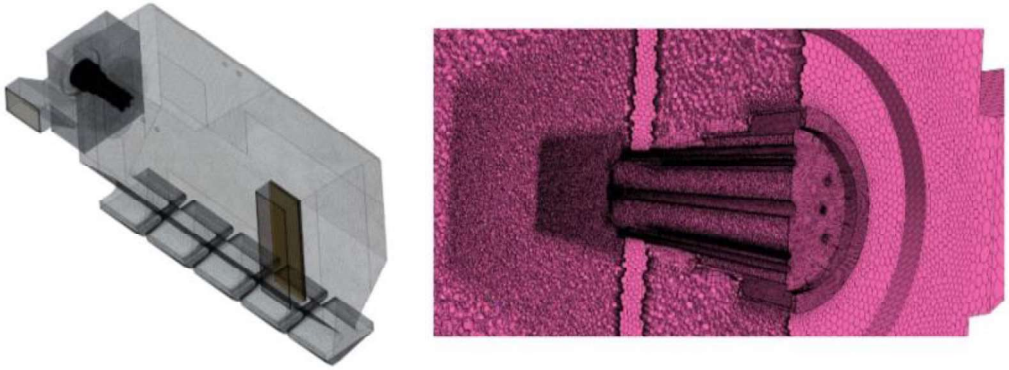

Figure 4. View of the mesh domain (left) and detail in the burner area (right)**.**

For each configuration, a steady state computation is performed with turbulence modeled by a RANS approach and standard 2 equations closure. A simplified chemistry approach has been employed, and the combustion is treated with the Flamelet Generated Manifold (FGM) [7]. The 325 reaction and 53 species mechanism GRI-Mech 3.0 [8] is chosen to model both the natural gas combustion and the NOx emission production. Compressible ideal gas approach is employed for the equation of state and to account for radiation a Discrete Ordinates Method is used, with absorption coefficients calculation based on Weighted Sum of Grey Gases Model, in which a mean optical path is computed on the whole fluid domain.

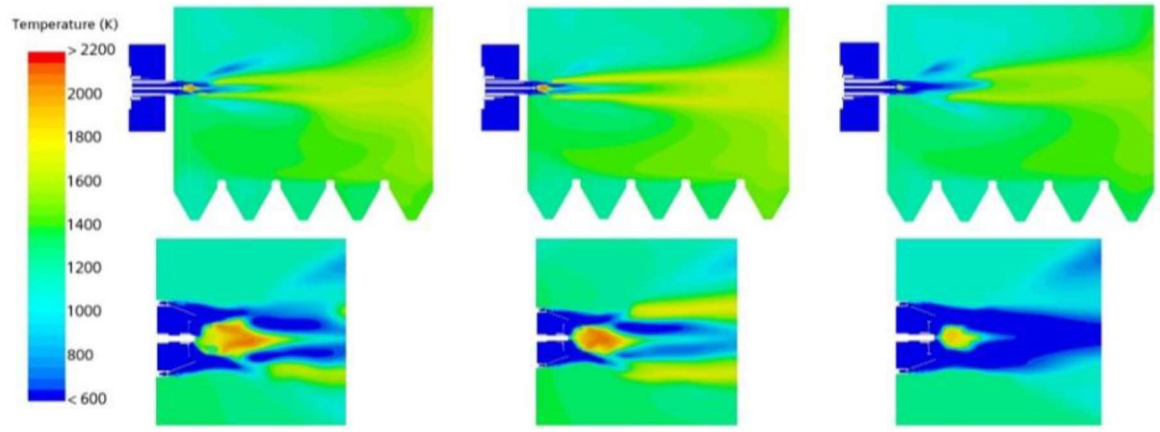

Figure 5. Contours of temperature in the XY plane (z=0), Case 1 on the left, Case 2 middle, Case 3 on the right.

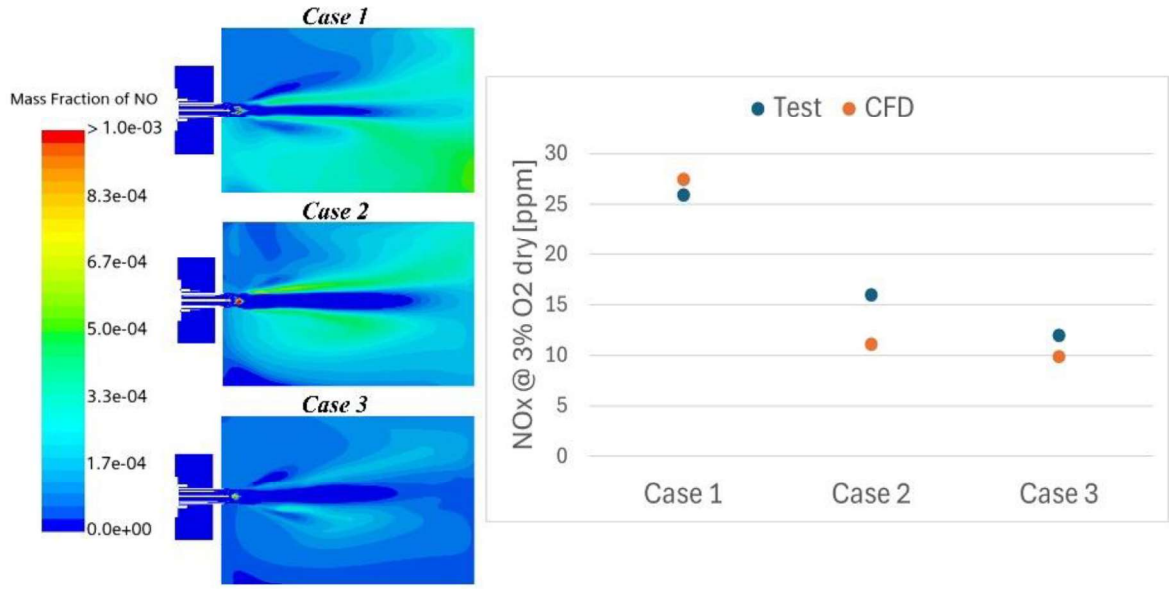

Figure 6. Contours of the NOx mass fraction on the XY plane (z=0) (left) and comparison between the NOx emissions on a dry basis, 3@O2 measured in the tests and the numerical values (right).

From the study carried out, the three cases analyzed exhibit a relatively uniform temperature field (Figure 5), with moderate local temperature peaks, a sign of the

recirculation of combustion gases occurring within the chamber, typical condition for the MILD-type combustion case. However, higher gas temperatures characterize the burner near field, where a pilot stabilization flame is used (see Figure 5, pictures in the bottom row, with zoom of burner near field).
As shown in Table 1, the steam injection configuration resulted in a reduction of NOx of 35% compared to the standard operation, and the addition of EFGR, causes a further decrease of NOx is measured, with a total reduction of 50% opposed to Case 1. This behavior is also predicted well by the CFD simulations, as can be seen in Figure 6 from the NOx mass fraction contours (on the left) and the comparison of the results obtained from the experimental data and simulations (on the right), which demonstrates good concordance on the values and trend of NOx.

Conclusion

In this work, an industrial Low-NOx burner is experimentally and numerically investigated in three different operating conditions. The investigation leads to the convergence of experimental tests and computational approaches, enabling an in-depth understanding of the phenomena governing MILD burner behavior, thus through the integration of experimental data and CFD simulations.
The test data allows validation of the adopted numerical model, and the considerable agreement between CFD results and experimental values of the NOx emissions shows that this methodology is reliable and usable for the design of industrial equipment, from the early stages up to the optimization of geometries.

References

[1] J.M. Ballester, C. Dopazo, N. Fueyo, M. Hernández, P.J. Vidal, “Investigation of low-NOx strategies for natural gas combustion”, *Fuel, 76, 1997*, 435-446.
[2] E.C. Zabetta, M. Hupa, K. Saviharju, “Reducing NOx emissions using fuel staging, air staging, and selective noncatalytic reduction in synergy”, *Ind. Eng. Chem. Res., 44, 2005*, 4552-4561.
[3] M. De Joannon, G. Langella, F. Beretta, A. Cavaliere, C. Noviello, "Mild Combustion: Process Features and Technological Constrains”, *Combustion Science and Technology, 153, 2000*, 33-50.
[4] J.A. Wünning, J.G. Wünning, “Flameless Oxidation to reduce thermal NO-formation”, *Progress in Energy and Combustion Science, 23, 1997*, 81-94.
[5] I.B. Özdemir, N. Peters, “Characteristics of the reaction zone in a combustor operating at mild combustion”, *Experiments in Fluids, 30, 2001*, 683-695.
[6] Simcenter STAR-CCM+ 2023.06 User Guide.
[7] Van Oijen, J. A. and De Goey, L.P.H. Modelling of premixed laminar flames using flamelet-generated manifolds. Combust. Sci. Technol., 16:113, 2000.
[8] http://www.me.berkeley.edu/gri_mech/

Development of a low-NO_x Micro-Mixing Gas Turbine Burner for High-H_2 Content Blends

A. Di Nardo, E. Giacomazzi, M. Cimini, G. Troiani, G. Calchetti, D. Cecere
eugenio.giacomazzi@enea.it
TERIN-DEC-CCT Laboratory, ENEA, C.R. Casaccia, S.M. di Galeria (Rome), Italy

Abstract
Aiming to a new and original burner geometry for gas turbines, potentially capable of operating with mixtures of natural gas and hydrogen in the range 0-100% H_2 with limited NO_x emissions, this work focuses on a device operating with a H_2 content larger than 50% by volume. The geometry was initially designed by means of several RANS simulations, optimizing reactants mixing and reducing the risk of flashback; LES simulations of some specific conditions were performed to check potential combustion dynamics issues. Then, the suggested solution was partially tested experimentally on a prototype.

Introduction
In the context of moving towards less reliance on fossil fuels, gas turbine plants operating with hydrogen/methane blends represent an important solution for decarbonizing the thermal power generation sector and for the sustainability of the energy transition [1]. However, it is important to emphasize that to have a significant impact on reducing CO_2 emissions, it is necessary to work with blends containing a high proportion of hydrogen.
When discussing fuel-flexibility currently, it refers to the ability of a gas turbine to operate with hydrogenated blends, where hydrogen is mixed with other gaseous fuels. These blends range from hydrogen-enriched natural gas (HENG) to ammonia. Although their tendency to exhibit thermos-acoustic instabilities, DLE (Dry Low Emissions) combustion technologies are the state of art to operate gas turbines with pollutant emissions below the limits set by the European Industrial Emission Directives (IED).
The maximum allowable concentration of hydrogen in DLE gas turbines varies significantly from one manufacturer to another [2]. The variation is due to differences in combustion temperatures and combustion technologies used across different classes. The pursuit of a combustion strategy for high-H_2 content blends with low NO_x emissions is a focal point for gas turbine manufacturers [3]. Currently, NO_x emissions are often controlled by derating the machine, meaning reducing its power output. It's also observed that adding H_2 to natural gas affects the start-up and shutdown procedures of the machines. Additionally, the machines will need to maintain a suitable degree of operational flexibility, meaning they must reliably and safely vary power output quickly to meet changes in energy demand.

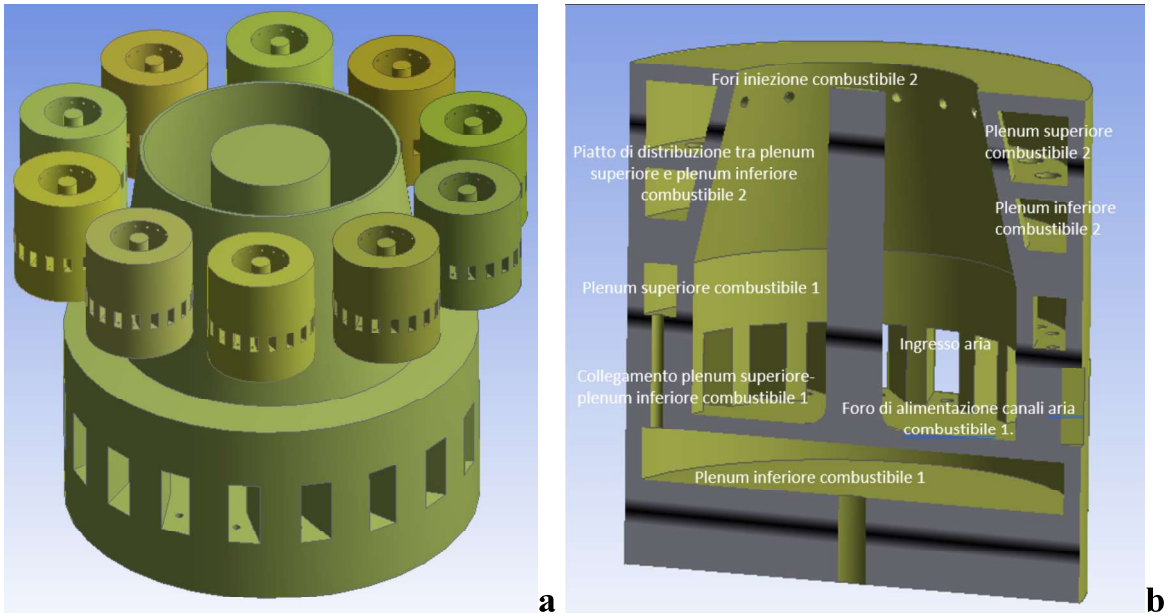

Figure 1. Complete burner (a); section of a crown system burner (b).

The developed burner configuration

Present results come from a project aiming to identify a low-emission fuel-flexible burner technology, build a prototype, and test it in an off-machine test facility. The design target machine is the TURBEC T100 microturbine.

An entirely original construction and operating strategy was devised. This involves two independent lean-premixed swirl burners (Fig. 1a) with flame aerodynamic stabilization: one central (330 kW_t) for low hydrogen content mixtures and one coaxial (crown burner system, consisting of 10 burners of 33 kW_t) for high hydrogen content mixtures. To independently operate the two burners, two separate air plenums have been provided, one for the central burner and one for the crown system, fed from a common source. By controlling their flow rates through an active control system, the operation of the gas turbine can be adjusted based on the hydrogen content in the incoming HENG mixture and the machine load.

This article deals with the development and first characterizations of one of the burners in the coaxial crown system, operating with high hydrogen content, i.e., higher than 50% by volume. To mitigate flashback risks the burner must be sized to ensure sufficiently high efflux velocities and low residence times in the mixer. To achieve these characteristics, the crown system burners were designed by hybridizing a typical swirl configuration (providing flame aerodynamic stabilization via central recirculation or vortex breakdown) with micro-mixing concepts.

The even number of burners in the crown system has alternating swirl flow directions, clockwise/counterclockwise, so that in the contact zone between the flows of two adjacent burners, the velocity vectors have the same direction.

In its final configuration, the burner (Fig. 2b) consists of 18 inclined channels through which air flows. Fuel is injected into each channel in crossflow at two opposing points (holes' diameter, 0.75 mm), facilitating fuel penetration into a

significant portion of the air flow, although it does not diffuse throughout the entire channel height. The dual injection necessitates two fuel plenums: the main fuel inlet feeds the lower plenum, which is then connected to the upper plenum through channels between the air conduits. The high number of channels and injection holes accelerates mixing through distributed fuel injection. Fuel and oxidizer complete mixing inside a premixing chamber of sufficient axial length (20 mm) to uniformize fuel concentration. The initially cylindrical chamber narrows towards the outlet to accelerate flow (exit diameter, 15 mm). The tangential velocity component imparts the initial rotation to the flow, necessary to achieve a swirl flow number SN = 1 at the burner outlets. Simultaneously, this rotation facilitates effective and rapid mixing between air and fuel in the premixing chambers.
For the first prototype of the crown system burner, it was equipped with an additional, independent diffusive fuel injection system (holes' diameter, 0.6 mm), located just before the outlet section, to experimentally evaluate its potential for very high concentrations of hydrogen in the fuel mixture.

The RANS development strategy
The sizing and optimization of the burners were conducted using RANS (Reynolds-Averaged Navier-Stokes) simulations with Ansys-Fluent 2019R1 software, focusing on mixing (non-reactive simulations). The computational grid has approximately five million cells. The "k-ε realizable" turbulence model was adopted, coupled to the Eddy Dissipation Concept (EDC) model with 46 chemical reactions and 17 species in reactive simulations. Transport properties were computed using kinetic gas theory. Simulations were performed at an operating pressure of 4.5 bar.
The representative burner of the crown system was studied for mixtures 50% and 100% H_2 at the nominal power level of 33 kW_t and maintaining constant air flow rate. It is observed that, the average nominal equivalence ratio ϕ decreases with increasing H_2 content: 0.5 and 0.43, for 50 and 100% H_2 respectively (ϕ used here are preliminary).
The objective was to design a burner that optimally mixes the reactants, reduces the risk of flashback, and is characterized by low NO_x emissions. After identifying the optimal configuration, the fuel supply system was also simulated to assess pressure losses and flow distribution through various channels and injection ports. Additionally, heat transfer through the burner material was simulated to estimate the preheating effect of the fuel due to the incoming air at 560°C.
A simple swirling configuration was initially chosen. Upon initial assessment of the dimensions and footprint of the central burner, it became apparent that the length of the lateral burners needed to be very short. Reducing this length created a dangerous central depression, potentially leading to the return of hot gases throughout the premixing chamber. Therefore, it became necessary to add a central body whose width was optimized to achieve a sufficiently high axial velocity profile at the outlet, particularly in the area adjacent to it. With this configuration, however, the length of the premixing chamber proved insufficient to ensure uniform mixing between fuel

and air. For this reason, additional and properly located fuel injections were added in the air channels, imposing a geometric configuration with an additional fuel plenum. An example of the obtained equivalence ratio distribution is in Fig. 2 (left): ϕ at the outlet section generally exhibits a radial distribution, with two inner and/or outer rings richer in fuel and a central ring poorer in fuel. The flow is highly swirled at the exit plane of the burner, exhibiting velocities of approximately 115 m/s, as shown in Fig. 2 (right).

The reactive simulations show that as the H_2content increases, the flame shortens. Such reduction is very noticeable when it is fueled with 100% H_2. Moreover, the flow velocities of the reactive mixture for which the burner was designed seem sufficient to prevent flame flashback in the premixing chamber. In the opposite case, i.e., with 50% H_2, the flame appears quite elongated and stretched.

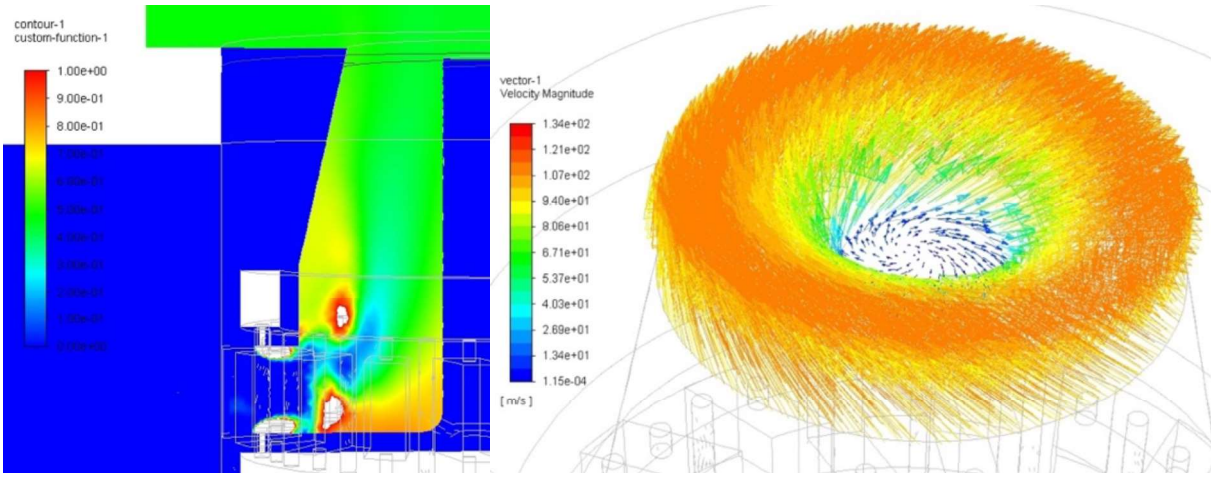

Figure 2. Equivalence ratio distribution for the 50%CH_4-50%H_2 fuel mixture (exit average value 0.5) (left). Velocity vectors at the exit (right).

LES and combustion dynamics

The LES simulations use the in-house parallel code HeaRT and ENEA's CRESCO supercomputing facility. The code solves the compressible Navier–Stokes equations with staggered finite-difference schemes, employing the dynamic Smagorinsky and LTSM models for subgrid terms. Convective terms are handled with the AUSM+-up method and WENO interpolation, while diffusive fluxes use a second-order central difference scheme.

The computational domain is a 60° cylindrical sector, 0.10 m in length, and 0.05 m in radius. The chamber starts with a quiescent flow at 874 K, and the fuel jet is injected through an annular section using a boundary condition from RANS simulations. The mesh has 400 × 300 × 64 grid points, totaling about 7.68 million cells. Chemical reactions follow the Glarborg et al. mechanism [4] for H_2, with 21 species and 109 reactions. Wilke's formula and Mathur's expression are used for viscosity and thermal conductivity, respectively, with preferential diffusion based on Hirschfelder and Curtiss law.

Figure 3 displays (left) snapshots of temperature fields of two 100% H_2 premixed

flames with different equivalence ratios. At ϕ=0.43, temperatures exceed 2000 K near the jet entrance, indicating the ignition zone with intense turbulence fostering efficient combustion. A strong recirculation bubble is observed near the jet axis, sustaining continuous ignition of fuel. At ϕ=0.30, temperatures peak below 1700 K with a longer flame length, showing less intense turbulence and quicker dissipation of high-temperature areas.
In both flames, the combustion region is confined to the internal shear layer, with intermittent combustion occurring in the external shear layer due to strong vortices detached from the flame tip flapping motion (not visible). Flame front topology is clear looking at the heat release rate (HRR) distribution on the right of Fig. 3. The flame at ϕ=0.43 exhibits more intense combustion and greater heat release rate. In contrast, at ϕ=0.30, the HRR is significantly reduced, indicating weaker combustion, and the flame length increases. Additionally, at ϕ=0.43, the flame front appears corrugated but not fragmented, unlike the other case where the flame front appears discontinuous in certain regions.

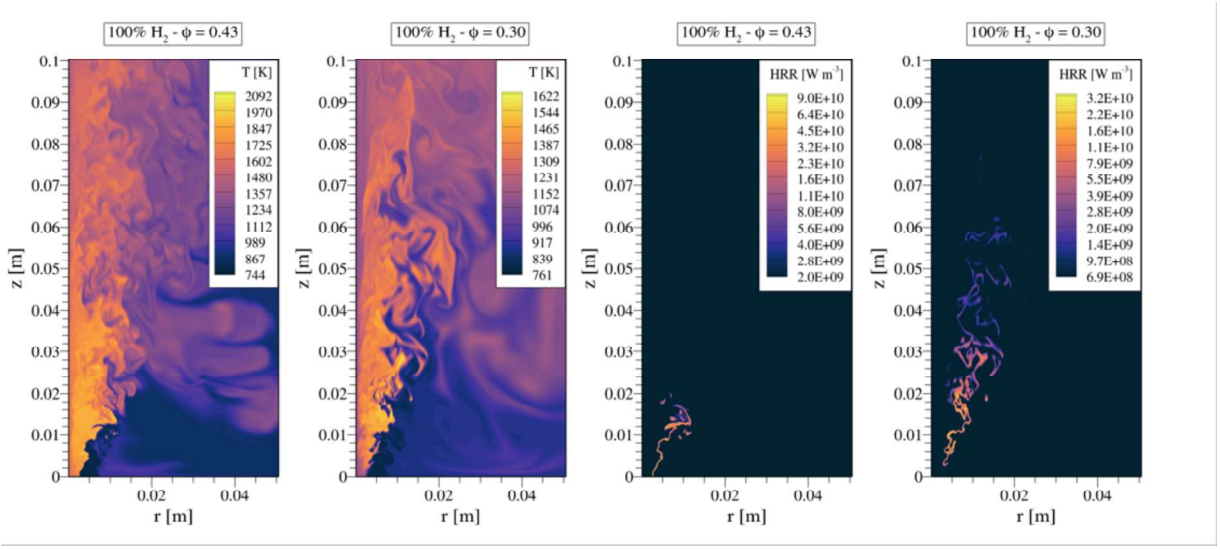

Figure 3. Snapshots of temperature field for 100% H_2 at different equivalence ratios.

Experimental tests

The conceptual burner for the crown system, designed for high-H_2 content fuel mixtures, has been mechanically designed and constructed. The prototype is shown in Fig. 4: the burner is on the left (about the diameter of a €1 coin), while it is assembled in its feeding system on the right.
The initial experimental tests aim to identify the stable ignition range of the burner at 1 and 4.5 bar, with various nominal powers and different hydrogen percentages in the HENG blend, while altering the nominal equivalence ratio. Figure 4, on the right, shows some initial results at 1 bar; further tests are planned, also aimed at quantifying NOx emissions. The initial results in Fig. 4 highlight critical flashback issues due to the central body for high hydrogen content: the central recirculation zone causes a strong impingement of hot gas products on its surface, making it incandescent.

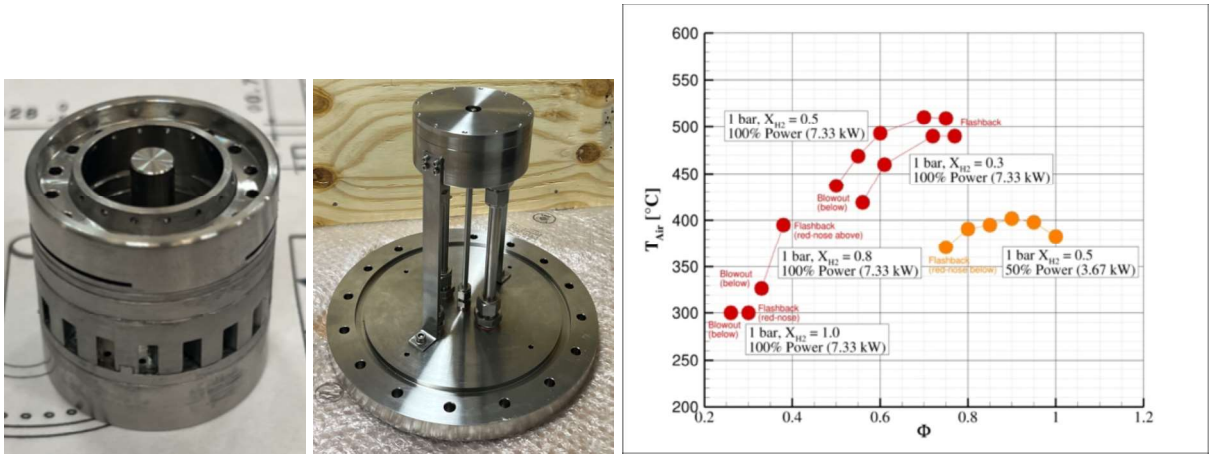

Figure 4. First prototype of the micro-mixing burner alone (left) and assembled in its feeding system (center); initial flame stability results from experimental tests at 1 bar (right).

Conclusions and future work

A combustion strategy capable of potentially operating over a wide range of natural gas/hydrogen mixtures has been identified through RANS simulations, focusing on the defined crown system burner for high-H_2 content blends. Some LES simulations were performed to examine combustion dynamics issues before constructing a representative prototype. Ongoing experimental tests will validate the adopted combustion strategy and suggest appropriate modifications. Consequently, the device may undergo improvements, and numerical studies will be conducted on integration with the feed system and liner for future implementation on the TURBEC T100 microturbine.

References

[1] E. Giacomazzi, G. Troiani, A. Di Nardo, G. Calchetti, D. Cecere, G. Messina, S. Carpenella, “Hydrogen Combustion: Features and Barriers to its Exploitation in the Energy Transition”, Energies, Special Issue ``Advances in Hydrogen Energy III", 16(20):7174 (1-29), 2023.

[2] D. Cecere, E. Giacomazzi, A. Di Nardo, G. Calchetti, “Gas Turbine Combustion Technologies for Hydrogen Blends”, Energies, Section A5 ``Hydrogen Energy", 16(19):6829 (1-29), 2023.

[3] D. Cecere, S. Carpenella, E. Giacomazzi, A. Stagni, A. Di Nardo, G. Calchetti, “Effects of hydrogen blending and exhaust gas recirculation on NO_x emissions in laminar and turbulent CH_4/Air flames at 25 bar”, International Journal of Hydrogen Energy, 49(B):1205-1222, 2024.

[4] Glarborg, Peter, et al. "Modeling nitrogen chemistry in combustion." Progress in energy and combustion science, 67: 31-68, 2018.


THE COMBUSTION INSTITUTE
1954

SESSION XI

Reaction Kinetics


THE COMBUSTION INSTITUTE
1954

Reduced-order condensed-phase kinetic models for polyethylene thermal degradation

A. Locaspi, T. Faravelli
tiziano.faravelli@polimi.it
CRECK Modeling Lab, DCMIC, Politecnico di Milano, Italy

Abstract
In a circular economy perspective, plastic wastes (PW) can be a source of chemicals, energy vectors and fuels. Pyrolysis, gasification, and partial oxidation technologies can be employed to produce chemicals, fuels, or energy. Modelling the thermochemical valorization requires first the definition of suitable condensed phase pyrolysis mechanisms for each constituent. This work proposes a reduced and a multi-step condensed-phase kinetic model for polyethylene (PE) thermal degradation for CFD applications. The former model employs 50 species and 480 reactions, while the latter involves 10 species and 10 reactions. The degradation rate and the selectivity to the different products is obtained from a validated semi-detailed model. The kinetic mechanisms are complemented by the thermochemistry of gas, liquid, and solid-phase species, accounting for phase-transition through pseudo-chemical reactions. Model validations are performed by comparison with experimental data in terms of mass loss, heat fluxes and product distribution profiles. Extending the proposed approach to other polymers and considering secondary gas-phase reactions offers a powerful tool to model PW chemical recycling processes.

Introduction
Industrial scale implementation of thermochemical recycling is a key step towards circular and sustainable chemical and energy industries [1]. Product distribution optimization, process/reactor design, and pollutant control largely benefit from fluid dynamics and chemical kinetic modelling tools, thus motivating the present work. Studies on PW mixtures have only been emerging recently, while single polyolefins condensed-phase degradation has been extensively studied in the past decades [2]. Several models have been presented for polyethylene (PE) pyrolysis, most being one-step or highly detailed mechanisms [1]. The former describe only polymer mass-loss, while the latter achieve high detail in volatile predictions but are computationally expensive. Industrial applications require accurate but flexible models able to predict the key physico-chemical steps of the degradation, i.e., residence times, heat requirements and product distribution. Reduced-order models capture the phenomena involved at a lower computational cost.
This work proposes a methodology to derive reduced-order CHEMKIN-like condensed-phase kinetic models. A reduced and a multi-step model are obtained for PE pyrolysis, by lumping of a validated semi-detailed mechanism [3]. The resulting

kinetic models offer two levels of compromise between accuracy and cost and prove able to describe a wide range of operating conditions. The models are complemented by thermochemistry of all species. Further work will address secondary gas-phase reactions, while coupling these models to other polymer models enables describing PW valorization. The proposed models are freely available on GitHub [4].

Reduced semi-detailed mechanism (PE-50-480)

The semi-detailed model for PE [3] follows the Functional Groups (FG) methodology, distinguishing polymeric chains in High (HMW) and Low Molecular Weight (LMW) species. The former are represented with pseudo-species representative of the polymer chemical moieties, the latter with species of interest. The reduced mechanism follows the same approach and describes the HMW chains with the same mid- (MC) and end-chain (EC) units. A species representative of the crystalline polymer is also introduced, together with its melting reaction. The LMW distribution is described with real species for $C<C_5$ and by vertical lumping of the $C>C_5$ range introducing paraffin, olefin, and diolefin for C_7, C_{16}, C_{30}, and C_{60}.
A single radical isomer is introduced for each stable species. For instance, as shown in Figure 1, HMW chains decompose forming terminal EC radicals (P-$\dot{C}_{40}H_{80}$_T) that propagate by unzipping, backbiting or stabilize to "P-$C_{40}H_{81}$". H-abstraction on this EC forms a secondary radical (P-$\dot{C}_{40}H_{80}$) that decomposes by β-scission. The reduced model lumps them both into "P-$\dot{C}_{40}H_{80}$", which undergoes all reactions of the isomers. The selectivity between the pathways is obtained by weighting on the temperature-dependent ratio between the two isomers [5]. The reduced kinetic model employs 50 gas + liquid species and 480 liquid reactions, i.e., a decrease of ~60% and ~85% in species and reactions compared to the semi-detailed mechanism [3].

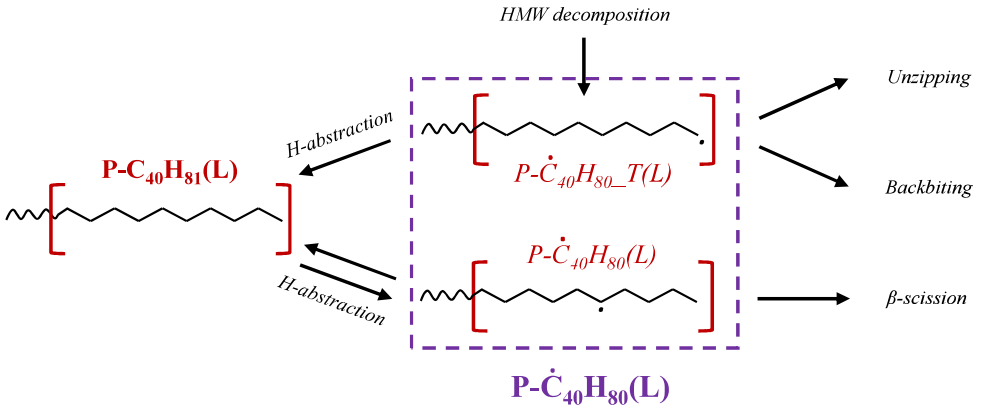

Figure 1. Representation of the radical isomer lumping for EC paraffin radicals.

Multi-step fully lumped mechanism (PE-10-10)

The multi-step model describes only the key aspects of the degradation process to reduce the computational cost. HMW chains are represented only by the crystalline and molten mid-chains, using the same carbon numbers as the reduced model. The LMW distribution is described by real species for the permanent gases (C_2H_4, C_3H_8,

C_3H_6, C_4H_6) and by lumped species representative of the petroleum cuts (C_5-C_{60}). Only the olefins are included, introducing NC_7H_{14} for oil cuts (C_5-C_{10}), $C_{16}H_{32}$ for diesel cuts (C_{11}-C_{20}) and $C_{30}H_{60}$ for waxes (C_{21+}). All species form in gas-phase, except for $C_{30}H_{60}$(L) that can undergo liquid-phase degradation before evaporating.
The multi-step mechanism is sketched in Figure 2. The crystalline phase melts as in the reduced model, and the molten polymer decomposes through 4 major pathways: backbone degradation, allyl formation, backbiting and unzipping. Each step is represented by a lumped reaction that accounts for the products of the semi-detailed mechanism. The rate of backbone degradation is estimated from the steady-state assumption on the total radical pool and assuming β-scissions are rate determining [6]. The selectivity to the other pathways is the same as the reduced model. Overall, this mechanism employs 10 gas + liquid species and 10 reactions, i.e., respectively a decrease of 92% and 99.7% compared to the semi-detailed mechanism [3].

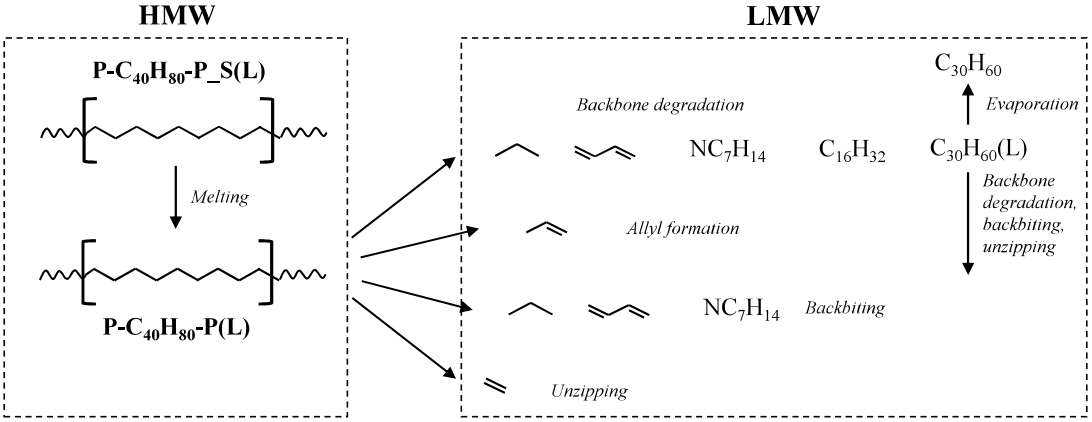

Figure 2. Schematic representation of the multi-step reaction mechanism.

Thermochemistry

The proposed mechanisms involve only irreversible reactions, and the estimation of thermodynamic properties allows to perform energy balances. Species properties are computed starting from gas-phase approaches [7]. Liquid-phase thermochemistry is differentiated according to the species critical temperature (T_c). For $T>T_c$ the gas-phase NASA values are employed, while at $T<T_c$ evaporation properties [8,9] are employed to evaluate the liquid-phase polynomials. To avoid the discontinuity at $T=T_c$, the transition temperature between the liquid and gas polynomials is defined such that the species enthalpy is continuous. On the other hand, the specific heat is intrinsically discontinuous.
The enthalpy and heat capacities of molten MC and EC are evaluated with the same approach, assuming a $T_c \rightarrow \infty$. Conversely, their entropies are estimated as the difference between two real chains of 100 and 110 MC units. The thermochemistry of the crystalline phase is estimated from literature data on heat capacities and melting enthalpies [10]. Above the melting temperature, the Einstein functional form is employed to constrain the high T limit for the heat capacity.

Model Validation

The proposed models are validated with the semi-detailed model [3] and a wide range of experimental data from the scientific literature in terms of mass-loss profiles, heat fluxes, and product distribution as shown in Figure 3 and 4.

Figure 3.a shows the comparison in terms of mass-loss profiles. Both reduced-order models reproduce the polymer degradation with similar accuracy compared to the semi-detailed model. While differences are observed, these are within the author-to-author experimental variability. At low T, the reduced model predicts slightly longer degradation times, possibly because of underestimation of allylic reactivity. The multi-step model predicts a smoother degradation profile, as the simplified reaction kinetics do not account for the time-varying reactivity.

Figure 3.b shows the comparison in predicted heat fluxes at 10°C/min. The models employ the same thermochemistry, and differences are related to the variations in mass-loss predictions. The melting peak is correctly described by the simplified kinetic approach. Conversely, the models underestimate the heat fluxes in the 200-400°C, although a wide scattering is also observed in terms of experimental data. Further experimental work is required to validate the proposed approach.

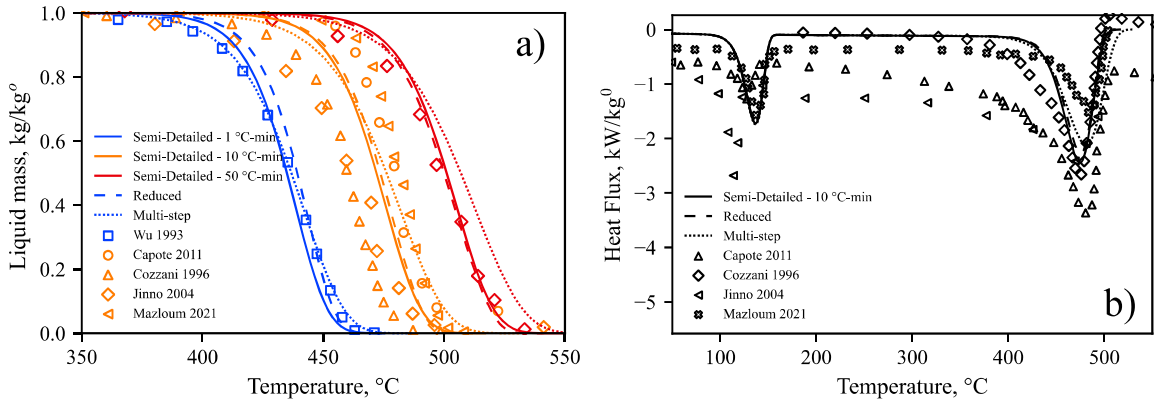

Figure 3. Model validation with data [11–15] on: a) mass-loss, b) heat fluxes.

Figure 4 shows the comparison in terms of mass distribution data. The semi-detailed and reduced models predict the detailed carbon distribution and the differences in unsaturation. Conversely, because of the strong lumping employed, the multi-step model describes only the petroleum cuts formed. Overall, all models capture the trend in the variation of product yields across the considered temperature range. Differences are observed, as the multi-step model neglects CH_4 formation, and the reduced one overestimates C_2H_4. Considering C_3 yields, the semi-detailed and reduced model show similar predictions, while the multi-step mechanism overestimates them. The multi-step model underestimates oil-cuts and underestimates diesel-cuts at high T, possibly due to the strong lumping. The higher oil yields of the reduced model are consequence of the strong simplification in selectivity between terminal and internal radicals.

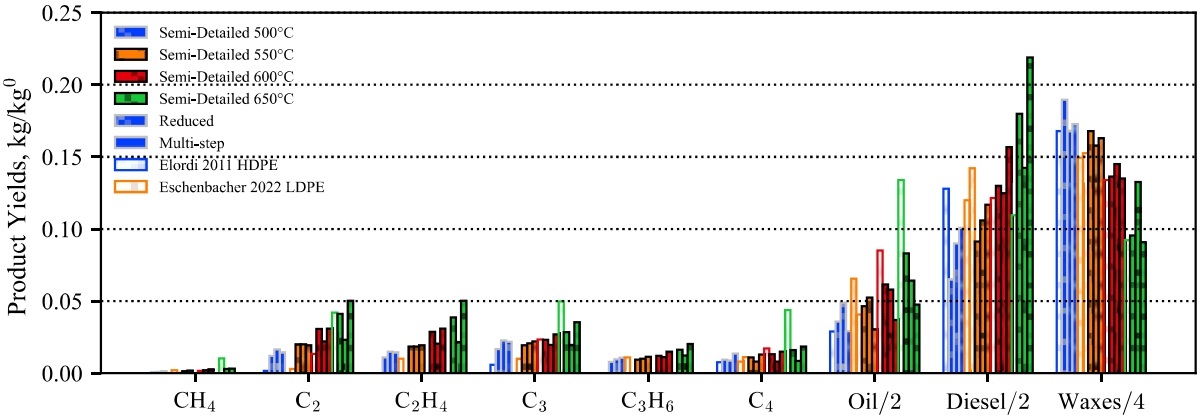

Figure 4. Model validation with mass product distribution data [16,17].

Conclusions

This work proposes a methodology to derive reduced-order condensed-phase kinetic models, employing PE as case-study for validation. A reduced and a multi-step model are proposed, coupled with the estimation of thermochemical properties. The reduced model lumps radical isomers and involves 50 species and 500 reactions, while the multi-step mechanism simplifies the radical chemistry in few global steps and involves 10 species and 10 reactions. The framework is validated with literature mass-loss profiles, heat fluxes, and product yields. Future activity will address evaluation of gas-phase reactions and development of similar reduced models also for other polymers of interest to describe PW valorization.

Acknowledgements

The authors thank M. Pelucchi and A. Frassoldati for their valuable suggestions in model development. This project has received funding from the European Union's Horizon Europe research and innovation programme under the HORIZON-CL4-2021-TWIN-TRANSITION-01 grant agreement No 101058412. Views and opinions expressed are however those of the author(s) only and do not necessarily reflect those of the European Union or HADEA. Neither the European Union nor the granting authority can be held responsible for them.

References

[1] Dogu O., Pelucchi M., Van de Vijver R., Van Steenberge P.H.M., D'hooge D.R., Cuoci A., Mehl M., Frassoldati A., Faravelli T., Van Geem K.M., "The chemistry of chemical recycling of solid plastic waste via pyrolysis and gasification: State-of-the-art, challenges, and future directions", *Prog. Energy Combust. Sci.* 84: 100901 (2021).

[2] Harmon R.E., Sribala G., Broadbelt L.J., Burnham A.K., "Insight into Polyethylene and Polypropylene Pyrolysis: Global and Mechanistic Models", *Energy & Fuels* 35: 6765–75 (2021).

[3] Locaspi A., Pelucchi M., Mehl M., Faravelli T., "Towards a lumped approach for solid plastic waste gasification: polyethylene and polypropylene

pyrolysis", *Waste Manag.* 156: 107–17 (2022).
[4] CRECK Modeling Lab, *Kinetic-Mechanisms*, https://github.com/CRECKMODELING/Kinetic-Mechanisms, cited 29 April, 2024.
[5] Pegurri A., Dinelli T., Pratali Maffei L., Faravelli T., Stagni A., "Coupling chemical lumping to data-driven optimization for the kinetic modeling of dimethoxymethane (DMM) combustion", *Combust. Flame* 260: 113202 (2024).
[6] Ranzi E., Dente M., Faravelli T., Bozzano G., Fabini S., Nava R., Cozzani V., Tognotti L., "Kinetic modeling of polyethylene and polypropylene thermal degradation", *J. Anal. Appl. Pyrolysis* 40–41: 305–19 (1997).
[7] Burke S.M., Simmie J.M., Curran H.J., "Critical evaluation of thermochemical properties of C1-C4 species: Updated group-contributions to estimate thermochemical properties", *J. Phys. Chem. Ref. Data* 44: 13101 (2015).
[8] Kolská Z., Růžička V., Gani R., "Estimation of the Enthalpy of Vaporization and the Entropy of Vaporization for Pure Organic Compounds at 298.15 K and at Normal Boiling Temperature by a Group Contribution Method", *Ind. Eng. Chem. Res.* 44: 8436–54 (2005).
[9] Nannoolal Y., Rarey J., Ramjugernath D., "Estimation of pure component properties: Part 3. Estimation of the vapor pressure of non-electrolyte organic compounds via group contributions and group interactions", *Fluid Phase Equilib.* 269: 117–33 (2008).
[10] Gaur U., Wunderlich B., "Heat Capacity and Other Thermodynamic Properties of Linear Macromolecules. V. Polystyrene", AIP Publishing, 1982.
[11] Chao-Hsiung Wu, Ching-Yuan Chang, Jwo-Luen Hor, Shin-Min Shih, Leo-Wang Chen, Feng-Wen Chang, "On the thermal treatment of plastic mixtures of MSW: Pyrolysis kinetics", *Waste Manag.* 13: 221–35 (1993).
[12] Capote J., Alvear D., Abreu O., Lazaro M., Puente E., Pyrolysis characterization of a linear low density polyethylene, Fire Safety Science, 2011, pp.877–88.
[13] Cozzani V., Nicolella C., Rovatti M., Tognotti L., "Influence of Gas-Phase Reactions on the Product Yields Obtained in the Pyrolysis of Polyethylene", *Ind. Eng. Chem. Res.* 36: 342–8 (1997).
[14] Jinno D., Gupta A.K., Yoshikawa K., "Thermal Decomposition Characteristics of Critical Components in Solid Wastes", *Environ. Eng. Sci.* 21: 65–72 (2004).
[15] Mazloum S., Aboumsallem Y., Awad S., Allam N., Loubar K., "Modelling pyrolysis process for PP and HDPE inside thermogravimetric analyzer coupled with differential scanning calorimeter", *Int. J. Heat Mass Transf.* 176: 121468 (2021).
[16] Elordi G., Olazar M., Lopez G., Artetxe M., Bilbao J., "Product Yields and Compositions in the Continuous Pyrolysis of High-Density Polyethylene in a Conical Spouted Bed Reactor", *Ind. Eng. Chem. Res.* 50: 6650–9 (2011).
[17] Eschenbacher A., Varghese R.J., Abbas-Abadi M.S., Van Geem K.M., "Maximizing light olefins and aromatics as high value base chemicals via single step catalytic conversion of plastic waste", *Chem. Eng. J.* 428: 132087 (2022).

A Group Preserving Time Integration Scheme for Chemistry

L. Angelilli*, V. Raman*
Email: langelil@umich.edu
* Department of Aerospace Engineering, University of Michigan, Ann Arbor, MI 48105, USA

Abstract
The integration of the chemical system always presents considerable challenges due to the wide variety of time scales embedded within. Stiff integrators, necessary for the stability properties they offer, allow the system to evolve over significant time steps. However, backward integration generally becomes computationally expensive as the size of the chemical kinetics mechanism increases. Since a nonlinear ODE can always be recast as a Lie group action, we can constrain the integration onto the manifold with a Group Preserving Scheme (GPS). This property allows for the definition of high-order, explicit, unconditionally stable time integration schemes that are also Jacobian free. The performance of the GPS, compared in terms of computational time and accuracy with the canonical integrator CVODE, reveals a tenfold speed-up while preserving the same accuracy for large mechanisms.

Introduction
The field of computational chemistry frequently encounters the challenge of solving ordinary differential equations (ODEs) that arise in the modeling of chemical kinetics. These equations often exhibit stiff behavior due to the vastly different reaction time scales present within the system. Traditional numerical methods based on backward time integration, while broadly effective, can sometimes fail to maintain the inherent geometric properties of the underlying physical processes, leading to potential inaccuracies and inefficiencies.
Another approach to deal with stiffness is to adaptively filter the fast time scales according to the Computational Singular Perturbation (CSP) principles. This approach, encapsulated by the CSP solver [1], leverages a local low-dimensional manifold derived from the CSP fast/slow decomposition. It adaptively mitigates stiffness by selectively eliminating rapid scales from the vector of chemical source terms, leading to a simplified set of non-stiff equations. These equations can be integrated with explicit schemes using larger time-steps. However, the CSP solver depends on generating a costly on-the-fly basis known as the CSP projector, derived from the eigensystem of the Jacobian matrix associated with the local chemical source terms.
A second strategy introduces a data-based reduced-order model (ROM) designed to mitigate the stiffness derived from various chemical time scales [2]. The goal is to create a ROM that serves as a fluid surrogate for tracking the time evolution of the

thermochemical state vector (comprising temperature and species mass fractions) throughout a complex, stiff, and nonlinear ignition sequence. The approach utilizes an encode-forecast-decode strategy, incorporating a nonlinear autoencoder (AE) for reducing dimensionality (through encoding and decoding) combined with a neural ordinary differential equation (NODE) to model the system dynamics within the latent space provided by the AE.

The main issue of employing these techniques is that they are computationally expensive when the size of the mechanism becomes large and Lie group integrators present a promising solution to these challenges. For over a hundred years, Lie groups have been crucial in shaping our understanding of the geometry inherent in differential equations. It is widely thought that the concept of Lie groups, as part of the broader framework of differential geometry, is extremely useful in developing advanced numerical methods for discretizing ODEs while preserving their invariant properties. By maintaining the geometric structure and invariance of the original ODEs, these new methods are more precise, more stable, and more efficient than traditional numerical approaches [3].

This approach is particularly advantageous in the context of chemical kinetics, where the preservation of certain invariants—like total mass or energy—can be crucial for achieving physically realistic and stable simulations.

In this paper, we explore the application of Lie group integrators to the domain of chemistry, focusing on their potential to enhance the accuracy and stability of simulations compared to conventional numerical methods.

Numerical Methods

This section summarizes the numerical approach adopted to formulate the time integration schemes.

The chemistry evolution is described through a stiff ODE

$$\frac{d\boldsymbol{y}}{dt} = \boldsymbol{f}(\boldsymbol{y})$$

Where **y** represents the state vector of the $N_s$species mass fractions and the RHS $\boldsymbol{f}(\boldsymbol{y})$ the chemical source term modeled by the Arrhenius law. From a mathematical perspective, the **y**(t) is a curve in R^N parametrized by the time t that goes from the initial condition to the equilibrium point. Recalling a fundamental theorem of differential geometry, since the curve is uniquely determined, we can define an *atlas* and finite number of *maps* to represent the curve, the y is a manifold. Additionally, the tangent to **y**(t) is given by **f**(**y**), which is always defined. Since the tangent bundle is defined everywhere, the manifold is differentiable.

The main goal of this manuscript is to formulate a numerical scheme that constrains the integration to the manifold itself following Liu's idea of Group Preserving Scheme [3-4]. This is possible if and only if the tangent bundle can be expressed as a left Lie group action on the manifold, which means that there exists an operator H such that

$$\frac{d\boldsymbol{y}}{dt} = \boldsymbol{f}(\boldsymbol{y}) = \boldsymbol{H}(\boldsymbol{y})\boldsymbol{y}$$

And this operator must be differentiable, invertible and the inverse must be differentiable as well. To define a suitable operator **H**, consider the augmented system $\mathbf{x} = [\mathbf{y}\ ||\mathbf{y}||]^T$. The time evolution of x is then

$$\frac{d}{dt}\begin{pmatrix}\boldsymbol{y}\\ ||\boldsymbol{y}||\end{pmatrix} = \begin{pmatrix}\mathbf{0}_{N_s\times N_s} & \dfrac{\boldsymbol{f}}{||\boldsymbol{y}||}\\ \dfrac{\boldsymbol{f}^T}{||\boldsymbol{y}||} & 0\end{pmatrix}\begin{pmatrix}\boldsymbol{y}\\ ||\boldsymbol{y}||\end{pmatrix} = \boldsymbol{H}\begin{pmatrix}\boldsymbol{y}\\ ||\boldsymbol{y}||\end{pmatrix}$$

The operator **H** is a *Special Orthogonal* Lie group ($SO(N_s)$), then we can integrate on manifold. The milestone of the integration on manifold is that we can define a linear operator linear **A** (Lie algebra) such that

$$\begin{pmatrix}\boldsymbol{y}\\ ||\boldsymbol{y}||\end{pmatrix}_{n+1} = \boldsymbol{A}\begin{pmatrix}\boldsymbol{y}\\ ||\boldsymbol{y}||\end{pmatrix}_{n}$$

And is function of the Lie group. The Lie theorem guarantees that for each Lie group there exists a Lie algebra. A canonical way to define **A** is by the exponential mapping, i.e. we consider the direct resolution of Eq. then

$$\boldsymbol{A} = \exp(\boldsymbol{H}\Delta t)$$

Although the exponential mapping is generally the best way of proceeding, it does not perform well when f tends to 0, i.e. in the neighborhood of the initial condition and equilibrium point, with a subsequent stiffer integration. For this reason, the Cayley transform is more suitable to describe the corresponding Lie algebra

$$\boldsymbol{A}_n = Cay(\Delta t\boldsymbol{H}_n)$$
$$= \begin{pmatrix}\boldsymbol{I}_{N_s} + \dfrac{4\Delta t^2}{4||\boldsymbol{y}_n||^2-\Delta t^2||\boldsymbol{f}_n||^2}\boldsymbol{f}_n\boldsymbol{f}_n^T & \dfrac{4\Delta t||\boldsymbol{y}_n||}{4||\boldsymbol{y}_n||^2-\Delta t^2||\boldsymbol{f}_n||^2}\boldsymbol{f}_n\\ \dfrac{4\Delta t||\boldsymbol{y}_n||}{4||\boldsymbol{y}_n||^2-\Delta t^2||\boldsymbol{f}_n||^2}\boldsymbol{f}_n^T & \dfrac{4||\boldsymbol{y}_n||^2+\Delta t^2||\boldsymbol{f}_n||^2}{4||\boldsymbol{y}_n||^2-\Delta t^2||\boldsymbol{f}_n||^2}\end{pmatrix}$$

Taking only the first line of the RHS of Eq. we obtain a first order Group Preserving Scheme

$$\boldsymbol{y}_{n+1} = \boldsymbol{y}_n + \frac{4\left|\left|\boldsymbol{y}_n\right|\right|^2 + 2\Delta t\boldsymbol{f}_n\cdot\boldsymbol{y}_n}{4\left|\left|\boldsymbol{y}_n\right|\right|^2-\Delta t^2\left|\left|\boldsymbol{f}_n\right|\right|^2}\Delta t\boldsymbol{f}_n = \boldsymbol{y}_n + \eta_n\boldsymbol{f}_n$$

Note that if $\boldsymbol{f}_n = \mathbf{0}$, $\eta_n = 1$ then the scheme can handle equilibrium points. However, to have a proper integration scheme $\eta_n > 0$, then it is necessary to impose another condition on the time step. In particular,

$$\left|\left|\boldsymbol{f}_n\right|\right| \leq L||\boldsymbol{y}_n||$$

Where L is the Lipschitz constant defined as the maximum absolute value of the eigenvalues of the Jacobian of the system. Since we want to build a Jacobian-free scheme, we will impose L arbitrarily large and function of the time step as

$$L = C \left|\left|\boldsymbol{f}_n\right|\right| / \left|\left|\boldsymbol{y}_n\right|\right| \text{ where } C = 10^{11}\Delta t_{global}$$

Where Δt_{global} is the prescribed time step of the simulation. To guarantee stability we need to integrate with smaller substeps defined as

$$\Delta t_{local} = \frac{1 - e^{-L\Delta t_{global}}}{L}$$

This ensures that the integration scheme is unconditionally stable.

Furthermore, to better reconstruct the trajectory, we want to use higher order integration schemes. Following the Butcher tableau to determine the weights of the 4th order Runge-Kutta scheme, we can write

$$\boldsymbol{k}_1 = \boldsymbol{f}(\boldsymbol{y}_n) \qquad \eta_1^c = \frac{4||\boldsymbol{y}_n||^2 + 2(\Delta t/2)\boldsymbol{f}_n \cdot \boldsymbol{y}_n}{4||\boldsymbol{y}_n||^2 - (\Delta t/2)^2||\boldsymbol{f}_n||^2}(\Delta t/2)$$

$$\boldsymbol{y}_2 = \boldsymbol{y}_n + \eta_1^c\boldsymbol{k}_1 \qquad \boldsymbol{k}_2 = \boldsymbol{f}(\boldsymbol{y}_2) \qquad \eta_2^c = \frac{4||\boldsymbol{y}_n||||\boldsymbol{y}_2|| + 2(\Delta t/2)\boldsymbol{f}_n \cdot \boldsymbol{y}_n}{4||\boldsymbol{y}_n||^2 - (\Delta t/2)^2||\boldsymbol{f}_n||^2}(\Delta t/2)$$

$$\boldsymbol{y}_3 = \boldsymbol{y}_n + \eta_2^c\boldsymbol{k}_2 \qquad \boldsymbol{k}_3 = \boldsymbol{f}(\boldsymbol{y}_3) \qquad \eta_3^c = \frac{4||\boldsymbol{y}_n||||\boldsymbol{y}_3|| + 2(\Delta t/2)\boldsymbol{f}_n \cdot \boldsymbol{y}_n}{4||\boldsymbol{y}_n||^2 - (\Delta t/2)^2||\boldsymbol{f}_n||^2}(\Delta t/2)$$

$$\boldsymbol{y}_4 = \boldsymbol{y}_n + \eta_3^c\boldsymbol{k}_3 \qquad \boldsymbol{k}_4 = \boldsymbol{f}(\boldsymbol{y}_4)$$

$$\boldsymbol{F}_n = \frac{1}{6}(\boldsymbol{k}_1 + 2\boldsymbol{k}_2 + 2\boldsymbol{k}_3 + \boldsymbol{k}_4) \quad \eta_n = \frac{4||\boldsymbol{y}_n||||\boldsymbol{y}_3|| + 2\Delta t\boldsymbol{f}_n \cdot \boldsymbol{y}_n}{4||\boldsymbol{y}_n||^2 - \Delta t^2||\boldsymbol{f}_n||^2}\Delta t$$

$$\boldsymbol{y}_{n+1} = \boldsymbol{y}_n + \eta_n\boldsymbol{F}_n$$

To have a 4th order group preserving scheme.

Results

This section shows the performances of the Lie Group Preserving Scheme. To assess the performances of the integrator, we consider a constant volume and energy reactor of a n-dodecane oxygen mixture at the pressure of 10 bar and we compare the performances against the stiff integrator CVODE.

Figure 1 shows the execution time of a time step (t_{wall}) in function of the physical time of the simulation. The Group Preserving Scheme is 10~12 times faster than CVODE before achieving the equilibrium solution, while the evaluation at the equilibrium point is about 100 times faster.

Figure 2 shows a comparison of the temperature and key species profiles to analyze the accuracy of the proposed solver. In particular, the Lie integrator has been tested with three different time steps (10^{-9}, 10^{-8} and 10^{-7}) and the reference profiles are computed with Cantera. The Group Preserving Scheme accurately reconstructs the Cantera solution for any species independently from the choice of the time step. The only small discrepancy is observed for $\Delta t = 10^{-7}$s for HO_2 implying that the scheme is robust.

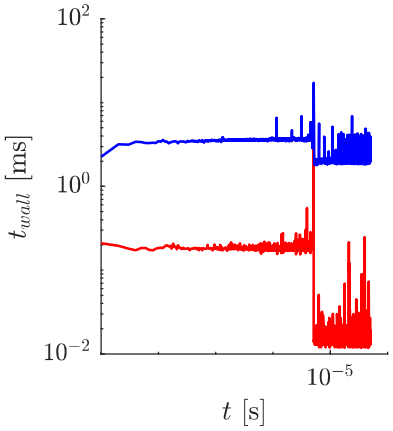

Figure 1 Execution time for the evaluation of each time step of a batch reactor.

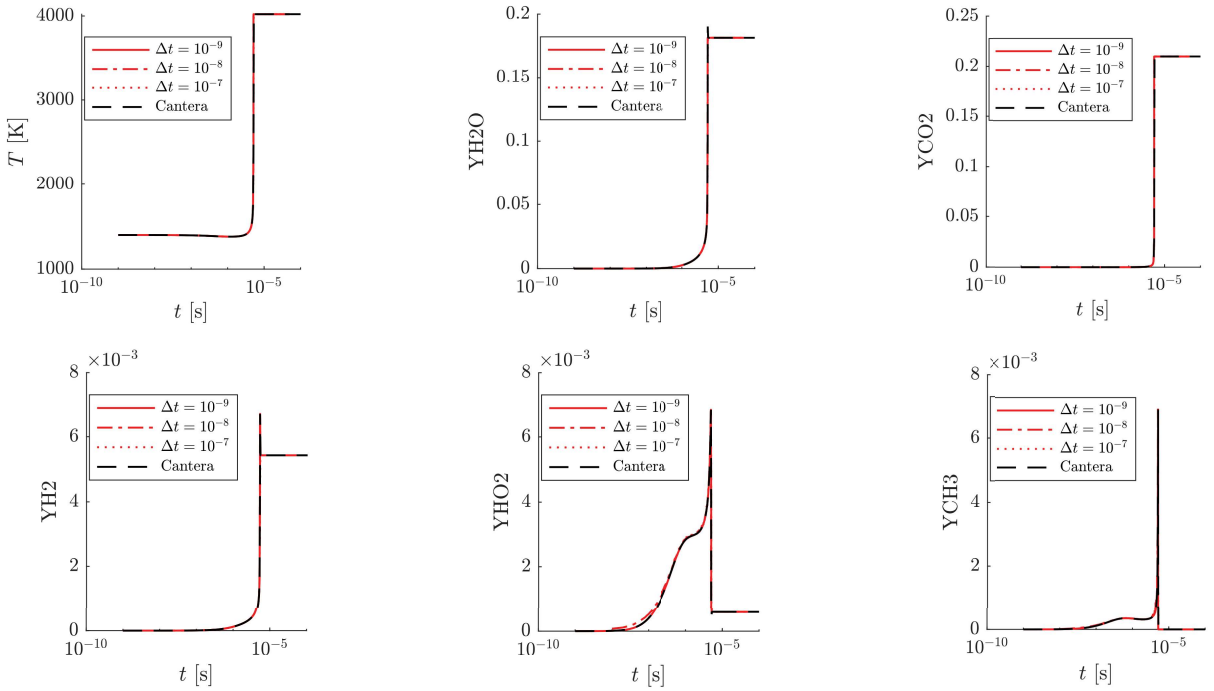

Figure 2 Comparison of the batch reactor with the Lie integrator with different time steps and the Cantera solution.

Conclusion

A Group Preserving Scheme based on the Lie group theory has been presented and its performances in terms of accuracy and speed are compared against the canonical solvers CVODE and Cantera. The new integrator achieves a speedup of 10 times during the actual evolution of the system and 100 times for the evaluation of the equilibrium point preserving the same accuracy as Cantera. The robustness of a manifold-constrained time integration scheme has been proved and this opens to a possible coupling with a full CFD solver.

References

[1] Galassi, Riccardo Malpica, et al. "An adaptive time-integration scheme for stiff chemistry based on computational singular perturbation and artificial neural networks." Journal of Computational Physics 451 (2022): 110875.

[2] Vijayarangan, Vijayamanikandan, et al. "A data-driven reduced-order model for stiff chemical kinetics using dynamics-informed training." Energy and AI 15 (2024): 100325.

[3] Liu, C. "Nonstandard group-preserving schemes for very stiff ordinary differential equations." Computer Modeling in Engineering and Sciences 9.3 (2005): 255.

[4] Lee, Hung-Chang, and Chein-Shan Liu. "The fourth-order group preserving methods for the integrations of ordinary differential equations." Computer Modeling in Engineering and Sciences (CMES) 41.1 (2009): 1.

Combining Metadynamics and Mean Force Integration for studying chemical reactions in solution: an application to backbiting of poly-Butyl Acrylate.

F. Serse*, A. Bjola, M. Salvalaglio**, M. Pelucchi***
Francesco.serse@polimi.it
* CRECK Modelling Lab, Politecnico di Milano, Piazza Leonardo da Vinci 32, Milan, Italy;
** Thomas Young Centre and Department of Chemical Engineering, University College London, London, WC1E 7JE, United Kingdom

Abstract
Free radical polymerization (FRP) and pyrolysis processes are fundamental technologies with wide-ranging applications in fields such as material synthesis and recycling. Understanding the underlying reaction mechanisms and considering the effect of solvents is crucial for the design and scale-up of such processes. However, since pyrolysis lacks selectivity and radical intermediates are hard to measure due to their extremely short lifetimes, rate coefficients from experimental campaigns on this subject are scarce. Nevertheless, experiments on free radical polymerization have been a flourishing field of study in past two decades. Knowledge of rate parameters of elementary reactions in solution or in bulk is key for formulating a valid kinetic mechanism. To this day, individual kinetic rate parameters of radical chain propagations, depropagations as well as isomerizations (backbiting) can be accessed experimentally through Pulsed Laser Polymerization technique (PLP) coupled with Size Exclusion Cromatography (SEC) [1] as well as semibatch solution polymerization coupled with Nuclear Magnetic Resonance (NMR) [2]. The resulting rate coefficients are gathered in the IUPAC Database for standard monomers which represents the gold standard for the validation of theoretical calculations. In particular, the experimental studies taken as reference [1-2] report the propagation, backbiting and β-scission rate coefficients for poly-Butyl Acrylate in bulk and in solvent (mainly a mixture of ortho/meta/para-xylene). In this work, accelerated molecular dynamics in conjunction with Mean Force Integration (MFI) have been employed for exploring the free energy landscape of the backbiting of poly-Butyl Acrylate (PBA) in gas phase as well as in solution with non-polar (o-/m-/p-xylene) and polar (water) solvents (Fig. 1).
The potential energy of the system has been partitioned such that the reactant molecule (i.e. the BA trimer) is described by a quantum tight binding potential (GFN1 xTB) whereas the surrounding solvent is treated with the classical Generalized Amber Force Field (GAFF). The electrostatic coupling between the reactant (QM) and the solvent environment (MM) has been modelled through a

Coulomb potential. The free energy landscape is recovered from a metadynamics [3] simulation by means of the Mean Force Integration (MFI) algorithm implemented in [4]. This implementation of the MFI reconstructs an analytical expression for the mean thermodynamic force in the collective variables space $\nabla F_t(\boldsymbol{s})$ up to a given time t, where $F_t(\boldsymbol{s})$ refers to the Helmholtz free energy. As reported in [4,5], the mean force has two components, namely the gradient with respect to s of the natural logarithm of the biased probability density $p_b^t(\boldsymbol{s})$ and the gradient of the bias potential $V_t(\boldsymbol{s})$ accumulated up to time t, as shown in eq. (1).

$$\nabla F_t(\boldsymbol{s}) = -k_B T \nabla \ln p_b^t(\boldsymbol{s}) - \nabla V_t(\boldsymbol{s}) \quad (1)$$

Where k_B is the Boltzmann constant. The space of collective variables for the sampling of 1:5 backbiting is defined by the distance between the end chain radical and the hydrogen in fifth position (see Fig 1a).

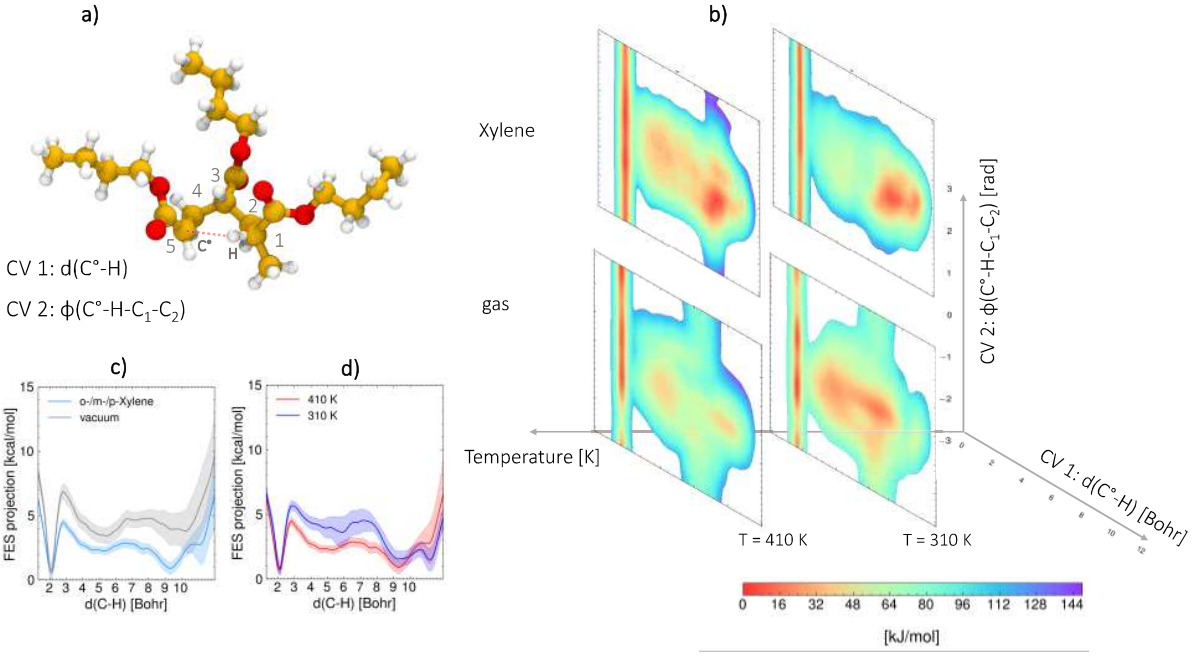

Figure 1. a) model molecule and CVs definition for the 1:5 backbiting; b) bivariate free energy surface in vacuum and in xylene solvent at 310 K and 410 K; c) marginal free energy profiles together with the standard deviation along the C-C distance in vacuum and in xylene solvent at T=410 K; d) marginal free energy profiles together with the standard deviation along the C-C distance in xylene solvent at 310 K and 410 K.

Rate constants are evaluated from the zero-point energy corrected free energy barriers of activation based on the rare events generalized Transition State Theory (TST) [6].

The newly found rate constants are introduced into a detailed kinetic mechanism from the literature [7]. In this previous study, the rate parameters of β-scission,

backbiting and tertiary propagation were used as degrees of freedom to match experimental profiles of monomer concentration. The introduction the kinetic parameters in xylene of backbiting as well as β-scission from our previous study [8] allow to match experiments using the tertiary propagation rate constant only as degree of freedom. The update kinetic scheme is reported in Table 1, whereas the predicted concentration profiles are shown in Fig. 2.

Table 1. Initiated radical polymerization mechanism of PBA.

Reaction	**Pre-exponent (1/s)**	**Activation energy (J/mol)**
Initiator decomposition	6.78E+15	147200
Propagation	1.80E+7	17400
Chain transfer to monomer	1.60E-2	15200
Tertiary propagation	7.90E+6	27800
Backbiting	1.88E+8	32600
β-scission	1.50E+13	88200
Termination	2.57E+8	2400
Chain transfer to solvent	176.00	32200

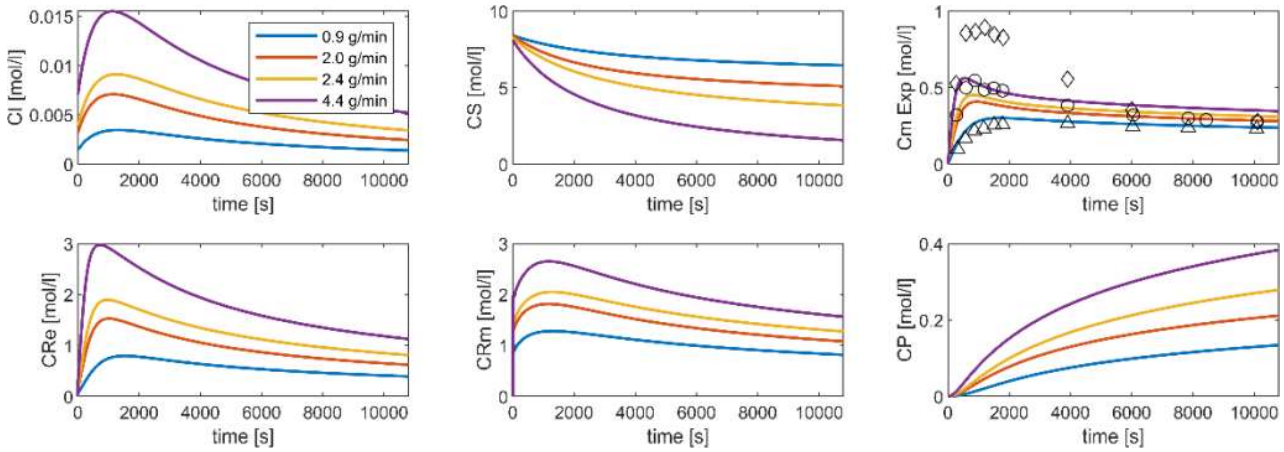

Figure 2. Concentration profiles in the starved feed semi-batch polymerization of PBA at 130°C for different monomer inlet flowrates. CI and CI. stand for initiator and its radical concentrations, CS stands for solvent concentration, Cm is the monomer concentration, CRe and CRm is the concentration of end-chain and mid-chain radicals, CP is the polymer concentration.

The updated mechanism is also applied to the thermal self-initiated polymerization of BA. A recent experimental study [] reported the effect of different solvents on the BA polymerization rates in a batch reactor allowing to validate our computational prediction of solvent effects on kinetic constants. In the absence of initiator I, the polymerization is triggered by thermal self-initiation. The Arrhenius parameters of this elementary reaction are unknown in the literature and have here been used as

degree of freedom to match the experiments. The values of this reaction that show better agreement with experiments in bulk is the following:

Reaction	Pre-exponent (1/s)	Activation energy (J/mol)	Order
Thermal self-initiation	7340	81600	0.3

Supposing that the solvent does not significantly affect thermal self-initiation, we show that solvent effects on the secondary reactivity, namely β-scission and backbiting, of BA can be responsible for the change in polymerization rate (Fig. 3).

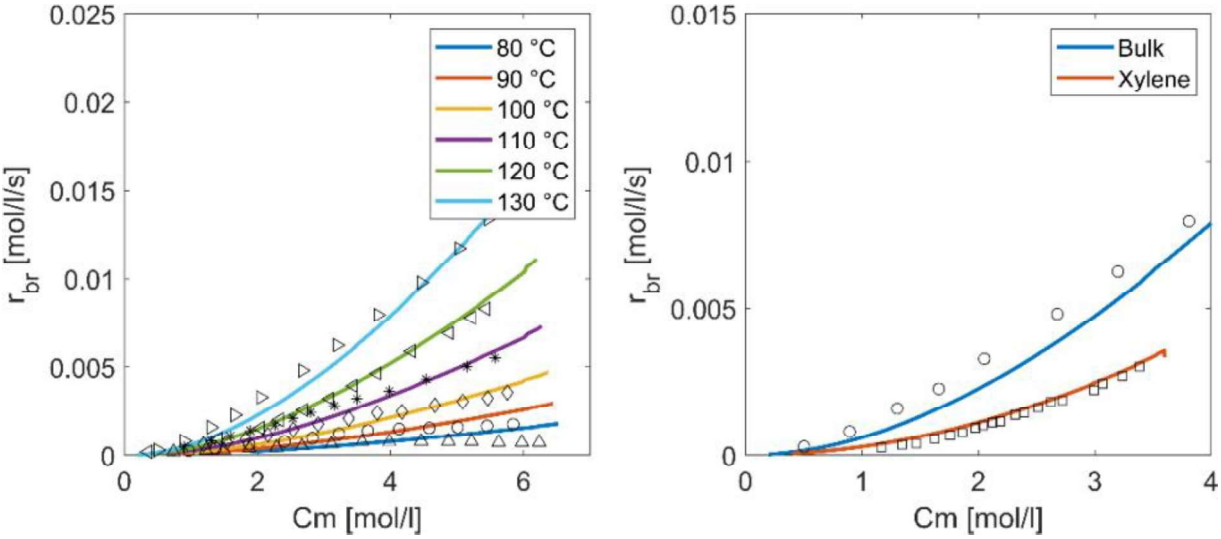

Figure 3. Comparison between model prediction and experiments of BA polymerization rate [mol/l/s]; left: polymerization in bulk in the temperature range 80-130 °C; right: predicted and experimental polymerization rates in bulk and in xylene at 130°C.

The global sensitivity analysis performed on self-initiation, backbiting and β-scission (Fig. 4) shows that these three reactions are highly important for the correct description of the polymerization rate.

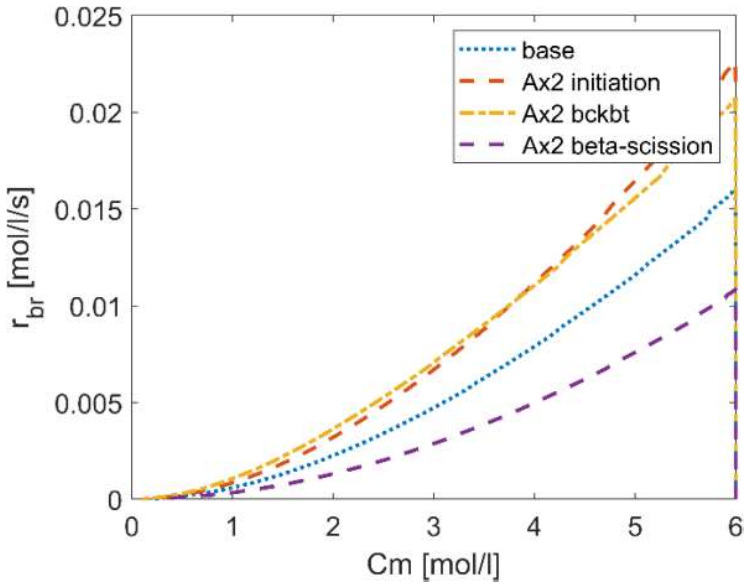

Figure 4. Global sensitivity analysis of polymerization rate [mol/l/s] against monomer concentration [mol/l] to thermal self-initiation, backbiting and β-scission reactions.

References

[1] Michael Buback, Robert G. Gilbert, Robin A. Hutchinson, Bert Klumperman, Frank-Dieter Kuchta, Bart G. Manders, Kenneth F. O'Driscoll, Gregory T. Russell, and Johannes Schweer. Critically evaluated rate coefficients for free-radical polymerization, 1. propagation rate coefficient for styrene. Macromolecular Chemistry and Physics, 196(10):3267–3280, 1995.

[2] Adam N. F. Peck and Robin A. Hutchinson. Secondary reactions in the high-temperature free radical polymerization of butyl acrylate. Macromolecules, 37(16):5944–5951, 2004.

[3] A. Laio and M. Parrinello, Proceedings of the National Academy of Sciences99.20 (2002): 12562-12566.

[4] Veselina Marinova and Matteo Salvalaglio. Timeindependent free energies from metadynamics via mean force integration. The Journal of Chemical Physics, 151(16):164115, oct 2019.

[5] Bjola A, Salvalaglio M. Estimating Free Energy Surfaces and their Convergence from multiple, independent static and history-dependent biased molecular-dynamics simulations with Mean Force Integration. ChemRxiv. 2024; doi:10.26434/chemrxiv-2024-83h5q.

[6] Reaction Rate Theory and Rare Events; Elsevier Science, 2017.

[7] Adam N. F. Peck and Robin A. Hutchinson. Macromolecules 2004 37 (16), 5944-5951. doi: 10.1021/ma049621t.
[8] Serse F, Bjola A, Salvalaglio M, Pelucchi M. Unveiling solvent effects on β-scissions through Metadynamics and Mean Force Integration. ChemRxiv. 2024; doi:10.26434/chemrxiv-2024-rn2rz This content is a preprint and has not been peer-reviewed.
[9] Mätzig, J.; Drache, M.; Beuermann, S. Self-Initiated Butyl Acrylate Polymerizations in Bulk and in Solution Monitored By In-Line Techniques. Polymers 2021, 13, 2021. https://doi.org/10.3390/polym13122021.

Gasoline Surrogate Combustion with Ozone Addition

F. Anaclerio*, S. M. Camporeale, V. Magi*** F. Fornarelli*,*****

Fabio.anaclerio@unifg.it
* Dept. of Scienze Agrarie, Alimenti, Risorse Naturali e Ingegneria, University of Foggia, 71122 Foggia, Italy
** Dept. of Mechanics, Mathematics and Management, Politechnic-University of Bari, 70125 Bari, Italy
*** School of Engineering, University of Basilicata, 85100 Potenza, Italy
**** Italian Nat. Group of Mathematical Physics of the Italian Nat. Inst. of High Mathematics, 00185 Rome, Italy

Abstract
In the present work, a numerical investigation on the laminar flame speed of Toluene Reference Fuel (TRF)/air/ozone mixtures has been carried out for different equivalence ratios, reactants temperatures and ozone concentrations. The 1-D numerical simulations have been performed with two modified chemical kinetic reaction mechanisms for TRF. The oxidative reactivity of the fuel has been improved thanks to the addition of ozone. Indeed, preliminary results show that ozone enhances the laminar flame speed and decreases the flame thickness of TRF/air mixture in the concentration range of 0-7000 ppm. For reactants temperature of 358 K at ambient pressure and for an ozone concentration of 7000 ppm, the increase in laminar flame speed is about 13% under lean conditions whereas it is about 4% under stoichiometric conditions. This work shows that the laminar flame speed is greatly influenced by ozone for unburned reactants temperatures greater than 550 K. Lean conditions enhance this behavior compared to the stoichiometric condition.

Introduction
The Laminar Flame Speed (LFS) is an important quantity to describe the reactivity, diffusivity and exothermicity of a fuel/air mixture. In combustion systems, LFS directly influences the combustion efficiency and pollutant emissions. In this context, the scientific research is focusing on the development of unconventional combustion strategies with the aim of reducing emissions and fuel consumption and increasing thermal efficiency. These strategies include the use of alternative fuels characterized by high LFS under lean conditions, and the use of standard fuel/air mixture enriched with either oxygen or chemical reactive species. Among them, ozone (O_3) is a promising chemical reactive species for increasing LFS, stabilizing the combustion variability, and controlling the ignition delay time. Indeed, the reaction $O_3 + N_2 \leftrightarrow O + O_2 + N_2$ plays a key role in the ozone decomposition for influencing LFS. Halter *et al.* [1] studied the role of ozone in methane/air combustion employing experimental and numerical approaches. The authors showed that, considering 2369 ppm of ozone at 300 K and 1 bar, LFS significantly increases and

the flame thickness decreases. Wang *et al.* [2] investigated the influence of different concentrations of ozone in the range 0-7000 ppm for the methane/air flames. They showed that LFS increases linearly with the ozone concentration. Furthermore, the highest increase has been observed for lean mixture conditions. Gao *et al.* [3] investigated, both experimentally and numerically, the influence of ozone on LFS of methane, propane, and ethylene. The results show that the LFS enhancement is more pronounced especially at high pressures. D'Amato *et al.* [4] numerically studied the influence of ozone on the methane/air for the ozone concentration in the range 0-7000 ppm. They confirmed that ozone addition improves LFS at high temperatures and pressures, and they extended these findings to an iso-octane/air mixture. In recent works, ozone has been employed to improve the thermal efficiency, emissions, and cycle-to-cycle variability of Spark-Ignition (SI) engines. Anaclerio *et al.* [5] proposed the use of ozone in SI engines fueled with gasoline/air/ozone mixtures under lean conditions. Their results indicated that ozone addition has a strong influence on the combustion process resulting in higher in-cylinder pressure with a reduction of burn delay, combustion phase and burn duration. In this work, a ternary mixture of iso-octane/n-heptane/toluene, named Toluene Reference Fuel (TRF) with 63/20/17 mol.% [6, 7] has been used as gasoline surrogate. A detailed kinetic mechanism for TRF with O_3 and a skeletal mechanism are proposed and validated to highlight the role of ozone on the LFS of commercial gasoline. The importance of the equivalence ratio and of the reactant temperature on the LFS is investigated and discussed for lean ($\phi = 0.6$) and stoichiometric conditions.

The Mathematical Model

Numerical simulations are carried out by using Cantera numerical code [8] to simulate adiabatic freely propagating laminar flames. The differential governing equations for one-dimensional premixed steady-state flame equations (state, mass continuity, species continuity, momentum and thermal energy equations) are solved. The initial gas temperature, pressure, and mixture composition are set. Two different reaction mechanisms for TRF with an ozone sub-mechanism [1] and Saxena NO_x sub-mechanism [9] are employed. Table 1 shows the number of species and reactions of each mechanism.

Table 1. Number of species and reactions of the TRF-O_3 detailed and skeletal mechanisms.

Mechanism	Type	Species	Reactions
Det_TRF_O_3	Detailed	507	17860
Skel_TRF_O_3	Skeletal	171	3535

Model Validation

The two reaction mechanisms have been validated (without ozone) against measurements for various equivalence ratios [15] and for mixtures of commercial

gasoline with air. The comparison is shown in Figure 1.a) [10-14] at 358 K and 1 bar and in Figure 1.b) at 373 K and 10 bar. Figure 1 shows that the numerical results are within the uncertainty range of the measurements. Furthermore, the figure shows that for rich mixtures ($\phi > 1.0$) higher LFS is found with the detailed mechanism. On the other hand, under lean conditions, the differences between the two mechanisms are negligible and are in fair agreement with the experimental data. To the best of the authors' knowledge, there are no data available in the literature for mixtures of gasoline with ozone.

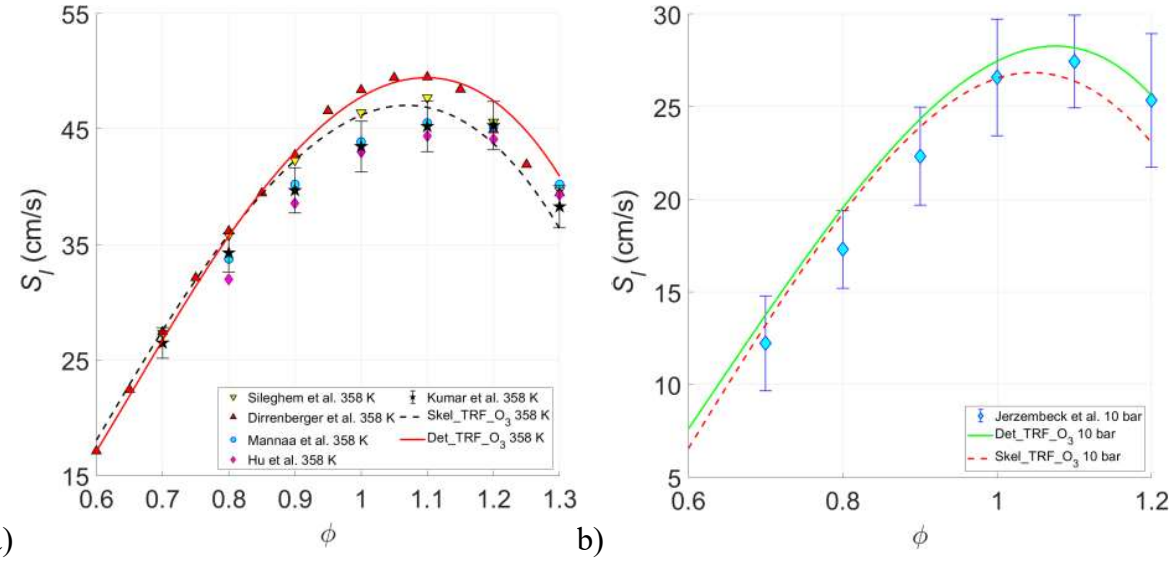

a) b)

Figure 1. Gasoline/air mixtures at 358 K and 1 bar [10-14] (a) and 373 K and 10 bar [15] (b) for different equivalence ratios.

Results and Discussion

Firstly, the analysis has been carried out for TRF/air/ozone mixtures at 358 K and ambient pressure for two different ozone concentrations, i.e. 2330 ppm and 7000 ppm. Then, the influence of the reactants' temperature on the LFS has been discussed for both stochiometric and lean conditions.

The influence of ozone

Figure 2.a) shows the laminar flame speed at 358 K and ambient pressure for different equivalence ratios and three ozone concentrations, i.e. 0, 2330 and 7000 ppm, by using the skeletal reaction mechanism. The enhancement of LFS has been defined as follows: $\varepsilon\ [\%] = (S_l - S_{l0})/S_{l0} \cdot 100$, where S_l and S_{l0} are the LFS with and without ozone, respectively. The results suggest that a) the presence of ozone increases the LFS across the entire set of equivalence ratios and b) the LFS increases more as the ozone concentration increases. Figure 2.b compares the percentage increase of LFS with the two chemical kinetic mechanisms. The highest LFS increase has been found for ultra-lean conditions ($\phi = 0.5$) and with 7000 ppm of ozone for both mechanisms. Specifically, such percentage increase is about 13.3%

and 11.8% for the detailed and skeletal mechanism, respectively. Furthermore, a gradual reduction of the LFS increase is observed as the equivalence ratio increases up to a minimum under about stoichiometric conditions for both kinetic mechanisms. Thereafter, LFS enhancement begins to increase again for slightly rich mixture conditions.

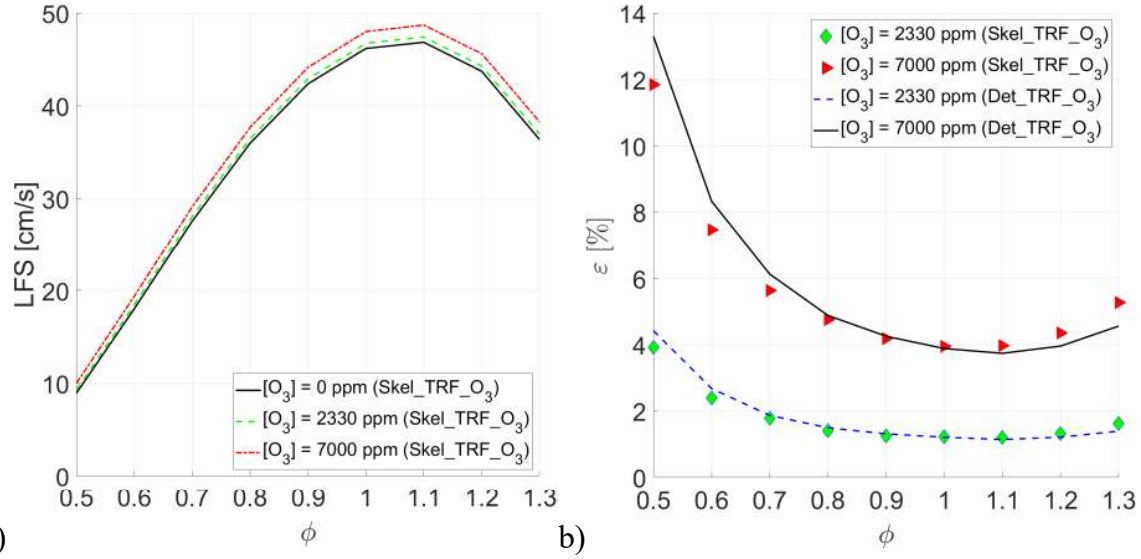

a) b)

Figure 2. LFS of TRF/air without and with different ozone concentrations vs equivalence ratios at 358 K and 1 bar (a). LFS enhancement for different ozone concentrations for both skeletal and detailed chemical kinetic mechanisms (b).

Under lean conditions ($\phi = 0.6$), the burnt gas temperature increases by 8.5% with an increase of 6.7%, 5.2%, 7.9% and 16.7% of the mole fractions of O, OH, H and HO_2, respectively. Under the same lean conditions, the flame thickness, defined as $\delta_l = (T_{max} - T_{min})/max(\nabla T)$, is 0.70 mm for the TRF/air flame without ozone and decreases to 0.68 mm when 7000 ppm of ozone is added to the mixture.

The influence of temperature

Several unburned mixture temperatures, ranging from 358 K to 700 K, for ozone concentrations of 0, 2330 and 7000 ppm at 1 bar have been considered. Figures 5.a) shows the LFS as a function of the unburned gas temperature for different ozone concentrations under stoichiometric and lean conditions ($\phi = 0.6$). Figures 5.b) gives the LFS slope with respect to the unburned temperature ($dS(T)/dT$). The LFS of the mixture without ozone smoothly increases with the temperature for both stoichiometric and lean conditions. On the other hand, the presence of ozone in the mixture significantly influences the LFS for temperatures higher than 550 K. Indeed, Figure 5.b) shows that the LFS variation with ozone increases linearly up to about 475 K for both stoichiometric and lean mixture conditions. For higher temperatures, the LFS slope starts to increase significantly until it reaches a maximum at about 600 K. The results show that for both ozone concentrations, i.e. 2330 ppm and 7000 ppm, an unburned gas temperature of about 550 K represents the threshold beyond which ozone strongly influences the oxidation mechanism of TRF.

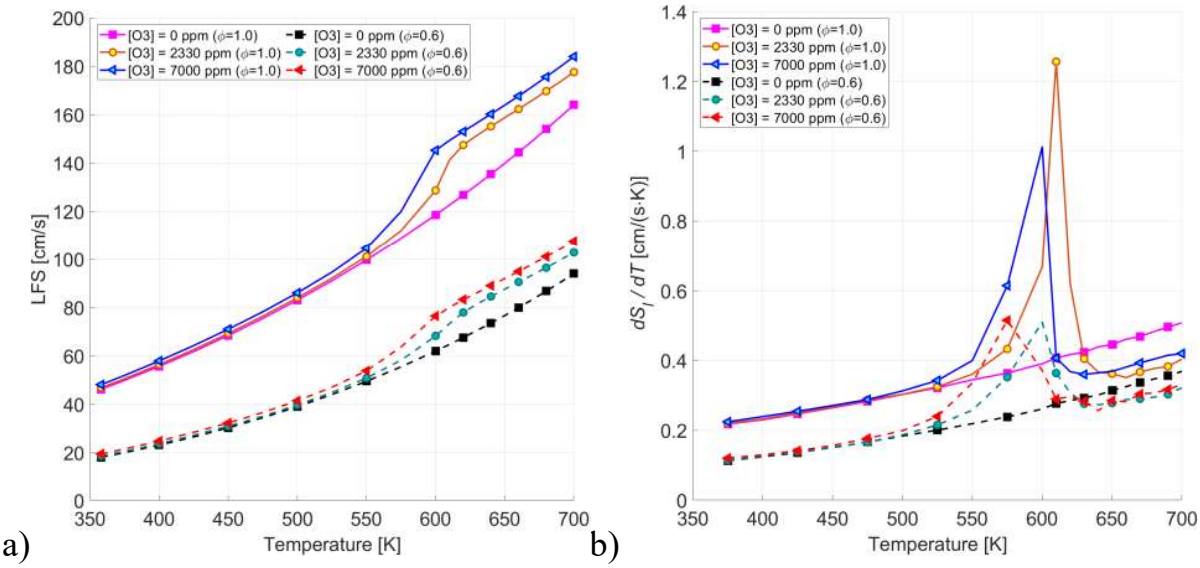

a) b)

Figure 5. LFS of TRF/air/O_3 mixtures (a) and LFS slope (b) vs unburned mixture temperature under stoichiometric and lean conditions at ambient pressure (1 bar).

Conclusions

In this work, the influence of ozone addition on the combustion of TRF/air flames has been investigated. One-dimensional numerical simulations have been performed to compute the laminar flame speed by using two chemical kinetic mechanisms, detailed vs skeletal.

The results can be summarized as follow:

- under lean conditions ($\phi = 0.5$), at 358 K and 1 bar, the presence of ozone in the TRF/air mixture increases the laminar flame speed of about 13%, whereas under stoichiometric conditions, such increase is about 4%;
- under lean conditions, the presence of ozone favors the increase of the main radicals and the reduction of the flame thickness;
- the influence of ozone becomes more relevant at high reactants temperatures, showing a sharp increase in the laminar flame speed over 550 K.

References

[1] F. Halter, P. Higelin, and P. Dagaut, Experimental and Detailed Kinetic Modeling Study of the Effect of Ozone on the Combustion of Methane, *Energy & Fuels* 2011 25 (7), 2909-2916.

[2] Z.H. Wang, L. Yang, B. Li, Z.S. Li, Z.W. Sun, M. Aldén, K.F. Cen, A.A. Konnov, Investigation of combustion enhancement by ozone additive in CH4/air flames using direct laminar burning velocity measurements and kinetic simulations, *Combustion and Flame*, 2012 159(1), 120-129.

[3] P. Saxena, F. A. Williams, Numerical and experimental studies of ethanol flames, *Proceedings of the Combustion Institute*, 2007 31(1), 1149-1156.

[4] M. D'Amato, A. Viggiano, V. Magi, A numerical investigation on the laminar flame speed of methane/air and iso-octane/air mixtures with ozone

addition, *Combustion and Flame*, 2022, 241, 112145.

[5] Anaclerio, F., Saponaro, G., Mancaruso, E., Mazzarella, C. et al., An Experimental Characterization of Gasoline/Ozone/Air Mixtures in Spark Ignition Engines, SAE Technical Paper 2023-24-0039, 2023.

[6] Ranzi, E., Frassoldati, A., Stagni, A., Pelucchi, M., Cuoci, A., Faravelli, T., Reduced kinetic schemes of complex reaction systems: Fossil and biomass derived transportation fuels, *International Journal of Chemical Kinetics*, 2014, 46 (9), pp. 512-542.

[7] B.M. Gauthier, D.F. Davidson, R.K. Hanson, Shock tube determination of ignition delay times in full-blend and surrogate fuel mixtures, *Combustion and Flame*, Volume 139(4), 2004.

[8] David G. Goodwin, Harry K. Moffat, Ingmar Schoegl, Raymond L. Speth, and Bryan W. Weber. *Cantera: An object-oriented software toolkit for chemical kinetics, thermodynamics, and transport processes*. https://www.cantera.org, 2023. Version 3.0.0. doi:10.5281/zenodo.8137090.

[9] P. Saxena, F. A. Williams, Numerical and experimental studies of ethanol flames, *Proceedings of the Combustion Institute*, 2007 31(1), 1149-1156.

[10] L. Sileghem, V.A. Alekseev, J. Vancoillie, K.M. Van Geem, E.J.K. Nilsson, S. Verhelst, A.A. Konnov, Laminar burning velocity of gasoline and the gasoline surrogate components iso-octane, n-heptane and toluene, *Fuel*, 2013 (112), 355-365.

[11] P. Dirrenberger, P.A. Glaude, R. Bounaceur, H. Le Gall, A. Pires da Cruz, A.A. Konnov, F. Battin-Leclerc, Laminar burning velocity of gasolines with addition of ethanol, *Fuel*, 2014, 115, 162-169.

[12] O. Mannaa, S. Mansour, W. L. Roberts, S. H. Chung, Laminar burning velocities at elevated pressures for gasoline and gasoline surrogates associated with RON, *Combustion and Flame*, 2015, 162 (6), 2311-2321.

[13] E. Hu, Z. Xu, Z. Gao, J. Xu, Z. Huang, Experimental and numerical study on laminar burning velocity of gasoline and gasoline surrogates, *Fuel*, 2019, 256, 115933.

[14] Rohit Kumar, Sudarshan Kumar, Formulation of a three-component gasoline surrogate model using laminar burning velocity data at elevated mixture temperatures, *Fuel*, 2021, 306, 121581.

[15] S. Jerzembeck, N. Peters, P. Pepiot-Desjardins, H. Pitsch, Laminar burning velocities at high pressure for primary reference fuels and gasoline: Experimental and numerical investigation, *Combustion and Flame*, 156 (2), 2009, 292-301.

Development of reduced chemical kinetic mechanism for combustion of ammonia-hydrogen blends

Fekadu Mosisa Wako[1], Simone Castellani[1], Antonio Andreini[1]
fekadumosisa.wako@unifi.it
[1] Department of Industrial Engineering, University of Florence, Via Santa Marta 3, 50139 Florence, Italy

Abstract
To achieve a reduced kinetic mechanism for comprehensive prediction of ammonia-hydrogen mixture combustion, a detailed kinetic mechanism with 32 species and 213 reactions was used. Directed relation graph with error propagation (DRGEP) as a primary reduction method, reaction path analysis and rate of production analysis were utilized as further refining approaches to simplify the mechanism. The reduction conditions covers; $\varphi = 0.5–2.0$, temperature of 600–1500 K, and pressure 1–10 bar. The final reduced mechanism consisting 18 species and 28 reactions has been used to predict main combustion parameters, such as laminar flame speed (SL), Ignition delay times (IDT) and NOx profiles. The results were compared with available experimental data and simulation results from the detailed mechanism. From the results, it is evident that the reduced mechanism captured the investigated parameters trend fairly well and are in good agreement with the experimental data and simulation results from the detailed mechanism, confirming its accuracy to represent combustion chemistry of the blend under the investigated conditions.

Introduction
Ammonia (NH_3) and hydrogen (H_2), as carbon-free energy sources, hold great promise in addressing concerns related to global warming. However, both have individual drawbacks that present challenges to their sole widespread adoption. Ammonia's low reactivity results in several limitations, including a low laminar flame speed, high auto-ignition temperature, narrow flammability limit and significant toxicity [1], which hinder its practical applications. Similarly, hydrogen's high reactivity lead to flashback, especially in lean premixed combustion scenarios [2]. These challenges underscore the importance of innovative approaches to effectively harness their benefits while addressing their inherent limitations. In this regard, blending NH_3 and H_2, presents a promising solution to address their individual limitations, notably enhancing reactivity while mitigating flashback issues [1]. Yet, understanding their combustion behavior in practical applications requires computationally affordable kinetic models. While utilizing detailed chemistry for high-fidelity simulation offers precision, it comes with significant computational costs and challenges. Thus, there is a critical need to develop reduced and computationally affordable kinetic mechanism. To this aim, Nozari et al.[3] developed reduced mechanism for NH_3-H_2 combustion by modifying the Konnov

mechanism [4], focusing on SL and NOx generation. But, the model overlooked IDT and ignored trace species. Otomo et al. [5] proposed the UT-LCS mechanism offering better predictions for SL, IDT and NOx emissions. Shrestha et al. [6] further improved to better predict SL. Despite significant efforts, most mechanisms remain in the range of 200–300 reactions and 30–50 species, which are still computationally heavy. In this regard, this study is aimed to develop a more simplified and computationally affordable mechanism for NH_3-H_2 blends.

Mechanism Reduction

A graph-based skeletal mechanism approach, employing DRGEP [7] was used to reduce the mechanism. DRGEP builds species dependency paths based on reactants and key products information, removing less critical species and reactions [7]. Mechanism reduction was performed in Cantera with python-based Automatic Mechanism Reduction (pyMARS) program [8]. Cantera, is an open-source software that allows simulations involving chemical kinetics [9] and pyMARS is specific program in Cantera built for mechanism reduction [8]. Detailed mechanism with 32 species and 213 reactions [10] was used as starting mechanism.

DRGEP simulation: The detailed mechanism undergoes a preliminary reduction process using DRGEP method at the following conditions; 600−1500 K, 1–10 bar, φ=0.5−2.0 and cutoff threshold 0.01. Key intermediate species; NH_2, NH, HNO, and NNH were defined as key target components, along with fuels, oxidizer and combustion products. After DRGEP calculations based on the specified conditions, a semi-detailed mechanism with 28 species and 171 reactions was obtained.

Reaction Path Analysis (RPA) and Rate of Production (ROP) Analysis: To further simplify the semi-detailed mechanism, RPA and ROP analysis were performed at; 300–1500 K, 1−10 bar, φ=0.5−2 and 25−75% H_2. Through this, key species from combustion of NH_3-H_2 mixtures were identified and retained in the mechanism, resulting in reduced mechanism consisting 18 species and 28 reactions.

Mechanism Validation

Laminar Flame Speed and Ignition Delay Times

In this section, the reduced mechanism is validated by computing SL and IDT. All simulations were performed using the open-source Cantera suite [9], with appropriate reactor modules to mimic real-world combustion conditions. An adaptive grid was determined based on criteria such as the maximum acceptable ratio among adjacent solutions (ratio=3), maximum first derivative for adjacent solutions (slope=0.06), and maximum acceptable second derivative for adjacent solutions (curve=0.12) [11]. SL was estimated assuming a 1D laminar flame model whereas IDT was simulated assuming 0D reactor model. The validation covers; 298–1500 K, 1–10 bar, φ=0.4–2 and H_2 fraction of 40–75%. Results were validated against experimental data from relevant literatures where available and simulation results from the detailed mechanism.

NOx emission profile

In this section, the reduced mechanism has been used to investigate the NOx emission trend from the combustion of a perfectly premixed mixture of 25% NH_3 – 75% vol. H_2 at constant equivalence ratio (φ) of 0.29, temperature of 498 K and pressures of 1.1, 1.5 and 2 bar. A chemical reactor network (CRN) comprising perfectly stirred reactor (PSR) and plug flow reactor (PFR) models were used for the investigation. Simulations were conducted in Cantera software.

Results and discussion

Laminar flame speed: Figures 1–3, depicted the SL results from both mechanisms compared with experimental data from the literatures. From the results, it is evident that the reduced mechanism effectively captured the SL trend under the specified conditions. The close agreement between the two mechanisms and the experimental data demonstrates the capability of the reduced chemistry to represent the combustion behavior of the NH_3-H_2 mixtures.

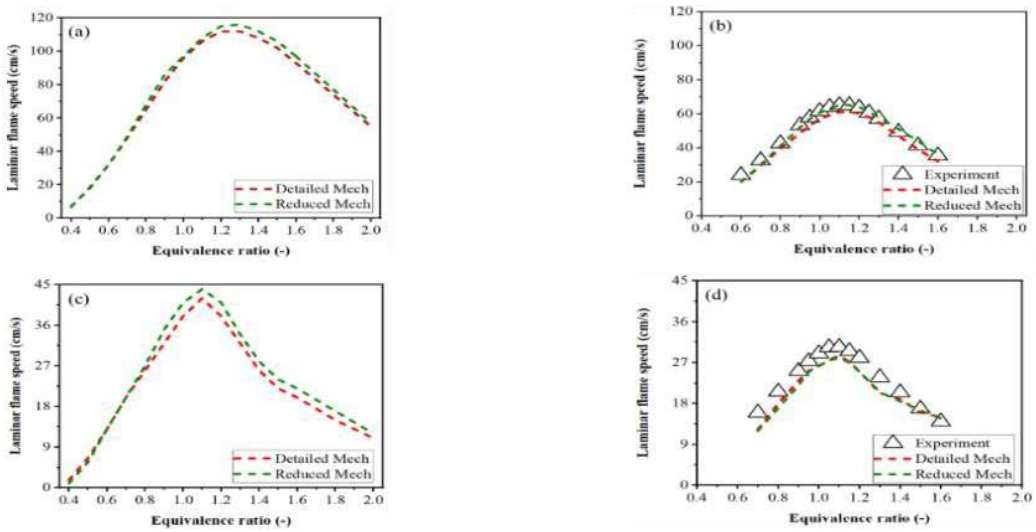

Figure 1. SL for NH_3–H_2 blends at 298 K and 1 bar; a) 25/75%, b) 40/60%, c) 50/50%, d) 60/40%. Symbols; experimental data [12, 13], lines; simulation results.

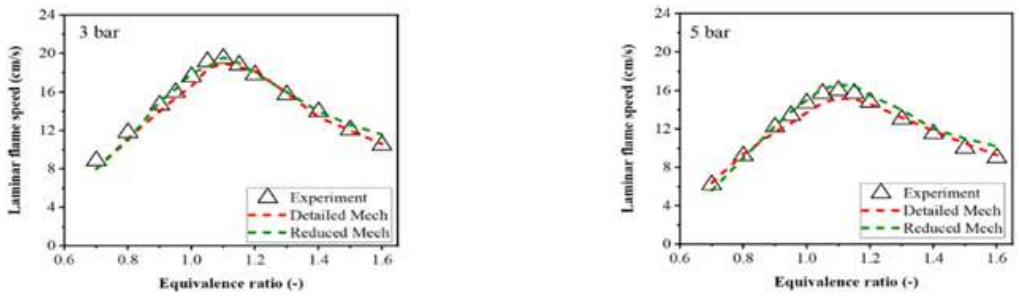

Figure 2. SL for 60%NH_3 + 40%H_2 at 298 K, 3–5 bar; a) 3 bar, b) 5 bar. Symbols; experimental data [12, 13], lines; simulation results.

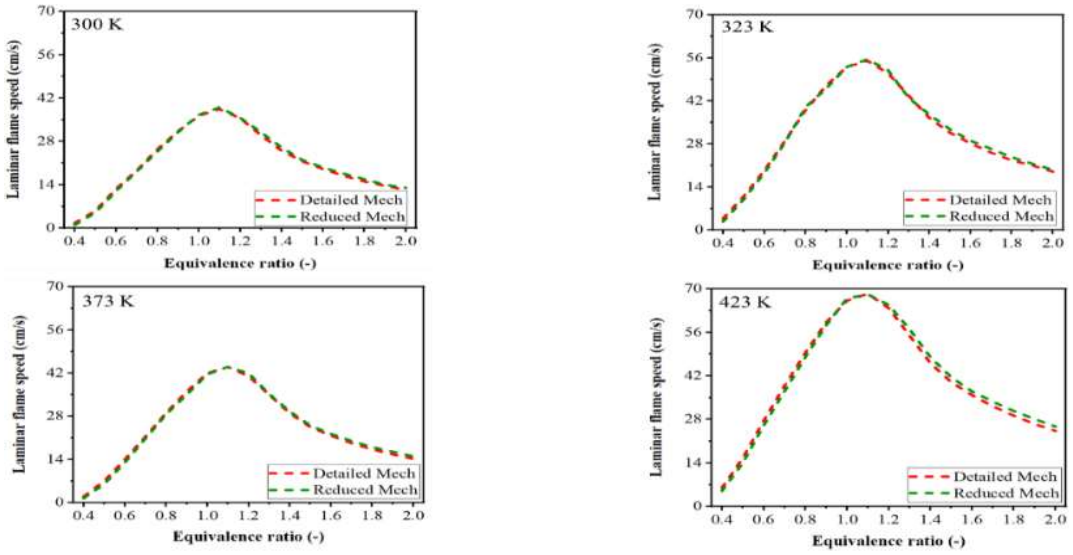

Figure 3. SL for 50%NH_3+50%H_2, 1bar, 300–423 K. Lines; simulation results.

Ignition Delay Times: Figure 4, depicted the IDT results obtained using the reduced and detailed mechanisms. The results reveal good agreement between the two mechanisms, confirming the capability of the reduced mechanism to capture the IDT trend under the studied conditions.

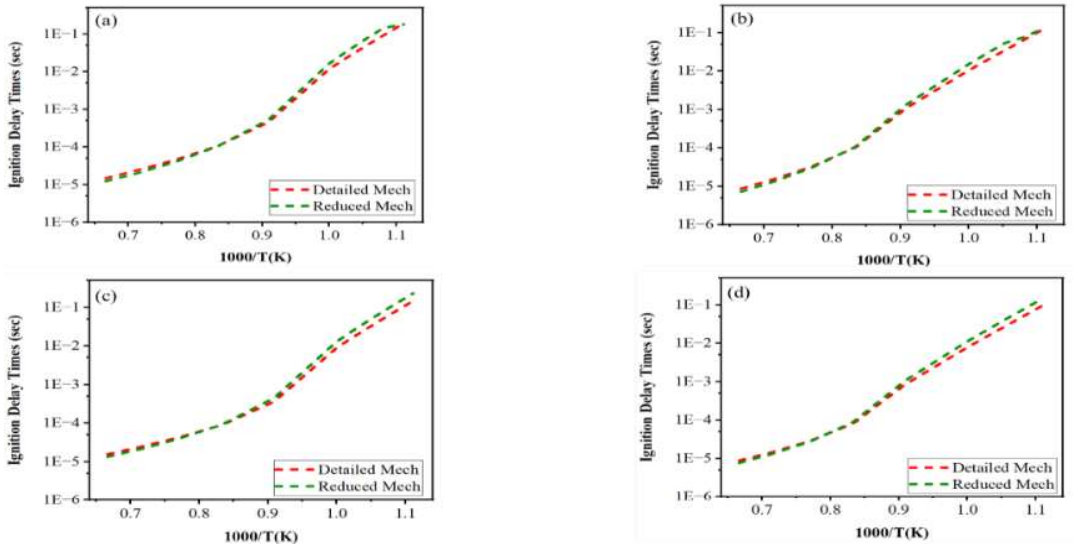

Figure 4. IDT data for 50%NH_3+50%H_2 at 850–1500 K, 5– 10 bar, φ=0.5–1.0; a) φ = 0.5, 5 bar, b) φ = 0.5, 10 bar, c) φ = 1.0, 5 bar, d) φ = 1.0, 10 bar

NOx Emissions: Figure 5 shows the fraction of NOx emission results obtained from the reduced mechanism compared against experimental campaign from Mozzatta et al. [14]. Despite few discrepancies, the reduced mechanism fairly captured the experimental trend. Increasing pressure led to decreased NOx due to improved combustion conditions (i.e., complete combustion) inhibiting NOx formation.

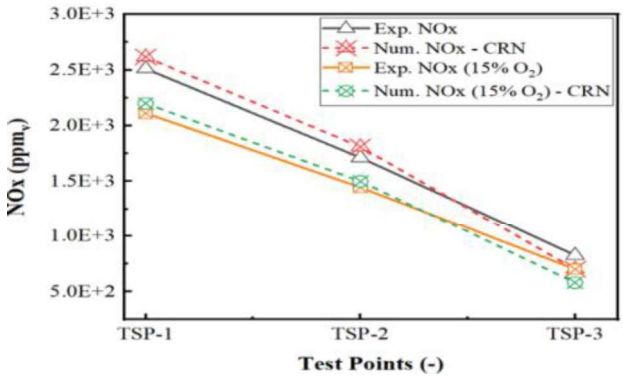

Figure 5. NOx emission results. Solid lines; experimental data [14], broken lines; simulation results for TSP-1 (1.1 bar), TSP-2 (1.5 bar), and TSP-3 (2 bar).

The pressure dependency of the NOx fraction can be attributed to the varying consumption pathways of NO over the different pressures, as illustrated in Figure 6. From the pathways, it is evident that R_1 and R_2 reactions are the primary contributors to NO consumption, with their impact becoming more pronounced at 2 bar. In the same way, R_3–R_5 have slight or no effect across the different pressures.

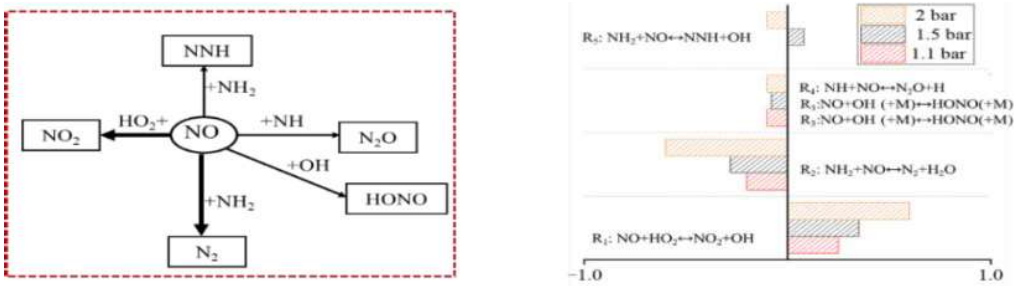

Figure 6. Main NOx consumption pathways at 498 K, φ=0.29, 1.1–2 bar

Conclusion

The detailed mechanism with 32 species and 213 reactions was simplified to 18 species and 28 reactions using the DRGEP method. The reduced mechanism was validated for key combustion parameters over ranges of reaction conditions, showing reliability and accuracy for studying NH_3-H_2 combustion properties.

Acknowledgements

National Recovery and Resilience Plan, Mission 4 Component 2–Investment 1.4–National Center for HPC, Big Data and Quantum Computing–funded by the European Union –NextGenerationEU – CUP (B83C22002830001) is acknowledged.

References

[1] Awad, O.I., et al., *"Characteristics of NH3/H2 blend as carbon-free fuels: a review"*. Int. J. Hydrogen Energy, 2023. **48**(96): p. 38077-38100. doi.10.1016/j.ijhydene.2022.09.096

[2] Syred, N., *A review of oscillation mechanisms and the role of the precessing vortex core (PVC) in swirl combustion systems.* Progress in Energy and Combustion Science, 2006. **32**(2): p. 93-161. doi.10.1016/j.pecs.2005.10.002

[3] Nozari, H. and A. Karabeyoğlu, *"Numerical study of combustion characteristics of ammonia as a renewable fuel and establishment of reduced reaction mechanisms".Fuel,* 2015. **159**: p. 223-233. doi.10.1016/j.fuel.2015.06.075

[4] Konnov, A.A., *"Implementation of the NCN pathway of prompt-NO formation in the detailed reaction mechanism".* Combust. Flame, 2009. **156**(11): p. 2093-2105. doi.10.1016/j.combustflame.2009.03.016

[5] Otomo, J., et al., *"Chemical kinetic modeling of ammonia oxidation with improved reaction mechanism for ammonia/air and ammonia/hydrogen/air combustion".* Int. J. Hydrogen Energy., 2018. **43**(5): p. 3004-3014. doi.10.1016/j.ijhydene.2017.12.066

[6] Shrestha, K.P., et al., *"An experimental and modeling study of ammonia with enriched oxygen content and ammonia/hydrogen laminar flame speed at elevated pressure and temperature".* Proc. Combust. Inst., 2021. **38**(2): p. 2163-2174. doi.10.1016/j.proci.2020.06.197

[7] Pepiot-Desjardins, P. and H. Pitsch, *"An efficient error-propagation-based reduction method for large chemical kinetic mechanisms".* Combust. Flame, 2008. **154**(1-2): p. 67-81. doi.10.1016/j.combustflame.2007.10.020

[8] Mestas, P., P. Clayton, and K. Niemeyer, *"pyMARS: automatically reducing chemical kinetic models in Python".* J. Open Source Softw., 2019. **4**(41). doi: 10.21105/joss.01543

[9] Goodwin, D., *An open-source, extensible software suite for CVD process simulation.* CVD XVI and EUROCVD, 2003. **14**(40): p. 2003-08.

[10] Shrestha, K.P., et al., *"Detailed kinetic mechanism for the oxidation of ammonia including the formation and reduction of nitrogen oxides".* Energy & fuels, 2018. **32**(10): p. 10202-10217. doi.10.1021/acs.energyfuels.8b01056

[11] Pio, G., M. Carboni, and E. Salzano, *"Realistic aviation fuel chemistry in computational fluid dynamics".*Fuel, 2019. **254**:p.115676. doi.10.1016/j.fuel.2019.115676

[12] Lhuillier, C., et al., *"Experimental investigation on laminar burning velocities of ammonia/hydrogen/air mixtures at elevated temperatures".* Fuel, 2020. **263**: p. 116653. doi.10.1016/j.fuel.2019.116653

[13] Wang, S., et al., *"Experimental study and kinetic analysis of the laminar burning velocity of NH3/syngas/air, NH3/CO/air and NH3/H2/air premixed flames at elevated pressures".* Combust. Flame., 2020. **221**: p. 270-287. doi.10.1016/j.combustflame.2020.08.004

[14] Mazzotta, L., et al., *Modeling Ammonia-Hydrogen-Air Combustion and Emission Characteristics of a Generic Swirl Burner.* J. Eng. Gas Turbine. Power., 2024. **146**(9): p. 091022. doi.org/10.1115/1.4064807

SECONDARY GAS-PHASE REACTIONS OF POLYETHYLENE PYROLYSIS: SEMI-DETAILED AND GLOBAL KINETICS

A. Pegurri, A. Locaspi, M. Mehl, M. Pelucchi, A. Stagni, T. Faravelli
tiziano.faravelli@polimi.it
Department of Chemistry, Materials, and Chemical Engineering "G. Natta",
Politecnico di Milano, Milano, 20133, Italy

Abstract
This paper introduces a semi-detailed mechanism and a global one for the gas-phase pyrolysis of polyethylene (PE). The semi-detailed kinetic model for long-chain olefins is developed by analogy to short olefin and long paraffin gas-phase semi-detailed mechanisms, effectively predicting olefin reactivity and products' distribution under varied conditions. This mechanism serves as a basis for deriving a global kinetic model that balances accuracy, flexibility, and computational efficiency. A numerical optimization of its kinetic rates is performed to improve its agreement with the semi-detailed model. Both models are coupled to the fully lumped CRECK mechanism for the PE pyrolysis in the condensed phase. Validation in different reactor setups confirms the models' capability to predict products' distributions. Despite minor discrepancies, the global mechanism effectively reproduces the behavior of the semi-detailed model. Overall, this work lays a robust foundation for optimizing plastic recycling processes, crucial to recovering high-value olefins from solid plastic waste in a circular economy.

Introduction
Chemical recycling of plastic waste is a fundamental step to achieving a sustainable chemical industry. Polyethylene (PE) is among the most widespread polymers, and thermochemical recycling through pyrolysis and gasification has been proven effective in recovering valuable raw chemicals [1]. Fluid dynamics and chemical kinetic modeling tools significantly aid in optimizing product distribution and process design. Nevertheless, compact kinetic models are required to limit the computational costs. Modeling the chemical transformation of polymers is complex, requiring a dual description of the liquid phase decomposition of the polymer's backbone and the subsequent degradation of gas products. PE condensed reactivity has been successfully described through a lumped approach [2] and reduced to a 10-species multi-step model with good accuracy. However, these models fail to predict the increased yield of light olefins observed under industrial-relevant conditions ($T > 650°C$) because of secondary gas-phase reactions. While the gas phase reactivity of long-chain linear paraffins has been extensively studied [3], the major products of PE degradation are long-chain linear olefins, and their reactivity has yet

to be successfully and comprehensively described. A semi-detailed model and a compact global scheme for the secondary reactivity of PE pyrolysis are presented in this work. A numerical optimization of the global kinetic rates is performed to improve the agreement with the semi-detailed mechanism while retaining generality [4].

Semi-detailed kinetic mechanism

The semi-detailed kinetic model describes the secondary reactivity of hydrocarbons produced from the condensed-phase PE pyrolysis, predicting the main products' distribution. Employing hierarchy and modularity principles, the model includes the detailed reactivity of smaller species ($C_{n\leq4}$) through the CRECK kinetic framework [5]. Both vertical and horizontal lumping techniques are applied to the heavier species to ensure compactness [6]. Long-chain linear olefins are the major components of waxes and oils and are assumed to represent the entire carbon distribution for $C_{n>4}$. In line with the liquid-phase model [7], three olefins are chosen to describe industrially interesting cuts: NC_7H_{14} for oil, $NC_{16}H_{32}$ for diesel, and $NC_{30}H_{60}$ for waxes. Their reactivity is described through initiation reactions and H-abstractions, whose kinetic parameters were determined by applying the established method of rate rules and accounting for the higher stability of the radicals in the allylic position. Cyclization and retro-ene reaction classes have been neglected to simplify the modeling in this stage, despite their possible role in aromatics production. H-abstractions on the long-chain olefins are assumed to form directly lower molecular weight decomposition products, by tracking their relative selectivity to the different abstracting sites [8]. This assumption is based on the short lifetime of alkyl radicals ($10^6\ s$) and strongly reduces the number of species and reactions involved. The semi-detailed gas-phase mechanism involves 64 species and 1260 reactions.

Global kinetic mechanism

Global kinetic models aim to describe the overall decomposition rate of the reacting mixture and correctly estimate the main products' distribution. Coherently with the condensed-phase model [7], the presented PE gas-phase global kinetics includes 12 species: three long-chain linear olefins (NC_7H_{14}, $NC_{16}H_{32}$, and $NC_{30}H_{60}$) as major components of the pyrolysis oils and waxes; one short-chain species for paraffins (C_3H_8), two for olefins (C_3H_6, and C_2H_4), and two for diolefins (C_4H_6 and C_3H_4) to account for different degree of products' saturation; two small species of interest (CH_4 and H_2); an inert; and benzene representing the aromatic fraction. The proposed reactivity involves six decomposition reactions (two for each long-chain olefin), and four growth reactions forming aromatics from smaller species. This approach is flexible enough to reproduce the high-temperature consumption of short-chain olefins to form aromatics. The kinetic rates were estimated to match the apparent kinetics of the semi-detailed model: a steady-state assumption was made on the total radical concentration to calculate apparent pre-exponential factors, activation

energies, and reaction orders. The kinetic rates were optimized with OptiSMOKE++ [4] to match the semi-detailed mechanism's results in a broad range of plug flow reactors (PFRs). Relevant conditions for PE pyrolysis were selected for a total of 384 combinations: six temperatures in the range $700°C < T < 1000°C$; two pressures (1 atm and 2 atm); eight residence times in the range $0.008\ s < \tau < 1.0\ s$; and four different ratios of C_7:C_{16}:C_{30} in the reacting mixture to account for the expected variability in the composition of pyrolysis products. The outlet concentrations of six species were targeted: the three long-chain olefins to track their overall reactivity; C_4H_6 and C_2H_4 as the main products of interest; and the aromatics fraction represented by benzene. A factor of ~5 was allowed as the maximum variation for the reaction rates, to obtain satisfying results without radically changing the estimated kinetics. The global gas-phase mechanism includes 12 species and 10 reactions, and well reproduces the results of the semi-detailed mechanism in the investigated conditions.

Model validation

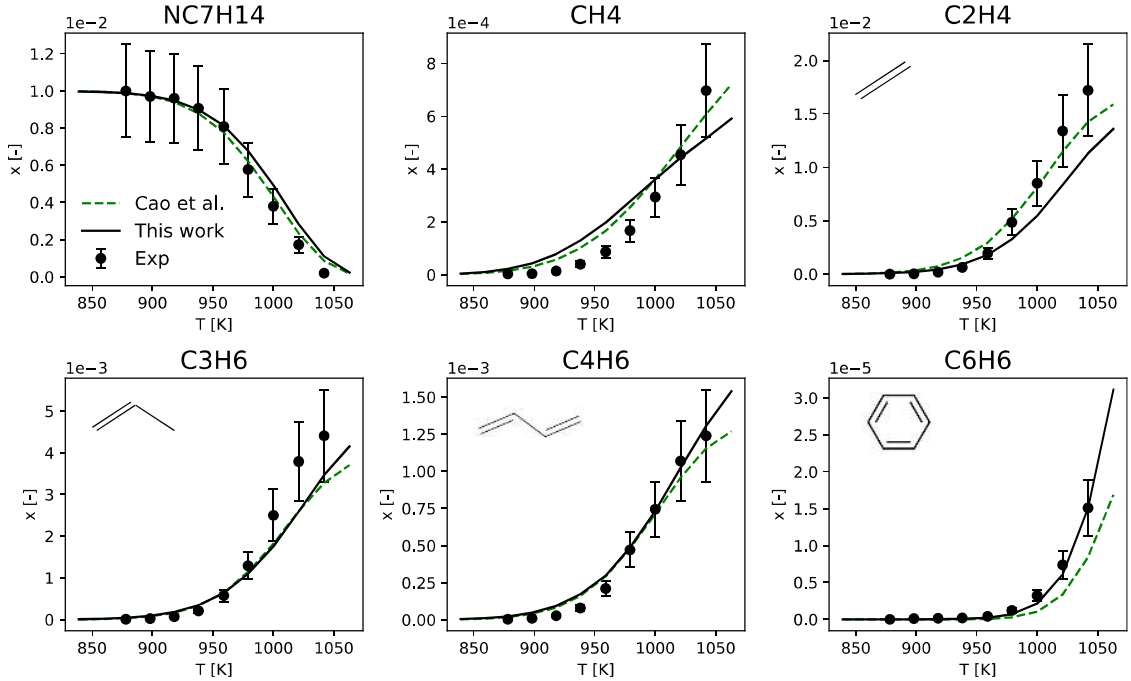

Figure 1. Outlet molar fractions from the pyrolysis of n-heptene, as measured in a PFR at atmospheric pressure and $\tau \cong 0.15\ s$ (dots) [9], and simulated with the semi-detailed model (continuous) and the model by Cao et al. [9] (dashed).

The validation of the gas-phase reactivity of polymers remains challenging due to the multi-phase nature of the process and the complex transport phenomena involved, making it difficult to isolate experimental data at kinetic-relevant conditions. For this reason, the reactivity of each olefin as modeled in the semi-detailed mechanism was validated independently, before addressing the whole mixture. The NC_7H_{14} pyrolysis was compared to the experimental data and detailed mechanism (350 species) by Cao et al. [9]. The soundness of the approach is

confirmed by the satisfactory results obtained in a PFR reported in Fig. 1. To the authors' knowledge, no experimental data are available in the literature for the pyrolysis of $NC_{16}H_{32}$ and $NC_{30}H_{60}$. Hence, their kinetics are validated by mutual comparison, verifying that their main products coherently follow a progression from NC_5H_{10} to $NC_{30}H_{60}$, as expected from the hierarchical nature of radical chain chemistry.

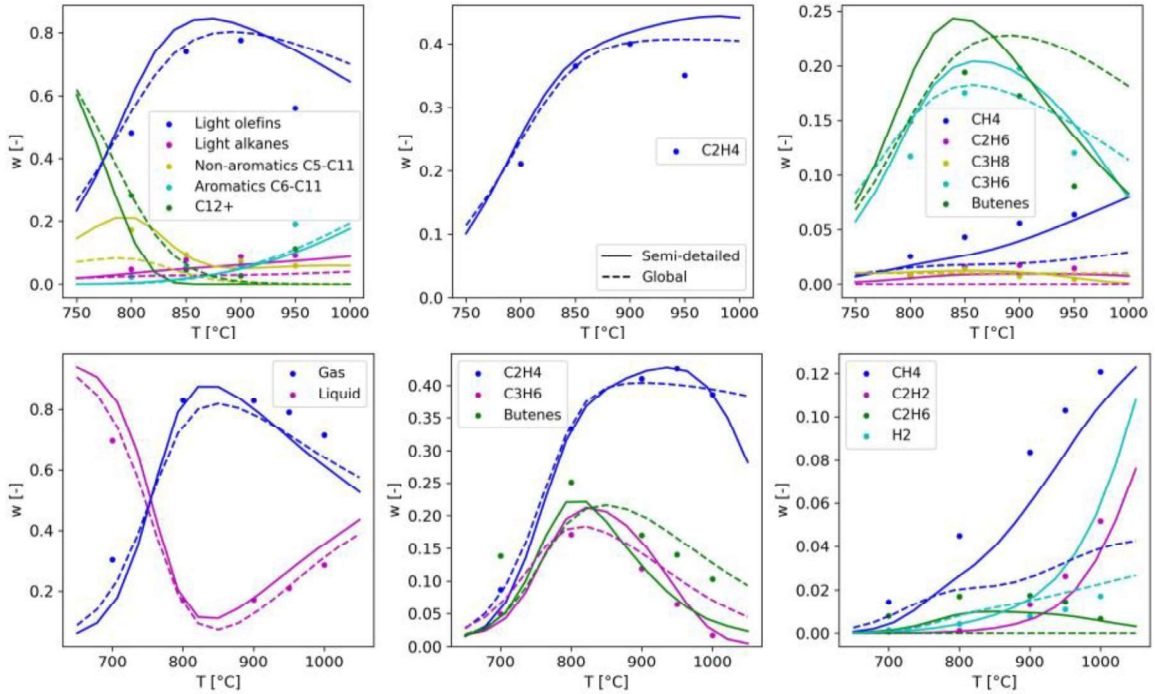

Figure 2. Outlet mass fractions from the gas-phase reactivity of PE pyrolysis products at atmospheric pressure. First row with $\tau = 0.016\ s$ [10] and second row with $\tau = 0.4\ s$ [11]. Experimental data (points) and simulation results from semi-detailed (continuous) and global (dashed) mechanisms are reported.

The semi-detailed and global models are validated in set-ups where the pyrolysis of PE ($T = 500°C$) and the further cracking of the gas products ($T = 700 - 1000°C$) are conducted in two separate steps [10,11], decoupling the effects of the secondary reactions from the liquid phase reactivity. By knowing the composition of the pyrolysis products entering the secondary cracking stage, errors in the modeling of the condensed reactivity can be excluded. The predictions of both models in the cracking of PE products at atmospheric pressure and different residence times ($\tau = 0.016 - 0.8\ s$) are presented in Fig. 2 with the experimental data. The semi-detailed mechanism correctly predicts the long olefins reactivity, light products' distribution, and the aromatics' production at the investigated conditions. Some inconsistencies emerge for high temperatures ($T > 900°C$) and short residence times ($\tau = 0.016\ s$), but errors in the physical reactor model assumption (ideal PFR) cannot be excluded, since residence times are difficult to estimate, and temperature profiles are unavailable. C_2H_4 model predictions in the two investigated datasets deviate from the experimental data in the opposite way, further supporting the over-simplified

reactor modeling hypothesis. Despite the inherent limitations, the global mechanism generally reproduces the behavior of the semi-detailed mechanism with minor discrepancies. For example, CH_4 and H_2 productions are underestimated, given the limited number of species and reactions. The accuracy of several target species is recovered through optimization: C_2H_4 and C_4H_6 as the main products of interest, benzene for the aromatics, and the long-chain olefins for the mixture reactivity.

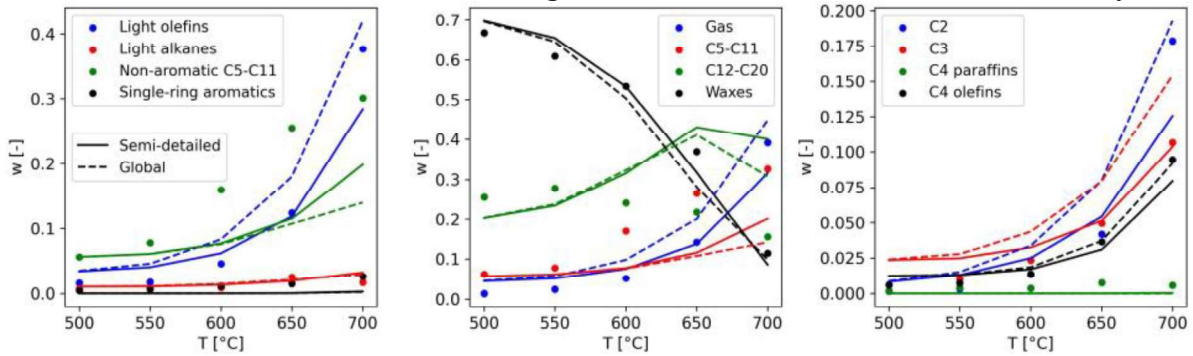

Figure 3. Outlet mass fractions of species and carbon distributions of PE pyrolysis products, in a spouted bed reactor at atmospheric pressure. Experimental data (points) [12] and simulation results from semi-detailed (continuous) and global (dashed) mechanisms are reported.

The mechanisms are also validated in more complex setups, such as a spouted bed reactor [12], where liquid- and gas-phase reactivity simultaneously occur. While these configurations do not allow fine control of the products' composition, they better represent most industrial processes. In the present work, only ideal reactor models are adopted, but inhomogeneity of reactor temperature and estimations of residence times are possibly sources of uncertainties for model predictions. Moreover, the gas-phase reactivity is decoupled from the polymer one: this neglects mutual interactions and assumes an average ratio between volatiles and inert gas flow rates, introducing further uncertainty in the validation. Overall, the results in Fig. 3 are encouraging despite the errors in the oil and diesel cuts. The production of light olefins follows the experimental trends, reflecting both models' capabilities in predicting PE secondary reactivity and showing promising potential in their adoption for reactor modeling and process optimization.

Conclusions

This work presents a semi-detailed mechanism and a global one for the gas-phase pyrolysis of PE. The semi-detailed kinetic model is developed leveraging rate rules and reaction classes, well-predicting olefins reactivity and products' distribution in the studied conditions. The global kinetic model is then obtained by exploiting an apparent kinetics approach, balancing accuracy and computational efficiency. The validation of the two mechanisms in different reactor set-ups confirms their potential for optimizing plastic recycling processes, critical for producing high-value olefins from solid plastic waste in a circular economy perspective.

Acknowledgments
This project has received funding from the European Union's Horizon Europe research and innovation program under the HORIZON-CL4-2021-TWIN-TRANSITION-01 grant agreement 101058412. Views and opinions expressed are however those of the authors only and do not necessarily reflect those of the European Union or HADEA. Neither the European Union nor the granting authority can be held responsible for them.

References

[1] S. Madanikashani, L.A. Vandewalle, S. De Meester, J. De Wilde, K.M. Van Geem, Multi-Scale Modeling of Plastic Waste Gasification: Opportunities and Challenges, *Materials*. 15 (2022) 4215.
[2] A. Locaspi, M. Pelucchi, M. Mehl, T. Faravelli, Towards a lumped approach for solid plastic waste gasification: Polyethylene and polypropylene pyrolysis, *Waste Management*. 156 (2023) 107–117.
[3] E. Ranzi, A. Frassoldati, S. Granata, T. Faravelli, Wide-Range Kinetic Modeling Study of the Pyrolysis, Partial Oxidation, and Combustion of Heavy n-Alkanes, (2005).
[4] M. Fürst, A. Bertolino, A. Cuoci, et al., OptiSMOKE++: A toolbox for optimization of chemical kinetic mechanisms, *Comput Phys Commun*. 264 (2021) 107940.
[5] E. Ranzi, A. Frassoldati, A. Stagni, et al., Reduced Kinetic Schemes of Complex Reaction Systems: Fossil and Biomass-Derived Transportation Fuels, *Int J Chem Kinet*. 46 (2014) 512–542.
[6] E. Ranzi, M. Dente, A. Goldaniga, G. Bozzano, T. Faravelli, Lumping procedures in detailed kinetic modeling of gasification, pyrolysis, partial oxidation and combustion of hydrocarbon mixtures, *Prog Energy Combust Sci*. 27 (2001) 99–139.
[7] CRECK Modeling Lab, Kinetic-Mechanisms, (2024). *https://github.com/CRECKMODELING/Kinetic-Mechanisms*
[8] E. Ranzi, M. Dente, T. Faravelli, G. Pennati, Prediction of Kinetic Parameters for Hydrogen Abstraction Reactions, *COMBUSTION SCIENCE AND TECHNOLOGY*. 95 (1993) 1–50.
[9] C. Cao, W. Li, Q. Xu, et al., Probing pyrolysis chemistry of 1-heptene pyrolysis with insight into fuel molecular structure effects, *Combust Flame*. 227 (2021) 79–94.
[10] M. Artetxe, G. Lopez, G. Elordi, et al., Production of light olefins from polyethylene in a two-step process: Pyrolysis in a conical spouted bed and downstream high-temperature thermal cracking, *Ind Eng Chem Res*. 51 (2012) 13915–13923.
[11] Z. Fu, F. Hua, S. Yang, H. Wang, Y. Cheng, Evolution of light olefins during the pyrolysis of polyethylene in a two-stage process, *J Anal Appl Pyrolysis*. 169 (2023) 105877.

[12] G. Elordi, M. Olazar, G. Lopez, M. Artetxe, J. Bilbao, Product Yields and Compositions in the Continuous Pyrolysis of High-Density Polyethylene in a Conical Spouted Bed Reactor, *Ind Eng Chem Res*. 50 (2011) 6650–6659.


THE COMBUSTION INSTITUTE
1954

SESSION XII

Emission and contaminants mitigation, formation and monitoring including incineration


THE COMBUSTION INSTITUTE
1954

THE EFFECT OF STRAIN RATE ON NANOPARTICLES AND SOOT IN ETHYLENE COUNTERFLOW FLAMES BLENDED WITH ETHANOL AND OME_3

V. Esposito*, M. Sirignano*
vincenzo.esposito9@unina.it
*Dipartimento di Ingegneria Chimica, dei Materiali e della Produzione Industriale,
Università degli Studi di Napoli Federico II, Napoli, 80125, Italy

Abstract
Nowadays, the levels of carbon dioxide in the atmosphere have reached alarming values. In order to decrease or halt global warming, and thus mitigate climate change, the ongoing challenge is to reduce dependence on fossil fuels. Biofuels, especially ethanol, emerge as valuable substitutes for traditional fossil fuels due to their lower carbon emissions. Additionally, among e-fuels, the oligomers of dimethyl ether (DME) – oxymethylene ethers (OMEs) – stand out as potential alternatives for achieving carbon-neutral combustion in diesel engines. Therefore, this work delves into investigating the impact of strain rate on nanoparticles and soot in counterflow diffusion flames (CDFs) of ethylene, ethylene/ethanol, and ethylene/OME_3 using in-situ spectroscopic diagnostics to advance cleaner combustion technologies.

Introduction
In the 20th century, the urgency of transitioning from fossil fuels to sustainable renewable energy is crucial. Among several eco-friendly alternatives, biofuels and e-fuels are being widely explored. Biofuels, especially ethanol - the most frequently produced - can emit less carbon than traditional fossil fuels when blended with conventional gasoline or diesel fuel in existing engines [1]. In the Power-to-Fuel (PtF) technology, oxymethylene ethers (OMEs) as e-fuels, and particularly OME_3, are promising candidates for achieving carbon-neutral combustion, as additives or substitutes in diesel engines [2,3]. Understanding soot formation in turbulent diffusion flames is critical because of its propensity to enhance combustion efficiency. In the context of turbulent diffusion flames, the CDFs delve into the dependence on the characteristic flow time scale of soot formation. In CDFs, the flow time is represented by the strain rate [4]. While strain rate is generally known to reduce soot, understanding of nanoparticle formation remains limited. The strain rate (up to 206.92 s^{-1}) effect for ethylene is here investigated along with ethanol and for the first time OME_3. This study aims to elucidate the intricate relationship between strain rate, oxygenated fuel, and soot and nanoparticle formation in soot forming (SF) flame configuration, characterized by two distinct zones: a pyrolytic and an oxidative zone. In order to provide the impact of strain rate on particle

formation, a pulsed Nd:YAG laser with an excitation source at 266 nm is used. The resulting insights contribute to developing cleaner combustion technologies, especially in blending oxygenated fuels with traditional ones. Further research is recommended for broader applicability, considering high strain rates and varied dilution conditions.

Materials and Methods

The counter-flow burner system is the same as in previous works [5-7]. It consists of two vertically positioned jet nozzles (I.D. 2.54 cm), separated by a constant distance of 1.5 cm. The oxidizer stream was introduced from the upper nozzle, while the fuel stream was introduced by the lower nozzle. Nozzle velocities were varied from 10 cm/s to 80 cm/s (at STP), corresponding to a global strain rate (K), calculated according to [8], which ranged from 25.86 s^{-1} to 206.92 s^{-1}. Ethanol and OME_3 concentrations (20% of total carbon fed) were introduced into the fuel stream, where they are electrically pre-heated at 150 °C to ensure their complete evaporation. The total carbon flow rate is kept constant through the different fuel blends, providing a direct comparison of the results. In the investigated flames (Table 1), the flame front is always on the oxidizer side of the stagnation plane, indicating the soot forming (SF) counterflow diffusion flames configuration. It is worth to underline that as in the fuel stream as in the oxidizer stream, the fuels and oxidizer molar fractions were balanced with nitrogen (75% and 79%, respectively).

Table 1. Strain rate and stream compositions of the investigated flames.

	Fuel stream					**Oxidizer stream**
	Pure C_2H_4	C_2H_4/EtOH		C_2H_4/OME_3		
K [s^{-1}]	$y_{C_2H_4}$ [-]	$y_{C_2H_4}$ [-]	y_{EtOH} [-]	$y_{C_2H_4}$ [-]	y_{OME_3} [-]	y_{O_2} [-]
25.86	**0.25**	**0.20**	**0.05**	**0.20**	**0.020**	**0.21**
38.80	**0.25**	**0.20**	**0.05**	**0.20**	**0.020**	**0.21**
51.73	**0.25**	**0.20**	**0.05**	**0.20**	**0.020**	**0.21**
103.46	**0.25**	**0.20**	**0.05**	**0.20**	**0.020**	**0.21**
206.92	**0.25**	**0.20**	**0.05**	**0.20**	**0.020**	**0.21**

The experimental diagnostic is similar to that used in previous works [5-7]. Spatially and spectrally resolved Laser-Induced Emission (LIE) measurements were performed using the fourth harmonic (266 nm) of a pulsed Nd:YAG laser as the excitation source. Laser-Induced Fluorescence (LIF), attributed to nanoparticles, Laser-Induced Incandescence, attributed to soot, and scattering, coupled with the capability of the entire burner assembly to move up or down with respect to the sampling point (spatial resolution of 0-1-0.2 mm), have allowed to well characterize the flames at different locations between the two opposed jet nozzles.

Results and discussions

In Figure 2a it is possible to observe the effect of strain rate in the pure ethylene counterflow flames, plotting scattering, LIF@350 nm, and LII@500nm profiles. As expected, due to the reduced residence time available for nucleation and growth, a general intense decrease is observed in the signals as the strain rate increases. The stagnation plane was hardly individuated to be located between 6.0 and 6.2 mm, because of the difficulty of detecting it above the gas phase for high strain rates.

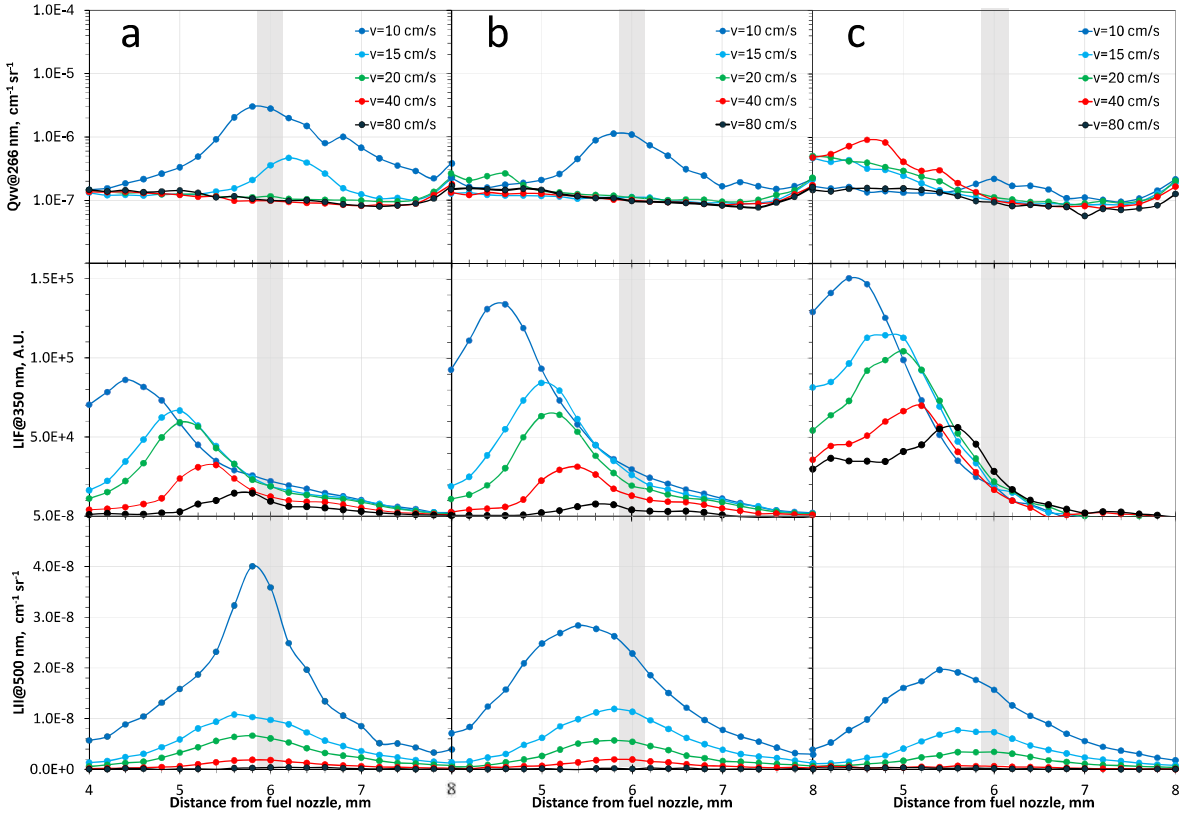

Figure 2 LIE signals measured at different wavelengths in the pure ethylene (a), ethylene/ethanol (b), and ethylene/OME_3 (c) CDFs at different strain rates.

The same trends were observed in the counterflow diffusion flames of ethylene/ethanol and ethylene/OME_3 at different strain rates (Figure 2b-2c).
A direct comparison of scattering, LIF@350nm, and LII@500nm for the three fuel blends with a strain rate of 38.8 s^{-1}, is presented in Figure 3. It is possible to observe the increasing LIF signal in the pyrolytic zone for the two oxygenated fuel blends, with OME_3 showing a more significant reduction in large soot particles detected by LII. On the right side of Figure 4 (left side), LII@500nm and LIF@350nm normalized signals against the strain rate are reported. Full dots and empty squares indicate the normalization of the signals on the maximum in the fuel zone and oxidant zone, respectively. The pure ethylene flame presents different trends in the pyrolytic and oxidant zones, with LII decreasing from K=25.86 s-1 to K=38.8 s-1. OME_3 has a trend similar to pure ethylene, indicating less sensitivity to strain rate but generally results in decreased particle formation due to the absence of C-C bonds.

Moreover, the ethanol blend exhibits a more effective reduction in particle nucleation and growth in the pyrolytic zone.
Finally, soot volume fraction profiles for the three fuel blends at different strain rates have been calculated. Their maximum values were plotted against strain rate such as their normalization in Figure 4 (right side), and once again it is demonstrated that when the strain rate rises, the former consequence is a reduction in soot formation.

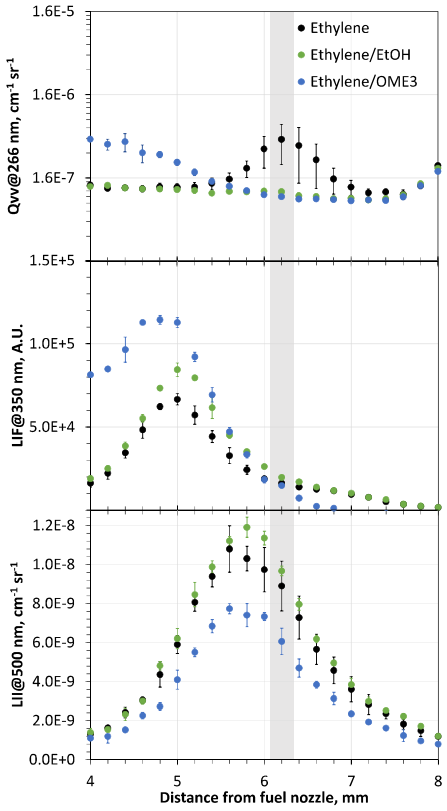

Figure 3 LIE signals measured at different wavelengths in CDFs of pure ethylene, ethylene/ethanol, and ethylene/OME_3 at a strain rate of K=38.8 s^{-1} (left side).

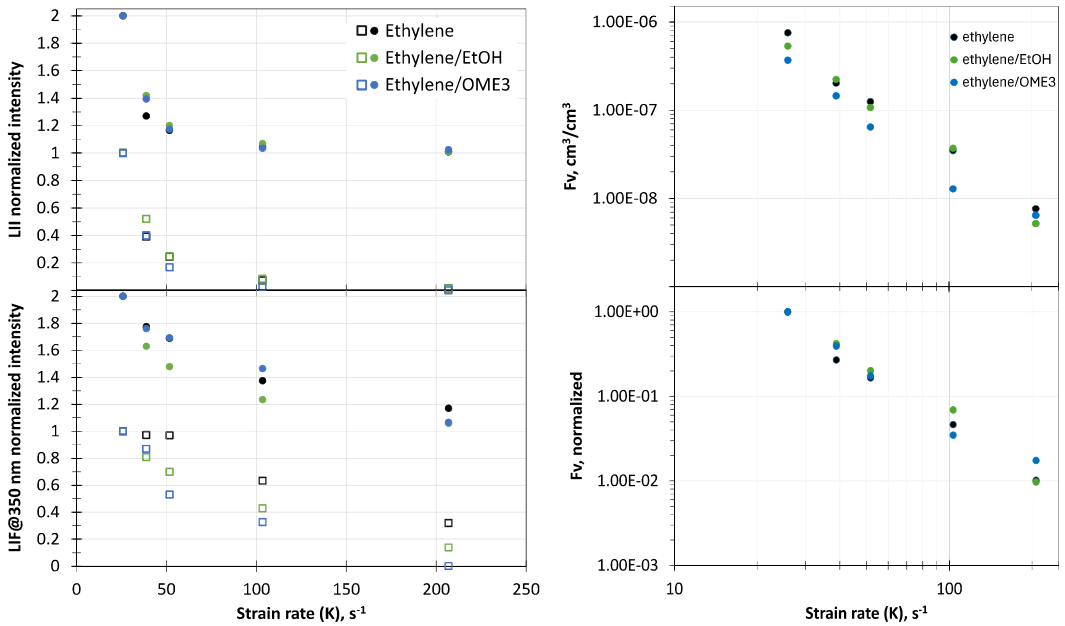

Figure 4 LII@500nm (top) and LIF@350nm (bottom) normalized intensity vs strain rate (left side). Soot volume fraction (top) and normalized soot volume fraction (bottom) vs strain rate for the three fuel blends (right side).

Conclusions

This study has examined the strain rate effect on nanoparticles and soot in counterflow diffusion flames (CDFs) of pure ethylene, ethylene/ethanol, and ethylene/OME_3. Using the fourth harmonic (266nm) of a pulsed Nd:YAG laser it was possible to analyse flame dynamics:

- Particle nucleation and growth are inhibited by decreasing strain rate.
- There is a non-linear strain rate effect on particle formation, and this latter sees the contributions of both pyrolytic (smaller particles due to dominant nucleation and coagulation) and oxidant zones.
- In the pyrolytic zone ethanol and OME3 increase particle formation, effect that goes to diminishes at higher strain rates.
- OME_3 presents a lower sensitivity to strain rate because of its higher reactivity and lack of C-C bonds.

References

[1] Cherwoo, L., Gupta, I., Flora, G., Verma, R., Kapil, M., Arya, S.K., et al. "Biofuels an alternative to traditional fossil fuels: A comprehensive review", *Sustain. Energy Technol. Assessments.* 60: 103503 (2023).

[2] Nemmour, A., Inayat, A., Janajreh, I., Ghenai, C., "Green hydrogen-based E-fuels (E-methane, E-methanol, E-ammonia) to support clean energy transition: A literature review". *Int. J. Hydrogen Energy*. 48:29011-33 (2023).

[3] Lumpp, B., Rothe, D., Pastötter, C., Lämmermann, R., Jacob, E., "OXYMETHYLENE ETHERS AS DIESEL FUEL ADDITIVES OF THE FUTURE", *MTZ world.w..* 72:34-8 (2011).

[4] Chung, S.H., Law, C.K., "An invariant derivation of flame stretch", *Combust Flame.* 55: 123-5 (1984).

[5] Salamanca, M., Sirignano, M., D'Anna, A., "Particulate formation in premixed and counter-flow diffusion ethylene/ethanol flames". *Energy Fuels.* 26(10), 6144-6152 (2012).

[6] Sirignano, M., Collina, A., Commodo, M., Minutolo, P., D'Anna, A., "Detection of aromatic hydrocarbons and incipient particles in an opposed-flow flame of ethylene by spectral and time-resolved laser induced emission spectroscopy". *Combust. Flame.* 159(4), 1663-1669 (2012).

[7] Sirignano, M., Bartos, D., Conturso, M., D'Anna, A., Masri, A.R., "Detection of nanostructures and soot in laminar premixed flames", *Combust. Flame.* 176:299-308 (2017).

[8] Seshadri, K., Williams, F.A., "Laminar flow between parallel plates with injection of a reactant at high Reynolds number.", *Int. J. Heat Mass Transf.* 21:251-3 (1978).

Newest methodology for flare validation

V. Ceglie*, [a], A. Ferrante[b], S. M. Camporeale[a], M. Torresi[a], D. Laera[a], A. Saponaro[b], S. Kretzschmar[c] , R. Withnall[c]

*vito.ceglie@poliba.it
[a] Polytechnic University of Bari, Department of Mechanics, Mathematics & Management, via Orabona 4, 70125, Bari, Italy
[b] Centro Combustione Ambiente SpA (CCA, Sofinter Group), via Milano km 1, 600, Gioia del Colle (BA), 70023, Italy
[c] Greens Combustion Ltd (GCL), A31 Arena Business Center, Holyroad Close Poole, Dorset, BH17 7FJ,(UK)

Abstract
The oxidation by burning of disposed gases containing combustible elements such as volatile organic compounds (VOCs), natural gas (or methane), carbon monoxide (CO), and hydrogen (H_2) is known as 'Flaring'. This process is used to manage the safe disposal of waste and emergency relief gasses generated by refineries, petroleum production, chemical industries, ammonia fertilizer plants, etc. Flaring is typically used for day-to-day waste disposal as well as the last line of defense in an emergency blow down condition. In recent years as efforts have been made to reduce global CO_2 and CO_2eq emissions, flares have been recognized as significant sources both of carbon dioxide and methane, it is also acknowledged that as flares have primarily been considered safety relief devices little rigorous focus has been made to understand their emissions under all operating conditions. Consequently, there is a strong interest among operators and suppliers in both understanding and maximizing the combustion efficiency of flares. In response to this challenge, CCA, headquartered in Gioia del Colle (BA) Italy, in cooperation with GCL, has pioneered a new methodology for precisely measuring flare efficiency on an industrial scale.

Introduction
The efficiency of flare combustion is influenced by several key factors: the flammability, auto-ignition temperature, net heating value, density [1], mixing of gases within the flare's combustion zone [2]. Incomplete combustion, known as "inefficient" flaring, can lead to the release of unburned fuel [3], volatile organic compounds [4], and carbonous soot or black carbon [5, 6, 7]. Since most flare gas contains a high concentration of methane [8], a short-lived climate pollutant with a significantly higher global warming potential than CO_2 [7], inefficient flaring can emerge as a major source of greenhouse gas emissions.
The direct measurements of the flare performance in open space are particularly difficult to be realized and the repeatability and accuracy of the results are far to be optimal, furthermore determination of the impact of such variables such as flare gas composition, cross wind and simulated rain has proved challenging. In order to eliminate these difficulties, at the CCA testing site in Gioia del Colle Italy a new

methodology for flare validation has been implemented. By the use of the 48 MW boiler test rig combustion chamber as an envelope volume to confine the flare combustion process it is possible to control both cross wind velocity, combustion duty and exhaust composition in reliable end repeatability conditions. The test facility also brings together state of the art gas blending stations with access to multiple feed gas compositions.
A testing method validation has been performed and a preliminary test measurement executed on a generic flare tip model properly designed in accordance with good engineering practice, are here presented.
Three distinct elevated flare reacting flow mixing regimes have been identified as possible conditions to be investigated by this new methodology. (see Figure 1) [9]

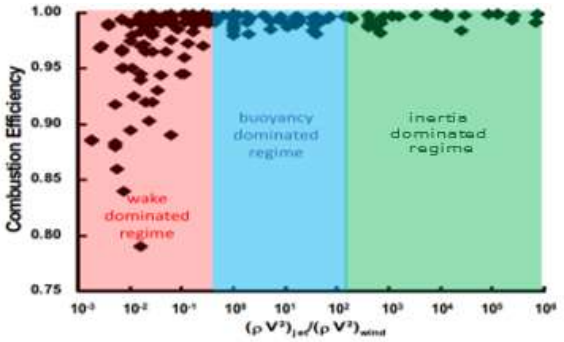

Figure 1: Combustion efficiency as a function of momentum flux ratio. [9]

Firstly, in the **inertia-dominated regime** in which the high-velocity jet facilitates jet-mixing, resulting in consistently high combustion efficiencies. The inertia dominated regimes are typical of flares operating under emergency and blow down conditions, this typically occurs only across 5% of a flares operating life. The second is the **buoyancy-dominated regime** where the velocity decreases and eddy quenching or stripping becomes possible. The last is the **wake-dominated regime** characterized by low velocity or high crosswind where the flame is drawn downwards and stabilizes within the vortex trail off the stack. A flare will typically spend almost 95% of its life operating under these lower flow conditions.

Experimental Rig in the CCA Testing Area

At the CCA testing area several combustion processes can be simulated and tested on an industrial scale by means important testing infrastructures. The CCA boiler test rig was designed in order to test boiler burners of up to 48 MW capacity. This furnace, one of the largest in Europe, continues to be utilized by CCA for assessing various boiler burner technologies across different fuel types. Its dimension is 4.5 meters in width, 6 meters in height, and 12 meters in length internally. With its closed design, the rig enables precise measurements of O_2, CO, CH_4, other unburnt hydrocarbons, and CO_2 at its outlet. View ports along the length of the chamber allow for detailed flame monitoring as well as emissions probing at the flame. This detailed flame monitoring could be crucial for further extrapolation to CFD analysis and

validation. A schematic representation of the facility is illustrated in Figure 2.

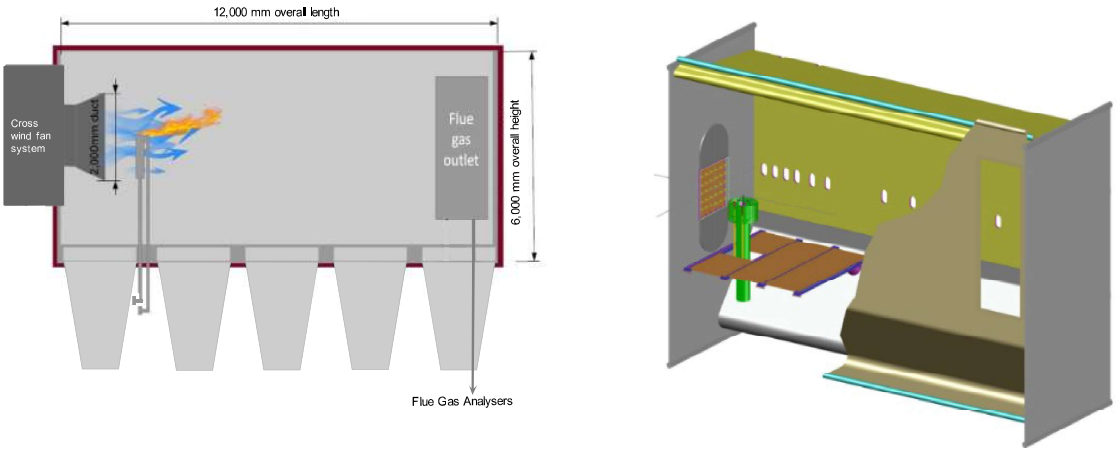

Figure 2: CCA furnace used for flare testing.

To conduct flare tests, modifications were made to the inlet, enabling the wind simulation by means of air supply through a square injector upstream the fare 1.514 x 1.515 meters size. Flow straighteners were installed in the air inlet to minimize turbulence. Two high-capacity fans are utilized to deliver ambient temperature air at rates of up to 138 tons per hour, resulting in crosswind speeds of up to 14 meters per second (equivalent to 50 km/h or 27 knots), typical of wind speeds at flare elevations which can reach heights of 200m. A demonstrative test campaign will be conducted on a benchmark flare tip supplied by Greens Combustion Ltd. . The 16-inch pipe flare is equipped with an integral wind shield, flame retention devices and two pilots. has been positioned 2 meters downstream from the air inlet. This range of flare size is sufficiently large to produce combustion and destruction efficiency results that are not scale dependent. The expected flare flow range for the experiments is from 0.5 to 2.0 MW. This range ensures the flame's complete development downwind of the flare tip, without any contact with the walls, ceiling, or floor of the working section. In order to ensure adequate aerodynamic similarity with the performance of industrial flare, calculations were conducted on the scaled-down version of full-size flare.

Probes and analyzers on experimental rig

Gas composition at the combustion chamber outlet was analyzed via extractive sampling of both wet and dry flue gases. A heat-traced sampling line delivered wet flue gases to an FTIR (Fourier Transform Infrared Spectroscopy) calibrated for CH_4, CO, and CO_2 measurement, as well as to a RATFISCH analyzer for total hydrocarbon assessment. Another sampling line directed flue gases to a cooling system, removing water vapor and providing dry flue gases to HORIBA PG350, and NOx analyzers.

In order to validate the test rig metering devices, a comparison between the theoretical CO_2 and that measured via HORIBA PG350 was made. Figure 3 presents the comparison between the experimental CO_2 emissions measured with respect to

the theoretical ones. The squared R value of the correlation is $R^2 = 0.9929$, showing a high goodness of the measurements.

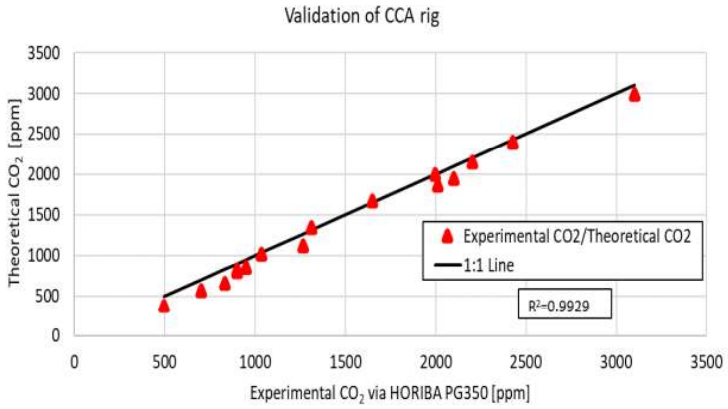

Figure 3: Validation of CCA metering devices.

Flare Efficiency Parameters

To assess the efficiency of flares, three key parameters are commonly used: Flare Combustion Efficiency (CE), Destruction Efficiency (DE), and Destruction and Removal Efficiency (DRE). These parameters quantify how effectively flares oxidize hydrocarbon components. In the literature, different way to calculate these parameters are applied, in this paper that are calculate as following:

Combustion Efficiency (CE): This parameter measures the proportion of total hydrocarbons (THC) completely burned in the flare to produce CO_2 and water vapor. It is expressed as the ratio of the volume concentration of emitted $[CO_2]$ to the sum of $[CO_2]$, [CO], and unburned hydrocarbons $[THC_w]$.

$$CE = \frac{[CO_2]}{[CO_2] + [CO] + [THC_w]}$$

Destruction Efficiency (DE): DE quantifies the extent to which introduced hydrocarbons undergo oxidation into non-hydrocarbon compounds (CO_2, CO, and water vapor). It is calculated as the ratio of the sum of $[CO_2]$ and [CO] to the sum of $[CO_2]$, [CO], and unburned hydrocarbons.

$$DE = \frac{[CO_2] + [CO]}{[CO_2] + [CO] + [THC_w]}$$

Destruction and Removal Efficiency (DRE): DRE, like DE, assesses the transformation of hydrocarbons into non-hydrocarbon forms. However, it is determined by comparing the mass flow rates of hydrocarbons entering and leaving the flare.

$$DRE = 1 - \frac{\dot{m}_{out}}{\dot{m}_{in}}$$

Results

During the initial test campaign, 16 distinct test conditions were recorded. The flue gas composition was recorded every second. The fuel flow was varied in a range of 90.46 to 12.7 kg/h, which given the 16-inch tip diameter, corresponded to velocity from 26.8 to 3.7 cm/s (typical range for the *"low pressure"* flare kind, in that we can identify as "wake dominated regime"). After this validation, the Combustion Efficiency (CE) and Destruction Efficiency (DE) were compared. Figure 4 shows that the differences between CE and DE exists when CE is less than 96%. The squared R value of the correlation is $R^2 = 0.99$, showing a good agreement between CE an DE. The right side of the figure displays a frame capturing the flare in a wake-dominated regime, examined in CCA.

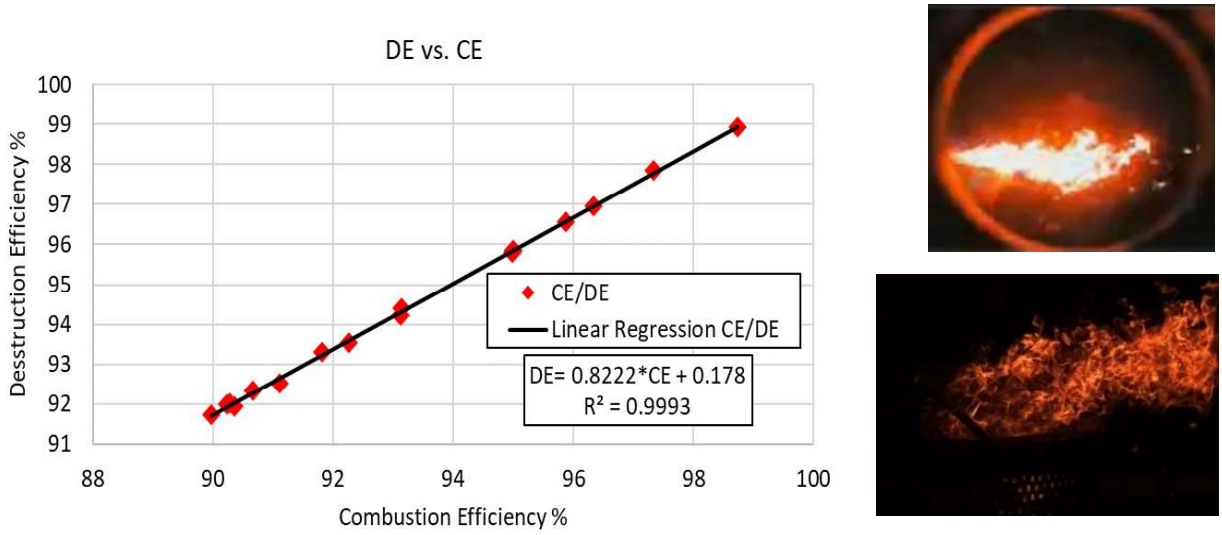

Figure 4: Combustion Efficiency vs. Destruction Efficiency

Figure 5 presents the combustion and destruction efficiency in function of wind velocity. During this testing regime it was found that combustion and destruction efficiencies decreased from almost 99% at low cross wind to around 90% when wind speed increased to near 11.5 m/s, Further tests were conducted at higher wind speeds and low flare flow conditions where flare combustion efficiency dropped to 75% at 14 m/s cross wind speed. These efficiencies notably surpassed those typically observed in 1 to 4'' pipeflares and their subsequent correlations, indicating that industrial-sized flares are less prone to combustion efficiency reduction in high crosswind conditions however while the flare will remain alight in these conditions combustion and destruction efficiency is substantially impacted. The presence of a wind shield and flame retention devices on the tested flare tip likely contributed to mitigating the impact of wind speed on combustion and destruction efficiency. These tests were carried out in "wake dominated regime". In future, this experimental methodology can be used in order to test flares in "inertia dominated regime". Furthermore, testing should be expanded to understand the impact on combustion efficiency as a flares component such as the windshield start to degrade over time.

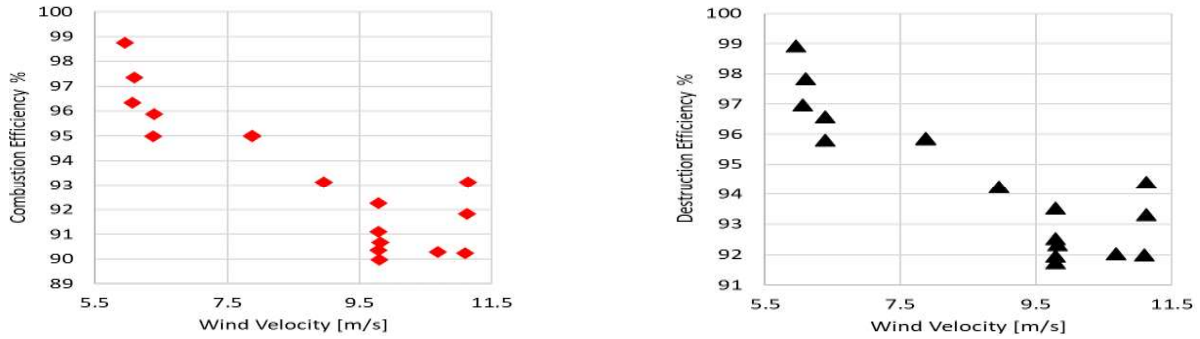

Figure 5: Effect of cross wind velocity on combustion and destruction efficiency

Conclusions

The paper underlines the possibility to be effective in the carbon emission control improving the flaring operation by a deeper understanding of the combustion process. A new testing capability can be used to measure in controlled and repeatability condition, different flare nozzles in scaled size. This new tool, available in an open testing platform, can be used as a basic to understand and validate different solutions and functional models.

References

[1] D. Shore, "Letter from Flaregas Corporation to William Vatavuk," U.S. Environmental Protection Agency, Research Triangle Park, NC, October 3, 1990.

[2] U.S. Envoiromental Protection Agency, "Compilation of Air Pollution emissions Factors," AP-42 Chapter 13,5 Research Triangle Park: U.S. Environmental Protection Agency, Office of Air Quality Planning and Standard, April 2015.

[3] A. Gvakharia, E. A. Kort, A. Brandt, J. Peischl, T. B. Ryerson, J. P. Schwarz, M. L. Smith and C. Sweeney, "Methane, black carbon, and ethane emissions from natural gas flares in the Bakken Shale, North Dakota.," *Environmental Science & Technology,* vol. 51, no. 9, pp. 5317-5325, 2017.

[4] W. B. Knighton, S. C. Herndon, J. F. Franklin, E. C. Wood, J. Wormhoudt, W. Brooks, E. C. Fortner and D. T. Allen, "Direct measurement of volatile organic compound emissions from industrial flares using real-time online techniques: Proton Transfer Reaction Mass Spectrometry and Tunable Infrared Laser Differential Absorption Spectroscopy," *Industrial & engineering chemistry research,* vol. 51, no. 39, pp. 12674-12684, 2012.

[5] B. M. Conrad and M. R. JOHNSON, "Mass absorption cross-section of flare-generated black carbon: Variability, predictive model, and implications.," *Carbon,* vol. 149, pp. 760-771, 2019.

[6] C. L. Weyant, P. B. Shepson, R. Subramanian, M. O. L. Cambaliza, A. Heimburger, D. McCabe, E. Baum, B. H. Stirm and T. C. Bond, "Black carbon emissions from associated natural gas flaring.," *Environmental science & technology,* vol. 50, no. 4, pp. 2075-2081, 2016.

[7] E. C. Fortner, W. A. Brooks, T. B. Onasch, M. R. Canagaratna, P. Massoli, J. T. Jayne, J. P. Franklin, W. B. Knighton, J. Wormhoudt, W. D. R., C. E. Kolb and S. C. Herndon, "Particulate emissions measured during the TCEQ comprehensive flare emission study.," *Industrial & engineering chemistry research,* vol. 51, no. 39, pp. 12586-12592, 2012.

[8] M. R. Johnson and A. R. Coderre, "Compositions and greenhouse gas emission factors of flared and vented gas in the Western Canadian Sedimentary Basin.," *Journal of the Air & Waste Management Association,* vol. 62, no. 9, pp. 992-1002., 2012.

[9] J. Seebold, P. Gogoloek, J. Pohl and R. Schwartz, "Practical implications of prior research on today's outstanding flare emissions questions and a research program to answer them.," in *AFRC-JFRC 2004 Joint International Combustion Symposium*, Maui, HI, 2004.

Experimental Investigation on PFAS Remediation Through Civil Sludge Combustion Processes.

M. Urciuolo[1], R. Migliaccio[1], B. Ciccone[1,4,], G. Ruoppolo[1], M. Baric[2], A. de Folly d'Auris[2], S. Frisario[3], D. Panepinto[4], G. Premoli[5], B. Ruffino[4], M. Zanetti[4]*

biagio.ciccone@stems.cnr.it
[1]Istituto di Scienze e Tecnologie per l'Energia e la Mobilità Sostenibili, Consiglio Nazionale delle Ricerche, P. le V. Tecchio, 80, 80125 Napoli, Italy
[2]Eni SpA, via Felice maritano 26, San Donato Milanese, Italy
[3]Eni Rewind Spa, Piazza Boldrini 1, San Donato Milanese, Italy
[4] Dipartimento di Scienza Applicata e Tecnologia (DISAT), Politecnico di Torino, C.so Duca degli Abruzzi 24-10129, Torino, Italy
[5]LabAnalysis Environmental Science Srl, via Europa 5, Casanova Lonati (Italy)

Abstract
Incineration process represents a valid solution for Poly-FluoroAlkyl Substances (PFAS) treatment. This study investigates the thermal degradation of sludge containing PFAS and coming from a municipal wastewater treatment plant, by employing a laboratory-scale bubbling fluidized bed combustor operating at 850°C. By utilizing samples of untreated municipal sludge and sludge spiked with a known PFAS mixture, the research could achieve a high analytical sensitivity, enabling a comprehensive evaluation of PFAS combustion efficiency. Preliminary results elucidated the distribution of fluorinated molecules within the combustion byproducts, shedding light on the PFAS degradation pathways during incineration.

Introduction
The term PFAS (Per- and Poly-FluoroAlkyl Substances) refers to a wide family of organic compounds characterized by partial or complete saturation of carbon atoms with fluorine [**1**]. Normally used in various industrial applications (from paper food packaging to firefighting foams), their stubborn resistance to degradation and their tendency to bioaccumulation and migration has raised concerns about ecological and health threats for human beings. Neurodevelopmental disorders, increased risk of thyroid diseases and cancer risk have been identified as possible outcomes of PFAS exposure [**2**]. PFAS are transferred from the industry to the environment via wastewater treatment plants (WWTP), where PFAS precursors are converted into PFAS mainly via biochemical reactions, e.g., N-ethyl per-fluorooctane sulfonamide (N-EtFOSA) and N-ethyl per-fluorooctane sulfonamidoethanol (N-EtFOSE) are transformed into PFOS (perfluorooctane sulfonate). Alternatively, PFAS originally present in industrial products are released into wastewaters.
High PFAS concentrations have been detected both in wastewater itself and in the sludges produced within the wastewater treatments in different countries like China,

the US and Germany [**1**]. High molecular weight PFAS compounds are less volatile and more hydrophobic, thus they exhibit a strong tendency to adsorb onto sludge matrices reaching concentrations up to thousands of nanograms per gram of dry weight.
In this context, efficient and safe treatment approaches for PFAS removal from municipal sludge is of outstanding importance to limit their spread into the environment. Up to date, different technologies have been studied for PFAS remediation, among which physical (adsorption), thermochemical and biochemical routes **[1].** Incineration of municipal sludges at high temperatures (800-900°C) is one of the possible strategies studied to degrade PFAS molecules [3], but more research is needed on the fate of PFAS compounds, on the degradation efficiency and on the fluorinate molecules distribution within the combustion flue gas and the ash. In this work, results from a preliminary experimental campaign of municipal sludge combustion are presented. PFAS thermal degradation during sludge incineration has been studied using a laboratory-scale bubbling fluidized bed combustor operated at 850°C and atmospheric pressure.

Materials and methods

Different combustion tests were performed using a laboratory scale bubbling fluidized bed combustor (40 mm ID and 1 m height) at a constant temperature of 850°C and a fluidization velocity of 0.5 m/s. The residence time was 2 s. Silica sand (300-400 μm) has been used as bed material. A metallic filter, kept at 300°C to avoid vapor condensation, was used to collect elutriated particles. A schematic representation of the experimental setup is reported in Figure 1.

The fuel (sludge) was continuously fed through a mechanical-pneumatic system consisting of a loading hopper positioned on a screw feeder that transports the solid particles into a little jar into which a flow of air pneumatically injects the particles at the base of the bed. For this reason, the fuel was crushed and sieved to small particles (<1 mm). During each experimental run, the fuel feeding rate was adjusted to have a stable oxygen concentration of 4-6% in the flue gas. Proximate and ultimate analyses were performed according to ASTM and UNI standards using a LECO TG701 thermogravimetric balance (ASTM D5142), LECO CS144 (ASTM D 4239) and a LECO CHN 628 elemental analyzer (ASTM D5373), respectively. The calorific value was determined using a PARR 6200 calorimeter (ASTM D 5865) with a Mahler calorimeter bomb. Metal analyses were performed by ICP-MS (Agilent 7500CE) after dissolution of the samples by microwave-assisted acid digestion, in accordance with US-EPA Methods 3051 and 3052. All measurements were repeated at least three times. Flue gas analysis has been performed online for O_2, CO, CO_2, and NO_x concentration.

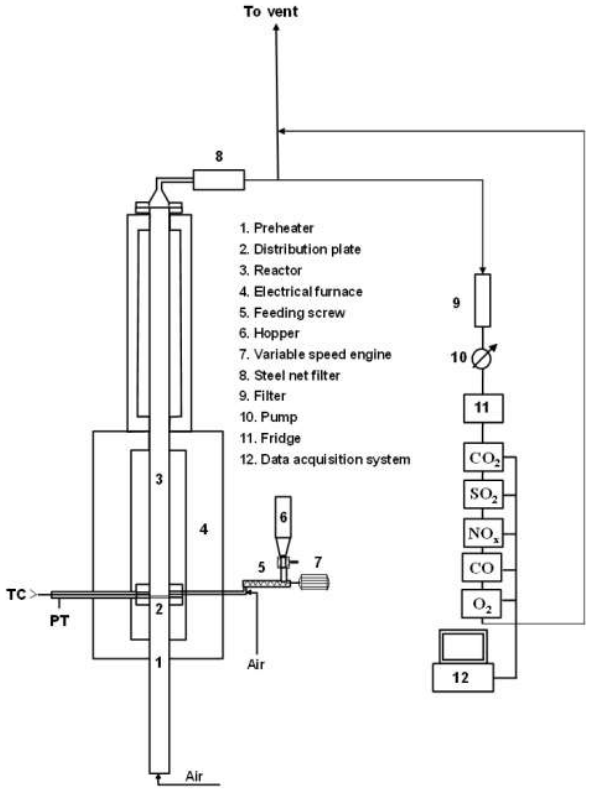

Figure 1. Laboratory scale fluidized bed combustor used in the experimental campaign.

Sampling and analysis of PFAS has been conducted by an external laboratory, which employed specific advanced techniques for high resolution evaluation of these contaminants. To assess the efficiency of PFAS destruction in the incineration process, the sludge was spiked with known amounts of 5 representative PFAS compounds, as shown in Table 1. The PFAS enrichment of the sludge was necessary, given the low concentrations of PFAS present in the actual starting sludge, to allow adequate analytical sensitivity. Spiked sludge samples exhibited PFAS concentrations surpassing those found in raw sludge by a factor of 100.

Table 1. PFAS content in spiked sludge.

Compound	**Sludge 1[mg/kg]**	**Sludge 2[mg/kg]**
PFBS	1.9	0.2
PFTeDA	1.8	0.5
PFOA	1.9	1.7
PFBA	2.0	2.4
PFOS	1.0	0.9
Total PFAS	8.5	5.8

The representative characteristics of the dry sludge used in the experimental campaign are reported in Table 2. The ICP analysis shows high concentration of some elements, especially Fe (~4%wt.), P (~3%wt.) and Ca (~2%wt.).

Table 2. Proximate and ultimate analyses of the sludge samples (as received, %wt).

Analysis	**Sludge 1**	**Sludge 2**
Moisture	4.7	4.5
Volatiles	65.3	61.3
Fixed carbon	8.1	4.9
Ash	21.9	29.4
Carbon	36.2	31.6
Hydrogen	5.4	4.6
Nitrogen	5.7	6.1
Sulfur	0.98	0.96
Clorine	0.12	0.075
Fluorine	0.018	0.0112
Oxygen (by difference)	25.0	22.8
LHV [kJ/kg]	15139	13457

Table 3 illustrates the experimental conditions of the combustion tests, particularly referring to the fuel feed rate and excess of combustion air.

Table 3. Operating conditions for the experimental tests.

Name	**N°1**	**N°2**	**N°3**	**N°4**	**N°5**	**N°6**	**N°7**	**N°8**
Feed, g/h	119.7	115.5	126.8	113.2	103.6	101.1	103.4	99.3
Power, kW_{th}	0.491	0.474	0.533	0.476	0.387	0.378	0.386	0.371
Air excess, %	18	22	12	26	58	62	58	65

Results and discussion

Tests from N°1 to N°4 were performed using a lower excess air (20-30%) compared to tests N°5 to N°8 (50-60%). This difference significantly influenced the efficiency of the combustion process in terms of pollutant emissions and ashes recovery from the combustor. From Table 4 it can be noted that higher O_2 content in the reactor lead to a reduction in CO and NO_x production from 2500-3000 ppm to 1100-1300 ppm and from 2500-3200 ppm to 1000-1600 ppm respectively. A more complete combustion is achieved when oxygen is in large excess, reaching a 99% combustion

efficiency. The fly ash concentration and their carbon content are comparable to values obtained in other experiments [4].

Table 4. Main results from the sludge incineration tests.

Name	N°1	N°2	N°3	N°4	N°5	N°6	N°7	N°8
Testing time, h	4	4	4	4	2	2	4	4
Combustion efficiency, %	96.4	96.3	96.3	95.5	98.94	98.96	99.02	98.86
Mean composition of flue gas v/v.								
O_2, %	3.89	4.07	4.21	4.88	7.37	6.39	6.79	6.95
CO_2, %	14.19	13.98	14.32	13.27	11.14	12.00	11.72	11.56
CO, ppm	2801	2871	2506	2614	1178	1243	1122	1306
NO_x, ppm	2900	3200	2500	2700	1000	1174	1487	1608
Flowrate and concentration of ash								
Fly ash, g/h	10.10	10.74	14.57	10.84	4.8	5.93	8.55	8.03
Carbon in Fly ash, g/h	0.019	0.03	0.168	0.146	0.006	0.007	0.01	0.01
Fly Ash concentration, mg/Nm^3	17451	18519	25123	18686	8266	10220	14742	13845
Bottom ash, g/h	17.3	17.0	10.7	13.4	23.1	19.3	21.1	22.6

Results from the experimental campaign suggest that the mean PFAS abatement efficiency was from 99.95 to 99.97%. The analysis conducted on the flue gas revealed the presence of only PFBS with a concentration of 10.6-37.2 ng/Nm^3 when the O_2 excess was lower (tests N°1 to N°4), while both PFOS and PFTeDA were detected with a mean concentration of 4.0 and 6.5 ng/Nm^3 during the other tests. In summary, in the exhaust gases only 3 out of 5 compounds were not eliminated by the incineration process in the fluidized bed combustor but the concentration was reduced by 6 orders of magnitude compared to the initial one. As for the residual ash from the combustion process, PFAS concentrations ranged from 200-600 ng/kg in the bottom ashes to 3000-24000 ng/kg in the fly ashes.

Conclusions

Incineration of municipal sludge samples spiked with a known amount of 5 different PFAS compounds was performed using a fluidized bubbling bed combustor operated at 850°C. The experimental campaign aimed to assess the efficacy of the combustion process for the abatement of persistent PFAS compounds. Some preliminary results showed that the mean PFAS destruction in the incineration process was always greater than 99.9%. Only PFBS, PFOS ad PFTeDA were detected in the flue gas with a concentration of 4-10 ng/Nm^3, while a PFAS concentration in the order of 200 – 24000 ng/kg was detected in the residual ashes.

References

[1] Zhou, T., Li, X., Liu, H., Dong, S., Zhang, Z., Wang, Z., Li, J., Nghiem, L.D., Khan, S.J., Wang, Q., "Occurrence, fate, and remediation for per-and polyfluoroalkyl substances (PFAS) in sewage sludge: A comprehensive review", *J. Hazard. Mater.* 466: 133637 (2024).

[2] Lenka, S. P., Kah, M., & Padhye, L. P., "A review of the occurrence, transformation, and removal of poly-and perfluoroalkyl substances (PFAS) in wastewater treatment plants", *Water res.* 199: 117187 (2021).

[3] Garg, A., Shetti, N. P., Basu, S., Nadagouda, M. N., Aminabhavi, T. M., "Treatment technologies for removal of per-and polyfluoroalkyl substances (PFAS) in biosolids", *Chem. Eng. J.*, *453*: 139964 (2023).

[4] Cammarota, A., Cammarota, F., Chirone, R., Ruoppolo, G., Solimene, R. & Urciuolo, M., "Fluidized Bed Combustion of Pelletized Sewage Sludge in a Pilot Scale Reactor", *Combustion Science and Technology*, 191:9, 1661-1676, (2019) DOI: 10.1080/00102202.2019.1605363

An experimental study on the catalytic cracking of tar: the effect of gas residence time

V. Arconati*, C. Boccia*, F. Parrillo*, F. Ardolino*, G. Ruoppolo, U. Arena***

vincenzo.arconati@unicampania.it

*Department of Environmental, Biological, Pharmaceutical Sciences and Technologies – University of Campania "Luigi Vanvitelli", Via Vivaldi 43-81100, Caserta, Italy

**Institute of Sciences and Technologies for Sustainable Energy and Mobility, National Research Council-CNR. P.le Tecchio 1, 80125, Naples, Italy

Abstract

Gasification is the thermochemical conversion of a carbonaceous solid or liquid material into a synthesis gas (syngas), composed by H_2, CO, CO_2, CH_4, and lower amounts of light hydrocarbons, together with different organic and inorganic impurities and particulates. These contaminants must be removed to allow syngas utilization in different high-added value applications, such as high efficiency electric energy generation, production of fuels, and synthesis of building block chemicals [1]. Among the different syngas contaminants, tars are probably the main compounds to deal with. Tar is a mixture of several heavy hydrocarbons having a high dew point, which leads to operational and environmental problems, including clogs and corrosion of pipelines and auxiliary devices, catalyst damage, smelly gas release, and production of industrial wastewater. Tar catalytic cracking is a promising technology for hot syngas clean-up processes, allowing to convert tars and preserve their chemical energy, thereby increasing syngas heating value.

Metal-supported catalysts are recognized as efficient catalysts in these processes [2]. Most of the available studies investigated the effects of temperature and tar concentration on the catalyst performance and on the deactivation mechanisms. This study investigated the effect of the gas residence time (varied from 0.055 s to 0.11 s and 0.165 s) by using an iron-supported catalyst (Fe/γ-Al_2O_3) under different steam concentrations (0% and 7.5%), keeping constant the temperature at 750 °C and 800 °C, and using naphthalene as a tar model. The results were used to identify the optimal operating conditions and to provide data useful for the design of a novel tar cracking reactor.

Materials and methods

Tar model compound and catalyst preparation. Naphthalene ($C_{10}H_8$) was selected as tar model compound since it is the main and most stable tar compound found in tar mixtures produced from waste and biomass gasification processes [1]. The active phase was pure iron, supported on γ-alumina (γ-Al_2O_3) spheres, having a diameter of 1 mm, a specific surface area of 150-170 m^2/g, and pore volume of 0.45 cm^3/g [3].

The catalyst, named Fe/γ-Al_2O_3 (3% wt), was prepared by wet impregnation dissolving $Fe(NO_3)_3 \cdot 9H_2O$ (98+%, Sigma-Aldrich®) in water and adding a suitable amount of γ-Al_2O_3. The catalyst was dried at 120 °C for 12 hours and then calcined with air at 850 °C. The complete characterization of the support and fresh catalyst is shown in Table 1.

Table 1. Physical properties and inorganic composition of the fresh catalyst Fe/γ-Al_2O_3 and its support γ-Al_2O_3.

Physical properties		
	γ-Al_2O_3	**Fe/γ-Al_2O_3**
Surface Area (m^2/g)	150-170	147
Pore Volume (cm^3/g)	0.45	0.47
ICP-MS analysis (mg/kg)		
Mn	15	-
Fe	217	30000
Cu	118	-

Experimental setup and procedures. The experimental tests were carried out in a bench-scale tubular quartz reactor with an internal diameter of 14 mm and a total height of 600 mm (Figure 1).

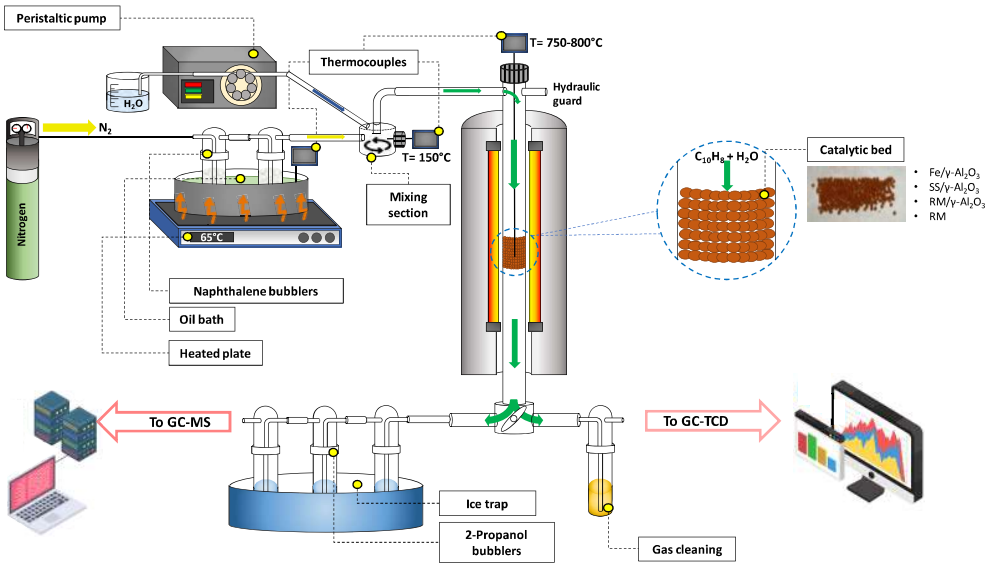

Figure 1. Schematic representation of the experimental apparatus.

Nitrogen was used as carrier gas and fed to two bubblers, each containing 20 g of naphthalene crystals, kept in an oil bath at 65 °C to allow the vaporization of a fixed amount of naphthalene. Water was fed by a peristaltic pump (Ismatec Regloo Digital 2-Channel®) and evaporated in a 15 cm pipe kept at 150 °C, before being mixed with nitrogen and naphthalene in a mixing section. All the lines were kept at 150 °C to

avoid the condensation of steam and naphthalene. After the system reached the steady state, the gases were sent to the reactor heated to the desired temperature and containing the catalytic bed. The product gases (such as H_2, CO, CO_2, N_2, CH_4) were cleaned by water and naphthalene in an oil bubbler and then analyzed by a gas chromatograph equipped with a thermal conductivity detector (GC-TCD, Agilent 3000a Micro GC®) every 3 minutes. The residual naphthalene was collected by a sampling section consisting of three bubblers with 2-propanol at 0 °C, and then analyzed by a gas chromatograph coupled to a mass spectrometer (GC-MS, Agilent HP6890/HP5975®). The first sample was collected 5 min after the start to assess the initial conversion efficiency, while the following samples were collected every 30 min for the first two hours of testing, and then every hour until the end of the tests. Finally, the reactor was purged with nitrogen and cooled down to room temperature. The operating conditions used in the experimental tests were based on the typical values found at the exit of a biomass/waste gasifier [4]. Naphthalene concentration was 22.5 mg/L_N, and its conversion was tested in the absence and presence of 7.5% of steam, at 750 °C and 800 °C. The mass of catalyst was varied from 3.9 g to 2.6 g and 1.3 g to change the gas residence time from 0.165 s to 0.11 s and 0.055 s, respectively.

Results and discussion

Time evolution of hydrogen. Figure 2 shows the H_2 production as measured during tests carried out at 750 °C and 800°C, without and with steam, for the different residence times.

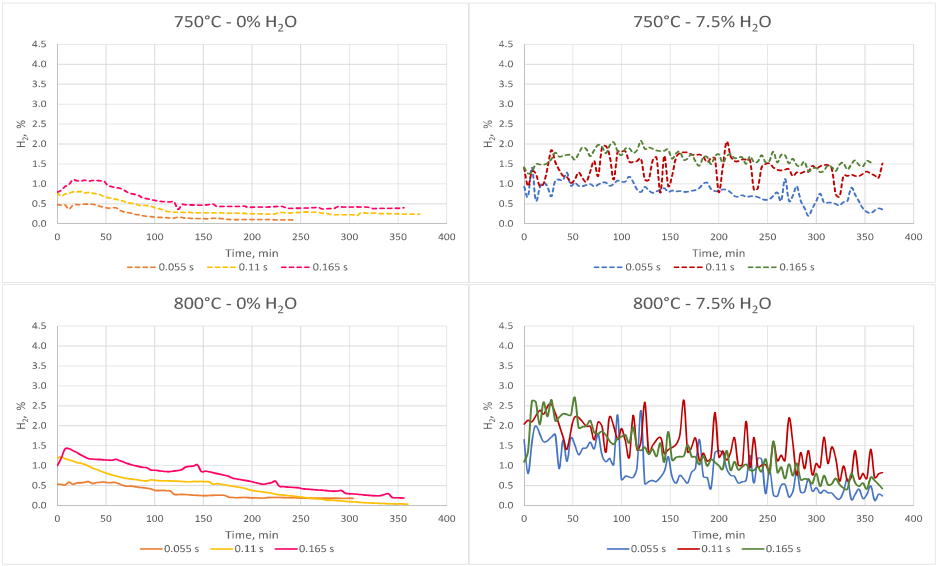

Figure 2. Time evolution of H_2 under the different operating conditions tested.

Without steam, the increase of the residence time led to slightly higher hydrogen concentrations at both temperatures, which can be related to the longer time of contact that naphthalene has with the active sites on the catalyst surface [5]. In the tests with steam, at 750°C, the positive effect of longer residence times on the

hydrogen concentration was confirmed, whereas at 800 °C, the decrease of hydrogen due to catalyst deactivation by coke deposition appeared more pronounced for the longer residence times.

Naphthalene conversion efficiency. The naphthalene conversion efficiency was calculated by means of the equation 1:

$$X_{C_{10}H_8} = \frac{[C_{10}H_8]_{IN} - [C_{10}H_8]_{OUT}}{[C_{10}H_8]_{IN}} \quad (1)$$

Figure 3 shows its values at different temperatures and residence times, without and with steam. At both temperatures tested, the steam improved the tar cracking process, due to the expected (and remarkable) role of the water-gas and steam reforming reactions. The conversion efficiency, like the hydrogen production, increased with the residence time due to the longer contact time between naphthalene and catalyst [6].

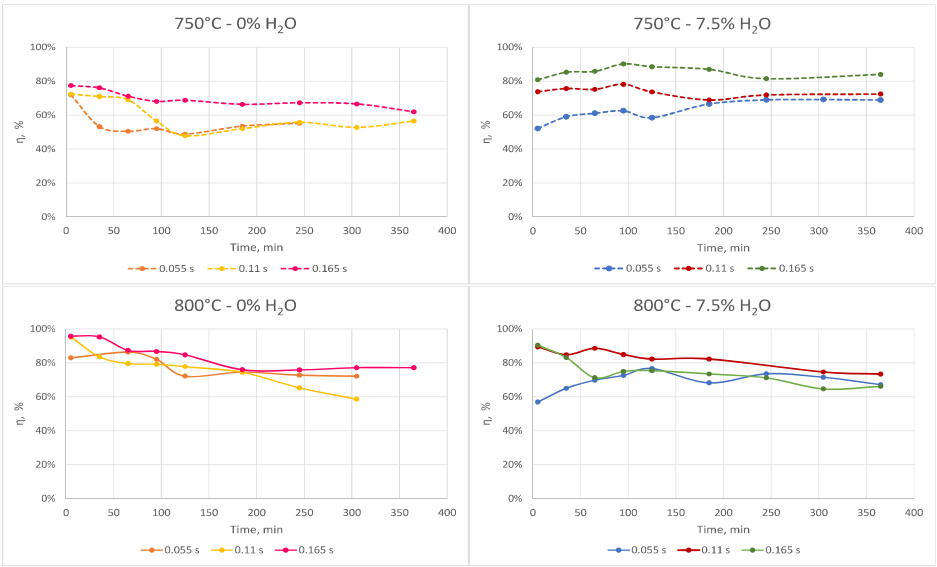

Figure 3. Naphthalene conversion efficiencies under the different operating conditions tested.

At 750 °C without steam, after the first 90 min, the conversion efficiencies at 0.055 s and 0.11 s had similar values of around 50% until the end of the test, due to coke deposition. Efficiencies were higher with a residence time of 0.165 s. Tests without steam and at higher temperature show still higher conversion efficiencies.
The presence of steam allowed for high values of efficiencies the whole duration of the tests, since the coke deposited on the catalyst surface was partially converted by water-gas and steam reforming reactions. As observed in the hydrogen trends, the effect of the residence time was less pronounced when the temperature is increased to 800 °C.

Mass variation of catalyst. The mass of catalyst was measured at the beginning (m_{in}) and end of each test (m_{out}). Equation 2 was used to calculate its variation in a time-specific unit, allowing for comparison of tests with different durations:

$$\Delta_{wt}\,, mg/min = \frac{m_{out} - m_{in}}{t_{tot}} \quad (2)$$

Figure 4 shows the mass variation under the different operating conditions tested. The lowest mass variation was observed at the residence time of 0.055 s, for both the steam concentration. The reduced contact time leads to a lower coke formation on the catalyst surface, confirming the results observed above. The larger mass variations in the test with longer residence time were only partially compensated by the steam presence that activates water-gas and steam reforming reactions.

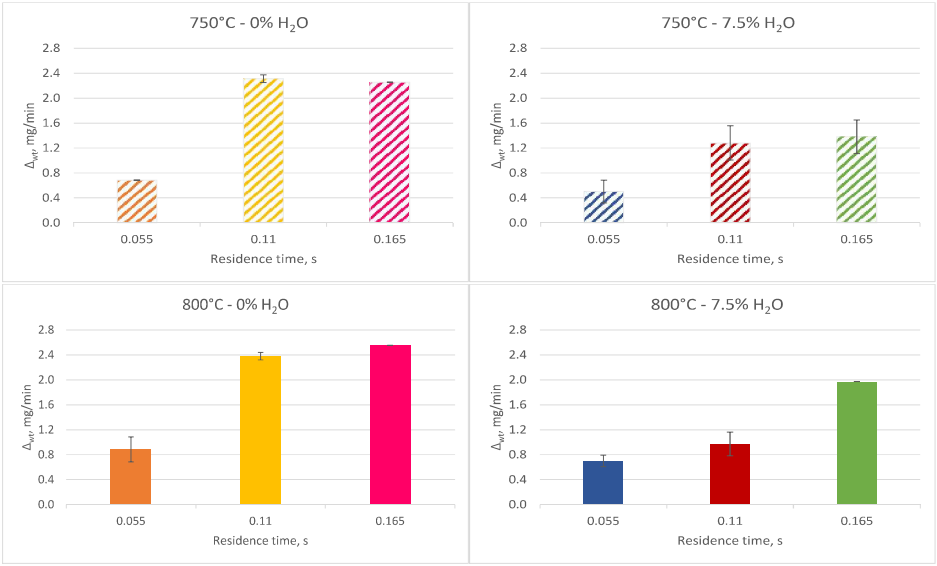

Figure 4. Time specific mass variation of the catalysts at the different operating condition tested.

Conclusions

Fe/γ-Al_2O_3 catalyst was tested using naphthalene as a tar model at a temperature of 750 °C and 800 °C, by varying the steam concentrations (0% and 7.5%) and residence times (0.055 s, 0.11 s, 0.165 s). The results show an increase of hydrogen evolution, naphthalene conversion efficiency, and catalyst mass variation with residence time, suggesting a general process improvement**.** This effect is less pronounced at the highest operating condition of 800 °C and 7.5% of steam, where the hydrogen yield and naphthalene conversion appear rather similar to the values obtained at the shorter residence time.

These results could be useful to implement a kinetic study of the reactions involved in the cracking process and to provide data for the design of a tar cracking reactor.

References

[1] Boccia, C., Parrillo, F., Ruoppolo, G., Commodo, M., Berruti, F., Arena, U., "The effect of steam concentration on hot syngas cleaning by activated carbons", *Fuel Processing Technology* 224:107033 (2021)

[2] Guan, G., Kaewpanha, M., Hao, X., Abudula, A., "Catalytic steam reforming of biomass tar: Prospects and challenges", *Renewable and Sustainable Energy Reviews*, 58:450-461 (2016)

[3] Miccio, F., Picarelli, A., Ruoppolo, G., "Increasing tar and hydrocarbons conversion by catalysis in bubbling fluidized bed gasifiers", *Fuel Processing Technology*.141:31-37 (2016)

[4] Arena, U., Fluidized bed gasification, Chap. 17 in *Fluidized Bed Technologies for Near-Zero Emission Combustion and Gasification*, Fabrizio Scala, 2013, p. 765

[5] Morgalla, M., Lin, L., Strand, M., "Decomposition of benzene using char aerosol particles dispersed in a high-temperature filter", *Energy* 118 :1345-1352 (2017)

[6] Zhurka, M.D., McCue, A.J., Kechagiopoulos, P.N., "Reaction pathways of phenol steam reforming over Rh and Ni-Co based catalysts supported on γ-Al_2O_3", *Fuel*. 364: 131102 (2024).

ACCURATE MODELLING OF NO_X EMISSION IN A COKE-OVEN-BATTERY WITH VALIDATION AGAINST TEST DATA

G. Rossiello*, T. Vela*, A. Vicentini **, D. Ettorre*,
S.B. Ahmadpanah*, and M. Torresi***.**
corresponding author gianluca.rossiello@seamthesis.com
* SEAMTHESIS Srl, Via IV Novembre, 156 – 29122 Piacenza, ITALY
** PAUL WURTH Italia SpA (SMS group), Via Balleydier 7 – 16149 Genova, ITALY
*** DMMM, Department of Mechanics, Mathematics and Management, Polytechnic University of Bari, Via Re David, 200 – 70125 Bari, ITALY

Abstract
In the present work, CFD simulations are used to provide an overview of a heating flue combustion chamber, a typical unit of a coke oven battery, that uses coke oven gas as fuel, with a focus on the production of NO_x, which is, along with carbon monoxide, the main source of pollution that must be minimized at the design stage and controlled during operation. In contrast to the most common approaches available in the literature, the proposed method is based on a detailed chemical reaction mechanism, with 24 species and 134 reactions, derived by reduction from the C1-C3 Polymers, and capable of accurately estimating the concentrations and distributions of radical and intermediate species, involved in NO_x formation by thermal and reaction mechanisms, and "destruction" by reburn phenomenon. The production of oxides of nitrogen pollutants is simulated by thermal and reaction mechanisms, also taking into account the reburn of NO_x. In this work, it is shown that the reburn mechanism is essential to correctly assess emission levels under the operating conditions of the heater combustion chamber. Numerical results were also validated through comparison with flue gas outlet temperature and NO_x emission at the furnace outlet.
The numerical results are shown and shed light on the peculiar characteristics of combustion in the heating stack. Finally, the content of NO_2 pollutants in the dry flues obtained from the numerical simulation is compared with the experimental data, showing almost perfect agreement. As a further result, modeling with and without reburn effect of NO is compared, showing its extreme significance.

Context and motivation
The ongoing energy transition is particularly challenging in sectors [1], such as the steel industry, where a combination of fuel flexibility, use of innovative processes, thermal efficiency, and increasingly restrictive emission limits, with a focus on nitrogen oxides (NO_x), are required. In this context, and particularly in the steel industry, advanced and validated design tools are needed to meet market needs by

optimizing processes and designing new plants, ensuring high efficiency and, at the same time, reduced emissions, under a wider range of operating conditions. In this framework, CFD (Computational Fluid Dynamics) is an extremely useful tool both for the analysis and design of individual equipment and for the optimization of the entire process.
In the specific case of coke oven batteries, the simulation of flow and combustion within the combustion chamber involves several relevant physical phenomena, which the modeling must take into account, mainly turbulence, heat exchange by conduction, convection and radiation, the chemical reaction between fuel and oxidant, and NO_x production. Therefore, validation of such complex models through comparison against experimental data coming from on-site measurements is particularly valuable for researchers and designers, and in the present study it was done by taking advantage of Paul Wurth's integrated work covering the entire process from design to commissioning and testing of the entire plant and the coke oven-battery in particular.
The key topics of this work are, therefore, the analysis of CFD fluid dynamic simulations, carried out on a combustion chamber, a typical unit of a coke oven battery, and the comparison of the results with experimental data from plant testing. The study aims at describing and providing advanced modeling validated with process data for the simulation combustion of a coke oven battery chamber which is able to accurately estimate NO_x emissions, which represent a pollutant extremely noxious both for human health and for the environment, frequently undergoing severe regulations which often require costly flues post-treatments to be met.

Problem description

In general, coke oven battery is an equipment to produce processed coke from the distillation of coal, made by a series of alternating heating flues and coking chambers, placed in rows to maximize the heat transfer rate.
The considered geometrical model consists of one “unit”, including one heating chamber, two heating wall portions and a chamotte refractory portion (Figure 1). Each individual chamber is divided into: an upward heating flue, where air and fuel are supplied and combustion occurs, and a downward heating flue, from which flue gases exit. Combustion air is divided into primary air in the base duct and secondary air at the lower and upper levels. To improve the combustion process by internal FGR (Flue Gas Recirculation) [2] two windows are symmetrically located at the lower level and act as recirculation ports (Figure 1).

Numerical modelling

CFD analyses are conducted with the Ansys Fluent-v17.2 [3]. The computational fluid and solid domains are discretized by a polyhedral mesh of about 3 million elements, obtained by a multi-block approach, generating smaller cells close to complex geometries, such as staging ports and COG inlet to correctly capture flows and combustion details.

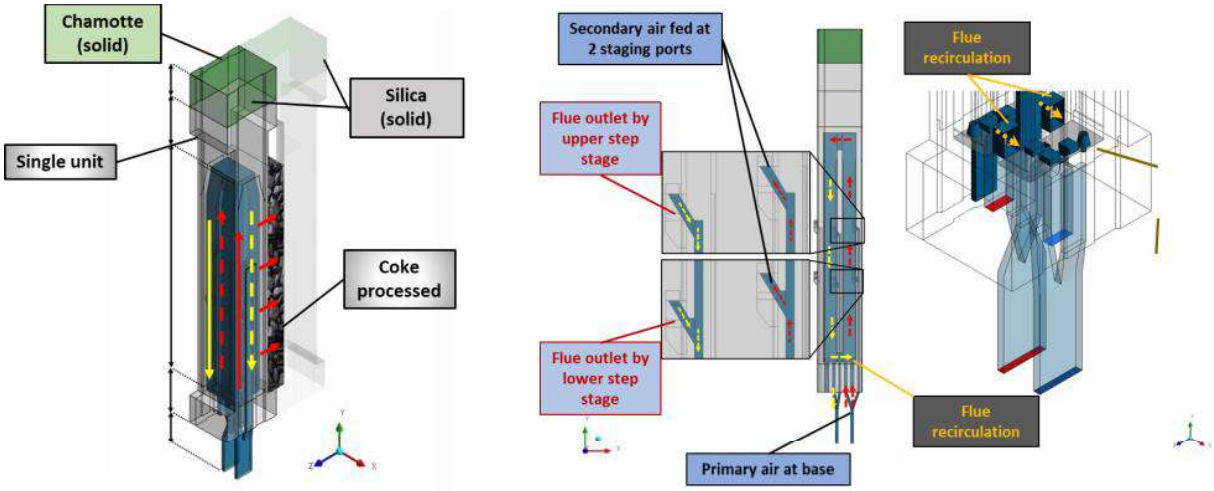

Figure 1. Heating flue chamber: isometric view (left), side view (middle) and isometric view of basement detail (right).

Numerical modeling is based on a stationary RANS (Reynolds Averaged Navier-Stokes equations) approach, in particular, the two-equation k-ε model with standard wall functions at solid boundaries are used for turbulent flow. The equation of state follows an ideal gas approach, with density depending on both temperature and absolute pressure. Combustion in coke ovens is controlled by two phenomena that occur in series: mixing of the reagents and then the chemical oxidation reactions. It is therefore the combination of fluid dynamics (mixing) and chemistry that determines the structure of the flame (extension and maximum temperature) and the level of NO_x emissions. The turbulent-chemistry interaction is modelled using the most advanced eddy dissipation concept (EDC) [4], with in situ adaptive tabulation (ISAT) model [5] to improve computational efficiency.

The need to have a direct and accurate prediction of NO_x and CO, which exploits the species and intermediates calculated in the combustion simulation, and the use of gaseous fuels derived from the steel process, such as coke oven gas (COG), has required the use of a more detailed kinetic scheme. The detailed mechanism chosen is the Polimi-23, which is a reduction of the complete C1-C3 scheme of the Politecnico di Milano for hydrocarbon combustion, with 23 species and 134 reactions. The addition of a 24th species, the intermediate CH, is necessary to "activate" the NO_x reburn mechanism, which is crucial for emission prediction, as shown in the results part.

Pollutant emissions are calculated by a post-processing method, which takes into account three mechanisms: the first is the Zeldovich mechanism, which involves the formation of thermal NO_x, and a second contribution from prompt effect. Fuel NO_x can be neglected, given the low content of nitrogen compounds in the fuel. Finally, the reburn mechanism is included, which is of paramount importance for accurate emission estimation in this case. Local turbulent fluctuations, which greatly affect NO_x production rates, are considered with a tabulated pdf approach based on temperature and species fluctuations.

To account for radiation within the gas and between the gas and the walls a Discrete Ordinates method (DO) is used, with absorption coefficients calculation based on WSGGM (Weighted Sum of Grey Gases Model) algorithm, in which a mean optical path is computed on the whole fluid domain. Finally heat conduction in solid is treated solving the Laplace equation with specific thermal conductivity for different materials.

Results

The experimental data from the plant are shown in Table 1 in the third line and are used to set up the CFD simulation and to carry out the comparison of the numerical simulation results with the experimental texts and validation of the model. In the composition used for the simulation because butane C_4H_{10} is not available among the species in the kinetic scheme used, it is replaced by the same amount (by mass) of ethane C_2H_6, as in the fourth line. The fuel flow rate for the individual chamber is estimated from the total measured fuel flow rate, while the air mass flow rate is calculated from the design value of the outlet oxygen content. The heat transfer coefficient between the wall and the coke is adjusted by matching the CFD brick temperature value to the experimental value. Finally, the concentration of nitrogen dioxide measured in the outlet flues is used as a verification and validation parameter for the model (
Table 2).

Table 1. Fuel composition, computed, and for CFD setup.

	CH_4	CO_2	CO	H_2O	H_2	C_2H_6	C_4H_{10}	N_2
Units	%	%	%	%	%	%	%	%
Exp. data	34.43	6.39	15.52	6.86	10.06	--	4.82	21.92
CFD set-up	34.43	6.39	15.52	6.86	10.06	4.82	--	21.92

Table 2. Process data by test/measurements, computed, and from CFD results

	Exp. data	CFD set-up
COG Inlet temperature	550 [°C]	550 [°C]
COG Flow rate	All chambers = 17'545 [Nm^3/h]	Single chamber = 19.56 [Nm^3/h]
AIR Inlet temperature	1200 [°C]	1200 [°C]
Outlet O_2	4.77÷5.18% [%vol. Dry basis]	Design: 4.95 [%vol. Dry basis]
NO_2	395 [mg/Nm^3] @ 5% O_2 dry out	394 [mg/Nm^3] @ 5% O_2 dry out
Outlet temperature	1274* [°C]	1274* [°C] (*tuned*)

Simulation results show a temperature field characterized by a high-temperature flame zone located at COG / air jets interface, with a peak above 1800°C, where the

highest concentrations of NO occur. A relevant concentration of hydrocarbon radical/intermediates CH_x is produced in the rich flame zone, which are involved in the reburn NO depletion mechanism (Figure 3).

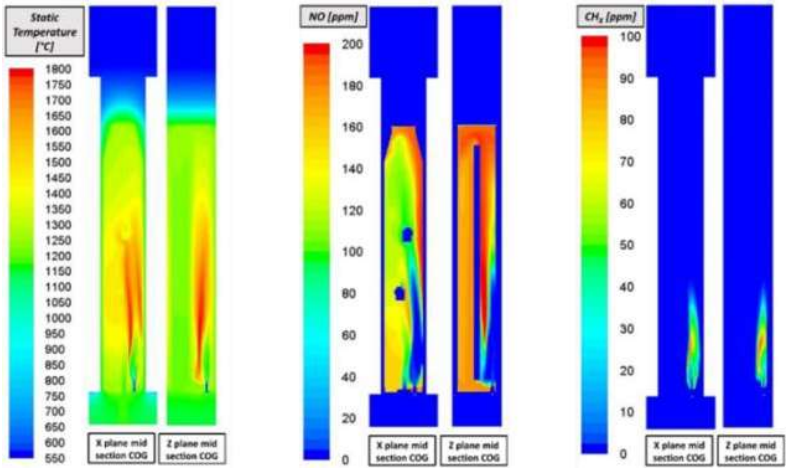

Figure 2. CFD results: contours of main fields on two planes cutting COG inlet.

As shown in Figure 3, the rates of thermal and prompt NO formation, and the rate of depletion due to reburning have the same order of magnitude, clearly explaining the relevant effect of reburn and why it cannot be neglected when simulating coke-oven-batteries. The thermal formation term is high in the fuel-air mixing zone where high gas temperature is combined with oxygen availability. On the other hand, the reburn NO depletion rate is high (in absolute value) where two conditions are met: NO and CHx intermediates are available, and temperature is above 1600 [K].

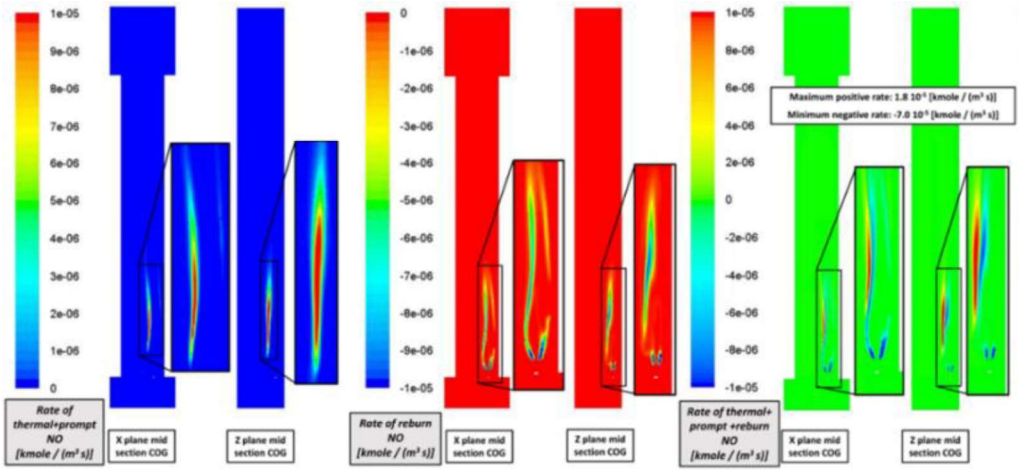

Figure 3. Rates of NO production/deplation: thermal+prompt (left), reburn (middle) mechanisms and thermal+prompt+reburn (right).

The validation of the CFD overall modelling and simulation approach is obtained comparing CFD NO_x emission estimation (394 mg/Nm^3) against the experimental data (395 mg/Nm^3), which shows almost perfect agreement (Table 1).Without the

NO reburn mechanism, a completely wrong value is obtained: 979 mg/Nm^3 versus 395 mg/Nm^3 of the tests, as shown in Figure 4.

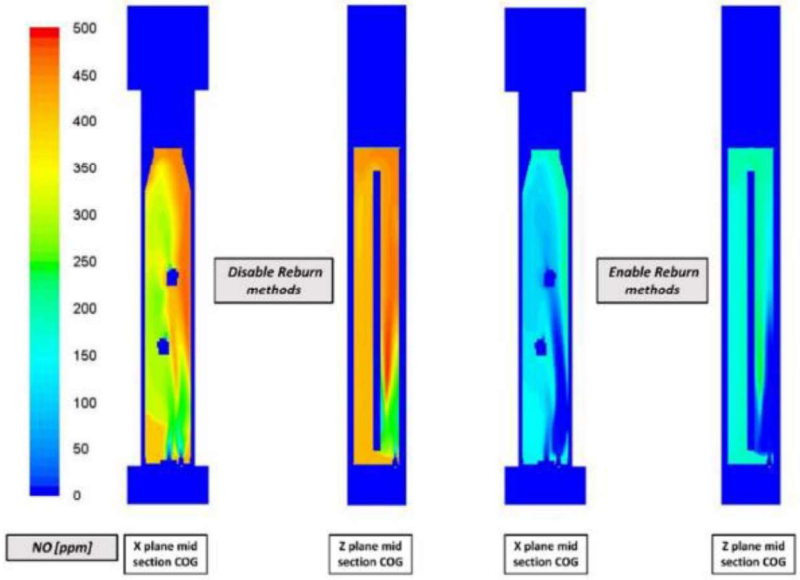

Figure 4. NO content with (right) and without (left) reburn mechanism**.**

Conclusion

In this paper, a comprehensive procedure for CFD modelling of coke oven battery combustion, with emphasis on NO_x emission calculation, is proposed to be an effective tool for design and optimization. The model is based on a detailed combustion mechanism and NO_x post-processing calculation, including thermal mechanism, thrust mechanism and rebound mechanism, based on the species fields (CH_x) calculated in the combustion simulation. The modelling approach was validated by comparing CFD results with experimental data from plant tests, demonstrating excellent agreement and the fundamental importance of the reburn reduction mechanism. The model needs no further tuning to be used for optimization of the heating combustion chamber design.

References

[1] WEO-2021 World Energy Outlook, International Energy Agency, Paris, France, 2021.

[2] Stanislaw Gamrat, Jakub Poraj, Jakub Bodys, Jacek Smolka, Wojciech Adamczyk. Influence of external flue gas recirculation on gas combustion in a coke oven heating system, Fuel Processing Technology, Volume 152, 2016, Pages 430-437.

[3] ANSYS Fluent, Users and Theory Guide, ANSYS, Inc., v.17.2, 2017.

[4] Gran IR, Magnussen BF. A Numerical Study of a Bluff-Body Stabilized Diffusion Flame. Part 1. Influence of Turbulence Modeling and Boundary Conditions.Combust Sci Technol 1996.

[5] S.B. Pope (1997) Computationally efficient implementation of combustion chemistry using in situ adaptive tabulation, Combustion Theory and Modelling, 1:1, 41-63, DOI: 10.1080/713665229.


THE COMBUSTION INSTITUTE
1954

WORK IN PROGRESS POSTERS


THE COMBUSTION INSTITUTE
1954

EXPERIMENTAL INVESTIGATION OF THE EFFECT OF S/V RATIO IN TUBULAR QUARTZ REACTORS ON THERMAL METHANE CRACKING

Gaia Lo Conte, Emmanuel Busillo, Maria Paola Bracciale, Paolo De Filippis, Benedetta de Caprariis
gaia.loconte@uniroma1.it
Department of Chemical Engineering Materials Environment, Sapienza University of Rome

Abstract
Experimental tests of non-catalytic thermal methane cracking have been conducted at different temperatures (950, 975 and 1000°C) and with different initial methane flow rates (25, 50 and 100 ml/min) in tubular quartz reactors (i.d.=1-1,5 cm). Tests have been carried out using empty and packed bed reactors with constant heated length (L=20 cm) to investigate the influence of the surface-to-volume ratio (S/V) on methane conversion, carbon products morphology and their relative contributions to the overall carbon balance. A comparison between the two cases has been made to highlight the effects of S/V ratio on surface reactions with respect to the homogeneous ones for the carbon formation. Higher conversions and increased deposited carbon production have been obtained at the highest temperatures tested and in the presence of packed beds (highest S/V). Carbon deposited on the surfaces has resulted to be a dense carbon matrix, morphologically different from carbon nanoparticles produced in the gas phase. Further studies are required in order to accurately investigate the properties of the carbons produced and pave the way to tune desired carbon properties, allowing, in the future, the coupling of sustainable turquoise hydrogen generation with the production of high added value materials.

A PRELIMINARY STUDY ON THE ORIGIN OF OXYGEN BONDED IN SOOT PARTICLES IN ETHANOL/ETHYLENE PREMIXED FLAME

C. Russo*, V. Esposito*, **, A. Tregrossi*, B. Apicella*, M. Sirignano**
vincenzo.esposito9@unina.it
*Istituto di Scienze e Tecnologie per l'Energia e la Mobilità Sostenibili – CNR – P. le V. Tecchio, 80 – 80125 Napoli, Italy
**Università degli Studi di Napoli Federico II – Dipartimento di Ingegneria Chimica, dei Materiali e della Produzione Industriale – P. le V. Tecchio, 80 – 80125 Napoli, Italy

Abstract
The objective of this study is to elucidate the source of oxygen incorporation into soot particles generated during ethanol combustion. The composition of carbon particulate matter (PM) and flame structure were investigated in fuel-rich premixed flames of ethylene and ethylene blended with ethanol (20% of total carbon fed) at atmospheric pressure. Analysis of the composition of gaseous species, conducted through probe sampling and gas chromatographic techniques, revealed that ethanol had a minor influence on the production of carbon monoxide (CO) and carbon dioxide (CO_2), while also delaying the formation of hydrocarbons. Carbon particulate matter (PM) and its fractions were subjected to laser desorption ionization-time of flight mass spectrometry (LDI-TOFMS) analysis to investigate the origin of oxygen integration: a fraction encompassing species smaller than 20 nm to isolate organic carbon and primary particles; a fraction soluble in dichloromethane; and a fraction soluble in acetonitrile, aimed at isolating organic carbon and its lighter fraction enriched in polycyclic aromatic hydrocarbons (PAHs), respectively. Fourier-transform mass spectrometry (FFT) analysis revealed mass discrepancies indicative of oxygen presence in ethanol-derived samples, particularly in the total particulate matter and small particle fractions, with negligible oxygen content in the soluble fractions. This finding challenges the traditional assumption regarding the role of oxy-PAHs in particle oxygenation. Consequently, attention was redirected toward small hydrocarbons such as aldehydes, with acetaldehyde emerging as a potential candidate for oxygen incorporation into particles. Acetaldehyde was found to be more prevalent in ethanol flames, supporting this hypothesis. Strategies aimed at reducing the formation of specific aldehydes, like acetaldehyde, could provide insights for mitigating particle oxygen content levels and their effects on human health.

A DNS STUDY OF TURBULENT PREMIXED AMMONIA-AIR FLAMES

R. Intranuovo*, F.G. Schiavone*, D. Laera*
raffaele.intranuovo@poliba.it
* DMMM, Polytechnic University of Bari, Bari, Italy

Abstract
In the current energy transition process, *ammonia* (NH_3) is gaining momentum as a fuel for carbon-free combustion, owing to properties such as high bulk energy density, relatively simple storage if compared with pure hydrogen (H_2), and a global developed economy. Still, given its toxic and corrosive nature, and its unfavorable combustion properties, research is needed to make it a feasible solution [1]. As part of the PRIN PNRR 2022 *"Reactant"* Project, the present work proposes a numerical study to characterize the combustion properties of perfectly premixed NH_3 (pure or doped with H_2) flames when submitted to Homogeneous Isotropic Turbulence (HIT). First, few recent detailed reaction mechanisms [2-3] are compared with an experimental dataset to select the most suitable scheme to predict NH_3/air laminar combustion properties, i.e., laminar flame speed (Fig. 1) and adiabatic flame temperature. Then, an Analytically Reduced Chemistry (ARC) version of the selected mechanism is used in the high-fidelity CFD code AVBP (https://www.cerfacs.fr/avbp7x/) to perform Direct Numerical Simulations (DNS) of a turbulent 3D stochiometric flat ammonia flame, a canonical configuration commonly adopted in the literature [4]. Preliminary results (Fig. 1) show hydrogen preferential diffusion on positively wrinkled regions, impacting local equivalence ratio, Heat Release Rate (HRR) and NO_x concentration. Multiple turbulence levels ranging from low to high Karlovitz numbers will be investigated in the future.

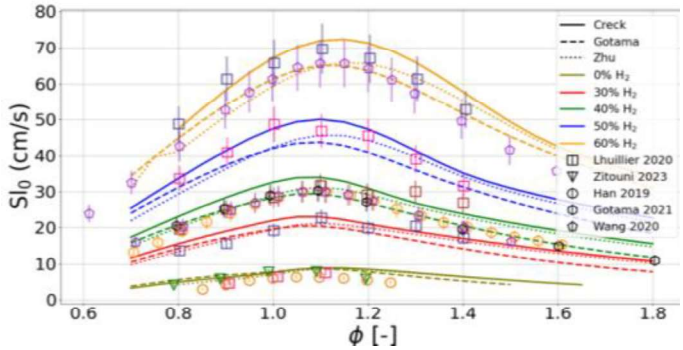

Figure 1. Flame speed for different schemes and comparison with experiments.

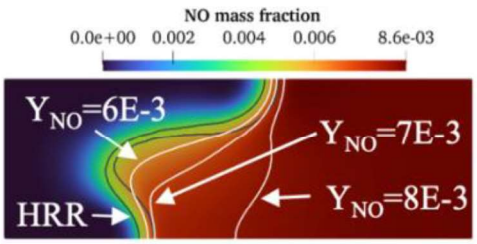

Figure 2. NO mass fraction for (70%NH_3+30%H_2)/air flame at $\phi = 1$ (HRR = 1.9 GW/m^3).

Acknowledgements
This research was funded by the National Recovery and Resilience Plan (NRRP), Mission 4, Component 2, Investment 1.1, Call for tender No. 1409 published on 14.9.2022 by the Italian Ministry of University and Research (MUR), funded by the European Union – NextGenerationEU D53D23018150001, Grant Assignment Decree No. 1385 adopted on 01/09/2023 by the MUR.

References
[1] A. Valera-Medina et al., Energy & Fuels 35.9 (2021) 6964-7029.
[2] Y. Zhu et al., Combustion and Flame 260 (2024) 113239.
[3] T. Cai et al., Chemical Engineering Journal 458 (2023) 141391.
[4] C. Netzer et al., Combustion and Flame 232 (2021) 111520.

Multi-Fidelity Numerical Simulations of a Swirled Turbulent Spray Flame: Impact of Chemical Reaction Modelling

Matteo Blandino*, Jacopo Liberatori*, Davide Cavalieri*, Mauro Valorani*, Pietro Paolo Ciottoli*
matteo.blandino@uniroma1.it
*Sapienza, Università di Roma, Rome, Italy, 00184

Abstract
Aviation, before COVID-19, was responsible for 2.5 - 4% of the total CO_2 emissions and recent projections report that the demand for air transport is expected to double by 2040 [1]. In this scenario, Sustainable Aviation Fuels (SAFs) represent the solution in the near-term, since their adoption does not require any modification of existing propulsive systems. Therefore, numerous experimental campaigns based on the SAF surrogates defined by the National Jet Fuels Combustion Program (NJFCP) have been conducted, offering a basis for evaluating the physical and chemical properties of SAFs [2]. Experimental investigations carried out with laboratory-scale burners with jet-engine combustors-like conditions and spray injectors are essential to understanding the flame dynamics and the interaction between the liquid droplets, the turbulent flow field, and combustion phenomena. Aiming at the same purpose, Computational Fluid Dynamics (CFD) can be employed to analyze the wide range of alternative fuels, exploiting the reduced time requirements and versatility with respect to experimental testing. The authors present a comprehensive analysis of the effects of the chemical reaction modelling on the n-heptane spray flame of the Cambridge burner [3]. Firstly, adopting an Eulerian-Lagrangian numerical framework, both the URANS and LES model are compared to the experimental data. Thus, the efficacy of the well-established Flamelet-Generated Manifold (FGM) model is examined. To take into account the droplet evaporation phenomenon and its coupling with the gaseous phase, non-adiabatic flamelets are employed in the tabulation process. Results revealed an optimal alignment with experimental data regarding flame topology for both the URANS and LES models. Finally, a finite-rate chemistry approach is investigated. The computational expense associated with using the same chemical mechanism used for flamelet tabulation would be excessive. Hence, a mechanism reduction driven by Computational Singular Perturbation (CSP) is proposed. This reduction specifically focuses on the Low-Temperature Chemistry (LTC) pathway, which is indicative of the spray-flame interaction, as well as multi-regime combustion in the lab-scale burner under consideration. Research on numerical simulations with finite-rate chemistry is currently underway.

[1] IATA, “Global outlook for air transport: highly resilient, less robust”, 2024
[2] Edwards, J., “Reference jet fuels for combustion testing”, AIAA, 2017.
[3] Yuan R., Kariuki J., Mastorakos E. , “Measurements in swirling spray flames at blow-off”, Int. J. of Spray and Comb. Dyn. 10.3, 2018.

BIOHYDROGEN PRODUCTION VIA STEAM REFORMING OF PYROLYSIS BIO-OIL

E. Mulu Fetene*, M. Troiano*, R. Solimene, P. Salatino***
elshadaymulu.fetene@unina.it
*Dipartimento di Ingegneria Chimica, dei Materiali e della Produzione Industriale, Università degli Studi di Napoli Federico II, P.le Tecchio 80, 80125 Napoli (Italy)
**Istituto di Scienze e Tecnologie per l'Energia e la Mobilità Sostenibili, Consiglio Nazionale delle Ricerche, P.le Tecchio 80, 80125 Napoli (Italy)

Abstract
Biohydrogen production from fast pyrolysis of biomass is becoming increasingly attractive as a convenient path to produce green hydrogen at affordable costs. Bio-oil can be converted to hydrogen via reforming or gasification processes. Catalytic steam reforming is the best alternative to produce high quality biohydrogen at lower reaction temperature. The combined fast-pyrolysis/steam reforming process for biohydrogen production is analyzed from a variety of perspectives.
Process layout. Two basic options may be considered, based on in-line or off-line combination of the pyrolytic and reforming stages. The in-line setup avoids using condensation and volatilization sections, a feature that makes this scheme cost-effective. Possible drawbacks are operational problems at the reforming stage due to contaminats associated with bio-oil. The off-line setup is characterized by remarkable flexibility as to the operational parameters of either conversion stages, and is better suited to hybrid delocalized/centralized biomass exploitation schemes. One further degree-of-freedom regards the choice of processing bio-oil as a whole, or selected fractions of it resulting from simple fractionation stages.
Design and operation of the steam reformer. Gas-solid fluidization is the reference technology for the design and operation of the steam reformer, due to the excellent thermal performance and multiphase contacting patterns of fluidized bed converters. However there are still some key issues to be addressed. Dispersion/mixing pattern of highly viscous and unstable bio-oil upon upon feeding to a fluidized bed may be problematic, and deserves better characterization and control. Moreover, effective contact between bio-oil vapours and the catalyst may be jeopardized by the aggregative behaviour of fluidized beds, especially in the bubbling fluidization regime. Careful reactor design and control of fluidization patterns is required to prevent gas phase segregation and inefficient vapour/catalyst contact.
Catalyst formulation. Bio-oils are characterized by complex and widely variable nature. Bio-oil components and specific contaminants may cause catalysts deactivation, hence loss of conversion and/or selectivity to biohydrogen. Catalyst formulation must be optimized with reference to the specific feedstock and process layout to ensure maximum productivity and stability.

Elucidating optical and chemical characteristics of laser irradiated soot particles

Francesca Migliorini*, Roberto Dondé*, Andrea Luccotti, Mauro Fasoli***, Matteo Tommasini**, Silvana De Iuliis***

francesca.migliorini@cnr.it

* CNR-ICMATE, Institute of Condensed Matter Chemistry and Technologies for Energy, CNR, Milano, Italy

** Department of Chemistry, Materials, and Chemical Engineering "G. Natta", Politecnico di Milano, Milano, Italy

*** Department of Material Science, Bicocca University of Milano, Milano, Italy

Abstract

Laser irradiation can induce various physical and chemical changes in soot nanoparticles making them suitable for specific applications in different areas.

In this work, we couple extinction measurements with FT-IR and Raman spectroscopy for a comprehensive understanding of the modifications taking place in soot nanoparticles after laser irradiation, elucidating the optical, chemical, and structural characteristics of the particles under investigation.

Particles are sampled from a premixed flame at two distinct heights above the burner, representing two different aging stages, and sent to an irradiation tube where IR-laser irradiation happens in excess of exhaust gases.

While nascent particles exhibit minimal modification under laser irradiation, we observe significant alterations in absorption properties, inner particle structures, and specific surface functionalities upon heating mature particles with one or ten laser pulses. Additionally, the presence of oxygenated species in mature particles, particularly those spectroscopically correlated with graphene oxide, suggests the occurrence of specific chemical reaction pathways when particles are irradiated in an environment rich in exhaust gases.

The results open up new possibilities for the development of advanced materials with tailored properties, contributing to the advancement of technology and the transition towards a more sustainable and circular economy.

Acknowledgement

The authors would like to acknowledge the financial support from the PRIN project 2022SEYHXP: ''UPcycling SOOT for sustainable nanocomposites-based wearable sensors (UP – SOOT)".

Flame Spray Synthesis of nanooxide for energy application

S. De Iuliis*, F. Migliorini*, A. Pozio, F. Bozza**, R. Donnini*, R. Dondé***
Silvana.deiuliis@cnr.it
*CNR-ICMATE, via Cozzi 53 – 20125 Milano, Italy
**ENEA, C.R. Casaccia, Via Anguillarese 301, 00123 Rome, Italy

Abstract
Flame spray pyrolysis (FSP) is considered one of the most scalable and cost-effective technologies for preparing well-controlled nanooxides which find applications as catalysts, biomaterials, sensors, to cite a few [1-2].
Compared to other synthesis techniques such as solid state reaction or wet methods, it has the advantage of avoiding detrimental steps (e.g. grinding, intensive milling, washing, or heat treatment). This method allows obtaining homogeneous nanoparticles as a nucleation process from the gas phase (gas-to-particle conversion). To this purpose economical precursors (e.g. nitrates) and solvents are used to synthesize a wide variety of possible material compositions with high production yields.
In the present work we investigate the relation between FSP solvents and particle formation focusing on solvent parameters such as boiling point, enthalpy of reaction and possibility for carboxylation. To this purpose, XRD, SEM and TEM analysis is performed in order to assess the impact of the solvent on particles size and crystallinity. Examples of the application of these flame-spray synthetized oxide nanoparticles in electrocatalysis for H_2 production are also presented.

Acknowledgement
This research was funded by the European Union – NextGeneration EU from the Italian Ministry of Environment and Energy Security POR H2 AdP MMES/ENEA with involvement of CNR and RSE, PNRR - Mission 2, Component 2, Investment 3.5 "Ricerca e sviluppo sull'idrogeno", CUP: B93C22000630006

References
1. R Strobel and S. E. Pratsinis, Effect of solvent composition on oxide morphology during flame spray pyrolysis of metal nitrates, Phys. Chem. Chem. Phys., 2011, 13, 9246–9252
2. A. Pozio, F. Bozza, N. Lisi, R. Chierchia, F. Migliorini, R. Donde, S. De Iuliis, Cobalt Oxide Synthesis via Flame Spray Pyrolysis as Anode Electrocatalyst for Alkaline Membrane Water Electrolyzer. Materials 2022, 15, 4626.

Mixture composition influence on schlieren images for simulated premixed H_2-air flame

M. Orlando*, F. Iapaolo*, F. Cozzi*
mattia.orlando@polimi.it
* Politecnico di Milano, Dipartimento di Energia, Via Lambruschini 4, Milano, Italy.

Abstract

Schlieren techniques are widely utilized for flame characterization, and ongoing research at Politecnico di Milano focuses on employing tomographic Background Oriented Schlieren (BOS) technique to measure temperature distribution in an axis-symmetric $H_2 - air$ premixed flame. The initial step in this process involves tomographic reconstruction of the refractive index distribution from the ray deflection measured from the BOS images. However, due to the unknown exact composition of the mixture, an assumption of constant composition (i.e., uniform Gladstone-Dale constant) must be made, which can significantly affect temperature accuracy.

The primary objective of this study is to analyze the dependency of refractive index and deflection on composition and how these parameters vary with changing equivalence ratios. This analysis is conducted through a 1-D planar simulation of an H_2-air laminar premixed flame. Additionally, the study aims to assess whether similar outcomes can be achieved with an axis-symmetric refractive index field simulating a Bunsen-type burner flame.

The flame simulation employs the CANTERA Python suite with the FreeSolver tool and a kinetic mechanism model for H_2 combustion. Refractive index computation in both 1D and axis-symmetric cases considers the real mixture composition, and three different scenarios assuming Gladstone-Dale constants for fresh mixture, exhaust gases, and air, applied uniformly.

For deflection estimation, a ray tracing algorithm is utilized, involving integration of a simplified form of the ray equation. Analysis of the 1D-case reveals that assuming a constant fresh mixture composition yields the most accurate results, with similar trends observed in the axis-symmetric case. Differences in results are lower for lean mixtures and increase for rich mixtures.

These findings deepen the understanding of composition's impact on deflections in Schlieren techniques and will facilitate accurate temperature estimation of the experimental H_2-air premixed flame through tomographic BOS.

Investigation of injector geometry effects on flow dynamics in hydrogen double-swirl burners

F. Cozzi*, F. Iapaolo*, D. Bezzi*, L.Sala*
francesca.iapaolo@polimi.it
*Politecnico di Milano, Dipartimento di Energia, Via Lambruschini 4, Milano, Italy.

Abstract
In present days, hydrogen represents a possible substitute in combustion applications, since it burns with no CO2 release in the ambient. Due to its high reactivity and high temperatures with respect to traditional fuels, hydrogen increases the flashback propensity and enhances NOx emissions. The aim of this study is to design an atmospheric double-swirl burner fed by hydrogen characterized by low NOx emissions and study the influence of the injector geometry on the flow field structure in isothermal conditions.
The burner consists of a central premixed swirled injector, placed inside an annular co-rotating swirled air flow. These streams are injected into an octagonal combustion chamber. The chamber is equipped with quartz windows to facilitate camera access for performing isothermal Stereo-PIV measurements. Due to this requirement, an equivalent airflow rate is used instead of hydrogen. The tests are conducted considering an equivalent thermal power of 12 kW, a secondary air split ratio of 0.6 and a global equivalence ratio of 0.45. The average flow field is analysed for various injector geometries, investigating the impact of axial holes presence and injector diameter on the flow characteristics.
From Stereo-PIV measurements emerges that the geometry has a limited impact on the swirl number. The presence of corner recirculation vortex CRV and central reverse flow zone CRFZ emerges in all the examined geometries, nevertheless it is reduced by a decrease of the injector diameter.
The current findings represent an initial phase preceding the evaluation of the burner in reactive scenarios. Furthermore, these results will be useful for validating and enhancing a numerical simulation, thereby enabling a more profound comprehension of how injector geometry and operating parameters impact the flow dynamics.

PERFORMANCE OF AN AUGER REACTOR FOR BIO-OIL PRODUCTION FROM CONTAMINATED BIOMASS

D.Amato*, P. Giudicianni*, C.M. Grottola*, R. Ragucci*
davide.amato@stems.cnr.it
**Institute of Sciences and Technologies for Sustainable Energy and Mobility (STEMS), National Research Council (CNR), Naples, Italy*

Abstract
CERESiS European project aims to develop, assess and validate integrated biofuel production pathways linking land decontamination to appropriate bioenergy crops and environmentally and economically efficient advanced biofuel production. The thermochemical process considered for the production of biofuels and key biofuel precursors from contaminated biomasses is Fast/Intermediate Pyrolysis (FP/IP).
The optimal ranges of operating conditions were properly tuned to take into account the presence of Potentially Toxic Elements (PTE) in the feedstock. Solid residence time and carrier gas flow rate have been selected as key influential parameters since, they greatly affect not only the liquid yield and quality but also the distribution of PTE, especially Heavy Metals (HM) in the three pyrolysis products (char, bio-oil and gas). The process conditions were optimized with the aim of reducing as much as possible the translocation of HM in the liquid product in such a way as to facilitate the subsequent purification process. With this in mind, a screw reactor was preferred to other pyrolysis technologies operating under fast pyrolysis conditions. This choice shifted the pyrolysis conditions from fast to intermediate (100-500 °C/min), thus penalizing the liquid yield. Nevertheless, in the presence of heavy metals, a compromise had to be pursued between maximizing liquid yield and minimizing solids elutriation phenomena.
The reactor configuration was changed several times during the project to achieve the desired pyrolysis temperature; the final configuration was then used to test the effect of the other operational parameters (solid residence time and nitrogen flow rate) and identify the optimal operating conditions.
The optimized system was then employed to test several contaminated biomasses. The system was able to convert all the considered biomasses, both woody and herbaceous, obtaining moderate variability in pyrolysis products yields and bio-oil composition. This confirms that the designed system, based on an auger reactor, is a robust pyrolysis system; the quality of the produced bio-oil could be further improved by optimizing also the condensation section of the pyrolysis system.

RATE RULE MODELING OF PAH GROWTH

Niccolò Fanari, Luna Pratali Maffei*, Tiziano Faravelli
*luna.pratali@polimi.it

The kinetic modeling of the pyrolysis and combustion of polycyclic aromatic hydrocarbons (PAHs) is crucial to address practical challenges in the current energy transition, such as the evolution of carbonaceous nanoparticles formation that is also interesting for the synthesis of high-value carbon materials [1].
Quantum mechanical calculations are extensively used to develop fundamentally-based kinetic models, however a fully detailed approach is impractical for large PAHs. In this work, we apply a theory-based lumped approach for the definition of reaction classes and rate rules to describe the kinetics of PAHs growth through two relevant reaction classes i.e., the HACA mechanism and the recombination of benzyl-like radicals with propargyl [2]. Based on literature theoretical calculations, our in-house master equation based lumping tool was combined with PSSA to obtain rate constants of global reactions to be implemented in CRECK kinetic model. First, we refined the rate rule definition for the rate constants for 1-ring to 4-ring aromatics. Then, we updated the model with the newly derived rate constants.
The left panel of Fig. 1 depicts the new HACA rate rule adopted with respect to the one previously adopted in the model at 1 atm. The new estimates decreases at high temperatures. Fig. 1 also shows the impact of the new rate rule on the predictions of $C_{10}H_8$ and $C_{12}H_8$ experimental profiles from C_2H_4 pyrolysis [3]. As expected, the $C_{10}H_8$ formation is lower due to the lower rate, while the mole fraction of $C_{12}H_8$ increases due to the slightly higher concentration of its precursor ($C_{10}H_7$).

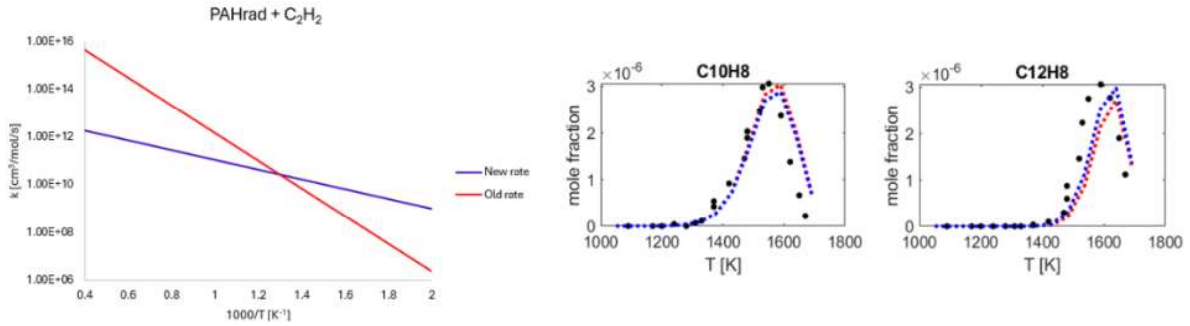

Figure 1: Comparison of the new and old rate rules for the HACA mechanism (left) and associated impact on kinetic simulations of C2H4 pyrolysis (right).

References

[1] N. Islam and B. K. Saikia, Chemosphere, vol. 303, p. 135027,2022
[2] L. Pratali Maffei , PhD thesis, 2022.
[3] W. Sun, A. Hamadi, S. Abid, N. Chaumeix, and A. Comandini,Combust Flame, vol. 220, pp. 257–271, 2020

CFD modeling of a scale-bridging burner in MILD Combustion conditions

V. Rosati, V. Castro, G. Ariemma, P. Sabia, G. Sorrentino, R. Ragucci and M. de Joannon

Vincenzo.rosati@stems.cnr.it

Istituto di Scienze e Tecnologie per l'Energia e la Mobilità sostenibili - Consiglio Nazionale delle Ricerche, Napoli, Italy

Abstract

The present work search for provide deep insights into methane oxidation in a cyclonic flow field chamber that present a geometry modification respect to previous works [1] to improve the strong internal recirculation of burnt products that allows the development of a moderate or intense low-oxygen dilution (MILD) combustion regime over a wide range of operating conditions. The analysis consists in a series of steady-state Favre averaged Navier-Stokes (FANS) simulations to evaluate the thermochemical processes taking place within the reactor and to assess the suitability of existing computational fluid dynamics (CFD) models to describe the turbulence–chemistry interactions in such a scale-bridging configuration. The evaluation is performed with respect to the renormalization group (RNG) k-ε turbulence closure model, using as kinetic mechanisms GRI-Mech 3.0, as well as different turbulent combustion approaches, the flamelet generated manifold (FGM) and the partially stirred reactor (PaSR) models. The consistency of the numerical predictions is checked by direct comparison with experimental results obtained in terms of temperature profiles collected locally inside the reactor at multiple positions. The temperature field is rather uniform within the reactor, especially that predicted by PaSR whereas FGM shows higher temperature values mainly near the walls. A reasonable agreement is reached by comparison in the mid plane by PaSR method denoting a difference below the 15% and in the outlet section with a difference under the 10% respect the experimental results. PaSR predicts an early ignition zone respect to Giuntini et al. [1]. The new geometry presents an improvement to the recirculation.

Reference

[1] Lorenzo Giuntini, Lorenzo Frascino, Giovanni Battista Ariemma, Chiara Galletti, Giancarlo Sorrentino, and Raffaele Ragucci. Performance Assessment of Modeling Approaches for Moderate or Intense Low-Oxygen Dilution Combustion in a Scale-Bridging Burnen. *Energy & Fuels* 2023 *37* (13), 9500-9513.

Acknowledgement

This ENCODING project has received funding from the European Union's Horizon Europe research and innovation programme under the Marie Skłodowska-Curie grant agreement No 101072779.

The results of this publication/presentation reflect only the author(s) view and do not necessarily reflect those of the European Union. The European Union can not be held responsible for them.

Scaling of a cyclonic flow field under MILD conditions

V. Castro, V. Rosati, G. Ariemma, P. Sabia, G. Sorrentino, R. Ragucci and M. de Joannon

vicente.castro@stems.cnr.it

Istituto di Scienze e Tecnologie per l'Energia e la Mobilità Sostenibili – STEMS-CNR

Napoli – ITALY

Abstract

In recent years, decarbonization in the energy sector has become a primary concern. To address this challenge, research has focused on developing new combustion technologies capable of meeting energy demands without increasing greenhouse gas emissions or producing solid particles such as soot.

Moderate or intense low oxygen dilution (MILD) combustion has emerged as a feasible option due to its low emissions of pollutants such as NOx and solid particles. This technology is characterized by the absence of a visible flame and low visible emissions, which poses a challenge for the control and stabilization of the oxidation process.

One of the key variables to consider in the design of a burner operating under MILD conditions is the fluid dynamics configuration. A cyclonic flow configuration appears to be appropriate for ensuring good mixing between the reactants and establishing internal conditions that maintain a stable oxidation process. The parameters involved in the correct stabilization process to achieve MILD combustion have been studied by this group using a Laboratory Unit Cyclonic Burner (LUCY).

In the present work, a new burner was designed to be more optically accessible. This burner is a reduced version of LUCY in terms of dimensions but maintains the same aspect ratio while reducing thermal power by a quarter. To ensure similar fluid dynamics behavior inside the new burner, the design process was verified using CFD simulations under different geometric conditions. Furthermore, the residence time distribution was analyzed to verify the mean residence time of the reactants inside the burner, ensuring an appropriate conversion process.

Acknowledgement

This ENCODING project has received funding from the European Union's Horizon Europe research and innovation programme under the Marie Skłodowska-Curie grant agreement No 101072779.

The results of this publication/presentation reflect only the author(s) view and do not necessarily reflect those of the European Union. The European Union cannot be held responsible for them.

EFFECT OF ETHANOL ADDITION ON SOOT PARTICLE FORMATION IN A MINIATURE INVERTED SOOT GENERATOR

G. Bladier*, A. Pignatelli, V. Vernocchi***, G. Motta****, M. Gualtieri****, G. De Falco*****, A. Sannino**, P. Minutolo*****, P. Prati***, A. D'Anna*, D. Massabò***, M. Commodo*****

gabriele.bladier@unina.it

* Università degli Studi di Napoli Federico II – DICMaPI– Napoli
**Università degli Studi di Napoli Federico II – Dip. di Fisica – Napoli
***Università di Genova & INFN – Dip. di Fisica – Genova
****Università degli Studi di Milano-Bicocca – Dip. di Scienze dell'Ambiente e della Terra – Milano
*****Ist. di Scienze e Tecnologie per l'Energia e la Mobilità Sostenibili – CNR – Napoli

Abstract

The present study is aimed at investigating the effect of ethanol addition on the total amount and the size distribution of soot particles produced by an ethylene flame in a Miniature Inverted Soot Generator (MISG).

The MISG is a combustion-based soot generator working as an inverted flame burner. It allows to obtain a stable generation of soot particles thanks to the stability of its co-flow diffusion flame, that shows a reduced flickering of the flame tip.

Ethanol is one of the most studied and used oxygenated additives and it is chosen as it can be obtained from biomass at reasonable cost. Three different flame conditions are investigated: one of pure ethylene as a reference flame and two with a higher amount of ethanol (10% and 20% with respect to the total carbon fed). The equivalence ratio of the three flames is kept constant at 0.124 to operate the MISG with a partially open-tip flame, leading to a particle size distribution function peaked at less than 100 nm. The analysis of the particle size distribution functions is performed by means of a nano-Differential Mobility Analyzer (nano-DMA) to detect the smaller particles and then integrated by using a Dekati Electrical Low-Pressure Impactor (ELPI). The results exhibit a general reduction of the number concentration of soot particles as a function of the amount of ethanol added to the flame. Moreover, the trend showed by the particle size distributions is the one expected for the MISG partially open-tip flame. Finally, Raman spectroscopy measurements are carried out on the ELPI filter stages to evaluate the effect of ethanol addition on the chemistry of the flame-formed carbon nanoparticles. The resulting Raman spectra show a more intense peak D for the soot particles produced by the ethanol-doped flames, corresponding to a larger size of the aromatic domains.

Acknowledgements: The authors thank the PRIN 2022 project 2022CH87SA: "Investigating atmospheric fate and Toxicological properties of Biofuels Emitted ultrafine particles with a SimulaTion chamber (IT-BEST)" for financial support.

Preferential diffusion effects on tabulated chemistry methods for hydrogen/methane and hydrogen/ammonia blends

B. Cassese[1,2], G. Sorrentino[1], M. De Joannon[1], R. Ragucci[1]
biagio.cassese@stems.cnr.it
1.Istituto di Scienze e Tecnologie per l'Energia e la Mobilità sostenibili - Consiglio Nazionale delle Ricerche, Napoli, Italy.
2. Università degli Studi di Napoli, Dipartimento di Ingegneria Industriale, Napoli, Italy.

Abstract
Advancements in more efficient combustion systems heavily rely on understanding the fundamental combustion characteristics of the different energy carriers and numerical simulation has a fundamental role in that. However, detailed chemistry simulation can be computationally prohibitive for industrial design workflows. Tabulated chemistry methods stand out as a promising approach, offering a cost-effective method for maintaining accuracy in simulations. Manifold generation is a pivotal aspect of tabulated chemistry methods as it delineates the range of thermochemical states accessible during the simulation. Preferential diffusion is one of the dominant effects that must be included when hydrogen is used as a fuel. The present work aims at numerically investigate the effect of preferential diffusion on flamelet-generated manifolds for different hydrogen-methane and hydrogen-ammonia blends. Extinguish counterflow diffusion flames are used for the generation of the manifold, solved by CHEM1D with two different transport models. As expected, preferential diffusion effects are predominant at high hydrogen molar fractions and become negligible at concentrations lower than 0.5. Preferential diffusion affects the shape of the manifold, i.e. higher diffusion of the progress variable species towards leaner and richer mixture fractions. Contours of the progress variable source term show higher peaks for the unity-Lewis case, due to the absence of diffusive transport, while a wider reaction zone is observed for the mixture-averaged case. Hence, manifolds are deeply affected by preferential diffusion, emphasizing the necessity of its incorporation into flamelet equations.

Acknowledgements
This research was partly funded by the European Union, NextGenerationEU in the framework of the National Sustainable Mobility Center - MOST, CN00000023, Italian Ministry of University and Research Decree n. 1033— 17/06/2022, Spoke 12, CUP B43C22000440001 and by the National Recovery and Resilience Plan (NRRP), Mission 4, Component 2, Investment 1.1, Call for tender No. 1409 published on 14.9.2022 by the Italian Ministry of University and Research (MUR), funded by the European Union – NextGenerationEU – Project Title REACTANT – CUP B53D23026970001, Grant Assignment Decree No. 1385 adopted on 01/09/2023 by the Italian Ministry of Ministry of University and Research (MUR).

EXPERIMENTAL AND NUMERICAL STUDY OF THE COMBUSTION CHARACTERISTICS OF SAF COMPONENTS

M. V. Manna*, P. Sabia*, M. de Joannon*, R. Ragucci*
mariavirginia.manna@stems.cnr.it
**Institute of Sciences and Technologies for Sustainable Energy and Mobility (STEMS), National Research Council (CNR), Naples, Italy*

Abstract
The aviation industry is responsible for over 2% of global human-induced CO_2 emissions and 12% of CO_2 emissions within the transport sector. To reduce the carbon footprint of aviation, it is essential to develop renewable alternative fuels. Sustainable Aviation Fuels (SAFs) offer a promising solution by lowering reliance on fossil fuels and decreasing carbon emissions throughout their lifecycle. Despite meeting ASTM D7566 standards, SAF production processes yield fuels with different hydrocarbon compositions compared to fossil jet fuels, characterized by higher iso-paraffin content and nearly negligible aromatic concentration. Currently, blending SAF with fossil jet fuels is necessary to meet required standards. Understanding the combustion properties of SAFs is crucial to increase the blending limit to 100%. This study investigates the oxidation of different SAF components to characterize mixture reactivity and speciation under conditions relevant to aircraft applications. Experimental tests were conducted in a Jet Stirred Flow Reactor, varying preheating temperatures, while maintaining a fixed residence time (0.37s), equivalence ratio (0.8), and dilution level (97%). Different bath gases were used to analyze oxidation behavior under vitiated air conditions. Detailed kinetic mechanisms were employed to validate their predictive capabilities against experimental data. Results revealed notable differences among the components. Isooctane showed higher reactivity at low temperatures but reduced reactant conversion between 1000-1200K, indicating a “NTC-like” behavior. Conversely, decane exhibited greater reactivity within this temperature range. Methylcyclohexane and toluene ignited at higher temperatures. Additionally, CO_2 and H_2O were found to influence fuel oxidation behavior. Further experimental and numerical research is planned to examine the impact of fuel mixture composition on overall oxidation behavior, focusing on the high branched-hydrocarbon content typical of SAF compositions.

Acknowledgments
The authors gratefully acknowledge the European Defence Fund (EDF) for the financial support through the NEUMANN project. Views and opinions expressed are however those of the authors only and do not necessarily reflect those of the European Union.

ICE for FUTURE On/Off-road MOBILITY @ Bosch

M. Iacobazzi*, D. Nuccio*, M. R. Gaballo*,
N. Medoro*, A. Arvizzigno*
e-mail: mariarosaria.gaballo@it.bosch.com
* Centro Studi Componenti per Veicoli S.p.A., Bosch,
Via delle Ortensie 19, Zona Industriale, 70026, Italy

Abstract

As part of its "Green Deal", the goal of the European Union (EU) is to achieve zero net emissions of greenhouse gases (GHG) across all sectors by 2050. This goal can only be achieved with carbon-neutral energy carriers and accordingly compatible powertrains, replacing combustion engine powered vehicles using fossil energy carriers such as diesel and gasoline prevalent today.

A transition period will see the utilization of different fuels for the internal combustion engines. From one side Bosch is supporting the transition and, as example, a comparison between generic EN590 diesel fuel and an innovative Eni HVO fuel from renewable feedstocks has been carried out on a heavy-duty powertrain (for off highway applications) installed on a dyno bench in CVIT.

From the other side, in the direction to achieve the "2050" target, Bosch is supporting the path to a global hydrogen economy by developing key technologies along the entire hydrogen value chain. These include electrolyzes for hydrogen production, fuel cell technology for stationary and mobile applications, and components for the hydrogen internal combustion engine, such as the hydrogen injection system.

Bosch has set up a broad program for the development of components, combustion processes and operating strategies for hydrogen engines. The H_2 ICE development starts from the optically accessible single-cylinder unit, which is essential for clarifying the fundamental phenomena and goes through the steps to the full engine with the associated exhaust gas aftertreatment. Hydrogen direct injection shows a very attractive engine concept using the synergies of operating strategy, hydrogen injection system, air system and exhaust gas aftertreatment.

For the combustion design a toolchain including numerical and experimental paths are developed. 0D/1D/3D CFD simulations are applied to the optimization of the mixing process and combustion in real engine conditions at CVIT.

Innovative and Sustainable Internal Combustion Engine

G.M. Miceli, A. Miceli
giuseppemaria.miceli@gmail.com
aristide.miceli@yahoo.it

Abstract
Heart Combustion Engine S. r. l. is an Italian startup that has developed an innovative internal combustion engine. This engine, patented in Europe and being implemented in other non-European countries, is characterized by one or more cylinders, inside which a piston with variable strokes slides. This piston performs the intake, compression, burst and exhaust phases with the aid of the rotation of two crankshafts through an angle of 360°. We have successfully completed a fully functioning single-cylinder prototype, which showed a 37% increase in expansion volume compared to intake volume. The engine can operate using petrol and is also compatible with a wide range of fuels used in combustion engines. The latter operates following a four-stroke cycle with a total duration of 360°, unlike the traditional cycle which requires 720°, and despite this it manages to develop a power increased by 130% compared to similar traditional engines which aspirate the same quantity of air. A distinctive feature of our engine is the ability to adjust degrees of suction versus expansion to suit project specifications, offering greater flexibility than traditional engines that operate on fixed 180° steps. Additionally, our engine allows significant variations in the compression ratio via a simple drive which has been integrated into the approved patent. Another improving feature is evident in the expansion phase, where the connecting rod connected to the piston descends almost parallel to the cylinder walls, significantly reducing friction on the cylinder surface. Our engine has been designed to suit a wide range of applications, including traditional combustion engines, hybrid engines, marine engines, electric generators and cogenerators. The cycle can be customized in various ways to meet specific needs. The thermodynamic calculations carried out demonstrate a significant reduction in the temperature of the exhaust gases, greater than 154°C in the prototype created. Internal energy recovery per cycle has an extremely positive impact on the sustainability of the engine.

TORREFACTION EXPERIMENTS FOR A VIABLE PRODUCTION OF SOLID BIO-FUELS FROM HAZELNUT INDUSTRY RESIDUES

Michele Miccio[1], Michela Fraganza[1], Paola Brachi[2], Renata Migliaccio[2], Blandine Tauleigne[3], Donatella Albanese[1], Stefano Giovanni Acierno[1], Aisylu Zainutdinova[4]

mmiccio@unisa.it

[1] Department of Industrial Engineering, Università degli Studi di Salerno - Via Giovanni Paolo II 132, 84084 Fisciano (SA), Italy

[2] Inst. of Sciences and Technologies for Energy and Sustainable Mobility, STEMS-CNR, P.le Tecchio 80, 80125 Napoli, Italy

[3] Department of Chemical Engineering, Clermont Auvergne University, Sigma Clermont, 20 avenue Blaise Pascal, 63178 AUBIERE CEDEX, France

[4] Dept. of Production Safety and Industrial Ecology, The Ufa State Aviation Technical University, Ulitsa Karla Marksa 12, 450077 Ufa, The Republic of Bashkortostan, Russia

Abstract

Hazelnut (Corylus avellana L.) is one of the most abundant tree nuts in human food. Turkey is the world leading producer, contributing over 72% to the global production, followed by Georgia, Spain and Italy. The Campania region has been the leader in the production of hazelnut in 2020, with about 480000 q and with less than half in the province of Avellino. The hazelnut skin (perisperm), hard shell (pericarp), green leafy cover/husk (floral bracts) and the hazelnut tree leaves are the by-products of roasting, cracking, shelling/hulling, and harvesting processes, respectively.

This work is part of a R&D project, with both lab-scale experiments and process simulation, aimed at valorization of the above non-edible parts. In particular, fresh hazelnut husks, which hold the hazelnut on the tree and remain attached to it in the early season harvesting, and cuticles from roasted Mortarella cultivar are considered; they are feedstocks yielding bioactive compounds (substances of chemical-food-pharmaceutical interest, such as the polyphenols as antioxidants) by extraction process and/or “renewable” solid fuels by thermochemical processing of residues.

This poster reports results of torrefaction as a “mild” thermochemical conversion process: experiments were carried out in a lab-scale, nitrogen-fluidized bed apparatus consisting of a tubular steel column, 38 mm ID and 350 mm high, surrounded by an electric heating tape, in *batch* mode with respect to biomass. Three temperature levels (200, 250 and 300 °C) are explored with a reaction time of 5 min. The results confirm the well-known trends in the literature that both the Mass Yield MY and the Energy Yield EY decrease with increasing torrefaction temperature. The fluidized torrefaction of such highly fragile materials is feasible and works smoothly. However, the feedstock is to be reduced from an original wide-cut size to a more processable size interval for fluidized bed operation, e.g., 2-4 mm.

EXOTIC BEHAVIOR OF OZONE-DOPED METHANE COFLOWING DIFFUSION FLAMES

E.A. Scelzo*, A. Pignatelli, L. Basta*, F. Sasso*, F. Picca*, M. Commodo***, P. Minutolo***, A. D'Anna***

emanuelealberto.scelzo@unina.it

*Università degli Studi di Napoli Federico II – Dipartimento di Ingegneria Chimica, dei Materiali e della Produzione Industriale – P. le V. Tecchio, 80 – 80125 Napoli, Italy

* Università degli Studi di Napoli Federico II – Dipartimento di Fisica "Ettore Pancini" – Via Cintia, 21 - 80126 Napoli, Italy

***Istituto di Scienze e Tecnologie per l'Energia e la Mobilità Sostenibili – CNR – P. le V. Tecchio, 80 – 80125 Napoli, Italy

Abstract


THE COMBUSTION INSTITUTE
1954

46th Meeting of The Italian Section of The Combustion Institute

Organizing and Scientific Committee

Dr. Mario Commodo (CNR-STEMS)
Prof. Davide Laera (Politecnico di Bari)
Prof. Sergio Camporeale (Politecnico di Bari)
Dr. Giancarlo Sorrentino (CNR-STEMS)
Dr. Gianluigi De Falco (CNR-STEMS)
Mr. Francesco Gabriele Schiavone (Politecnico di Bari)
Dr. Antonio Tregrossi (CNR-STEMS)

Local Organizer

Dipartimento di Meccanica, Matematica e Management
Politecnico di Bari,Via Orabona 4 - 70125 Bari
website: www.dmmm.poliba.it

Dipartimento Meccanica Matematica Management

MUR Dipartimento di Eccellenza 2018-2022 2023-2027

Supporting Institutions

Consiglio Nazionale delle Ricerche
STEMS
Istituto di Scienze e Tecnologie per l'Energia e la Mobilità Sostenibili

Supporting Partners

CCA CENTRO COMBUSTIONE AMBIENTE

ASICI
Associazione Sezione Italiana del Combustion Institute
P.le V. Tecchio, 80
80125 Napoli – Italia
ASICI website: www.combustion-institute.it
E-mail: m.commodo@irc.cnr.it
Telephone: +39 081 7682256


THE COMBUSTION INSTITUTE
1954

ISBN 978-88-88104-29-4